

# **Relativistic Quantum Chemistry Applied to Actinides**

**by**

**Samuel Omonigho Odoh**

**A Thesis submitted to the Faculty of Graduate Studies of**

**The University of Manitoba**

**in partial fulfillment of the requirements of the degree of**

**DOCTOR OF PHILOSOPHY**

**Department of Chemistry**

**University of Manitoba**

**Winnipeg, Canada**

**Copyright © 2012 by Samuel O. Odoh**

# Table of Contents

|   |      |
|---|------|
| Table of Contents .....   | i    |
| List of Figures .....   | iv   |
| List of Tables .....  | xi   |
| List of Abbreviations .....   | xvii |
| Abstract .....  | xix  |
| Acknowledgement .....   | xxi  |
| Chapter 1- Introduction .....   | 1    |
| 1.1. The Actinide Elements and their Uses .....                       | 1    |
| 1.2. Chemical Properties of Actinides .....                           | 4    |
| 1.3. Theoretical Studies of Actinide Complexes .....                  | 9    |
| 1.3.1. The Schrödinger Equation .....                                 | 9    |
| 1.3.2. The Variational Principle and Electronic Basis Sets.....       | 10   |
| 1.3.3. The Hartree-Fock Method and Post Hartree-Fock Approaches ..... | 13   |
| 1.3.4. Density Functional Theory .....                                | 17   |
| 1.3.5. Relativistic Effects .....                                     | 21   |
| 1.3.6. Solvation Effects .....  | 25   |

|   |     |
|---|-----|
| 1.4. Organization of this Thesis .....  | 26  |
| 1.5. References .....   | 29  |
| Chapter 2- Performance of Relativistic Effective Core Potentials for DFT Calculations on Actinide Compounds .....   | 36  |
| Chapter 3- Theoretical Study of the Structural Properties of Plutonium IV and VI Complexes .....  | 64  |
| Chapter 4- Theoretical Study of the Structural and Electronic Properties of Plutonyl Hydroxides .....   | 98  |
| Chapter 5- DFT Study of Uranyl Peroxo Complexes with H <sub>2</sub> O, F <sup>-</sup> , OH <sup>-</sup> , CO <sub>3</sub> <sup>2-</sup> and NO <sub>3</sub> <sup>-</sup> .... | 151 |
| Chapter 6- Theoretical Study of the Reduction of Uranium(VI) Aquo Complexes on Titania Particles and by Alcohols .....  | 195 |
| Chapter 7- QM and QM/MM Study of Uranyl Fluorides in the Gas Phase, Aqueous Phase and in the Hydrophobic Cavities of Tetrabrachion .....                                      | 231 |
| Chapter 8- Novel and Stable U(V)/U(V) Binuclear Complexes Formed by Oxo-functionalization of Axial Oxo Atoms .....  | 269 |
| Chapter 9- Theoretical Study of a Gas-Phase Binuclear Uranyl Hydroxo Complex, [(UO <sub>2</sub> ) <sub>2</sub> (OH) <sub>5</sub> ] <sup>-</sup> .....                         | 295 |
| Chapter 10- Summary and Future Studies of Actinide Complexes .....  | 325 |
| 10.1. Summary .....   | 325 |

|  |     |
|--|-----|
| 10.2. Future Studies of Actinide Complexes Specific to this Thesis .....       | 328 |
| 10.3. General Directions for Computational Studies of Actinide Complexes ..... | 330 |
| References .....   | 331 |
| List of Publications .....   | 336 |

## List of Figures

|   |    |
|---|----|
| Figure 1.1: The actinides in the periodic table of elements .....   | 2  |
| Figure 1.2: The aquo complexes of U(VI) and U(IV) .....   | 8  |
| Figure 1.3: Schematic description of the chapters in this thesis .....  | 28 |
| Figure 2.1: Absolute Deviations of the Vibrational Wavenumbers, $\text{cm}^{-1}$ for NUN, $\text{NUO}^+$ and CUO computed using Stuttgart RECPs with the aug-cc-pVTZ ligand basis set and the AE four-component method with the L2 basis set .....  | 44 |
| Figure 2.2: Distorted Planar T-Shaped Structure of $\text{UO}_3(\text{g})$ .....  | 46 |
| Figure 2.3: Absolute Deviations of the Vibrational Wavenumbers, $\text{cm}^{-1}$ , for $\text{UO}_3$ and $\text{UF}_6$ computed using Stuttgart RECPs with the aug-cc-pVTZ ligand basis set and the AE four-component method with the L2 basis set .....  | 50 |
| Figure 2.4: Absolute Deviations of the Enthalpy Changes, $\text{kJ/mol}$ for Reactions 1-5 computed using Stuttgart RECPs with the aug-cc-pVTZ ligand basis set and the AE four-component method .....  | 55 |
| Figure 3.1: (Left) The $\text{An}=\text{O}_{\text{yl}}$ bond lengths ( $\text{\AA}$ ) in the bare actinyl moieties, $\text{AnO}_2^{2+}$ as well as the $\text{An}=\text{O}_{\text{yl}}$ and average $\text{An}-\text{OH}_2$ bond lengths ( $\text{\AA}$ ) in the pentaquo complexes, $[\text{AnO}_2(\text{H}_2\text{O})_5]^{2+}$ . (Right) The actinyl symmetric and asymmetric stretching vibrational frequencies ( $\text{cm}^{-1}$ ) in the bare actinyl moieties, $\text{AnO}_2^{2+}$ and the pentaquo complexes, $[\text{AnO}_2(\text{H}_2\text{O})_5]^{2+}$ . ..... | 74 |
| Figure 3.2: (Left) The $\text{An}=\text{O}_{\text{yl}}$ bond lengths ( $\text{\AA}$ ) in the bare actinyl moieties, $\text{AnO}_2^{1+}$ as well as the $\text{An}=\text{O}_{\text{yl}}$ bond lengths and average $\text{An}-\text{OH}_2$ bond lengths ( $\text{\AA}$ ) in the pentaquo complexes,   |    |

$[\text{AnO}_2(\text{H}_2\text{O})_5]^{1+}$ . (Right) The actinyl symmetric and asymmetric stretching vibrational frequencies ( $\text{cm}^{-1}$ ) in the bare actinyl moieties,  $\text{AnO}_2^{1+}$  and the pentaquo complexes,  $[\text{AnO}_2(\text{H}_2\text{O})_5]^{1+}$ . These values were obtained with the obtained using the PBE functional and PCM solvation model .....75

Figure 3.3: A. The cis (top) and trans (bottom) isomers of the  $\text{PuO}_2\text{Cl}_2(\text{H}_2\text{O})_2$  complex. B. The cis (top) and trans (bottom) isomers of the  $\text{PuO}_2\text{Cl}_2(\text{H}_2\text{O})_3$  complex .....80

Figure 3.4: A) The decrease in the  $\text{An}=\text{O}_{yl}$  and  $\text{An}-\text{Cl}$  bond lengths ( $\text{\AA}$ ) on addition of  $2\text{Cs}^+$  to the  $[\text{AnO}_2\text{Cl}_4]^{2-}$  complexes. B) The increase in the actinyl stretching vibrational frequencies ( $\text{cm}^{-1}$ ) on addition of  $2\text{Cs}^+$  to the  $[\text{AnO}_2\text{Cl}_4]^{2-}$  complexes .....81

Figure 3.5: The optimized structure of plutonyl diaquo-dinitrate,  $\text{PuO}_2(\text{NO}_3)_2(\text{H}_2\text{O})_2$  obtained using the B3LYP functional .....85

Figure 3.6: The optimized structures of several plutonium (IV) complexes: A)  $\text{Pu}(\text{H}_2\text{O})_8^{4+}$ , B)  $\text{Pu}(\text{NO}_3)_2^{2+}$ , C)  $\text{Pu}(\text{NO}_3)_4(\text{H}_2\text{O})_3$  and D)  $\text{Pu}(\text{NO}_3)_6^{2-}$  calculated with the B3LYP functional in the aqueous phase .....89

Figure 4.1: Optimized structures of the aquo-hydroxo  $[\text{PuO}_2(\text{H}_2\text{O})_{5-n}(\text{OH})_n]^{2-n}$  complexes obtained at the BP86/B2 level with the COSMO solvation model .....105

Figure 4.2: Optimized structures of the aquo-hydroxo  $[\text{PuO}_2(\text{H}_2\text{O})_{4-n}(\text{OH})_n]^{2-n}$  complexes obtained at the BP86/B2 level with the COSMO solvation model .....106

Figure 4.3: Optimized structures of the bis-plutonyl aquo tetrahydroxo and dihydroxo complexes obtained at the B3LYP/B3 level in the gas phase .....114

|   |     |
|---|-----|
| Figure 4.4: Structures of $[(\text{PuO}_2)_3(\text{H}_2\text{O})_6(\text{O})(\text{OH})_3]^+$ obtained at the BP86/B2/COSMO level. The $C_{3V}$ structure is shown on the left while the structure with a bridging aquo group is shown on the right ..... | 115 |
| Figure 4.5: Scheme depicting the formation and decomposition of the $\mu_3$ -oxo hexagonal trimetallic core of the trimer aquo-hydroxo complexes .....  | 127 |
| Figure 4.6: The molecular orbitals of $[\text{PuO}_2]^{2+}$ .....   | 129 |
| Figure 4.7: The energy levels of the $[\text{AnO}_2]^{2+}$ optimized at the BP86/B2 level with the COSMO model .....  | 130 |
| Figure 4.8: Selected occupied alpha spin MOs of $[\text{PuO}_2(\text{OH})_4]^{2-}$ .....  | 132 |
| Figure 4.9: The energy levels of the $[\text{AnO}_2(\text{OH})_4]^{2+}$ optimized at the BP86/B2 level with the COSMO model .....   | 134 |
| Figure 4.10: The 39th to 62nd MOs of $[(\text{PuO}_2)_2(\text{OH})_2]^{2+}$ of alpha spin .....   | 136 |
| Figure 4.11: Selected alpha spin MOs of the trimer complex, $[(\text{PuO}_2)_3(\text{O})(\text{OH})_3]^+$ .....   | 139 |
| Figure 4.12: Abbreviated energy level diagram of the $[(\text{AnO}_2)_3(\text{O})(\text{OH})_3]^+$ complexes .....  | 142 |
| Figure 5.1: The structures of $\text{UO}_2^{2+}$ and its peroxo derivatives optimized at the B3LYP/B1 level in aqueous solution .....   | 156 |
| Figure 5.2: The molecular orbitals of $\text{UO}_2(\text{O}_2)$ . The geometry of this complex was optimized with the PCM approach and the B3LYP functional .....   | 159 |

|   |     |
|---|-----|
| Figure 5.3: Simulated IR spectra of $\text{UO}_2^{2+}$ and its peroxo derivatives obtained at the at the B3LYP/B1 level in aqueous solution .....   | 160 |
| Figure 5.4: MO-26 and MO-27 of the $\text{C}_{2v}$ structure of $\text{UO}_2(\text{O}_2)_2^{2-}$ .....  | 163 |
| Figure 5.5: The structures of $\text{UO}_2(\text{H}_2\text{O})_5^{2+}$ and its peroxo derivatives optimized at the B3LYP/B1 level in aqueous solution .....   | 166 |
| Figure 5.6: The structures of $\text{UO}_2\text{F}_4^{2-}$ and its peroxo derivatives optimized at the B3LYP/B1 level in aqueous solution .....   | 170 |
| Figure 5.7: The structures of $\text{UO}_2(\text{OH})_4^{2-}$ and its peroxo derivatives optimized at the B3LYP/B1 level in aqueous solution .....  | 173 |
| Figure 5.8: MO-30 of cis and trans- $\text{UO}_2(\text{O}_2)_2(\text{OH})_2^{4-}$ .....   | 176 |
| Figure 5.9: The structures of $\text{UO}_2(\text{CO}_3)_3^{4-}$ and its peroxo derivatives optimized at the B3LYP/B1 level in aqueous solution .....  | 178 |
| Figure 6.1: Possibilities for charge transfer to U(VI) complexes adsorbed on $\text{TiO}_2$ crystals or nanoparticles .....   | 199 |
| Figure 6.2: Structure of $\text{UO}_2^{2+}$ adsorbed at the rutile (110) surface at the bridging oxygen atoms .....   | 204 |
| Figure 6.3: Total and partial electronic density of states (DOS) obtained for a clean rutile (110) slab while using with the PBE functional (left) and the PBE+U approach (right, $U=4.2$ eV) ..... | 206 |

Figure 6.4: Total and partial electronic density of states (DOS) obtained for hydroxylated rutile (110) slabs with the PBE+U approach (U=4.2 eV for Ti 3d and U=4.0 eV for U 5f) .....207

Figure 6.5: Total and partial electronic density of states (DOS) obtained for rutile (110) slabs with an adsorbed  $\text{UO}_2^{2+}$  group obtained with the PBE+U approach (U=4.2 eV for Ti-3d and U=4.0 eV for U-5f).....210

Figure 6.6: Total and partial electronic density of states (DOS) obtained for stoichiometric (left) and surface hydroxyl defected (right) rutile (110) slabs with adsorbed  $[\text{UO}_2(\text{H}_2\text{O})_3]^{2+}$  obtained with the PBE+U approach (U=4.2 eV for Ti-3d and U=4.0 eV for U-5f) .....211

Figure 6.7: Electronic energy levels and frontier molecular orbitals obtained at the BP86/TZP level for the a  $\text{Ti}_{38}\text{O}_{76}-[\text{UO}_2(\text{H}_2\text{O})_3]^{2+}$  surface-adsorbate complex .....212

Figure 6.8: Calculated spin distributions of a rutile (110) slab with a surface-adsorbed  $[\text{UO}_2(\text{H}_2\text{O})_3]^{2+}$  moiety and a surface hydroxyl defect. These calculations were carried out with the PBE+U approach .....215

Figure 6.9: Electronic energy levels and MOs of a non-stoichiometric cluster (with a surface hydroxyl)-adsorbate complex .....216

Figure 6.10: The quenching of the lowest triplet excited state of  $[\text{UO}_2(\text{H}_2\text{O})_5]^{2+}$  by water and organic alcohols .....221

Figure 7.1: Top: the right handed coiled coil protein of Tetrabrachion. Bottom: two monomer chains of the RHCC tetramer .....233

|   |     |
|---|-----|
| Figure 7.2: Aqueous phase structures of the $[\text{UO}_2\text{F}_n(\text{H}_2\text{O})_{5-n}]^{2-n}$ complexes optimized at the BP86/TZP/ZORA/COSMO level .....  | 240 |
| Figure 7.3: Left: Variation of the Mulliken charges on the uranium atom (black) and uranyl moiety (red) and the fluoro-2p contribution to the HOMO-1 orbital (blue) with increasing number of fluoride ligands. Right: Variation of the U=O bond lengths (black) and bond orders (red) with increasing number of fluoride ligands ..... | 246 |
| Figure 7.4: Selected frontier molecular orbitals of $[\text{UO}_2\text{F}_n(\text{H}_2\text{O})_{5-n}]^{2-n}$ complexes. The member structures were optimized at the ADF/ZORA/BP86/TZP/COSMO .....  | 248 |
| Figure 7.5: The atoms of the isoleucine residues (represented as green crosses) at the n-terminal end of cavity two .....   | 255 |
| Figure 8.1: Two common motifs for cation-cation interactions between uranyl groups .....  | 272 |
| Figure 8.2: The recently synthesized $\text{U}_2\text{O}_4$ Pacman complex, <b>1a</b> .....   | 273 |
| Figure 8.3: Optimized structure of the yttrium dimer complex obtained at the PBE/L1 level. The O, U and Y atoms are in red, dark green and light green colours respectively .....   | 274 |
| Figure 8.4: The lithium-chloride monomer salt of the yttrium dimer complex, <b>2</b> . The dioxo-uranium core with Li and Y oxo-functionalization are shown on the right .....  | 275 |
| Figure 8.5: Molecular orbitals of primary $\sigma$ - and $\pi$ - character in the unrestricted singlet state of <b>1a</b> .....   | 280 |
| Figure 8.6: The (a) HOMO-172 (bonding with respect to the two U atoms) with an energy of -1.094 a.u. and (b) its antibonding counterpart, both containing contributions from U-5f and O-2s orbitals .....   | 281 |

Figure 9.1: The three low energy structures of  $(\text{UO}_2)_2(\text{OH})_5^-$  obtained at the B3LYP/TZVP level  
.....301

Figure 9.2: Calculated IR spectra for the  $\mu_2$ -dihydroxo (black),  $\mu$ -hydroxo-CCI (blue) and  $\mu$ -hydroxo-di-CCI (red) structures of  $(\text{UO}_2)_2(\text{OH})_5^-$  obtained using the B3LYP functional  
.....308

Figure 9.3: Other possible structure of  $(\text{UO}_2)_2(\text{OH})_5^-$ . Their energies at the B3LYP (and MP2 //B3LYP) levels are given relative to that of the  $\mu$ -hydroxo-di-CCI structure  
.....313

Figure 9.4: Low energy structures of the bis-uranyl hydroxo complexes,  $(\text{UO}_2)_2(\text{OH})_n^{4-n}$   
.....316

## List of Tables

|   |    |
|---|----|
| Table 1.1: Electronic ground state configurations of the actinide elements .....  | 5  |
| Table 1.2: The various oxidation states of the actinide elements .....  | 6  |
| Table 2.1: Vibrational Frequencies, $\text{cm}^{-1}$ , of NUN computed using Stuttgart RECPs with the aug-cc-pVTZ ligand basis set and the AE four-component method with the L2 basis set .....   | 42 |
| Table 2.2: Vibrational Frequencies, $\text{cm}^{-1}$ , of $\text{NUO}^+$ computed using Stuttgart RECPs with the aug-cc-pVTZ ligand basis set and the AE four-component method with the L2 basis set.....                                 | 43 |
| Table 2.3: Vibrational Frequencies, $\text{cm}^{-1}$ , of CUO computed using Stuttgart RECPs with the aug-cc-pVTZ ligand basis set and the AE four-component method with the L2 basis set .....   | 45 |
| Table 2.4: Calculated Bond Lengths (in $\text{\AA}$ ) and Bond Angles (in degrees) of $\text{UO}_3$ (g) computed using Stuttgart RECPs with the aug-cc-pVTZ ligand basis set and the AE four-component method with the L2 basis set ..... | 48 |
| Table 2.5: Calculated Bond Lengths (in $\text{\AA}$ ) and Bond Angles (in degrees) of $\text{UO}_3$ (g) computed using Stuttgart RECPs with the aug-cc-pVTZ ligand basis set and the AE four-component method with the L2 basis set ..... | 49 |
| Table 2.6: Vibrational Frequencies, $\text{cm}^{-1}$ , of $\text{UF}_6$ computed using Stuttgart RECPs with the aug-cc-pVTZ ligand basis set and the AE four-component method with the L2 basis set .....                                 | 51 |
| Table 2.7: Calculated enthalpy changes*, kJ/mol for Reactions 1-5 computed using Stuttgart RECPs and the AE four-component method .....   | 53 |

|  |     |
|--|-----|
| Table 3.1: The calculated bond lengths (Å) and plutonyl vibrational frequencies (cm <sup>-1</sup> ) of the bare PuO <sub>2</sub> <sup>2/1+</sup> and actinyl aquo PuO <sub>2</sub> (H <sub>2</sub> O) <sub>5</sub> <sup>2/1+</sup> systems obtained using DFT in the gaseous and aqueous phases .....  | 71  |
| Table 3.2: The calculated structural properties (bond lengths in Å and vibrational frequencies in cm <sup>-1</sup> ) of the chloride complexes of the plutonyl (VI) cation obtained using the B3LYP functional. The values obtained with the PBE functional are given in parenthesis .....   | 77  |
| Table 3.3. The calculated structural properties (bond lengths in Å and vibrational frequencies in cm <sup>-1</sup> ) of the nitrate complexes of the plutonyl (VI) cation obtained using the B3LYP functional in the gaseous and aqueous phases. The values obtained with the PBE functional are given in parenthesis .....  | 84  |
| Table 3.4: The calculated bond lengths (Å) of the AnO <sub>2</sub> (NO <sub>3</sub> ) <sub>2</sub> (H <sub>2</sub> O) <sub>2</sub> , AnO <sub>2</sub> (NO <sub>3</sub> ) <sub>2</sub> (TBP) <sub>2</sub> <sup>a</sup> , AnO <sub>2</sub> Cl <sub>2</sub> (H <sub>2</sub> O) <sub>2</sub> and AnO <sub>2</sub> Cl <sub>2</sub> (TPPO) <sub>2</sub> <sup>a</sup> complexes obtained using the B3LYP functional with RECPs in the gaseous phase ..... | 86  |
| Table 3.5: The calculated Pu-OH <sub>2</sub> and Pu-O <sub>water/nitrate</sub> bond lengths of the aquo, nitrate and aquo-nitrate complexes of the plutonium (IV) cation obtained using DFT in the gaseous and aqueous phases .....  | 88  |
| Table 4.1: Calculated structural properties of [PuO <sub>2</sub> (H <sub>2</sub> O) <sub>5</sub> ] <sup>2+</sup> and [PuO <sub>2</sub> (H <sub>2</sub> O) <sub>4</sub> (OH)] <sup>+</sup> . The bond distances are given in Å while the vibrational frequencies (asymmetric/symmetric plutonyl stretching modes) are given in cm <sup>-1</sup> .....   | 106 |

Table 4.2: Calculated structural properties of  $[\text{PuO}_2(\text{H}_2\text{O})_3(\text{OH})_2]$  and  $[\text{PuO}_2(\text{H}_2\text{O})_2(\text{OH})_3]^-$ . The bond distances are given in Å while the vibrational frequencies (asymmetric/symmetric plutonyl stretching modes) are given in  $\text{cm}^{-1}$  .....108

Table 4.3: Calculated structural properties of  $[\text{PuO}_2(\text{H}_2\text{O})_2(\text{OH})_2]$  and  $[\text{PuO}_2(\text{H}_2\text{O})(\text{OH})_3]^-$ . The bond distances are given in Å while the vibrational frequencies (asymmetric/symmetric plutonyl stretching modes) are given in  $\text{cm}^{-1}$  .....109

Table 4.4: Calculated structural properties of  $[\text{PuO}_2(\text{OH})_4]^{2-}$  and  $[\text{PuO}_2(\text{OH})_5]^{3-}$ . The bond distances are given in Å while the vibrational frequencies (asymmetric/symmetric plutonyl stretching modes) are given in  $\text{cm}^{-1}$  .....110

Table 4.5: Calculated Mayer bond orders of the plutonyl aquo-hydroxo complexes obtained at the PBE/B1 level in the gaseous phase .....111

Table 4.6: Calculated structural properties of the plutonyl dimer complexes. The bond lengths are in Å and the calculated IR intensities ( $\text{km/mol}$ ) are given in parenthesis .....113

Table 4.7: Calculated structural properties of the  $\mu_3$ -oxo motifs of the trimeric complex,  $[(\text{PuO}_2)_3(\text{H}_2\text{O})_6(\text{O})(\text{OH})_3]^+$ . The bond lengths are given in Å, bond angles in degrees while vibrational frequencies are presented in  $\text{cm}^{-1}$  .....115

Table 4.8: Calculated uranyl stretching vibrational frequencies ( $\text{cm}^{-1}$ ) of uranium aquo hydroxo complexes obtained at the PBE/B1 level .....118

Table 4.9: Calculated reaction energies ( $\text{kcal/mol}$ ) for the formation of the dimer and trimer actinyl hydroxo complexes in the aqueous phase .....122

|   |     |
|---|-----|
| Table 4.10: Calculated reaction energies (kcal/mol) obtained actinyl hydrolysis reactions at the BP86/B2 while using the COSMO solvation model .....  | 124 |
| Table 4.11: Energies, atomic contributions and descriptions of the MOs of $[(\text{PuO}_2)_2(\text{OH})_2]^{2+}$ at the B3LYP/B3 level. The orbital energies are scaled such that the HOMO is at 0.00 eV .....                                    | 137 |
| Table 4.12: Energies (eV), individual atomic contributions and descriptions of the MOs of $[(\text{PuO}_2)_3(\text{O})(\text{OH})_3]^+$ at the B3LYP/B3 level. The orbital energies are scaled such that the HOMO is at 0.00 eV .....             | 141 |
| Table 5.1: Energies and characters of the MOs of the dioxouranium (VI) peroxides in aqueous solution obtained at the B3LYP/B1 level. MO energies are given in eV .....  | 158 |
| Table 5.2: Calculated structural properties and vibrational frequencies of $\text{UO}_2^{2+}$ and its peroxo derivatives obtained at the B3LYP/B1 level in aqueous solution .....   | 161 |
| Table 5.3: Calculated structural properties and vibrational frequencies ( $\text{cm}^{-1}$ ) of $\text{UO}_2(\text{H}_2\text{O})_5^{2+}$ and its peroxo derivatives obtained at the B3LYP/B1 level in the gas-phase and in aqueous solution ..... | 165 |
| Table 5.4: Calculated structural properties and vibrational frequencies of $\text{UO}_2\text{F}_4^{2-}$ and its peroxo derivatives obtained at the B3LYP/B1 level in aqueous solution .....   | 168 |
| Table 5.5: Calculated structural properties and vibrational frequencies of $\text{UO}_2(\text{OH})_4^{2-}$ and its peroxo derivatives obtained at the B3LYP/B1 level in aqueous solution .....  | 172 |
| Table 5.6: Calculated structural properties and vibrational frequencies ( $\text{cm}^{-1}$ ) of $\text{UO}_2(\text{CO}_3)_3^{4-}$ and its peroxo derivatives obtained at the B3LYP/B1 level in the gas-phase and in aqueous solution .....        | 180 |

|  |     |
|--|-----|
| Table 5.7: Calculated structural properties and vibrational frequencies ( $\text{cm}^{-1}$ ) of $\text{UO}_2(\text{NO}_3)_3^-$ and its peroxy derivatives obtained at the B3LYP/B1 level in the gas-phase and in aqueous solution .....  | 181 |
| Table 5.8: The calculated Mayer bond orders in various uranyl complexes and their peroxy derivatives obtained at the B3LYP/B2 level using structures optimized at the B3LYP/B1 level. ....   | 184 |
| Table 6.1: Calculated structural features and properties of U(VI) complexes obtained with the PBE functional in the gas phase .....  | 203 |
| Table 6.2: Calculated reaction energies (kcal/mol) obtained for R6 in aqueous solution obtained at the PBE/TZP and B3LYP/TZP levels in addition to the calculated structural and electronic properties of the triplet state uranyl-quencher complexes .....                            | 219 |
| Table 7.1: Calculated and experimental structural parameters of the $[\text{UO}_2\text{F}_n(\text{H}_2\text{O})_{5-n}]^{2-n}$ complexes .....  | 241 |
| Table 7.2: Aqueous phase calculated ligand binding energies in kcal/mol, Mayer bond orders for the U=O Bond and atomic Mulliken charges on uranium atoms in the $\text{UO}_2\text{F}_n(\text{H}_2\text{O})_{5-n}]^{2-n}$ complexes obtained at the ADF/ZORA/TZP/BP86/COSMO level ..... | 247 |
| Table 7.3: Calculated relative energies (kcal/mol), frontier gaps (eV) and structural features of the two orientations of the $[\text{UO}_2\text{F}_5]^{3-}$ complex in the hydrophobic cavities of tetrabrachion...   | 256 |
| Table 7.4: Computed structural parameters cisplatin in the gaseous and aqueous phases and of two randomly selected orientations of cisplatin embedded in the cavity two (largest cavity) of the RHCC protein obtained using RECPs .....  | 260 |

|   |     |
|---|-----|
| Table 8.1: Calculated and experimental structural parameters of 1a in the ferromagnetic triplet electronic state and antiferromagnetic broken-symmetry state (in parentheses) .....   | 279 |
| Table 8.2: Calculated reaction free energies ( $\Delta G_{298}$ , kcal/mol) required to transaminate the unoccupied amine site of several Pacman complexes with a <i>cis</i> -uranyl group .....  | 284 |
| Table 8.3: Calculated atomic charges on the uranium and oxo- atoms of the uranyl Pacman complex, $\text{UO}_2(\text{Py})(\text{H}_2\text{L})$ , and its pentavalent and reductively oxo-functionalized derivatives obtained at the PBE/AE/4-component level (and at the B3LYP/RECP level) ..... | 284 |
| Table 8.4: The calculated and experimental structural parameters (bond lengths in Å and angles in degrees) for the monomer complexes .....  | 286 |
| Table 8.5: The calculated and experimental structural parameters (bond lengths in Å and angles in degrees) for the dimer complexes .....  | 288 |
| Table 9.1: Calculated relative energies (kcal/mol) of the three low energy structures of $(\text{UO}_2)_2(\text{OH})_5^-$ .....   | 302 |
| Table 9.2. Calculated bond lengths (Å) and bond orders of the low energy structures of $(\text{UO}_2)_2(\text{OH})_5^-$ obtained at the B3LYP/TZVP level .....  | 303 |
| Table 9.3. Calculated IR vibrational frequencies ( $\text{cm}^{-1}$ ) of the low energy structures of $(\text{UO}_2)_2(\text{OH})_5^-$ obtained at the B3LYP/TZVP level .....   | 307 |
| Table 9.4. Calculated bond lengths (Å), bond orders and vibrational frequencies ( $\text{cm}^{-1}$ ) of a few gas-phase mono-nuclear uranium complexes obtained at the B3LYP/TZVP level .....   | 310 |
| Table 9.5. Relative energies (kcal/mol) of the low energy structures of $(\text{UO}_2)_2(\text{OH})_n^{4-n}$ , (n=2, 3, 4 and 6) obtained at the DFT and ab initio levels .....   | 315 |

## List of Abbreviations

|         |  |
|---------|--|
| AE      | All-Electron   |
| BO      | Born-Oppenheimer   |
| CASSCF  | Complete Active Space Self Consistent Field  |
| CASPT2  | CASSCF with 2 <sup>nd</sup> -Order Perturbative Treatment of Dynamical Correlation |
| CCI     | Cation-Cation Interactions   |
| CCSD    | Coupled Cluster Singles and Doubles  |
| CCSD(T) | Coupled Cluster Singles and Doubles with Perturbative Triples                      |
| CCSDTQ  | Coupled Cluster Singles, Doubles, Triples and Quadruples                           |
| CI      | Configuration Interaction  |
| DKH     | Douglas Kroll Hess   |
| DFT     | Density Functional Theory  |
| ECP     | Effective Core Potentials  |
| FW      | Foldy-Wouthuysen   |
| GGA     | Generalized Gradient Approximations  |
| GTOs    | Gaussian Type Orbitals   |
| HF      | Hartree-Fock   |
| HK      | Hohenberg-Kohn   |
| HLNW    | High Level Nuclear Waste   |
| HOMO    | Highest Occupied Molecular Orbitals  |
| IR      | Infra-Red  |
| KS      | Kohn-Sham  |
| LCAO    | Linear Combination of Atomic Orbitals  |
| LC-ECP  | Large Core Effective Core Potentials   |

|                 |   |
|-----------------|---|
| LDA             | Local Density Approximation                     |
| LUMO            | Lowest Occupied Molecular Orbitals              |
| MO              | Molecular Orbital                               |
| MP <sup>n</sup> | Møller-Plesset Perturbation Theory of nth Order |
| NBO             | Natural Bond Orbitals                           |
| NMR             | Nuclear Magnetic Resonance                      |
| NOCV            | Natural Orbitals for Chemical Valence           |
| PBE             | Perdew Burke and Enzerhof GGA Functional        |
| PCM             | Polarizable Continuum Model                     |
| Post HF         | Post HF approaches                              |
| PUREX           | Plutonium URanium EXtraction                    |
| RECP            | Relativistic Effective Core Potentials          |
| SCF             | Self Consistent Field                           |
| SC-ECP          | Small-Core Effective Core Potentials            |
| STOs            | Slater Type Orbitals                            |
| UA0             | United Atom Topological Model                   |
| UEG             | Uniform Electron Gas                            |
| WIPP            | Waste Isolation Pilot Plant                     |
| ZORA            | Zeroth Order Regular Approximation              |

## Abstract

Of the many available computational approaches, density functional theory is the most widely used in studying actinide complexes. This is generally because it incorporates electron correlation effects and is computationally inexpensive for modestly sized compounds.

The first chapter of this thesis is an introductory chapter in which some basic concepts of electronic structure theory are discussed. The rest of this thesis is a compilation of several studies of the structural and electronic properties of a range of actinide compounds using predominantly density functional theory. The performances of the basis set/relativistic components as well as the density functional component of theoretical calculations were examined in Chapters 2 and 3 respectively. In Chapters 4, 5, 6 and 7, the electronic structures and properties of actinide species in the environment were explored. The speciation of actinyl aquo-hydroxo species at increasing pH values were studied in Chapter 4. In Chapter 5, the structural and electronic properties of uranyl peroxo complexes with other environmentally important ligands were studied. The adsorption of uranyl complexes to geochemical surfaces was studied in Chapter 6. In addition, the mechanistic pathways to the reduction of these complexes on surfaces and alcohols were examined. In chapter 7, the complexes formed by the uranyl moiety with the aquo and fluoride ligands were studied in gas and aqueous phases. The interactions of uranyl pentafluoride with a protein were examined using a hybrid QM/MM approach. Overall these studies (Chapters 4, 5, 6 and 7) provided valuable insights into the speciation and reduction of actinide species in the environment. In Chapter 8, the properties of novel pentavalent uranium complexes were studied using density functional theory. These complexes have promising roles in the retardation of uranium, via U(VI)-U(IV) reduction, in the environments of nuclear storage repositories. In

Chapter 9, the existence of cation-cation interactions in an hexavalent bis-uranyl hydroxo complex was examined using density functional theory and wavefunction methods. In Chapter 10, a summary of the works compiled in this thesis is presented. Future directions for work on the chemistry of actinide complexes were also included in this chapter.

## **Acknowledgement**

I would like to thank my supervisor, Dr Georg Schreckenbach, for the opportunity to work under him towards this degree over the last few years. His patience, support, encouragement, friendly approach and critical thinking have been invaluable along the way to this degree. In the same vein, I would like to thank the members of my advisory committee, Dr Mario Bieringer, Dr Peter Budzelaar and Dr Mostafa Fayek for their help, advice, criticism and support during the work towards this degree.

I am indebted to all the present and former members of the Schreckenbach group at the University of Manitoba. The postdoctoral and research fellows, Grigory Shamov, Qing-Jiang Pan and Abu Asaduzamman were very helpful during the early stages of my doctoral program. Their help with the various projects I worked on as well as on-going collaboration after their departure from the group is highly appreciated.

I would like to thank all members of my family. Without the encouragement of my loving wife, Sarah Odoh, my sister, Mary Odoh, and my parents (Godwin and Caroline Odoh), it would not have been possible to complete this degree. I am eternally grateful to my brothers, Emmanuel and Daniel Odoh for their support and understanding.

# Chapter 1: Introduction

## 1.1 The actinides and their uses.

The actinides or actinoids are the elements with atomic numbers from 89 to 103 on the periodic table of elements.<sup>1-2</sup> They are named after the first member of this series, actinium. The position of these elements on the periodic table is shown in Figure 1.1. The actinide series correspond to filling of the 5f shell (mostly) and the actinides are therefore f-block elements. The only exception to this is lawrencium which is a d-block element.<sup>3</sup> The other members of the f-block are the lanthanides. These are the elements from lanthanum to lutetium which possess gradually filled 4f shells.

Of the actinides, only uranium and thorium are found in substantial quantities in nature. Protactinium and actinium are also found in nature. All the other actinides are artificial elements produced through various nuclear reactions of primordial uranium. In terms of abundance, uranium and thorium exist at average concentrations of about 2-4 and 6 parts per million (ppm) in the earth crust. Examples of thorium minerals are thorianite ( $\text{ThO}_2$ , 88% Th), thorite ( $\text{ThSiO}_4$ , 72% Th) and brabantite ( $\text{CaTh}(\text{PO}_4)_2$ , 50% Th). The most common uranium ore is uraninite ( $\text{UO}_2$ , 88% U). Others include Rutherfordine ( $\text{UO}_2(\text{CO}_3)$ , 72% U) and schoepite [ $(\text{UO}_2)_8\text{O}_2(\text{OH})_{12} \cdot 12\text{H}_2\text{O}$ , 73% U]. Np, Pu, Cm, Bk and Cf are sometimes formed by natural transmutation of uranium ores and so are found in minute quantities in these minerals.<sup>4</sup>

The actinides have found their greatest applications in the production of energy via controlled nuclear fission and in the production of nuclear weapons. These uses are underpinned

| Group →     | 1        | 2        | 3        | 4         | 5         | 6         | 7         | 8         | 9         | 10        | 11        | 12        | 13         | 14        | 15         | 16        | 17         | 18         |
|-------------|----------|----------|----------|-----------|-----------|-----------|-----------|-----------|-----------|-----------|-----------|-----------|------------|-----------|------------|-----------|------------|------------|
| ↓ Period    |          |          |          |           |           |           |           |           |           |           |           |           |            |           |            |           |            |            |
| 1           | 1<br>H   |          |          |           |           |           |           |           |           |           |           |           |            |           |            |           |            | 2<br>He    |
| 2           | 3<br>Li  | 4<br>Be  |          |           |           |           |           |           |           |           |           |           | 5<br>B     | 6<br>C    | 7<br>N     | 8<br>O    | 9<br>F     | 10<br>Ne   |
| 3           | 11<br>Na | 12<br>Mg |          |           |           |           |           |           |           |           |           |           | 13<br>Al   | 14<br>Si  | 15<br>P    | 16<br>S   | 17<br>Cl   | 18<br>Ar   |
| 4           | 19<br>K  | 20<br>Ca | 21<br>Sc | 22<br>Ti  | 23<br>V   | 24<br>Cr  | 25<br>Mn  | 26<br>Fe  | 27<br>Co  | 28<br>Ni  | 29<br>Cu  | 30<br>Zn  | 31<br>Ga   | 32<br>Ge  | 33<br>As   | 34<br>Se  | 35<br>Br   | 36<br>Kr   |
| 5           | 37<br>Rb | 38<br>Sr | 39<br>Y  | 40<br>Zr  | 41<br>Nb  | 42<br>Mo  | 43<br>Tc  | 44<br>Ru  | 45<br>Rh  | 46<br>Pd  | 47<br>Ag  | 48<br>Cd  | 49<br>In   | 50<br>Sn  | 51<br>Sb   | 52<br>Te  | 53<br>I    | 54<br>Xe   |
| 6           | 55<br>Cs | 56<br>Ba |          | 72<br>Hf  | 73<br>Ta  | 74<br>W   | 75<br>Re  | 76<br>Os  | 77<br>Ir  | 78<br>Pt  | 79<br>Au  | 80<br>Hg  | 81<br>Tl   | 82<br>Pb  | 83<br>Bi   | 84<br>Po  | 85<br>At   | 86<br>Rn   |
| 7           | 87<br>Fr | 88<br>Ra |          | 104<br>Rf | 105<br>Db | 106<br>Sg | 107<br>Bh | 108<br>Hs | 109<br>Mt | 110<br>Ds | 111<br>Rg | 112<br>Cn | 113<br>Uut | 114<br>Fl | 115<br>Uup | 116<br>Lv | 117<br>Uus | 118<br>Uuo |
| Lanthanides | 57<br>La | 58<br>Ce | 59<br>Pr | 60<br>Nd  | 61<br>Pm  | 62<br>Sm  | 63<br>Eu  | 64<br>Gd  | 65<br>Tb  | 66<br>Dy  | 67<br>Ho  | 68<br>Er  | 69<br>Tm   | 70<br>Yb  | 71<br>Lu   |           |            |            |
| Actinides   | 89<br>Ac | 90<br>Th | 91<br>Pa | 92<br>U   | 93<br>Np  | 94<br>Pu  | 95<br>Am  | 96<br>Cm  | 97<br>Bk  | 98<br>Cf  | 99<br>Es  | 100<br>Fm | 101<br>Md  | 102<br>No | 103<br>Lr  |           |            |            |

**Figure 1.1:** The actinides in the periodic table of elements.<sup>5</sup>

by the radioactive behavior of the actinide elements. Radioactivity is the ability of an unstable nucleus to lose energy and decay to other nucleus/nuclei by emitting ionizing radiation. Although all isotopes of the actinides are radioactive, the  $^{235}\text{U}$  isotope of uranium is the most commonly used fissile material in nuclear reactors. Bombardment of this isotope with a neutron leads to its fragmentation into smaller nuclei and emission of 2-3 other neutrons. As a result of the release of more neutrons than were used in the initiation process, the fission of  $^{235}\text{U}$  becomes self-sustaining after a critical mass (about 52 kg) is attained. This chain-reaction of neutron-induced fission of  $^{235}\text{U}$  is controlled in nuclear reactors. The heat produced is used to generate electricity. Currently, about 7% of total global energy consumption and 14% of global electricity consumption is produced from nuclear reactors using some fissionable actinide isotope.<sup>6</sup>

There are however significant drawbacks to the use of the actinide elements in nuclear reactors to generate energy.<sup>7</sup> Firstly, significant portions of the nuclear fuel used in fission reactors are not consumed and end up as waste, generally a mixture of U, Pu and other actinides. Some constituents of the radioactive waste, especially fissile plutonium, can be separated and reused in nuclear weapons and other reactors. The plutonium uranium extraction process, PUREX, is one such method for extracting fissile actinides from spent nuclear fuel. It is however the case that spent fuel and nuclear waste are highly hazardous and toxic to living things as well as the environment. There is therefore a need to keep nuclear waste and spent fuel from contaminating the environment. The half-life of a radionuclide (radioactive nucleus) is the period of time it takes it to lose half of its radioactivity. The actinides with very long half-lives found in nuclear waste pose strong challenges to waste storage, disposal and management strategies. <sup>232</sup>U has the shortest half-life (68.9 years) of the uranium isotopes while <sup>238</sup>U has the longest half-life (4.5 billion years). <sup>237</sup>Np and <sup>239</sup>Pu are also found in nuclear waste and have half-lives of about 2 million and 24,000 years respectively. The rather long periods of time needed for these radioisotopes to lose their radioactivity, relative to the average human life span, means that it is well nigh impossible to prevent eventual dispersal into the environment, waste management approaches such as geologic disposal and transmutation notwithstanding. For this reason, it is very important that we have a clear understanding of the dispersal and migration of actinide elements, their speciation in the environment, their interaction with abiotic surfaces as well as with biotic organisms and the mechanisms behind their toxicity to animal and plant life.<sup>8</sup> There is a need to understand the overall chemistry occurring at already contaminated sites (that are here and now).

The actinides are also used in coloring glasses and ceramics ( $\text{UO}_2$ )<sup>9</sup>, smoke detectors (Am as alpha emission source)<sup>10</sup>, and gas mantles (Th).  $^{239}\text{Pu}$  is extensively used in the nuclear weapons industry while  $^{238}\text{Pu}$  is used in heart pacemakers and deep-sea diving suits as a source of energy.<sup>11</sup> It was used as heating source for the astronauts who participated in the Apollo space missions. It is particularly suited for these roles as it emits relatively harmless alpha particles.  $^{239}\text{Pu}$  is now being used as a nuclear fuel in fast-breeder reactors. Depleted uranium is used in making battle armors and projectiles. The ability of actinide elements and their compounds to efficiently catalyze reactions is under continuing investigation.

## 1.2 Chemical properties of the actinides

There have been a large number of studies examining the chemical properties of the actinide elements and their compounds. For the sake of brevity we here focus on their oxidation states and electronic configurations. The electronic ground state configurations of the actinide elements are given in Table 1.1. The 5f, 6d and 7s electrons are close in energy to each other as a result of the relative destabilization of the 5f orbitals due to relativistic effects. The implication of this is that the actinides can have a variety of oxidation states as any number of ionized electrons can be removed from the energetically close valence energy levels. The various oxidation states existing for each of the actinide elements are shown in Table 1.2. The presence of multiple oxidation states for the actinides has significant ramifications to their speciation in the environment as the stability and hydrolytic behavior of each actinide elements differ for different oxidation states. This is particularly common for the light actinides (U, Np and Pu) which in some cases exhibit more than one oxidation state in the same solution. As expected, the stabilities of the different oxidation states depend on the electronic configuration (and resulting stability) of the resulting ion. For example, the +2 oxidation state is known to be only transiently

**Table 1.1:** Electronic ground state configurations of the actinide elements. The noble gas core structure of radon, [Rn], is used to depict the electronic configurations. The atomic number, Z, of each element is also given.<sup>1</sup>

| Element      | Z  | Configuration                                       | Element     | Z   | Configuration  |
|--------------|----|---|-------------|-----|--|
| Actinium     | 89 | [Rn]6d <sup>1</sup> 7s <sup>2</sup>                 | Berkelium   | 97  | [Rn]5f <sup>9</sup> 7s <sup>2</sup>                  |
| Thorium      | 90 | [Rn]6d <sup>2</sup> 7s <sup>2</sup>                 | Californium | 98  | [Rn]5f <sup>10</sup> 7s <sup>2</sup>                 |
| Protactinium | 91 | [Rn]5f <sup>2</sup> 6d <sup>1</sup> 7s <sup>2</sup> | Einsteinium | 99  | [Rn]5f <sup>11</sup> 7s <sup>2</sup>                 |
| Uranium      | 92 | [Rn]5f <sup>3</sup> 6d <sup>1</sup> 7s <sup>2</sup> | Fermium     | 100 | [Rn]5f <sup>12</sup> 7s <sup>2</sup>                 |
| Neptunium    | 93 | [Rn]5f <sup>4</sup> 6d <sup>1</sup> 7s <sup>2</sup> | Mendelevium | 101 | [Rn]5f <sup>13</sup> 7s <sup>2</sup>                 |
| Plutonium    | 94 | [Rn]5f <sup>6</sup> 7s <sup>2</sup>                 | Nobelium    | 102 | [Rn]5f <sup>14</sup> 7s <sup>2</sup>                 |
| Americium    | 95 | [Rn]5f <sup>7</sup> 7s <sup>2</sup>                 | Lawrencium  | 103 | [Rn]5f <sup>14</sup> 6d <sup>1</sup> 7s <sup>2</sup> |
| Curium       | 96 | [Rn]5f <sup>7</sup> 6d <sup>1</sup> 7s <sup>2</sup> |             |     |  |

stable for all the actinide elements (with the exception of Nobelium, due to the presence of a stable fully filled 5f sub-shell). Similarly the half-filled 5f<sup>7</sup> electronic configuration implies that the +4 oxidation state is most stable for Berkelium. The different oxidation states for these elements result in a rich redox chemistry and consequently colorful chemistry in solution. For example aqueous solutions of uranium in the +3, +4 and +6 oxidation states have visible colors of brown-red, green and yellow respectively. The +4 and +6 oxidation states are most important for uranium. They form the oxides, UO<sub>2</sub> and UO<sub>3</sub> respectively. The +5 oxidation state of uranium is generally unstable as it disproportionates to the +4 and +6 oxidation states.<sup>12</sup> The different actinide oxidation states also generally have different solubility and stability in aqueous

**Table 1.2:** The various oxidation states of the actinide elements.

|              |               |             |         |
|--------------|---------------|-------------|---------|
| Actinium     | 3             | Berkelium   | 3, 4    |
| Thorium      | 3, 4          | Californium | 2, 3, 4 |
| Protactinium | 3, 4, 5       | Einsteinium | 2, 3    |
| Uranium      | 3, 4, 5, 6    | Fermium     | 2, 3    |
| Neptunium    | 3, 4, 5, 6, 7 | Mendelevium | 2, 3    |
| Plutonium    | 3, 4, 5, 6, 7 | Nobelium    | 2, 3    |
| Americium    | 3, 4, 5, 6    | Lawrencium  | 3       |
| Curium       | 3, 4, 5       |             |         |

environments.<sup>8</sup> Uranium in the +6 state, U(VI), is generally more soluble in water than the +4 oxidation state, U(IV), which tends to form insoluble precipitates. To deter contamination of the aquatic environment and the ecological zones of cities and countries by radioactive uranium from spent fuel or mill tailings, it is preferable that U(VI) compounds are reduced to the +4 oxidation state. This is because the U(IV) compounds are significantly less soluble in water and therefore migrate more slowly than U(VI) species and are more amenable to retardation and deposition strategies.<sup>8</sup> An interesting example of the role the differing oxidation states play in the environmental chemistry of the actinide elements has been described by Runde.<sup>8</sup> Plutonium is a rather problematic element in the waste isolation pilot plant, WIPP, depository, in New Mexico, USA. This is because the high chloride soil content of the depository preferentially stabilizes

Pu(VI) which is more soluble (and thus more environmentally mobile) than Pu(IV). In contrast, the alkaline waters of the Yucca Mountain nuclear waste storage site dissolve Np about a thousand times more easily than Pu. As such Np is the problematic element at Yucca Mountain, Nevada, USA.<sup>8</sup>

The +3 and +4 actinide ions exist as discrete ions which are hydrated in solution as  $\text{An}(\text{H}_2\text{O})_n^{+3/+4}$  species. The +5 and +6 oxidation states however hydrolyze water in aqueous solutions to form actinyl,  $\text{AnO}_2^+$  and  $\text{AnO}_2^{2+}$  ions respectively. The  $\text{An}^{+3/+4}$  and  $\text{AnO}_2^{+/2+}$  ions form a large number of coordination complexes by binding various types of ligands. This is due to the hard acid nature of these ions. They form strong complexes with hard bases such as anionic or oxygen donating ligands. Examples of such complexes are thorium nitrate ( $\text{Th}(\text{NO}_3)_4 \cdot 5\text{H}_2\text{O}$ ), actinide halides ( $\text{AnX}_4$ ,  $\text{An} = \text{Th}, \text{U}, \text{Np}$  and  $\text{Pu}$ ,  $\text{X} = \text{F}, \text{Cl}$  and  $\text{Br}$ ) and uranium carbonate,  $\text{UO}_2(\text{CO}_3)_3^{4-}$ . Complexes formed with organic ligands are also well known. The overall coordination number of the  $\text{An}^{+3/+4}$  and  $\text{AnO}_2^{+/2+}$  ions depend on the size and shape (steric effect) of the ligands. For example, the effective coordination numbers for aquo ligands to these ions are 8-10 and 9-12 for the trivalent and tetravalent ions respectively and 4-5 and 5-6, especially for the aquo ligand, for the pentavalent and hexavalent actinyl species respectively. The aquo ions for U(VI) and U(IV) with coordination numbers of 5 and 8 respectively are shown in Figure 1.2.

As uranium is the most abundant and most widely used actinide element, a larger (compared to the other actinides) proportion of experimental studies have focused in synthesizing and characterizing its complexes. Although there has been recent progress in the synthesis and characterization of diverse uranium complexes, there are still a lot of experimental

challenges to our understanding of the behavior of these elements and their compounds in the environment. A few of them are: 1) the need for difficult handling techniques as a result of the

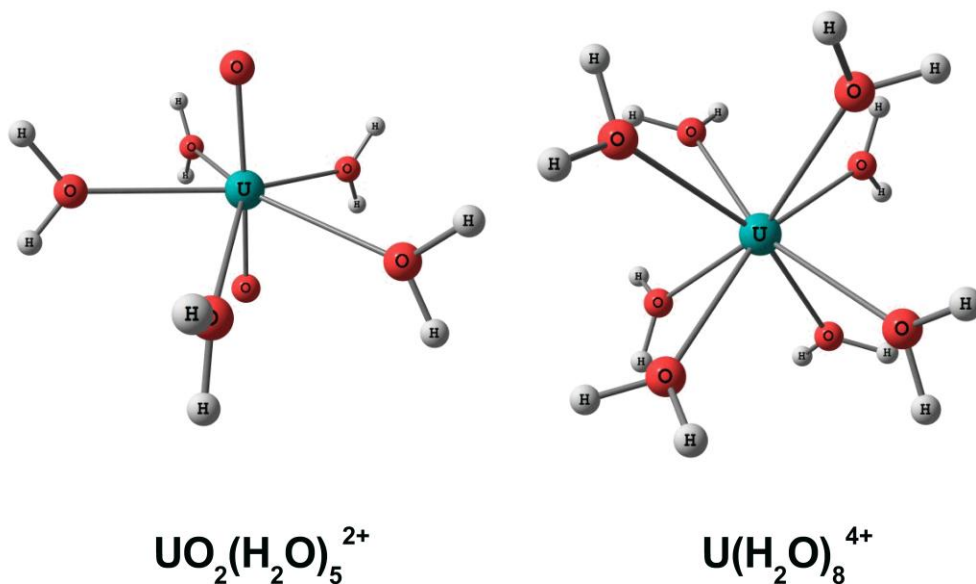


**Figure 1.2:** The aquo complexes of U(VI) and U(IV).

toxicity and radioactivity of the actinide elements and the relative scarcity of the actinide elements. This is especially true for the trans-uranium elements. In many cases, several different oxidation states might be simultaneously present in solution further complicating the work of experimental chemists. In contrast, computational studies are relatively cheap, safe and can be used to either complement available experimental data or bridge any gaps in our understanding of the properties of actinide complexes.

### 1.3 Theoretical studies of actinide complexes.

#### 1.3.1 The Schrödinger equation

All theoretical approaches employed in this thesis begin with a formulation of the time-independent adiabatic approximation of the Schrödinger equation.<sup>13</sup> In these methods, the Schrödinger equation is essentially recast to take advantage of the Born-Oppenheimer (BO) approximation<sup>14</sup> which allows the motion of the nuclei and electrons to be uncoupled. The physical meaning of the BO approximation is an assumption that the nuclei moves at negligible speeds compared to the electrons. The nuclei are assumed to be stationary in comparison to the fast moving electrons. This separation of the nuclear and electronic motion allows for an easier evaluation of the electron-nuclei, nuclei-nuclei interactions as well as the nuclear kinetic energies.

$$\hat{H}\Psi = E\Psi \quad (1.1)$$

$$\hat{H} = \hat{H}_{electron} + V_{nuclei} \quad (1.2)$$

$$\hat{H}_{electron} + V_{nuclei} \Psi_{electron} = E_{electron}\Psi_{electron} \quad (1.3)$$

$$\hat{H}_{electron} = T_{electron} + V_{electron-nuclei} + V_{electron-electron} \quad (1.4)$$

$V_{nuclei}$  is constant at each molecular geometry (BO approximation) and so can be removed. This allows us to recast Equation 1.1 into the electronic Schrodinger equation, Equation 1.3. The variational minimization of the energy results in the ground state wavefunction,  $\Psi$  and the lowest electronic energy,  $E$ , obtained during the variational minimization depends parametrically on the nuclear positions. The components of Equation 1.4 are the kinetic energy of the electrons, the electron-nuclei interaction potential and the electron-

electron interaction potential. The minimization of the energy, complete solution of the Schrödinger equation, is however not tractable except for the smallest systems such as  $H_2$ ,  $H_2^+$ , and  $He^+$ . The reason for this is the  $3N$ -dimensional nature of the electronic wavefunction, where  $N$  is the number of electrons. The electron-electron interaction part,  $V_{electron-electron}$ , of the Hamiltonian is also very difficult to evaluate.

### 1.3.2 The variational principle and electronic basis sets.

Examination of Equation 1.3 shows us that it has an infinite number of solutions. Assuming we are working with the electronic Schrodinger equation, the electronic energy obtained with an arbitrary wavefunction can be written as in Equation 1.5. The solution that yields the lower bound to the energy,  $E_{el}$ , yields the correct ground state wave-function. The lower bound to the energy is labeled as  $E_0$ . The variational principle in lay-man terms simply states “if there are two wavefunctions for a system, the one that produces the lower energy better represents the ground state wavefunction of the system and in fact the true ground state wavefunction yields the lowest energy,  $E_0$ ”. According to the variational principle, if the exact ground state wavefunction is used in Equation 1.5, the lowest electronic energy will be obtained. Thus Equation 1.5 can be generalized to Equation 1.6.

$$E_{el} = \frac{\langle \Psi | \hat{H} | \Psi \rangle}{\langle \Psi | \Psi \rangle} \quad (1.5)$$

$$E_{el} = \frac{\langle \Psi | \hat{H} | \Psi \rangle}{\langle \Psi | \Psi \rangle} \geq E_0 \quad (1.6)$$

It is immediately obvious that to get a given value of  $E_{el}$  as described in Equation 1.6, we need a trial wavefunction, its quality (seen as  $E_{el} - E_0$ ) notwithstanding. For atomic and molecular systems, electronic trial wavefunctions need to fulfill two important properties. Firstly as electrons are fermions, the trial wavefunction must be anti-symmetric under particle interchange.

$$\Psi(x_1, x_2) = -\Psi(x_2, x_1) \quad (1.7)$$

And secondly, no two identical electrons (or fermions in general) can occupy the same quantum state simultaneously. This is called the Pauli Exclusion Principle. The Slater determinant is an expression that conforms to these two conditions for multielectronic systems.<sup>15</sup> It is written as a determinant consisting of several orthonormal spin-orbitals each of which describe the position and spin of an electron.

$$\Psi(r_1, r_2, \dots, r_N) = \frac{1}{\sqrt{N!}} \begin{vmatrix} \phi_1(r_1) & \phi_2(r_1) & \dots & \phi_N(r_1) \\ \phi_1(r_2) & \phi_2(r_2) & \dots & \phi_N(r_2) \\ \vdots & \vdots & & \vdots \\ \phi_1(r_N) & \phi_2(r_N) & \dots & \phi_N(r_N) \end{vmatrix} \quad (1.8)$$

There are generally two classes of functions used to represent atomic spin-orbitals in modern electronic structure theory.<sup>16</sup> The first are called Slater type orbitals (STOs) which are modeled using the exponentially decaying electronic distribution ( $e^{-\zeta r}$ ) of the hydrogen atom. As they correspond to a real atom, they accurately describe the cusp condition at the atomic center. There are however significant computational challenges to calculating the integrals of an exponential decay function. In most cases, numerical solutions to the integrals of these functions are needed. The cusp at the atomic center is also difficult to handle computationally. The Gaussian type orbitals (GTOs) are a more tractable class of orbitals. Such orbitals possess

analytical solutions to their integrals. The disadvantages of using GTOs are: 1) wrong cusp conditions and 2) overall poor long range behavior as they decay much faster than STOs,  $e^{-ar^2}$  instead of  $e^{-\zeta r}$ . A widely used approach to circumvent these disadvantages is to use several GTOs to represent a single basis function according to Equation 1.9. The coefficients,  $C_i$ , are fit to ensure agreement with the radial electronic distribution of the hydrogen atom.

$$C_1 e^{-b_1 r^2} + C_2 e^{-b_2 r^2} + C_3 e^{-b_3 r^2} \quad (1.9)$$

In molecular systems, the atomic basis sets are combined to represent a molecular orbital (MO) as shown in Equation 1.10. This is called the Linear Combination of Atomic Orbitals principle (LCAO). The coefficients,  $S_i$ , describe the contribution of each atomic orbital to the MO. Prior to going forward, we note that the constituent atomic orbitals of an MO can contain one basis function (either an STO or GTO). These types of basis sets are said to be of single- $\zeta$  quality. Those containing two, three and four basis functions per atomic orbital are said to be of double- $\zeta$ , triple- $\zeta$  and quadruple- $\zeta$  basis sets. Polarization functions (basis functions with higher angular momentum) as well as diffuse basis functions can be added to each atomic orbital to respectively allow for a better description of electron correlation and anionic systems or excited electronic states. In some cases, the basis function is partitioned into a core and valence part. This is generally rooted in the idea that core electrons are generally chemically inactive and not involved in bond formation or ionization processes. A more complete explanation of the variational principle and the other concepts briefly described here can be found in most modern computational chemistry textbooks.<sup>16-17</sup>

$$\phi = \sum_{i=1}^N S_i \varphi_i \quad (1.10)$$

### 1.3.3 The Hartree-Fock method and Post Hartree-Fock approaches.

At the Hartree-Fock level, a Fock operator consisting of one-electron kinetic energy, the nucleus-electron interaction potential and the Hartree-Fock potential is defined, Equation 1.11. The Hartree-Fock method is the direct result of applying the variational method to the Slater determinant, Equation 1.8, in the electronic Schrödinger equation, Equation 1.1. The first two terms of Equation 1.11 (the electron kinetic energies and nucleus-electron interaction potentials) are one-electron operators describing the motion of an  $i^{\text{th}}$  electron in the field of the nuclei. These are combined into the  $\hat{h}_i$  term of Equation 1.12. The Hartree-Fock potential consists of the Coulomb ( $\hat{J}_j$ ) and exchange ( $\check{K}_j$ ) operators. It is a two-electron operator that describes inter-electron repulsion. The former,  $\hat{J}_j$ , describes the classical Coulombic repulsion between the electron and the  $j^{\text{th}}$  electron. The exchange operator,  $\check{K}_j$ , defines the electron exchange energy and it essentially switches the spin orbital of the  $i^{\text{th}}$  electron with that of the  $j^{\text{th}}$  electron. The Hartree-Fock Hamiltonian is then described as the sum of the Fock operators for all electrons in the system, Equation 1.14.<sup>18-19</sup>

$$F_i = -\frac{1}{2}\nabla^2 + \sum_k^{Nuclei} \frac{Z_k}{r_{ik}} + V_i^{HF}\{J\} \quad (1.11)$$

$$F_i = \hat{h}_i + \sum_k^N \hat{J}_j - \check{K}_j \quad (1.12)$$

$$\hat{H}_{HF} = \sum_i^n F_i = \sum_i^n \hat{h}_i + \sum_k^N \hat{J}_{ij} - \check{K}_{ij} \quad (1.13)$$

This equation allows us to write the Hartree-Fock (HF) energy as

$$E_{HF} = \sum_{i=1}^N \hat{h}_{ii} + \frac{1}{2} \sum_{i=1}^N \sum_{j=1}^N \hat{J}_{ij} - \check{K}_{ij} = \sum_{i=1}^N \epsilon_i + \frac{1}{2} \sum_{j=1}^N (\hat{J}_{ij} - \check{K}_{ij}) \quad (1.14)$$

It becomes immediately obvious that HF theory, from the definition of the Hartree-Fock potential, is a mean-field approximation in which each electron moves in an average field generated by the remaining (n-1) electrons. There are two very important deficiencies to the HF solution with a single Slater determinant. The first relates to the difference between the instantaneous electron-electron interaction of the real system and the mean field interaction experienced by each electron in HF theory. This is called dynamical correlation. The second deficiency is labeled as non-dynamical correlation and relates to deficiencies caused by the use of a single Slater determinant to describe the system. Non-dynamical correlation is particularly large for systems with near-degenerate energy levels. As such the true wavefunction of such systems consist of several coefficient-weighted Slater determinants. The sum of the dynamical and non-dynamical correlation is called the correlation energy and is defined as the difference between the ground state electronic energy and the HF energy.

$$E_{correlation} = E_0 - E_{HF} = E_{non-dynamical\ correlation} + E_{dynamical\ correlation} \quad (1.15)$$

It is important to note that although the contribution of electron correlation to the total electronic energy is small (~1%), its omission in most cases leads to large errors in calculated structural and electronic properties as well as reaction energies. There are various approaches to improving the HF approach. The only post Hartree-Fock approaches employed in this work are the second-order Møller-Plesset perturbation theory, MP2 and the coupled cluster singles and doubles and perturbatively included triples, CCSD(T), approaches.

In Møller-Plesset perturbation theory,<sup>20-21</sup> the unperturbed Hamiltonian,  $\hat{H}^0$ , is the sum of the one-electron Fock operators in Equation 1.13, and the Hartree-Fock wavefunction is an eigenfunction of  $\hat{H}^0$  which yields an eigenvalue equal to the sum of the one electron energies of the occupied spin orbitals. The electron correlation (dynamical correlation as the single Slater determinant is still employed) is described as a perturbation,  $\hat{H}'$ , to  $\hat{H}^0$ .

$$\hat{H} = \lambda\hat{H}' + \hat{H}^0 \quad (1.16)$$

Essentially a subset of the general time-independent perturbation theory of Rayleigh and Schrödinger<sup>22</sup>, Møller-Plesset perturbation theory assumes that all Slater determinants corresponding to the excitation of electrons from the occupied to the virtual orbitals are also eigenfunctions of  $\hat{H}^0$  with an eigenvalue equal to the sum of the one electron energies of their occupied spin orbitals. The wavefunction and energy can be expanded in terms of the perturbation.

$$\psi_i = \psi_i^{(0)} + \lambda\psi_i^{(1)} + \lambda^2\psi_i^{(2)} + \dots \quad (1.17)$$

$$E_i = E_i^{(0)} + \lambda E_i^{(1)} + \lambda^2 E_i^{(2)} + \dots \quad (1.18)$$

Substitution of these equations into the electronic Schrödinger equation yields a series of equations conforming to the general formula:  $E_i^0 = \langle \psi_i^0 | \hat{H}^0 | \psi_i^0 \rangle$  and  $E_i^n = \langle \psi_i^0 | \hat{H}' | \psi_i^{n-1} \rangle$ . The sum of  $E_i^0$  and  $E_i^1$  describes the HF energy (combination of the one-electron energy and the Hartree-Fock potential). The various Møller-Plesset perturbation (MP) approaches are named according to the degree of correlation correction included with the HF potential. For example, in MP2,  $E_i^2 = \langle \psi_i^0 | \hat{H}' | \psi_i^1 \rangle$  is included. Lastly, it should be noted that the higher orders of the MP<sup>n</sup> approaches are not necessarily convergent with respect to total energies.<sup>16</sup>

In coupled cluster theory, an infinite exponential cluster operator acts on the Hartree-Fock wavefunction to generate a full configuration interaction, CI, solution accounting for electron correlation, Equation 1.19.<sup>23</sup> The coupled cluster approaches are labeled according to the level at which the expansion coefficients,  $\check{T}$ , are truncated, Equation 1.20.<sup>24</sup> As an example, truncation at the single and double excitations level leads to the coupled cluster singles and doubles approach (CCSD). The most popular coupled cluster approach involves the inclusion of triple excitations into the CCSD wavefunction in a perturbative (Møller-Plesset) manner, Equation 1.16. This method is called the CCSD(T) approach. The CCSD(T) method is often referred to as the gold standard of computational chemistry as it has been shown to yield highly accurate (< 1 kcal/mol) reaction energies, transition state barriers and structure.<sup>24-25</sup> It is also a compromise between computational expense and the more accurate CCSDTQ and higher order coupled cluster approaches.

$$\Psi_{CC} \geq e^{\check{T}} \Psi_{HF} \geq \quad (1.19)$$

$$e^{\check{T}} = 1 + \check{T}_1 + \check{T}_2 + \frac{\check{T}_1^2}{2} + \frac{\check{T}_2^2}{2} + \check{T}_1\check{T}_2 + \dots \quad (1.20)$$

To briefly review, the major deficiency of HF theory is the lack of an appropriate treatment of the instantaneous interaction between electrons as well as the single reference nature of the Slater determinant employed. This neglect of electron correlation and mean field approximation to inter-electron repulsion has dramatic effects on calculated bond energies, vibrational frequencies and bond lengths in molecular species.<sup>16</sup> The MP<sup>n</sup> and coupled cluster approaches become increasingly expensive at higher orders. The energy convergence of the MP<sup>n</sup> methods is in many cases oscillatory at increasingly higher orders. These approaches also experience significant spin contaminations when employed for open shell (unrestricted HF

wavefunction) systems. The coupled cluster techniques are only computationally feasible (at the current moment) for the smallest of molecules. They also require basis sets of at least triple- $\zeta$  quality.

### 1.3.4 Density Functional Theory

Most of the calculations in this thesis were carried out under the framework of density functional theory (DFT). Although it has its roots in the much earlier Thomas-Fermi model<sup>26-27</sup> and the work of Slater on the  $X\alpha$  exchange functional<sup>15, 28</sup>, modern DFT is based on the two fundamental Hohenberg-Kohn (HK) theorems.<sup>29</sup> The first HK theorem states that the ground state electron density,  $\rho(\mathbf{r})$ , uniquely determines the external potential  $V(\mathbf{r})$ . The determination of  $V(\mathbf{r})$  allows for the exact formulation of the Hamiltonian and thus the wavefunction. The second HK theorem states that the ground state energy can be obtained variationally. This is due to the fact that any new density generates a new external potential leading to a new wavefunction. The energy, a functional of the density, is the sum of the external potential,  $\int \rho(\mathbf{r}) V(\mathbf{r}) d\mathbf{r}$ , the kinetic energy,  $T[\rho]$  and electron-electron interaction energy,  $E_{ee}[\rho]$ , Equation 1.21. The  $E_{ee}[\rho]$  term contains both the classical Coulombic interactions and the non-classical electron-electron interactions.

$$E[\rho] = \int \rho(\mathbf{r}) V(\mathbf{r}) d\mathbf{r} + T[\rho] + E_{ee}[\rho] \quad (1.21)$$

$$E[\rho] = \frac{\langle \Psi | \hat{H} | \Psi \rangle}{\langle \Psi | \Psi \rangle} \geq E_0[\rho] \quad (1.22)$$

Kohn-Sham DFT is the most widely used form of DFT. The basic assumption to this framework is the stipulated existence of a system of non-interacting electrons with exactly the

same density as the system of interest, one with interacting electrons.<sup>30</sup> For the system of non-interacting electrons, the  $E_{ee}$  term of Equation 1.21 by definition becomes zero. An analogous equation to the Fock equations of HF theory (Equations 1.11-1.14) allows us to construct Kohn-Sham spin orbitals.  $E_s \rho r$  in Equation 1.23 is the energy of the spin orbitals generated for the non-interacting system. Equation 1.24, is an eigen-value equation for Kohn-Sham particles and is reminiscent of the Fock equations at the Hartree-Fock level, Equation 1.12.

$$E_s \rho r = \rho r V r dr - \frac{1}{2} \nabla^2 \quad (1.23)$$

$$\hat{h}_i^{KS} \psi_i = \epsilon_i \psi_i \quad (1.24)$$

The one-electron Hamiltonian for the Kohn-Sham particles is given as

$$\hat{h}_i^{KS} = -\frac{1}{2} \nabla^2 + V_{eff} r \quad (1.25)$$

The effective external potential is defined as

$$V_{eff} r = V r + \frac{\rho r'}{r - r'} dr + V_{xc} r \quad (1.26)$$

The energy of the Kohn-Sham system is then given as

$$E_{KS} \rho r = \sum_i^N \epsilon_i - \frac{\rho r \rho r'}{r - r'} dr dr' + E_{xc} \rho r - V_{xc} r \rho r dr \quad (1.27)$$

The exchange-correlation term,  $E_{xc} \rho r$ , is a composite term containing: 1) the kinetic energy of a system of interacting electrons minus the kinetic energy of a system with non-interacting electrons with exactly the same density and 2) the electron-electron interaction (total electron exchange and correlation) minus the classical Coulomb interaction. Working backwards, we can

see that the Schrödinger equation has essentially been recast with energy as functional of density. If the exact exchange-correlation term is known, a full solution to the Schrödinger equation will have been obtained. Although a large number of possible exchange-correlation functionals have been proposed and tested over the years,<sup>31-36</sup> the exact nature of this functional remains unknown. This functional is often split into the exchange functional and the correlation functional.

$$E_{xc}[\rho, r] = E_x[\rho, r] + E_c[\rho, r] \quad (1.28)$$

The earliest known exchange-correlation functional is called the local density approximation (LDA) and is based on the fictitious system of a uniform electron gas, UEG. This system has an infinite number of electrons and uniform density all throughout. The exchange energy of a UEG is a functional of its density, Equation 1.29. The correlation part of the exchange-correlation functional was parameterized using highly accurate Monte Carlo calculations on the UEG. This work was done by Ceperley and Alder.<sup>37</sup> Modern modifications such as that of Vosko, Wilk and Nusair are available in most modern ab initio software packages.<sup>38</sup> Testing of the performance of the LDA functional for actinide molecules reveals that it generally leads to bond lengths that are slightly shorter than experimental values as well as reaction energies that deviate significantly from the experimental values. LDA is however particularly suited for metallic periodic systems where the electron density changes only very slowly.<sup>16-17</sup>

$$E_x[\rho, r] = \frac{-3}{4} \frac{3}{\pi} \int \rho^{\frac{1}{3}}(r) dr \quad (1.29)$$

The most common modifications to the LDA functional involve attempts to correct for rapidly changing electron densities found in molecular systems. The generalized gradient approximation, GGA, functionals were the first corrections to find widespread usage for molecular systems. In these functionals the gradient of the density is included in the formulation of the exchange-correlation functional, Equation 1.30. The  $f\left(\frac{\nabla\rho}{\rho^3}\right)$  term is the gradient parameter and provides a better description of the electron exchange in regions where there are changes in the electron density. The GGA functionals provided vast improvement on the agreement between the calculated ionization, atomization and binding energies and the experimental values.<sup>16</sup> Rigorous tests have however found that they generally tend to slightly overestimate the lengths of the bonds in actinide complexes.<sup>39-43</sup> The PBE functional is a non-empirical GGA functional and was widely used in the works compiled in this thesis.<sup>44-45</sup>

$$E_x \rho r = \int \rho^{\frac{4}{3}} r f\left(\frac{\nabla\rho}{\rho^3}\right) dr \quad (1.30)$$

The next stages of modification to the exchange-correlation functional encompass the hybrid and meta-GGA functionals. Additional information regarding the density is included as the Laplacian of the density and the non-interacting kinetic energy in the meta-GGA functionals. No meta-GGA functionals were employed in the works compiled in this thesis. Regarding the hybrid functionals, the gradient corrected GGA functionals are combined with explicit Hartree-Fock exchange. An example of the general mixing of GGAs with Hartree-Fock exchange as seen in the Becke three parameter functionals is shown in Equation 1.31. This combination is based on the adiabatic connection formula which allows us to write the exchange-correlation formula as a combination of the Hartree-Fock exchange and some DFT exchange-correlation functional.

The most widely used functional in the works compiled in this thesis and all of computational actinide chemistry in general is the B3LYP functional.<sup>46-47</sup> It combines some portion of the Hartree exchange with the B88 exchange and LYP correlation functionals using the formula:

$$E_{xc} = E_{xc}^{LDA} + 0.20 E_x^{HF} - E_x^{LDA} + 0.72 E_x^{GGA} - E_x^{LDA} + 0.81 E_c^{GGA} - E_c^{LDA} \quad (1.31)$$

The B88 exchange functional of Becke and the popular LYP correlation functional of Lee Yang and Parr are the GGA functionals employed in the B3LYP functional. Extensive testing by various authors have shown this particular functional to be suited for calculating the structural properties of actinide complexes, their vibrational frequencies as well as their reaction energies.<sup>39, 41-43, 48</sup> Other examples of hybrid functionals include B3PW91 and BHandH.<sup>16</sup>

Other functionals employed in this work are the long-range corrected hybrid functional, CAM-B3LYP<sup>49</sup>, the half and half functional of Becke, BHandH<sup>46</sup>, and the B3LYP functional with dispersion corrections using Grimme's third scheme, B3LYP-D3.<sup>33</sup>

### 1.3.5 Relativistic effects

The time-independent Schrödinger equation<sup>13, 22</sup> is only valid for non-relativistic systems. As the atomic number,  $Z$ , increases in heavier nuclei, the speeds of the core-electrons approach the speed of light. At such speeds, relativistic effects become important in the electronic structure of the atoms, ions and compounds of heavy nuclei. Generally the major effects in molecular systems are propagated by the contraction and stabilization of s and p orbitals as well as the expansion and destabilization of d and f orbitals.<sup>50-52</sup> Relativistic effects increase according to  $Z^2/c^2$  down the periodic table, where  $c$  is the speed of light, 137 in atomic units. The Dirac equation, Equation 1.32, was formulated in 1929 to describe the one-electron energies of relativistic systems<sup>53</sup> and is similar to the earlier Klein-Gordon equation<sup>54</sup>. In the Dirac equation,

$\alpha$  and  $\beta$  are  $4 \times 4$  matrices, Equations 1.33-1.35,  $V$  is the external potential and the wavefunction is a four component column spinor, Equation 1.36, containing the large component,  $\Psi_L$ , and the small component,  $\Psi_s$ . The large and small components respectively describe the positive and negative energy solutions found on either side of  $2mc^2$ . The small component solutions correspond to positrons while the large component solutions correspond to electrons. The up or down arrows in Equation 1.36 indicate the particle spin of the electrons and positrons. The coupling between the positronic and electronic parts of the wavefunction can be removed through the Foldy-Wouthuysen (FW) transformation.<sup>55</sup> The Pauli and Zeroth order regular approximation (ZORA) Hamiltonians were obtained by first order FW transformation of the Dirac-Coulomb-Breit Hamiltonian expanded in a series of  $c^{-2}$  and  $E/(2mc^2 - V)$ .<sup>56-57</sup> Calculations in which the spin components are projected out of the four-component Dirac equation are known as scalar-relativistic calculations while those in which the small-component is projected out are two-component approximations to the full Dirac equation. In these sets of equations (Equations 1.32-1.36),  $I$  is the two-dimensional identity matrix,  $\sigma$  represents the Pauli spin matrices in a compact form and  $p$  is the momentum.

$$(c\alpha \cdot p + \beta mc^2 + V)\Psi = E\Psi \quad (1.32)$$

$$\alpha = \begin{pmatrix} 0 & \sigma \\ \sigma & 0 \end{pmatrix} \quad (1.33)$$

$$\sigma_x = \begin{pmatrix} 0 & 1 \\ 1 & 0 \end{pmatrix}, \sigma_y = \begin{pmatrix} 0 & -i \\ i & 0 \end{pmatrix}, \sigma_z = \begin{pmatrix} 1 & 0 \\ 0 & -1 \end{pmatrix} \quad (1.34)$$

$$\beta = \begin{pmatrix} I & 0 \\ 0 & I \end{pmatrix} \quad (1.35)$$

$$\Psi = \begin{pmatrix} \Psi_L \uparrow \\ \Psi_L \downarrow \\ \Psi_S \uparrow \\ \Psi_S \downarrow \end{pmatrix} \quad (1.36)$$

Modern quantum-chemical calculations generally include relativistic effects using any one of the ZORA<sup>56-57</sup>, the Douglas-Kroll-Hess<sup>58-59</sup> unitary transformation and relativistic effective core potentials (ECP)<sup>60-61</sup>. The ZORA and ECP approaches were employed in the calculations summarized in this thesis. We however here focus on discussing the use of relativistic ECPs as they were used in nearly all the studies included in this work.

The realization that the core electrons unlike their valence counterparts are chemically inert and not involved in bond formation implies that they can be completely frozen (frozen-core approximation) or replaced by an effective core potential (ECP) without any massive loss in accuracy. The overall Hamiltonian used in the ECP calculations is transformed into Equation 1.37 below. In this equation,  $V_{PP} r_i$  contains the Coulomb and exchange operators for the valence electrons and potential to account for the core electrons. The kinetic and electron-electron correlation terms are completely non-relativistic.

$$\hat{H} = -\frac{1}{2}\nabla^2 + \sum_{i<j} \frac{1}{r_{ij}} + \sum_i V_{PP} r_i \quad (1.37)$$

The design of ECPs usually starts from all-electron basis set calculations on an atom of the desired element. The design could either be for non-relativistic ECPs in which case an HF (and in some cases post-HF) wave-function is employed or for relativistic ECPs in which some approximation to the Dirac equation (in most cases, the quasi relativistic Pauli Hamiltonian) is used. For the latter, all relativistic effects are embedded in the  $V_{pp}$  term of Equation 1.37. The designers of either flavor of ECPs however face certain challenges:<sup>62-63</sup> A) Would the ECP be

constructed such that it replicates the shapes and energies and shapes of the orbitals (shape-consistent ECPs) or would it be an energy-consistent ECP which would replicate some electronic property (ionization potentials, electron affinities or electronic spectra) of the atom? The energy-consistent ECPs are the most widely used variety as a result of the availability of experimental data regarding the electronic properties of most atoms. B) Where is the core-valence boundary? In other words, which orbitals should be placed in the core region to be replaced by the ECP and which should be in the valence region? For the actinide elements, this particular question is non-trivial given the semi-core nature of the 6s and 6p orbitals as well as the participation of the 5f orbitals in bond formation.

There are two commonly used types of energy-consistent ECPs used in computational studies of actinide systems.<sup>64-66</sup> The design of the small-core (SC) ECPs is such that 60 (principal quantum number,  $n < 5$  shells) core electrons are represented with a pseudopotential while the remaining ( $n \geq 5$  shells) electrons (30 for thorium, 32 for uranium as examples) are represented by valence basis sets. For the second variety, the large-core (LC) ECPs, 78 core electrons are replaced by a pseudopotential. As the core-region covered by the pseudopotential is larger for the LC-ECPs, they provide even greater time savings than the SC-ECPs. However, it has been shown that SC-ECPs generally tend to provide better agreements between experimental and calculated structural parameters and reaction energies. In Chapter 2 and works by other authors, the performance of the SC-ECPs and LC-ECPs designed by Stuttgart-Cologne group relative to experimental results (of the structure and reaction energies of several uranium complexes) are compared to those obtained using a full scalar relativistic four-component approximation to the Dirac equation.<sup>41-43</sup>

### 1.3.6 Solvation Effects

The effect of a solvent environment on the nature, speciation/chemical form and spectra of actinide complexes can be significant. For example for the meta-stable U(V) complexes, an aqueous solvent is sufficiently oxidizing to prevent their isolation and characterization.<sup>12, 67-71</sup> Experimental NMR studies of  $\text{UO}_2^{2+}$  in alkaline solution have shown the existence of fast oxygen exchange processes.<sup>48, 72-74</sup> It should be noted that the behaviors of actinide species in solutions are in no way uniform. For example, a comparison of the speciation diagrams of  $\text{UO}_2^{2+}$  and  $\text{PuO}_2^{2+}$ , indicated that although the pentaquo complex is dominant for both species in highly acidic solutions, the uranyl moiety forms trinuclear (in addition to binuclear) species,  $[(\text{UO}_2)_3(\text{OH})_5]^+$  and  $[(\text{UO}_2)_3(\text{OH})_7]^{2-}$  at modest to high pH values while its plutonyl counterpart forms mainly the binuclear species,  $[(\text{PuO}_2)_2(\text{OH})_2]^{2+}$  with negligible concentrations of trinuclear plutonyl complexes, even at high pH values.<sup>75-77</sup> The inclusion of solvent effects, when needed, is therefore very important in modern computational actinide chemistry.

One approach for describing the effect of a solvent environment on the structure, speciation and electronic properties of actinide complexes involves adding a large number of solvent molecules around the solute molecule. As an example, to study the uranyl ion in aqueous solution, the  $\text{UO}_2^{2+}$  ion could be surrounded by a cubic box containing water molecules with an overall density of about  $1.0 \text{ g/cm}^3$ . Vibrational frequency analyses and other calculations are then carried out on this solute-solvent box after the structural optimizations. This explicit approach to modeling solvation effects can be extremely computationally demanding as the number of solvent molecules increase. In addition, the introduction of so many solvent molecules implies the existence of a large number of possible minima and transition state structures. This further complicates any search for the global minimum structure.<sup>16</sup>

For the implicit solvation models,<sup>78-82</sup> a polarizable continuum or conductor-like model with electrostatic and entropic properties that match that of the desired solvent is employed. For these solvation models, the size/shape of the solvent-excluded cavity around the solute molecule has to be defined. The molecular free energy in solution is calculated as a sum of the electrostatic, dispersion-repulsion and cavitation energy contributions, Equation 1.38.

$$G_{solution} = G_{electrostatic} + G_{dispersion-repulsion} + G_{cavitation} \quad (1.38)$$

The cavity can be described such that each atom in a molecule is represented by individual spheres, individual cavity models, or for the united atom models, in which the hydrogen atoms are included in the spheres of the atoms to which they are directly bonded. Most software suites allow the user to specify the formation of the cavity from various tesserae as well as the radii of each cavity. The implementation of the polarizable continuum solvation model<sup>83-84</sup> (PCM) in the Gaussian 03 suites of programs<sup>85</sup> was used in most of the work compiled in this thesis. Gutowski et al.<sup>86-87</sup> have previously explored the suitability of this model and other solvation models for describing the effect of solvent environments on the structures and stabilities of actinide complexes. It has been shown that implicit model calculations on  $\text{AnO}_2^{2+}$  and  $\text{AnO}_2^+$  ions with a first solvation sphere containing 4-6 explicit water molecules accurately reproduces the structure and properties of these ions in highly acidic aqueous solutions.<sup>41-42, 88</sup>

## 1.4 Organization of this Thesis

This thesis is written in a sandwich style agglomeration of several manuscripts published or submitted in peer-reviewed scientific journals during the course of the doctoral program. The over-arching aim of the dissertation is to further our understanding of actinide chemistry by using computational methods. In each chapter, we try to answer particular questions regarding

the structure and properties of actinide complexes. The structural and electronic properties as well as the chemistry of actinide species in the gaseous, aqueous and solid phases are examined using theoretical calculations. In addition, the performances of the various theoretical methods used were also examined. Each chapter is followed by a list of references. The basic outline of this thesis is illustrated in Figure 1.3.

A brief introduction to actinide chemistry and the computational methods used in this thesis are presented in Chapter 1. In Chapter 2, we attempted to benchmark the performance of LC-ECP and SC-ECPs against an all-electron basis set four-component scalar-relativistic approach in the framework of DFT. This chapter essentially answers the question: how much accuracy can be obtained with ECP calculations? And how accurate are DFT calculations employing relativistic ECPs compared to those employing all-electron electron basis sets with a four-component approximation to the Dirac Hamiltonian?

In Chapters 3, 4 and 5, several questions regarding the aqueous chemistry of actinide complexes were studied using DFT calculations. The ability of DFT, a single-reference theory to accurately describe the structure of plutonium complexes is confirmed in Chapter 3. It is very important to ensure that the structures of open-shell plutonium complexes can be well-predicted by the single reference Kohn-Sham DFT approach before using the approach in studying their speciation and energetics. Given that we found DFT to be well suited to predicting the structures of plutonyl (VI) complexes in Chapter 3, we proceeded to studying the structural properties, speciation and energetics of the  $\text{PuO}_2^{2+}$  in acidic and alkaline aqueous solutions in Chapter 4. This study allowed us to explain the differences between the trinuclear species-dominated uranyl chemistry at modest-high pH and the binuclear species-dominated plutonyl chemistry at similar pH values. In Chapter 5, DFT calculations were used to explore the structure and speciation of

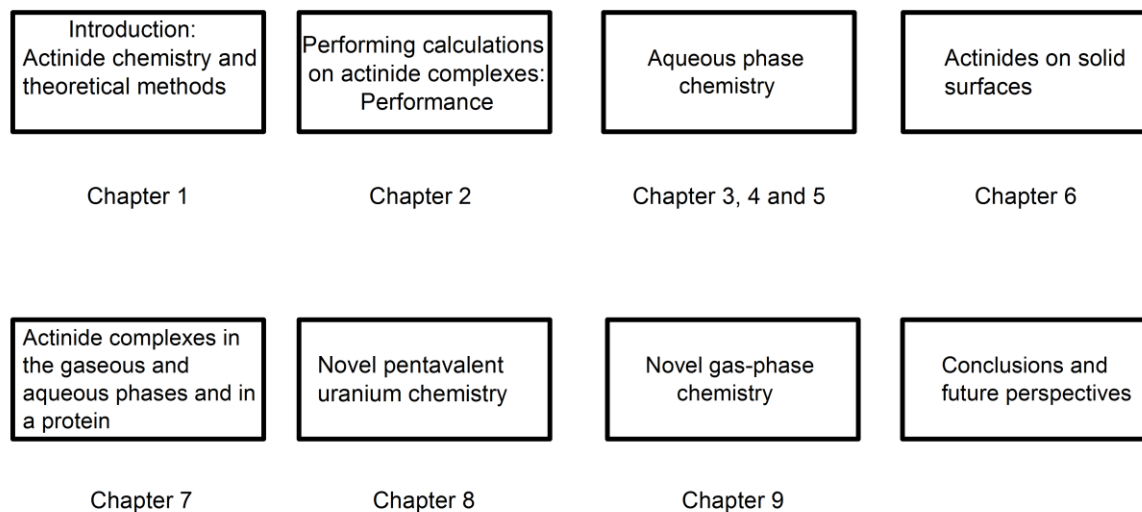


**Figure 1.3:** Schematic description of the chapters in this thesis

mononuclear uranyl peroxy complexes in aqueous solution. These complexes are possibly the building blocks of the well-known crystalline polynuclear uranyl-peroxide species.

In the next chapter, Chapter 6, the adsorption, electronic structure and reactions of uranium complexes on geochemical surfaces were studied using a combination of periodic and molecular DFT calculations. A comprehensive study of the structure and bonding as well as the electronic properties of uranyl fluorides in the gas-phase, aqueous phase and in the cavities of a protein is presented in Chapter 7. This study encompasses three of the phases (except for the solid phase) in which actinides in the environment can be found.

The next two chapters (Chapters 8 and 9) concentrate on novel uranium chemistry. As previously noted<sup>8</sup>, the U(V) ion is metastable as it disproportionates to U(VI) and U(IV). New

experimental breakthroughs have however led to the synthesis of stable U(V) species. The structural and electronic properties of two binuclear U(V)/U(V) complexes formed by oxo-functionalization of axial oxo atoms are studied in Chapter 8. In Chapter 9 however, the structure of a binuclear U(VI)/U(VI) complex formed by laser ablation of UO<sub>3</sub> is studied. Particular attention was given to possible structural motifs featuring cation-cation interactions.

In Chapter 10, the results from the various studies compiled in this thesis are presented. The linkages between the different chapters and how each chapter relates to the goal of effective nuclear waste storage and environmental remediation of nuclear waste sites are discussed. Finally, future directions for the works compiled in this thesis as well as for computational actinide chemistry in general are discussed.

## 1.5. References

1. Kaltsoyannis, N.; Scott, P., *The f elements*,. 1 ed.; Oxford University Press: Oxford, 1999.
2. Cotton, F. A.; Wilkinson, G., *Advanced Inorganic Chemistry*. 1 ed.; John Wiley and Sons: New York, 1988.
3. Eliav, E.; Kaldor, U.; Ishikawa, Y., *Phys. Rev. A* **1995**, 52 (1), 291-296.
4. <http://www.mindat.org/>. (Assessed July 23<sup>rd</sup>, 2012)
5. Holmes, D. <http://californiahomeopath.com/issue/the-california-homeopath-volume-14-1/article/the-actinides-the-ultimate-challenge>. (Assessed July 23<sup>rd</sup>, 2012)
6. <http://www.world-nuclear.org/info/inf01.html>. (Assessed July 23<sup>rd</sup>, 2012)
7. Ewing, R. C.; Runde, W.; Albrecht-Schmitt, T. E., *Mrs Bulletin* **2010**, 35 (11), 859-866.

8. Runde, W. The Chemical Interactions of Actinides in the Environment *Los Alamos Science* [Online], 2000.
9. Betti, M., *J. Environ. Radioactiv.* **2003**, *64* (2-3), 113-119.
10. Clain, A. F.; de Aquino, J. O.; Domingues, M. D. F., *Quim. Nova* **1999**, *22* (5), 677-678.
11. <https://www.ornl.gov/ptp/collection/Miscellaneous/pacemaker.htm>. (Assessed July 23<sup>rd</sup>, 2012)
12. Graves, C. R.; Kiplinger, J. L., *Chem. Commun.* **2009**, (26), 3831-3853.
13. Schrodinger, E., *Annalen Der Physik* **1926**, *79* (4), 361-U8.
14. Born, M.; Oppenheimer, R., *Annalen Der Physik* **1927**, *84* (20), 0457-0484.
15. Slater, J. C., *Phys. Rev.* **1951**, *81* (3), 385-390.
16. Cramer, C. J., *Essentials of Computational Chemistry -Theories and Models*. 2 ed.; John Wiley & Sons Ltd: London, 2005.
17. Jensen, F., *Introduction to Computational Chemistry*. Wiley: Chichester, 1999.
18. Hartree, D. R., *P. Camb. Philos. Soc.* **1928**, *24*, 89-110.
19. Hartree, D. R., *P. Camb. Philos. Soc.* **1928**, *24*, 111-132.
20. Moller, C.; Plesset, M. S., *Phys. Rev.* **1934**, *46* (7), 0618-0622.
21. Pople, J. A.; Binkley, J. S.; Seeger, R., *Int. J. Quantum Chem.* **1976**, 1-19.
22. Schrodinger, E., *Annalen Der Physik* **1926**, *80* (13), 437-490.
23. Cizek, J., *J. Chem. Phys.* **1966**, *45* (11), 4256-&.
24. Purvis, G. D.; Bartlett, R. J., *J. Chem. Phys.* **1982**, *76* (4), 1910-1918.
25. Kendall, R. A.; Dunning, T. H.; Harrison, R. J., *J. Chem. Phys.* **1992**, *96* (9), 6796-6806.
26. Thomas, L. H., *P. Camb. Philos. Soc.* **1927**, *23*, 542-548.
27. Fermi, E., *Rend. Accad. Lincei* **1927**, *6*, 602-607.

28. Slater, J. C., *Adv. Quantum Chem.* **1972**, 6, 1-.
29. Hohenberg, P.; Kohn, W., *Phys. Rev. B* **1964**, 136 (3B), B864-&.
30. Kohn, W.; Sham, L. J., *Phys. Rev.* **1965**, 140 (4A), 1133-&.
31. Cohen, A. J.; Mori-Sanchez, P.; Yang, W. T., *Chem. Rev.* **2012**, 112 (1), 289-320.
32. Cramer, C. J.; Truhlar, D. G., *Phys. Chem. Chem. Phys.* **2009**, 11 (46), 10757-10816.
33. Grimme, S.; Antony, J.; Ehrlich, S.; Krieg, H., *J. Chem. Phys.* **2010**, 132 (15).
34. Kozuch, S.; Gruzman, D.; Martin, J. M. L., *J. Phys. Chem. C* **2010**, 114 (48), 20801-20808.
35. Zhao, Y.; Truhlar, D. G., *Chem. Phys. Lett.* **2011**, 502 (1-3), 1-13.
36. Zhao, Y.; Truhlar, D. G., *J. Chem. Theory Comput.* **2011**, 7 (3), 669-676.
37. Ceperley, D. M.; Alder, B. J., *Phys. Rev. Lett.* **1980**, 45 (7), 566-569.
38. Vosko, S. H.; Wilk, L.; Nusair, M., *Can. J. Phys.* **1980**, 58 (8), 1200-1211.
39. Batista, E. R.; Martin, R. L.; Hay, P. J., *J. Chem. Phys.* **2004**, 121 (22), 11104-11111.
40. Odoh, S. O.; Schreckenbach, G., *J. Phys. Chem. A* **2011**, 115 (48), 14110-14119.
41. Schreckenbach, G.; Shamov, G. A., *Acc. Chem. Res.* **2010**, 43 (1), 19-29.
42. Shamov, G. A.; Schreckenbach, G., *J. Phys. Chem. A* **2005**, 109 (48), 10961-10974.
43. Shamov, G. A.; Schreckenbach, G.; Vo, T. N., *Chem-Eur. J.* **2007**, 13 (17), 4932-4947.
44. Perdew, J. P.; Burke, K.; Ernzerhof, M., *Phys. Rev. Lett.* **1996**, 77 (18), 3865-3868.
45. Perdew, J. P.; Burke, K.; Ernzerhof, M., *Phys. Rev. Lett.* **1997**, 78 (7), 1396-1396.
46. Becke, A. D., *J. Chem. Phys.* **1993**, 98 (7), 5648-5652.
47. Stephens, P. J.; Devlin, F. J.; Chabalowski, C. F.; Frisch, M. J., *J. Phys. Chem.* **1994**, 98 (45), 11623-11627.
48. Schreckenbach, G.; Hay, P. J.; Martin, R. L., *Inorg. Chem.* **1998**, 37 (17), 4442-4451.

49. Yanai, T.; Tew, D. P.; Handy, N. C., *Chem. Phys. Lett.* **2004**, 393 (1-3), 51-57.
50. Pyykko, P., *Chem. Rev.* **1988**, 88 (3), 563-594.
51. Pyykko, P.; Desclaux, J. P., *Acc. Chem. Res.* **1979**, 12 (8), 276-281.
52. Pyykko, P.; Li, J.; Runeberg, N., *J. Phys. Chem.* **1994**, 98 (18), 4809-4813.
53. Dirac, P. A. M., *Proc. Roy. Soc. Ser. A, 1929, 123, 714.* **1929**, 123, 714-.
54. Polyanin, A. D., *Handbook of Linear Partial Differential Equations for Engineers and Scientists.* Chapman & Hall/CRC: 2002.
55. Foldy, L. L.; Wouthuysen, S. A., *Phys. Rev.* **1950**, 78 (1), 29-36.
56. Dyllal, K. G.; van Lenthe, E., *J. Chem. Phys.* **1999**, 111 (4), 1366-1372.
57. van Lenthe, E.; Ehlers, A.; Baerends, E. J., *J. Chem. Phys.* **1999**, 110 (18), 8943-8953.
58. Reiher, M.; Wolf, A., *J. Chem. Phys.* **2004**, 121 (5), 2037-2047.
59. Wolf, A.; Reiher, M.; Hess, B. A., *J. Chem. Phys.* **2002**, 117 (20), 9215-9226.
60. Küchle, W.; Dolg, M.; Stoll, H.; Preuss, H., *Mol. Phys.* **1991**, 74 (6), 1245-1263.
61. Küchle, W.; Dolg, M.; Stoll, H.; Preuss, H., *J. Chem. Phys.* **1994**, 100 (10), 7535-7542.
62. Dolg, M.; Cao, X. Y., *Chem. Rev.* **2012**, 112 (1), 403-480.
63. Stoll, H.; Metz, B.; Dolg, M., *J. Comput. Chem.* **2002**, 23 (8), 767-778.
64. Cao, X. Y.; Dolg, M., *J. Mol. Struct-Theochem* **2004**, 673 (1-3), 203-209.
65. Cao, X. Y.; Dolg, M., *Coordin. Chem. Rev.* **2006**, 250 (7-8), 900-910.
66. Cao, X. Y.; Dolg, M.; Stoll, H., *J. Chem. Phys.* **2003**, 118 (2), 487-496.
67. Arnold, P. L.; Pecharman, A. F.; Love, J. B., *Angew. Chem. Int. Edit.* **2011**, 50 (40), 9456-9458.
68. Fortier, S.; Hayton, T. W., *Coordin. Chem. Rev.* **2010**, 254 (3-4), 197-214.

69. Ikeda, A.; Hennig, C.; Tsushima, S.; Takao, K.; Ikeda, Y.; Scheinost, A. C.; Bernhard, G., *Inorg. Chem.* **2007**, *46* (10), 4212-4219.
70. Mizuoka, K.; Grenthe, I.; Ikeda, Y., *Inorg. Chem.* **2005**, *44* (13), 4472-4474.
71. Mizuoka, K.; Ikeda, Y., *Inorg. Chem.* **2003**, *42* (11), 3396-3398.
72. Clark, D. L.; Conradson, S. D.; Donohoe, R. J.; Keogh, D. W.; Morris, D. E.; Palmer, P. D.; Rogers, R. D.; Tait, C. D., *Inorg. Chem.* **1999**, *38* (7), 1456-1466.
73. Shamov, G. A.; Schreckenbach, G., *J. Am. Chem. Soc.* **2008**, *130* (41), 13735-13744.
74. Szabo, Z.; Grenthe, I., *Inorg. Chem.* **2007**, *46* (22), 9372-9378.
75. Rao, L. F.; Tian, G. X.; Di Bernardo, P.; Zanonato, P., *Chem-Eur. J.* **2011**, *17* (39), 10985-10993.
76. Reilly, S. D.; Neu, M. P., *Inorg. Chem.* **2006**, *45* (4), 1839-1846.
77. Zanonato, P.; Di Bernardo, P.; Bismondo, A.; Liu, G. K.; Chen, X. Y.; Rao, L. F., *J. Am. Chem. Soc.* **2004**, *126* (17), 5515-5522.
78. [http://www.nd.edu/~wschnei1/courses/CBE\\_547/Lectures/implicit\\_solvation\\_models.pdf](http://www.nd.edu/~wschnei1/courses/CBE_547/Lectures/implicit_solvation_models.pdf).  
(Assessed July 23<sup>rd</sup>, 2012)
79. Cramer, C. J.; Truhlar, D. G., *Chem. Rev.* **1999**, *99* (8), 2161-2200.
80. Cramer, C. J.; Truhlar, D. G., *Acc. Chem. Res.* **2008**, *41* (6), 760-768.
81. Tomasi, J.; Mennucci, B.; Cammi, R., *Chem. Rev.* **2005**, *105* (8), 2999-3093.
82. Tomasi, J.; Persico, M., *Chem. Rev.* **1994**, *94* (7), 2027-2094.
83. Miertus, S.; Scrocco, E.; Tomasi, J., *Chem. Phys.* **1981**, *55* (1), 117-129.
84. Miertus, S.; Tomasi, J., *Chem. Phys.* **1982**, *65* (2), 239-245.
85. Frisch, M. J. T., G. W.; Schlegel, H. B.; Scuseria, G. E.; Robb, M. A.; Cheeseman, J. R.; Montgomery, Jr., J. A.; Vreven, T.; Kudin, K. N.; Burant, J. C.; Millam, J. M.; Iyengar, S. S.;

Tomasi, J.; Barone, V.; Mennucci, B.; Cossi, M.; Scalmani, G.; Rega, N.; Petersson, G. A.; Nakatsuji, H.; Hada, M.; Ehara, M.; Toyota, K.; Fukuda, R.; Hasegawa, J.; Ishida, M.; Nakajima, T.; Honda, Y.; Kitao, O.; Nakai, H.; Klene, M.; Li, X.; Knox, J. E.; Hratchian, H. P.; Cross, J. B.; Bakken, V.; Adamo, C.; Jaramillo, J.; Gomperts, R.; Stratmann, R. E.; Yazyev, O.; Austin, A. J.; Cammi, R.; Pomelli, C.; Ochterski, J. W.; Ayala, P. Y.; Morokuma, K.; Voth, G. A.; Salvador, P.; Dannenberg, J. J.; Zakrzewski, V. G.; Dapprich, S.; Daniels, A. D.; Strain, M. C.; Farkas, O.; Malick, D. K.; Rabuck, A. D.; Raghavachari, K.; Foresman, J. B.; Ortiz, J. V.; Cui, Q.; Baboul, A. G.; Clifford, S.; Cioslowski, J.; Stefanov, B. B.; Liu, G.; Liashenko, A.; Piskorz, P.; Komaromi, I.; Martin, R. L.; Fox, D. J.; Keith, T.; Al-Laham, M. A.; Peng, C. Y.; Nanayakkara, A.; Challacombe, M.; Gill, P. M. W.; Johnson, B.; Chen, W.; Wong, M. W.; Gonzalez, C.; and Pople, J. A. Gaussian 03, Revision C.02. 2004.

86. Cocalia, V. A.; Gutowski, K. E.; Rogers, R. D., *Coordin. Chem. Rev.* **2006**, *250* (7-8), 755-764.

87. Gutowski, K. E.; Dixon, D. A., *J. Phys. Chem. A* **2006**, *110* (28), 8840-8856.

88. Moskaleva, L. V.; Kruger, S.; Spörl, A.; Rosch, N., *Inorg. Chem.* **2004**, *43* (13), 4080-4090.

## Preface to Chapter 2

This chapter is based on a manuscript published in the journal “*Journal of Physical Chemistry A*”. The full citation of the paper is as follows:

Samuel O. Odoh and Georg Schreckenbach, “Performance of relativistic effective core potentials in DFT calculations on actinide compounds” *Journal of Physical Chemistry A*, **2010**, 114, 1957.

The actinide atoms are at the tail-end of the periodic table of elements. As such, the use of all-electron basis sets in theoretical examination of the structure and properties of actinide complexes are computationally expensive. The use of effective core pseudopotentials (ECPs) in such calculations reduces the computational burden. In addition, the ECPs are usually constructed in a careful manner as to include relativistic treatment of the actinide atoms. In this work, we compared the performance of two types of ECPs in predicting the structure and reaction free energies of several small actinide complexes against all-electron basis set calculations.

All the calculations in the published manuscript and compiled in this chapter were carried out by Samuel O. Odoh. The manuscript was prepared together with Prof. Georg Schreckenbach.

Copyright permissions have been obtained from the American Chemical Society and the other authors.

## **Chapter 2: Performance of Relativistic Effective Core Potentials in DFT Calculations on Actinide Compounds**

### **Abstract**

Density functional theory (DFT) calculations using relativistic effective core potentials (RECPs) have emerged as a robust and fast method of calculating the structural parameters and energy changes of the thermochemical reactions of actinide complexes. A comparative investigation of the performance of the Stuttgart small-core and large-core RECPs in DFT calculations has been carried out. The vibrational frequencies and reaction enthalpy changes of several uranium (VI) compounds computed using these RECPs were compared to those obtained using DFT and a four-component one-electron scalar relativistic approximation of the full Dirac equation with large all-electron basis sets (AE). The relativistic AE method is a full solution of the Dirac equation with all spin-components separated out. This method gives the ‘correct’ answer (with respect to scalar relativity) which should be closest to experimental values when an adequate density functional is used and in the absence of significant spin-orbit effects. The small-core RECP generally show better agreement with the four-component scalar-relativistic AE method than the large-core RECP. We conclude that the 5s, 5p and 5d orbitals are important in determining the chemistry of actinide complexes. Instances in which large-core RECPs give better agreement with experimental data are attributed to either experimental uncertainties or error cancellations.

## Introduction

There has been recent progress in the use of quantum mechanical methods to compute the structural parameters of actinide compounds.<sup>1-3</sup> Several approaches have been used to include relativistic effects, electron correlation and solvation effects into calculations on actinide complexes.<sup>4</sup> To incorporate relativistic effects, various approximations to the full Dirac Hamiltonian have been used in combination with all-electron (AE) basis sets.<sup>5</sup> The literature contains many examples in which the Douglas-Kroll-Hess (DKH) approximation<sup>6-8</sup>, the Zeroth Order Regular Approximation<sup>9-11</sup> (ZORA) and other such approximations have been used to include relativistic effects in calculations on actinides.<sup>12-16</sup> The use of specially-designed effective core potentials in place of AE basis sets is another means of including relativistic effects.<sup>17</sup> These relativistic effective core potentials (RECPs) and their associated valence basis sets have been used in calculations at the density functional theory (DFT),<sup>16,18</sup> second order Møller-Plesset Perturbation theory<sup>19-21</sup> (MP2) and coupled cluster (CCSD(T))<sup>20-22</sup> levels of theory. There are two popular flavors of RECPs for the uranium atom and other early actinides, large-core RECPs with the 5f to 7s orbitals treated as valence orbitals (78 core electrons on uranium) and small-core RECPs which include the 5s, 5p and 5d orbitals in the valence shell as well (60 core electrons on uranium).

The use of actinide RECPs and associated basis sets in DFT calculations have emerged as a fast and relatively accurate method of computing the properties of actinide complexes.<sup>16,18</sup> The effects of the density functional(s) of choice on computational results have been examined.<sup>21</sup> The performance of the two types of RECPs mentioned above in DFT computations of the thermochemical reaction energy changes, vibrational frequencies and bond lengths of actinide compounds have been compared by various authors.<sup>16,18,23-27</sup> It has been generally noted that

DFT calculations with large-core RECPs often yield less accurate results in comparison to those using AE methods and also to those using small-core RECPs.

With the release of another set of RECPs by the Stuttgart-Dresden-Bonn (Stuttgart) group<sup>28</sup>, Marsden and coworkers compared the performance of the small-core and large-core RECPs produced specifically by this group.<sup>29-30</sup> The vibrational frequencies of various U(VI) compounds (NUN, NUO<sup>+</sup>, CUO, UO<sub>3</sub> and UF<sub>6</sub>) and the enthalpy changes of various reactions involving several uranium fluorides and oxyfluorides were computed using DFT and the Stuttgart RECPs. The computed values were statistically compared to experimental values and to results obtained with the (large-core) Los Alamos RECP and its double-zeta valence basis set (LANL2DZ).<sup>31</sup> They concluded from their calculations that similar degrees of accuracy were obtained when using large-core and small-core RECPs to compute vibrational frequencies. The large-core RECP was found to give somewhat better enthalpy changes than its small-core counterpart for the thermochemical reactions that were studied.

This work is a further assessment of the performance of the RECPs from the Stuttgart group. We have performed DFT calculations using the one-electron four-component scalar relativistic method<sup>32</sup> implemented in the Priroda code<sup>33</sup> with large all-electron (AE) basis sets. The reaction enthalpy changes and vibrational wavenumbers obtained with the AE four-component method are then compared with those obtained with the RECPs from the Stuttgart group. In this way, we can separate effects of the relativistic approximation (such as the comparison of LC- and SC-RECPs) from effects of the model chemistry (DFT exchange-correlation functional, basis set convergence). Thus fortuitous error cancellations leading to occasions and possibly conclusions where the large-core RECP performs as well or even better than the small-core RECP can be identified.

## Computational Details

DFT calculations were performed to obtain the optimized geometries and vibrational frequencies of three linear triatomic molecules (NUN, NUO<sup>+</sup> and CUO), UO<sub>3</sub> and UF<sub>6</sub>. The enthalpy changes associated with the gas phase reactions of several U(VI) compounds were also computed (reactions 1-5). Three generalized gradient approximation (GGA), PBE<sup>34-35</sup>, BPBE<sup>35-36</sup> and BLYP<sup>36-37</sup> and two hybrid functionals, B3LYP<sup>38-39</sup> and PBE0<sup>34-35</sup> were used in combination with tight energy and geometry convergence criteria. The AE calculations were carried out with the Priroda code.<sup>33,40</sup> Priroda employs a four-component one-electron scalar relativistic approximation to the full Dirac equation with all spin-orbit terms separated out and neglected.<sup>32</sup> We have previously examined the performance of DFT calculations with the four-component method implemented in the Priroda program.<sup>18,41</sup> Two types of AE basis sets implemented in the Priroda code were used for all the atoms. These basis sets named L1 and L2 are of double- and triple-zeta quality respectively for the large component (cc-pVDZ and cc-pVTZ) respectively<sup>40,42</sup>. They also include the appropriate kinetically balanced basis sets for the small component. In Priroda, vibrational constants using the hybrid functionals were obtained with numerical frequency analysis, whereas analytical frequencies were used for the GGA functionals.

The Stuttgart large-core and small-core RECPs for uranium<sup>28, 43-44</sup> and their associated valence basis sets were used in DFT calculations in both the Gaussian 03<sup>45</sup> and NWchem<sup>46-47</sup> suites of programs. All g-type functions on the uranium atom were removed from the valence basis sets. To provide some insight into basis set dependency, the 6-31+G\*, 6-311+G\*, 6-311++G(3df,3pd) and aug-cc-pVTZ basis sets were used to describe the hydrogen, nitrogen, oxygen and fluorine atoms in separate calculations. The same set of density functionals as employed in Priroda were employed in these calculations. Ultra-fine and xfine grids were used in

all calculations performed using Gaussian 03 and NWChem respectively. Tight self-consistent field (SCF) and geometry optimization criteria were used in all calculations carried out in Gaussian 03 and NWChem. Similar settings were employed for both the RECP and AE calculations. The reaction enthalpy changes at 298K were calculated as the sum of the changes in the electronic energy and the calculated enthalpy corrections.

## Results and Discussion

**Vibrational Constants of Triatomic Compounds.** NUN, NUO<sup>+</sup> and CUO are U(VI) compounds iso-electronic with UO<sub>2</sub><sup>2+</sup>. The IR spectra of these compounds trapped in argon and neon matrices have been measured and reported.<sup>48-50</sup> Theoretical calculations of the bond-lengths and vibrational constants of these compounds have been carried out by Pyykkö and co-workers using large-core quasi-relativistic pseudopotentials at the Hartree-Fock level.<sup>51</sup> Gagliardi and Roos carried out complete active space (CASPT2) calculations using the Stuttgart small-core RECP on these compounds and obtained results in agreement with experimental data<sup>52</sup>. Marsden and co-workers have also reported the harmonic and an-harmonic vibrational frequencies of these compounds calculated with DFT and RECPs.<sup>29-30</sup> The symmetric and asymmetric stretching vibrational wavenumbers for NUN, NUO<sup>+</sup> and CUO computed using the small-core and large-core RECPs with the aug-cc-pVTZ ligand basis set are compared to those obtained using the AE method in Tables 2.1-2.3. Deviations of the values computed using the large- and small- core RECPs from the AE method are presented graphically in Figure 2.1.

For NUN, vibrational frequencies computed using the small-core RECP show good agreement with those obtained using the AE method regardless of the basis set or functional used. The average deviation between the small-core RECP and AE results is 2 cm<sup>-1</sup> which is less

than the experimental uncertainty of about  $10\text{ cm}^{-1}$ . However, the values obtained with the large-core RECP deviate from both the small-core RECP and AE results by  $3\text{-}25\text{ cm}^{-1}$ . The observed deviation is particularly pronounced for the IR-active and more intense anti-symmetric stretching vibration. The anti-symmetric stretching vibrational frequencies calculated with the PBE and BPBE GGA functionals and the small-core RECP or AE methods agree very well with the experimental values, as well as with the high-level CASPT2 ab initio results.<sup>52</sup> A similar level of agreement is maintained even after the inclusion of estimated matrix effects. There is a systematic  $20\text{-}25\text{ cm}^{-1}$  underestimation of the calculated frequencies obtained using the BLYP functional when compared to the other GGA functionals. This underestimation is observed for all three methods with which relativistic effects are included. As previously noted, the hybrid functionals generally over-bind the selected triatomic molecules leading to higher vibrational frequencies.<sup>29-30,51</sup>

The general argument that the small-core RECP better reflects the results obtained with the AE method still remains valid for the calculated frequencies of CUO and NUO<sup>+</sup>, Figure 2.1. A close examination of Tables 2.1-2.3 reveals the possibility of significant error cancellation when comparing the values obtained with the large-core RECP to the experimental values. The seemingly better agreement between the large-core RECP results obtained using hybrid functionals and the experimental values is an artifact of the systematic underestimation of the results obtained with the small-core RECP and AE methods. The comparison of the vibrational frequencies of NUN, NUO<sup>+</sup> and CUO obtained using the large-core and small-core RECPs to experimental values by the Marsden group is dominated by hybrid functionals.<sup>30</sup> This is despite the fact that the GGA functionals (BP86 and BLYP) that were used gave better agreement with experimental values when used with the small-core RECP. A bias of their comparison table

towards hybrid functionals for which the values obtained using the large-core RECP systematically underestimates the small-core RECP values while excluding GGA functionals

**Table 2.1:** Calculated vibrational frequencies,  $\text{cm}^{-1}$ , of NUN.

| Experiment <sup>a</sup> | 1077    |         | (1089) <sup>b</sup> |                      | $\omega(\text{anti.sym.})$ |                             |
|-------------------------|---------|---------|---------------------|----------------------|----------------------------|-----------------------------|
|                         | LC RECP | SC RECP | AE                  | LC RECP <sup>c</sup> | SC RECP <sup>c</sup>       | CASPT2/SC RECP <sup>d</sup> |
| PBE                     | 1021.9  | 1030.0  | 1033.6              |                      |                            | 1015                        |
|                         | 1056.8  | 1081.4  | 1080.5              |                      |                            | 1072                        |
| BPBE                    | 1015.3  | 1025.7  | 1027.3              |                      |                            |                             |
|                         | 1052.8  | 1078.6  | 1075.2              |                      |                            |                             |
| BLYP                    | 987.2   | 997.3   | 1000.8              |                      |                            |                             |
|                         | 1026.8  | 1051.1  | 1050.3              | 1038                 | 1064                       |                             |
| B3LYP                   | 1076.4  | 1072.0  | 1074.4              |                      |                            |                             |
|                         | 1097.5  | 1115.2  | 1113.0              | 1105                 | 1125                       |                             |
| PBE0                    | 1117.8  | 1112.4  | 1115.8              |                      |                            |                             |
|                         | 1134.2  | 1151.2  | 1149.4              | 1141                 | 1161                       |                             |

<sup>a</sup> References <sup>48</sup>. <sup>b</sup> Antisymmetric stretch; experimental vibrational frequencies corrected for matrix effects are in parenthesis. <sup>c</sup> Reference <sup>30</sup>. <sup>d</sup> Reference <sup>52</sup>. For Tables 2.1, 2.2 and 2.3, the calculated frequencies obtained with each functional are given for symmetric (top) and asymmetric stretching modes.

**Table 2.2:** Calculated vibrational frequencies,  $\text{cm}^{-1}$ , of  $\text{NUO}^+$ .

| Experiment <sup>a</sup> | 970 (979) $\omega(\text{OU})$ |         |        | 1119 (1134) $\omega(\text{NU})$ |                      |                              |
|-------------------------|-------------------------------|---------|--------|---------------------------------|----------------------|------------------------------|
|                         | LC RECP                       | SC RECP | AE     | LC RECP <sup>c</sup>            | SC RECP <sup>c</sup> | CASPT2, SC RECP <sup>c</sup> |
| PBE                     | 954.5                         | 962.4   | 962.4  |                                 |                      | 1023                         |
|                         | 1101.5                        | 1134.8  | 1134.8 |                                 |                      | 1134                         |
| BPBE                    | 952.0                         | 961.0   | 958.7  |                                 |                      |                              |
|                         | 1097.2                        | 1131.3  | 1124.1 |                                 |                      |                              |
| BLYP                    | 920.7                         | 931.4   | 932.8  | 932                             | 933                  |                              |
|                         | 1068.2                        | 1099.4  | 1095.7 | 1078                            | 1099                 |                              |
| B3LYP                   | 997.3                         | 998.6   | 997.2  | 1003                            | 999                  |                              |
|                         | 1167.8                        | 1186.2  | 1180.8 | 1174                            | 1184                 |                              |
| PBE0                    | 1038.0                        | 1035.0  | 1034.1 | 1042                            | 1038                 |                              |
|                         | 1210.6                        | 1230.2  | 1225.0 | 1218                            | 1229                 |                              |

<sup>a</sup> Reference<sup>49</sup>. <sup>b</sup> Experimental vibrational frequencies corrected for matrix effects are in parenthesis. <sup>c</sup> Reference<sup>30</sup>. <sup>d</sup> Reference<sup>52</sup>.

(like the popular PBE and BPBE) that give greater agreements with experimental values creates a situation in which it appears that the large-core RECP performs better or at least as well as the small-core RECP. Tables 2.1-2.3 contain direct comparisons of the vibrational wavenumbers for these triatomic compounds computed using the RECPs to the values obtained with a full AE scalar-relativistic one-electron Dirac equation solution. A cursory look reveals that the RECP with 60 core electrons always agrees better with the AE method, Figure 2.1. Occasions in which

the large-core RECP appears to give better agreement with the experiment can then be easily seen as error cancellation due to the hybrid density functionals (typically overestimating the vibrational wavenumbers) and the nature of the large-core RECP (typically leading to smaller vibrational wavenumbers than those obtained using the small-core RECP and AE method).

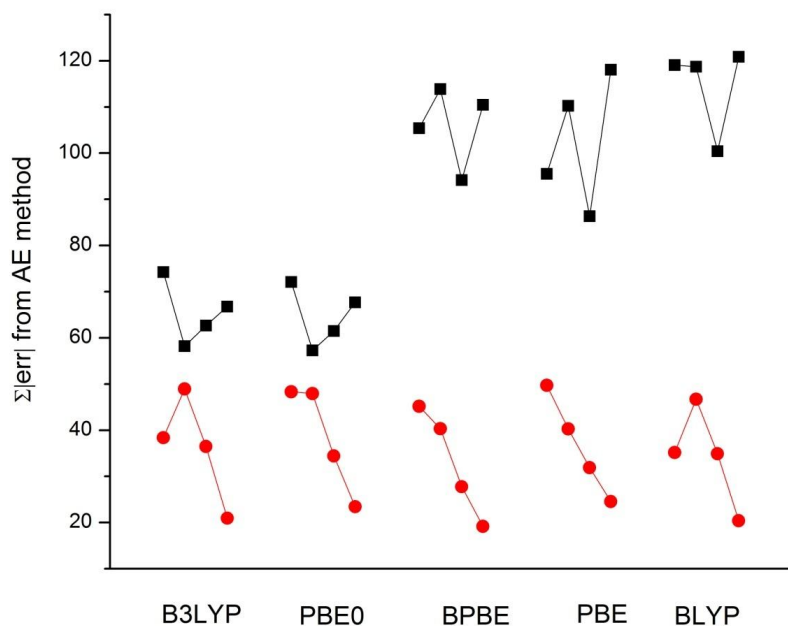


**Figure 2.1:** Absolute deviations of the vibrational wavenumbers,  $\text{cm}^{-1}$  for NUN,  $\text{NUO}^+$  and CUO computed using Stuttgart RECPs from the values obtained with the AE four-component method (small-core RECP in red circles and large-core RECP in black squares. Ligand basis sets are 6-31+G(d), 6-311+G(d), 6-311++G(3df, 3pd) and aug-cc-pVTZ from Left to Right).

**Table 2.3:** Calculated vibrational frequencies,  $\text{cm}^{-1}$ , of CUO.

| Experiment <sup>a</sup> |         |         | 872    | (881)                | $\omega(\text{OU})$  |                                 |  |
|-------------------------|---------|---------|--------|----------------------|----------------------|---------------------------------|--|
|                         |         |         | 1047   | (1062) <sup>b</sup>  | $\omega(\text{CU})$  |                                 |  |
|                         | LC RECP | SC RECP | AE     | LC RECP <sup>c</sup> | SC RECP <sup>c</sup> | CASPT2,<br>SC RECP <sup>d</sup> |  |
| PBE                     | 842.4   | 867.0   | 869.9  |                      |                      | 870                             |  |
|                         | 1076.6  | 1094.6  | 1086.5 |                      |                      | 1077                            |  |
| BPBE                    | 840.8   | 861.4   | 865.3  |                      |                      |                                 |  |
|                         | 1073.4  | 1088.0  | 1082.0 |                      |                      |                                 |  |
| BLYP                    | 821.3   | 839.7   | 846.1  | 819                  | 842                  |                                 |  |
|                         | 1051.5  | 1055.5  | 1050.8 | 1012                 | 1064                 |                                 |  |
| B3LYP                   | 871.3   | 884.6   | 890.6  | 876                  | 886                  |                                 |  |
|                         | 1114.1  | 1134.4  | 1130.6 | 1107                 | 1142                 |                                 |  |
| PBE0                    | 908.6   | 919.0   | 920.3  | 913                  | 917                  |                                 |  |
|                         | 1051.5  | 1181.6  | 1171.9 | 1147                 | 1183                 |                                 |  |

<sup>a</sup> Reference <sup>50</sup>. <sup>b</sup> Experimental vibrational frequencies corrected for matrix effects are in parenthesis. <sup>c</sup> Reference <sup>30</sup>. <sup>d</sup> Reference <sup>52</sup>.

**Vibrational Constants of  $\text{UO}_3$  and  $\text{UF}_6$ .** A distorted planar T-shaped structure was obtained for  $\text{UO}_3$  in all our calculations, Table 2.4 and Figure 2.2. The calculated  $2b_2$  and  $2a_1$  vibrations of  $\text{UO}_3$  and all the vibrational frequencies of the  $\text{UF}_6$  molecule are presented in Tables 2.5 and 2.6 respectively. The hybrid functionals, B3LYP (and PBE0 for  $\text{UF}_6$ ) show better agreement with experimental results than the GGA functionals used. This is in contrast to the situation observed

for the triatomic molecules above. The performance of the hybrid functionals in calculating the vibrational frequencies of  $\text{UO}_3$ ,  $\text{UF}_6$ ,  $\text{UO}_2\text{F}_2$  and  $\text{UO}_2(\text{OH})_2$  become relevant when comparing the reaction enthalpy changes calculated using hybrid and GGA functionals in the section below. A quick look at Table 2.5 shows that for the functional (B3LYP) that yields the best agreement with the experimental values, the calculations using the small-core RECP and the AE method outperform the calculations employing the large-core RECP. Generally, our computed vibrational wavenumbers are less than those obtained in the work of Marsden when basis sets of similar triple- $\zeta$  quality are used.<sup>30</sup> This may be due to different choices of optimization criteria (we use tight optimization and energy convergence criteria in all our calculations).

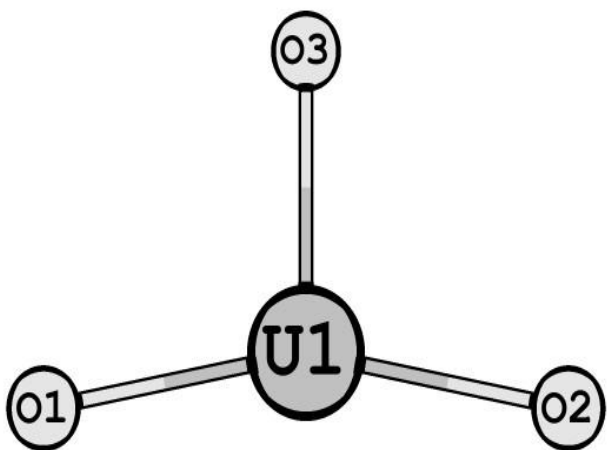


**Figure 2.2:** Distorted Planar T-Shaped Structure of  $\text{UO}_3$  (g)

The small-core RECP gives structural properties in better agreement with the AE method than the large-core RECP. As an example, the wavenumbers of the  $2a_1$  and  $2b_2$  vibrations of  $\text{UO}_3$  computed using the large-core RECP underestimate and overestimate the values obtained using the two other methods respectively. This relationship between the values computed using the

large-core and small-core RECPs is already obvious from the calculated bond-lengths and bond angles of the  $\text{UO}_3$  molecule as shown in Table 2.4. Although, the distorted planar T-shaped structure was obtained for  $\text{UO}_3$  in all our calculations, the calculations with the large-core RECP generally gave longer U-O<sub>3</sub> bonds and smaller O<sub>1</sub>-U-O<sub>3</sub> bond angles when compared with the small-core RECP and AE calculations. In addition, large-core RECP calculations result in shorter U-O<sub>1</sub>/O<sub>2</sub> bonds and larger O<sub>1</sub>-U-O<sub>2</sub> angles. Thus the smaller and larger values respectively of the  $2a_1$  (U=O<sub>3</sub>) and asymmetric  $2b_2$  (O<sub>1</sub>=U=O<sub>2</sub>) vibrational wavenumbers obtained with the large-core RECP are not unexpected. Also, the experimental splitting ( $106\text{ cm}^{-1}$ ) of the  $2b_2$  and  $2a_1$  vibrational modes is better reproduced by the small-core RECP and AE methods ( $110.14$  and  $102.48\text{ cm}^{-1}$  respectively) than by the large-core RECP ( $139.08\text{ cm}^{-1}$ ) when used with the hybrid functionals.

The vibrational frequencies of  $\text{UF}_6$  computed using the small-core RECP are in good agreement with the previous work of Hirao using a similar RECP and basis sets.<sup>53</sup> It can be seen in Table 2.6 that the large-core RECP gives an erroneous ordering or description of the  $t_{1u}$  and  $t_{2g}$  vibrations for all basis sets and density functionals used. This was also observed by Hirao and co-workers and also in the calculations of Hay and Martin as well as Schreckenbach and co-workers.<sup>1,17</sup> However, the correct wavenumber ordering of the  $t_{1u}$  and  $t_{2g}$  vibrations was obtained from calculations using the ZORA Hamiltonian with the BP86 functional and a triple-zeta basis set performed by Kovács and Konings.<sup>54</sup> The calculated vibrational wavenumbers of the  $\text{UF}_6$  molecule previously obtained by other groups are in agreement with the values shown in Table 2.6.<sup>1,17,53,55</sup> Surprisingly however, the erroneous ordering of the  $t_{1u}$  and  $t_{2g}$  vibrational wavenumbers was not observed in the large-core RECP calculations of the Marsden group.<sup>30</sup>

**Table 2.4:** Calculated<sup>a</sup> bond lengths (in Å) and bond angles of gaseous UO<sub>3</sub>.

|       | LC RECP |       | SC RECP |       | AE    |       |
|-------|---------|-------|---------|-------|-------|-------|
| PBE   | 1.798   | 1.863 | 1.820   | 1.858 | 1.823 | 1.859 |
|       | 100.4   | 159.3 | 101.7   | 156.7 | 102.4 | 155.2 |
| BPBE  | 1.799   | 1.864 | 1.821   | 1.858 | 1.827 | 1.862 |
|       | 100.5   | 159.0 | 101.9   | 156.2 | 102.9 | 154.2 |
| BLYP  | 1.817   | 1.881 | 1.844   | 1.876 | 1.847 | 1.877 |
|       | 101.8   | 156.5 | 104.3   | 151.3 | 105.0 | 150.1 |
| B3LYP | 1.780   | 1.852 | 1.803   | 1.848 | 1.807 | 1.850 |
|       | 99.8    | 160.4 | 100.5   | 159.0 | 101.1 | 157.8 |
| PBE0  | 1.761   | 1.834 | 1.780   | 1.830 | 1.783 | 1.832 |
|       | 98.5    | 163.1 | 98.9    | 162.3 | 99.4  | 161.3 |

<sup>a</sup> The parameters are ordered as  $r(\text{U-O}_1/\text{O}_2)$ ,  $r(\text{U-O}_3)$ ,  $\angle\text{O}_1\text{-U-O}_3$  and  $\angle\text{O}_1\text{-U-O}_2$  respectively

**Table 2.5:** Calculated vibrational frequencies,  $\text{cm}^{-1}$ , of  $\text{UO}_3$ .

| Experiment <sup>a</sup> | 760.3 (768)              |         | 2a <sub>1</sub> (U=O <sub>3</sub> )                 |                      |                      |                       |
|-------------------------|--------------------------|---------|---|----------------------|----------------------|-----------------------|
|                         | 865.3 (875) <sup>b</sup> |         | 2b <sub>2</sub> (O <sub>1</sub> =U=O <sub>2</sub> ) |                      |                      |                       |
|                         | LC RECP                  | SC RECP | AE  | LC RECP <sup>c</sup> | SC RECP <sup>c</sup> | ADF/ZORA <sup>d</sup> |
| PBE                     | 727.1                    | 751.5   | 757.7   |                      |                      | 758.3                 |
|                         | 854.0                    | 843.6   | 843.6   |                      |                      | 849.0                 |
| BPBE                    | 726.7                    | 751.6   | 755.0   |                      |                      |                       |
|                         | 853.9                    | 841.7   | 838.8   |                      |                      |                       |
| BLYP                    | 700.5                    | 729.4   | 736.7   | 712                  | 727                  |                       |
|                         | 823.3                    | 806.7   | 809.2   | 840                  | 809                  |                       |
| B3LYP                   | 756.2                    | 775.3   | 781.6   | 766                  | 779                  |                       |
|                         | 891.0                    | 879.3   | 879.9   | 906                  | 891                  |                       |
| PBE0                    | 788.8                    | 803.9   | 809.7   | 798                  | 812                  |                       |
|                         | 927.6                    | 919.5   | 918.0   | 942                  | 935                  |                       |

<sup>a</sup> Experimental vibrational wavenumbers corrected for matrix effects are in parenthesis. <sup>b</sup> Reference <sup>56</sup>. <sup>c</sup> Reference <sup>30</sup>. <sup>d</sup> Reference <sup>21</sup>.

Several general trends observed in the calculated wavenumbers of the triatomic molecules and previously by other workers were also observed in the computed values of the vibrational frequencies of  $\text{UO}_3$ ,  $\text{UF}_6$ ,  $\text{UO}_2\text{F}_2$ , and  $\text{UO}_2(\text{OH})_2$ . The GGA functionals under-bind the atoms in these molecules leading to vibrational frequencies lower than those obtained with hybrid functionals. Also, of the GGA functionals considered, the BLYP functional systematically underestimates the other GGAs (PBE and BPBE) by approximately  $10\text{-}30 \text{ cm}^{-1}$ . This is most

noticeable for stretching vibrations. The small-core RECP is always in better agreement with the four-component scalar-relativistic AE method employed in this work. The deviations of the vibrational wavenumbers of  $\text{UO}_3$  and  $\text{UF}_6$  computed with the large-core and small-core RECPs from those obtained using the AE method are presented in Figure 2.3.

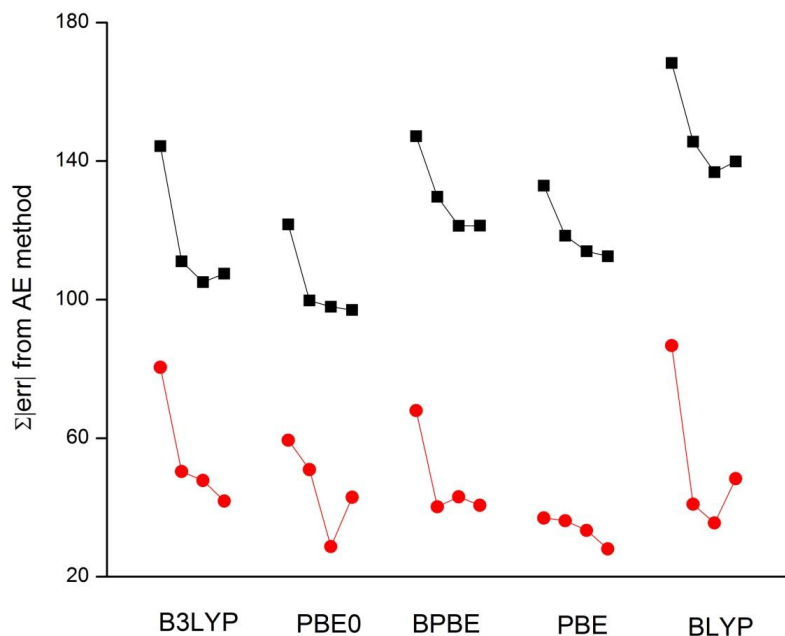


**Figure 2.3:** Absolute deviations of the vibrational wavenumbers,  $\text{cm}^{-1}$ , for  $\text{UO}_3$  and  $\text{UF}_6$  computed using Stuttgart RECPs from the values obtained with the AE four-component method (small-core RECP in red circles and large-core RECP in black squares. Ligand basis sets are 6-31+G(d), 6-311+G(d), 6-311++G (3df, 3pd) and aug-cc-pVTZ from left to right).

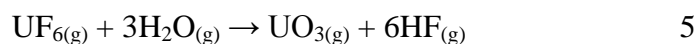
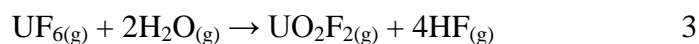
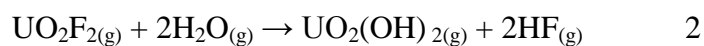
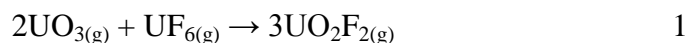
**Table 2.6:** Calculated vibrational frequencies,  $\text{cm}^{-1}$ , of  $\text{UF}_6$ .

|                         | $t_{2u}$ | $t_{1u}$ | $t_{2g}$ | $e_g$ | $t_{1u}$ | $a_{1g}$ |
|-------------------------|----------|----------|----------|-------|----------|----------|
| Experiment <sup>a</sup> | 143      | 186      | 200      | 540   | 634      | 672      |
| Large-core RECP         |          |          |          |       |          |          |
| B3LYP                   | 143.5    | 187.9    | 184.2    | 515.2 | 613.4    | 645.8    |
| PBE0                    | 148.5    | 189.8    | 188.5    | 525.6 | 631.3    | 669.4    |
| PBE                     | 139.5    | 179.7    | 173.5    | 501.1 | 591.4    | 609.1    |
| BPBE                    | 140.3    | 180.6    | 173.5    | 500.4 | 590.7    | 608.2    |
| BLYP                    | 136.8    | 178.5    | 170.2    | 490.4 | 576.0    | 591.7    |
| Small-core RECP         |          |          |          |       |          |          |
| B3LYP                   | 137.4    | 181.6    | 191.9    | 527.3 | 610.3    | 654.5    |
| PBE0                    | 138.7    | 182.2    | 193.0    | 537.0 | 627.6    | 676.4    |
| PBE                     | 130.0    | 173.1    | 182.6    | 516.4 | 590.8    | 624.4    |
| BPBE                    | 130.1    | 173.6    | 183.3    | 516.4 | 590.3    | 623.7    |
| BLYP                    | 129.6    | 172.3    | 183.2    | 506.7 | 575.8    | 607.9    |
| AE-4-Component          |          |          |          |       |          |          |
| B3LYP                   | 137.7    | 183.0    | 198.1    | 536.5 | 618.1    | 662.7    |
| PBE0                    | 139.1    | 184.5    | 199.8    | 545.5 | 635.8    | 683.6    |
| PBE                     | 130.3    | 175.6    | 187.4    | 525.4 | 599.1    | 632.1    |
| BPBE                    | 131.9    | 176.8    | 189.4    | 520.9 | 593.5    | 626.6    |
| BLYP                    | 130.0    | 175.4    | 188.6    | 517.0 | 585.7    | 617.2    |

<sup>a</sup> Reference <sup>57</sup>

Generally, the vibrational wavenumbers computed using the small-core RECP tend to converge toward the values computed with the AE method as the quality of the basis set is increased. The structural parameters computed with the small-core RECP with a triple-zeta basis set can be used in lieu of an AE calculation with some degree of confidence, Figures 2.1 and 2.3, Tables 2.1-2.6.

**Enthalpy of Reaction.** The enthalpy changes associated with the thermochemical reactions studied in this work have been reported experimentally by Privalov and co-workers as -311 kJ/mol, 65 kJ/mol, 187 kJ/mol, -184 kJ/mol and 435 kJ/mol for reactions 1-5 respectively.<sup>19</sup>



It should be noted that there are uncertainties of 15-50 kJ/mol associated with the experimental data obtained. There have been several attempts to calculate the enthalpy changes associated with these reactions. The Privalov group also calculated the reaction enthalpy changes using MP2, B3LYP and CCSD(T) with the Stuttgart small-core RECP. The inclusion of diffuse functions in the basis sets was found to result in more accurate enthalpy changes by the Marsden group<sup>30</sup>. Shamov and co-workers computed the enthalpy changes of reactions 1, 4 and 5, among others using the same AE method used in this work<sup>21</sup>. They compared the AE reaction enthalpy changes to those obtained using the small-core RECP and ZORA/ADF methods. Actually, a

close examination of Table 2.7 in their work reveals great agreement between the results obtained with the AE method, ZORA/ADF method and the small-core RECP when larger basis sets are used.

The calculated enthalpy changes obtained using the AE method with the triple-zeta quality L2 basis and the Stuttgart RECPs with the aug-cc-pVTZ basis set used on oxygen, fluorine and hydrogen are presented in Tables 2.7. From Figure 2.4, it is obvious that the enthalpy changes calculated using the small-core RECP are in much better agreement with the AE method than those obtained using the large-core RECP. The small-core and large-core RECP enthalpy changes are generally within 0-50 and 10-100 kJ/mol of the values obtained using the AE method, respectively. The enthalpy changes computed with the small-core RECP and AE method converge dramatically towards the experimental data as the number of diffuse functions in the basis set is increased. This is also observed for calculations in which the large-core RECP was used, albeit not uniformly. This is in line with previous observation of improvements in the calculated enthalpy change when diffuse functions are added to the basis set.

The reaction enthalpy changes calculated using hybrid functionals with the small-core RECP and AE method for reactions 1, 2 and 4 are in good agreement with the experimental data. Privalov and co-workers suggested that the rather large errors in the calculated values obtained for reactions 2, 3 and 5 arise from the poor description of HF in these reactions. This was refined by Marsden and co-workers as possibly due to the performance of the functionals in calculating

**Table 2.7:** Calculated enthalpy changes<sup>\*</sup>, kJ/mol for Reactions 1-5 computed using Stuttgart RECPs and the AE four-component method.

| Reaction | Method     | Functional |        |        |        |        |
|----------|------------|------------|--------|--------|--------|--------|
|          |            | B3LYP      | PBE0   | PBE    | BPBE   | BLYP   |
| 1        | LC RECP    | -326.5     | -355.8 | -218.8 | -218.6 | -210.5 |
|          | SC RECP    | -281.4     | -305.9 | -197.4 | -198.8 | -191.5 |
|          | AE-Method  | -275.9     | -302.0 | -196.8 | -198.4 | -187.7 |
|          | Experiment | -311       |        |        |        |        |
| 2        | LC RECP    | 106.7      | 103.0  | 98.9   | 100.0  | 102.5  |
|          | SC RECP    | 95.9       | 91.2   | 89.5   | 90.9   | 95.0   |
|          | AE-Method  | 95.2       | 90.6   | 89.8   | 92.5   | 94.4   |
|          | Experiment | 65         |        |        |        |        |
| 3        | LC RECP    | 181.4      | 166.6  | 220.7  | 197.2  | 218.4  |
|          | SC RECP    | 248.4      | 227.7  | 282.7  | 261.8  | 286.8  |
|          | AE-Method  | 274.8      | 248.4  | 312.6  | 279.7  | 321.4  |
|          | Experiment | 187        |        |        |        |        |
| 4        | LC RECP    | -147.2     | -158.2 | -120.7 | -108.0 | -112.0 |
|          | SC RECP    | -169.0     | -175.6 | -151.1 | -139.4 | -144.2 |
|          | AE-Method  | -180.1     | -184.6 | -164.9 | -146.5 | -160.1 |
|          | Experiment | -184       |        |        |        |        |
| 5        | LC RECP    | 435.5      | 427.7  | 440.3  | 405.2  | 432.9  |
|          | SC RECP    | 513.3      | 494.5  | 524.3  | 492.1  | 526.0  |

|            |       |       |       |       |       |
|------------|-------|-------|-------|-------|-------|
| AE-Method  | 550.1 | 523.7 | 567.4 | 518.8 | 575.9 |
| Experiment | 435   |       |       |       |       |

\* Experimental values are from reference <sup>19</sup>. The aug-cc-pVTZ ligand basis was used in the RECP calculations while the triple-zeta L2 basis was used in the AE calculations.

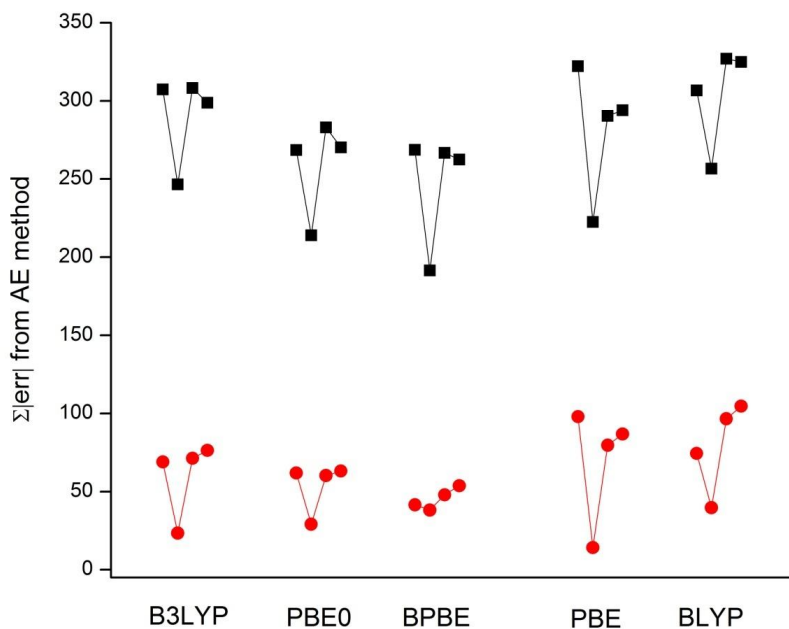


**Figure 2.4:** Absolute deviations of the enthalpy changes, kJ/mol for reactions 1-5 computed using Stuttgart RECPs from the values obtained with the AE four-component method (small-core RECP in red circles and large-core RECP in Black Squares). Ligand basis sets are 6-31+G(d), 6-311+G(d), 6-311++G (3df, 3pd) and aug-cc-pVTZ from left to right)

the electron affinity of the F atom.<sup>30</sup> It is worthy of note that the calculations that employ the small-core RECP and AE method perform very well for the reaction with no fluoride involved (Reaction 4). It could be argued that treatment of the fluorides is a pathologic problem for these methods. The large discrepancies between the experimental values and those obtained using hybrid functionals with small-core RECP and AE method is an indication of the poor performance of approximate DFT in predicting the enthalpy changes of Reactions 2, 3, and 5. It has been previously shown that CCSD(T) calculations using either a four-component scalar-relativistic method with all-electron basis sets or the small-core RECP give results in greater agreement with experimental values.<sup>21,30</sup> Although, the energy changes obtained in calculations using the large-core RECP give exceptional agreement with experimental values for Reactions 3 and 5, it is obvious that this is due to fortuitous error cancellation. In any case, the right comparison is between the values obtained with the AE and RECP methods and not between the results of the RECP methods and the experimental values.

## **Conclusions**

We have carried out a comparative study of the performance of the Stuttgart small-core and large-core RECPs against an all-electron method that employs DFT and a four-component one-electron scalar-relativistic approximation. The vibrational wavenumbers of several uranium compounds and the enthalpy changes associated with the thermochemical reactions of several uranium fluorides and oxyfluorides were calculated using the RECPs and the AE method.

The structural parameters and reaction enthalpy changes computed using DFT and the four-component one-electron scalar relativistic AE method are the ‘correct DFT’ values. Granted these values may deviate significantly from experimental data as has been previously shown, the

values computed using the small-core RECP are generally in greater agreement than those obtained using the large core RECP. The importance of the 5s, 5p and 5d orbitals in describing the chemistry of the selected actinide compounds have been made obvious. As has been previously discussed this somewhat counterintuitive result can be understood as follows. In ECP methods, pseudo-orbitals are used for the valence orbitals that, by construction, lack the nodal structure (core wiggles) arising from the orthogonality requirements with respect to the core shells.<sup>4</sup> By adding the 5s, 5p and 5d orbitals to the calculations, we effectively reintroduce the outermost such core wiggle to the higher orbitals. This core wiggle may well stretch into regions of space that are relevant to bonding, and it would thus be required for an accurate description of the chemistry of these systems. We should note that the neglect of core-polarization and correlation has been put forward as an alternative explanation of the differences between large- and small-core ECPs.<sup>28</sup>

Discrepancies between the experimental data and the values computed with the AE could be due to non-suitability of approximate DFT in studying the selected system, significant spin-orbit effects or experimental errors. Instances in which the large-core RECP appear to give better results than the small-core RECP and AE method are in our opinion due to error cancellations (basis sets, functionals and RECPs errors). One could, of course, argue that accurate results obtained through error cancellations are still valuable results. While this argument has its merits, there is no guarantee, as far as we can tell, that this error cancellation is transferable between different types of uranium compounds or to different oxidation states of the uranium atom. Thus we conclude based on the findings in this work that the use of large-core RECPs for calculations on actinide complexes is not recommended anymore.

## References

1. Schreckenbach, G.; Hay, P. J.; Martin, R. L., *J. Comput. Chem.* **1999**, *20*, 70.
2. Vallet, V.; Macak, P.; Wahlgren, U.; Grenthe, I., *Theor. Chem. Acc.* **2006**, *115*, 145.
3. Kaltsoyannis, N.; Hay, P. J.; Li, J.; Blaudeau, J. P.; Bursten, B. E., Theoretical Studies of the Electronic Structure of Compounds of the Actinides. In *The Chemistry of the Actinide and Transactinide Elements, 3rd ed*, 3 ed.; Morss, L. R.; Edelstein, N. M.; Fuger, J.; Katz, J. J., Eds. Springer: Dordrecht, The Netherlands, 2006; Vol. 3, pp 1893.
4. Schreckenbach, G.; Shamov, G. A., *Acc. Chem. Res.* **2009**, in print 10.1021/ar800271r.
5. Dirac, P. A. M., *Proc. R. Soc. London, Ser. A* **1928**, *117*, 610.
6. Douglas, M.; Kroll, N. M., *Ann. Phys.* **1974**, *82*, 89.
7. Hess, B. A., *Phys. Rev. A: At. Mol. Opt. Phys.* **1986**, *33*, 3742.
8. Reiher, M., *Theor. Chem. Acc.* **2006**, *116*, 241.
9. Faas, S.; Snijders, J. G.; van Lenthe, J. H.; van Lenthe, E.; Baerends, E. J., *Chem. Phys. Lett.* **1995**, *246*, 632.
10. van Lenthe, E., *J. Comput. Chem.* **1999**, *20*, 51.
11. van Lenthe, E.; Baerends, E. J.; Snijders, J. G., *J. Chem. Phys.* **1993**, *99*, 4597.
12. Peralta, J. E.; Batista, E. R.; Scuseria, G. E.; Martin, R. L., *J. Chem. Theory Comput.* **2005**, *1*, 612.
13. Cao, X. Y.; Moritz, A.; Dolg, M., *Chem. Phys.* **2008**, *343*, 250.
14. van Wüllen, C., *J. Comput. Chem.* **1999**, *20*, 51.
15. Infante, I.; Visscher, L., *J. Comput. Chem.* **2004**, *25*, 386.
16. Garcia-Hernandez, M.; Lauterbach, C.; Krüger, S.; Matveev, A.; Rösch, N., *J. Comput. Chem.* **2002**, *23*, 834.

17. Hay, P. J.; Martin, R. L., *J. Chem. Phys.* **1998**, *109*, 3875.
18. Shamov, G. A.; Schreckenbach, G., *J. Phys. Chem. A* **2005**, *109*, 10961.
19. Privalov, T.; Schimmelpfennig, B.; Wahlgren, U.; Grenthe, I., *J. Phys. Chem. A* **2002**, *106*, 11277.
20. Schimmelpfennig, B.; Privalov, T.; Wahlgren, U.; Grenthe, I., *J. Phys. Chem. A* **2003**, *107*, 9705.
21. Shamov, G. A.; Schreckenbach, G.; Vo, T. N., *Chem. Eur. J.* **2007**, *13*, 4932.
22. Rotzinger, F. P., *Chem. Eur. J.* **2007**, *13*, 800.
23. Straka, M.; Kaupp, M., *Chem. Phys.* **2005**, *311*, 45.
24. de Jong, W. A.; Harrison, R. J.; Nichols, J. A.; Dixon, D. A., *Theor. Chem. Acc.* **2001**, *107*, 22.
25. Batista, E. R.; Martin, R. L.; Hay, P. J., *J. Chem. Phys.* **2004**, *121*, 11104.
26. Vetere, V.; Maldivi, P.; Adamo, C., *J. Comput. Chem.* **2003**, *24*, 850.
27. Tsushima, S.; Uchida, Y.; Reich, T., *Chem. Phys. Lett.* **2002**, *357*, 73.
28. Lim, I. S.; Stoll, H.; Schwerdtfeger, P., *J. Chem. Phys.* **2006**, *124*, 034107.
29. Clavaguera-Sarrio, C.; Ismail, N.; Marsden, C. J.; Begue, D.; Pouchan, C., *Chem. Phys.* **2004**, *302*, 1.
30. Iche-Tarrat, N.; Marsden, C. J., *J. Phys. Chem. A* **2008**, *112*, 7632.
31. Hay, P. J.; Wadt, W. R., *J. Chem. Phys.* **1985**, *82*, 270.
32. Dylla, K. G., *J. Chem. Phys.* **1994**, *100*, 2118.
33. Laikov, D. N.; Ustynyuk, Y. A., *Russ. Chem. Bull.* **2005**, *54*, 820.
34. Perdew, J. P.; Burke, K.; Ernzerhof, M., *Phys. Rev. Lett.* **1996**, *77*, 3865.
35. Perdew, J. P.; Burke, K.; Ernzerhof, M., *Phys. Rev. Lett.* **1997**, *78*, 1396.

36. Becke, A. D., *Phys. Rev. A: At. Mol. Opt. Phys.* **1988**, 38, 3098.
37. Lee, C. T.; Yang, W. T.; Parr, R. G., *Phys. Rev. B: Condens. Matter* **1988**, 37, 785.
38. Becke, A. D., *J. Chem. Phys.* **1993**, 98, 5648.
39. Stephens, P. J.; Devlin, F. J.; Chabalowski, C. F.; Frisch, M. J., *J. Phys. Chem.* **1994**, 98, 11623.
40. Laikov, D. N. *Priroda Code 6*. 2006.
41. Shamov, G. A.; Schreckenbach, G., *J. Phys. Chem. A* **2006**, 110, 9486.
42. Laikov, D. N., *Chem. Phys. Lett.* **2005**, 416, 116.
43. Küchle, W.; Dolg, M.; Stoll, H.; Preuss, H., *Mol. Phys.* **1991**, 74, 1245.
44. Küchle, W.; Dolg, M.; Stoll, H.; Preuss, H., *J. Chem. Phys.* **1994**, 100, 7535.
45. Frisch, M. J. T., G. W.; Schlegel, H. B.; Scuseria, G. E.; Robb, M. A.; Cheeseman, J. R.; Montgomery, Jr., J. A.; Vreven, T.; Kudin, K. N.; Burant, J. C.; Millam, J. M.; Iyengar, S. S.; Tomasi, J.; Barone, V.; Mennucci, B.; Cossi, M.; Scalmani, G.; Rega, N.; Petersson, G. A.; Nakatsuji, H.; Hada, M.; Ehara, M.; Toyota, K.; Fukuda, R.; Hasegawa, J.; Ishida, M.; Nakajima, T.; Honda, Y.; Kitao, O.; Nakai, H.; Klene, M.; Li, X.; Knox, J. E.; Hratchian, H. P.; Cross, J. B.; Bakken, V.; Adamo, C.; Jaramillo, J.; Gomperts, R.; Stratmann, R. E.; Yazyev, O.; Austin, A. J.; Cammi, R.; Pomelli, C.; Ochterski, J. W.; Ayala, P. Y.; Morokuma, K.; Voth, G. A.; Salvador, P.; Dannenberg, J. J.; Zakrzewski, V. G.; Dapprich, S.; Daniels, A. D.; Strain, M. C.; Farkas, O.; Malick, D. K.; Rabuck, A. D.; Raghavachari, K.; Foresman, J. B.; Ortiz, J. V.; Cui, Q.; Baboul, A. G.; Clifford, S.; Cioslowski, J.; Stefanov, B. B.; Liu, G.; Liashenko, A.; Piskorz, P.; Komaromi, I.; Martin, R. L.; Fox, D. J.; Keith, T.; Al-Laham, M. A.; Peng, C. Y.; Nanayakkara, A.; Challacombe, M.; Gill, P. M. W.; Johnson, B.; Chen, W.; Wong, M. W.; Gonzalez, C.; and Pople, J. A. *Gaussian 03, Revision C.02*. 2004.

46. Bylaska, E. J. d. J., W. A.; Govind N.; Kowalski K.; Straatsma, T. P.; Valiev, M.; Wang, D.; Apra, E.; Windus, T. L.; Hammond, J.; Nichols, P.; Hirata, S.; Hackler, M. T.; Zhao, Y.; Fan, P. -D.; Harrison, R. J.; Dupuis, M.; Smith, D. M. A.; Nieplocha, J.; Tipparaju, V.; Krishnan, M.; Wu, Q.; Van Voorhis, T.; Auer, A. A.; Nooijen, M.; Brown, E.; Cisneros, G.; Fann, G. I.; Fruchtl, H.; Garza, J.; Hirao, K.; Kendall, R.; Nichols, J. A.; Tsemekhman, K.; Wolinski, K.; Anchell, J.; Bernholdt, D.; Borowski, P.; Clark, T.; Clerc, D.; Dachsel, H.; Deegan, M.; Dyall, K.; Elwood, D.; Glendening, E.; Gutowski, M.; Hess, A.; Jaffe, J.; Johnson, B.; Ju, J.; Kobayashi, R.; Kutteh, R.; Lin, Z.; Littlefield, R.; Long, X.; Meng, B.; Nakajima, T.; Niu, S.; Pollack, L.; Rosing, M.; Sandrone, G.; Stave, M.; Taylor, H.; Thomas, G.; van Lenthe, J.; Wong, A.; and Zhang, Z. NWChem, A Computational Chemistry Package for Parallel Computers, Version 5.1". 2007.
47. Kendall, R. A.; Apra, E.; Bernholdt, D. E.; Bylaska, E. J.; Dupuis, M.; Fann, G. I.; Harrison, R. J.; Ju, J. L.; Nichols, J. A.; Nieplocha, J.; Straatsma, T. P.; Windus, T. L.; Wong, A. T., *Comput. Phys. Commun.* **2000**, *128*, 260.
48. Hunt, R. D.; Yustein, J. T.; Andrews, L., *J. Chem. Phys.* **1993**, *98*, 6070.
49. Zhou, M. F.; Andrews, L., *J. Chem. Phys.* **1999**, *111*, 11044.
50. Andrews, L.; Liang, B. Y.; Li, J.; Bursten, B. E., *Angew. Chem. Int. Ed.* **2000**, *39*, 4565.
51. Pyykkö, P.; Li, J.; Runeberg, N., *J. Phys. Chem.* **1994**, *98*, 4809.
52. Gagliardi, L. A.; Roos, B. O., *Chem. Phys. Lett.* **2000**, *331*, 229.
53. Han, Y. K.; Hirao, K., *J. Chem. Phys.* **2000**, *113*, 7345.
54. Kovács, A.; Konings, R. J. M., *J. Mol. Struc.-Theochem* **2004**, *684*, 35.
55. Han, Y. K., *J. Comput. Chem.* **2001**, *22*, 2010.
56. Zhou, M. F.; Andrews, L.; Ismail, N.; Marsden, C., *J. Phys. Chem. A* **2000**, *104*, 5495.

57. McDowell, R. S.; Asprey, L. B.; Paine, R. T., *J. Chem. Phys.* **1974**, *61*, 3571.

## Preface to Chapter 3

This chapter is based on a manuscript published in the journal “*Journal of Physical Chemistry A*”. The full citation of the paper is as follows:

Samuel O. Odoh and Georg Schreckenbach, “Theoretical study of the structural properties of Pu(IV) and Pu(VI) Complexes” *Journal of Physical Chemistry A*, **2010**, 114, 1957.

Density functional theory (DFT) is a single reference approach. The implication of this is that it is not a fully rigorous approach for studying multi-reference systems, i.e. systems in which the ground electronic state contains two or more nearly degenerate determinants. Open-shell actinide ions such as Pu(VI) and Pu(IV) are  $f^2$  and  $f^4$  systems.

All the calculations in the published manuscript and compiled in this chapter were carried out by Samuel O. Odoh. The manuscript was prepared together with Prof. Georg Schreckenbach.

Copyright permissions have been obtained from the American Chemical Society and the other authors.

# Chapter 3: Theoretical Study of the Structural Properties of Plutonium IV and VI Complexes

## Abstract

The structural properties of several plutonium (IV) and (VI) complexes have been examined in the gaseous and aqueous phases using Kohn-Sham density functional theory calculations with scalar relativistic effective core potentials and the polarizable continuum solvation model. The aquo and nitrate complexes of  $\text{PuO}_2^{2+}$  and  $\text{Pu}^{4+}$  were considered in addition to the aquo-chloro complexes of  $\text{PuO}_2^{2+}$ . The nitrate and chloro- complexes formed with triphenylphosphine oxide (TPPO) and tributylphosphate (TBP) respectively were also studied. The structural parameters of the plutonyl complexes were compared to their uranyl and neptunyl analogues. The bond lengths and vibrational frequencies of the plutonyl complexes can generally be computed with sufficient accuracy with the pure PBE density functional with shorter bond lengths being predicted by the B3LYP functional. The structural parameters of the  $[\text{PuO}_2\text{Cl}_2\text{L}_2]$  systems formed with TPPO and TBP as well as the aqueous  $[\text{PuO}_2\text{Cl}_2(\text{H}_2\text{O})_3]$  complex are matched to previous experimental results. Overall, the inclusion of ligands in the equatorial region results in significant changes in the stretching frequency of the plutonyl group. The structural features of the plutonyl (VI) systems are rather similar to those of their  $5f^0$  uranyl and  $5f^1$  neptunyl counterparts. For the Pu(IV) aquo and nitrate complexes, the average of the calculated Pu-OH<sub>2</sub> and Pu-O<sub>nitrate</sub> bond lengths are generally within 0.04 Å of the reported experimental values. Overall Kohn-Sham DFT can be used successfully in predicting the structures of this diverse set of Pu(VI) and Pu(IV) complexes.

## Introduction

The speciation and mobility of actinide complexes in the environment depend on the prevailing pH, ligand concentration as well as the presence of oxidizing agents. It is therefore important to study the structural, redox and photochemical properties of actinide compounds using experimental and theoretical approaches. On the theoretical side, there has been tremendous progress in the use of quantum mechanical methods in probing the structure and electronic properties of actinide complexes.<sup>1-24</sup> The incorporation of relativistic effects, electron correlation, and when needed, solvation effects have drastically increased the accuracy and utility of such methods. Increasingly, Kohn-Sham density functional theory (DFT) has emerged as a method of choice for carrying out calculations on uranium (VI) complexes as a result of its speed, good treatment of electron correlation and the strongly single-reference character of these  $5f^0$  compounds. The presence of valence shell electrons in  $5f^n$  ( $n \neq 0$ ) complexes often results in a multitude of low-lying states that are nearly degenerate with the electronic ground state. In such cases, there is the possibility that single reference approaches will predict the wrong electronic ground state, or would have large spin contamination or poor energy convergence attributes with the 5f-electrons hopping between the nearly-degenerate orbitals. For a sizeable fraction of actinide complexes, the wavefunction is distinctly multi-reference in character making single reference approaches like Kohn-Sham DFT (simply DFT from here onwards) at best less rigorous or at worst unsuitable. Increasingly however, scalar-relativistic DFT has been shown to successfully predict the structural properties, thermochemistry and bonding of open-shell actinide systems.<sup>20, 22, 25-27</sup> This has often been attributed to the atomic character of the occupied 5f orbitals ensuring little difference in the general chemical bonding schemes of the different electronic states formed by the different 5f occupations.<sup>27</sup>

For the case of the plutonyl (VI) moiety,  $\text{PuO}_2^{2+}$ , DFT predicts the  $^3\text{H}_g$  ground state in agreement with more sophisticated correlated ab initio methods.<sup>28</sup> This, in addition makes the accuracy of DFT in predicting the geometrical structures of plutonyl complexes unsurprising.<sup>25-26, 29</sup> It should however be noted that the calculated structural parameters obtained from scalar-relativistic DFT are accurate even though the true  $^3\text{H}_g$  ground state is an admixture of equal proportions of two determinants each with a normalization factor of  $1/\sqrt{2}$ . The calculated structural properties for plutonyl complexes obtained using DFT can therefore be compared to available experimental data to further assess the performance of density functionals in predicting their speciation and equilibrium structures. In their calibration work, Ismail et al.<sup>28</sup> obtained similar  $\text{Pu}=\text{O}_{yl}$  bond lengths and vibrational frequencies for the  $\text{PuO}_2^{2+}$  group with the B3LYP functional and the approximate quadratic coupled cluster approach. Indeed, it appears that the structural features obtained using the B3LYP functional are also in very good agreement with those obtained with the scalar relativistic and spin-orbit corrected variants of the complete active space, CASSCF, approach after correcting for dynamic correlations using second-order perturbation theory, CASPT2.<sup>30</sup> A more general work by Clavaguera-Sarrio et al.<sup>27</sup> found out that the description of the electronic ground state, structural and vibrational properties of open-shell actinide systems are described by DFT with accuracy on par with those obtained with the CASPT2 approach. The structures of carbonate and aquo complexes of Pu(VI) have also been examined using DFT in conjunction with perturbation theory and coupled cluster approaches.<sup>20, 25-26, 31</sup> These works showed that DFT methods can sufficiently provide a quantitative estimate of the equilibrium number of equatorial ligands in acidic aqueous conditions.

Plutonium complexes are significantly less studied with experimental techniques than their uranium counterparts for reasons of toxicity and safety. The possibility of producing

nuclear weapons from stolen plutonium is viewed as a significant risk by many global powers. Theoretical calculations on plutonium complexes can then be used to either complement available experimental data or to bridge the gaps in our knowledge of these complexes. On the experimental side, Gaunt et al.<sup>32</sup> have recently characterized the crystal structure of the plutonyl (VI) dinitrate,  $[\text{PuO}_2(\text{NO}_3)_2(\text{H}_2\text{O})_2]$ , complex using X-ray diffraction and spectroscopic methods. In contrast, they found only negligible formation of the dinitrate in aqueous solutions with the mononitrates,  $[\text{PuO}_2(\text{NO}_3)(\text{H}_2\text{O})_x]^+$ , being dominant despite the weak nitrate complexation by the plutonyl entity. There is significantly less theoretical data on plutonyl nitrate complexes in contrast to their counterpart aquo,<sup>20, 25, 29</sup> carbonate,<sup>33</sup> hydroxo<sup>31</sup> and plutonium (VI) fluoride<sup>4, 9</sup> complexes. This is most likely due to the weak complexation of nitrates by actinyl groups in general despite the importance of nitrates and nitric acid in industrial nuclear processes.

There is however available experimental data on the structures of actinide (IV) nitrate  $[\text{An}(\text{NO}_3)_n(\text{H}_2\text{O})_m]^{4-n}$ , complexes making assessment of the performance of theoretical methods easier.<sup>34-35</sup> The  $\text{Pu}^{4+}$  cation has a  $5f^4$  electronic configuration and is known to coordinate with 5 or 6 nitrate ligands with both species existing in aqueous solutions at very high nitrate concentrations. Recently, Horowitz and Marston used scalar-relativistic calculations to accurately predict the structures of U(IV), Np(IV) and Pu(IV) aquo complexes.<sup>29</sup> In addition, they obtained relatively accurate redox potentials for the Pu(III)/Pu(IV) redox couple using spin-orbit corrected DFT. This and other reports<sup>20, 25-27, 31</sup> would suggest that DFT should be able to at the least correctly predict the structural features and to some extent correctly predict the speciation of Pu(IV) nitrate complexes.

In this work, the reliability of DFT calculations in predicting the geometrical features and vibrational frequencies of diverse gaseous and aqueous phase plutonium (IV) and (VI)

complexes is further examined. The aim is to extend the application of DFT in predicting the structures of plutonium complexes beyond the extensively examined aquo, carbonate and hexahalide complexes. This is done by appraising its capability in studying other plutonium complexes not extensively studied using theoretical approaches. In this work, the structures of the pentaquo, aquo-chloro and nitrate complexes of  $\text{PuO}_2^{2+}$  are examined. The dinitrate and dichloro complexes formed with organic ligands such as tributylphosphate (TBP) and triphenylphosphine oxide (TPPO) were also examined in addition to the  $[\text{AnO}_2\text{Cl}_4]^{2-}$  and their cesium salts,  $\text{Cs}_2[\text{AnO}_2\text{Cl}_4]$  (An=U, Np and Pu). These diverse ligand environments should allow us to gain insights into the nature of the Pu-ligand interaction, the vibrational spectra of these molecules as well as the ability of DFT to provide sufficiently accurate structures for these molecules. The comparison of the uranium, neptunium and plutonium complexes will also provide insights into any structural changes down the actinide series. Only the aquo,  $[\text{Pu}(\text{H}_2\text{O})_8]^{4+}$  and nitrate  $[\text{Pu}(\text{NO}_3)_n(\text{H}_2\text{O})_m]^{4-n}$ , complexes are considered for the +4 oxidation state.

### **Computational Details**

The geometries of all the complexes in this work were fully optimized without symmetry constraints in the gaseous and when needed aqueous phases. The optimized structures were confirmed as local minima structures using vibrational frequency analysis. The calculated vibrational frequencies were obtained using the harmonic approximation. Although this work is mainly focused on plutonium complexes, we have compared some of these complexes with their uranium and neptunium counterparts. We have only compared compounds in which the actinide atoms possess the same oxidation states. Scalar relativistic effective core pseudopotentials (RECPs) were used in this work. The RECP calculations were carried out with the Gaussian 03<sup>36</sup>

suite of programs. The Stuttgart small-core<sup>37-38</sup> (60 core electrons represented by a pseudopotential) RECPs and associated valence basis sets were used for the actinide atoms while the aug-cc-pVDZ basis was used on all other atoms. The uranium, neptunium and plutonium valence basis sets were augmented with diffuse f-type functions having exponent of 0.005, 0.005 and 0.05 respectively. All g-type functions were however removed from the actinide valence basis sets. This small-core pseudopotential has been shown to result in very good agreements with all-electron basis set calculations as well as experimental structural parameters and reaction energies.<sup>13, 19-20, 22</sup> To examine the basis set dependence of the energetics of the complexes studied in this work, the aug-cc-pVTZ basis was also used on the hydrogen, nitrogen, oxygen and chlorine atoms in the molecular structures optimized with the double- $\zeta$  basis. The hybrid B3LYP<sup>39-40</sup> and pure DFT PBE<sup>41-42</sup> functionals were used in these calculations. The numerical integration of the exchange-correlation portion of the density functionals were carried out using ultra-fine grids. All the complexes studied in this work had negligible spin contaminations in the unrestricted DFT ground states. Deviations of more than 3.5% from the expected  $S(S+1)$  values were taken as the hallmark of ‘significant’ spin contamination. The solution phase calculations were carried out with the polarizable continuum solvation (PCM) model.<sup>43</sup> All solution phase calculations were carried out in water. The default atomic radii in the Gaussian 03 code were used in the calculations. It should be mentioned that no imaginary frequencies were obtained for the complexes optimized in aqueous solution using the PCM model. The gas phase and aqueous phase frequency analyses calculations were carried out analytically. Tight geometry optimization and energy convergence criteria were stipulated in all the calculations. The various gas-phase optimized structures for each molecule were used as starting structures for optimization using the

PCM model. Only the bidentate coordination mode was considered for all the nitrate complexes studied in this work.<sup>34-35</sup>

## Results and Discussion

**Bare  $\text{PuO}_2^{2/1+}$  and aquo plutonyl (VI/V) complexes.** The calculated structural parameters of the bare  $\text{PuO}_2^{2/1+}$  and pentaquo plutonyl (VI/V) complexes obtained using RECPs are presented in Table 3.1. Starting from the naked plutonyl dication,  $\text{PuO}_2^{2+}$ , the calculated Pu=O bond length obtained with the B3LYP functional in the gas phase is in good agreement with those obtained using the CASPT2 and AQCC approaches.<sup>28, 30</sup> Also, there is good agreement between the calculated stretching vibrational frequencies of the plutonyl entity obtained using the B3LYP functional and these more sophisticated approaches. The use of the PBE functional results in longer Pu=O bonds and consequently lower vibrational frequencies. The decrease in the vibrational frequencies caused by employing a GGA functional is on the order of 78-85  $\text{cm}^{-1}$ . Similar effects have been observed in the performance of the PW91 and B3LYP functionals in predicting the structural features of  $\text{PuN}_2$ .<sup>27</sup> The Pu=O bond of the bare  $\text{PuO}_2^{2+}$  is slightly longer by about 0.03 Å when the B3LYP functional and PCM solvation model are employed. This increase in length results in stretching vibrational frequencies of similar magnitude as those obtained when the GGA functional is used in the gas-phase. Employing the GGA functional with the PCM solvation model results in very good agreement between the calculated and experimental Pu=O bond lengths. This also brings about very good agreement (within 6  $\text{cm}^{-1}$  and 2  $\text{cm}^{-1}$  respectively) between the calculated and experimental symmetric and asymmetric stretching vibrational frequencies. It seems that employing the GGA functional with the PCM solvation model in calculations on the bare plutonyl entity, although questionable on theoretical

**Table 3.1:** The calculated bond lengths ( $\text{\AA}$ ) and plutonyl vibrational frequencies ( $\text{cm}^{-1}$ ) of the bare  $\text{PuO}_2^{2/1+}$  and actinyl aquo  $\text{PuO}_2(\text{H}_2\text{O})_5^{2/1+}$  systems obtained using DFT in the gaseous and aqueous phases

| System                                    | Parameter            | Gas    |        | Solution |        | Expt. <sup>a</sup> |
|---|----------------------|--------|--------|----------|--------|--------------------|
|   |                      | PBE    | B3LYP  | PBE      | B3LYP  |                    |
| $\text{PuO}_2^{2+}$                       | Pu=O <sub>yl</sub>   | 1.704  | 1.669  | 1.738    | 1.703  |                    |
|   | $\nu_{\text{symm}}$  | 919.3  | 1006.1 | 842.0    | 916.1  |                    |
|   | $\nu_{\text{asymm}}$ | 1044.1 | 1122.7 | 964.1    | 1024.1 |                    |
| $\text{PuO}_2(\text{H}_2\text{O})_5^{2+}$ | Pu=O <sub>yl</sub>   | 1.741  | 1.712  | 1.748    | 1.718  | 1.74               |
|   | Pu-OH <sub>2</sub>   | 2.465  | 2.460  | 2.441    | 2.435  | 2.41               |
|   | $\nu_{\text{symm}}$  | 848.5  | 918.0  | 829.7    | 898.3  | 835                |
|   | $\nu_{\text{asymm}}$ | 971.0  | 1031.1 | 937.5    | 991.4  | 962                |
| $\text{PuO}_2^{1+}$                       | Pu=O <sub>yl</sub>   | 1.737  | 1.723  | 1.788    | 1.776  |                    |
|   | $\nu_{\text{symm}}$  | 870.2  | 911.4  | 761.9    | 792.4  |                    |
|   | $\nu_{\text{asymm}}$ | 968.4  | 1007.6 | 839.3    | 863.4  |                    |
| $\text{PuO}_2(\text{H}_2\text{O})_5^{1+}$ | Pu=O <sub>yl</sub>   | 1.788  | 1.774  | 1.801    | 1.788  | 1.81               |
|   | Pu-OH <sub>2</sub>   | 2.583  | 2.590  | 2.565    | 2.568  | 2.47               |

|                      |       |       |       |       |     |
|----------------------|-------|-------|-------|-------|-----|
| $\nu_{\text{symm}}$  | 782.2 | 817.2 | 753.2 | 786.0 | 748 |
| $\nu_{\text{asymm}}$ | 874.0 | 908.0 | 818.0 | 843.2 |     |

---

<sup>a</sup> References <sup>61, 64</sup>.

grounds, is sufficient in predicting the structural parameters in acidic solutions. The agreement between the experimental and calculated Pu=O bond lengths and vibrational frequencies suggest that the effect of explicitly adding aquo ligands in the first hydration sphere around the plutonyl dication should be minimal. Comparison of the aqueous phase structures obtained for  $\text{PuO}_2^{2+}$  and  $[\text{PuO}_2(\text{H}_2\text{O})_5]^{2+}$  using the GGA functional, Table 3.1, shows a minute elongation of the Pu=O<sub>yl</sub> bonds by about 0.01 Å, suggesting that the Pu-OH<sub>2</sub> interaction is very weak. There is also a minimal decrease in the O<sub>yl</sub>=Pu=O<sub>yl</sub> angle by less than 0.6° upon insertion of five water molecules into the first hydration sphere. The symmetric stretching vibrational frequency calculated with the PBE functional is lower in  $[\text{PuO}_2(\text{H}_2\text{O})_5]^{2+}$  but is still within 5.3 cm<sup>-1</sup> of the experimental value while the asymmetric counterpart is now about 24.5 cm<sup>-1</sup> away from the experimental value and the value obtained for  $\text{PuO}_2^{2+}$ . The structural features and vibrational frequencies computed with the RECPs are in agreement<sup>44</sup> with those obtained with the all-electron basis set with the ZORA<sup>45-46</sup> approach. In addition, the discrepancies between the geometrical parameters obtained in the scalar-relativistic and spin-orbit corrected calculations are small.<sup>44</sup> This is in agreement with previous results and also indicates that using the small-core pseudopotential with GGA functionals results in geometrical parameters of sufficient accuracy.<sup>31,</sup>

<sup>47</sup> The use of the B3LYP functional with RECPs in optimizing the geometry of  $[\text{PuO}_2(\text{H}_2\text{O})_5]^{2+}$  results in Pu=O<sub>yl</sub> bond lengths about 0.03 Å smaller than the experimental value.<sup>35</sup> The average

of the Pu-OH<sub>2</sub> bond lengths is only slightly smaller than that obtained with the PBE functional. The error in the calculated Pu-OH<sub>2</sub> bond lengths is smaller than that obtained for the U-OH<sub>2</sub> bonds in the counterpart uranyl complex, Figure 3.1. The vibrational frequency of the symmetric stretching of the plutonyl entity in [PuO<sub>2</sub>(H<sub>2</sub>O)<sub>5</sub>]<sup>2+</sup> obtained with the B3LYP functional is still much larger than the experimental values. This agrees with previous experience that showed hybrid functionals give vibrational frequencies that are generally higher than the experimental value.<sup>10, 13, 19-20, 22</sup> A scaling factor of 0.92-0.98 is often required to bring sufficient accordance with the experimental data. The asymmetric O=Pu=O vibration obtained with the B3LYP functional in the aqueous phase is not much better than that obtained with the PBE functional. A scaling factor of about 0.93 appears sufficient in bringing a match between the experimental and calculated vibrational frequencies obtained with the B3LYP functional. Overall however, introduction of the five aquo ligands in the first solvation sphere only results in about 0.01-0.015 Å elongation of the Pu=O<sub>y1</sub> bonds and a decrease in the stretching vibrational frequencies by between 12 and 33 cm<sup>-1</sup>.

In general, examination of the bond lengths and O=An=O stretching vibrational frequencies calculated for the bare, AnO<sub>2</sub><sup>2+</sup> and [AnO<sub>2</sub>(H<sub>2</sub>O)<sub>5</sub>]<sup>2+</sup> complexes of uranium, neptunium and plutonium indicates that the B3LYP functional generally results in slightly shorter bonds while the PBE functional results in better O=An=O stretching vibrational frequencies, Figure 3.1. The elongation of the An=O<sub>y1</sub> and An-OH<sub>2</sub> bonds upon reduction to the +5 oxidation state is well known, Figure 3.2. The experimental values of the asymmetric O=An=O vibration frequencies are accurately predicted by aqueous phase calculations on the bare AnO<sub>2</sub><sup>n+</sup> cations with the PBE functional even though inclusion of the first hydration sphere is necessary in reducing the differences between the experimental and calculated values of the

symmetric O=An=O vibrations. These observations have been previously reported.<sup>31</sup> Overall, it appears that the performance of DFT is in no way significantly worse for the  $\text{PuO}_2^{n+}$  systems than for the  $\text{UO}_2^{n+}$  systems, Figures 3.1 and 3.2. Regarding the fortuity of the agreement between the calculated and experimental vibrational frequencies, there is the age-old case of "getting good results by error cancellations". At the current level of theory, the results (both the calculated values and the trends between the calculated and experimental values) suggest that these types of calculations can be used in future combined theoretical and experimental works. The applicability to uranium and neptunium complexes is also advantageous.

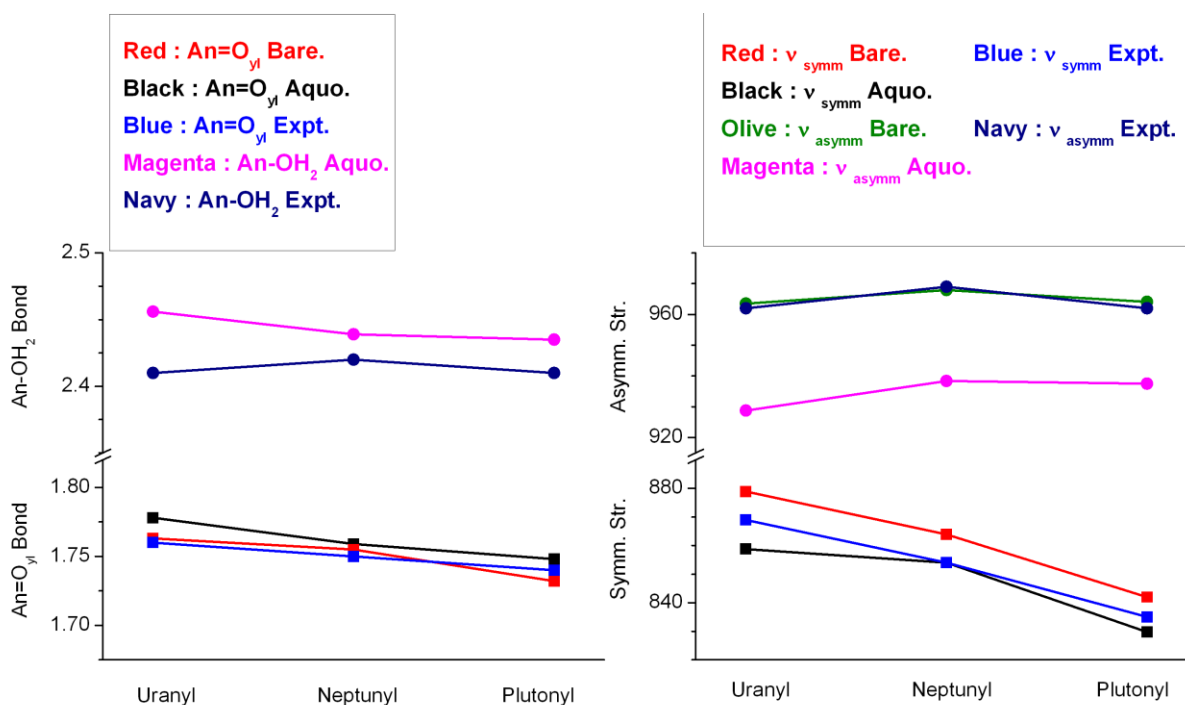


**Figure 3.1:** (Left) The  $\text{An}=\text{O}_{\text{yl}}$  bond lengths ( $\text{\AA}$ ) in the bare actinyl moieties,  $\text{AnO}_2^{2+}$  as well as the  $\text{An}=\text{O}_{\text{yl}}$  and average  $\text{An}-\text{OH}_2$  bond lengths ( $\text{\AA}$ ) in the pentaquo complexes,  $[\text{AnO}_2(\text{H}_2\text{O})_5]^{2+}$ . (Right) The actinyl symmetric and asymmetric stretching vibrational frequencies ( $\text{cm}^{-1}$ ) in the bare actinyl moieties,  $\text{AnO}_2^{2+}$  and the pentaquo complexes,  $[\text{AnO}_2(\text{H}_2\text{O})_5]^{2+}$ . These values were obtained with the obtained using the PBE functional and PCM solvation model.

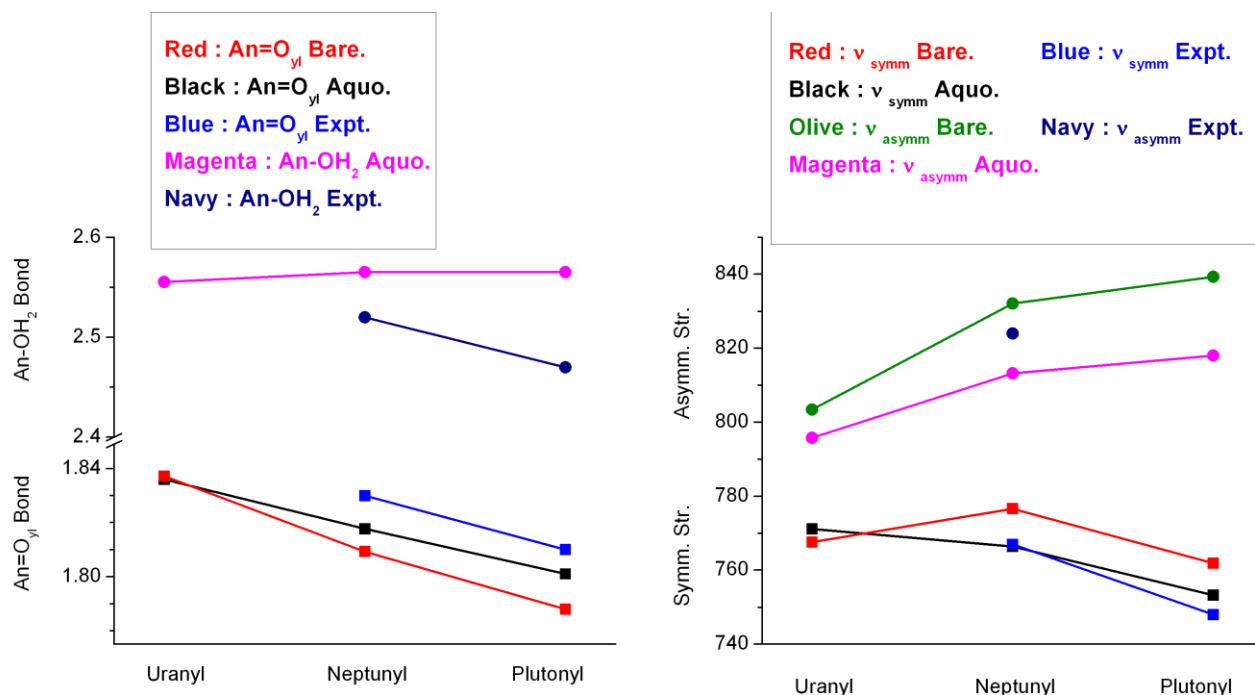


**Figure 3.2:** (Left) The An=O<sub>yl</sub> bond lengths (Å) in the bare actinyl moieties, AnO<sub>2</sub><sup>1+</sup> as well as the An=O<sub>yl</sub> bond lengths and average An-OH<sub>2</sub> bond lengths (Å) in the pentaquo complexes, [AnO<sub>2</sub>(H<sub>2</sub>O)<sub>5</sub>]<sup>1+</sup>. (Right) The actinyl symmetric and asymmetric stretching vibrational frequencies (cm<sup>-1</sup>) in the bare actinyl moieties, AnO<sub>2</sub><sup>1+</sup> and the pentaquo complexes, [AnO<sub>2</sub>(H<sub>2</sub>O)<sub>5</sub>]<sup>1+</sup>. These values were obtained with the PBE functional and PCM solvation model.

**Plutonyl (VI) chloro complexes.** Runde et al.<sup>48</sup> identified the mono- and bis-chloro (and a possible tri-chloro) complexes formed with the PuO<sub>2</sub><sup>2+</sup> moiety in sodium chloride solutions. They found the chloro-complexes to occur at greater concentrations in such solutions than the pentaquo ion with the mono-chloride complex being most stable. From the X-ray absorption spectra in solution, they and Conradson et al.<sup>35</sup> provided the geometrical parameters of plutonyl complexes formed at various chloride concentrations. Regarding the bis-chloride complex,

[PuO<sub>2</sub>Cl<sub>2</sub>(H<sub>2</sub>O)<sub>2</sub>], Berthon et al.<sup>49</sup> recently used DFT analysis to confirm the greater stability of the trans isomer of [PuO<sub>2</sub>Cl<sub>2</sub>(TPPO)<sub>2</sub>], TPPO=triphenylphosphine oxide. This structure is analogous to trans-[PuO<sub>2</sub>Cl<sub>2</sub>(H<sub>2</sub>O)<sub>2</sub>] which our solution phase calculations with the B3LYP functional shows to be essentially iso-energetic with its cis-isomer. The energy difference, ΔG(cis-trans), between the geometrical isomers of [PuO<sub>2</sub>Cl<sub>2</sub>(H<sub>2</sub>O)<sub>2</sub>] was calculated as 3.5 and 0.0 kcal/mol when the B3LYP functional was employed in the gaseous and aqueous phases, respectively. Single-point calculation with the aug-cc-pVTZ basis (for O, Cl and H atoms) on the geometries optimized at the double-ζ level reduces the cis-trans energy difference to about 0.0 kcal/mol in the aqueous phase. The magnitude of the energy differences calculated suggests that both structures are iso-energetic with ready inter-conversion in aqueous solutions. The greater stability of the trans- structure of [PuO<sub>2</sub>Cl<sub>2</sub>(TPPO)<sub>2</sub>] is most likely due to steric repulsion.

Structurally, The Pu=O<sub>y1</sub>, Pu-OH<sub>2</sub> and Pu-Cl bond lengths in the trans-isomer of [PuO<sub>2</sub>Cl<sub>2</sub>(H<sub>2</sub>O)<sub>2</sub>] were calculated as 1.736, 2.417 and 2.643 Å, respectively, in the aqueous phase with the B3LYP functional, Table 3.2. The Pu-OH<sub>2</sub> bonds are slightly longer (2.444 Å) in the cis-isomer. The calculated Pu=O<sub>y1</sub> bond lengths are in agreement with the experimental value of 1.75 Å which is relatively unchanged from those in the pentaquo complex. The calculated Pu-OH<sub>2</sub> and Pu-Cl bonds are however significantly shorter than the values of 2.49 and 2.70 Å respectively reported by Conradson et al.<sup>35</sup> and Runde et al.<sup>48</sup> It should however be noted that the calculated Pu-Cl bonds obtained for the [PuO<sub>2</sub>Cl<sub>2</sub>(H<sub>2</sub>O)<sub>2</sub>] complexes in this work are in good agreement with those obtained for the PuO<sub>2</sub>Cl<sub>2</sub>L<sub>2</sub> complexes from DFT calculations (2.634-

**Table 3.2:** The calculated properties (bond lengths in Å and frequencies in cm<sup>-1</sup>) of plutonyl chloro-aquo complexes obtained using the B3LYP (and PBE) functional.<sup>a</sup> W is used to represent the aquo ligand (H<sub>2</sub>O).

| Complex <sup>b</sup>                            | Gas Phase       |        |        |                           | Aqueous Solution |        |        |                           |           |
|---|-----------------|--------|--------|---------------------------|------------------|--------|--------|---------------------------|-----------|
|   | O <sub>yl</sub> | Aquo   | Chloro | $\nu_{\text{symm/asymm}}$ | O <sub>yl</sub>  | Aquo   | Chloro | $\nu_{\text{symm/asymm}}$ |           |
| PuO <sub>2</sub> Cl <sub>4</sub> <sup>2-</sup>  | 1.74            |        | 2.73   | 824/941                   | 1.75             |        | 2.70   | 816/917                   |           |
|   | (1.77)          |        | (2.71) | (763/878)                 | (1.78)           |        | (2.67) | (756/858)                 |           |
| PuO <sub>2</sub> Cl <sub>3</sub> W <sub>1</sub> | 1.74            | 2.59   | 2.67   | 845/961                   | 1.74             | 2.52   | 2.68   | 833/934                   |           |
|   | (1.77)          | (2.62) |        | (776/898)                 | (1.77)           | (2.53) | (2.67) | (769/877)                 |           |
| PuO <sub>2</sub> Cl <sub>2</sub> W <sub>2</sub> | Cis-            | 1.74   | 2.51   | 2.59                      | 852/967          | 1.74   | 2.44   | 2.64                      | 848/946   |
|   |                 | (1.77) | (2.52) | (2.58)                    | (800/914)        |        |        |                           |           |
|   | Trans-          | 1.74   | 2.48   | 2.60                      | 850/967          | 1.74   | 2.42   | 2.64                      | 845/945   |
|   |                 | (1.76) | (2.51) | (2.60)                    | (795/915)        | (1.77) | (2.42) | (2.62)                    | (786/891) |
| PuO <sub>2</sub> Cl <sub>2</sub> W <sub>3</sub> | Cis-            | 1.73   | 2.62   | 2.63                      | 859/973          | 1.73   | 2.53   | 2.67                      | 847/947   |
|   |                 | (1.77) | (2.62) | (2.63)                    | (785/909)        | (1.77) | (2.55) | (2.66)                    | (780/890) |

|   |        |        |        |           |        |        |        |           |
|---|--------|--------|--------|-----------|--------|--------|--------|-----------|
| Trans-  | 1.73   | 2.55   | 2.67   | 864/980   | 1.73   | 2.53   | 2.69   | 848/948   |
|   | (1.76) | (2.55) | (2.67) | (798/919) | (1.76) | (2.53) | (2.68) | (784/892) |
| Expt. <sup>c</sup>                              |        |        |        |           | 1.75   | 2.49   | 2.70   |           |
| PuO <sub>2</sub> Cl <sub>1</sub> W <sub>4</sub> | 1.73   | 2.53   | 2.58   | 879/995   | 1.73   | 2.48   | 2.64   | 867/965   |
|   | (1.76) | (2.54) | (2.57) | (813/934) | (1.76) | (2.50) | (2.62) | (802/910) |
| Expt. <sup>c</sup>                              |        |        |        |           | 1.75   | 2.43   | 2.75   |           |

<sup>a</sup> The calculated Pu-O<sub>yl</sub>, Pu-OH<sub>2</sub> and Pu-Cl bond lengths are given. <sup>b</sup> W is used to represent the aquo ligand (H<sub>2</sub>O). <sup>c</sup> Reference <sup>48</sup>

2.637 Å)<sup>49</sup> and experimental measurements (2.630 Å).<sup>48</sup> Interestingly, addition of another aquo ligand to the equatorial region results in elongation of the Pu-Cl bonds to 2.679 and 2.689 Å in the cis- and trans- isomers of [PuO<sub>2</sub>Cl<sub>2</sub>(H<sub>2</sub>O)<sub>3</sub>] respectively, Table 3.2 and Figure 3.3. This is in much better agreement with the measurements of Runde et al.<sup>48</sup> The Pu-OH<sub>2</sub> bonds also increase to 2.534 and 2.522 Å in the cis- and trans- isomers respectively in much better agreement with the EXAFS value of 2.49 Å.<sup>48</sup> The calculated structural features thus allow us to identify the previously characterized aqueous phase complexes characterized as [PuO<sub>2</sub>Cl<sub>2</sub>(H<sub>2</sub>O)<sub>3</sub>] rather than [PuO<sub>2</sub>Cl<sub>2</sub>(H<sub>2</sub>O)<sub>2</sub>] for which there are many analogous PuO<sub>2</sub>Cl<sub>2</sub>L<sub>2</sub> solid-state species. Such structural differences between the di-aquo and tri-aquo species can also be observed in the bis-chloro complexes formed with the uranyl group.<sup>2</sup> For [PuO<sub>2</sub>Cl<sub>2</sub>(H<sub>2</sub>O)<sub>3</sub>], the trans- structure is about 5.9 and 1.6 kcal/mol more stable than the cis- structure in the gas and aqueous phase calculations with the B3LYP functional respectively. This larger energy difference implies the

trans- isomer should be significantly predominant in aqueous solutions. It can be directly related to the increased steric crowding compared to  $[\text{PuO}_2\text{Cl}_2(\text{H}_2\text{O})_2]$ . Also, the structural features of the trans- complex are in slightly better agreement with the experimental reports, Table 3.2.

The O=Pu=O asymmetric stretching vibration has been observed between 908 to 918  $\text{cm}^{-1}$  in previous solid-state measurements of the IR spectra of various  $\text{PuO}_2\text{Cl}_2\text{L}_2$ -type complexes.<sup>50</sup> Calculations with the PBE functional on  $[\text{PuO}_2\text{Cl}_2(\text{H}_2\text{O})_2]$  in the gas-phase predict the asymmetric stretching vibration frequency of O=Pu=O to be 914.9 and 914.4  $\text{cm}^{-1}$  for the trans- and cis- structures respectively, Table 3.2. It should be noted that the gas-phase calculations also predict this vibrational frequency mode to be at 971.0  $\text{cm}^{-1}$  in  $[\text{PuO}_2(\text{H}_2\text{O})_5]^{2+}$ . The agreement between the values calculated for the  $\text{PuO}_2\text{Cl}_2\text{L}_2$  and  $[\text{PuO}_2\text{Cl}_2(\text{H}_2\text{O})_2]$  complexes indicates considerable decrease in the plutonyl vibrational frequencies upon introduction of the chloride ligands into the equatorial region. It appears that the role of the organic ligand is minimal in this effect. Indeed the asymmetric vibrational mode of the plutonyl group in trans- $[\text{PuO}_2\text{Cl}_2(\text{TPPO})_2]$  was calculated at 916.7  $\text{cm}^{-1}$  in the gas-phase using the PBE functional, adequately agreeing with the peak at 920  $\text{cm}^{-1}$  observed in the solid state IR spectrum.

In the  $[\text{PuO}_2\text{Cl}_2(\text{H}_2\text{O})_3]$  complex, the asymmetric O=Pu=O stretching vibration is between 908.7 and 919.3  $\text{cm}^{-1}$  in the gas phase and between 889.7 and 892.4  $\text{cm}^{-1}$  in the aqueous phase, Table 3.2. It appears that the magnitude of the O=Pu=O asymmetric stretching vibration frequency is much more dependent on the introduction of two chloride ligands into the equatorial region and less so on the number of aquo ligands in the complex. The symmetric vibrational frequencies of the plutonyl moiety in  $[\text{PuO}_2\text{Cl}_2(\text{H}_2\text{O})_3]$  were calculated to be between 780.3-784.4  $\text{cm}^{-1}$  in the aqueous phase, a drastic reduction from the 829.7  $\text{cm}^{-1}$  (and 835  $\text{cm}^{-1}$ ) calculated (and experimentally measured) for the pentaquo complex. The reduction of both the

symmetric and asymmetric stretching vibrations of the O=Pu=O group by 45 to 60  $\text{cm}^{-1}$  upon introduction of two chloride ligands into the equatorial region is supported by the theoretical calculations in this work and previously reported experimental results.<sup>50</sup>

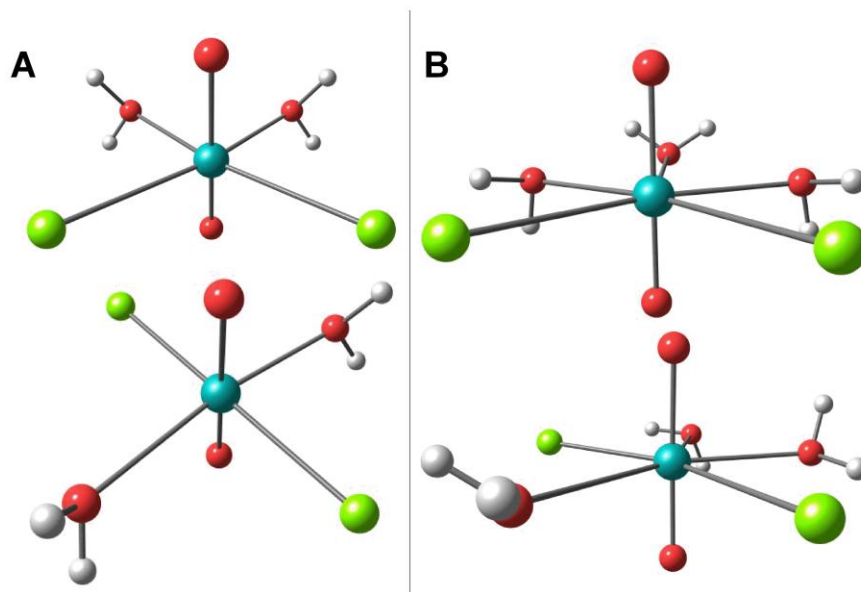


**Figure 3.3:** A) The cis (top) and trans (bottom) isomers of the  $\text{PuO}_2\text{Cl}_2(\text{H}_2\text{O})_2$  complex. B) The cis (top) and trans (bottom) isomers of the  $\text{PuO}_2\text{Cl}_2(\text{H}_2\text{O})_3$  complex.

The mono-chloro complexes formed at lower concentrations were calculated as having shorter Pu-OH<sub>2</sub> and Pu=O<sub>yl</sub> bonds than the bis-chloro complexes, Table 3.2. This is in agreement with the experimental reports. The Pu-Cl bond length in  $[\text{PuO}_2\text{Cl}(\text{H}_2\text{O})_4]^+$  was calculated as 2.642 Å in the aqueous solution significantly underestimating the experimental value of 2.75 Å for the Pu-Cl bonds in the complex formed by  $\text{PuO}_2^{2+}$  at lower chloride concentrations in acidic aqueous media. The experimental report of much longer (by about 0.05 Å) Pu-Cl bonds in the

complex formed at lower chloride concentrations is surprising as similar effects are absent in the uranyl counterparts.<sup>51-52</sup> Indeed after replacement of all the aquo ligands by chloride anions, the Pu-Cl bonds in  $[\text{PuO}_2\text{Cl}_4]^{2-}$  were calculated to be only about 2.697 Å in length in aqueous solution. The calculated Pu-Cl bond lengths of  $[\text{PuO}_2\text{Cl}_4]^{2-}$  in the gas and aqueous phases are in agreement with the theoretical results of Austin et al.<sup>31</sup> They are also near the range of 2.653-2.671 Å previously reported in experimental works on crystalline  $\text{Cs}_2[\text{AnO}_2\text{Cl}_4]$  complexes.<sup>53-55</sup>

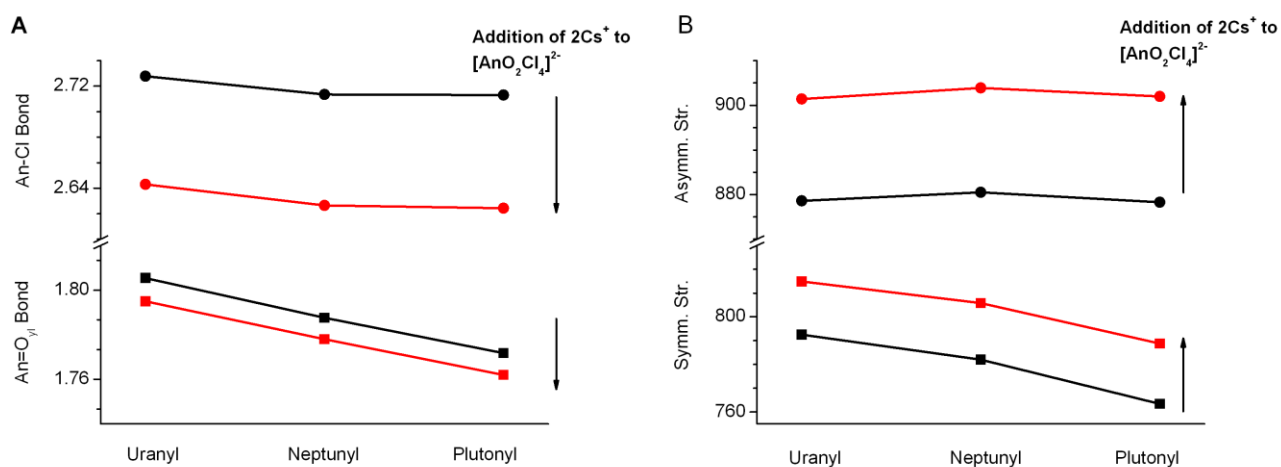


**Figure 3.4:** A) The decrease in the An=O<sub>yl</sub> and An-Cl bond lengths (Å) on addition of 2Cs<sup>+</sup> to the  $[\text{AnO}_2\text{Cl}_4]^{2-}$  complexes. B) The increase in the actinyl stretching vibrational frequencies (cm<sup>-1</sup>) on addition of 2Cs<sup>+</sup> to the  $[\text{AnO}_2\text{Cl}_4]^{2-}$  complexes. The structural features of the anionic and neutral complexes were calculated with the PBE functional and are depicted with black and red squares respectively. The experimental values<sup>56, 59</sup> of the symmetric vibrational frequencies in solid  $\text{Cs}_2[\text{UO}_2\text{Cl}_4]$  and  $\text{Cs}_2[\text{NpO}_2\text{Cl}_4]$  are 832 and 802 cm<sup>-1</sup> respectively. The calculated values for these complexes are within 17 cm<sup>-1</sup> and 4 cm<sup>-1</sup> of the experimental reports respectively.

For the  $[\text{AnO}_2\text{Cl}_4]^{2-}$  complexes in general, Figure 3.4, the trends in the calculated bond lengths and vibrational frequencies in the gas phase are similar to those observed in the pentaquo uranyl, neptunyl and plutonyl complexes, Figure 3.1. The attachment of cesium atoms to two chloride ligands in a trans- arrangement allows us to simulate the single-crystal units of the  $\text{Cs}_2[\text{AnO}_2\text{Cl}_4]$  complexes. The calculations show the cesium salts should have shorter An-Cl bonds (by about 0.09 Å for the non-cesiated chloride ligands although the ones with Cs salts maintain the same bond lengths found in the  $[\text{AnO}_2\text{Cl}_4]^{2-}$  species) than the counterpart  $[\text{AnO}_2\text{Cl}_4]^{2-}$  complexes, Figure 3.4. The difference between the An=O<sub>yl</sub> bonds in the gas phase anionic and neutral salts are more modest (less than 0.01 Å). Overall these changes upon the addition of two cesium ions bring the An-Cl and An=O<sub>yl</sub> bonds in agreement with available solid state experimental<sup>53-55</sup> reports on the actinyl complexes. The symmetric and asymmetric stretching vibrational frequencies of the actinyl entities are larger in the cesium complexes, Figure 3.4. The calculated values of the symmetric and asymmetric vibrations of actinyl entity in the cesiated neptunyl and uranyl complexes are in good agreement with the values reported by Denning.<sup>56-59</sup>

**Plutonyl (VI) nitrate complexes.** Gaunt et al.<sup>32</sup> recently crystallized plutonyl (VI) diaquo-dinitrate and characterized it using X-ray diffraction techniques. The crystalline dinitrate they obtained had two water molecules in a trans- arrangement in the equatorial region. They however observed only negligible dinitrate formation in aqueous solutions even at very low pH values. The aqueous solution of  $\text{PuO}_2^{2+}$  in acidic nitrate solutions shows very weak coordination of the nitrate ligand with the mononitrate complex being the dominant species. The calculated structural parameters of a few structures of the mononitrate, dinitrate and trinitrate complexes are given in Table 3.3. For the diaquo-dinitrate characterized by Gaunt et al.<sup>32</sup>, Figure 3.5, the

experimental Pu=O<sub>yl</sub> bond length of 1.727 Å is well replicated by the B3LYP/RECPs calculations as 1.728 Å. The calculated Pu-OH<sub>2</sub> bond lengths at 2.534 Å are however significantly larger than the experimental values, 2.450 Å. Such a large discrepancy was also seen between the calculated and experimental U-OH<sub>2</sub> bonds in the work on the analogous U(VI) complex by Gutowski et al.<sup>6</sup> and Prestianni et al.<sup>16</sup> The Hartree-Fock calculations on the uranyl nitrate and sulfate complexes by Craw et al.<sup>60</sup> also yielded this over-estimation of the U-OH<sub>2</sub> bond lengths. The bonds between the actinide atom and the coordinating oxygen atoms of the two nitrate groups in [PuO<sub>2</sub>(NO<sub>3</sub>)<sub>2</sub>(H<sub>2</sub>O)<sub>2</sub>] were calculated to be about 2.469 Å in length, a value near the average value of 2.497 Å obtained in the X-ray diffraction study. It should be noted that the unit cell of the dinitrate in the experimental study contains two independent molecules. There appears to be a mismatch between the calculated and experimental relative magnitudes of the Pu-O<sub>nitrate</sub> and Pu-OH<sub>2</sub> bond lengths due to the significant overestimation of the latter.

The symmetric O=Pu=O and coordinated nitrate stretching vibrational frequencies of the dinitrate are Raman active and were measured at 844 and 756 cm<sup>-1</sup>, respectively in the solid phase.<sup>32</sup> The calculated infrared values for these frequencies are 866.9 and 741.9 cm<sup>-1</sup>, respectively at the B3LYP/RECP level in the gas phase, Table 3.3. The experimental value of the plutonyl symmetric stretching vibrational frequency is over-estimated by approximately 23 cm<sup>-1</sup> at this level. The calculated values for these vibrations in the aqueous phase are 847.7 and 748.4 cm<sup>-1</sup> respectively. This suggests that, if the diaquo-dinitrate complex is formed in solution, the symmetric stretching frequency of the plutonyl entity should be lower than that obtained in the gas phase and also lower than the experimental value of this vibrational mode in the [PuO<sub>2</sub>(H<sub>2</sub>O)<sub>5</sub>]<sup>2+</sup> complex.<sup>61</sup> The absence of any peaks around 820-830 cm<sup>-1</sup> in the Raman spectrum of

**Table 3.3:** The calculated structural properties (bond lengths in Å and vibrational frequencies in cm<sup>-1</sup>) of the plutonyl nitrate complexes obtained using the B3LYP functional in the gaseous and aqueous phases.

|  | Gas Phase       |       |         |                         |                      | Aqueous Solution |       |         |                         |                      |
|--|-----------------|-------|---------|-------------------------|----------------------|------------------|-------|---------|-------------------------|----------------------|
|  | O <sub>yl</sub> | Aquo  | Nitrate | ν <sub>symm/asymm</sub> | ν <sub>nitrate</sub> | O <sub>yl</sub>  | Aquo  | Nitrate | ν <sub>symm/asymm</sub> | ν <sub>nitrate</sub> |
| [PuO <sub>2</sub> (NO <sub>3</sub> ) <sup>1-</sup>                 | 1.708           |       | 2.364   | 911.4/1001.0            | 669.3                | 1.719            |       | 2.437   | 871.4/980.1             | 698.8                |
| [PuO <sub>2</sub> (NO <sub>3</sub> )W <sub>4</sub> ] <sup>1+</sup> | 1.733           | 2.592 | 2.420   | 867.2/993.1             | 746.6                | 1.733            | 2.552 | 2.486   | 863.0/970.1             | 748.6                |
| [PuO <sub>2</sub> (NO <sub>3</sub> ) <sub>2</sub> W <sub>2</sub> ] | 1.740           | 2.531 | 2.462   | 850.2/976.1             | 746.5                | 1.743            | 2.512 | 2.477   | 847.7/948.6             | 748.4                |
| Expt. <sup>a</sup>   | 1.727           | 2.432 | 2.497   | 844                     | 756                  |                  |       |         |                         |                      |
| [PuO <sub>2</sub> (NO <sub>3</sub> ) <sub>3</sub> ] <sup>1-</sup>  | 1.738           |       | 2.487   | 850.1/965.3             | 747.7                | 1.737            |       | 2.483   | 845.9/943.1             | 745.8                |

<sup>a</sup> Reference <sup>32</sup>

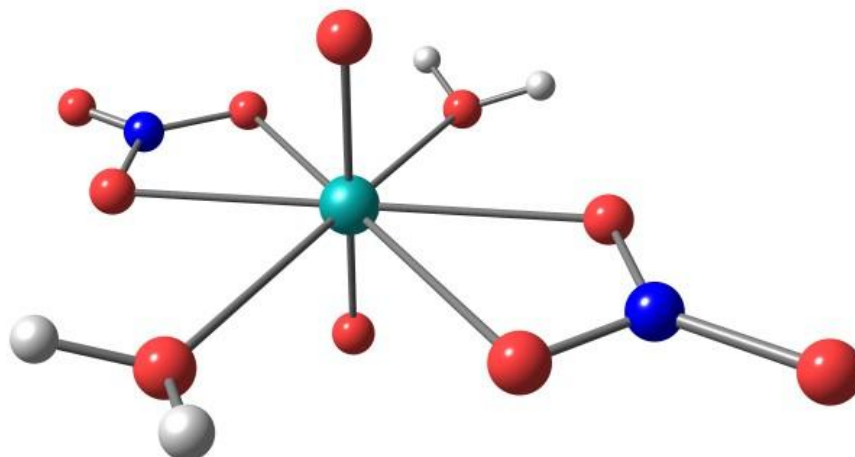


**Figure 3.5:** The optimized structure of plutonyl diaquo-dinitrate,  $\text{PuO}_2(\text{NO}_3)_2(\text{H}_2\text{O})_2$  obtained using the B3LYP functional.

the plutonyl moiety in acidic nitrate solutions most likely suggests negligible formation of the dinitrate in agreement with the conclusion of Gaunt et al.<sup>32</sup> The peak observed at  $836\text{ cm}^{-1}$  in the aqueous solution of  $\text{PuO}_2^{2+}$  in concentrated nitric acid corresponds to the symmetric stretching frequency in the pentaquo complex.

The nitrate counterparts of the  $[\text{PuO}_2\text{Cl}_2\text{L}_2]$  complexes,  $[\text{PuO}_2(\text{NO}_3)_2\text{L}_2]$ , are of great importance in the nuclear processing industry. In summary organic ligands are used in liquid-liquid extraction of actinide compounds from complex acidic solutions. Plutonyl nitrate is extracted with tributylphosphate, TBP, in the PUREX extraction process.<sup>62</sup> The structural parameters of the  $[\text{AnO}_2(\text{NO}_3)_2(\text{H}_2\text{O})_2]$  and  $[\text{AnO}_2(\text{NO}_3)_2(\text{TBP})_2]$  complexes (An = U, Np and Pu), optimized in the gas phase are presented in Table 3.4. Overall, there appears to be quite little change in the  $\text{An}=\text{O}_{\text{yl}}$  bond lengths between the corresponding  $[\text{AnO}_2(\text{NO}_3)_2(\text{H}_2\text{O})_2]$  and

**Table 3.4:** The calculated bond lengths (Å) of the  $\text{AnO}_2(\text{NO}_3)_2(\text{H}_2\text{O})_2$ ,  $\text{AnO}_2(\text{NO}_3)_2(\text{TBP})_2^{\text{a}}$ ,  $\text{AnO}_2\text{Cl}_2(\text{H}_2\text{O})_2$  and  $\text{AnO}_2\text{Cl}_2(\text{TPPO})_2^{\text{a}}$  complexes obtained using the B3LYP functional with RECPs in the gaseous phase

|                                    |       | $\text{AnO}_2(\text{NO}_3)_2(\text{H}_2\text{O})_2$ |       |       | $\text{AnO}_2(\text{NO}_3)_2(\text{TBP})_2^{\text{a,b}}$ |       |       |
|------------------------------------|-------|---|-------|-------|--|-------|-------|
|                                    |       | U   | Np    | Pu    | U  | Np    | Pu    |
| An=O <sub>yl</sub>                 | Calc. | 1.769   | 1.748 | 1.740 | 1.768  | 1.749 | 1.743 |
|                                    | Expt. | 1.754-1.763   |       | 1.727 | 1.77   | 1.75  | 1.75  |
| An-O <sub>nitrate</sub>            | Calc. | 2.483   | 2.469 | 2.462 | 2.516  | 2.496 | 2.489 |
|                                    | Expt. | 2.477-2.513   |       | 2.497 | 2.54   | 2.51  | 2.50  |
| An-OH <sub>2</sub> /O <sub>p</sub> | Calc. | 2.546   | 2.546 | 2.531 | 2.428  | 2.385 | 2.443 |
|                                    | Expt. | 2.446-2.457   |       | 2.432 | 2.41   | 2.38  | 2.40  |
|                                    |       | $\text{AnO}_2\text{Cl}_2(\text{H}_2\text{O})_2$     |       |       | $\text{AnO}_2\text{Cl}_2(\text{TPPO})_2^{\text{a,c}}$    |       |       |
| An=O <sub>yl</sub>                 | Calc. | 1.773   | 1.754 | 1.737 | 1.777  | 1.763 | 1.751 |
|                                    | Expt. |   |       |       | 1.753-1.767  | 1.751 | 1.747 |
| An-Cl                              | Calc. | 2.622   | 2.604 | 2.597 | 2.650  | 2.627 | 2.629 |
|                                    | Expt. |   |       |       | 2.645-2.673  | 2.622 | 2.630 |
| An-OH <sub>2</sub> /O <sub>p</sub> | Calc. | 2.509   | 2.494 | 2.478 | 2.352  | 2.330 | 2.326 |

|       |             |       |       |
|-------|-------------|-------|-------|
| Expt. | 2.300-2.339 | 2.288 | 2.302 |
|-------|-------------|-------|-------|

<sup>a</sup> TPPO and TBP are abbreviations for triphenylphosphine oxide and tributylphosphate respectively. <sup>b</sup> Reference <sup>63</sup>. <sup>c</sup> Reference <sup>49, 65-67</sup>

[AnO<sub>2</sub>(NO<sub>3</sub>)<sub>2</sub>(TBP)<sub>2</sub>] complexes. The structural features of the uranyl, neptunyl and plutonyl complexes are all rather similar with minimal change across the series, Table 3.4. This as well as the calculated bond distances are in good agreement with the experimental reports of den Auwer et al.<sup>63</sup> This is also the case in the [AnO<sub>2</sub>Cl<sub>2</sub>(TPPO)<sub>2</sub>] complexes, Table 3.4. Due to electronegativity differences, the An-O<sub>phosphine</sub> bonds in the [AnO<sub>2</sub>(NO<sub>3</sub>)<sub>2</sub>(TBP)<sub>2</sub>] complexes are shorter than the An-OH<sub>2</sub> bonds in their [AnO<sub>2</sub>(NO<sub>3</sub>)<sub>2</sub>(H<sub>2</sub>O)<sub>2</sub>] counterparts, Table 3.4. This is also evident in the dichloro- complexes. This goes back to the ionic nature of the equatorial bonds in actinyl complexes.

**Plutonyl (IV) aquo and nitrate complexes.** The ability of DFT to successfully predict the structural features of Pu(IV) complexes has been demonstrated recently by Horowitz et al.<sup>29</sup> The Pu-OH<sub>2</sub> bond length in the [Pu(H<sub>2</sub>O)<sub>8</sub>]<sup>4+</sup> complex was calculated as 2.39 Å in good agreement with the experimental value of 2.38 Å. Our calculations in the aqueous phase yield Pu-OH<sub>2</sub> bond lengths of 2.392 and 2.393 Å with the B3LYP and PBE functionals respectively, Table 3.5. The dinitrate, tetranitrate and hexanitrate complexes of Pu<sup>4+</sup> are known to be the dominant species in acidic aqueous nitrate solutions. The pentanitrate and hexanitrate are thought to be present at high nitrate concentrations in acidic aqueous solutions. The geometries of the [Pu(NO<sub>3</sub>)<sub>n</sub>]<sup>4-n</sup> (n=2-6) complexes were optimized using both density functionals employed in this work. The

**Table 3.5:** The calculated Pu-OH<sub>2</sub> and Pu-O<sub>water/nitrate</sub> bond lengths of the aquo, nitrate and aquo-nitrate complexes of the plutonium (IV) cation obtained using DFT in the gaseous and aqueous phases

|   | PBE   |          | B3LYP |          | Expt. <sup>a</sup> |
|---|-------|----------|-------|----------|--------------------|
|   | Gas   | Solution | Gas   | Solution |                    |
| [Pu(H <sub>2</sub> O) <sub>8</sub> ] <sup>4+</sup>                                | 2.428 | 2.393    | 2.416 | 2.393    | 2.39               |
| [Pu(NO <sub>3</sub> ) <sub>2</sub> ] <sup>2+</sup>                                | 2.231 | 2.419    | 2.214 | 2.390    | ‘2.42’             |
| [Pu(NO <sub>3</sub> ) <sub>3</sub> ] <sup>1+</sup>                                | 2.304 | 2.450    | 2.298 | 2.411    |                    |
| [Pu(NO <sub>3</sub> ) <sub>4</sub> ] <sup>0</sup>                                 | 2.385 | 2.438    | 2.376 | 2.434    |                    |
| [Pu(NO <sub>3</sub> ) <sub>4</sub> (H <sub>2</sub> O) <sub>3</sub> ] <sup>0</sup> | 2.504 | 2.511    |       | 2.500    | 2.46               |
| [Pu(NO <sub>3</sub> ) <sub>5</sub> ] <sup>1-</sup>                                | 2.456 | 2.474    | 2.449 | 2.469    |                    |
| [Pu(NO <sub>3</sub> ) <sub>5</sub> (H <sub>2</sub> O)] <sup>1-</sup>              | 2.509 | 2.507    |       | 2.502    |                    |
| [Pu(NO <sub>3</sub> ) <sub>6</sub> ] <sup>2-</sup>                                | 2.534 | 2.524    | 2.529 | 2.520    | 2.48               |

<sup>a</sup> References<sup>34-35</sup>

nitrate ligands were coordinated to the Pu<sup>4+</sup> cation in a bidentate fashion, Figure 3.6. It should be noted that the EXAFS experiments of Allen et al.<sup>34</sup> found average Pu-O<sub>water/nitrate</sub> bond lengths of 2.42, 2.46 and 2.49 Å respectively for the heptaaquo-dinitrate, triaquo-tetranitrate and hexanitrate species. The average of the calculated Pu-O<sub>nitrate</sub> bond lengths in the dinitrate,

tetranitrate and hexanitrate species obtained with the B3LYP functional in aqueous solution are 2.399, 2.438 and 2.520 Å respectively, Table 3.5. This indicates that in the absence of aquo ligands, the Pu-O<sub>nitrate</sub> bond lengths can vary between 2.399 and 2.520 Å. The Pu-O<sub>water</sub> bonds would then be expected to slightly increase the average Pu-O<sub>water/nitrate</sub> bond lengths in the [Pu(NO<sub>3</sub>)<sub>n</sub>(H<sub>2</sub>O)<sub>11-2n</sub>]<sup>4-n</sup> complexes. Indeed optimization of the [Pu(NO<sub>3</sub>)<sub>4</sub>(H<sub>2</sub>O)<sub>3</sub>] and [Pu(NO<sub>3</sub>)<sub>5</sub>(H<sub>2</sub>O)<sub>1</sub>]<sup>1-</sup> aquo-nitrate complexes results in longer (0.03-0.07 Å) average Pu-O<sub>water/nitrate</sub> bonds.

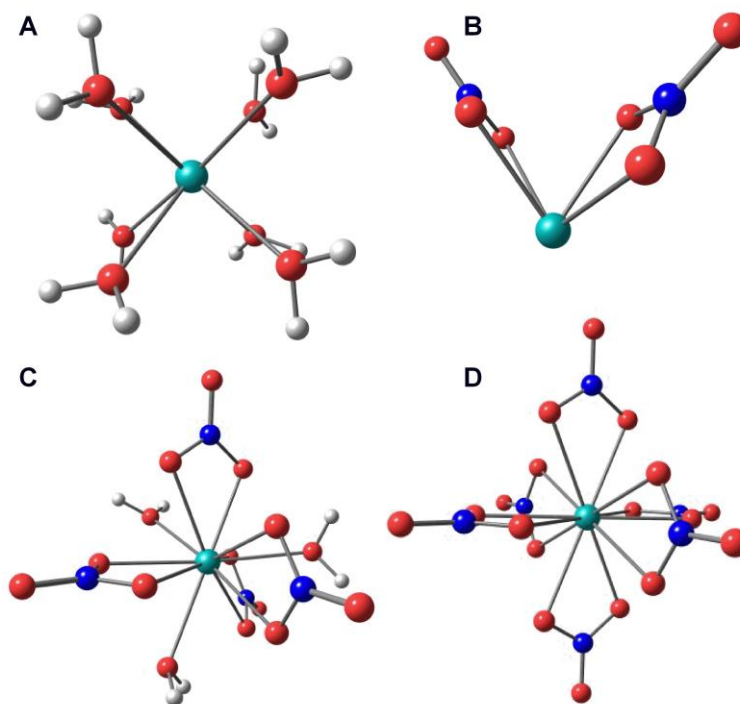


**Figure 3.6:** The optimized structures of several plutonium (IV) complexes: A) Pu(H<sub>2</sub>O)<sub>8</sub><sup>4+</sup>, B) Pu(NO<sub>3</sub>)<sub>2</sub><sup>2+</sup>, C) Pu(NO<sub>3</sub>)<sub>4</sub>(H<sub>2</sub>O)<sub>3</sub> and D) Pu(NO<sub>3</sub>)<sub>6</sub><sup>2-</sup> calculated with the B3LYP functional in the aqueous phase.

## Conclusions

We have performed a comprehensive characterization of the structural properties of several plutonyl (VI) and plutonium (IV) complexes using scalar relativistic Kohn-Sham DFT calculations with small-core effective core pseudopotentials. The aquo, chloro and nitrate complexes were examined in the gas and aqueous phases in addition to the complexes formed with a few organic ligands. The calculations in aqueous solvents were carried out using the PCM solvation model.

Overall, good performance can be obtained by using the hybrid B3LYP functional in calculating the structural parameters of the plutonyl (VI) and plutonium (IV) complexes or by using the PBE functional in predicting the signature infrared and Raman active vibrational frequencies of these complexes either in the gas-phase (solid-state single crystals) or aqueous phases. The use of the vibrational frequencies predicted by these functionals in addition with experimental infrared or Raman spectroscopic data promises to be a strong tool in confirming the identity of plutonium complexes that might be isolated or prepared in the future. It should be noted that the calculated vibrational frequencies rely on the harmonic approximation. Deviations between the experimental and calculated vibrational frequencies can therefore be expected. The agreement between the two is however sufficient for future combined theoretical and experimental work on actinide complexes. In terms of geometrical parameters, the plutonyl complexes are rather very reminiscent of their counterpart uranyl and neptunyl counterparts with usually minimal changes in the associated bond lengths (0.01-0.03 Å) and bond angles. The only problematic point seems to be the calculation of the An-OH<sub>2</sub> bond lengths in the diaquo-dinitrate complexes. It might be necessary to explicitly include water molecules in the second coordination sphere around the actinyl entity for good agreement between the experimental and

calculated An-OH<sub>2</sub> bond lengths. We have extended the use of DFT in predicting the structure of plutonium (IV) complexes beyond the octaquo complexes. The calculated and experimental geometrical parameters in the nitrate and aquo-nitrate complexes agree to within 0.02-0.04 Å.

It would appear that DFT calculations can be used in predicting sufficiently accurate structural parameters for such complexes, the lack of rigor in not fully accounting for the various nearly-degenerate electronic states (correct ground state?) and their multi-reference characters notwithstanding. The scope of the current work is limited to examining the structural features of the selected molecules with limited examination of the ability of DFT to correctly predict the speciation, coordination numbers and hydration energies of these plutonium compounds. Going forward, the use of spin-orbit coupled wave function approaches in predicting the electronic structure and spectroscopic properties of small to medium-sized actinide species holds some appeal for us.

## References

1. Batista, E. R.; Martin, R. L.; Hay, P. J., *J. Chem. Phys.* **2004**, *121*, 11104.
2. Bühl, M.; Sieffert, N.; Golubnychiy, V.; Wipff, G., *J. Phys. Chem. A* **2008**, *112*, 2428.
3. Clavaguera-Sarrio, C.; Ismail, N.; Marsden, C. J.; Begue, D.; Pouchan, C., *Chem. Phys.* **2004**, *302*, 1.
4. Gagliardi, L.; Willetts, A.; Skylaris, C. K.; Handy, N. C.; Spencer, S.; Ioannou, A. G.; Simper, A. M., *J. Am. Chem. Soc.* **1998**, *120*, 11727.
5. Garcia-Hernandez, M.; Lauterbach, C.; Krüger, S.; Matveev, A.; Rösch, N., *J. Comput. Chem.* **2002**, *23*, 834.

6. Gutowski, K. E.; Cocalia, V. A.; Griffin, S. T.; Bridges, N. J.; Dixon, D. A.; Rogers, R. D., *J. Am. Chem. Soc.* **2007**, *129*, 526.
7. Han, Y. K., *J. Comput. Chem.* **2001**, *22*, 2010.
8. Han, Y. K.; Hirao, K., *J. Chem. Phys.* **2000**, *113*, 7345.
9. Hay, P. J.; Martin, R. L., *J. Chem. Phys.* **1998**, *109*, 3875.
10. Iche-Tarrat, N.; Marsden, C. J., *J. Phys. Chem. A.* **2008**, *112*, 7632.
11. Kaltsoyannis, N.; Hay, P. J.; Li, J.; Blaudeau, J. P.; Bursten, B. E., Theoretical Studies of the Electronic Structure of Compounds of the Actinides. In *The Chemistry of the Actinide and Transactinide Elements*, 3rd ed, 3 ed.; Morss, L. R.; Edelstein, N. M.; Fuger, J.; Katz, J. J., Eds. Springer: Dordrecht, The Netherlands, 2006; Vol. 3, pp 1893.
12. Kovács, A.; Konings, R. J. M., *J. Mol. Struct-Theochem* **2004**, *684*, 35.
13. Odoh, S. O.; Schreckenbach, G., *J. Phys. Chem. A* **2010**, *114*, 1957.
14. Peralta, J. E.; Batista, E. R.; Scuseria, G. E.; Martin, R. L., *J. Chem. Theory Comput.* **2005**, *1*, 612.
15. Perron, H.; Roques, J.; Domain, C.; Drot, R.; Simoni, E.; Catalette, H., *Inorg. Chem.* **2008**, *47*, 10991.
16. Prestianni, A.; Joubert, L.; Chagnes, A.; Cote, G.; Ohnet, M. N.; Rabbe, C.; Charbonnel, M. C.; Adamo, C., *J. Phys. Chem. A.* **2010**, *114*, 10878.
17. Schimmelpfennig, B.; Privalov, T.; Wahlgren, U.; Grenthe, I., *J. Phys. Chem. A.* **2003**, *107*, 9705.
18. Schreckenbach, G.; Hay, P. J.; Martin, R. L., *J. Comput. Chem.* **1999**, *20*, 70.
19. Schreckenbach, G.; Shamov, G. A., *Acc. Chem. Res.* **2010**, *43*, 19.
20. Shamov, G. A.; Schreckenbach, G., *J. Phys. Chem. A* **2005**, *109*, 10961.

21. Shamov, G. A.; Schreckenbach, G., *J. Phys. Chem. A* **2006**, *110*, 9486.
22. Shamov, G. A.; Schreckenbach, G.; Vo, T. N., *Chem-Eur. J.* **2007**, *13*, 4932.
23. Vallet, V.; Macak, P.; Wahlgren, U.; Grenthe, I., *Theor. Chem. Acc.* **2006**, *115*, 145.
24. Vallet, V.; Wahlgren, U.; Schimmelpfennig, B.; Moll, H.; Szabo, Z.; Grenthe, I., *Inorg. Chem.* **2001**, *40*, 3516.
25. Cao, Z. J.; Balasubramanian, K., *J. Chem. Phys.* **2005**, *123*.
26. Chaudhuri, D.; Balasubramanian, K., *Chem. Phys. Lett.* **2004**, *399*, 67.
27. Clavaguera-Sarrio, C.; Vallet, V.; Maynau, D.; Marsden, C. J., *J. Chem. Phys.* **2004**, *121*, 5312.
28. Ismail, N.; Heully, J. L.; Saue, T.; Daudey, J. P.; Marsden, C. J., *Chem. Phys. Lett.* **1999**, *300*, 296.
29. Horowitz, S. E.; Marston, J. B., *J. Chem. Phys.* **2011**, *134*.
30. La Macchia, G.; Infante, I.; Raab, J.; Gibson, J. K.; Gagliardi, L., *Phys. Chem. Chem. Phys.* **2008**, *10*, 7278.
31. Austin, J. P.; Sundararajan, M.; Vincent, M. A.; Hillier, I. H., *Dalton T.* **2009**, 5902.
32. Gaunt, A. J.; May, I.; Neu, M. P.; Reilly, S. D.; Scott, B. L., *Inorg. Chem.* **2011**, *50*, 4244.
33. Chaudhuri, D.; Balasubramanian, K., *Chem. Phys. Lett.* **2004**, *399*, 67.
34. Allen, P. G.; Veirs, D. K.; Conradson, S. D.; Smith, C. A.; Marsh, S. F., *Inorg. Chem.* **1996**, *35*, 2841.
35. Conradson, S. D.; Abney, K. D.; Begg, B. D.; Brady, E. D.; Clark, D. L.; den Auwer, C.; Ding, M.; Dorhout, P. K.; Espinosa-Faller, F. J.; Gordon, P. L.; Haire, R. G.; Hess, N. J.; Hess, R. F.; Keogh, D. W.; Lander, G. H.; Lupinetti, A. J.; Morales, L. A.; Neu, M. P.; Palmer, P. D.;

Paviet-Hartmann, P.; Reilly, S. D.; Runde, W. H.; Tait, C. D.; Veirs, D. K.; Wastin, F., *Inorg. Chem.* **2004**, *43*, 116.

36. Frisch, M. J. T., G. W.; Schlegel, H. B.; Scuseria, G. E.; Robb, M. A.; Cheeseman, J. R.; Montgomery, Jr., J. A.; Vreven, T.; Kudin, K. N.; Burant, J. C.; Millam, J. M.; Iyengar, S. S.; Tomasi, J.; Barone, V.; Mennucci, B.; Cossi, M.; Scalmani, G.; Rega, N.; Petersson, G. A.; Nakatsuji, H.; Hada, M.; Ehara, M.; Toyota, K.; Fukuda, R.; Hasegawa, J.; Ishida, M.; Nakajima, T.; Honda, Y.; Kitao, O.; Nakai, H.; Klene, M.; Li, X.; Knox, J. E.; Hratchian, H. P.; Cross, J. B.; Bakken, V.; Adamo, C.; Jaramillo, J.; Gomperts, R.; Stratmann, R. E.; Yazyev, O.; Austin, A. J.; Cammi, R.; Pomelli, C.; Ochterski, J. W.; Ayala, P. Y.; Morokuma, K.; Voth, G. A.; Salvador, P.; Dannenberg, J. J.; Zakrzewski, V. G.; Dapprich, S.; Daniels, A. D.; Strain, M. C.; Farkas, O.; Malick, D. K.; Rabuck, A. D.; Raghavachari, K.; Foresman, J. B.; Ortiz, J. V.; Cui, Q.; Baboul, A. G.; Clifford, S.; Cioslowski, J.; Stefanov, B. B.; Liu, G.; Liashenko, A.; Piskorz, P.; Komaromi, I.; Martin, R. L.; Fox, D. J.; Keith, T.; Al-Laham, M. A.; Peng, C. Y.; Nanayakkara, A.; Challacombe, M.; Gill, P. M. W.; Johnson, B.; Chen, W.; Wong, M. W.; Gonzalez, C.; and Pople, J. A. Gaussian 03, Revision C.02. 2004.

37. Küchle, W.; Dolg, M.; Stoll, H.; Preuss, H., *Mol. Phys.* **1991**, *74*, 1245.

38. Küchle, W.; Dolg, M.; Stoll, H.; Preuss, H., *J. Chem. Phys.* **1994**, *100*, 7535.

39. Becke, A. D., *J. Chem. Phys.* **1993**, *98*, 5648.

40. Stephens, P. J.; Devlin, F. J.; Chabalowski, C. F.; Frisch, M. J., *J. Phys. Chem.* **1994**, *98*, 11623.

41. Perdew, J. P.; Burke, K.; Ernzerhof, M., *Phys. Rev. Lett.* **1996**, *77*, 3865.

42. Perdew, J. P.; Burke, K.; Ernzerhof, M., *Phys. Rev. Lett.* **1997**, *78*, 1396.

43. Miertus, S.; Scrocco, E.; Tomasi, J., *Chem. Phys.* **1981**, *55*, 117.

44. Odoh, S. O., *Unpublished results*.
45. van Lenthe, E., *J. Comput. Chem.* **1999**, *20*, 51.
46. van Lenthe, E.; Baerends, E. J.; Snijders, J. G., *J. Chem. Phys.* **1993**, *99*, 4597.
47. Odoh, S. O.; Walker, S. M.; Meier, M.; Stetefeld, J.; Schreckenbach, G., *Inorg. Chem.* **2011**, *50*, 3141.
48. Runde, W.; Reilly, S. D.; Neu, M. P., *Geochim. Cosmochim. Ac.* **1999**, *63*, 3443.
49. Berthon, C.; Boubals, N.; Charushnikova, I. A.; Collison, D.; Cornet, S. M.; Auwer, C.; Gaunt, A. J.; Kaltsoyannis, N.; May, I.; Petit, S.; Redmond, M. P.; Reilly, S. D.; Scott, B. L., *Inorg. Chem.* **2010**, *49*, 9554.
50. Balakris.P. V; Patil, S. K.; Sharma, H. D.; Venkatas.H. V, *Can. J. Chemistry* **1965**, *43*, 2052.
51. Allen, P. G.; Bucher, J. J.; Shuh, D. K.; Edelstein, N. M.; Reich, T., *Inorg. Chem.* **1997**, *36*, 4676.
52. Hennig, C.; Tutschku, J.; Rossberg, A.; Bernhard, G.; Scheinost, A. C., *Inorg. Chem.* **2005**, *44*, 6655.
53. Watkin, D. J.; Denning, R. G.; Prout, K., *Acta Crystallogr. C* **1991**, *47*, 2517.
54. Wilkerson, M. P.; Arrington, C. A.; Berg, J. M.; Scott, B. L., *J. Alloy Compd.* **2007**, *444*, 634.
55. Wilkerson, M. P.; Scott, B. L., *Acta Crystallogr. E* **2008**, *64*, I5.
56. Denning, R. G., *Struct. Bond.* **1992**, *79*, 215.
57. Denning, R. G., *J. Phys. Chem. A.* **2007**, *111*, 4125.
58. Denning, R. G.; Morrison, I. D., *Chem. Phys. Lett.* **1991**, *180*, 101.
59. Denning, R. G.; Norris, J. O. W.; Brown, D., *Mol. Phys.* **1982**, *46*, 325.

60. Craw, J. S.; Vincent, M. A.; Hillier, I. H.; Wallwork, A. L., *J. Phys. Chem.* **1995**, *99*, 10181.
61. Madic, C.; Begun, G. M.; Hobart, D. E.; Hahn, R. L., *Inorg. Chem.* **1984**, *23*, 1914.
62. [http://www.ne.doe.gov/pdfFiles/NRCseminarreprocessing\\_Terry\\_Todd.pdf](http://www.ne.doe.gov/pdfFiles/NRCseminarreprocessing_Terry_Todd.pdf).
63. Den Auwer, C.; Revel, R.; Charbonnel, M. C.; Presson, M. T.; Conradson, S. D.; Simoni, E.; Le Du, J. F.; Madic, C., *J. Synchrotron Radiat.* **1999**, *6*, 101.
64. Basile, L. J.; Sullivan, J. C.; Ferraro, J. R.; Labonvil.P, *Appl. Spectrosc.* **1974**, *28*, 142.
65. Akona, S. B.; Fawcett, J.; Holloway, J. H.; Russell, D. R.; Leban, I., *Acta Crystallogr. C* **1991**, *47*, 45.
66. Alcock, N. W.; Roberts, M. M.; Brown, D., *J. Chem. Soc.-Dalton Trans.* **1982**, 25.
67. Bombieri, G.; Brown, D.; Graziani, R., *J. Chem. Soc.-Dalton Trans.* **1975**, 1873.

## Preface to Chapter 4

This chapter is based on a manuscript published in the journal “*Inorganic Chemistry*”. The full citation of the paper is as follows:

Samuel O. Odoh, Justine A. Reyes and Georg Schreckenbach, “Theoretical Study of the Structural and Electronic Properties of Plutonyl Hydroxides”, *Inorg. Chem.* **2012**, submitted.

All the calculations in the main body of the published manuscript and compiled in this chapter were carried out by Samuel O. Odoh. The manuscript was prepared together with Justine A. Reyes and Prof. Georg Schreckenbach. Justine A. Reyes was an undergraduate research fellow in the Department of Chemistry, University of Manitoba.

A crucial difference between the speciation of hexavalent uranyl and plutonyl complexes in aqueous solutions at high pH has been reported. The uranyl speciation system contains a significant amount of the trimeric (and heavier) complex at modest to high pH values. This contrasts with the plutonyl system in which little or negligible amounts of the trimer complex was observed. In this chapter the structure and electronic properties of plutonyl aquo-hydroxo complexes are examined using density functional theory. The origin of the differences in the mole-fractions of the uranyl and plutonyl trimeric complexes in the actinyl aquo-hydroxo speciation diagrams was also determined.

Copyright permissions have been obtained from the American Chemical Society and the other authors.

## Chapter 4: Theoretical Study of the Structural and Electronic

### Properties of Plutonyl Hydroxides

#### Abstract

Previous experimental reports have revealed major differences between the uranyl and plutonyl hydrolysis systems. The uranyl hydrolysis is dominated by trimeric and polynuclear species while the plutonyl system is dominated by a dimer complex with relatively low mole-fractions for the trimer. To fully understand the origins of this discrepancy, the structural and electronic properties of the monomeric, dimeric and trimeric plutonyl hydroxo complexes as well as the hydrolysis reactions of  $[\text{PuO}_2(\text{H}_2\text{O})_4]^{2+}$  have been theoretically examined using scalar-relativistic density functional theory. The stabilities of the plutonyl hydroxo complexes were also compared to those of their uranyl and neptunyl analogues. The trends in the structures of the plutonyl hydroxo complexes are generally similar to those observed in their uranyl counterparts. The calculated plutonyl symmetric stretching vibrational frequencies were used to match previously reported experimental Raman peaks at 833, 817, 826 and 794  $\text{cm}^{-1}$  to  $[\text{PuO}_2(\text{H}_2\text{O})_5]^{2+}$ ,  $[\text{PuO}_2(\text{H}_2\text{O})_4(\text{OH})]^+$ ,  $[(\text{PuO}_2)_2(\text{OH})_2(\text{H}_2\text{O})_6]^{2+}$  and  $[(\text{PuO}_2)_2(\text{OH})_4(\text{H}_2\text{O})_4]$  respectively. The assignment of the experimental peak at 805  $\text{cm}^{-1}$  is equivocal as it could be assigned to either  $[(\text{PuO}_2)_2(\text{OH})_4(\text{H}_2\text{O})_4]$  or  $[(\text{PuO}_2)_3(\text{H}_2\text{O})_6(\text{O})(\text{OH})_3]^+$ . The calculated reaction energies,  $\Delta E_{\text{reaction}}$ , for the hydrolysis of  $[\text{AnO}_2(\text{H}_2\text{O})_5]^{2+}$  complexes show that the formation of the dihydroxo dimer is significantly more exothermic than the formation of the trimer. The formation of the uranyl trimer complex by hydrolysis of  $[\text{UO}_2(\text{H}_2\text{O})_5]^{2+}$  is however about 6.2 kcal/mol more exothermic than the case in the plutonyl system. This calculated  $\Delta\Delta E_{\text{reaction}}$  agrees very well with

experimental estimates of 6.32 kcal/mol and could explain the dominance of the trimer in the uranyl system in contrast to its minor role in the plutonyl hydrolysis system. The greater oxophilicity of the uranyl group results in greater stabilization of its trimeric complex, in comparison to that of plutonyl, by dehydration of two hydroxo groups to form a  $\mu_3$ -oxo group. The presence of a bridging aquo ligand in the trimer ring also destabilizes the uranyl system to a far greater extent than its plutonyl analog. These critical differences are manifested in the  $\mu_3$ -oxo atomic 2p contributions to the actinyl- $\pi(d)/\mu_3O$ -2p orbitals as well as the extent to which the  $\pi(f/d)/\sigma(Pu-\mu_3O)$  orbitals are stabilized. These two factors decrease down the U, Np and Pu series.

## Introduction

The +6 oxidation state of plutonium is dominated by the plutonyl moiety in aqueous media.<sup>1-2</sup> The environmental dominance of the hydroxide and carbonate ligands and the toxicity and safety issues associated with plutonium make it important to study the properties of the plutonyl hydroxide and carbonate species. There have been several experimental and theoretical studies of the speciation, structure and electronic properties of plutonyl carbonates.<sup>3-6</sup> On the other hand, hydrolysis of plutonyl complexes<sup>7-9</sup> has been studied to a much lesser extent than that of their uranyl counterparts.<sup>10-26</sup> The practical effect of this is a distinct scarcity of experimental data regarding the speciation and solution thermodynamics, structure and electronic properties of plutonyl hydroxides in contrast to the situation for uranium. Recently, Neu et al. pointed out a significant difference between the U(VI) and Pu(VI) hydrolysis systems.<sup>9</sup> The plutonyl hydrolysis system is dominated by the dimeric product,  $[(PuO_2)_2(OH)_2(H_2O)_6]^{2+}$ , while the uranyl system is dominated by the trimeric complex,  $[(UO_2)_3(OH)_5]^+$ , and other polynuclear species in highly alkaline solutions. They could however not characterize the structural

properties of the plutonyl dimer complex using extended X-ray absorption fine structure (EXAFS).<sup>9</sup> In addition, they found no evidence for the formation of higher polynuclear species such as  $[(\text{PuO}_2)_3(\text{OH})_5]^+$  or  $[(\text{PuO}_2)_4(\text{OH})_7]^+$ . It should be however noted that they used very dilute solutions, with concentrations between  $10^{-2}$  and  $10^{-5}$  M Pu(VI). On the other hand, Rao et al. recently reported their potentiometric and calorimetric work on the hydrolysis of Pu(VI) in slightly acidic solutions at variable temperatures.<sup>8</sup> The formation of  $[(\text{PuO}_2)_3(\text{OH})_5]^+$  was invoked in attempts to fit their calorimetric and potentiometric data. Going further back, the formation of a tetrameric complex rather than  $[(\text{PuO}_2)_3(\text{OH})_5]^+$  was invoked by Madic et al. in their evaluation of the pH dependence of the Raman active plutonyl asymmetric stretching vibrational modes of the hydrolysis products.<sup>7</sup>

The seeming disparity in the final conclusions of these experimental works<sup>7-9</sup> and the general scarcity of EXAFS structural data for plutonyl complexes represent a significant gap in our knowledge of the similarity and differences between the hydrolysis of the plutonyl group and that of its uranium and neptunium analogues. In addition, if one adheres to the conclusions of Neu et al.<sup>9</sup> regarding the absence or negligible concentration of the trimeric species, there is at the current moment only speculative insights for why this is the case as well as for why in contrast the uranyl hydrolysis system is dominated by the trimeric and polynuclear complexes. Theoretical calculations can however be used to provide information regarding the structural properties and stabilities of the plutonyl hydroxo complexes. Kohn-Sham density functional theory (DFT) is a powerful method that is rigorously only suited for single-reference systems. A large number of open-shell actinide systems, amongst which are the Pu(VI) complexes, are however not entirely single-reference in nature. The ground electronic states in these complexes often contain several determinants each corresponding to particular occupation of the actinide 5f

orbitals. As such, the use of single-reference theoretical approaches in computing the properties of these complexes is not fully rigorous. On the other hand, the use of DFT calculations in predicting the structural features and vibrational frequencies of plutonyl complexes, as well of other open-shell actinide systems, has been reported by various workers.<sup>3, 5, 27-34</sup> The non-bonding natures of the unpaired 5f electrons of the open-shell actinide systems ensures that there are, to a first approximation, no differences in the bonding schemes of the different electronic states corresponding to the different occupations of the 5f orbitals.

In this work, we have examined the structural and electronic properties of the monomeric, dimeric and trimeric plutonyl hydroxides using scalar-relativistic DFT calculations. The calculated structural properties of hydrolyzed plutonyl complexes are compared to available EXAFS data<sup>35</sup> while the calculated vibrational frequencies are compared to the Raman spectroscopic measurements of Madic et al.<sup>7</sup> The aim is to use theoretical calculations to fully identify which species are present in the plutonyl hydrolysis pH speciation diagram. In addition, the reaction energies for forming the monomeric, dimeric and polynuclear plutonyl hydroxides are compared to those of their neptunyl and uranyl counterparts in a bid to understand the origin(s) of the differences in the hydrolysis systems of these actinides.

### **Computational Details.**

All DFT calculations in this work were carried out with the ADF<sup>36-37</sup>, Gaussian 03<sup>38</sup> and Priroda<sup>39</sup> codes. Calculations employing relativistic effective core potentials (RECPs) to describe the plutonium atoms were carried out with Gaussian 03 while those employing all-electron (AE) basis sets were carried out with the ADF and Priroda codes. In cases with difficult convergence attributes, the plutonyl-hydroxo cores,  $[[\text{PuO}_2(\text{OH})_n]^{2-n}]_x$ , were first optimized before step-wise

addition of each aquo ligand. After the gas-phase geometry optimizations, vibrational frequencies were calculated using the harmonic approximation in order to confirm the minima nature of the optimized structures on the potential energy surfaces. The properties of the triplet, quintet and septet multiplet states are reported for the monomeric, dimeric and trimeric plutonyl species respectively. The deviations between the calculated and expected  $S(S+1)$  values for these multiplet states were in all cases less than 3.5%. Attempts to examine other multiplet states, such as the quintet state for the trimeric complexes and the antiferromagnetic singlet states for the dimeric complexes were abandoned as a result of massive spin contaminations (greater than 10% deviation from the exact  $S(S+1)$  value). Reaction energies were calculated as  $\Delta E$  by employing the total electronic energies of the reactants and products in an aqueous medium. In Priroda and Gaussian 03, ultra-fine grids were used in the numerical integration of the exchange-correlation portion of the density functionals. The grid size refers to the use of a grid-based numerical integration step in the evaluation of the exchange-correlation energies. An integration parameter of 6.0 was employed for the calculations carried out using the ADF code. To examine trends and allow for comparison, a similar approach was employed for the uranium and neptunium analogues of the plutonyl complexes studied in this work. The high-spin electronic states of the neptunyl complexes (triplet and quartet states for the dimer and trimers respectively) were also used.

A scalar-relativistic approximation to the full Dirac equation was used in the AE calculations carried out with the Priroda code. In this case, all the spin-orbit terms were separated out and neglected.<sup>40</sup> This approach, when used with the PBE functional has been shown to lead to accurate structural parameters, redox potentials and reaction energies for actinide complexes.<sup>34, 41-42</sup> A basis of double- $\zeta$  quality (cc-pVDZ) was used for all the elements for the

large component with the corresponding kinetically-balanced basis sets for the small component.<sup>39</sup> The combination of the PBE functional and this all-electron basis set is labeled as PBE/B1. Mayer bond orders<sup>43</sup> were calculated after the geometry optimizations. All the calculations carried out at this level were performed in the gas-phase.

The scalar relativistic ZORA approach<sup>44-46</sup> was employed with triple- $\zeta$  polarized (TZP) all electron basis sets in the calculations carried out with the ADF code. No core atomic orbitals were frozen in these calculations. The BP86 functional was used in optimizing the geometries of all the uranyl, neptunyl and plutonyl molecules in both the gaseous and aqueous phases. This level is labeled the BP86/B2 level. In ADF, the aqueous phase calculations were carried out using the conductor-like screening solvation model, COSMO.<sup>47</sup> The radii of the U, Np, Pu, O and H atoms were taken as 2.34, 2.34, 2.34, 1.72 and 1.30 respectively. The variations of the calculated reaction energies were found to be generally negligible for actinide solvation radii between 2.24 and 2.44 Å.

In the RECPs calculations, the Stuttgart small-core scalar-relativistic pseudopotential was used to describe the plutonium atoms.<sup>48-49</sup> The pseudopotential was used to represent 60 core electrons in plutonium while the remaining 34 electrons were represented by the associated valence basis set. All g-type functions were removed from the valence basis set to increase computational efficiency. The 6-31+G\* basis was used to describe all the other atoms in the molecules, except for hydrogen atoms for which the 6-31G basis was employed. This combination of the RECP for the plutonium atoms and the 6-31+G\*/6-31G bases for the non-actinide atoms is labeled as B3. The B3LYP functional was employed in the RECP computations. The effects of a solvent environment on the calculated reaction energies were evaluated with single-point calculations on the geometries optimized at B3LYP/B3 level in the

gas-phase while employing the polarizable continuum solvation (PCM) model.<sup>50</sup> The default atomic radii of the united atom topological model (UA0) in Gaussian 03 were used in the calculations. To examine trends and allow for comparison, a similar approach was employed for the uranium and neptunium analogues of the plutonyl complexes studied in this work.

## Results and Discussion

**Structural Properties.** The optimized structures of the monomeric plutonyl aquo-hydroxide complexes obtained at the BP86/B2 level in the aqueous phase are shown in Figures 4.1 and 4.2. The structural parameters and plutonyl stretching vibrational frequencies obtained for these molecules are collected in Tables 4.1-4.4. At this level, the Pu-O<sub>y1</sub> bonds were calculated to be about 1.76 Å long in the pentaquo plutonyl complex, [PuO<sub>2</sub>(H<sub>2</sub>O)<sub>5</sub>]<sup>2+</sup>, slightly longer than the experimental value of 1.75 Å.<sup>35</sup> The calculated Pu-OH<sub>2</sub> bond lengths for the equatorial ligands in this complex are also a good match for the experimental value of 2.41 Å. The experimental Pu-O<sub>y1</sub> and Pu-OH<sub>2</sub> bond distances were determined from EXAFS spectroscopy in solution.<sup>35</sup> From a methodological perspective, the calculated Pu-O<sub>y1</sub> bond lengths obtained in the gas phase are slightly shorter than those obtained in aqueous solution. The use of the hybrid functional leads to even shorter Pu-O<sub>y1</sub> bonds, Table 4.1.

Examination of the optimized structures of [PuO<sub>2</sub>(H<sub>2</sub>O)(OH)<sub>4</sub>]<sup>2-</sup>, [PuO<sub>2</sub>(H<sub>2</sub>O)<sub>2</sub>(OH)<sub>3</sub>]<sup>-</sup> and [PuO<sub>2</sub>(H<sub>2</sub>O)<sub>3</sub>(OH)<sub>2</sub>], Figure 4.1, shows that an aquo ligand in these complexes is found in the second solvation sphere, about 3.68-4.00 Å from the plutonium atoms. Energetically, the complexes with an aquo ligand in the second coordination sphere are generally favored in the gas phase mostly due to the hydrogen bonding with the equatorial hydroxo ligands. This was found to be the case at the BP86/B2 and B3LYP/B3 levels. In the aqueous phase calculations, there is a

dramatic reduction in the calculated binding energy of the water ligand in the 2<sup>nd</sup> coordination sphere. The removal of the second sphere aquo ligand from  $[\text{PuO}_2(\text{H}_2\text{O})(\text{OH})_4]^{2-}$ ,  $[\text{PuO}_2(\text{H}_2\text{O})_2(\text{OH})_3]^-$  and  $[\text{PuO}_2(\text{H}_2\text{O})_3(\text{OH})_2]$  were actually calculated to be exothermic at the BP86/B3 level while employing the COSMO solvation model. As a result,  $[\text{PuO}_2(\text{OH})_4]^{2-}$ ,  $[\text{PuO}_2(\text{H}_2\text{O})(\text{OH})_3]^-$  and  $[\text{PuO}_2(\text{H}_2\text{O})_2(\text{OH})_2]$ , Figure 4.2, are most likely the preferred species in solution. In addition, the calculated energies obtained in the gaseous and aqueous phases also show that  $[\text{PuO}_2(\text{OH})_4]^{2-}$  is preferred to its pentahydroxo counterpart,  $[\text{PuO}_2(\text{OH})_5]^{3-}$ . It should be noted that this does not imply the absence of a second coordination sphere. Rather, more (than one) explicit water molecules are required for a stable second sphere.

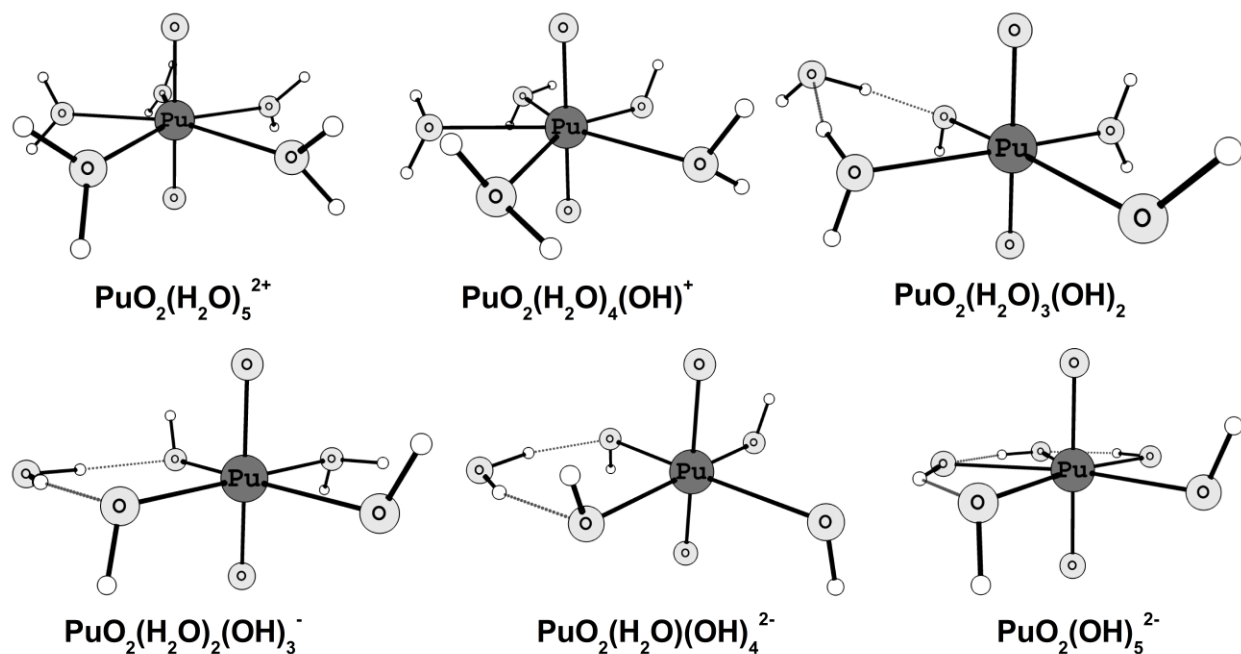


**Figure 4.1:** Optimized structures of the aquo-hydroxo  $[\text{PuO}_2(\text{H}_2\text{O})_{5-n}(\text{OH})_n]^{2-n}$  complexes obtained at the BP86/B2 level with the COSMO solvation model.

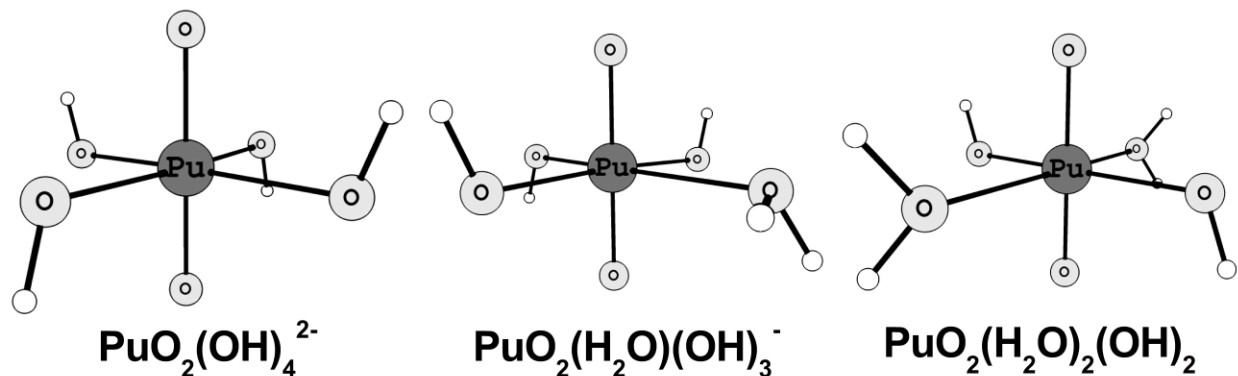


**Figure 4.2:** Optimized structures of the aquo-hydroxo  $[\text{PuO}_2(\text{H}_2\text{O})_{4-n}(\text{OH})_n]^{2-n}$  complexes obtained at the BP86/B2 level with the COSMO solvation model.

**Table 4.1:** Calculated structural properties of  $[\text{PuO}_2(\text{H}_2\text{O})_5]^{2+}$  and  $[\text{PuO}_2(\text{H}_2\text{O})_4(\text{OH})]^+$ . The bond distances are given in Å while the vibrational frequencies (asymmetric/symmetric plutonyl stretching modes) are given in  $\text{cm}^{-1}$ .

|              | $[\text{PuO}_2(\text{H}_2\text{O})_5]^{2+}$ |                    |                | $[\text{PuO}_2(\text{H}_2\text{O})_4(\text{OH})]^+$ |       |                    |            |
|--------------|---|--------------------|----------------|---|-------|--------------------|------------|
|              | Bond Lengths (Å)                            |                    | Freq.          | Bond Lengths (Å)                                    |       |                    | Freq       |
|              | Pu-O <sub>y1</sub>                          | Pu-OH <sub>2</sub> |                | Pu-O <sub>y1</sub>                                  | Pu-OH | Pu-OH <sub>2</sub> |            |
| PBE/B1       | 1.75  | 2.46               | 969/853        | 1.77  | 2.11  | 2.53-2.56          | 922, 814   |
| BP86/B2      |   |                    |                |   |       |                    |            |
| Gaseous      | 1.74  | 2.46               | 976/856        | 1.77  | 2.13  | 2.53-2.57          | 925, 815   |
| Aqueous      | 1.76  | 2.41               | 925/827        | 1.78  | 2.14  | 2.50-2.53          | 875, 787   |
| B3LYP/B3     |   |                    |                |   |       |                    |            |
| Gaseous      | 1.72  | 2.47               | 1032/911       | 1.74  | 2.11  | 2.53-2.57          | 979, 864   |
| <i>Expt.</i> | <i>1.75</i>                                 | <i>2.41</i>        | <i>962/833</i> |   |       |                    | <i>817</i> |

<sup>a</sup> EXAFS measurements in aqueous solution; Ref<sup>35</sup>

There is a sequential increase in the Pu-O<sub>y1</sub> bond lengths as an aquo ligand is replaced by a hydroxo group. This is the case at the PBE/B1, BP86/B2 and B3LYP/B3 levels of theory in both the gaseous and aqueous phases, Tables 4.1-4.4. For example, at the BP86/B2 level in solution, the Pu-O<sub>y1</sub> bonds become progressively weaker by about 0.01-0.03 Å as more hydroxo ligands are coordinated in the equatorial region. This increase in bond lengths is reflected in the decrease in the calculated Pu-O<sub>y1</sub> Mayer bond orders, Table 4.5. The bond orders decrease from 2.38 in the pentaquo complex to 2.25 in the pentahydroxo complex. Although the gradual decrease in Pu-O<sub>y1</sub> bond strength as indicated by the bond order is small, it correlates very well with the increasing bond lengths. This phenomenon is not unique to the plutonyl hydroxides and similar effects have been observed in uranyl fluorides<sup>51</sup> and uranyl hydroxides, to name a few.<sup>52</sup> The magnitude of the Pu-O<sub>y1</sub> bond orders indicate that the Pu-O bonds in the plutonyl moiety have significant triple bond character and the weakening of these bonds down the plutonyl aquo-hydroxo series could at first glance be attributed to decreasing  $\pi$ -bonding interactions between the plutonium and axial oxo atoms. The Pu-OH bonds also become progressively longer down the series with increasing number of hydroxide groups. The Pu-OH bond length increases from 2.14 Å in [PuO<sub>2</sub>(H<sub>2</sub>O)<sub>4</sub>OH]<sup>+</sup> to 2.28 Å in [PuO<sub>2</sub>(OH)<sub>4</sub>]<sup>2-</sup> and 2.26-2.53 Å in [PuO<sub>2</sub>(OH)<sub>5</sub>]<sup>3-</sup> at the BP86/B2 level in the COSMO calculations. This correlates with the decreasing Pu-OH bond orders down the series. This trend is present in both the [PuO<sub>2</sub>(H<sub>2</sub>O)<sub>4-n</sub>OH]<sub>n</sub>.H<sub>2</sub>O]<sup>2-n</sup> and [PuO<sub>2</sub>(H<sub>2</sub>O)<sub>4-n</sub>OH]<sub>n</sub><sup>2-n</sup> series of complexes, Tables 4.5. For the terminal hydroxo complex, [PuO<sub>2</sub>(OH)<sub>4</sub>]<sup>2-</sup>, the calculated Pu-O<sub>y1</sub> and Pu-OH bond lengths obtained at the BP86/B2 level are within 0.05 Å of the EXAFS data.<sup>35</sup>

The aqueous environment as modeled by the COSMO solvation model generally tends to alter the Pu-O<sub>y1</sub> and Pu-OH bonds by less than 0.02 Å. In contrast the major structural effect of

**Table 4.2:** Calculated structural properties of  $[\text{PuO}_2(\text{H}_2\text{O})_3(\text{OH})_2]$  and  $[\text{PuO}_2(\text{H}_2\text{O})_2(\text{OH})_3]^-$ . The bond distances are given in Å while the vibrational frequencies (asymmetric/symmetric plutonyl stretching modes) are given in  $\text{cm}^{-1}$ .

|          | $[\text{PuO}_2(\text{H}_2\text{O})_3(\text{OH})_2]$ |            |                    | Freq.   | $[\text{PuO}_2(\text{H}_2\text{O})_2(\text{OH})_3]^-$ |           |                    | Freq    |
|----------|---|------------|--------------------|---------|---|-----------|--------------------|---------|
|          | Pu-O <sub>yl</sub>                                  | Pu-OH      | Pu-OH <sub>2</sub> |         | Pu-O <sub>yl</sub>                                    | Pu-OH     | Pu-OH <sub>2</sub> |         |
| PBE/B1   | 1.79  | 2.18, 2.20 | 2.47,2.58          | 900/795 | 1.81  | 2.20,2.20 | 2.67               | 863/758 |
|          |   |            | 3.68               |         |   | 2.29      | 3.80               |         |
| BP86/B2  |   |            |                    |         |   |           |                    |         |
| Gaseous  | 1.79  | 2.18, 2.20 | 2.49,2.59          | 894/785 | 1.81  | 2.22,2.22 | 2.70               | 854/749 |
|          |   |            | 3.73               |         |   | 2.29      | 3.91               |         |
| Aqueous  | 1.80  | 2.16, 2.22 | 2.46,2.48          |         | 1.82  | 2.19,2.23 | 2.57               |         |
|          |   |            | 3.77               |         |   | 2.25      | 3.83               |         |
| B3LYP/B3 |   |            |                    |         |   |           |                    |         |
| Gaseous  | 1.75  | 2.17, 2.20 | 2.52,2.59          | 951/838 | 1.77  | 2.21,2.22 | 2.72               | 913/799 |
|          |   |            | 3.71               |         |   | 2.30      | 3.84               |         |

the solvent environment is shortening of the Pu-OH<sub>2</sub> bonds. We give two examples of this phenomenon here. For  $[\text{PuO}_2(\text{H}_2\text{O})_5]^{2+}$ , the Pu-OH<sub>2</sub> bonds were calculated to be shorter by 0.05 Å after the introduction of solvent effects at the BP86/B2 level, Table 4.1. The gas phase structure of  $[\text{PuO}_2(\text{H}_2\text{O})(\text{OH})_3]^-$  is such that the lone aquo ligand interacts with one of the hydroxo groups. This leads to a longer Pu-OH<sub>2</sub> bond as well as one unusually long Pu-OH bond of about 2.32 Å. Optimization in solution removes this effect, Figure 4.2, resulting in Pu-OH<sub>2</sub> and Pu-OH bonds that are 2.58 Å and 2.21 Å long respectively, Table 4.3.

**Table 4.3:** Calculated structural properties of  $[\text{PuO}_2(\text{H}_2\text{O})_2(\text{OH})_2]$  and  $[\text{PuO}_2(\text{H}_2\text{O})(\text{OH})_3]^-$ . The bond distances are given in Å while the vibrational frequencies (asymmetric/symmetric plutonyl stretching modes) are given in  $\text{cm}^{-1}$ .

|          | $[\text{PuO}_2(\text{H}_2\text{O})_2(\text{OH})_2]$ |       |                    |         | $[\text{PuO}_2(\text{H}_2\text{O})(\text{OH})_3]^-$ |           |                    |          |
|----------|---|-------|--------------------|---------|---|-----------|--------------------|----------|
|          | Bond Lengths (Å)                                    |       |                    | Freq.   | Bond Lengths (Å)                                    |           |                    | Freq.    |
|          | Pu-O <sub>y1</sub>                                  | Pu-OH | Pu-OH <sub>2</sub> |         | Pu-O <sub>y1</sub>                                  | Pu-OH     | Pu-OH <sub>2</sub> |          |
| PBE/B1   | 1.80  | 2.14  | 2.54               | 884/782 | 1.81  | 2.18,2.31 | 2.70               | 853/ 749 |
| BP86/B2  |   |       |                    |         |   |           |                    |          |
| Gaseous  | 1.80  | 2.15  | 2.55               | 875/772 | 1.81  | 2.20,2.32 | 2.73               | 842/736  |
| Aqueous  | 1.81  | 2.15  | 2.48               | 826/748 | 1.82  | 2.21      | 2.58               | 793/ 716 |
| B3LYP/B3 |   |       |                    |         |   |           |                    |          |
| Gaseous  | 1.76  | 2.16  | 2.55               | 931/820 | 1.78  | 2.19,2.30 | 2.75               | 899/789  |

The calculated structural properties of the dimeric species,  $[(\text{PuO}_2)_2(\text{OH})_2(\text{H}_2\text{O})_6]^{2+}$  and  $[(\text{PuO}_2)_2(\text{OH})_4(\text{H}_2\text{O})_4]$  are presented in Table 4.6. For these complexes, the structures of various conformers arising from the different orientations of the terminal hydrogen atoms in the pendant and bridging hydroxo groups were optimized and only the most stable structures are shown in Figure 4.3. We can employ a simple approach to describing the structures of the dimeric complexes. These complexes are  $\mu_2$ -dihydroxo complexes as the two plutonyl moieties are bridged by two hydroxo ligands. To a first approximation, the bridging hydroxo groups in  $[(\text{PuO}_2)_2(\text{OH})_2(\text{H}_2\text{O})_6]^{2+}$  are shared between the  $\text{PuO}_2^{2+}$  groups, such that it appears that each  $\text{PuO}_2^{2+}$  group is bonded to approximately one hydroxo group. On the other hand, each  $\text{PuO}_2^{2+}$  group is bonded to about two hydroxo groups in the tetrahydroxo complex,

$[(\text{PuO}_2)_2(\text{OH})_4(\text{H}_2\text{O})_4]$ . Now given this simple model, the calculated Pu-O<sub>yl</sub> bonds in these complexes, Table 4.6, are within the ranges suggested by the trends obtained for the mononuclear complexes, Tables 4.1 and 4.3. Likewise the calculated Pu-O<sub>yl</sub> bond orders in the dihydroxo and tetrahydroxo binuclear complexes are of the same magnitude as those found in  $[\text{PuO}_2(\text{H}_2\text{O})_4(\text{OH})]^+$  and  $[\text{PuO}_2(\text{H}_2\text{O})_2(\text{OH})_2]$  respectively, Table 4.5.

**Table 4.4:** Calculated structural properties of  $[\text{PuO}_2(\text{OH})_4]^{2-}$  and  $[\text{PuO}_2(\text{OH})_5]^{3-}$ . The bond distances are given in Å while the vibrational frequencies (asymmetric/symmetric plutonyl stretching modes) are given in  $\text{cm}^{-1}$ .

| $[\text{PuO}_2(\text{OH})_4]^{2-}$ | Bond Lengths (Å)   |             |           | PuO <sub>2</sub> Str. ( $\text{cm}^{-1}$ ) | $[\text{PuO}_2(\text{OH})_5]^{3-}$ |          |           |
|------------------------------------|--------------------|-------------|-----------|--|------------------------------------|----------|-----------|
|                                    | Pu-O <sub>yl</sub> | Pu-OH       | Asym, Sym |  | Pu-O <sub>yl</sub>                 | Pu-OH    | Asym, Sym |
| PBE/B1                             | 1.85               | 2.27        | 808, 690  | 1.85                                       | 2.402                              |          |           |
| BP86/B2                            |                    |             |           |  |                                    |          |           |
| Gaseous                            | 1.85               | 2.29        | 788, 699  | 1.84                                       | 2.46                               | 776, 656 |           |
| Aqueous                            | 1.85               | 2.25        | 756, 683  | 1.85                                       | 2.26-2.53                          |          |           |
| B3LYP/B3                           |                    |             |           |  |                                    |          |           |
| Gaseous                            | 1.81               | 2.28        | 837, 727  | 1.80                                       | 2.45                               | 840, 723 |           |
| <i>Expt</i>                        | <b>1.80</b>        | <b>2.30</b> |           |  |                                    |          |           |

**Table 4.5:** Calculated Mayer bond orders of the plutonyl aquo-hydroxo complexes obtained at the PBE/B1 level in the gaseous phase.

|   | Pu-O <sub>yl</sub> | Pu-OH <sub>pendant</sub> | Pu-OH <sub>bridging</sub> | Pu-OH <sub>2</sub> |
|---|--------------------|--------------------------|---------------------------|--------------------|
| Monomers  |                    |                          |                           |                    |
| [PuO <sub>2</sub> (H <sub>2</sub> O) <sub>5</sub> ] <sup>2+</sup>                                     | 2.38               |                          |                           | 0.47               |
| [PuO <sub>2</sub> (H <sub>2</sub> O) <sub>4</sub> (OH)] <sup>+</sup>                                  | 2.36               | 1.40                     |                           | 0.36-0.38          |
| [PuO <sub>2</sub> (H <sub>2</sub> O) <sub>3</sub> (OH) <sub>2</sub> ]                                 | 2.34               | 1.04/1.15                |                           | 0.39/0.50          |
| [PuO <sub>2</sub> (H <sub>2</sub> O) <sub>2</sub> (OH) <sub>2</sub> ]                                 | 2.34               | 1.30                     |                           | 0.36               |
| [PuO <sub>2</sub> (H <sub>2</sub> O) <sub>2</sub> (OH) <sub>3</sub> ] <sup>-</sup>                    | 2.31               | 0.93/1.09/1.12           |                           | 0.08/0.38          |
| [PuO <sub>2</sub> (H <sub>2</sub> O)(OH) <sub>3</sub> ] <sup>-</sup>                                  | 2.31               | 0.89-1.21                |                           | 0.37               |
| [PuO <sub>2</sub> (OH) <sub>4</sub> ] <sup>2-</sup>   | 2.28               | 1.10                     |                           |                    |
| [PuO <sub>2</sub> (OH) <sub>5</sub> ] <sup>3-</sup>   | 2.25               | 1.04                     |                           |                    |
| Dimers  |                    |                          |                           |                    |
| [(PuO <sub>2</sub> ) <sub>2</sub> (OH) <sub>2</sub> (H <sub>2</sub> O) <sub>6</sub> ] <sup>2+</sup>   | 2.36               |                          | 0.68                      | 0.40               |
| [(PuO <sub>2</sub> ) <sub>2</sub> (OH) <sub>4</sub> (H <sub>2</sub> O) <sub>4</sub> ]                 | 2.34               | 0.90                     | 0.66                      | 0.40               |
| Trimers   |                    |                          |                           |                    |
| [(PuO <sub>2</sub> ) <sub>3</sub> (H <sub>2</sub> O) <sub>6</sub> (O)(OH) <sub>3</sub> ] <sup>+</sup> | 2.33-2.35          | 0.85 for μ-oxo           | 0.70                      | 0.36               |

Going on to the other bonds, the Pu-OH<sub>2</sub> bonds are slightly longer in [(PuO<sub>2</sub>)<sub>2</sub>(OH)<sub>4</sub>(H<sub>2</sub>O)<sub>4</sub>], compared to [(PuO<sub>2</sub>)<sub>2</sub>(OH)<sub>2</sub>(H<sub>2</sub>O)<sub>6</sub>]<sup>2+</sup>, due to the interactions between the aquo ligands and the pendant hydroxo groups in this complex. The bonds between the plutonium atoms and the bridging hydroxo groups were calculated to be about 2.33-2.37 Å long. At the

PBE/B1 level, these bonds were calculated as having bond orders of 0.65-0.68, much smaller than the values of 0.89-1.40 obtained for the Pu-OH bonds in the monomer complexes or the value of 0.90 obtained for the pendant Pu-OH bonds in the binuclear tetrahydroxo complex, Table 4.5. The implication is a significant reduction in the  $\pi$ -donor character of the bridging OH groups as they each now form two  $\sigma$ -type bonds to the two plutonium atoms. The Pu-Pu distances in  $[(\text{PuO}_2)_2(\text{OH})_2(\text{H}_2\text{O})_6]^{2+}$  and  $[(\text{PuO}_2)_2(\text{OH})_4(\text{H}_2\text{O})_4]$  were calculated as 3.78 and 3.79 Å respectively at the BP86/B2 level in the COSMO calculations. As the covalent radius of plutonium is 1.87 Å, implying a Pu-Pu internuclear distance of about 3.74 Å, we can conclude that there is little covalent interaction between the actinide centers in these complexes. The calculated bond orders associated with the Pu-Pu distances are less than 0.2 in both dimer complexes. Tsushima et al. previously carried out EXAFS experiments on the analogous uranyl series.<sup>53</sup> They obtained a U-U distance of 3.88 Å for  $[(\text{UO}_2)_2(\text{OH})_2(\text{H}_2\text{O})_6]^{2+}$  which was in very good agreement with the results of the DFT calculations they had also carried out. We obtained a U-U distance of 3.87 Å for aqueous  $[(\text{UO}_2)_2(\text{OH})_2(\text{H}_2\text{O})_6]^{2+}$  at the BP86/B2 level, within 0.01 Å of the experimental and previous theoretical work. We note the contraction of the actinide-actinide distances by about 0.09 Å on going from the uranyl dimer complex to its plutonyl counterpart, consistent with the actinide contraction. The covalent radius of plutonium is about 0.1 Å smaller than that of uranium.

For the trimeric complex, It has been previously noted that  $[(\text{PuO}_2)_3(\text{H}_2\text{O})_6(\text{O})(\text{OH})_3]^+$  and  $[(\text{PuO}_2)_3(\text{H}_2\text{O})_6(\text{OH})_5]^+$  can't be distinguished from the often used acid-base titration experiments.<sup>53</sup> In their work on the uranyl analogue, Tsushima et al. obtained average U-U distances of 3.81-3.82 Å from their EXAFS experiments.<sup>53</sup> They concluded from these distances that there is a preference for  $[(\text{UO}_2)_3(\text{H}_2\text{O})_6(\text{O})(\text{OH})_3]^+$  rather than  $[(\text{UO}_2)_3(\text{H}_2\text{O})_6(\text{OH})_5]^+$ . At the

**Table 4.6:** Calculated structural properties of the plutonyl dimer complexes. The bond lengths are in Å and the calculated IR intensities (km/mol) are given in parenthesis.

|                             | [(PuO <sub>2</sub> ) <sub>2</sub> (OH) <sub>2</sub> (H <sub>2</sub> O) <sub>6</sub> ] <sup>2+</sup> |           |           |                  | [(PuO <sub>2</sub> ) <sub>2</sub> (OH) <sub>4</sub> (H <sub>2</sub> O) <sub>4</sub> ] |           |           |                  |
|-----------------------------|---|-----------|-----------|------------------|---|-----------|-----------|------------------|
|                             | PBE/B1  | BP86/B2   |           | B3LYP/B3         | PBE/B1  | BP86/B2   |           | B3LYP/B3         |
|                             | Gaseous   | Gaseous   | Aqueous   | Gaseous          | Gaseous   | Gaseous   | Aqueous   | Gaseous          |
| Pu-O <sub>yl</sub>          | 1.76  | 1.76      | 1.77      | 1.73             | 1.78  | 1.78      | 1.80      | 1.74-1.75        |
| Pu-OH <sub>bridging</sub>   | 2.32  | 2.32      | 2.32      | 2.33             | 2.33-2.35   | 2.34-2.35 | 2.35-2.36 | 2.37, 2.34       |
| Pu-OH <sub>pendant</sub>    |   |           |           |                  | 2.30  | 2.30      | 2.20      | 2.26-2.32        |
| Pu-OH <sub>2</sub>          | 2.51-2.53   | 2.52-2.55 | 2.43-2.52 | 2.53-2.55        | 2.58  | 2.61      | 2.59-2.60 | 2.58-2.59        |
| Pu-Pu                       | 3.82  | 3.80      | 3.78      | 3.84             | 3.71  | 3.74      | 3.79      | 3.75             |
| PuO <sub>2</sub> Str. Asym. | 944,938   | 947, 939  |           | 1004(446),996(0) | 917,908   | 912, 902  |           | 971(504),959(49) |
| PuO <sub>2</sub> Str. Sym.  | 831,825   | 829, 823  |           | 884(0),879(33)   | 804,793   | 804, 789  |           | 852(2),845(4)    |
| <b><i>Expt.</i></b>         | <b>826<sup>a</sup></b>  |           |           |                  | <b>805,793<sup>a</sup></b>  |           |           |                  |
| Bridging OH                 | 796,784   | 780, 778  |           | 844(184),838(0)  | 734,731   | 754, 748  |           | 783(205),780(13) |

<sup>a</sup> Raman spectroscopic measurements; Ref<sup>7</sup>

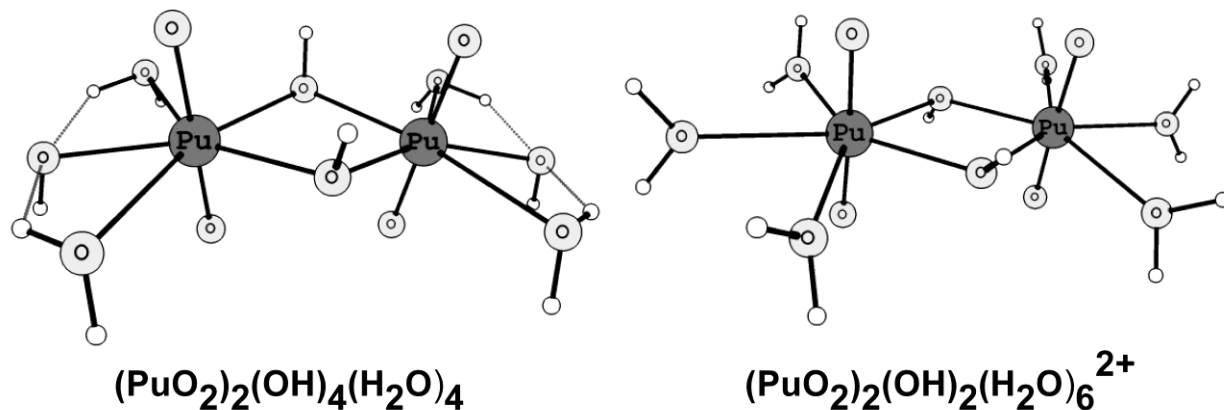


**Figure 4.3:** Optimized structures of the bis-plutonyl aquo tetrahydroxo and dihydroxo complexes obtained at the B3LYP/B3 level in the gas phase.

BP86/B2 level and with the COSMO solvation model, we obtained U-U distances of 3.82 Å for a  $C_{3V}$  structure for  $[(\text{UO}_2)_3(\text{H}_2\text{O})_6(\text{O})(\text{OH})_3]^+$ . The agreement between the EXAFS data of Tsushima et al.<sup>53</sup> and the result from the BP86/B2 model increases our confidence in the use of the  $C_{3V}$  structure in describing the plutonyl counterpart. The structural parameters of the optimized  $C_{3V}$   $\mu_3$ -oxo structure of  $[(\text{PuO}_2)_3(\text{H}_2\text{O})_6(\text{O})(\text{OH})_3]^+$  are presented in Table 4.7. This structure is shown in Figure 4.4. Similar to the case in the  $[(\text{PuO}_2)_2(\text{OH})_4(\text{H}_2\text{O})_4]$  dimer complex, the Pu-O<sub>yl</sub> bonds in this structure were calculated to be about 1.74 Å long at the B3LYP/B3 level in the gas phase, Table 4.7. The usual strengthening of the Pu-OH<sub>2</sub> bonds after optimization with an implicit solvation model is also observed for this complex at the BP86/B2 level. The Pu-Pu distances in this complex are 3.74 Å long, about 0.08 Å shorter than the U-U distances in  $[(\text{UO}_2)_3(\text{H}_2\text{O})_6(\text{O})(\text{OH})_3]^+$ .

**Table 4.7:** Calculated structural properties of the  $\mu_3$ -oxo motifs of the trimeric complex,  $[(\text{PuO}_2)_3(\text{H}_2\text{O})_6(\text{O})(\text{OH})_3]^+$ . The bond lengths are given in Å, bond angles in degrees while vibrational frequencies are presented in  $\text{cm}^{-1}$ .

|                             | PBE/B1        | BP86/B2       |         | B3LYP/B3 |
|-----------------------------|---------------|---------------|---------|----------|
|                             | Gaseous       | Gaseous       | Aqueous | Gaseous  |
| Pu-O <sub>yl</sub>          | 1.78          | 1.78          | 1.79    | 1.74     |
| Pu-OH <sub>bridging</sub>   | 2.42          | 2.41          | 2.40    | 2.39     |
| Pu- $\mu_3$ O               | 2.18          | 2.17          | 2.17    | 2.19     |
| Pu-OH <sub>2</sub>          | 2.58          | 2.60          | 2.56    | 2.54     |
| Pu-Pu                       | 3.71          | 3.73          | 3.74    | 3.72     |
| PuO <sub>2</sub> Str. Asym. | 913, 901, 903 | 917, 902, 902 |         |          |
| PuO <sub>2</sub> Str. Sym.  | 803, 784, 781 | 807,          |         |          |
| Bridging OH                 | 721, 715, 709 | 784, 748, 737 |         |          |

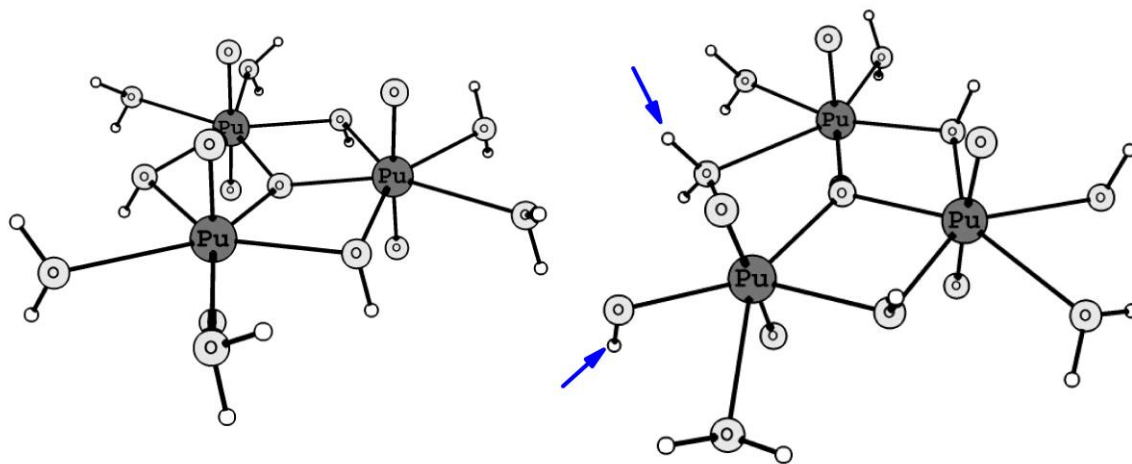


**Figure 4.4:** Structures of  $[(\text{PuO}_2)_3(\text{H}_2\text{O})_6(\text{O})(\text{OH})_3]^+$  obtained at the BP86/B2/COSMO level. The  $C_{3V}$  structure is shown on the left while the structure with a bridging aquo group is shown on the right.

Regarding the structure of the plutonyl trimer complex there are two points of note. Firstly, it remains to be seen whether the highly symmetrical  $C_{3V}$  structure is the global minimum structure on the potential energy surface. Tsushima et al. obtained another  $\mu_3$ -oxo structure that was about 9.8 kcal higher in energy than the lowest energy structure they obtained for  $[(UO_2)_3(H_2O)_6(O)(OH)_3]^+$ .<sup>53</sup> This structure has two bridging hydroxo groups, a bridging aquo group and a pendant hydroxo group. The plutonyl analogue is shown in Figure 4.4. Secondly, it still remains to be seen whether the  $[(AnO_2)_3(O)(OH)_3]^+$  core is preferred to the  $[(AnO_2)_3(OH)_5]^+$  core for plutonium as it was in the case of uranium.<sup>53</sup> The significance of these two points will be discussed later.

### **Vibrational Frequencies.**

The calculated plutonyl stretching vibrational frequencies of the monomeric plutonyl complexes are also collected in Tables 4.1-4.4. As the vibrational frequencies were calculated without correction for anharmonic effects, this implies that deviations from available experimental values cannot be fully avoided. The calculated structural features in Tables 4.1-4.4 show that the hybrid B3LYP functional generally over-binds the actinyl An-O<sub>yl</sub> bonds, relative to the GGA functionals. The shorter An-O<sub>yl</sub> bonds obtained with the B3LYP functional result in vibrational frequencies that are much higher than the experimental values. This agrees well with previous reports by other workers.<sup>33-34, 41-42, 51</sup> On the other hand, the solvent environment tends to reduce the calculated plutonyl stretching frequencies by about 20-40 cm<sup>-1</sup> at the BP86/B1 and B3LYP/B3 levels. This is also in accordance with literature experience.<sup>33, 51</sup> Given that the PBE functional, like most GGA functionals tends to slightly under-bind actinyl bonds in the gas-phase, there appears to be a serendipitous coincidence between the actinyl stretching vibrational frequencies obtained with the PBE functional in the gas-phase and the experimental values

obtained in the aqueous phase. The under-binding error of the GGA functional corrects for the non-inclusion of solvation effects. Taking  $[\text{PuO}_2(\text{H}_2\text{O})_5]^{2+}$  as an example, the gas-phase PBE/B1 values for the plutonyl symmetric and asymmetric stretching modes are 853 and 969  $\text{cm}^{-1}$ , Table 4.1, in good agreement with the solvent-phase experimental values of 833 and 962  $\text{cm}^{-1}$  for the symmetric and asymmetric  $\text{O}_{\text{yl}}\text{-Pu-O}_{\text{yl}}$  stretching modes respectively. The plutonyl stretching vibrational frequencies obtained in the gas-phase with the BP86/B2 approach are also close to the experimental value but are often lower than those obtained at the PBE/B1 level for the other monomeric plutonyl aquo-hydroxo complexes, Tables 4.1-4.4.

To further test the usefulness of the vibrational frequencies obtained at the PBE/B1 level for estimating experimental frequencies obtained in solution, we have calculated the vibrational frequencies of all the hydrolyzed uranyl aquo complexes. There are available IR and Raman experimental data for the vibrational frequencies of the uranyl hydrolysis products.<sup>22, 54</sup> The calculated uranyl stretching vibrational frequencies of  $[\text{UO}_2(\text{H}_2\text{O})_5]^{2+}$ ,  $[(\text{UO}_2)_2(\text{OH})_2(\text{H}_2\text{O})_6]^{2+}$  and  $[(\text{UO}_2)_3(\text{H}_2\text{O})_6(\text{O})(\text{OH})_3]^+$  obtained using the PBE/B1 approach are presented in Table 4.8. The calculated uranyl stretching modes of  $[\text{UO}_2(\text{H}_2\text{O})_5]^{2+}$ ,  $[(\text{UO}_2)_2(\text{OH})_2(\text{H}_2\text{O})_2]^{2+}$  and  $[(\text{UO}_2)_3(\text{OH})_3(\text{O})(\text{H}_2\text{O})_6]^{2+}$  are in good agreement with the experiment.<sup>22, 54</sup> The agreement between the calculated and experimental frequencies for these uranyl complexes, especially for the polymeric species, gives us tremendous confidence regarding the use of the PBE/B1 approach in predicting the vibrational frequencies of the species found in the plutonyl hydrolysis speciation diagram. The most significant deviation between the experimental and calculated frequencies was obtained for  $[\text{UO}_2(\text{OH})_4]^{2-}$ , Table 4.8. Overall, the use of the PBE/B1 approach in the gas-phase is desirable as it requires little or no scaling factor due to the opposing effects of hybrid exchange and solvation effects (as has been discussed above). It also helps that this

approach is based on a fully scalar-relativistic approach with large all-electron basis sets thus avoiding the core-valence issues of RECPs.

Madic et al. have characterized the evolution of the symmetric plutonyl stretching vibrational modes as a function of pH using Raman spectroscopy.<sup>7</sup> The symmetric and asymmetric plutonyl vibrational stretching modes in  $[\text{PuO}_2(\text{H}_2\text{O})_5]^{2+}$  were calculated to be at 853 and 969  $\text{cm}^{-1}$  respectively at the PBE/B1 level, Table 4.1. As previously noted, the replacement of an aquo ligand by a hydroxo ligand leads to elongation of the Pu-O<sub>yl</sub> bonds, Tables 4.1-4.4. This results in lower plutonyl stretching vibrational frequencies. The symmetric and asymmetric

**Table 4.8:** Calculated uranyl stretching vibrational frequencies ( $\text{cm}^{-1}$ ) of uranium aquo hydroxo complexes obtained at the PBE/B1 level.

|  | Calculated    |               | Experimental Data <sup>22, 54</sup> |            |
|--|---------------|---------------|-------------------------------------|------------|
|  | Symmetric     | Asymmetric    | Symmetric                           | Asymmetric |
| $[\text{UO}_2(\text{H}_2\text{O})_5]^{2+}$                         | 887           | 973           | 870                                 | 962        |
| $[\text{UO}_2(\text{H}_2\text{O})_4]^{2+}$                         | 894           | 981           |                                     |            |
| $[\text{UO}_2(\text{H}_2\text{O})_3(\text{OH})]^+$                 | 847           | 921           |                                     |            |
| $[\text{UO}_2(\text{H}_2\text{O})_2(\text{OH})_2]$                 | 810           | 883           |                                     |            |
| $[\text{UO}_2(\text{H}_2\text{O})(\text{OH})_3]^-$                 | 777           | 850           |                                     |            |
| $[\text{UO}_2(\text{OH})_4]^{2-}$                                  | 730           | 802           | 784                                 | 857        |
| $[(\text{UO}_2)_2(\text{H}_2\text{O})_6(\text{OH})_2]^{2+}$        | 855, 861      | 944, 936      | 854                                 | 943        |
| $[(\text{UO}_2)_2(\text{H}_2\text{O})_4(\text{OH})_4]$             | 829, 838      | 907, 918      |                                     |            |
| $[(\text{UO}_2)_3(\text{H}_2\text{O})_6(\text{O})(\text{OH})_3]^+$ | 822, 822, 831 | 898, 898, 921 | 836                                 | 923        |

stretching modes decrease to around 814 and 922  $\text{cm}^{-1}$  respectively in the first hydrolyzed monomer complex,  $[\text{PuO}_2(\text{H}_2\text{O})_4(\text{OH})]^+$ . Comparison of the speciation diagram obtained using calculated hydrolysis constants by Neu et al.<sup>9</sup> with that obtained by Madic et al.<sup>7</sup> using Raman spectroscopic measurements, suggests that the hydrolyzed species that is first formed at around pH 3-4 should possess a Raman active peak at 817  $\text{cm}^{-1}$ . Neu et al. identified this hydrolyzed species as  $[\text{PuO}_2(\text{H}_2\text{O})_4(\text{OH})]^+$  and concluded it to be the dominant monomeric plutonyl hydroxo complex. Our gas-phase PBE/B1 calculations predicted the Raman active symmetric  $\text{O}_{\text{yl}}\text{-Pu-O}_{\text{yl}}$  stretching mode for this complex to be at 814  $\text{cm}^{-1}$ . This stretching mode was calculated to be at 782  $\text{cm}^{-1}$  in the most stable dihydroxo complex,  $\text{trans-}[\text{PuO}_2(\text{H}_2\text{O})_2(\text{OH})_2]$ . The  $\text{trans-}$  dihydroxo complex is about 3.18 and 4.60 kcal/mol more stable than its  $\text{cis-}$  conformer at the BP86/B2 and B3LYP/B3 level in solution respectively. Despite this small energy difference between the  $\text{cis-}$  and  $\text{trans-}$  isomer, the experimental peak at 817  $\text{cm}^{-1}$  cannot be assigned to  $\text{cis-}[\text{PuO}_2(\text{H}_2\text{O})_2(\text{OH})_2]$  as it has a higher symmetric stretching vibrational frequency of 800  $\text{cm}^{-1}$ . It appears that the only possible assignment of the Raman peak at 817  $\text{cm}^{-1}$  is  $[\text{PuO}_2(\text{H}_2\text{O})_4(\text{OH})]^+$ , in good agreement with Neu et al.'s conclusions.<sup>9</sup>

There is also the option that the Raman peak at 817  $\text{cm}^{-1}$  could be assigned to the dimeric species,  $[(\text{PuO}_2)_2(\text{OH})_2(\text{H}_2\text{O})_6]^{2+}$  as Madic et al.<sup>7</sup> did or even to higher polynuclear species. There are two plutonyl groups in the dimeric complexes. For this reason, we find two sets of asymmetric and symmetric  $\text{O}_{\text{yl}}\text{-Pu-O}_{\text{yl}}$  vibrational stretching modes described as  $\nu_2+\nu_2'$ ,  $\nu_2-\nu_2'$ ,  $\nu_1+\nu_1'$  and  $\nu_1-\nu_1'$  with respect to the coupling of the individual plutonyl groups. For this dimeric dihydroxo complex, the  $\nu_2+\nu_2'$  stretching mode corresponds to the asymmetric stretching of the  $\text{Pu-O}_{\text{yl}}$  bonds on both plutonyl groups in the same direction. This mode is IR active while its counterpart, the  $\nu_2-\nu_2'$  mode is Raman active. For the symmetric stretching modes, the  $\nu_1+\nu_1'$

mode is Raman active, while the  $\nu_1-\nu_1'$  mode is IR active. The  $\nu_2+\nu_2'$ ,  $\nu_2-\nu_2'$ ,  $\nu_1+\nu_1'$  and  $\nu_1-\nu_1'$  modes were calculated as 944, 938, 831 and 825  $\text{cm}^{-1}$  respectively at the PBE/B1 level, Table 4.6. This suggests that the experimental Raman peak observed at 817  $\text{cm}^{-1}$  can still be assigned to  $[\text{PuO}_2(\text{H}_2\text{O})_3(\text{OH})]^+$  and not  $[(\text{PuO}_2)_2(\text{OH})_2(\text{H}_2\text{O})_6]^{2+}$ . However, the peak observed at 826  $\text{cm}^{-1}$  in the Raman spectra<sup>7</sup> can now be assigned to the  $\nu_1+\nu_1'$  mode of  $[(\text{PuO}_2)_2(\text{OH})_2(\text{H}_2\text{O})_6]^{2+}$ . This matches the speciation diagram of Neu et al.<sup>9</sup> but contravenes Madic et al.'s<sup>7</sup> assignment of the peak at 817  $\text{cm}^{-1}$  to  $[(\text{PuO}_2)_2(\text{OH})_2(\text{H}_2\text{O})_6]^{2+}$ . The suggestion is that even at the high Pu(VI) concentrations that their work was carried out in, the monomeric complex could still have been observed by Madic et al.<sup>7</sup>

Madic et al. also observed other peaks at 805  $\text{cm}^{-1}$  and 794  $\text{cm}^{-1}$  at slightly higher pH values in their experimental measurements.<sup>7</sup> Examination of the calculated vibrational frequencies in Tables 4.6 reveals that we can assign these peaks to the  $\nu_1+\nu_1'$  and  $\nu_1-\nu_1'$  modes of the tetrahydroxo dimer complex,  $[(\text{PuO}_2)_2(\text{OH})_4(\text{H}_2\text{O})_4]$ . The Raman active O-H wagging modes of the bridging hydroxo groups were calculated at 784  $\text{cm}^{-1}$  in  $[(\text{PuO}_2)_2(\text{OH})_2(\text{H}_2\text{O})_6]^{2+}$  and at around 734  $\text{cm}^{-1}$  in  $[(\text{PuO}_2)_2(\text{OH})_4(\text{H}_2\text{O})_4]$ , Table 4.6. These are most likely too low to warrant assignment to the experimental peaks at 805  $\text{cm}^{-1}$  and 794  $\text{cm}^{-1}$ . From experience, we note that the calculated vibrational frequencies obtained at the PBE/B1 level in nearly all cases either matches or over-estimates the experimental value.<sup>33-34, 41-42, 51</sup>

There are three sets of plutonyl asymmetric and symmetric vibrational frequencies in  $[(\text{PuO}_2)_3(\text{H}_2\text{O})_6(\text{O})(\text{OH})_3]^+$ . These are labeled as  $\nu_2+\nu_2'+\nu_2''$ ,  $\nu_2-\nu_2'$ ,  $\nu_2-\nu_2''$ , and  $\nu_1+\nu_1'-\nu_1''$ ,  $\nu_1-\nu_1'$  and  $\nu_1-\nu_1''$ , reflecting the direction of the individual Pu-O<sub>yl</sub> stretches. The symmetric vibrational modes were calculated to be at 855, 840 and 813  $\text{cm}^{-1}$  at the PBE/B1 level, Table 4.7. All these modes were found to be IR active suggesting that this complex was not the one observed in the

Raman spectra of Madic et al.<sup>7</sup> The mode calculated at 840 cm<sup>-1</sup> has the lowest IR intensity and assignment to the Raman experimental peak at 826 cm<sup>-1</sup> is tentatively possible. In addition, the  $\mu$ -hydroxo wagging vibrational frequencies are all infrared (IR) active and between 742-797 cm<sup>-1</sup>. For this reason, they most likely cannot account for the experimental Raman<sup>7</sup> peaks at 794 and 805 cm<sup>-1</sup>.

### **Energetics.**

The reaction energies for the formation of the plutonyl dimer and trimer complexes in solution are presented in Table 4.9. The difference in electronic energies of the reactants and products,  $\Delta E_{\text{reaction}}$ , were employed due to the difficulty of calculating the solvent phase thermal free energy corrections for the open-shell species at the BP86/B2 level. The calculations at the BP86/B2 level are expected to be more accurate as they use a triple- $\zeta$  basis set, thereby reducing basis set superposition errors, and include the effect of the aqueous environment on the structure of the relevant complexes. In contrast the B3LYP/B3 results were obtained from single-point calculations on the gas-phase geometries. The calculated energies presented in Table 4.9 are for the solvent phase reactions and as a result do not include corrections for basis set superposition errors (BSSE). Counterpoise calculations were carried out to estimate these errors for the dimerization of the  $[\text{AnO}_2(\text{H}_2\text{O})_2(\text{OH})_2]$  species in the gas phase. They amount to around 1.1-1.8 kcal/mol at the B3LYP/B3 level and are much lower (0.4-0.6 kcal/mol) at the BP86/B2 level. This is understandable given the triple- $\zeta$  nature of the basis sets employed in the BP86/B2 calculations.

Formation of the  $[(\text{AnO}_2)_2(\text{OH})_2(\text{H}_2\text{O})_6]^{2+}$  complexes by dimerization of the monomeric  $[\text{AnO}_2(\text{H}_2\text{O})_4(\text{OH})]^+$  complexes was calculated to be more endothermic than the agglomeration

of the pentaquo complex with  $[\text{AnO}_2(\text{H}_2\text{O})_4(\text{OH})_2]$  species. This is most likely an electrostatic effect. The production of the  $[(\text{AnO}_2)_2(\text{OH})_4(\text{H}_2\text{O})_4]$  complexes by dimerization of the  $[\text{AnO}_2(\text{H}_2\text{O})_2(\text{OH})_2]$  species were calculated to be less exothermic than the formation of their counterpart binuclear dihydroxo complexes. Examination of Table 4.9 shows that the formation of the trimer complexes, is more exothermic for the uranyl and neptunyl complexes by about 6 kcal/mol in comparison to the plutonyl complex. Assuming that thermochemical factors are dominant over kinetic factors, one can say from the calculated energies that the significance of the  $[(\text{AnO}_2)_3(\text{H}_2\text{O})_6(\text{OH})_3(\text{O})]^+$  species follows the trend  $\text{U} \approx \text{Np} > \text{Pu}$ .

It is however not fully clear that the reactions listed in Table 4.9 represent the dominant mechanisms for the formation of these bimetallic and trimetallic complexes. For this reason, the direct hydrolyses of the monomeric pentaquo complexes were also studied and the reaction energies are compiled in Table 4.10. The calculation of the reaction energies of the hydrolysis of the actinyl aquo complexes (estimation of their  $\text{pK}_a$  values) is rather difficult due to the issues regarding estimating the solvation free energies of a proton.<sup>55-57</sup> In this work we have used the hydronium ion in the reactions presented in Table 4.10. In aqueous solution, the driving force for the formation of the hydronium and hydroxide ions from water was calculated as 62.9 and 67.3 kcal/mol at the BP86/B2 and B3LYP/B3 levels respectively. These values correspond to  $\text{pK}_a$  values of 21.7 and 20.3 respectively in comparison to the experimental value of 15.7.

For the monomeric aquo-hydroxo complexes, the reactions become increasingly endothermic as the degree of hydrolysis is increased. The formation of  $[\text{UO}_2(\text{H}_2\text{O})_4(\text{OH})]^+$  and  $[\text{PuO}_2(\text{H}_2\text{O})_4(\text{OH})]^+$  were calculated to be endothermic in solution by about 10.1 and 9.5 kcal/mol respectively at the BP86/B2 level. These agree moderately well with the experimental values of 7.1 and 8.0 kcal/mol respectively. The possible sources of the residual errors in the

**Table 4.9:** Calculated reaction energies (kcal/mol) for the formation of the dimer and trimer actinyl hydroxo complexes in the aqueous phase.

| Reactions   | U     | Np    | Pu    |
|---|-------|-------|-------|
| <b>Dimers</b>   |       |       |       |
| <hr/>   |       |       |       |
| $2\text{AnO}_2(\text{H}_2\text{O})_4(\text{OH})^+ \rightarrow (\text{AnO}_2)_2(\text{H}_2\text{O})_6(\text{OH})_2^{2+} + 2\text{H}_2\text{O}$   |       |       |       |
| B3LYP/B3  | -4.8  | -1.9  | -7.5  |
| BP86/B2   | -4.1  | 2.4   | -4.2  |
| <hr/>   |       |       |       |
| $\text{AnO}_2(\text{H}_2\text{O})_2(\text{OH})_2 + \text{AnO}_2(\text{H}_2\text{O})_5^{2+} \rightarrow (\text{AnO}_2)_2(\text{H}_2\text{O})_6(\text{OH})_2^{2+} + \text{H}_2\text{O}$                   |       |       |       |
| B3LYP/B3  | -20.2 | -17.1 | -29.0 |
| BP86/B2   | -17.8 | -11.6 | -15.3 |
| <hr/>   |       |       |       |
| $2\text{AnO}_2(\text{H}_2\text{O})_2(\text{OH})_2 \rightarrow (\text{AnO}_2)_2(\text{H}_2\text{O})_4(\text{OH})_4$  |       |       |       |
| B3LYP/B3  | -12.6 | -7.6  | -2.0  |
| BP86/B2   | -12.9 | 0.3   | -5.1  |
| <hr/>   |       |       |       |
| <b>Trimers</b>  |       |       |       |
| <hr/>   |       |       |       |
| $(\text{AnO}_2)_2(\text{H}_2\text{O})_4(\text{OH})_4 + \text{AnO}_2(\text{H}_2\text{O})_4(\text{OH})^+ \rightarrow (\text{AnO}_2)_3\text{O}(\text{H}_2\text{O})_6(\text{OH})_3^+ + 3\text{H}_2\text{O}$ |       |       |       |
| B3LYP/B3  | -8.5  | -8.1  | -2.0  |
| BP86/B2   | -13.8 | -13.9 | -7.8  |
| <hr/>   |       |       |       |

calculated reaction energies are known (such as basis set errors, solvation model, reaction model, approximate nature of Kohn-Sham DFT and problems with the accuracy of the experimental reaction energies). For the dimer complexes, the reactions leading to the formation of the dihydroxo species are significantly less endothermic than similar reactions for the

tetrahydroxides. This would suggest that the dihydroxo species are most likely the dominant binuclear species in solution. Overall for the dimer and monomer aquo-hydroxo species, the reaction energies of the plutonium complexes are generally within 1.5 kcal/mol of those of their uranium counterparts. The formation of the trimer complexes is least endothermic for  $[(\text{UO}_2)_3(\text{H}_2\text{O})_6(\text{OH})_3(\text{O})]^+$  and most endothermic for  $[(\text{PuO}_2)_3(\text{H}_2\text{O})_6(\text{OH})_3(\text{O})]^+$ . Similar to the case in Table 4.9, there is a difference of about 6 kcal/mol between uranyl and plutonyl systems, Table 4.10.

**Table 4.10:** Calculated reaction energies (kcal/mol) obtained actinyl hydrolysis reactions at the BP86/B2 while using the COSMO solvation model.

| Reactions  | U     | Np   | Pu    |
|--|-------|------|-------|
| <b>Monomers</b>  |       |      |       |
| $\text{AnO}_2(\text{H}_2\text{O})_5^{2+} + \text{H}_2\text{O} \rightarrow \text{AnO}_2(\text{H}_2\text{O})_4(\text{OH})^+ + \text{H}_3\text{O}^+$        | 10.1  | 7.7  | 9.5   |
| Experimental <sup>8, 26</sup>  | 7.1   |      | 8.0   |
| $\text{AnO}_2(\text{H}_2\text{O})_5^{2+} + \text{H}_2\text{O} \rightarrow \text{AnO}_2(\text{H}_2\text{O})_2(\text{OH})_2 + 2\text{H}_3\text{O}^+$       | 33.8  | 29.4 | 30.2  |
| $\text{AnO}_2(\text{H}_2\text{O})_5^{2+} + 2\text{H}_2\text{O} \rightarrow \text{AnO}_2(\text{H}_2\text{O})(\text{OH})_3^- + 3\text{H}_3\text{O}^+$      | 63.8  | 60.1 | 63.0  |
| $\text{AnO}_2(\text{H}_2\text{O})_5^{2+} + 3\text{H}_2\text{O} \rightarrow \text{AnO}_2(\text{OH})_4^{2-} + 4\text{H}_3\text{O}^+$                       | 101.3 | 97.8 | 101.8 |
| <b>Dimers</b>  |       |      |       |
| $2\text{AnO}_2(\text{H}_2\text{O})_5^{2+} \rightarrow (\text{AnO}_2)_2(\text{H}_2\text{O})_6(\text{OH})_2^{2+} + 2\text{H}_3\text{O}^+$                  | 16.0  | 17.8 | 14.9  |
| $2\text{AnO}_2(\text{H}_2\text{O})_5^{2+} + 2\text{H}_2\text{O} \rightarrow (\text{AnO}_2)_2(\text{H}_2\text{O})_4(\text{OH})_4 + 4\text{H}_3\text{O}^+$ | 54.6  | 59.1 | 55.3  |
| <b>Trimers</b>   |       |      |       |
| $3\text{AnO}_2(\text{H}_2\text{O})_5^{2+} \rightarrow (\text{AnO}_2)_3\text{O}(\text{H}_2\text{O})_6(\text{OH})_3^+ + 5\text{H}_3\text{O}^+$             | 50.9  | 53.1 | 57.1  |

The consistency between the approximately 6 kcal/mol difference between the uranyl and plutonyl trimer systems raises some questions. Firstly, how significant is 6 kcal/mol or an equilibrium constant of 1, via  $e^{-\Delta G/RT}$ ? To recast this question, one wonders if 6 kcal/mol is enough to explain the low/negligible concentration of the plutonyl trimer in contrast to the significant mole fraction of the trimer in the uranyl hydrolysis system. This discrepancy in the percentage concentration of the trimeric uranyl and plutonyl complexes has been observed experimentally by Neu et al.<sup>9</sup> and Rao et al.<sup>8, 26</sup> Fortunately, Rao et al., as part of their long line of work on reaction energetics of actinide complexes<sup>58-62</sup>, have reported experimental energy data for the uranyl and plutonyl hydrolysis systems. The difference between the experimental hydrolysis reaction energies leading to the uranyl trimer (89.8 kJ/mol) and the plutonyl trimer (116.3 kJ/mol) is 26.4 kJ/mol (6.3 kcal/mol).<sup>8, 26</sup> The theoretically calculated difference in reaction energies between these actinide trimer systems,  $\Delta\Delta E_{\text{reaction}}$ , Tables 4.9 and 4.10, therefore coincides with the experimental work of Rao et al.<sup>8, 26</sup> This coincidence, most likely a result of error cancellation in the theoretical and experimental data sets, suggests that 6 kcal/mol is enough to explain the disparity in the experimental mole fractions of the uranyl and plutonyl trimer complexes. As a point of note, the gas-phase reaction energies (both  $\Delta E_{\text{reaction}}$  and  $\Delta G_{\text{reaction}}$ ) favor the formation of the uranyl trimer complex by up to 11.7 kcal/mol.

Secondly, it is important that the origin of this difference be explained. One possible suggestion would be that the septet electronic state does not represent the most stable multiplicity for the plutonyl trimer complex. Single point calculations with total multiplicities of 3 and 5 were carried out at the septet electronic state geometry at the PBE/B1, BP86/B2 and B3LYP/B3 levels in the gaseous and aqueous phases. All these states were found to be higher in energy than the septet state. Unfortunately, spin contaminations from the low-lying septet state make most of

the calculated energies for these states unreliable. The lowest spin contaminations were obtained at the PBE/B1 level. At this level, full optimization for total multiplicities of 3 and 5 for the plutonyl trimer complex shows that they are about 10.3 and 13.3 kcal/mol higher in energy than the septet state respectively. We can conclude with sufficient confidence that the presence of other electronic states lower in energy than the septet state is most likely not the origin of the phenomenon of differing trimer mole-fractions between the uranyl and plutonyl series.

The origin of this discrepancy between the hydrolysis systems has been speculated to be due to the greater oxophilicity of U(VI) in comparison to Pu(VI) by Neu et al.<sup>9</sup> Looking at the structure of  $[(\text{PuO}_2)_3(\text{H}_2\text{O})_6(\text{OH})_3(\text{O})]^+$ , Figure 4.4, this difference in oxophilicity is possibly manifest in the differences in the amount of stability conferred by the dehydration of the  $[(\text{AnO}_2)_3(\text{OH})_5]^+$  complexes to form the  $[(\text{AnO}_2)_3(\text{O})(\text{OH})_3]^+$  species. As we previously noted, both the  $[(\text{AnO}_2)_3(\text{OH})_5]^+$  and  $[(\text{AnO}_2)_3(\text{O})(\text{OH})_3]^+$  species consume five protons upon titration and as such can't be distinguished using potentiometric methods. We optimized the structures of the bare  $[(\text{AnO}_2)_3(\text{OH})_5]^+$  complexes at the B3LYP/B3 level in the gas phase and calculated the energies for their dehydration in solution. The most stable structures for the  $[(\text{AnO}_2)_3(\text{OH})_5]^+$  complexes feature a central  $\mu_3$ -hydroxo and a pendant hydroxo in addition to three bridging hydroxo groups. The dehydration energies for  $[(\text{UO}_2)_3(\text{OH})_5]^+$ ,  $[(\text{NpO}_2)_3(\text{OH})_5]^+$ , and  $[(\text{PuO}_2)_3(\text{OH})_5]^+$  to form the respective  $[(\text{AnO}_2)_3(\text{O})(\text{OH})_3]^+$  complex were calculated as -24.7, -16.7 and -3.5 kcal/mol respectively. The  $\mu_3$ -oxo atom therefore stabilizes the trimeric hexagonal core to a greater extent in the uranyl complex than it does in the plutonyl complex.

A scheme depicting the fragmentation of the trimer complex into the component dimer and monomer units is shown in Figure 4.5. In this scheme, the structures with bridging aquo group, labeled **5b**, are involved in formation and break-up of the trimetallic core. We note that

the oxophilicity argument via dehydration of the  $[(\text{AnO}_2)_3(\text{OH})_5]^+$  complexes minimizes the possible role of the **5b** complexes. In the final analysis, the  $[(\text{PuO}_2)_3(\text{OH})_5]^+$  complex as well as the **5b** species should be closer in energy to the hexagonal  $C_{3V}$  structure, **5a**, than the case in the analogous uranium system. This would imply that the formation of the trimeric core is more endothermic in the plutonyl system. The converse (easier fragmentation of the trimeric core)

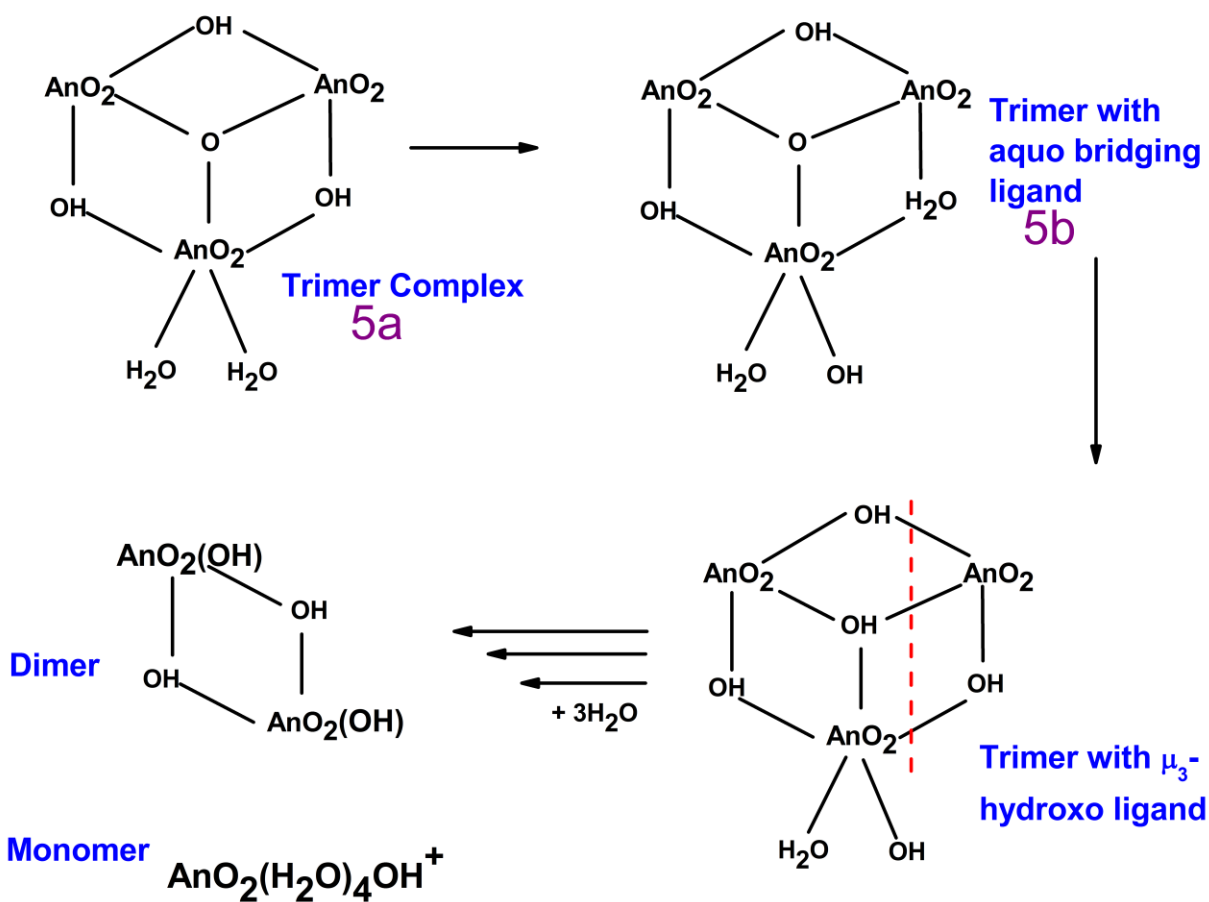


**Figure 4.5:** Scheme depicting the formation and decomposition of the  $\mu_3$ -oxo hexagonal trimetallic core of the trimer aquo-hydroxo complexes.

would be true for the backward reaction. The structure of the **5b** actinyl aquo-hydroxo complexes were optimized at the BP86/B2 level in aqueous solution, Figures 4.4 and 4.5. At this level, these structures are about 8.3, 5.6 and 0.9 kcal/mol higher in energy than the **5a** structures for the U, Np and Pu systems respectively.

It can be concluded that the higher-energy difference between the **5a** and **5b** structures for the uranyl trimer complex and to some extent the significant stability conferred by the  $\mu_3$ -oxo atom (after dehydration of  $[(\text{UO}_2)_3(\text{OH})_5]^+$ ) is responsible for its persistence in solution. The reverse of these are true for the analogous plutonyl system. The **5a** structure was found to be isoenergetic (0.9 kcal/mol) with its **5b** counterpart. The **5b** plutonyl complex also more easily transforms into the  $[(\text{AnO}_2)_3(\text{OH})_5]^+$  complex, 3.5 kcal/mol versus 24.7 kcal/mol for the uranyl system, which can then fragment to the dimer and monomer components.

### Electronic Structure.

Electronically, the valence molecular orbitals (MOs) of the plutonyl moiety are a pair of degenerate 5f orbitals, the  $\sigma(f)$  orbital, the  $\sigma(d)$  orbital and a pair each of  $\pi(f)$  and  $\pi(d)$  orbitals, Figure 4.6. This orbital framework is somewhat similar to that of the uranyl and neptunyl moieties with the exception of two degenerate singly occupied 5f orbitals. A comparison of the electronic structures of the plutonyl aquo-hydroxo complexes to those of their uranyl and neptunyl counterparts is interesting. The calculations at the BP86/B2 level using the COSMO model show that the An-O<sub>yl</sub>, An-OH and An-OH<sub>2</sub> bonds of the  $[\text{AnO}_2(\text{H}_2\text{O})_n(\text{OH})_{4-n}]^{2-n}$  complexes undergo a small contraction of about 0.03 Å between the uranium and plutonium analogues. The shorter An-O<sub>yl</sub> bonds in PuO<sub>2</sub><sup>2+</sup> compared to UO<sub>2</sub><sup>2+</sup> can be explained by larger 5f

contributions to the  $\sigma(f)$  and  $\pi(f)$  orbitals and well as lower 6p contributions to the  $\sigma(f)$  orbitals, Figure 4.6.

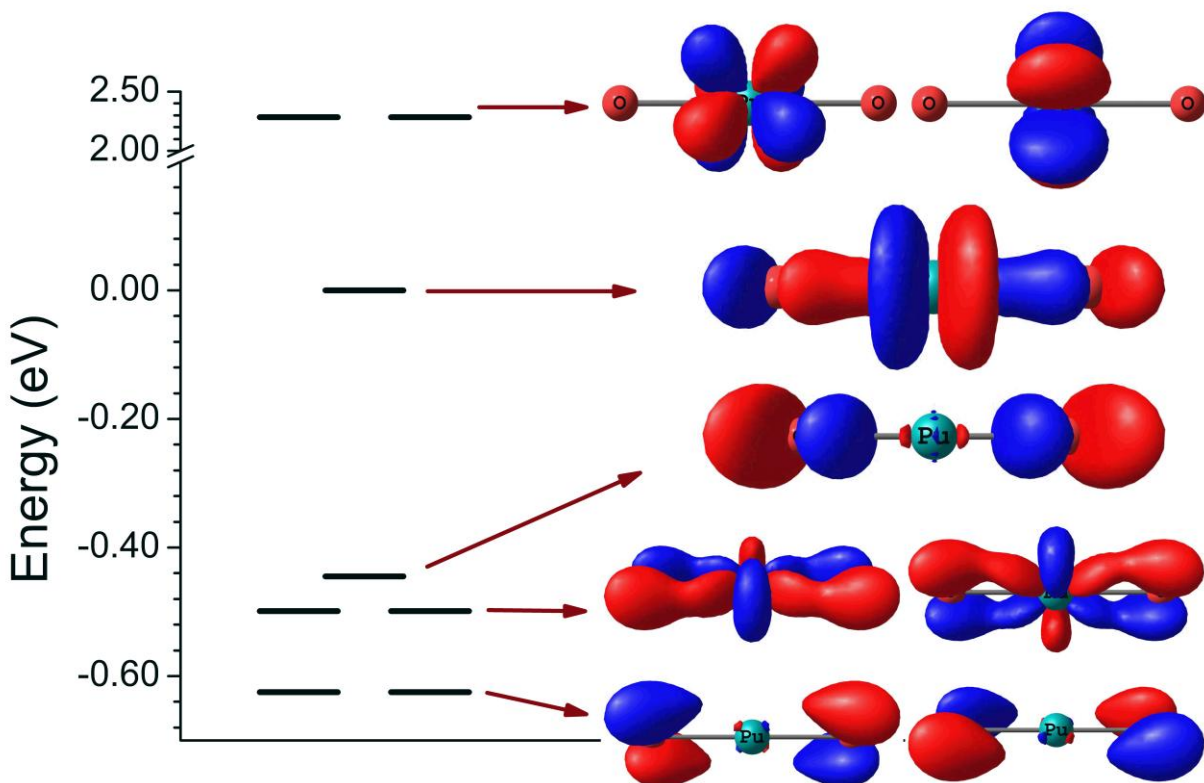


**Figure 4.6:** The  $\alpha$ -spin molecular orbitals of  $[\text{PuO}_2]^{2+}$ . All the orbitals contained in this picture are occupied by one electron. In order of decreasing energies, these are the two 5f orbitals (2.28 eV, 100% Pu-5f), the  $\sigma(f)$  orbital (0.00 eV, 61.4% 2p from each oxo atom, 14.4% 5f from Pu and 6.5% 6p from Pu), the  $\sigma(d)$  orbital (-0.45 eV, 38.7% 2p from each oxo atom, 12.1% 6d from Pu, 1% 7s from Pu), the two  $\pi(d)$  orbitals (-0.50 eV, 41.3% 2p from each oxo atom, 14.8% 6d from Pu) and the two  $\pi(f)$  orbitals (-0.63 eV, 43.7% 5f from Pu, 26.9% 2p from each oxo atom).

For example, the 5f orbital contribution to the  $\sigma(f)$  orbital increases from 57.1% to 57.5% and 61.4% down the U, Np and Pu series while the 6p orbital contribution decreases from 9.7% to 6.6%. Associated with the decreasing 6p and increasing 5f contributions to the  $\sigma(f)$  MO is its stabilization relative to the  $\sigma(d)$  orbital on going from  $\text{UO}_2^{2+}$  to  $\text{PuO}_2^{2+}$ . As a result of this stabilization, the  $\sigma(f)$  orbital is about 0.45 eV higher in energy than the  $\sigma(d)$  orbital in plutonyl in comparison to the case in uranyl and neptunyl where it is about 1.04 eV and 0.78 eV higher in energy respectively, Figure 4.6. The 5f contribution to the  $\pi(f)$  orbitals also increase down the series (31.2%, 37.3% and 43.7%). The resulting stabilization of the  $\pi(f)$  orbitals down the series actually results in a switching of the ordering of the  $\pi(f)$  and  $\pi(d)$  orbitals in plutonyl, Figure 4.7.

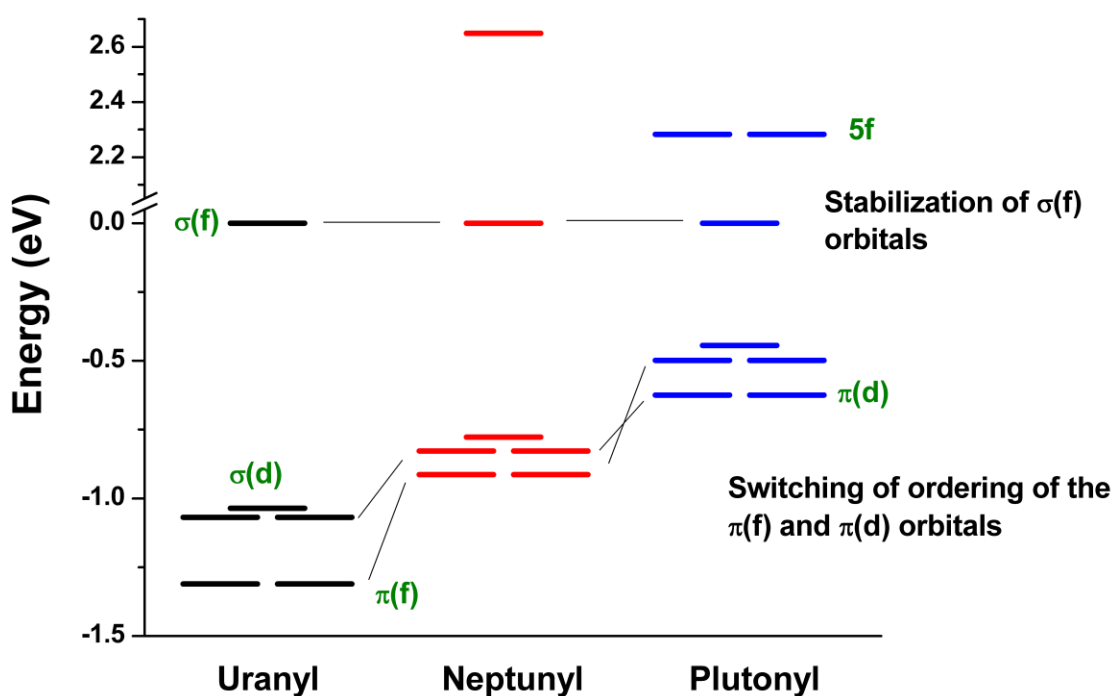


**Figure 4.7:** The energy levels of the  $[\text{AnO}_2]^{2+}$  optimized at the BP86/B2 level with the COSMO model. Only the  $\alpha$ -spin molecular orbitals (1 electron each) are shown for  $\text{NpO}_2^{2+}$  and  $\text{PuO}_2^{2+}$ .

The energy separation between these orbitals is 0.24 eV, 0.09 eV and -0.13 eV respectively in  $\text{UO}_2^{2+}$ ,  $\text{NpO}_2^{2+}$  and  $\text{PuO}_2^{2+}$ . The stabilization of the  $\sigma(\text{f})$  and  $\pi(\text{f})$  orbitals down the series is also seen at the B3LYP/B2 level.

The coordination of hydroxo ligand(s) to the plutonyl moiety results in significant stabilization of the  $\sigma(\text{d})$  orbital as it is the lowest plutonyl MO in the  $[\text{PuO}_2(\text{H}_2\text{O})_{4-n}(\text{OH})_n]^{2-n}$  complexes, Figure 4.8. The  $\sigma(\text{d})$  orbital in  $[\text{PuO}_2(\text{OH})_4]^{2-}$  has some minor bonding contributions (about 1.5% 2p each) from the equatorial ligands. The stabilization of the actinyl  $\sigma(\text{d})$  orbital has been previously observed by Kaltsoyannis et al.<sup>52</sup> in their study of uranyl aquo-hydroxo complexes. The  $\sigma(\text{f})$  orbital at -2.28 eV is also stabilized on hydrolysis but to a much lesser extent than its  $\sigma(\text{d})$  counterpart. The bonding overlap with the four OH ligands (about 4% 2p each) is stronger in the  $\sigma(\text{f})$  orbital than in the  $\sigma(\text{d})$  one, Figure 4.8. In contrast, the energies of the  $\pi(\text{f}/\text{d})$  orbitals are relatively unchanged between the bare cation and the tetrahydroxide. The description of these orbitals have however been altered in the hydroxide complex. The Pu-6d contributions to the plutonyl  $\pi$  orbitals are much lower in  $[\text{PuO}_2(\text{OH})_4]^{2-}$  than in  $\text{PuO}_2^{2+}$ . The Pu-6d contributions are about 2.7% in the  $\pi(\text{f})$  orbitals at -3.35 eV and 4.7% in the  $\pi(\text{f}/\text{d})$  orbitals at -2.97 eV, Figure 4.8. These are in contrast to the 14.8% Pu-6d contribution to the  $\pi(\text{d})$  orbitals at -0.50 eV in  $\text{PuO}_2^{2+}$ , Figure 4.6. The Pu-OH bonds are characterized by a pair of  $\pi$ -type orbitals at -2.24 eV. The orbital at -3.06 eV is of mixed  $\sigma(\text{Pu-OH})/\sigma(\text{Pu-O}_{\text{yl}})$  character due to 2p contributions of about 13% from each oxo atom as well as 14.2% 2p contributions from each hydroxo group. The decreased Pu-6d contributions to the  $\text{PuO}_2^{2+}$   $\pi$ -orbitals (-0.50 and -0.63 eV in Figure 4.6), increased Pu-5f contributions to the Pu-OH  $\pi$  orbitals (-2.24 eV in Figure 4.8) and increased 6d contributions to the mixed  $\sigma(\text{Pu-OH})/\sigma(\text{Pu-O}_{\text{yl}})$  orbitals down the  $[\text{PuO}_2(\text{OH})_n]^{2-n}$  series is a good explanation for the elongation of the Pu-O<sub>yl</sub> down the series. There is essentially

a transfer of actinyl 6d and 5f electron densities from the Pu-O<sub>yl</sub> to Pu-OH bonds. This explanation is also in line with Clark et al.'s speculation regarding the origin of a similar phenomenon in the analogous uranyl series.<sup>63</sup>

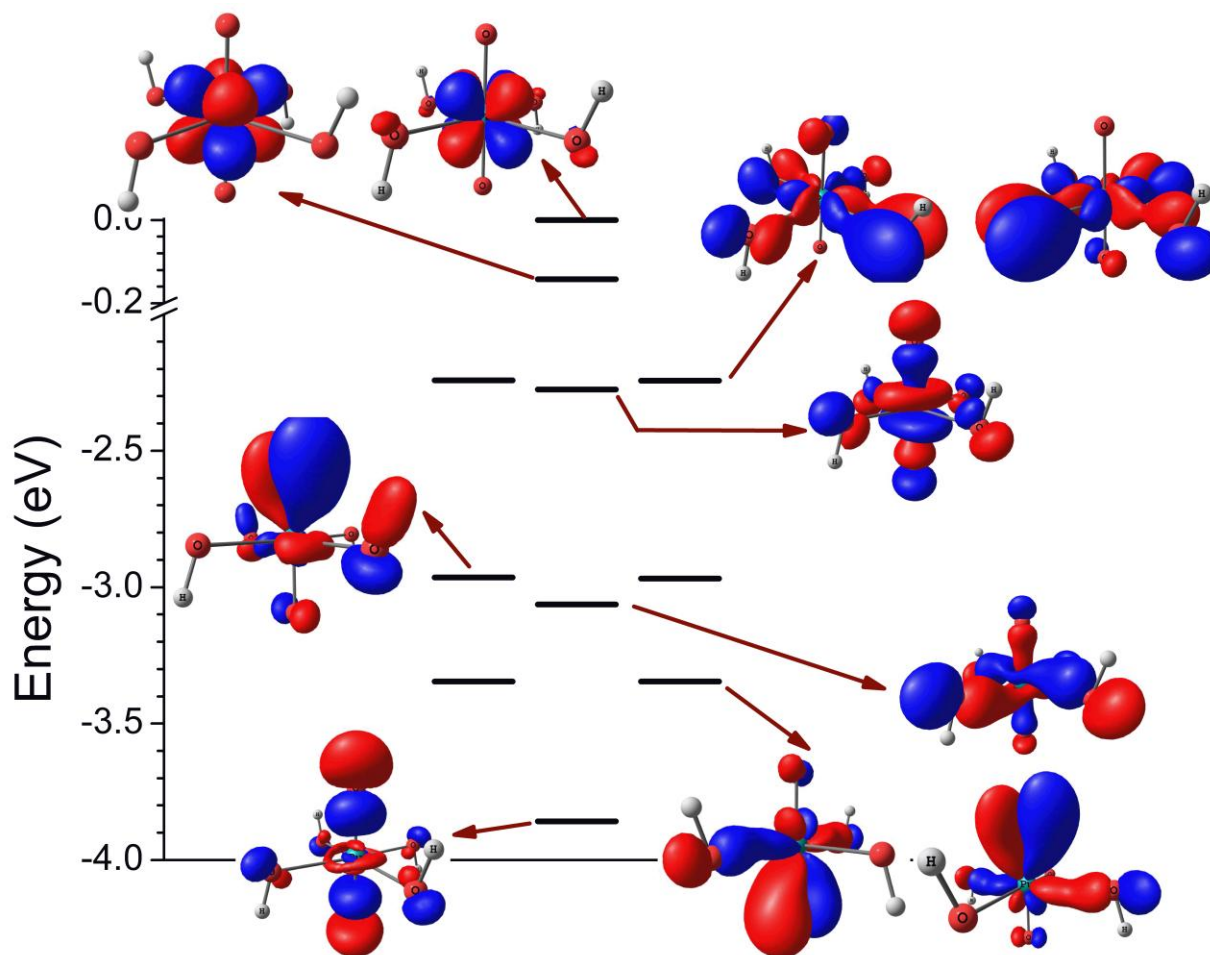


**Figure 4.8:** Selected occupied alpha spin MOs of  $[\text{PuO}_2(\text{OH})_4]^{2-}$ . In order of decreasing energies, these are the two 5f orbitals (0.00 eV, 88% Pu-5f; -0.14 eV, 100% Pu-5f), the  $\pi(\text{Pu-OH})$  orbitals (-2.24 eV, 29.5% 2p from each from two OH, 18% Pu-5f, 5% 2p from other OH), the  $\sigma(\text{Pu-O}$  and Pu-OH mixed) orbital (-2.28 eV, 4% from each OH, 36.6% Pu-5f, 5.7% Pu-6p, 16.7% from each oxo atom), the two  $\pi(\text{f/d})$  orbitals (-2.97 eV, 71% and 4% 2p from oxo atoms, 6.0% Pu-5f

and 4.7% Pu-6d), the  $\sigma$ (Pu-O and Pu-OH mixed) orbital (-3.06 eV, 11.7% Pu-5f, 1.0% Pu-6p, 5.7% Pu-6d, 13% 2p from each oxo and 14.2% 2p from each OH), the two  $\pi$ (f) orbitals (-3.35 eV, 58.5% and 2% 2p from the oxo atoms, 21.1% Pu-5f, 2.7% Pu-6d, 5% 2p from each OH) and the  $\sigma$ (d) orbital (-3.86 eV, 37.0% 2p from each oxo, 11.8% Pu-6d and 1.5% 2p from each hydroxo).

As noted for the bare actinyl complexes, there is a switching of the ordering of the  $\pi$ (d) and  $\pi$ (f) orbitals between  $\text{NpO}_2^{2+}$  and  $\text{PuO}_2^{2+}$  due to the stabilization of the  $\sigma$ (f) and  $\pi$ (f) orbitals across the U, Np and Pu series, Figure 4.7. In  $[\text{UO}_2(\text{OH})_4]^{2-}$ , the lower energy  $\pi$  orbitals at 0.48 eV above the  $\sigma$ (d) orbital, have about 6.0% U-6d and 9.1% U-5f contributions. On the other hand, the higher energy  $\pi$  orbitals at 0.88 eV, have 9.9% U-5f and 3.2% U-6d contributions. In the plutonyl analog, we find that the higher energy  $\pi$  orbitals (at -2.97 eV in Figure 4.8) contains about 6.0% Pu-5f and 4.7% Pu-6d atomic contributions while the lower  $\pi$  orbitals (at -3.35 eV in Figure 4.8) contain 21.1% Pu-5f and 2.7% Pu-6d contributions. This indicates that the more stable  $\pi$  orbitals in  $[\text{PuO}_2(\text{OH})_4]^{2-}$  are mainly of  $\pi$ (f) character in contrast to their mixed  $\pi$ (f/d) natures in the uranyl analogue. For the neptunyl analogue, the lower  $\pi$  orbital is 5.1% Np-6d and 12.6% Np-5f while the less stable  $\pi$  orbital is 4.3% Np-6d and 9.2% Np-5f. This switching in orbital character, especially for the  $\pi$ (f) and  $\sigma$ (f) orbitals across the U, Np and Pu series is also present in the aquo-hydroxo species intermediate between the bare dication and the tetrahydroxo species. The stabilization of the  $\sigma$ (f) orbital and the switching of the ordering of the  $\pi$ (f)/ $\pi$ (f/d) orbitals across the U, Np and Pu series of tetrahydroxo complexes is presented in Figure 4.9.

We also note that for  $[\text{PuO}_2(\text{OH})_4]^{2-}$ , the mixed  $\sigma(\text{Pu-OH})/\sigma(\text{Pu-O}_{yl})$ -type orbital at -3.06 eV in Figure 4.8 somewhat resembles the  $\sigma(\text{f})$  orbital at -2.28 eV. The orbital at -3.06 eV however has lower Pu-5f and O-2p contributions from the plutonyl entity. It has greater contributions from the equatorial hydroxo groups. There is a slight destabilization of this orbital down the U, Np and Pu series, Figure 4.9. Working backwards to  $[\text{UO}_2(\text{OH})_4]^{2-}$ , we find that the mixed  $\sigma(\text{Pu-OH}/\text{Pu-O})$ -type orbital has higher contributions from the hydroxo groups and less contributions from the plutonyl group suggesting it has greater An-OH character than the one found in the plutonyl analogue.

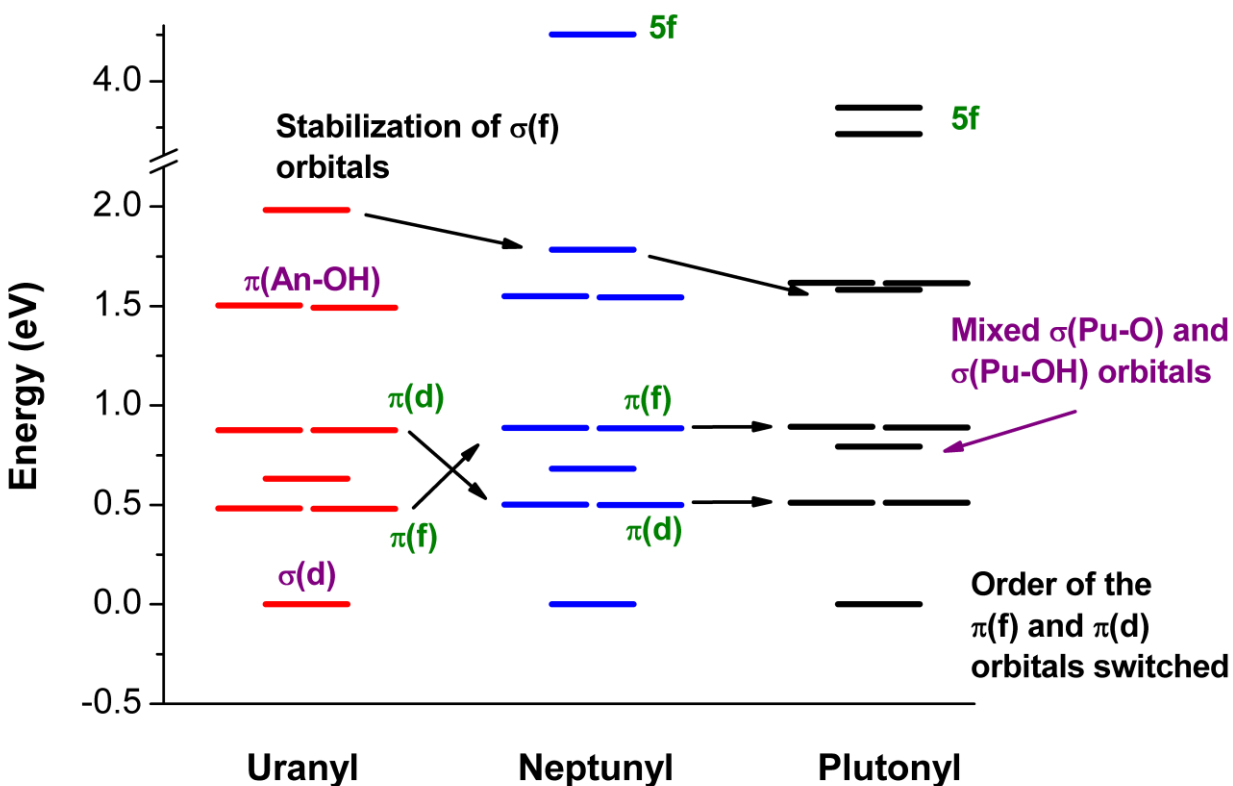


**Figure 4.9:** The energy levels of the  $[\text{AnO}_2(\text{OH})_4]^{2+}$  optimized at the BP86/B2 level with the COSMO model.

The monomeric plutonyl complexes possess one  $\sigma(f)$ , one  $\sigma(d)$ , two  $\pi(f)$  and two  $\pi(d)$ , orbitals of alpha spin in an unrestricted DFT picture. It is therefore logical to expect two  $\sigma(f)$ , two  $\sigma(d)$  and eight  $\pi(f/d)$  orbitals in the dimeric complexes. For simplicity, we select to analyze the electronic structure of gas-phase  $[(\text{PuO}_2)_2(\text{OH})_2]^{2+}$ , Figure 4.10. The aqueous phase electronic structure is qualitatively similar, especially regarding the atomic composition of the MOs. Overall, the general description of the electronic structure of this dimer complex and its tetrahydroxo counterpart,  $[(\text{PuO}_2)_2(\text{OH})_4]$ , are consistent at the B3LYP/B3 and BP86/B2 levels. MO-39 and MO-40 constitute the O-H bonds of the bridging hydroxo groups. The character and atomic contributions to these orbitals at the B3LYP/B2 level are presented in Table 4.11. They are semi-core orbitals found at about 1.6-2.2 eV and 2.2-2.4 eV below the valence actinyl orbitals at the BP86/B2 and B3LYP/B3 levels respectively. These orbitals are respectively bonding and antibonding across the bridging HO-OH groups. The  $\pi(d)$  and  $\pi(f)$  orbitals are found between 3.02 and 2.61 eV below the HOMO, Table 4.11. It appears that orbitals with contributions from the bridging OH groups are stabilized to a greater extent than those without. This was found to be the case in both the gaseous and aqueous phases. Several of the  $\pi$  orbitals found in this complex also possess  $\sigma(\text{Pu-OH})$  [MO-42, MO-44] and  $\sigma(d)$  [MO-48] characters. The  $\sigma(f)$  and  $\sigma(d)$  orbitals of plutonyl groups are found at slightly higher energies between -2.53 and -2.34 eV, Table 4.11. The  $\sigma(f)$  orbitals have contributions of about 3-4% from Pu 7p atomic orbitals while the  $\sigma(d)$  orbitals have admixtures of Pu-5f contributions of up to 9% in MO-48 and 5% in MO-52. The admixture of Pu-7p orbitals in  $\sigma(f)$  MOs is also seen in the monomeric hydroxides, as so is the admixture of Pu-5f and Pu-6d orbitals in  $\pi(d)$ ,  $\sigma(d)$  and  $\pi(f)$  MOs, Figures 4.6 and 4.8. The bridging Pu-OH bonds in  $[(\text{PuO}_2)_2(\text{OH})_2]^{2+}$  are supported by MO-53 and MO-54 which are formed by overlap of OH-2p and Pu-5f atomic contributions. There are

some  $O_{y1}$ -2p contributions to these orbitals. The remaining occupied orbitals are the four  $5f^1$  orbitals and the two orbitals for the lone electron pairs of the hydroxo ligands. The OH lone pair orbitals contain about 5-9% Pu 5f while MO-59, the  $5f^1$  orbital with highest energy has significant OH lone pair character. The first sets of virtual orbitals are empty 5f orbitals.

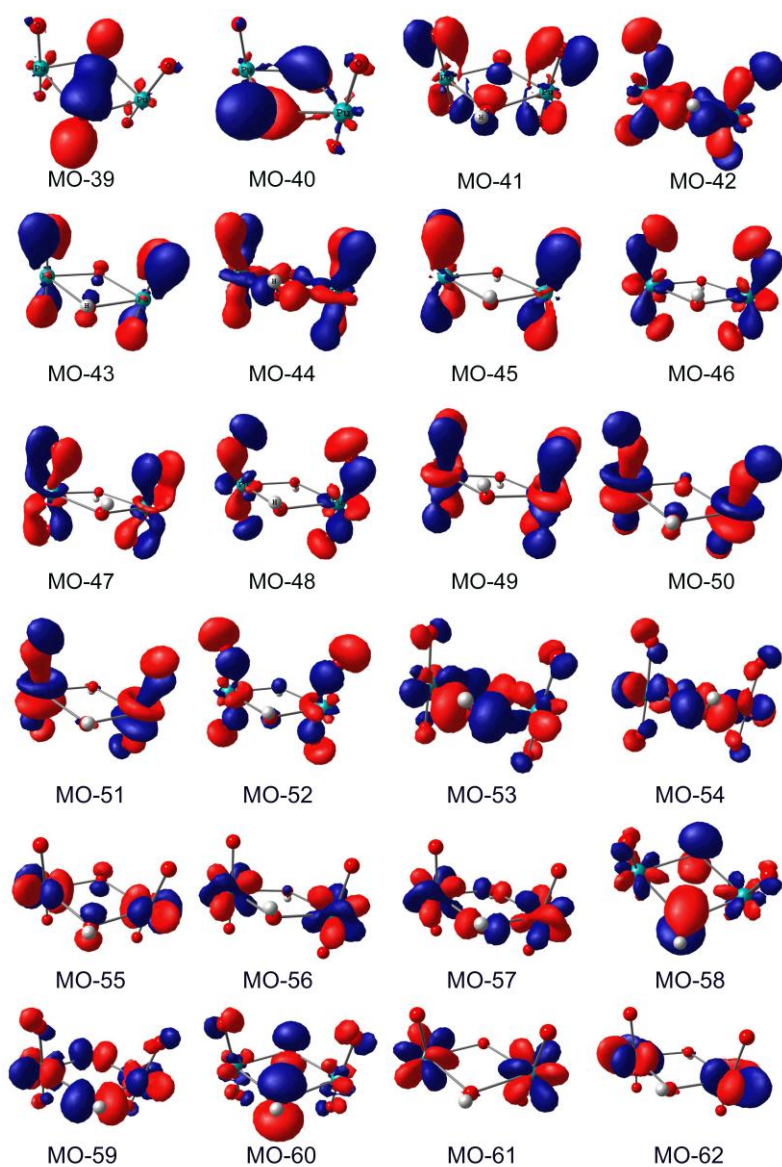


**Figure 4.10:** The 39<sup>th</sup> to 62<sup>nd</sup> MOs of  $[(PuO_2)_2(OH)_2]^{2+}$  of alpha spin.

**Table 4.11:** Energies, atomic contributions and descriptions of the MOs of  $[(\text{PuO}_2)_2(\text{OH})_2]^{2+}$  at the B3LYP/B3 level. The orbital energies are scaled such that the HOMO is at 0.00 eV.

| MO | Energy, eV | Atomic Contributions  | Description                             |
|----|------------|---|---|
| 39 | -5.19      | 3% 6d each Pu, 33% 2p each OH, 7% 1s each H                                   | $\sigma(\text{H-O-O-H})$                |
| 40 | -4.64      | 3% 5f each Pu, 2% 6d each Pu, 33% 2p each OH,<br>7% 1s each H                 | $\sigma(\text{O-H})$                    |
| 41 | -3.02      | 10% 6d each Pu, 15% 2p each $\text{O}_{yl}$ , 7% 2p each<br>OH                | $\pi(\text{d})$                         |
| 42 | -2.94      | 8% 5f each Pu, 5% 6d each Pu, 12% 2p each $\text{O}_{yl}$ ,<br>10% 2p each OH | $\pi(\text{f/d}), \sigma(\text{Pu-OH})$ |
| 43 | -2.90      | 10% 6d each Pu, 18% 2p each $\text{O}_{yl}$ , 5% 2p each<br>OH                | $\pi(\text{d})$                         |
| 44 | -2.86      | 16% 5f each Pu, 12% 2p each $\text{O}_{yl}$ , 8% 2p each OH                   | $\pi(\text{f}), \sigma(\text{Pu-OH})$   |
| 45 | -2.75      | 3% 5f each Pu, 9% 6d each Pu, 19% 2p each $\text{O}_{yl}$ ,                   | $\pi(\text{d})$                         |
| 46 | -2.72      | 13% 5f each Pu, 3% 6d each Pu, 16% 2p each $\text{O}_{yl}$ ,                  | $\pi(\text{f})$                         |
| 47 | -2.72      | 7% 5f each Pu, 8% 6d each Pu, 17% 2p each $\text{O}_{yl}$ ,                   | $\pi(\text{d/f})$                       |
| 48 | -2.64      | 9% 5f each Pu, 5% 6d each Pu, 18% 2p each $\text{O}_{yl}$ ,                   | $\pi(\text{f}), \sigma(\text{d})$       |
| 49 | -2.61      | 20% 5f each Pu, 14% 2p each $\text{O}_{yl}$ ,                                 | $\pi(\text{f})$                         |
| 50 | -2.53      | 27% 5f each Pu, 3% 6p each Pu, 8% 2p each $\text{O}_{yl}$ ,<br>3% 2p each OH  | $\sigma(\text{f})$                      |
| 51 | -2.38      | 26% 5f each Pu, 4% 6p each Pu, 9% 2p each $\text{O}_{yl}$ ,                   | $\sigma(\text{f})$                      |
| 52 | -2.34      | 5% 5f each Pu, 2% 2p each OH, 19% 2p each $\text{O}_{yl}$ ,<br>6% 6d each Pu  | $\sigma(\text{d})$                      |

|         |       |   |                   |
|---------|-------|---|-------------------|
| 53      | -1.72 | 13% 5f each Pu, 25% 2p each OH, 4% 2p each<br>O <sub>yl</sub> , 4% 6d each Pu | σ(Pu-OH)          |
| 54      | -1.59 | 26% 5f each Pu, 14% 2p each OH, 5% 2p each O <sub>yl</sub>                    | σ(Pu-OH)          |
| 55      | -1.15 | 44% 5f each Pu, 6% 2p each OH   | 5f                |
| 56      | -1.02 | 48% 5f each Pu  | 5f                |
| 57      | -0.89 | 40% 5f each Pu, 8% 2p each OH   | 5f                |
| 58      | -0.55 | 36% 2p each OH, 9% 5f each Pu   | OH lone pair      |
| 59      | -0.45 | 24% 5f each Pu, 20% 2p each OH, 2% 2p each O <sub>yl</sub>                    | 5f + OH lone pair |
| 60/HOMO | 0.00  | 38% 2p each OH, 5% 5f each Pu, 3% 2p each O <sub>yl</sub>                     | OH lone pair      |
| 61/LUMO | 3.55  | 49% 5f from each Pu   | 5f                |
| 62      | 3.67  | 48% 5f from each Pu   | 5f                |

The electronic structures of the trimer complexes,  $[(\text{PuO}_2)_3(\text{H}_2\text{O})_6(\text{OH})_3(\text{O})]^+$  and  $[(\text{PuO}_2)_3(\text{OH})_3(\text{O})]^+$  are too complicated to be fully described here. 18 actinyl (6  $\sigma$  and 12  $\pi$ ) orbitals are expected in these complexes, with these orbitals containing atomic contributions from each plutonyl group as well as from the bridging hydroxo and  $\mu_3$ -oxo groups. This is similar to the case of the dimeric dihydroxo complex. As an example, MO-72 in  $[(\text{PuO}_2)_3(\text{OH})_3(\text{O})]^{2-}$ , Figure 4.11, consists of  $\pi(f)$  contributions from each plutonyl group. The presence of the  $\mu_3$ -oxo bridge introduces not only oxo-bridge lone-pair orbitals but also results in the modification of some orbitals of the plutonyl groups. An example of the effect of the bridging oxo-group on the electronic structure is depicted in Figure 4.11. MO-63 at around -15.85 eV, Table 4.12, contains  $\pi(d)$  type contributions from each of the plutonyl groups which

overlap with 2p orbitals of the bridging oxo. The participation of the atomic 2p orbitals of the  $\mu_3$ -oxo atom to this particular orbital amounts to about 18%, Table 4.12.

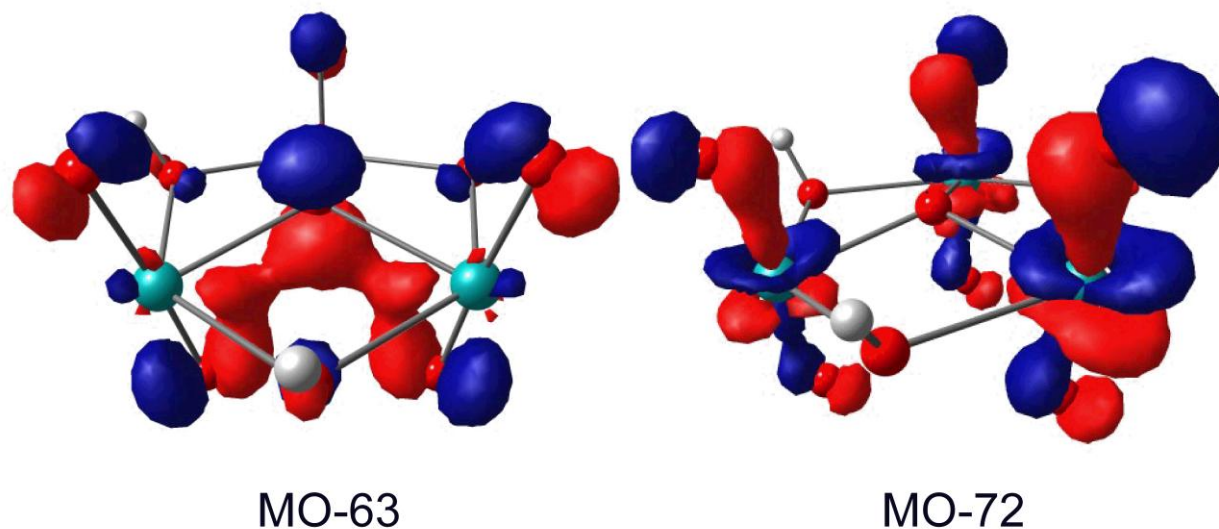


**Figure 4.11:** Selected alpha spin MOs of the trimer complex,  $[(\text{PuO}_2)_3(\text{O})(\text{OH})_3]^+$ .

We have previously noted that subsequent to the formation of the  $[(\text{AnO}_2)_3(\text{OH})_5]^+$  species, dehydration to the  $\mu_3$ -oxo complex (**5a** in Figure 4.5) with three bridging hydroxo ligands confers significant stability on the uranyl trimer complex,  $[(\text{UO}_2)_3(\text{O})(\text{OH})_3]^+$ , in contrast to its plutonyl analog,  $[(\text{PuO}_2)_3(\text{O})(\text{OH})_3]^+$ . The uranyl complex with a bridging aquo group (**5b** in Figure 4.5) is also less stable relative to the **5a** complex in comparison to the plutonyl system. It would be quite interesting to see whether the origin of this discrepancy can be found by examining the electronic structure of the oxo-trihydroxo trimer complexes. In the  $[(\text{AnO}_2)_3(\text{O})(\text{OH})_3]^+$  complexes, MOs 63-65 are actinyl- $\pi$ (f/d) orbitals with significant  $\sigma(\text{An}-\mu_3\text{O})$  characters. These orbitals are shown between -15.5 and -16.0 eV in Figure 4.12. The

contributions from the  $\mu_3$ -oxo to these three orbitals are highest in the U(VI) complex and lowest in the Pu(VI) trimer, Table 4.12. The greater participation of the 2p atomic contributions of the  $\mu_3$ -oxo atom to these orbitals correlates well with the greater oxophilicity of uranium centre and the role of the central oxo atom in further stabilizing the hexagonal  $(\text{UO}_2)_3(\text{OH})_3$  core. To further emphasize this particular point, we note that the splitting between MO-63 (the  $\pi(\text{d})/\mu_3\text{O}-2\text{p}$  orbital) and MO-64/MO-65 (the  $\pi(\text{f}/\text{d})/\sigma(\text{Pu}-\mu_3\text{O})$  orbitals) were calculated as 0.21, 0.26 and 0.33 eV for the U, Np and Pu complexes respectively at the B3LYP/B2 level in the gas phase.

MOs 66-67 are of actinyl- $\sigma(\text{d})$  character in the trimer complexes, Table 4.12. They also possess some  $\sigma(\text{An}-\text{OH})$  characters. The 5f contributions to these orbitals however increase from 0-2% to 4-5 % and 3-8% in the U(VI), Np(VI) and Pu(VI) trimers respectively. The increase in 5f contributions down the series is also noticeable for the actinyl- $\pi$  and  $\sigma(\text{f})$  orbitals, Figure 4.12. For example, in the U(VI) complex, the  $\pi(\text{d})$  orbitals (MO 68-72) have negligible U-5f contributions. In contrast, there are significant  $\pi(\text{f})-\pi(\text{d})$  mixing in the plutonyl complex. This  $\pi(\text{f})-\pi(\text{d})$  mixing down the series results in further stabilization of the  $\text{O}_{\text{yl}}=\text{An}=\text{O}_{\text{yl}}$  bonds and is reminiscent of the previously discussed switching of the energetic ordering of the  $\pi(\text{f})$  and  $\pi(\text{d})$  orbitals in the bare dications and monomer tetrahydroxo complexes on going from U to Pu, Figures 4.7 and 4.9.

**Table 4.12:** Energies (eV), individual atomic contributions and descriptions of the MOs of  $[(\text{PuO}_2)_3(\text{O})(\text{OH})_3]^+$  at the B3LYP/B3 level. The orbital energies are scaled such that the HOMO is at 0.00 eV. Scaling allows for easier presentation.

| MO | Atomic Participations  | Description  | Energy |
|----|--|--|--------|
| 63 | 7% Pu-6d, 5-12% O <sub>yl</sub> 2p, ~2% $\mu$ -OH, 18% $\mu_3(\text{O})$ 2p              | $\pi(\text{d})/\mu_3(\text{O}-2\text{p})$  | -15.85 |
| 64 | 3-6% Pu-5f, 3-5% Pu-6d, 23% $\mu_3(\text{O})$ 2p, 8-11% O <sub>yl</sub> 2p, 4% $\mu$ -OH | $\pi(\text{f}/\text{d}), \sigma(\text{Pu}-\mu_3\text{O})$                                | -15.52 |
| 65 | 4-8% Pu-5f, 4-5% Pu-6d, 22% $\mu_3(\text{O})$ 2p, 8-13% O <sub>yl</sub> 2p,              | $\pi(\text{f}/\text{d}), \sigma(\text{Pu}-\mu_3\text{O})$                                | -15.51 |
| 66 | 4% Pu-5f, 11% Pu-6d, 13% Pu-7s, 20-26% O <sub>yl</sub> 2p, 3% $\mu$ -OH                  | $\sigma(\text{d}) \text{Pu}'\text{-O}_{yl}$  | -15.09 |
| 67 | 3-8% Pu-5f, 9% Pu-6d, 12% Pu-7s, 14-20% O <sub>yl</sub> 2p, 2% $\mu$ -OH                 | $\sigma(\text{d}) \text{Pu}'\text{-O}_{yl}$<br>$\pi(\text{f}) \text{Pu}''\text{-O}_{yl}$ | -15.08 |
| 68 | 6-7% Pu-5f, 7% Pu-6d, 9% Pu-7s, 10-19% O <sub>yl</sub> 2p                                | $\pi(\text{d})$  | -15.05 |
| 69 | 3-11% Pu-5f, 3-8% Pu-6d, 3-29% O <sub>yl</sub> 2p  | $\pi(\text{f})$  | -15.00 |
| 70 | 8-9% Pu-5f, 6% Pu-6d, 7-27% O <sub>yl</sub> 2p   | $\pi(\text{f}/\text{d})$   | -14.97 |
| 71 | 3-4% Pu-5f, 3-7% Pu-6d, 3-30% O <sub>yl</sub> 2p   | $\pi(\text{d}/\text{f})$   | -14.91 |
| 72 | 10-18% Pu-5f, 3% Pu-6d, 2% Pu-6p, 3-15% O <sub>yl</sub> 2p                               | $\pi(\text{f})$  | -14.83 |
| 73 | 3-15% Pu-5f, 2-3% Pu-6d, 3-13% O <sub>yl</sub> 2p, 3% $\mu_3(\text{O})$ 2p               | $\pi(\text{f})/\sigma(\text{f})$   | -14.82 |
| 74 | 2-14% Pu-5f, 2% Pu-6d, 7-17% O <sub>yl</sub> 2p, 3% $\mu_3(\text{O})$ 2p                 | $\pi(\text{f})/\sigma(\text{Pu}-(\mu_3\text{-O}))$                                       | -14.81 |
| 75 | 3-7% Pu-5f, 2-4% Pu-6d, 5-19% O <sub>yl</sub> 2p, 3% $\mu_3(\text{O})$ 2p                | $\pi(\text{f})/\sigma(\text{f})$   | -14.79 |
| 76 | 7-11% Pu-5f, 2% Pu-6d, 2-21% O <sub>yl</sub> 2p, 2% $\mu$ -OH                            | $\pi(\text{f})$  | -14.78 |
| 77 | 7-9% Pu-5f, 2-3% Pu-6d, 11-25% O <sub>yl</sub> 2p, 2% $\mu$ -OH                          | $\pi(\text{f})$  | -14.71 |
| 78 | 4-13% Pu-5f, 3% Pu-6d, 2-38% O <sub>yl</sub> 2p, 2% $\mu$ -OH                            | $\sigma(\text{f})$   | -14.69 |

|    |   |      |        |
|----|---|------|--------|
| 79 | 10-24% Pu-5f, 3% Pu-6d, 2-21% O <sub>yl</sub> 2p,           | σ(f) | -14.44 |
| 80 | 2-20% Pu-5f, 2% Pu-6d, 2-3% Pu-6p, 6-17% O <sub>yl</sub> 2p | σ(f) | -14.44 |

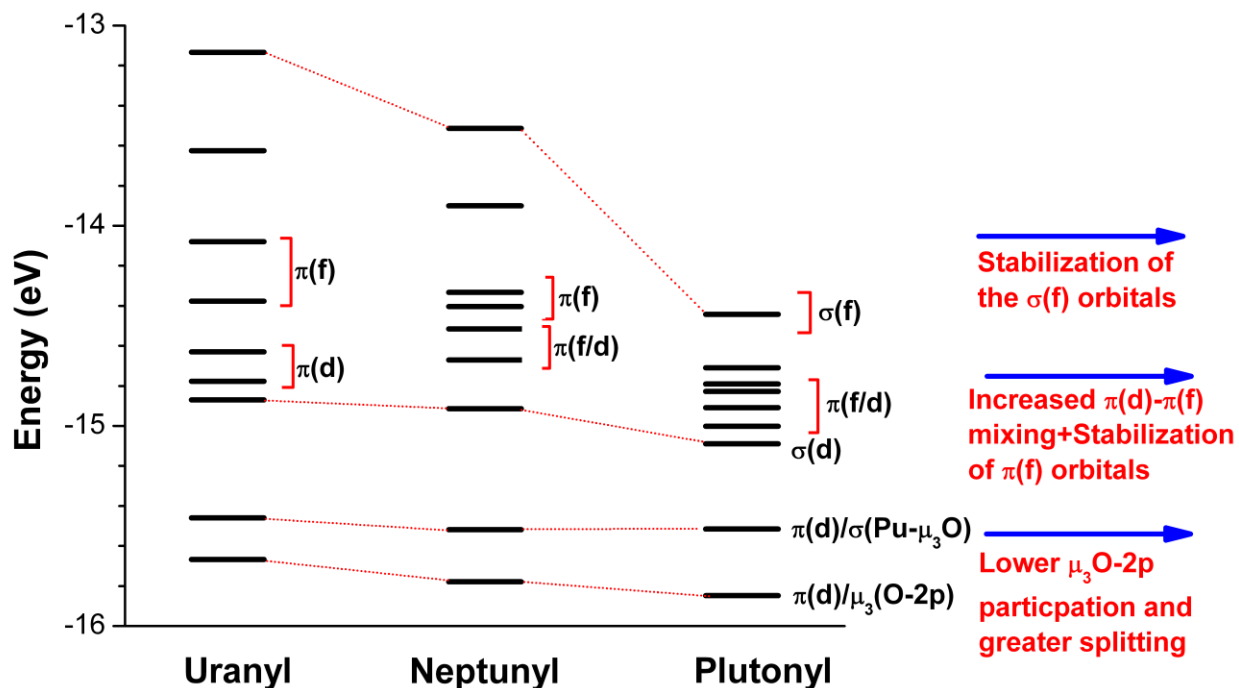


**Figure 4.12:** Abbreviated energy level diagram of the  $[(AnO_2)_3(O)(OH)_3]^+$  complexes.

## Conclusions

We have presented a comprehensive examination of the structure and electronic properties of monomeric, dimeric and trimeric plutonyl aquo-hydroxo complexes using scalar relativistic DFT calculations. The calculations in aqueous solvents were carried out using the PCM solvation model. The formation of the plutonyl complexes through both monomer agglomeration and the hydrolysis reactions of  $[PuO_2(H_2O)_5]^{2+}$  were examined. The trends in the

calculated reaction free energies for the formation of uranyl, neptunyl and plutonyl hydroxo complexes were discussed. The variation of the electronic structures of the complexes with increasing number of equatorial hydroxo ligands or increasing number of plutonyl groups were also examined.

The calculated structures of the monomeric plutonyl aquo-hydroxo complexes are in good agreement with previously reported experimental data. The Pu-O<sub>yl</sub> bonds become progressively weaker and longer as the number of equatorial hydroxo ligands is increased. Examination of the electronic structure of these complexes revealed the origin of this phenomenon to be a decrease in the Pu-6d contributions to the plutonyl  $\pi(d)$  orbitals and an increase in Pu-6d contributions to orbitals with plutonyl- $\sigma(d)/\sigma(\text{Pu-OH})$  and plutonyl- $\sigma(f)/\sigma/\pi(\text{Pu-OH})$  characters. This quantitative explanation of the weakening of the Pu-O<sub>yl</sub> bonds supports previous speculations regarding a Pu-6d overloading or competition between the axial O<sub>yl</sub> and equatorial hydroxos. Similar arguments are applicable to other actinide systems. The trend in weaker Pu-O<sub>yl</sub> bonds results in lower plutonyl stretching vibrational frequencies. We were able to assign the symmetric stretching modes of  $[\text{PuO}_2(\text{H}_2\text{O})_5]^{2+}$  and  $[\text{PuO}_2(\text{H}_2\text{O})_4(\text{OH})]^+$  to available Raman data. The Pu-O<sub>yl</sub> and Pu-OH distances in the plutonyl aquo-hydroxo complexes are generally about 0.03-0.04 Å and 0.01-0.02 Å shorter than similar bonds in their uranyl and neptunyl analogs respectively. The origin of these slight contractions is an increase in actinyl 5f participation in the  $\sigma(f)$  and  $\pi(f)$  orbitals down the U-Np-Pu series as well as increased stabilization of the  $\sigma(f)$  actinyl MO relative to the  $\sigma(d)$  MO.

The calculated reaction energies for the hydrolysis of  $[\text{PuO}_2(\text{H}_2\text{O})_5]^{2+}$  reveals the formation of the dimer complex,  $[(\text{PuO}_2)_2(\text{OH})_2(\text{H}_2\text{O})_6]^{2+}$ , is significantly more exothermic than the formation of the trimer complexes. This is also the case for the uranyl and neptunyl systems.

The formation of the uranyl trimer was however calculated to be about 6.2 kcal/mol more exothermic than the formation of the counterpart plutonyl complex. This  $\Delta\Delta E_{\text{reaction}}$  is sufficiently accurate due to systematic cancellation of errors and in good agreement with previously reported experimental value of 6.32 kcal/mol. The greater oxophilicity of U(VI) means that the dehydration of two hydroxo groups in  $[(\text{UO}_2)_3(\text{OH})_5]^+$  to yield a  $\mu_3$ -oxo group in  $[(\text{UO}_2)_3(\text{O})(\text{OH})_3]^+$ , is significantly more exothermic than for its plutonyl analogue. In addition, trimeric complexes with bridging aquo ligands are more stable for the plutonyl system than for the uranyl system. As these complexes are most likely involved in the fragmentation of the trimeric core, this is possibly the origin of the increased mole-fraction of the trimeric and higher polynuclear complexes in the uranyl hydrolysis speciation diagram. Comparison of the electronic structures of  $[(\text{UO}_2)_3(\text{O})(\text{OH})_3]^+$ ,  $[(\text{NpO}_2)_3(\text{O})(\text{OH})_3]^+$  and  $[(\text{PuO}_2)_3(\text{O})(\text{OH})_3]^+$ , reveals a critical difference in the degree of participation of the  $\mu_3$ -oxo 2p orbitals to the actinyl  $\pi(\text{d})/\mu_3\text{O}$ -2p orbitals. The  $\mu_3$ -oxo 2p contributions are highest in the U complex and lowest in the Pu complex. For this reason, the  $\pi(\text{f}/\text{d})/\sigma(\text{Pu}-\mu_3\text{O})$  orbitals are also least stabilized in the Pu complex.

The calculated frequencies of the plutonyl symmetric stretching vibrational modes in the dimer complex,  $[(\text{PuO}_2)_2(\text{OH})_2(\text{H}_2\text{O})_6]^{2+}$ , match previously reported Raman spectroscopic data. The accuracy of the calculated frequencies was ascertained by accurately predicting the Raman and IR stretching modes of  $[\text{UO}_2(\text{H}_2\text{O})_5]^{2+}$ ,  $[\text{UO}_2(\text{H}_2\text{O})_4(\text{OH})]^+$ ,  $[(\text{UO}_2)_2(\text{OH})_2(\text{H}_2\text{O})_6]^{2+}$ , and  $[(\text{UO}_2)_3(\text{O})(\text{OH})_3(\text{H}_2\text{O})_6]^+$ . The calculated reaction energies and the  $\Delta\Delta E_{\text{reaction}}$  indicate that the mole-fraction of the uranyl trimer should exceed that of the plutonyl trimer. At high plutonyl concentrations, the increase in the amount of trimer formed should correlate with the Raman peak at  $805\text{ cm}^{-1}$ .

The electronic structure of  $[(\text{PuO}_2)_2(\text{OH})_2]^{2+}$  is very similar to that of the monomer plutonyl hydroxo species. The various  $\pi(\text{d})$ ,  $\pi(\text{f})$ ,  $\sigma(\text{d})$  and  $\sigma(\text{f})$  orbitals are linear combinations of contributions from the two plutonyl groups. This is also the case in the trimer complex,  $[(\text{PuO}_2)_3(\text{OH})_3(\text{O})]^+$ , although some MOs (especially  $\pi$  orbitals) contain significant overlap with 2p contributions from the central  $\mu_3$ -oxo atom.

## References

1. Clark, D. L. H., S. S.; Jarvinen, G. D.; Neu, M. P. , *The Chemistry of the Actinide and Transactinide Elements*. 3rd ed.; Springer: Dordrecht, The Netherlands, 2006; Vol. 2.10., Pg 815.
2. Runde, W.; Reilly, S. D.; Neu, M. P., *Geochim. Cosmochim. Acta* **1999**, 63 (19-20), 3443-3449.
3. Austin, J. P.; Sundararajan, M.; Vincent, M. A.; Hillier, I. H., *Dalton T.* **2009**, (30), 5902-5909.
4. Balasubramanian, K.; Chaudhuri, D., *Chem. Phys. Lett.* **2008**, 450 (4-6), 196-202.
5. Chaudhuri, D.; Balasubramanian, K., *Chem. Phys. Lett.* **2004**, 399 (1-3), 67-72.
6. Clark, D. L.; Hobart, D. E.; Neu, M. P., *Chem. Rev.* **1995**, 95 (1), 25-48.
7. Madic, C.; Begun, G. M.; Hobart, D. E.; Hahn, R. L., *Inorg. Chem.* **1984**, 23 (13), 1914-1921.
8. Rao, L. F.; Tian, G. X.; Di Bernardo, P.; Zanonato, P., *Chem-Eur. J.* **2011**, 17 (39), 10985-10993.
9. Reilly, S. D.; Neu, M. P., *Inorg. Chem.* **2006**, 45 (4), 1839-1846.
10. Aberg, M., *Acta Chem. Scand.* **1970**, 24 (8), 2901-&.
11. Ahrland, S., *Acta Chem. Scand.* **1949**, 3 (4), 374-400.

12. Ahrland, S.; Hietanen, S.; Sillen, L. G., *Acta Chem. Scand.* **1954**, 8 (10), 1907-1916.
13. Cao, Z. J.; Balasubramanian, K., *J. Chem. Phys.* **2005**, 123 (11).
14. Choppin, G. R.; Mathur, J. N., *Radiochim. Acta* **1991**, 52-3, 25-28.
15. Gianguzza, A.; Milea, D.; Millero, F. J.; Sammartano, S., *Mar. Chem.* **2004**, 85 (3-4), 103-124.
16. Kato, Y.; Meinrath, G.; Kimura, T.; Yoshida, Z., *Radiochim. Acta* **1994**, 64 (2), 107-111.
17. Meinrath, G.; Kato, Y.; Yoshida, Z., *J. Radioanal. Nucl. Ch.* **1993**, 174 (2), 299-314.
18. Moll, H.; Reich, T.; Szabo, Z., *Radiochim. Acta* **2000**, 88 (7), 411-415.
19. Neuefeind, J.; Soderholm, L.; Skanthakumar, S., *J. Phys. Chem. A* **2004**, 108 (14), 2733-2739.
20. Nguyen-Trung, C.; Palmer, D. A.; Begun, G. M.; Peiffert, C.; Mesmer, R. E., *J. Solution Chem.* **2000**, 29 (2), 101-129.
21. Palmer, D. A.; NguyenTrung, C., *J. Solution Chem.* **1995**, 24 (12), 1281-1291.
22. Quiles, F.; Burneau, A., *Vib. Spectrosc.* **2000**, 23 (2), 231-241.
23. Sonnenberg, J. L.; Hay, P. J.; Martin, R. L.; Bursten, B. E., *Inorg. Chem.* **2005**, 44 (7), 2255-2262.
24. Toth, L. M.; Begun, G. M., *J. Phys. Chem.* **1981**, 85 (5), 547-549.
25. Tsushima, S.; Yang, T. X.; Suzuki, A., *Chem. Phys. Lett.* **2001**, 334 (4-6), 365-373.
26. Zanonato, P.; Di Bernardo, P.; Bismondo, A.; Liu, G. K.; Chen, X. Y.; Rao, L. F., *J. Am. Chem. Soc.* **2004**, 126 (17), 5515-5522.
27. Batista, E. R.; Martin, R. L.; Hay, P. J., *J. Chem. Phys.* **2004**, 121 (22), 11104-11111.
28. Cao, Z. J.; Balasubramanian, K., *J. Chem. Phys.* **2005**, 123 (11).

29. Clavaguera-Sarrio, C.; Vallet, V.; Maynau, D.; Marsden, C. J., *J. Chem. Phys.* **2004**, *121* (11), 5312-5321.
30. Craw, J. S.; Vincent, M. A.; Hillier, I. H.; Wallwork, A. L., *J. Phys. Chem.* **1995**, *99* (25), 10181-10185.
31. Horowitz, S. E.; Marston, J. B., *J. Chem. Phys.* **2011**, *134* (6).
32. Ismail, N.; Heully, J. L.; Saue, T.; Daudey, J. P.; Marsden, C. J., *Chem. Phys. Lett.* **1999**, *300* (3-4), 296-302.
33. Odoh, S. O.; Schreckenbach, G., *J. Phys. Chem. A* **2011**, *115* (48), 14110–14119.
34. Shamov, G. A.; Schreckenbach, G., *J. Phys. Chem. A* **2005**, *109* (48), 10961-10974.
35. Conradson, S. D.; et al, *Inorg. Chem.* **2004**, *43* (1), 116-131.
36. ADF2012.01, Theoretical Chemistry, Vrije Universiteit, Amsterdam, The Netherlands, <http://www.scm.com>.
37. te Velde, G.; Bickelhaupt, F. M.; van Gisbergen, S. J. A.; Fonseca Guerra, C.; Baerends, E. J.; Snijders, J. G.; Ziegler, T., *J. Comput. Chem.* **2001**, *22*, 931-967.
38. Frisch, M. J.; et al Gaussian 03, Revision C.02. 2004.
39. Laikov, D. N.; Ustynyuk, Y. A., *Russ. Chem. B+* **2005**, *54* (3), 820-826.
40. Dyllal, K. G., *J. Chem. Phys.* **1994**, *100* (3), 2118-2127.
41. Odoh, S. O.; Schreckenbach, G., *J. Phys. Chem. A* **2010**, *114* (4), 1957-1963.
42. Shamov, G. A.; Schreckenbach, G.; Vo, T. N., *Chem-Eur. J.* **2007**, *13* (17), 4932-4947.
43. Bridgeman, A. J.; Cavigliasso, G.; Ireland, L. R.; Rothery, J., *J. Chem. Soc. Dalton* **2001**, (14), 2095-2108.
44. Faas, S.; Snijders, J. G.; van Lenthe, J. H.; van Lenthe, E.; Baerends, E. J., *Chem. Phys. Lett.* **1995**, *246* (6), 632-640.

45. van Lenthe, E., *J. Comp. Chem.* **1999**, *20* (1), 51-62.
46. van Lenthe, E.; Baerends, E. J.; Snijders, J. G., *J. Chem. Phys.* **1993**, *99* (6), 4597-4610.
47. Pye, C. C.; Ziegler, T., *Theor. Chem. Acc.* **1999**, *101* (6), 396-408.
48. Küchle, W.; Dolg, M.; Stoll, H.; Preuss, H., *Mol. Phys.* **1991**, *74* (6), 1245-1263.
49. Küchle, W.; Dolg, M.; Stoll, H.; Preuss, H., *J. Chem. Phys.* **1994**, *100* (10), 7535-7542.
50. Miertus, S.; Scrocco, E.; Tomasi, J., *Chem. Phys.* **1981**, *55* (1), 117-129.
51. Odoh, S. O.; Walker, S. M.; Meier, M.; Stetefeld, J.; Schreckenbach, G., *Inorg. Chem.* **2011**, *50* (7), 3141-3152.
52. Ingram, K. I. M.; Haller, L. J. L.; Kaltsoyannis, N., *Dalton T.* **2006**, (20), 2403-2414.
53. Tsushima, S.; Rossberg, A.; Ikeda, A.; Muller, K.; Scheinost, A. C., *Inorg. Chem.* **2007**, *46* (25), 10819-10826.
54. Quiles, F.; Chinh, N. T.; Carteret, C.; Humbert, B., *Inorg. Chem.* **2011**, *50* (7), 2811-2823.
55. da Silva, G.; Kennedy, E. M.; Dlugogorski, B. Z., *J. Phys. Chem. A* **2006**, *110* (39), 11371-11376.
56. Jang, Y. H.; Goddard, W. A.; Noyes, K. T.; Sowers, L. C.; Hwang, S.; Chung, D. S., *J. Phys. Chem. B* **2003**, *107* (1), 344-357.
57. Liptak, M. D.; Shields, G. C., *J. Am. Chem. Soc.* **2001**, *123* (30), 7314-7319.
58. Di Bernardo, P.; Zanonato, P.; Bismondo, A.; Jiang, H. J.; Garnov, A. Y.; Jiang, J.; Rao, L. F., *Eur. J. Inorg. Chem.* **2006**, (22), 4533-4540.
59. Hummel, W.; Puigdomenech, I.; Rao, L. F.; Tochiyama, O., *Comptes Rendus Chimie* **2007**, *10* (10-11), 948-958.
60. Rao, L. F., *Chem. Soc. Rev.* **2007**, *36* (6), 881-892.

61. Reed, W. A.; Rao, L. F.; Zanonato, P.; Garnov, A. Y.; Powell, B. A.; Nash, K. L., *Inorg. Chem.* **2007**, *46* (7), 2870-2876.
62. Tian, G. X.; Rao, L. F., *J. Chem. Thermodyn* **2009**, *41* (4), 569-574.
63. Clark, D. L.; Conradson, S. D.; Donohoe, R. J.; Keogh, D. W.; Morris, D. E.; Palmer, P. D.; Rogers, R. D.; Tait, C. D., *Inorg. Chem.* **1999**, *38* (7), 1456-1466.

## Preface to Chapter 5

This chapter is based on a manuscript submitted to the journal “*Inorganic Chemistry*”. The full citation of the paper is as follows:

Samuel O. Odoh and Georg Schreckenbach, “DFT Study of Uranyl Peroxo Complexes with H<sub>2</sub>O, F<sup>-</sup>, OH<sup>-</sup>, CO<sub>3</sub><sup>2-</sup> and NO<sub>3</sub><sup>-</sup>”, *Inorg. Chem.*, **2012**, submitted.

In this chapter, the structures and electronic properties of complexes formed between uranyl, peroxo and other environmentally relevant ligands were studied using density functional theory. At high peroxide concentrations, actinyl species form polynuclear crystalline species. These species have been extensively studied using both experimental and theoretical techniques. The smaller uranyl peroxo complexes formed at lower concentrations with other ligands might be more relevant to the migration of radionuclides in the environment. In addition, a study of such complexes might provide insights into the origin (mechanism of formation) of the larger polynuclear uranium peroxides. Such a study is compiled in this chapter.

All the calculations in the published manuscript and compiled in this chapter were carried out by Samuel O. Odoh. The manuscript was prepared together with Prof. Georg Schreckenbach.

Copyright permissions have been obtained from the American Chemical Society and the other authors.

## Chapter 5: DFT Study of Uranyl Peroxo Complexes with H<sub>2</sub>O, F<sup>-</sup>, OH<sup>-</sup>, CO<sub>3</sub><sup>2-</sup> and NO<sub>3</sub><sup>-</sup>

### Abstract

The structural and electronic properties of monoperoxo and diperoxo uranyl complexes with aquo, fluoride, hydroxo, carbonate and nitrate ligands have been studied using scalar relativistic density functional theory (DFT). Only the complexes in which the peroxo ligands are coordinated to the uranyl moiety in a bidentate mode were considered. The calculated binding energies confirm that the affinity of the peroxo ligand for the uranyl group far exceeds that of the F<sup>-</sup>, OH<sup>-</sup>, CO<sub>3</sub><sup>2-</sup>, NO<sub>3</sub><sup>-</sup> and H<sub>2</sub>O ligands. The formation of the monoperoxo complexes from UO<sub>2</sub>(H<sub>2</sub>O)<sub>5</sub><sup>2+</sup> and HO<sub>2</sub><sup>-</sup> were found to be exothermic in solution. In contrast, the formation of the monouranyl-diperoxo, UO<sub>2</sub>(O<sub>2</sub>)<sub>2</sub>X<sub>2</sub><sup>4-</sup> or UO<sub>2</sub>(O<sub>2</sub>)<sub>2</sub>X<sup>4-/3-</sup> complexes were all found to be endothermic in aqueous solution. This suggests that the monoperoxo species are the terminal mono-uranyl peroxo complexes in solution, in agreement with recent experimental work. Overall, we find that the properties of the uranyl-peroxo complexes conform to well known trends: the coordination of the peroxo ligand weakens the U-O<sub>yl</sub> bonds, stabilizes the σ(d) orbitals and causes a mixing between the uranyl π- and peroxo σ and π orbitals. The weakening of the U-O<sub>yl</sub> bonds upon peroxide coordination results in uranyl stretching vibrational frequencies that are much lower than those obtained after the coordination of carbonato or hydroxo ligands.

## Introduction

The coordination of actinide ions to the peroxide group,  $O_2^{2-}$ , has been highlighted for use in nuclear separation technologies due to the crystallization of actinide peroxides complexes<sup>1</sup>, in addition to the intensification of the corrosion of uranium dioxide nuclear fuels after peroxide-induced oxidation.<sup>2-3</sup> The peroxide group has a very strong affinity for uranium resulting in insoluble polynuclear solids at high concentrations and pH.<sup>1, 4-7</sup> In fact, studdite,  $UO_4 \cdot 4H_2O$  and metastuddite,  $UO_4 \cdot 2H_2O$ , two hydrated uranyl peroxides, are the only known peroxide containing minerals and are formed from hydrogen peroxide generated by the  $\alpha$ -radiolysis of water.<sup>8</sup> Recently, the agglomeration of uranyl-peroxide units into nanoscale cage clusters has been the focus of several studies. Burns et al. have synthesized and characterized a variety of uranyl peroxide hydroxide polyhedral species.<sup>1, 4-7, 9</sup> These polynuclear clusters mostly adopt a cage-like motif with one of the largest of them being a  $[UO_2(OH)(O_2)]_{60}^{60-}$  complex which adopts the buckyball structure of Buckminsterfullerene. The reason behind the preference of the cage motif over the linear sheet motif in these and other uranyl-peroxide nanoclusters has been investigated by several workers using electronic structure calculations.<sup>10-11</sup> In their calculations Vlasisavljević et al. showed that the uranyl-peroxide-uranyl motif found in these clusters is inherently bent as a result of the covalent interaction across the U-O<sub>2</sub> bond.<sup>11</sup> They also demonstrated the effect of the size and electronegativity of the counterion on the dihedral U-O<sub>2</sub>-U angle.

It is however the case that the solution chemistry of uranyl peroxide has not been investigated to the same extent as its solid-state complexes. The solution chemistry of these peroxide complexes is particularly important in view of the environmental importance of migrating nuclear waste streams. Goff et al.<sup>12</sup> have shown that minute amounts of peroxide can be used to displace a carbonate group from aqueous solutions of  $UO_2(CO_3)_3^{4-}$ . Structural and

spectroscopic characterization of the peroxy-carbonato complex formed revealed it to be  $\text{UO}_2(\text{O}_2)(\text{CO}_3)_2^{4-}$  in the form of  $\text{K}_4[\text{UO}_2(\text{O}_2)(\text{CO}_3)_2]\cdot\text{H}_2\text{O}$ . The spectroscopic investigations of Meca et al. have also indicated the existence of two uranyl peroxide-hydroxide complexes at pH 12 in the absence of carbonate species.<sup>13</sup> These species were suggested to be  $\text{UO}_2(\text{O}_2)(\text{OH})_2^{2-}$  and  $\text{UO}_2(\text{O}_2)_2(\text{OH})_2^{4-}$ , with the latter, as expected, being more predominant at higher peroxide concentrations. More recently, Zanonato et al. examined the ternary peroxide-hydroxide system in a tetramethylammonium nitrate medium.<sup>14</sup> They found  $\text{UO}_2(\text{O}_2)(\text{OH})^-$  to be the dominant complex from pH 9.5 to 11.5 even though significant amounts of the binuclear complex,  $(\text{UO}_2)_2(\text{O}_2)_2(\text{OH})^-$ , was present at around pH 10.5. These studies suggest that the uranyl peroxide moiety,  $\text{UO}_2(\text{O}_2)$  could indeed form complexes with a wide variety of ligands in so far as the U(VI) and  $\text{O}_2^{2-}$  concentration is controlled, to prevent the complexity and precipitation engendered by polynuclear species. Nyman et al. have also recently reported the synthesis of two lithium salts of  $\text{UO}_2(\text{O}_2)_3^{4-}$ .<sup>15</sup> They suggested that these monomeric triperoxy systems could play a role in aqueous behavior, re-dissolution and self assembly characteristics of uranyl polynuclear peroxides.

The recent progress being made in the solvent phase and monomer chemistry of uranyl-peroxide species has motivated us to carry out a systematic computational study of the structural and electronic properties of the possible ternary uranyl peroxide complexes with fluoride, aquo, hydroxo, carbonate and nitrate ligands. Additionally, we have focused on the characteristic vibrational frequencies of these peroxy complexes, the relative stabilities of their various structures as well as the trends in their calculated structural properties. Ultimately the aim of the current work is to provide calculated structural data for the uranyl peroxy complexes. This will hopefully allow for an easier characterization of some these complexes should they be

synthesized in the future. All the calculations in this work have been carried out using scalar relativistic density functional theory (DFT). The use of DFT calculations as a complement to the available experimental stoichiometric and structural data of actinide complexes and in predicting the structures of as yet to be synthesized actinide species is well established.<sup>11, 16-41</sup>

## Computational Details

The geometry optimizations in this work were all carried out with the Gaussian 03 code.<sup>42</sup> Vibrational frequency analyses with the harmonic approximation were carried out after the geometry optimizations to characterize the local minima nature of the optimized structures on the potential energy surfaces. Most of the geometry optimizations and vibrational frequency calculations were carried out in aqueous solution while employing the polarizable continuum solvation (PCM) model.<sup>43</sup> In some cases, the gas phase structures of the complexes were also optimized and presented in this work, for comparison. In the PCM calculations, the default atomic radii of the united force field (UFF) in Gaussian 03 were employed. The peroxide complexes studied in this work were all found to be singlet species. The restricted singlet wavefunctions are stable with respect to conversion to unrestricted determinants and relaxation of the orbital symmetries. In all the calculations, only complexes with bidentate coordination between the uranium atoms and the peroxy group were considered. Ultra-fine grids were used in the numerical integration of the exchange-correlation portion of the density functional. Regarding basis sets, the Stuttgart small-core scalar-relativistic pseudopotential was used to describe the uranium atoms.<sup>44-46</sup> The pseudopotential represents 60 core electrons in uranium while the remaining 32 electrons were represented by the associated valence basis set. The design and use of this pseudopotential-basis set combination reduces the computational expense and allows a wise inclusion of scalar-relativistic effects. To further improve computational

efficiency, all g-type functions were removed from the valence basis set. The 6-31+G\* basis was used to describe oxygen, nitrogen, fluorine and carbon atoms while hydrogen atoms were described with the 6-31G basis. We label this scheme in which the uranium RECP and the 6-31+G\*/6-31G bases for the non-actinide atoms were employed as B1. The B3LYP<sup>47-49</sup> functional was employed in all the calculations carried out in this current work. Overall the B3LYP/B1 abbreviation is used to describe the functional and basis set combination employed in the calculations.

Single point calculations on the geometries optimized at the B3LYP/B1 level were carried out with a four-component scalar relativistic approach as implemented in the Priroda program.<sup>50</sup> These calculations allowed us to obtain the population based Mayer bond orders which are in our experience good reflections of the formal bond order.<sup>34, 37</sup> A basis of double- $\zeta$  quality (cc-pVDZ) was used for all the elements for the large component with the corresponding kinetically-balanced basis sets for the small component.<sup>51</sup> The B3LYP functional was also employed in the Priroda calculations. This combination of functional and basis set is labeled as B3LYP/B2.

## Results and Discussions

**UO<sub>2</sub><sup>2+</sup> and its peroxy derivatives.** The electronic structure of UO<sub>2</sub><sup>2+</sup> as well as those of its neptunium and plutonium analogues has been studied extensively.<sup>52-57</sup> At the B3LYP/B1 level and in aqueous solution, the valence region of this dication consists of the  $\sigma(f)$ ,  $\pi(f)$ ,  $\sigma(d)$  and  $\pi(d)$  orbitals at -11.1, -11.9, -12.2 and -12.2 eV respectively. The optimized geometries for UO<sub>2</sub><sup>2+</sup> and its peroxide derivatives, UO<sub>2</sub>(O<sub>2</sub>)<sub>n</sub><sup>2-n</sup>, obtained with the PCM solvation model, are shown in Figure 5.1. For the uranyl peroxide species, UO<sub>2</sub>(O<sub>2</sub>), UO<sub>2</sub>(O<sub>2</sub>)<sub>2</sub><sup>2-</sup> and UO<sub>2</sub>(O<sub>2</sub>)<sub>3</sub><sup>4-</sup>, the  $\sigma$

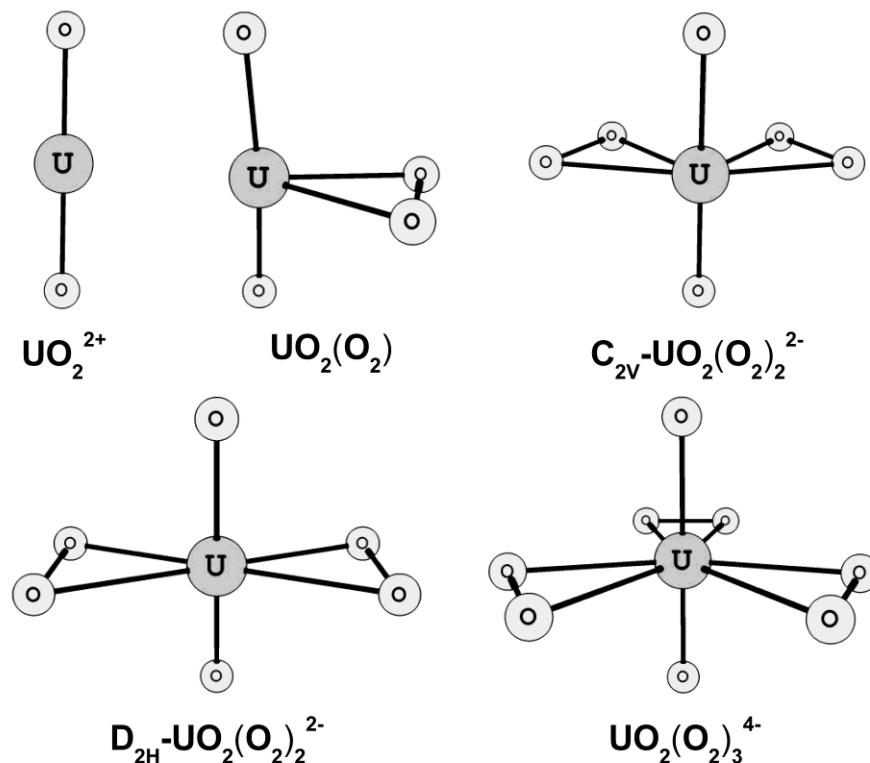


**Figure 5.1:** The structures of  $\text{UO}_2^{2+}$  and its peroxy derivatives optimized at the B3LYP/B1 level in aqueous solution. The  $\text{D}_{2h}$  structure of the uranyl diperoxide was found to be a transition state structure.

and  $\pi$  bonding orbitals of the peroxy ligand are found below the uranyl  $\sigma(\text{d})$  and  $\pi(\text{d})$  orbitals, Table 5.1. There is however substantial mixing between the  $\text{O}_2\text{-}\pi$  orbital and the uranyl  $\pi(\text{d})$  orbitals in  $\text{UO}_2(\text{O}_2)$ . In contrast, the  $\text{U-O}_{\text{peroxy}}$  bond orbitals between the uranyl and peroxy units are found above the uranyl  $\sigma(\text{f})$  orbitals. The uranyl and peroxy orbitals of  $\text{UO}_2(\text{O}_2)$  are shown in Figure 5.2. The coordination of the second and third peroxide ligands stabilizes the actinyl  $\pi(\text{f})$  orbitals such that there is significant  $\sigma(\text{O}_2)\text{-}\pi(\text{f})$  as well as  $\pi(\text{O}_2)\text{-}\pi(\text{d})$  mixing in the diperoxo and triperoxo complexes, Table 5.1. In addition, the uranyl  $\pi(\text{f})$  orbitals are stabilized below the  $\pi(\text{d})$

orbitals in  $\text{UO}_2(\text{O}_2)_3^{4-}$ . The nature of the  $\pi(\text{O}_2)$ - $\pi(\text{d})$  mixing is reminiscent of the  $\pi(\text{d})$ - $\mu_3\text{O}_2(2\text{p})$  orbitals that were recently reported in trimeric  $[(\text{AnO}_2)_3(\text{O})(\text{OH})_3]^+$  complexes of uranium and plutonium.<sup>58</sup> In that study, the degree of stability conferred by the central  $\mu_3$ -oxo ligand on the hexagonal trimer shape was found to be greater for the uranium complex and lower for the plutonium complex. A similar difference in the mixing of the  $\sigma(\text{O}_2)$  and  $\pi(\text{O}_2)$  orbitals with the uranyl and plutonyl  $\pi(\text{f})$  and  $\pi(\text{d})$  orbitals might also exist for the peroxide complexes. The  $\text{C}_{2\text{v}}$  structure of  $\text{UO}_2(\text{O}_2)_2^{2-}$  was calculated to be 3.1 kcal/mol more stable than its  $\text{D}_{2\text{h}}$  conformer in the aqueous phase. The energy difference in the gas phase was calculated as 1.2 kcal/mol. The  $\text{D}_{2\text{h}}$  structure is a transition state structure in both gaseous and aqueous media as it possesses imaginary frequencies of about  $37i \text{ cm}^{-1}$  and  $76i \text{ cm}^{-1}$  respectively in these media. These imaginary frequencies correspond to the equatorial bending of the  $\text{O}_2$ -U- $\text{O}_2$  group. The bent  $\text{O}_2$ -U- $\text{O}_2$  wing in the  $\text{C}_{2\text{v}}$  structure suggests a preference for circular polynuclear  $(\text{UO}_2(\text{O}_2)_2)_n$ -type species over the linear polymer species implied by the  $\text{D}_{2\text{h}}$  structure.

The calculated geometries of  $\text{UO}_2^{2+}$ ,  $\text{UO}_2(\text{O}_2)$ ,  $\text{UO}_2(\text{O}_2)_2^{2-}$  and  $\text{UO}_2(\text{O}_2)_3^{4-}$  obtained at the B3LYP/B1 level in aqueous solution are presented in Table 5.2. The calculated symmetric and asymmetric vibrational stretching modes of the uranyl groups in these complexes as well as the  $\text{O}_2$  stretching and U- $\text{O}_2$  stretching modes of the peroxides are also presented in Table 5.2. The  $\text{O}_{\text{yl}}\text{-U-O}_{\text{yl}}$  bond angle was calculated as  $180.0^\circ$ ,  $174.3^\circ$ ,  $171.6^\circ$  and  $180.0^\circ$  in  $\text{UO}_2^{2+}$ ,  $\text{UO}_2(\text{O}_2)$ ,  $\text{C}_{2\text{v}}\text{-UO}_2(\text{O}_2)_2^{2-}$  and  $\text{UO}_2(\text{O}_2)_3^{4-}$  respectively. There is a sequential weakening of the U- $\text{O}_{\text{yl}}$ , U- $\text{O}_{\text{peroxo}}$ , O- $\text{O}_{\text{peroxo}}$  bonds as the number of coordinated peroxide ligands are increased. The weaker U- $\text{O}_{\text{yl}}$  bonds result in lower uranyl stretching vibrational frequencies. The uranyl stretching modes in  $\text{UO}_2(\text{O}_2)_3^{4-}$  were calculated as  $662 \text{ cm}^{-1}$  for the asymmetric mode and  $646 \text{ cm}^{-1}$  for the symmetric mode. These are significantly lower than those obtained for the bare dication. To put

**Table 5.1:** Energies and characters of the MOs of the dioxouranium (VI) peroxides in aqueous solution obtained at the B3LYP/B1 level.

| UO <sub>2</sub> (O <sub>2</sub> ) |                |                         | UO <sub>2</sub> (O <sub>2</sub> ) <sub>2</sub> <sup>2-</sup> |                |                           | UO <sub>2</sub> (O <sub>2</sub> ) <sub>3</sub> <sup>4-</sup> |                |                           |
|-----------------------------------|----------------|-------------------------|--|----------------|---------------------------|--|----------------|---------------------------|
| MO                                | Energy<br>(eV) | Character               | MO   | Energy<br>(eV) | Character                 | MO   | Energy<br>(eV) | Character                 |
| 22                                | -11.32         | σ(O <sub>2</sub> )      | 26   | -10.07         | σ(O <sub>2</sub> )        | 30   | -9.19          | σ(O <sub>2</sub> )        |
| 23                                | -11.05         | π(O <sub>2</sub> )/π(d) | 27   | -9.77          | σ(O <sub>2</sub> )        | 31   | -8.89          | σ(O <sub>2</sub> )/σ(d)   |
| 24                                | -10.77         | π(O <sub>2</sub> )/π(d) | 28   | -9.64          | π(O <sub>2</sub> )/σ(d)   | 32   | -8.83          | σ(O <sub>2</sub> )        |
| 25                                | -9.84          | σ(d)                    | 29   | -9.58          | π(O <sub>2</sub> )/π(d)   | 33   | -8.82          | σ(O <sub>2</sub> )        |
| 26                                | -9.84          | π(d)                    | 30   | -9.38          | π(O <sub>2</sub> )/π(d/f) | 34   | -8.50          | π(O <sub>2</sub> )/π(d)   |
| 27                                | -9.35          | π(f)                    | 31   | -8.75          | π(O <sub>2</sub> )/π(f)   | 35   | -8.50          | π(O <sub>2</sub> )/π(d)   |
| 28                                | -9.35          | π(f)                    | 32   | -8.35          | σ(d)                      | 36   | -8.13          | π(O <sub>2</sub> )/σ(f)   |
| 30                                | -8.11          | σ(f)                    | 33   | -8.07          | π(d/f)                    | 37   | -7.75          | π(O <sub>2</sub> )/π(d/f) |
| 31                                | -7.40          | σ(U-O <sub>2</sub> )    | 34   | -7.69          | π(f)                      | 38   | -7.75          | π(O <sub>2</sub> )/π(d/f) |
|                                   |                |                         | 35   | -7.51          | π(d)                      | 39   | -7.28          | σ(d)                      |
|                                   |                |                         | 36   | -7.42          | π(f)                      | 40   | -6.50          | π(f)                      |
|                                   |                |                         | 37   | -6.57          | σ(f)                      | 41   | -6.50          | π(f)                      |
|                                   |                |                         | 38   | -6.03          | σ(U-O <sub>2</sub> )      | 42   | -6.42          | π(d)                      |
|                                   |                |                         |  |                |                           | 43   | -6.42          | π(d)                      |
|                                   |                |                         |  |                |                           | 44   | -5.61          | σ(f)                      |
|                                   |                |                         |  |                |                           | 45   | -5.06          | σ(U-O <sub>2</sub> )      |

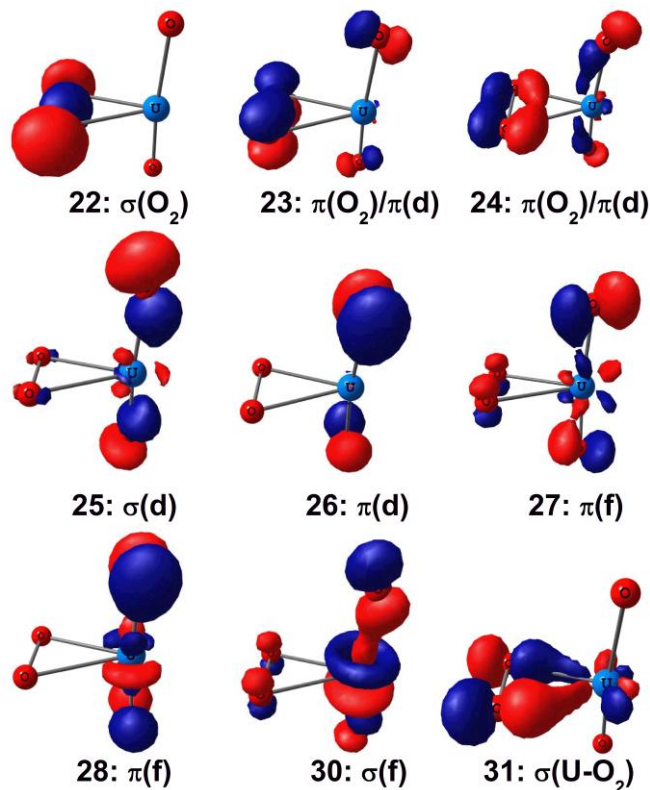


**Figure 5.2:** The molecular orbitals of  $\text{UO}_2(\text{O}_2)$ . The geometry of this complex was optimized with the PCM approach and the B3LYP functional.

this in perspective, the uranyl stretching modes in  $\text{UO}_2(\text{NO}_3)_3^-$  and  $\text{UO}_2(\text{CO}_3)_3^{4-}$ , two complexes also possessing bidentate anionic ligands, were calculated as 870 and 929  $\text{cm}^{-1}$  for the former and 775 and 811  $\text{cm}^{-1}$  in the latter. In addition, the longer  $\text{U-O}_{\text{peroxo}}$  and  $\text{O-O}_{\text{peroxo}}$  bonds result in lower frequencies for the  $\text{O}_2$  stretching and  $\text{U-O}_2$  stretching vibrational modes respectively. Similar elongations of the  $\text{U-O}_{\text{yl}}$  bonds have been observed in the uranyl hydroxide,  $\text{UO}_2(\text{OH})_n^{2-n}$ ,<sup>58-59</sup> and fluoride,  $\text{UO}_2\text{F}_n^{2-n}$ ,<sup>29</sup> complexes. The simulated IR spectra of  $\text{UO}_2^{2+}$ ,  $\text{UO}_2(\text{O}_2)$ ,  $\text{C}_{2v}$ - $\text{UO}_2(\text{O}_2)_2^{2-}$  and  $\text{UO}_2(\text{O}_2)_3^{4-}$  are shown in Figure 5.3. The vibrational modes associated with the stretching of the peroxo O-O bonds were found between 839 and 936  $\text{cm}^{-1}$ , Table 5.2, gradually

decreasing down the series and split across several frequencies in the diperoxo and triperoxo species. The calculated IR intensities of these peaks indicate that some of the O-O stretching should be observed in the Raman spectra of the peroxo complexes. The peak centered at around  $470\text{ cm}^{-1}$  in the simulated IR spectra of  $\text{UO}_2(\text{O}_2)$  and around  $400\text{ cm}^{-1}$  in  $\text{C}_{2v}\text{-UO}_2(\text{O}_2)_2^{2-}$  and  $\text{UO}_2(\text{O}_2)_3^{4-}$ , Figure 5.3, contains the  $\text{U-O}_{\text{peroxo}}$  stretching vibrations of which the symmetric mode has significantly higher IR intensities than the counterpart asymmetric mode. Similar to the case for the O-O stretching mode, the  $\text{U-O}_{\text{peroxo}}$  stretching vibrations are split into IR and Raman active modes in the higher peroxides. The  $\text{U-O}_{\text{yl}}$  bonds in  $\text{UO}_2(\text{O}_2)_3^{4-}$  optimized with the PCM

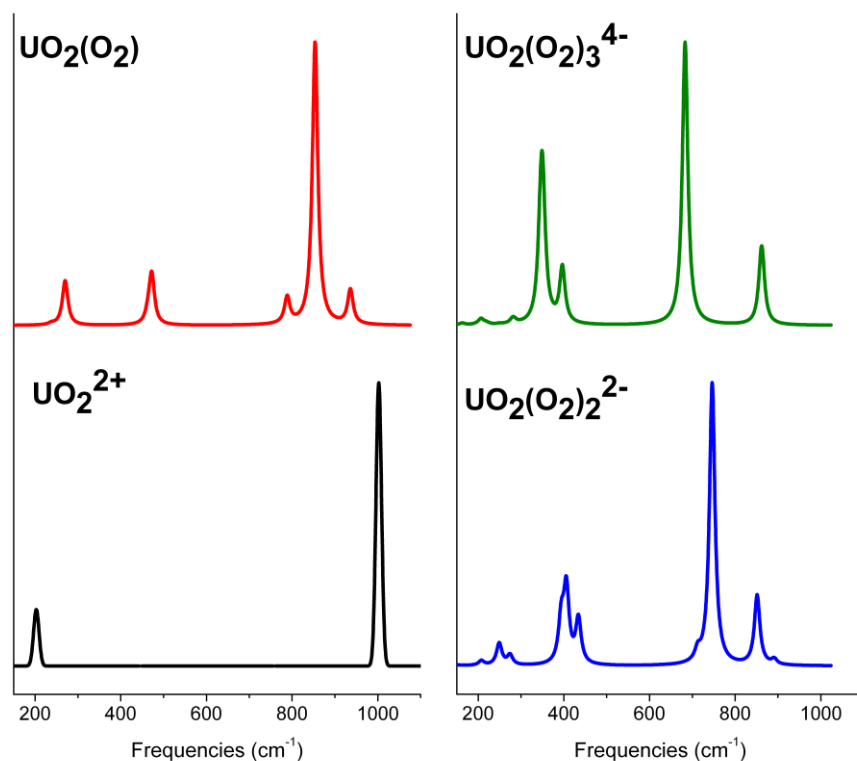


**Figure 5.3:** Simulated IR spectra of  $\text{UO}_2^{2+}$  and its peroxo derivatives obtained at the at the B3LYP/B1 level in aqueous solution.

**Table 5.2:** Calculated structural properties and vibrational frequencies of  $\text{UO}_2^{2+}$  and its peroxo derivatives obtained at the B3LYP/B1 level in aqueous solution.

|                                  | Bonds ( $\text{\AA}$ ) |                              |        | Vibrational Frequencies ( $\text{cm}^{-1}$ ) |      |                        |                          |                 |
|----------------------------------|------------------------|------------------------------|--------|--|------|------------------------|--------------------------|-----------------|
|                                  | U-O <sub>yl</sub>      | U-O                          | O-O    | Uranyl Stretching                            |      | O <sub>2</sub> stretch | U-O <sub>2</sub> stretch |                 |
|                                  |                        | peroxo                       | peroxo | Asymm.                                       | Sym. |                        | Symm.                    | Asymm.          |
| $\text{UO}_2^{2+}$               | 1.748                  |                              |        | 1002   | 920  |                        |                          |                 |
| $\text{UO}_2(\text{O}_2)$        | 1.810                  | 2.177                        | 1.442  | 854  | 789  | 936                    | 472                      | 464             |
| $\text{UO}_2(\text{O}_2)_2^{2-}$ |                        |                              |        |  |      |                        |                          |                 |
| $\text{C}_{2v}$                  | 1.866                  | 2.233/<br>2.260              | 1.471  | 746  | 712  | 891/851                | 434/394                  | 406/394         |
| $\text{D}_{2h}$                  | 1.861                  | 2.259                        | 1.467  | 755  | 713  | 891/856                | 393/392                  | 397/370         |
| $\text{UO}_2(\text{O}_2)_3^{4-}$ | 1.907                  | 2.323                        | 1.485  | 662  | 646  | 871/841/<br>839        | 378/354/<br>332          | 377/339/3<br>28 |
| Expt.                            | 1.846 <sup>a</sup>     | 2.303-<br>2.324 <sup>a</sup> |        |  |      |                        |                          |                 |

<sup>a</sup> X-ray structure of  $\text{Li}_4[\text{UO}_2(\text{O}_2)_3]_3 \cdot 10\text{H}_2\text{O}$ ; Reference <sup>15</sup>

model are about 0.05  $\text{\AA}$  longer than those found in solid  $\text{Li}_4[\text{UO}_2(\text{O}_2)_3]_3 \cdot 10\text{H}_2\text{O}$ , Table 5.2.<sup>15</sup> It is noted that the crystal structure indicated interactions between the lithium-bound water molecules and the peroxide oxygen ligands. In implicit solvation models, like the PCM model employed here, the effect of a solvent is included with a statistically average solvent described by its

dielectric constant, a macroscopic property. These models are not sufficient to describe the lithium-water and water-peroxo interactions in  $\text{Li}_4[\text{UO}_2(\text{O}_2)_3]_3 \cdot 10\text{H}_2\text{O}$ .

There are two types of  $\text{U-O}_{\text{peroxo}}$  bonds in the  $\text{C}_{2v}$  structure of  $\text{UO}_2(\text{O}_2)_2^{2-}$ , the proximal ones being about 0.03 Å longer than the distal ones, Figure 5.1. The  $\sigma(\text{O}_2)$  character of MO-26 in  $\text{C}_{2v}\text{-UO}_2(\text{O}_2)_2^{2-}$  is such that there is some overlap across the distal oxygen atoms of the two peroxo ligands, Figure 5.4. As this overlap is prohibited in the  $\text{D}_{2h}$  structure, by virtue of the trans arrangement of the equatorial peroxo groups, it is most likely the reason behind the greater stability of the  $\text{C}_{2v}$  structure. Examination of the MO energy levels reveals that MO 26 is about 0.30 eV (6.92 kcal/mol) below MO 27 ( $\sigma$  orbital antibonding across the O-O' distance, Figure 5.3) in  $\text{C}_{2v}\text{-UO}_2(\text{O}_2)_2^{2-}$ . In contrast, the energy difference between these orbitals is 0.08 eV (1.84 kcal/mol) in  $\text{D}_{2h}\text{-UO}_2(\text{O}_2)_2^{2-}$ . This discrepancy indicates a stabilization of MO-26 in the  $\text{C}_{2v}$  structure. The difference in the relative energies of these orbitals is however not sufficient to fully explain the greater stability of  $\text{C}_{2v}\text{-UO}_2(\text{O}_2)_2^{2-}$ . Increased contributions from uranium atomic orbitals, generally found in  $\text{D}_{2h}\text{-UO}_2(\text{O}_2)_2^{2-}$ , result in destabilization of molecular orbitals with predominantly peroxo character. The converse is true for orbitals with mainly uranyl character.

The  $\sigma(\text{U-O}_2)$  orbitals of the  $\text{U-O}_{\text{peroxo}}$  bonds are formed by overlap of the uranium 5f orbitals and the in-plane  $\pi$  antibonding orbitals of the peroxo ligand, Figure 5.2. There is some U-6d contribution, 8%, to the  $\sigma(\text{U-O}_2)$  orbital in  $\text{UO}_2(\text{O}_2)$ . The U-6d orbitals however do not participate in the  $\text{U-O}_{\text{peroxo}}$  bonds of  $\text{UO}_2(\text{O}_2)_2^{2-}$  and  $\text{UO}_2(\text{O}_2)_3^{4-}$ . The out-of-plane peroxo antibonding  $\pi$  orbitals are found at higher energies.

The absolute ligand binding energies for  $\text{UO}_2(\text{O}_2)$ ,  $\text{C}_{2v}\text{-UO}_2(\text{O}_2)_2^{2-}$  and  $\text{UO}_2(\text{O}_2)_3^{4-}$  were calculated as -121.5, -194.4 and -235.8 kcal/mol respectively at the B3LYP/B1 level in aqueous solution. These are the energies required to bind the peroxo ligands to the  $\text{UO}_2^{2+}$  and are equivalent to -121.5, -97.2 and -78.6 kcal/mol per peroxo group in these complexes respectively. The binding energies were obtained from the calculated electronic energies of the species involved in the reaction:  $\text{UO}_2^{2+}(\text{aq}) + n\text{O}_2^{2-}(\text{aq}) \rightarrow \text{UO}_2(\text{O}_2)_n^{2-2n}(\text{aq})$ . Although, the absolute binding energies become larger for successive coordination of a peroxo ligand, the calculated binding energies relative to the (n-1) species decrease down the series. A similar effect has been

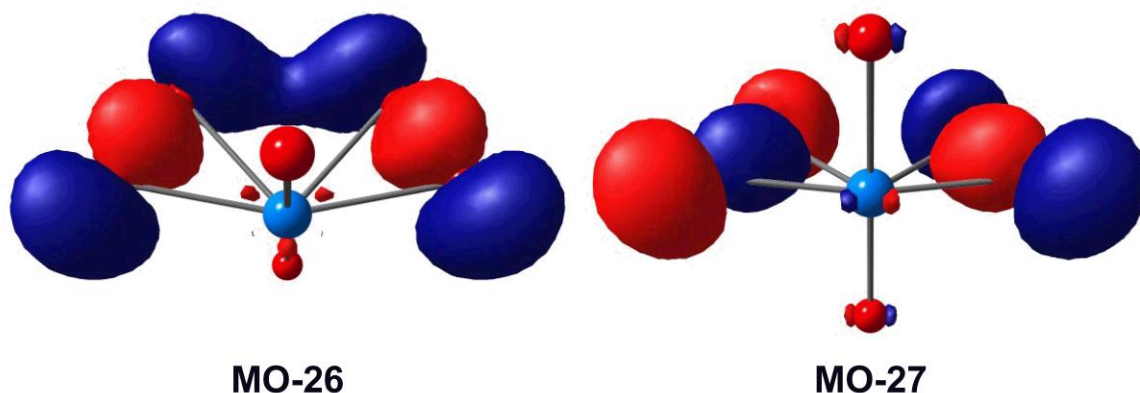


**Figure 5.4:** MO-26 and MO-27 of the  $\text{C}_{2v}$  structure of  $\text{UO}_2(\text{O}_2)_2^{2-}$ . The former is bonding with respect to the O-O' distance between the distal oxygen atoms of the peroxo group while the latter is antibonding. The distal U-O bonds are about 0.03 Å shorter than the proximal ones.

observed in our previous works on plutonyl hydroxides<sup>58</sup> and uranyl fluorides<sup>29</sup> as well as by other workers. For comparison, we also calculated the absolute ligand binding energies of  $\text{UO}_2(\text{OH})_4^{2-}$ ,  $\text{UO}_2(\text{NO}_3)_3^-$  and  $\text{UO}_2(\text{CO}_3)_3^{4-}$ . These were calculated as -167.8, -55.4 and -148.0 kcal/mol respectively, or -41.9, -18.5, -49.3 kcal/mol per ligand respectively. The implication of

this is that for the  $\text{UO}_2\text{L}_n$  species ( $\text{L} = \text{O}_2^{2-}$ ,  $\text{OH}$ ,  $\text{NO}_3^-$  or  $\text{CO}_3^{2-}$ ), the affinity of the uranyl group for the peroxide ligand far exceeds its affinity for the hydroxide, nitrate and carbonate ligands.

**Uranyl aquo complexes.** The uranyl chemistry in highly acidic solutions is dominated by the  $\text{UO}_2(\text{H}_2\text{O})_5^{2+}$  complex. The calculated bond lengths and vibrational frequencies of  $\text{UO}_2(\text{H}_2\text{O})_5^{2+}$  obtained in this work are presented in Table 5.3. Shamov et al. and several other workers have previously predicted the structure of this complex in the gas phase at the DFT level.<sup>16, 35-36, 59</sup> The calculated gas phase geometry of this complex obtained in this work is in good agreement with previous reports. Introduction of solvent effects with the continuum solvation model slightly weakens the  $\text{U-O}_{\text{yl}}$  bonds by about 0.01 Å but strengthens the  $\text{U-OH}_2$  interactions by about 0.05 Å. This is in accordance with previous computational work.<sup>28-29, 34-36</sup> The use of the solvation model brings the calculated  $\text{U-O}_{\text{yl}}$  and  $\text{U-OH}_2$  bond-lengths to within 0.01 and 0.03 Å of the available aqueous phase extended X-ray absorption fine structure, EXAFS, data of Allen et al.<sup>60</sup> The calculated uranyl stretching vibrational frequencies are reduced by about 20-53  $\text{cm}^{-1}$  in the solvent phase calculations. The experimental vibrational frequencies<sup>61-62</sup> of  $\text{UO}_2(\text{H}_2\text{O})_5^{2+}$  are within 41  $\text{cm}^{-1}$  of the calculated values obtained using the PCM model.

The replacement of aquo ligands in  $\text{UO}_2(\text{H}_2\text{O})_5^{2+}$  by an equatorial peroxy group forms  $\text{UO}_2(\text{H}_2\text{O})_4(\text{O}_2)$ ,  $\text{UO}_2(\text{H}_2\text{O})_3(\text{O}_2)$  or  $\text{UO}_2(\text{H}_2\text{O})_2(\text{O}_2)$ . This is particularly interesting given that the chemical formulas of the minerals studtite and metastudtite are  $\text{UO}_2(\text{H}_2\text{O})_4(\text{O}_2)$  and  $\text{UO}_2(\text{H}_2\text{O})_2(\text{O}_2)$  respectively. The optimized structures for the aquo-peroxy complexes are presented in Figure 5.5. Starting from gas phase  $\text{UO}_2(\text{H}_2\text{O})_5^{2+}$  and  $\text{HO}_2^-$ , as shown in the reaction below, the formation of the aquo-peroxy complexes were calculated to be very exothermic in the gas phase, between -158.2 kcal/mol for  $\text{UO}_2(\text{H}_2\text{O})_2(\text{O}_2)$  and -187.1 kcal/mol for  $\text{UO}_2(\text{H}_2\text{O})_4(\text{O}_2)$ .

**Table 5.3:** Calculated structural properties and vibrational frequencies ( $\text{cm}^{-1}$ ) of  $\text{UO}_2(\text{H}_2\text{O})_5^{2+}$  and its peroxy derivatives obtained at the B3LYP/B1 level in the gas phase and in aqueous solution.

|   | Bond Lengths (Å)  |                     |                       |                       | Uranyl Stretching |                  |
|---|-------------------|---------------------|-----------------------|-----------------------|-------------------|------------------|
|   | U-O <sub>yl</sub> | U-O <sub>aquo</sub> | U-O <sub>peroxy</sub> | O-O <sub>peroxy</sub> | Asymm.            | Symm.            |
| <hr/>   |                   |                     |                       |                       |                   |                  |
| $\text{UO}_2(\text{H}_2\text{O})_5^{2+}$                      |                   |                     |                       |                       |                   |                  |
| Gas phase   | 1.750             | 2.491               |                       |                       | 1026              | 937              |
| Solution  | 1.759             | 2.440-2.492         |                       |                       | 973               | 911              |
| Experimental  | 1.76 <sup>a</sup> | 2.41 <sup>a</sup>   |                       |                       | 965 <sup>b</sup>  | 870 <sup>b</sup> |
| <hr/>   |                   |                     |                       |                       |                   |                  |
| $\text{UO}_2(\text{O}_2)(\text{H}_2\text{O})_4$               |                   |                     |                       |                       |                   |                  |
| Gas phase   | 1.813             | 2.677/2.686         | 2.176                 | 1.426                 | 886               | 813              |
| Solution  | 1.815             | 2.644-2.666         | 2.195                 | 1.440                 | 840               | 789              |
| <hr/>   |                   |                     |                       |                       |                   |                  |
| $\text{UO}_2(\text{O}_2)(\text{H}_2\text{O})_3$               |                   |                     |                       |                       |                   |                  |
| Gas phase   | 1.814             | 2.593/2.600         | 2.162                 | 1.429                 |                   |                  |
| Solution  | 1.814             | 2.549-2.557         | 2.186                 | 1.445                 | 843               | 791              |
| <hr/>   |                   |                     |                       |                       |                   |                  |
| $\text{UO}_2(\text{O}_2)(\text{H}_2\text{O})_2$               |                   |                     |                       |                       |                   |                  |
| Gas phase   | 1.808             | 2.571               | 2.141                 | 1.435                 | 893               | 820              |
| Solution  | 1.813             | 2.562/2.612         | 2.179                 | 1.444                 | 844               | 788              |
| <hr/>   |                   |                     |                       |                       |                   |                  |
| Solution  |                   |                     |                       |                       |                   |                  |
| $\text{UO}_2(\text{O}_2)_2(\text{H}_2\text{O})^{2-}$          | 1.866             | 2.727               | 2.240/2.264           | 1.471                 | 739               | 704              |
| cis- $\text{UO}_2(\text{O}_2)_2(\text{H}_2\text{O})_2^{2-}$   | 1.862             | 2.725               | 2.251/2.275           | 1.469                 | 749               | 718              |
| trans- $\text{UO}_2(\text{O}_2)_2(\text{H}_2\text{O})_2^{2-}$ | 1.865             | 2.645               | 2.267/2.279           | 1.466                 | 741               | 709              |

<sup>a</sup> Reference <sup>60</sup> <sup>b</sup> References <sup>61-62</sup>

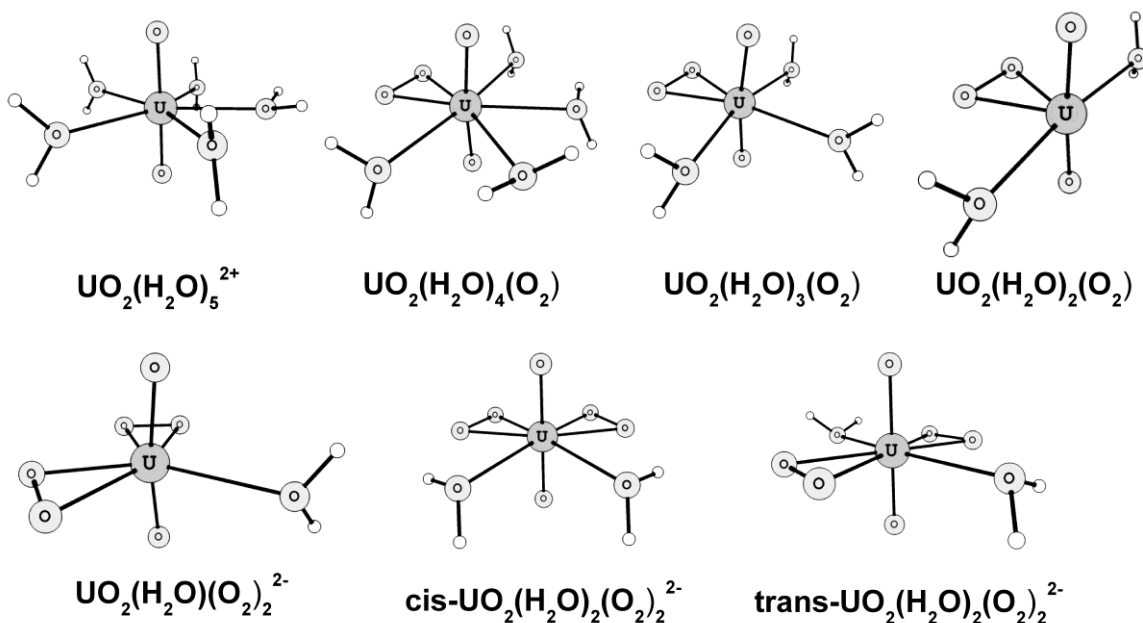


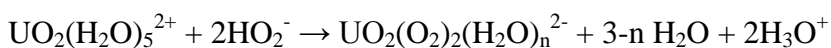
**Figure 5.5:** The structures of  $\text{UO}_2(\text{H}_2\text{O})_5^{2+}$  and its peroxo derivatives optimized at the B3LYP/B1 level in aqueous solution.



There is a drastic solvent effect, in excess of 150 kcal/mol, on these reactions. The formation of  $\text{UO}_2(\text{H}_2\text{O})_4(\text{O}_2)$  is still the most exothermic in the solution phase, about -13.7 kcal/mol, compared to -6.7 and -8.7 kcal/mol for  $\text{UO}_2(\text{H}_2\text{O})_2(\text{O}_2)$  and  $\text{UO}_2(\text{H}_2\text{O})_3(\text{O}_2)$  respectively. This implies that the preferred equatorial coordination number of uranyl aquo-peroxo complex in the gas phase and in solution is 6, larger than that in the case of  $\text{UO}_2(\text{H}_2\text{O})_5^{2+}$ .<sup>35-36, 63</sup> The  $\text{U}-\text{O}_{\text{yl}}$  bond lengths in the aquo-peroxo complexes are centered at 1.814 Å with minimal changes both in solution and as the number of aquo ligands are increased from 2 to 4, Table 5.3. This represents a weakening of about 0.055 Å from  $\text{UO}_2(\text{H}_2\text{O})_5^{2+}$ . The identical  $\text{U}-\text{O}_{\text{yl}}$  bond lengths in these aquo-peroxo complexes are reflected in the similar calculated uranyl stretching vibrational frequencies, Table 5.3. The presence of the equatorial aquo ligands also has little influence on the length of the peroxo O-O bond. As a result the O-O stretching mode of  $\text{UO}_2(\text{O}_2)$  calculated at

936 cm<sup>-1</sup> in solution is retained in the aquo-peroxo complexes with very little change in its frequency. The U-O<sub>peroxo</sub> bonds become slightly longer from UO<sub>2</sub>(O<sub>2</sub>)(H<sub>2</sub>O)<sub>2</sub> to UO<sub>2</sub>(O<sub>2</sub>)(H<sub>2</sub>O)<sub>4</sub>, weakening by 0.035 Å for the gaseous species and 0.016 Å in solution. The stretching modes associated with the U-O<sub>peroxo</sub> bonds are centered around 460-470 cm<sup>-1</sup> just as in UO<sub>2</sub>(O<sub>2</sub>), Figure 5.3. In contrast, the weakening of the U-OH<sub>2</sub> bonds after coordination of an equatorial peroxo ligand is significantly more pronounced, 0.08-0.20 Å in the gas phase and about 0.10 Å with the PCM model. The steric crowding between the aquo and peroxo ligands results in longer U-OH<sub>2</sub> bonds as the equatorial coordination number is increased.

It is reasonable to expect the formation of diperoxo species such as UO<sub>2</sub>(O<sub>2</sub>)<sub>2</sub>(H<sub>2</sub>O)<sup>2-</sup> or UO<sub>2</sub>(O<sub>2</sub>)<sub>2</sub>(H<sub>2</sub>O)<sub>2</sub><sup>2-</sup> at high peroxide concentrations. The calculated thermochemistry for the formation of these complexes in solution, via the reaction shown below, is however unfavorable. The reactions are endothermic for both UO<sub>2</sub>(O<sub>2</sub>)<sub>2</sub>(H<sub>2</sub>O)<sup>2-</sup>, 22.7 kcal/mol and UO<sub>2</sub>(O<sub>2</sub>)<sub>2</sub>(H<sub>2</sub>O)<sub>2</sub><sup>2-</sup>, 18.1 kcal/mol. In a similar manner, the formation of the triperoxo complex, UO<sub>2</sub>(O<sub>2</sub>)<sub>3</sub><sup>4-</sup>, from UO<sub>2</sub>(H<sub>2</sub>O)<sub>5</sub><sup>2+</sup>, is endothermic in aqueous solution by 77.8 kcal/mol.



**Uranyl fluoride complexes.** The structural properties of UO<sub>2</sub>F<sub>4</sub><sup>2-</sup> as well as those of species formed by substitution of the fluoride ligands by peroxo groups are presented in Table 5.4. These geometrical features were obtained at the B3LYP/B1 level while employing the PCM solvation model. The optimized geometries for these complexes are presented in Figure 5.6. The calculated structural parameters of UO<sub>2</sub>F<sub>4</sub><sup>2-</sup> are in good agreement with experimental data<sup>64</sup> and previous

**Table 5.4:** Calculated structural properties and vibrational frequencies of  $\text{UO}_2\text{F}_4^{2-}$  and its peroxo derivatives obtained at the B3LYP/B1 level in aqueous solution.

|  | Bonds (Å)          |        |        |                    | Vibrational Frequencies ( $\text{cm}^{-1}$ ) |                |                          |        |      |
|--|--------------------|--------|--------|--------------------|--|----------------|--------------------------|--------|------|
|  | U-O <sub>y1</sub>  | U-O    | O-O    | U-F                | Stretching Modes                             |                |                          |        |      |
|  |                    | peroxo | peroxo |                    | Uranyl                                       | O <sub>2</sub> | U-O <sub>2</sub> stretch |        |      |
|  |                    |        |        |                    | Asymm.                                       | Symm.          | Symm.                    | Asymm. |      |
| $\text{UO}_2\text{F}_4^{2-}$               | 1.826              |        |        | 2.216              | 822  | 786            |                          |        |      |
| Expt.                                      | 1.800 <sup>a</sup> |        |        | 2.260 <sup>a</sup> |  |                |                          |        |      |
| $\text{UO}_2\text{F}_3(\text{O}_2)^{3-}$   | 1.859              | 2.258  | 1.461  | 2.302              | 752  | 720            | 895                      | 405    | 390  |
| $\text{UO}_2\text{F}_2(\text{O}_2)^{2-}$   | 1.842              | 2.235  | 1.460  | 2.251              | 787  | 739            | 891                      | 411    | 400  |
|  |                    |        |        | 2.260              |  |                |                          |        |      |
| $\text{UO}_2\text{F}(\text{O}_2)_2^{3-}$   | 1.876              | 2.270- | 1.477  | 2.328              | 722  | 692            | 878/                     | 398    | 394  |
|  |                    | 2.284  |        |                    |  |                | 843                      |        |      |
| $\text{UO}_2\text{F}_2(\text{O}_2)_2^{4-}$ |                    |        |        |                    |  |                |                          |        |      |
| Cis  | 1.893              | 2.299- | 1.466  | 2.434              | 682  | 660            | 904/                     | 364/   | 380/ |
|  |                    | 2.317  |        |                    |  |                | 875                      | 340    | 352  |
| Trans                                      | 1.893              | 2.309  | 1.465  | 2.423              | 687  | 664            | 904                      | 352/   | 360/ |
|  |                    |        |        |                    |  |                | /                        | 345    | 343  |
|  |                    |        |        |                    |  |                | 880                      |        |      |

<sup>a</sup> Reference <sup>40</sup>

theoretical literature<sup>29, 64-65</sup>. The U-O<sub>y1</sub> bonds were calculated to be about 0.03 Å longer than the experimental bond length of 1.800 Å. In contrast, the U-F bonds are about 0.04 Å shorter than

the experimental value of 2.260 Å. The vibrational mode associated with the asymmetric stretching of the uranyl group was calculated as 822 cm<sup>-1</sup> in good agreement with the value obtained from experiment. The experimental data on the structural properties of this complex were obtained by EXAFS, measurements in aqueous solution.<sup>64</sup>

Structurally, the U-O<sub>yl</sub> bond lengths increase sequentially by about 0.02 Å down the UO<sub>2</sub>F<sub>4</sub><sup>2-</sup>, UO<sub>2</sub>F<sub>2</sub>(O<sub>2</sub>)<sup>2-</sup>, UO<sub>2</sub>F<sub>3</sub>(O<sub>2</sub>)<sup>3-</sup>, UO<sub>2</sub>F(O<sub>2</sub>)<sub>2</sub><sup>3-</sup> and UO<sub>2</sub>F<sub>2</sub>(O<sub>2</sub>)<sub>2</sub><sup>4-</sup> series. The U-F and U-O<sub>peroxo</sub> bonds also become progressively weaker down the series, Table 5.4. It is not entirely surprising that the U-O<sub>yl</sub>, U-F and U-O<sub>peroxo</sub> bonds are longer in UO<sub>2</sub>F<sub>3</sub>(O<sub>2</sub>)<sup>3-</sup> than in UO<sub>2</sub>F<sub>2</sub>(O<sub>2</sub>)<sup>2-</sup>, or in UO<sub>2</sub>F<sub>2</sub>(O<sub>2</sub>)<sub>2</sub><sup>4-</sup> than in UO<sub>2</sub>F(O<sub>2</sub>)<sub>2</sub><sup>3-</sup>. As previously noted, this trend towards weaker bonds as the number of equatorially coordinated anionic ligands is increased has been reported by various workers in uranyl hydroxides<sup>59, 66</sup>, fluorides<sup>29</sup>, carbonates<sup>20</sup> and nitrates<sup>20</sup>. Clark et al. suggested that the similar trend for the uranyl hydroxides was most likely due to competition between the axial oxo groups and the equatorial hydroxide ligands for the uranium 6d orbitals.<sup>66</sup> In our recent study of the plutonyl hydroxide complexes, [PuO<sub>2</sub>(H<sub>2</sub>O)<sub>4-n</sub>(OH)<sub>n</sub>]<sup>2-n</sup>, we found that the Pu-OH bond is supported by both π-type and σ-type bond orbitals, with increasing Pu-6d contributions to these orbitals as the number of equatorial hydroxide ligands is increased and simultaneous decrease in the Pu-6d contributions to the axial plutonyl π-orbitals.<sup>58</sup>

The binding energies of the fluoro groups to the uranyl peroxo cores, UO<sub>2</sub>(O<sub>2</sub>) or UO<sub>2</sub>(O<sub>2</sub>)<sub>2</sub><sup>2-</sup>, were calculated to be 23.9, 20.7, 13.6 and 5.2 kcal/mol per fluoro ligand in UO<sub>2</sub>F<sub>2</sub>(O<sub>2</sub>)<sup>2-</sup>, UO<sub>2</sub>F<sub>3</sub>(O<sub>2</sub>)<sup>3-</sup>, UO<sub>2</sub>F(O<sub>2</sub>)<sub>2</sub><sup>3-</sup> and UO<sub>2</sub>F<sub>2</sub>(O<sub>2</sub>)<sub>2</sub><sup>4-</sup> respectively. This correlates well with the increasing U-F bond lengths down the series, Table 5.4. The weakening of the U-O<sub>yl</sub> and U-O<sub>peroxo</sub> bonds as the number of equatorial ligands in the ternary fluoro-peroxo complexes are increased results in lower wavenumbers for the O<sub>yl</sub>-U-O<sub>yl</sub> stretching modes as well as the U-

$O_{\text{peroxo}}$  stretching modes, Table 5.4. The symmetric and asymmetric uranyl stretching modes decrease from respectively 786 and 822  $\text{cm}^{-1}$  in  $\text{UO}_2\text{F}_4^{2-}$  to respectively 739 and 787  $\text{cm}^{-1}$  in

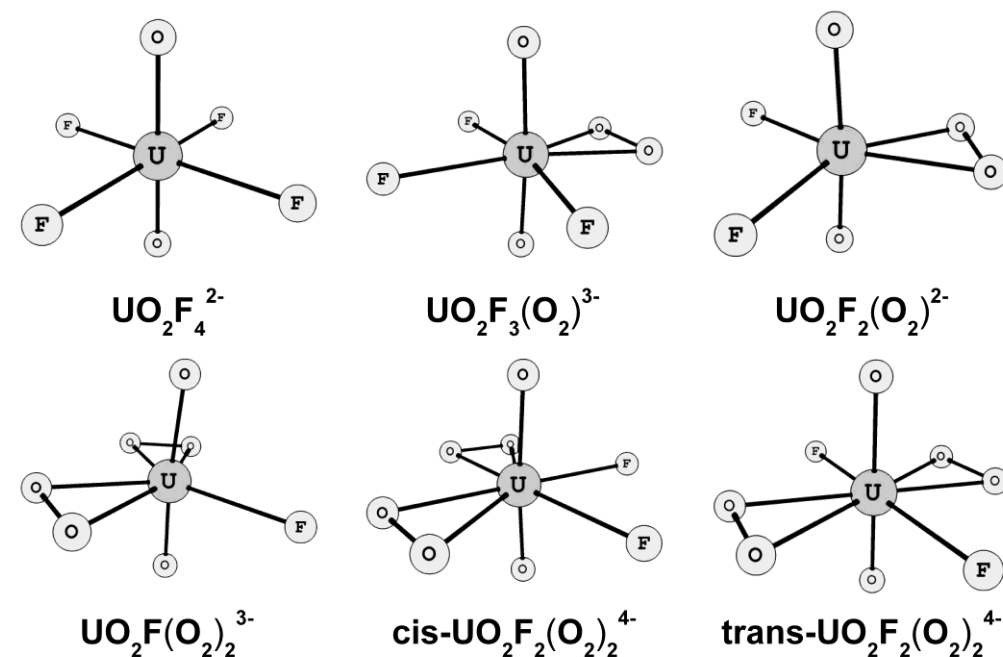
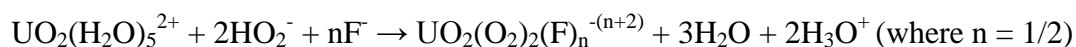


**Figure 5.6:** The structures of  $\text{UO}_2\text{F}_4^{2-}$  and its peroxo derivatives optimized at the B3LYP/B1 level in aqueous solution.

$\text{UO}_2\text{F}_2(\text{O}_2)^{2-}$ . The coordination of an extra fluoride ligand in the equatorial region of  $\text{UO}_2\text{F}_3(\text{O}_2)^{3-}$  further reduces the frequencies of these vibrational modes to 720 and 752  $\text{cm}^{-1}$  respectively, Table 5.4. The symmetric and asymmetric  $\text{U-O}_{\text{peroxo}}$  stretching modes also decrease from 400 and 411  $\text{cm}^{-1}$  in  $\text{UO}_2\text{F}_2(\text{O}_2)^{2-}$  to 390 and 405  $\text{cm}^{-1}$  in  $\text{UO}_2\text{F}_3(\text{O}_2)^{3-}$ . A similar pattern is also present in the fluoro-diperoxo and difluoro-diperoxo complexes, Table 5.4. We note that  $\text{UO}_2\text{F}_2(\text{O}_2)^{2-}$  is topologically similar to the  $\text{UO}_2(\text{O}_2)(\text{CO}_3)_2^{4-}$  ion. The asymmetric  $\text{U-O}_{\text{peroxo}}$  stretching mode of  $\text{UO}_2\text{F}_2(\text{O}_2)^{2-}$  calculated at 400  $\text{cm}^{-1}$  has a significantly lower IR intensity than

the symmetric mode calculated at 411 cm<sup>-1</sup>. The calculated peak at 400 cm<sup>-1</sup> is in a way similar to the peak observed at 413.1 cm<sup>-1</sup> in the Raman spectrum of K<sub>4</sub>[UO<sub>2</sub>(O<sub>2</sub>)(CO<sub>3</sub>)<sub>2</sub>].H<sub>2</sub>O.<sup>12</sup>

The reactions leading to the formation of the ternary fluoro-peroxo complexes from UO<sub>2</sub>(H<sub>2</sub>O)<sub>5</sub><sup>2+</sup> were studied at the B3LYP/B1 level in solution. These reactions take the form:



The calculated energies for these reactions are -44.9, -59.3, 10.9 and 14.1 kcal/mol for UO<sub>2</sub>F<sub>2</sub>(O<sub>2</sub>)<sup>2-</sup>, UO<sub>2</sub>F<sub>3</sub>(O<sub>2</sub>)<sup>3-</sup>, UO<sub>2</sub>F(O<sub>2</sub>)<sub>2</sub><sup>3-</sup> and UO<sub>2</sub>F<sub>2</sub>(O<sub>2</sub>)<sub>2</sub><sup>4-</sup> respectively. Firstly, the formation of the fluoro-diperoxo species in solution is endothermic, similar to the case with the aquo-diperoxo complexes. On the other hand, the reactions leading to the formation of the monoperoxo complexes are significantly exothermic in solution.

**Uranyl hydroxide complexes.** The geometries of the hydroxo and hydroxo-peroxo analogues of the fluoro and fluoro-peroxo complexes discussed above were also optimized at the B3LYP/B1 level in aqueous solution. The calculated structural parameters and vibrational frequencies are presented in Table 5.5 and the structures are shown in Figure 5.7. Aqueous phase EXAFS measurement by Moll et al. provided U-O<sub>y1</sub> and U-OH bonds lengths of 1.83 Å and 2.26 Å respectively for UO<sub>2</sub>(OH)<sub>4</sub><sup>2-</sup>.<sup>67</sup> The bond lengths obtained for these bonds from our theoretical calculations are within 0.02 Å of the EXAFS data, Table 5.5. The frequencies of the symmetric and asymmetric uranyl stretching vibrational modes in this complex were calculated to be 757 and 790 cm<sup>-1</sup> respectively in solution. In the gas phase, the calculated frequencies of these vibrational modes are 756 and 826 cm<sup>-1</sup> respectively. The frequencies of these vibrations were found to be 784 and 857 cm<sup>-1</sup> in aqueous phase measurement of the IR and Raman spectra of

**Table 5.5:** Calculated structural properties and vibrational frequencies of  $\text{UO}_2(\text{OH})_4^{2-}$  and its peroxy derivatives obtained at the B3LYP/B1 level in aqueous solution.

|   | Bonds (Å)          |        |        |                    | Vibrational Frequencies ( $\text{cm}^{-1}$ ) |                  |                  |        |     |
|---|--------------------|--------|--------|--------------------|--|------------------|------------------|--------|-----|
|   | U-O <sub>yl</sub>  | U-O    | O-O    | U-OH               | Stretching Modes                             |                  |                  |        |     |
|   |                    | peroxy | peroxy |                    | Uranyl                                       | O <sub>2</sub>   | U-O <sub>2</sub> |        |     |
|   |                    |        |        |                    | Asymm.                                       | Symm.            | Symm.            | Asymm. |     |
| $\text{UO}_2(\text{OH})_4^{2-}$               | 1.845              |        |        | 2.279              | 790  | 757              |                  |        |     |
| Expt.   | 1.830 <sup>a</sup> |        |        | 2.265 <sup>a</sup> | 857 <sup>b</sup>                             | 784 <sup>b</sup> |                  |        |     |
| $\text{UO}_2(\text{OH})_3(\text{O}_2)^{3-}$   | 1.871              | 2.281  | 1.464  | 2.342-             | 734  | 707              | 891              | 390    | 360 |
|   |                    |        |        | 2.396              |  |                  |                  |        |     |
| $\text{UO}_2(\text{OH})_2(\text{O}_2)^{2-}$   | 1.851              | 2.247  | 1.468  | 2.286              | 774  | 731              | 872              | 419    | 401 |
| $\text{UO}_2(\text{OH})(\text{O}_2)_2^{3-}$   | 1.879              | 2.275  | 1.481  | 2.344              | 718  | 689              | 870              | 393    | 378 |
|   |                    | 2.287  |        |                    |  |                  | 836              | 384    | 357 |
| $\text{UO}_2(\text{OH})_2(\text{O}_2)_2^{4-}$ |                    |        |        |                    |  |                  |                  |        |     |
| Cis   | 1.897              | 2.314  | 1.471  | 2.472              | 682  | 664              | 894              | 370    | 341 |
|   |                    | 2.330  |        |                    |  |                  | 869              | 349    |     |
| Trans   | 1.898              | 2.318  | 1.469  | 2.479              | 680  | 663              | 891              | 359    | 355 |
|   |                    |        |        |                    |  |                  | 872              | 336    | 330 |

<sup>a</sup> Reference <sup>67</sup>

<sup>b</sup> Reference <sup>68-69</sup>

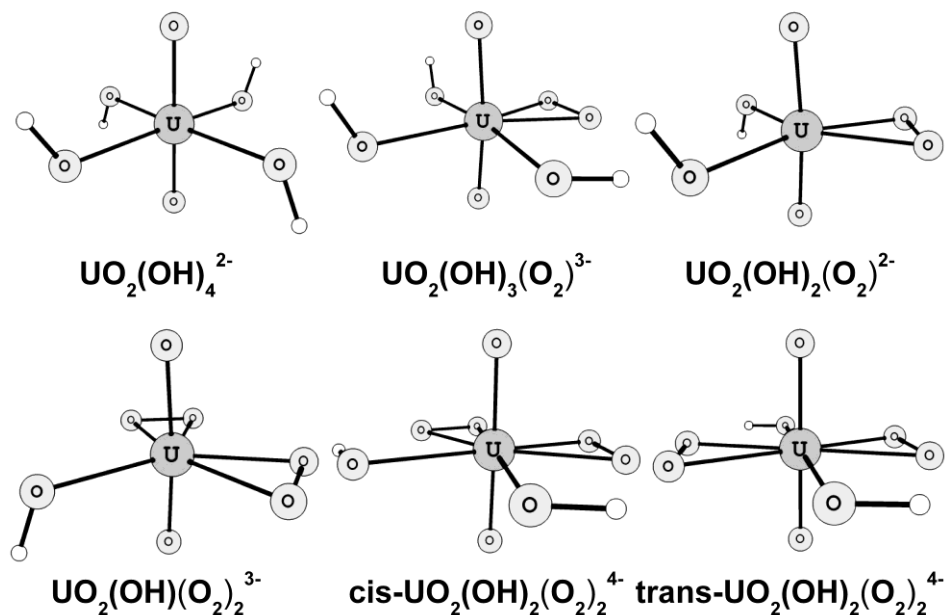
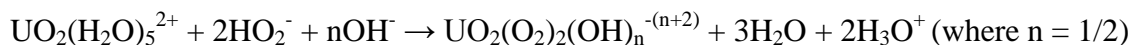


**Figure 5.7:** The structures of  $\text{UO}_2(\text{OH})_4^{2-}$  and its peroxo derivatives optimized at the B3LYP/B1 level in aqueous solution.

uranyl hydroxides by Quiles et al.<sup>68-69</sup> Clark et al. assigned the Raman peak at  $796\text{ cm}^{-1}$  to the symmetric uranyl stretching mode in their characterization of a cobalt salt of the tetrahydroxide,  $[\text{Co}(\text{NH}_3)_6]_2[\text{UO}_2(\text{OH})_4]_3 \cdot \text{H}_2\text{O}$ .<sup>66</sup> Overall, it appears that the calculated vibrational frequencies obtained in the aqueous phase deviate from the experimental values by  $30\text{-}70\text{ cm}^{-1}$ . Compared to the  $\text{UO}_2\text{F}_4^{2-}$  complex, Table 5.4, the  $\text{U-O}_{y1}$  and U-ligand (U-OH/U-F) bonds are about  $0.02$  and  $0.06\text{ \AA}$  longer in the tetrahydroxo complex, Table 5.5. The origin of this bond weakening in the hydroxo complex is most likely the differences in the extents to which the  $2p$  atomic orbitals of the equatorial ligands can compete with the oxo  $2p$  orbitals for the U- $6d$  orbitals. This is related to the  $\pi$ -donating abilities of the  $\text{OH}^-$  and  $\text{F}^-$  ligands. The longer  $\text{U-O}_{y1}$  bonds in  $\text{UO}_2(\text{OH})_4^{2-}$  is correlated with lower frequencies for the uranyl stretching modes in comparison to  $\text{UO}_2\text{F}_4^{2-}$ .

The reactions leading to the formation of  $\text{UO}_2(\text{OH})_2(\text{O}_2)^{2-}$ ,  $\text{UO}_2(\text{OH})_3(\text{O}_2)^{3-}$ ,  $\text{UO}_2(\text{OH})(\text{O}_2)_2^{3-}$  and  $\text{UO}_2(\text{OH})_2(\text{O}_2)_2^{4-}$  are similar to those written for the analogous fluoro-peroxo complexes:



The reaction energies for these are -57.7, -69.3, 6.3 and 8.1 kcal/mol for  $\text{UO}_2(\text{OH})_2(\text{O}_2)^{2-}$ ,  $\text{UO}_2(\text{OH})_3(\text{O}_2)^{3-}$ ,  $\text{UO}_2(\text{OH})(\text{O}_2)_2^{3-}$  and  $\text{UO}_2(\text{OH})_2(\text{O}_2)_2^{4-}$  respectively in aqueous solution. The formation of the ternary hydroxo-peroxo complexes is significantly less exothermic than the formation of the analogous fluoro-peroxo complexes. However like the aquo-diperoxo and fluoro-diperoxo complexes, the formation of the hydroxo-diperoxo species from  $\text{HO}_2^-$  was calculated to be endothermic in solution.

The optimized structures of the hydroxo-peroxo complexes are presented in Figure 5.7. The calculated  $\text{U-O}_{\text{yl}}$  bond lengths in these complexes, Table 5.5, are generally within 0.01 Å of those obtained for their fluoride counterparts, Table 5.4. As a result of this similarity in  $\text{U-O}_{\text{yl}}$  bond lengths, the calculated uranyl stretching vibrational frequencies of the hydroxo-peroxo species are generally within 20  $\text{cm}^{-1}$  of those of the fluoro-peroxides. The  $\text{U-O}_{\text{peroxo}}$  bonds were calculated to be about 2.247 and 2.281 Å long in  $\text{UO}_2(\text{OH})_2(\text{O}_2)^{2-}$  and  $\text{UO}_2(\text{OH})_3(\text{O}_2)^{3-}$  respectively, Table 5.5. These can be compared to 2.235 and 2.258 Å for the difluoro and trifluoro monoperoxides, Table 5.4. The calculated  $\text{U-O}_{\text{peroxo}}$  stretching modes are found in the range 330-419  $\text{cm}^{-1}$ , with the diperoxo species possessing two symmetric and two asymmetric  $\text{U-O}_{\text{peroxo}}$  stretching modes. This is similar to the case in the analogous fluoride complexes, Table 5.4, as well as in  $\text{UO}_2(\text{O}_2)_2$ , Table 5.2. Like the  $\text{U-O}_{\text{yl}}$  and  $\text{U-O}_{\text{peroxo}}$  bonds, the similarity of the

O-O<sub>peroxo</sub> bonds between the fluoro-peroxo and hydroxo-peroxo species results in similar calculated frequencies for the O<sub>2</sub> stretching vibrational modes.

The dihydroxo-diperoxo complex, UO<sub>2</sub>(OH)<sub>2</sub>(O<sub>2</sub>)<sub>2</sub><sup>4-</sup>, like its fluoride analogue has two conformers, a cis structure (C<sub>2v</sub> or butterfly arrangement of the peroxo ligands) and a trans structure (D<sub>2h</sub> arrangement of the peroxo ligands). The trans structure was found to be more stable than the cis conformer by 0.8 kcal/mol in aqueous solution. These structures are therefore iso-energetic, in contradiction to the case in UO<sub>2</sub>(O<sub>2</sub>)<sub>2</sub><sup>2-</sup>, where the cis orientation of the peroxo ligands is favored by 3.1 kcal/mol. To explain the energy difference between the two conformers of UO<sub>2</sub>(O<sub>2</sub>)<sub>2</sub><sup>2-</sup>, we examined the nature of the σ(O<sub>2</sub>)-type orbitals and found some overlap across the two peroxo groups in the C<sub>2v</sub> structure (see above and Figure 5.4). Examination of the low-energy valence orbitals of cis- and trans- UO<sub>2</sub>(OH)<sub>2</sub>(O<sub>2</sub>)<sub>2</sub><sup>4-</sup> reveals MO-30 to be of predominantly σ(O-H) character, Figure 5.8. These orbitals however have significant σ(O<sub>2</sub>)-type contributions. From an analysis of the orbital compositions, the σ(O<sub>2</sub>)-type contributions to MO-30 are larger for the trans conformer of UO<sub>2</sub>(OH)<sub>2</sub>(O<sub>2</sub>)<sub>2</sub><sup>4-</sup>. This compensates for the lacking overlap between the two peroxo units, Figure 5.4, and is responsible for the iso-energetic nature of the two conformers. Similar arguments are applicable to the fluoride analogues. As for UO<sub>2</sub>F<sub>2</sub>(O<sub>2</sub>)<sub>2</sub><sup>4-</sup>, attempts to optimize the structure of UO<sub>2</sub>(OH)<sub>2</sub>(O<sub>2</sub>)<sub>2</sub><sup>4-</sup> in the gas phase failed as the molecule fragmented into its component anionic pieces. Zehnder et al. have recently characterized Na<sub>6</sub>[UO<sub>2</sub>(O<sub>2</sub>)<sub>2</sub>(OH)<sub>2</sub>](OH)<sub>2</sub>·14H<sub>2</sub>O using single crystal X-ray diffraction techniques.<sup>70</sup> They found that the UO<sub>2</sub>(OH)<sub>2</sub>(O<sub>2</sub>)<sub>2</sub><sup>4-</sup> anion in Na<sub>6</sub>[UO<sub>2</sub>(O<sub>2</sub>)<sub>2</sub>(OH)<sub>2</sub>](OH)<sub>2</sub>·14H<sub>2</sub>O has two trans peroxo groups and two trans hydroxo ligands. Compared to Na<sub>6</sub>[UO<sub>2</sub>(O<sub>2</sub>)<sub>2</sub>(OH)<sub>2</sub>](OH)<sub>2</sub>·14H<sub>2</sub>O, (U-O<sub>yl</sub>, 1.862 Å; U-O<sub>peroxo</sub>, 2.289/2.308 Å; U-O<sub>OH</sub> 2.388 Å and O-O<sub>peroxo</sub>, 1.480 Å) the structural parameters of trans-UO<sub>2</sub>(OH)<sub>2</sub>(O<sub>2</sub>)<sub>2</sub><sup>4-</sup> that we optimized in

solution appears to be sufficiently close (within 0.03 Å), Table 5.5. The only exceptions are the U-OH bonds which are about 0.09 Å longer than those found in the sodium salt. To confirm the stabilization of the  $\text{UO}_2\text{F}_2(\text{O}_2)_2^{4-}$  and  $\text{UO}_2(\text{OH})_2(\text{O}_2)_2^{4-}$  species in solution, we checked that the errors in the total polarization charges obtained for the PCM calculations, a reflection of the portion of the density lying outside the cavity, were in all cases less than 0.05. We also examined the volume of the cavity and the spatial extent of the virtual molecular orbitals in the complexes.

**Uranyl carbonates and nitrates.** The formation of  $\text{UO}_2(\text{O}_2)(\text{CO}_3)_2^{4-}$  and  $\text{UO}_2(\text{O}_2)_2(\text{CO}_3)^{4-}$ , from  $\text{UO}_2(\text{H}_2\text{O})_5^{2+}$  by addition of  $\text{HO}_2^-$  and the carbonate ion follow the reaction

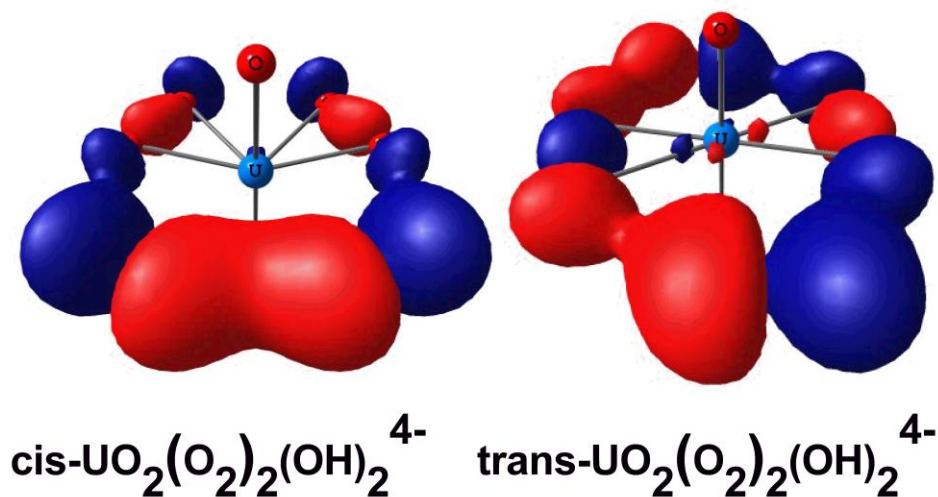


**Figure 5.8:** MO-30 of cis- and trans-  $\text{UO}_2(\text{O}_2)_2(\text{OH})_2^{4-}$ . These orbitals are mostly of  $\sigma(\text{O-H})$  character with substantial contributions from the O-O bonds of the peroxide.

The reaction energies were calculated as -59.8 and 6.3 kcal/mol for  $\text{UO}_2(\text{O}_2)(\text{CO}_3)_2^{4-}$  and  $\text{UO}_2(\text{O}_2)_2(\text{CO}_3)^{4-}$  respectively at the B3LYP/B1 level in aqueous solvent. For the analogous nitrate species,  $\text{UO}_2(\text{O}_2)(\text{NO}_3)_2^{2-}$  and  $\text{UO}_2(\text{O}_2)_2(\text{NO}_3)^{3-}$ , the reaction energies are -16.7 and 20.4 kcal/mol respectively. These reaction energies suggest that the diperoxo species should not be observed in solution. In a contemporaneous paper, Grenthe et al. have reported the speciation of the uranyl-peroxide-carbonate system using a combination of potentiometric and NMR measurements.<sup>71</sup>  $\text{UO}_2(\text{O}_2)(\text{CO}_3)_2^{4-}$  and  $\text{UO}_2(\text{O}_2)(\text{CO}_3)^{2-}$  were the only species with one uranyl group identified in their experiments. Most of the other species observed in their data contained two uranyl groups. The absence of  $\text{UO}_2(\text{O}_2)_2(\text{CO}_3)^{4-}$ , in the experimental speciation data of Grenthe et al., even at high  $\text{H}_2\text{O}_2$  concentrations, is in good agreement with the calculated reaction energies obtained in this work. The reaction energies for the formation of the nitrate-peroxo complexes are higher than those of their carbonate counterparts, in line with the fact that  $\text{NO}_3^-$  is a much weaker ligand for uranyl than  $\text{CO}_3^{2-}$ . The carbonate and carbonate-peroxo complexes are shown in Figure 5.9.

Structurally, the  $\text{U-O}_{y1}$  bonds are shorter in the nitrate complexes than in the counterpart carbonate complexes, Tables 6 and 7. Comparison of the nitrate-peroxo and carbonate-peroxo complexes to the fluoro-peroxo, Table 5.4, the hydroxo-peroxo, Table 5.5, and bare peroxo, Table 5.2, complexes indicates that the  $\text{U-O}_{y1}$  bonds become increasingly weaker as the interactions between the uranyl and equatorial ligands become stronger. The calculated  $\text{U-O}_{y1}$  bond lengths in  $\text{UO}_2(\text{CO}_3)_3^{4-}$  and  $\text{UO}_2(\text{NO}_3)_3^-$  obtained in either the gaseous phase or in solution are about 0.01-0.02 Å longer than the experimental values. It should be noted that the experimental values were obtained from solid state X-ray or neutron diffraction studies of alkali metal salts of  $\text{UO}_2(\text{CO}_3)_3^{4-}$  and  $\text{UO}_2(\text{NO}_3)_3^-$ .<sup>72-73</sup> Assuming that this discrepancy between the

calculated and experimental U-O<sub>yl</sub> bond lengths observed in the tricarbonate and trinitrate complexes can be transferred to the peroxo complexes brings the calculated U-O<sub>yl</sub> bond lengths

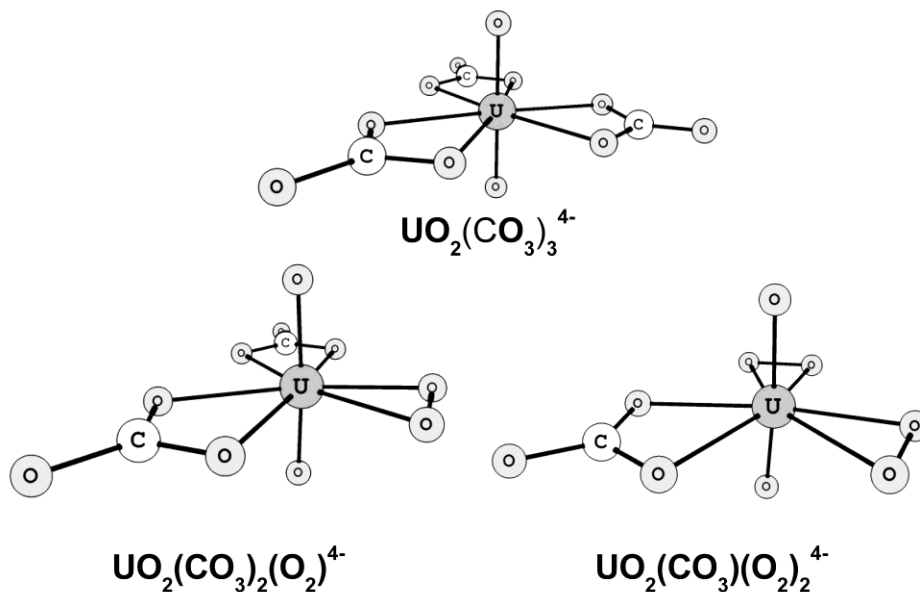


**Figure 5.9:** The structures of  $\text{UO}_2(\text{CO}_3)_3^{4-}$  and its peroxo derivatives optimized at the B3LYP/B1 level in aqueous solution. The analogous nitrate complexes possess similar structural frameworks.

in  $\text{UO}_2(\text{O}_2)(\text{CO}_3)_2^{4-}$  into agreement with the experimental value of 1.825-1.827 Å obtained from the crystallographic data of  $\text{K}_4[\text{UO}_2(\text{O}_2)(\text{CO}_3)_2] \cdot \text{H}_2\text{O}$ .<sup>12</sup>

The U-O<sub>nitrate</sub> bond length in  $\text{UO}_2(\text{NO}_3)_3^-$  was calculated as 2.503 and 2.500 Å in the gas and aqueous phases respectively, Table 5.7. In contrast, the solvent effect on the U-O<sub>carbonate</sub> bond length is significantly higher, Table 5.6. Similar to the U-O<sub>yl</sub> bonds, the U-O<sub>nitrate</sub> and U-O<sub>carbonate</sub> bonds become weaker on coordination of a peroxo group. In the calculations carried out in aqueous solution, the U-O<sub>carbonate</sub> bonds increase from 2.462 Å in the tricarbonate complex to

2.548 Å in the diperoxo-monocarbonate complex. The U-O<sub>nitrate</sub> bonds in the diperoxo-mononitrate complex are about 2.714 Å long. The U-O<sub>carbonate</sub> bonds distal to the peroxo group in UO<sub>2</sub>(O<sub>2</sub>)(CO<sub>3</sub>)<sub>2</sub><sup>4-</sup> are slightly shorter (by 0.005 and 0.002 Å in the gaseous and aqueous phases respectively) than those proximal to the peroxo group, Table 5.6. Similarly the distal U-O<sub>nitrate</sub> bonds in UO<sub>2</sub>(O<sub>2</sub>)(NO<sub>3</sub>)<sub>2</sub><sup>2-</sup> are shorter than their proximal counterparts by 0.047 and 0.030 Å in the gas and aqueous phases respectively, Table 5.7. The trend in the U-O<sub>peroxo</sub> bond lengths in the ternary peroxo-nitrate and peroxo-carbonate complexes is similar to those observed for the U-O<sub>yl</sub> and U-O<sub>carbonate/nitrate</sub> bonds.

In the calculations with the PCM solvation model, the bond between the oxygen atoms of the peroxide ligands was calculated to be about 1.442 Å long in UO<sub>2</sub>(O<sub>2</sub>)<sub>2</sub><sup>2-</sup> and 1.471 Å long in UO<sub>2</sub>(O<sub>2</sub>)<sub>2</sub><sup>2-</sup>, Table 5.2. This bond is slightly longer (about 1.460 Å) in the monoperoxo-fluoro complexes, Table 5.4, as well as in the monoperoxo-carbonate complex (1.459 Å) and in the monoperoxo-nitrate complex (1.451 Å). The calculated O-O bond length in UO<sub>2</sub>(O<sub>2</sub>)(CO<sub>3</sub>)<sub>2</sub><sup>4-</sup> is in good agreement with the experimental value of 1.469 Å obtained Goff et al.<sup>12</sup> in their work on K<sub>4</sub>[UO<sub>2</sub>(O<sub>2</sub>)(CO<sub>3</sub>)<sub>2</sub>].1H<sub>2</sub>O.

The calculated vibrational frequencies of the peroxo-carbonate and peroxo-nitrate complexes are also presented in Table 5.6 and Table 5.7 respectively. The modes associated with asymmetric and symmetric stretching of the uranyl group in UO<sub>2</sub>(CO<sub>3</sub>)<sub>3</sub><sup>4-</sup> were calculated as 839 cm<sup>-1</sup> and 773 cm<sup>-1</sup> respectively in the gas phase. This calculated symmetric stretching frequency is within the range obtained previously by Schlosser et al.<sup>32</sup> and de Jong et al.<sup>20</sup>. The inclusion of the solvent effects with the PCM model has little effect on the symmetric stretching frequency but reduces the asymmetric stretching mode by about 28 cm<sup>-1</sup> in comparison to the gas phase.

**Table 5.6:** Calculated structural properties and vibrational frequencies ( $\text{cm}^{-1}$ ) of  $\text{UO}_2(\text{CO}_3)_3^{4-}$  and its peroxy derivatives obtained at the B3LYP/B1 level in the gas phase and in aqueous solution.

|   | Bond Lengths ( $\text{\AA}$ ) |                          |                          |                       | Uranyl Stretching |                    |
|---|-------------------------------|--------------------------|--------------------------|-----------------------|-------------------|--------------------|
|   | U-O <sub>yl</sub>             | U-O <sub>carbonate</sub> | U-O <sub>peroxy</sub>    | O-O <sub>peroxy</sub> | Asymm.            | Symm.              |
| $\text{UO}_2(\text{CO}_3)_3^{4-}$             |                               |                          |                          |                       |                   |                    |
| Gas phase                                     | 1.822                         | 2.535                    |                          |                       | 839               | 773                |
| Solution                                      | 1.828                         | 2.462                    |                          |                       | 811               | 775                |
| Experimental                                  | 1.81 <sup>a</sup>             | 2.44 <sup>a</sup>        |                          |                       | 889 <sup>b</sup>  | 813 <sup>b</sup>   |
| $\text{UO}_2(\text{O}_2)(\text{CO}_3)_2^{4-}$ |                               |                          |                          |                       |                   |                    |
| Gas phase                                     | 1.848                         | 2.636/2.641              | 2.272                    | 1.461                 | 796               | 730                |
| Solution                                      | 1.856                         | 2.498/2.500              | 2.255                    | 1.459                 | 761               | 739                |
| Experimental                                  | 1.825-1.827 <sup>b</sup>      | 2.429-2.473 <sup>b</sup> | 2.238-2.255 <sup>b</sup> | 1.469 <sup>b</sup>    |                   | 766.5 <sup>b</sup> |
| $\text{UO}_2(\text{O}_2)_2(\text{CO}_3)^{4-}$ |                               |                          |                          |                       |                   |                    |
| Solution                                      | 1.883                         | 2.548                    | 2.286/2.296              | 1.475                 | 708               | 706                |

<sup>a</sup> Reference <sup>72</sup> <sup>b</sup> Reference <sup>74</sup> <sup>c</sup> Reference <sup>12</sup>

The calculated IR active asymmetric uranyl stretching frequency deviates from the experimental value by about  $71 \text{ cm}^{-1}$  in the aqueous phase while its symmetric counterpart has an error of about  $31 \text{ cm}^{-1}$ .<sup>74</sup> In contrast, the agreement between the B3LYP/B1 model and the experimental vibrational frequencies is improved for  $\text{UO}_2(\text{NO}_3)_3^-$ , Table 5.7. The symmetric stretching mode was calculated to have a frequency of  $870 \text{ cm}^{-1}$  in good agreement with solid state Raman spectroscopic measurements ( $876\text{-}886 \text{ cm}^{-1}$ ) of uranyl nitrate salts.<sup>75</sup> The gas phase calculations

provided a value of  $875\text{ cm}^{-1}$  for this vibrational mode, little change from the calculations with the PCM model and in good agreement with the solid-state crystal measurements. The frequencies of the uranyl asymmetric stretching vibrational mode were found to be  $943.1$  and  $967.2\text{ cm}^{-1}$  in the potassium and ammonium crystalline salts from solid-state IR measurements.<sup>75</sup> The calculated frequencies of this vibrational mode in the gaseous and aqueous phases are within  $14\text{-}38\text{ cm}^{-1}$  of these experimental values, Table 5.7.

For the peroxo derivative of  $\text{UO}_2(\text{CO}_3)_3^{4-}$  and  $\text{UO}_2(\text{NO}_3)_3^-$ , the calculated frequencies of the asymmetric and symmetric uranyl stretching modes decrease by  $30\text{-}55\text{ cm}^{-1}$  for each carbonate substitution in the peroxo-carbonate series, Table 5.6, and about  $70\text{-}100\text{ cm}^{-1}$  for each nitrate substitution in the peroxo-nitrate series, Table 5.7. For the mono-peroxo carbonate complex, the calculated frequencies of the symmetric uranyl stretching mode,  $739\text{ cm}^{-1}$  in solution and  $730\text{ cm}^{-1}$  in the gas phase, are in agreement with the experimental value of  $766.5\text{ cm}^{-1}$  obtained during Raman spectral measurements of  $\text{K}_4[\text{UO}_2(\text{O}_2)(\text{CO}_3)_2]\cdot\text{H}_2\text{O}$ .<sup>12</sup> Another notable vibrational mode in  $\text{UO}_2(\text{O}_2)(\text{CO}_3)_2^{4-}$  is the C-O stretch, calculated at  $1054\text{ cm}^{-1}$  in good agreement with the experimental value of  $1053\text{ cm}^{-1}$  in the potassium hydrate complex.<sup>12</sup> The vibrational mode associated with the C-O<sub>3</sub> bending of both carbonate groups (asymmetric out of plane deformations) is Raman active and was calculated to have frequencies of respectively  $847$  and  $842\text{ cm}^{-1}$  in the gaseous and aqueous phase calculations on  $\text{UO}_2(\text{O}_2)(\text{CO}_3)_2^{4-}$ . The same mode is also Raman active in the calculated spectra of  $\text{UO}_2(\text{CO}_3)_3^{4-}$ ,  $849$  and  $842\text{ cm}^{-1}$  in the gaseous and aqueous phases respectively. Peaks corresponding to this vibrational mode were observed between  $849$  and  $879\text{ cm}^{-1}$  in the combined Raman and infra-red (IR) work of Anderson et al.<sup>76</sup> on  $\text{K}_4[\text{UO}_2(\text{CO}_3)_3]$ . In addition, de Jong et al.<sup>20</sup> obtained a value of  $845\text{ cm}^{-1}$  in their theoretical study of uranyl carbonate using the local density approximation (LDA) with

**Table 5.7:** Calculated structural properties and vibrational frequencies ( $\text{cm}^{-1}$ ) of  $\text{UO}_2(\text{NO}_3)_3^-$  and its peroxy derivatives obtained at the B3LYP/B1 level in the gas phase and in aqueous solution.

|   | Bond Lengths ( $\text{\AA}$ ) |                        |                       |                       | Uranyl Stretching    |                      |
|---|-------------------------------|------------------------|-----------------------|-----------------------|----------------------|----------------------|
|   | U-O <sub>yl</sub>             | U-O <sub>nitrate</sub> | U-O <sub>peroxy</sub> | O-O <sub>peroxy</sub> | Asymm.               | Symm.                |
| $\text{UO}_2(\text{NO}_3)_3^-$                |                               |                        |                       |                       |                      |                      |
| Gas phase                                     | 1.776                         | 2.503                  |                       |                       | 957                  | 875                  |
| Solution                                      | 1.776                         | 2.500                  |                       |                       | 929                  | 870                  |
| Experimental                                  | 1.77 <sup>a</sup>             | 2.48-2.50 <sup>a</sup> |                       |                       | 943-967 <sup>b</sup> | 875-886 <sup>b</sup> |
| $\text{UO}_2(\text{O}_2)(\text{NO}_3)_2^{2-}$ |                               |                        |                       |                       |                      |                      |
| Gas phase                                     | 1.821                         | 2.662/2.709            | 2.187                 | 1.446                 | 858                  | 787                  |
| Solution                                      | 1.822                         | 2.589/2.619            | 2.198                 | 1.451                 | 824                  | 777                  |
| $\text{UO}_2(\text{O}_2)_2(\text{NO}_3)^{3-}$ |                               |                        |                       |                       |                      |                      |
| Solution                                      | 1.869                         | 2.714                  | 2.252/2.264           | 1.473                 | 735                  | 703                  |

<sup>a</sup> Reference <sup>73</sup> <sup>b</sup> Reference <sup>75</sup>

diffuse basis sets. We note that the peak at  $841.7 \text{ cm}^{-1}$  in the Raman spectrum of  $\text{K}_4[\text{UO}_2(\text{O}_2)(\text{CO}_3)_2] \cdot 2.5\text{H}_2\text{O}$  was however labeled as the O-O symmetric stretching mode by Goff et al.<sup>12</sup> The frequency of the O-O symmetric stretching mode in  $\text{UO}_2(\text{O}_2)(\text{CO}_3)_2^{4-}$  was however calculated to be at  $890$  and  $894 \text{ cm}^{-1}$  in the gas phase and in solution respectively. This particular mode was calculated to be at  $944 \text{ cm}^{-1}$  in PCM calculations on  $\text{H}_2\text{O}_2$  in contrast to the experimental value of  $875 \text{ cm}^{-1}$ . It is most likely the case that the assignment of the strong peak at  $841.7 \text{ cm}^{-1}$  to the O-O symmetric stretching mode by Goff et al. is correct given the seemingly large error in the calculated frequencies for this mode. The symmetric and asymmetric stretching

of the U-O<sub>peroxo</sub> bonds in UO<sub>2</sub>(O<sub>2</sub>)(CO<sub>3</sub>)<sub>2</sub><sup>4-</sup> were calculated respectively as 383 and 375 cm<sup>-1</sup> in the gas phase and 394 and 387 cm<sup>-1</sup> in solution. The asymmetric stretching modes, which were calculated to possess low IR intensities, might account for the peak at 431.0 cm<sup>-1</sup> in the Raman spectrum of K<sub>4</sub>[UO<sub>2</sub>(O<sub>2</sub>)(CO<sub>3</sub>)<sub>2</sub>].2.5H<sub>2</sub>O.

**Bond Orders in the uranyl and uranyl peroxo complexes.** The population-based Mayer bond orders obtained for all the bonds in the uranyl and uranyl peroxo complexes studied in this work are collected in Table 5.8. The calculated bond orders for the U-O<sub>yl</sub> bonds in UO<sub>2</sub><sup>2+</sup>, UO<sub>2</sub>(H<sub>2</sub>O)<sub>5</sub><sup>2+</sup>, UO<sub>2</sub>(NO<sub>3</sub>)<sub>3</sub><sup>-</sup>, UO<sub>2</sub>(OH)<sub>4</sub><sup>2-</sup>, UO<sub>2</sub>(CO<sub>3</sub>)<sub>3</sub><sup>4-</sup> and UO<sub>2</sub>F<sub>4</sub><sup>2-</sup> decrease down the series. The orders for these bonds range from 2.53 in the bare dication to 2.29 in the tetrafluoro complex. These values indicate that the U-O<sub>yl</sub> bonds possess significant triple bond character with the presence of equatorial ligands diminishing the triple bond nature. From the degree of perturbation of the U-O<sub>yl</sub> bonds, as seen in the bond order reduction, it appears that the aquo and nitrate ligands have the weakest covalent interaction with the uranyl groups. This is supported by the U-O<sub>water</sub> and U-O<sub>nitrate</sub> bond orders of 0.48 and 0.46-0.49 respectively that are far smaller than the U-O<sub>carbonate</sub>, U-F<sub>fluoride</sub> and U-O<sub>hydroxide</sub> bond orders respectively of 0.68, 1.02 and 1.07, Table 5.8. It is most likely that a competition between the U-O<sub>yl</sub> and U-X<sub>ligand</sub> bonds for uranium 6d atomic contributions result in the weakening of the U-O<sub>yl</sub> bonds with increasing  $\pi$ -donating abilities of the equatorial ligand. This correlates with the fact that the U-OH bonds have the highest bond order of the equatorial U-X<sub>ligand</sub> bonds. As previously mentioned, it has recently been shown that there is an increase in the actinide 6d contributions to the An-OH bonds and a simultaneous decrease in the An 6d contributions to the An-O<sub>yl</sub> bonds on progressing down the AnO<sub>2</sub><sup>2+</sup> to AnO<sub>2</sub>(OH)<sub>4</sub><sup>2-</sup> (An = U, Np and Pu) series.<sup>58</sup>

**Table 5.8.** The calculated Mayer bond orders in various uranyl complexes and their peroxo derivatives obtained at the B3LYP/B2 level using structures optimized at the B3LYP/B1 level.

|  | U-O <sub>yl</sub> | U-O <sub>peroxo</sub> | O-O <sub>peroxo</sub> | U-X <sub>ligand</sub> |  | U-O <sub>yl</sub> | U-O <sub>peroxo</sub> | O-O <sub>peroxo</sub> | U-X <sub>ligand</sub> |
|--|-------------------|-----------------------|-----------------------|-----------------------|--|-------------------|-----------------------|-----------------------|-----------------------|
| UO <sub>2</sub> <sup>2+</sup>  | 2.53              |                       |                       |                       | Halides  |                   |                       |                       |                       |
| UO <sub>2</sub> (O <sub>2</sub> )  | 2.42              | 1.23                  | 1.01                  |                       | UO <sub>2</sub> F <sub>4</sub> <sup>2-</sup>                                   | 2.29              |                       |                       | 1.02                  |
| C <sub>2v</sub> -UO <sub>2</sub> (O <sub>2</sub> ) <sub>2</sub> <sup>2-</sup>                | 2.31              | 1.05/1.08             | 0.98                  |                       | UO <sub>2</sub> (O <sub>2</sub> )F <sub>2</sub> <sup>2-</sup>                  | 2.31              | 1.07                  | 0.98                  | 1.00                  |
| UO <sub>2</sub> (O <sub>2</sub> ) <sub>3</sub> <sup>4+</sup>                                 | 2.25              | 1.03                  | 0.98                  |                       | UO <sub>2</sub> (O <sub>2</sub> )F <sub>3</sub> <sup>3-</sup>                  | 2.26              | 1.05                  | 0.99                  | 0.96                  |
| Aquo   |                   |                       |                       |                       | UO <sub>2</sub> (O <sub>2</sub> ) <sub>2</sub> F <sup>3-</sup>                 | 2.27              | 1.02                  | 0.97                  | 0.95                  |
| UO <sub>2</sub> (H <sub>2</sub> O) <sub>5</sub> <sup>2+</sup>                                | 2.43              |                       |                       | 0.46-0.49             | UO <sub>2</sub> (O <sub>2</sub> ) <sub>2</sub> F <sub>2</sub> <sup>4-</sup>    | 2.26              | 1.04                  | 0.99                  | 0.94                  |
| UO <sub>2</sub> (O <sub>2</sub> )(H <sub>2</sub> O) <sub>2</sub>                             | 2.40              | 1.20                  |                       | 0.34                  | Hydroxides   |                   |                       |                       |                       |
| UO <sub>2</sub> (O <sub>2</sub> )(H <sub>2</sub> O) <sub>3</sub>                             | 2.39              | 1.18                  | 1.00                  | 0.34                  | UO <sub>2</sub> (OH) <sub>4</sub> <sup>2-</sup>                                | 2.32              |                       |                       | 1.07                  |
| UO <sub>2</sub> (O <sub>2</sub> )(H <sub>2</sub> O) <sub>4</sub>                             | 2.39              | 1.17                  | 1.01                  | 0.30                  | UO <sub>2</sub> (O <sub>2</sub> )(OH) <sub>2</sub> <sup>2-</sup>               | 2.32              | 1.08                  | 0.98                  | 1.06                  |
| UO <sub>2</sub> (O <sub>2</sub> ) <sub>2</sub> (H <sub>2</sub> O) <sup>2-</sup>              | 2.31              | 1.06                  | 0.98                  | 0.24                  | UO <sub>2</sub> (O <sub>2</sub> )(OH) <sub>3</sub> <sup>3-</sup>               | 2.29              | 1.06                  | 0.98                  | 1.00-                 |
|  |                   |                       |                       |                       |  |                   |                       |                       | 1.03                  |
| UO <sub>2</sub> (O <sub>2</sub> ) <sub>2</sub> (H <sub>2</sub> O) <sub>2</sub> <sup>2-</sup> |                   |                       |                       |                       | UO <sub>2</sub> (O <sub>2</sub> ) <sub>2</sub> (OH) <sub>3</sub> <sup>3-</sup> | 2.28              | 1.02                  | 0.97                  | 1.02                  |
| Trans  | 2.30              | 1.00/1.04             | 0.98                  | 0.25                  | UO <sub>2</sub> (O <sub>2</sub> ) <sub>2</sub> (OH) <sub>2</sub> <sup>4-</sup> | 2.26              | 1.04                  | 0.99                  | 0.99                  |

|   |      |           |      |      |   |      |       |      |  |      |
|---|------|-----------|------|------|---|------|-------|------|--|------|
| Cis   | 2.32 | 1.00/1.04 | 0.97 | 0.24 | Nitrates                                      |      |       |      |  |      |
| Carbonates                                    |      |           |      |      | $\text{UO}_2(\text{NO}_3)_3^-$                | 2.38 |       |      |  | 0.48 |
| $\text{UO}_2(\text{CO}_3)_3^{4-}$             | 2.31 |           |      | 0.68 | $\text{UO}_2(\text{O}_2)(\text{NO}_3)_2^{2-}$ | 2.35 | 1.13  | 1.00 |  | 0.36 |
| $\text{UO}_2(\text{O}_2)(\text{CO}_3)_2^{4-}$ | 2.29 | 1.05      | 0.99 | 0.64 | $\text{UO}_2(\text{O}_2)_2(\text{NO}_3)^{3-}$ | 2.28 | 1.02- | 0.98 |  | 0.28 |
|   |      |           |      |      |   |      | 1.04  |      |  |      |
| $\text{UO}_2(\text{O}_2)_2(\text{CO}_3)^{4-}$ | 2.26 | 1.00-1.02 | 0.98 | 0.61 |   |      |       |      |  |      |

Going forward, we are interested in using more comprehensive charge and orbital decomposition schemes to examine the interplay between covalent and electrostatic interactions in determining the strength of the equatorial bonds in actinide complexes.

For the uranyl peroxy complexes,  $\text{UO}_2(\text{O}_2)$ ,  $\text{UO}_2(\text{O}_2)_2^{2-}$  and  $\text{UO}_2(\text{O}_2)_3^{4-}$ , the calculated bond orders for the  $\text{U}-\text{O}_{\text{yl}}$  bonds decrease from 2.42 to 2.25, reminiscent of the case for the fluoro, hydroxo, aquo, nitrate and carbonate complexes. The  $\text{U}-\text{O}_{\text{peroxy}}$  bond orders also decrease from 1.23 in the monoperoxy species to 1.03 in the triperoxy complex. The inclusion of other ligands in the equatorial region of  $\text{UO}_2(\text{O}_2)$  leads to a slight decrease in the  $\text{U}-\text{O}_{\text{yl}}$  bond orders. A similar case is observed for the  $\text{U}-\text{O}_{\text{peroxy}}$  bonds, with the calculated bond order depending on the binding strength of the other equatorial ligands. For the strongly binding carbonate, hydroxo and fluoro equatorial ligands, the  $\text{U}-\text{O}_{\text{peroxy}}$  bond orders are about 1.05-1.08 while for the weakly binding aquo and nitrate ligands, the  $\text{U}-\text{O}_{\text{peroxy}}$  bond orders are about 1.13-1.20. The bond orders for the O-O bonds of the peroxide ligand remain within the range 0.97-1.01 regardless of the number of peroxy groups in the complex as well as the nature of the other equatorial ligands.

## Conclusions

The structural and electronic properties of various uranyl peroxy complexes have been examined using scalar relativistic DFT calculations. The aqueous-phase structures of the peroxy complexes were modeled with the PCM solvation model. The reaction energies for the formation of the uranyl peroxy complexes from their parent uranyl complexes, the relative stabilities of the various structures of the peroxy complexes as well as the role of the equatorial peroxy group on the trans-cis transformation of the uranyl moiety were all examined in the gaseous and aqueous phases.

The affinity of the peroxo ligand for the uranyl group far exceeds that of the  $F^-$ ,  $OH^-$ ,  $CO_3^{2-}$ ,  $NO_3^-$  and  $H_2O$  ligands. The reactions leading to the formation of the various uranyl-monoperoxo complexes from  $UO_2(H_2O)_5^{2+}$  and  $HO_2^-$  were calculated to be significantly exothermic in both the gaseous and aqueous phases. As a result, the U(VI) and peroxo concentrations, both kinetic factors, are the major factors in experimentally identifying the mononuclear uranyl-peroxo species studied in this work. It should be noted however that the formation of the diperoxo  $UO_2(O_2)_2X_2^{4-}/UO_2(O_2)_2X^{4/3-}$  species from  $UO_2(H_2O)_5^{2+}$  and  $HO_2^-$  were all calculated to be endothermic in aqueous medium. This implies that the monouranyl-diperoxo complexes of the aquo, fluoro, hydroxo, carbonate and nitrate ligands would be absent in solution in very good agreement with recent experimental data. On the other hand, attempts to optimize the geometries of these complexes in the gas phase failed as they decomposed to the component anions. This indicates the crucial roles of counter-ions in the crystallization of the  $UO_2(O_2)_2X_2^{4-}/UO_2(O_2)_2X^{4/3-}$  species.

Examination of the electronic structures of the uranyl-peroxo complexes reveals that the  $U-O_{\text{peroxo}}$  bond is formed by overlap between U(VI) 5f orbitals and in-plane  $\pi$  antibonding orbitals of the peroxo ligand. The  $\sigma$  and  $\pi$  bonding orbitals between the oxygen atoms of the peroxo ligands are more stable than the orbitals of the uranyl moiety. There is however significant  $\pi$ - $\pi$  mixing between the orbitals of the peroxo ligand and the  $\pi(d)$  orbitals of the uranyl. The importance of  $\pi(O_2)$ - $\pi(f)$  mixing is higher for the diperoxo and triperoxo complexes as the inclusion of the second and third peroxo ligands further stabilizes the uranyl  $\pi(f)$  orbitals. For  $UO_2(O_2)_2^{2-}$ , a cis arrangement of the peroxo groups was calculated to be more stable than the  $D_{2h}$  structure which features a trans arrangement of the equatorial peroxo groups. The origin of this difference was found to be the presence of an overlap between the distal oxygen atoms of the

two peroxo groups in the  $\sigma(\text{O}_2)$  orbitals. In contrast for the  $\text{UO}_2(\text{O}_2)_2\text{X}_2^{4-}$  (for  $\text{X} = \text{F}^-$  and  $\text{OH}^-$ ) species, the structures with cis and trans peroxo groups are iso-energetic as the  $\sigma(\text{O}_2)$  orbitals now contain overlap with the  $\sigma(\text{O-H})$  and  $\text{F}_{2p}$  orbitals.

The trends in the structures of the uranyl-peroxo complexes with the  $\text{F}^-$ ,  $\text{OH}^-$ ,  $\text{CO}_3^{2-}$ ,  $\text{NO}_3^-$  and  $\text{H}_2\text{O}$  ligands are similar to those previously observed in other uranyl complexes. Inclusion of the peroxo ligand weakens the  $\text{U-O}_{\text{yl}}$  bonds resulting in sequentially decreasing uranyl vibrational frequencies. The O-O bond of the peroxo complexes is mostly centered at 1.455-1.480 Å and as such the O-O stretching vibrational mode is found between 840 and 940  $\text{cm}^{-1}$ . The calculated bond orders of the O-O bonds were found to be between 0.96-1.02, in good correlation with the little influence on the O-O bond lengths by the type and nature of equatorial ligands. The  $\text{U-O}_{\text{peroxo}}$  bond-lengths are somewhat more sensitive to the type and number of coordinated anionic ligands. The  $\text{U-O}_{\text{peroxo}}$  stretching modes were calculated to be between 330-419  $\text{cm}^{-1}$ , with the symmetric mode being IR active and the asymmetric mode, Raman active.

## References

1. Sigmon, G. E.; Ling, J.; Unruh, D. K.; Moore-Shay, L.; Ward, M.; Weaver, B.; Burns, P. C., *J. Am. Chem. Soc.* **2009**, *131*, 16648.
2. Clarens, F.; de Pablo, J.; Casas, I.; Gimenez, J.; Rovira, M.; Merino, J.; Cera, E.; Bruno, J.; Quinones, J.; Martinez-Esparza, A., *J. Nucl. Mater.* **2005**, *345*, 225.
3. Gimenez, J.; Clarens, F.; Casas, I.; Rovira, M.; de Pablo, J.; Bruno, J., *J. Nucl. Mater.* **2005**, *345*, 232.
4. Kubatko, K. A.; Forbes, T. Z.; Klingensmith, A. L.; Burns, P. C., *Inorg. Chem.* **2007**, *46*, 3657.

5. Ling, J.; Wallace, C. M.; Szymanowski, J. E. S.; Burns, P. C., *Angew. Chem. Int. Edit.* **2010**, *49*, 7271.
6. Sigmon, G. E.; Weaver, B.; Kubatko, K. A.; Burns, P. C., *Inorg. Chem.* **2009**, *48*, 10907.
7. Unruh, D. K.; Burtner, A.; Pressprich, L.; Sigmon, G. E.; Burns, P. C., *Dalton T.* **2010**, *39*, 5807.
8. Corbel, C.; Sattonnay, G.; Guilbert, S.; Garrido, F.; Barthe, M. F.; Jegou, C., *J. Nucl. Mater.* **2006**, *348*, 1.
9. Armstrong, C. R.; Nyman, M.; Shvareva, T.; Sigmon, G. E.; Burns, P. C.; Navrotsky, A., *P. Natl. Acad. Sci. USA* **2012**, *109*, 1874.
10. Miro, P.; Pierrefixe, S.; Gicquel, M.; Gil, A.; Bo, C., *J. Am. Chem. Soc.* **2010**, *132*, 17787.
11. Vlaisavljevich, B.; Gagliardi, L.; Burns, P. C., *J. Am. Chem. Soc.* **2010**, *132*, 14503.
12. Goff, G. S.; Brodnax, L. F.; Cisneros, M. R.; Peper, S. M.; Field, S. E.; Scoft, B. L.; Runde, W. H., *Inorg. Chem.* **2008**, *47*, 1984.
13. Meca, S.; Martinez-Torrents, A.; Marti, V.; Gimenez, J.; Casas, I.; de Pablo, J., *Dalton T.* **2011**, *40*, 7976.
14. Zanonato, P. L.; Di Bernardo, P.; Grenthe, I., *Dalton T.* **2012**, *41*, 3380.
15. Nyman, M.; Rodriguez, M. A.; Campana, C. F., *Inorg. Chem.* **2010**, *49*, 7748.
16. Austin, J. P.; Sundararajan, M.; Vincent, M. A.; Hillier, I. H., *Dalton T.* **2009**, 5902.
17. Batista, E. R.; Martin, R. L.; Hay, P. J., *J. Chem. Phys.* **2004**, *121*, 11104.
18. Bühl, M.; Sieffert, N.; Chaumont, A.; Wipff, G., *Inorg. Chem.* **2011**, *50*, 299.
19. Bühl, M.; Sieffert, N.; Chaumont, A.; Wipff, G., *Inorg. Chem.* **2012**, *51*, 1943.

20. de Jong, W. A.; Apra, E.; Windus, T. L.; Nichols, J. A.; Harrison, R. J.; Gutowski, K. E.; Dixon, D. A., *J. Phys. Chem. A* **2005**, *109*, 11568.
21. de Jong, W. A.; Harrison, R. J.; Nichols, J. A.; Dixon, D. A., *Theor. Chem. Acc.* **2001**, *107*, 22.
22. Garcia-Hernandez, M.; Lauterbach, C.; Krüger, S.; Matveev, A.; Rösch, N., *J. Comput. Chem.* **2002**, *23*, 834.
23. Han, Y. K., *J. Comput. Chem.* **2001**, *22*, 2010.
24. Han, Y. K.; Hirao, K., *J. Chem. Phys.* **2000**, *113*, 7345.
25. Hay, P. J.; Martin, R. L., *J. Chem. Phys.* **1998**, *109*, 3875.
26. Kovacs, A.; Konings, R. J. M., *J. Mol. Struct-Theochem.* **2004**, *684*, 35.
27. Odoh, S. O.; Schreckenbach, G., *J. Phys. Chem. A* **2010**, *114*, 1957.
28. Odoh, S. O.; Schreckenbach, G., *J. Phys. Chem. A* **2011**, *115*, 14110.
29. Odoh, S. O.; Walker, S. M.; Meier, M.; Stetefeld, J.; Schreckenbach, G., *Inorg. Chem.* **2011**, *50*, 3141.
30. Pereira, C. C. L.; Marsden, C. J.; Marcalo, J.; Gibson, J. K., *Phys. Chem. Chem. Phys.* **2011**, *13*, 12940.
31. Privalov, T.; Schimmelpfennig, B.; Wahlgren, U.; Grenthe, I., *J. Phys. Chem. A* **2002**, *106*, 11277.
32. Schlosser, F.; Moskaleva, L. V.; Kremleva, A.; Krüger, S.; Rösch, N., *Dalton T.* **2010**, *39*, 5705.
33. Schreckenbach, G.; Hay, P. J.; Martin, R. L., *J. Comput. Chem.* **1999**, *20*, 70.
34. Schreckenbach, G.; Shamov, G. A., *Acc. Chem. Res.* **2010**, *43*, 19.
35. Shamov, G. A.; Schreckenbach, G., *J. Phys. Chem. A* **2005**, *109*, 10961.

36. Shamov, G. A.; Schreckenbach, G., *J. Phys. Chem. A* **2006**, *110*, 12072.
37. Shamov, G. A.; Schreckenbach, G.; Vo, T. N., *Chem-Eur. J.* **2007**, *13*, 4932.
38. Straka, M.; Kaupp, M., *Chem. Phys.* **2005**, *311*, 45.
39. Tsushima, S.; Uchida, Y.; Reich, T., *Chem. Phys. Lett.* **2002**, *357*, 73.
40. Vallet, V.; Macak, P.; Wahlgren, U.; Grenthe, I., *Theor. Chem. Acc.* **2006**, *115*, 145.
41. Vukovic, S.; Watson, L. A.; Kang, S. O.; Custelcean, R.; Hay, B. P., *Inorg. Chem.* **2012**, *51*, 3855.
42. Frisch, M. J.; et al Gaussian 03, Revision C.02. 2004.
43. Miertus, S.; Scrocco, E.; Tomasi, J., *Chem. Phys.* **1981**, *55*, 117.
44. Küchle, W.; Dolg, M.; Stoll, H.; Preuss, H., *Mol. Phys.* **1991**, *74*, 1245.
45. Küchle, W.; Dolg, M.; Stoll, H.; Preuss, H., *J. Chem. Phys.* **1994**, *100*, 7535.
46. Lim, I. S.; Stoll, H.; Schwerdtfeger, P., *J. Chem. Phys.* **2006**, *124*.
47. Becke, A. D., *J. Chem. Phys.* **1993**, *98*, 5648.
48. Lee, C. T.; Yang, W. T.; Parr, R. G., *Phys. Rev. B.* **1988**, *37*, 785.
49. Stephens, P. J.; Devlin, F. J.; Chabalowski, C. F.; Frisch, M. J., *J. Phys. Chem.* **1994**, *98*, 11623.
50. Laikov, D. N.; Ustynyuk, Y. A., *Russ. Chem. B+* **2005**, *54*, 820.
51. Laikov, D. N., *Chem. Phys. Lett.* **2005**, *416*, 116.
52. Denning, R. G., *Struct. Bond.* **1992**, *79*, 215.
53. Denning, R. G., *J. Phys. Chem. A* **2007**, *111*, 4125.
54. Denning, R. G.; Foster, D. N. P.; Snellgrove, T. R.; Woodward, D. R., *Mol. Phys.* **1979**, *37*, 1089.

55. Denning, R. G.; Green, J. C.; Hutchings, T. E.; Dallera, C.; Tagliaferri, A.; Giarda, K.; Brookes, N. B.; Braicovich, L., *J. Chem. Phys.* **2002**, *117*, 8008.
56. Denning, R. G.; Snellgrove, T. R.; Woodwark, D. R., *Mol. Phys.* **1976**, *32*, 419.
57. Denning, R. G.; Snellgrove, T. R.; Woodwark, D. R., *Mol. Phys.* **1979**, *37*, 1109.
58. Odoh, S. O.; Reyes, J. A.; Schreckenbach, G., *Inorg. Chem.* **2012**, *submitted*.
59. Ingram, K. I. M.; Haller, L. J. L.; Kaltsoyannis, N., *Dalton T.* **2006**, 2403.
60. Allen, P. G.; Bucher, J. J.; Shuh, D. K.; Edelstein, N. M.; Reich, T., *Inorg. Chem.* **1997**, *36*, 4676.
61. Jones, L. H.; Penneman, R. A., *J. Chem. Phys.* **1953**, *21*, 542.
62. Toth, L. M.; Begun, G. M., *J. Phys. Chem.* **1981**, *85*, 547.
63. Tsushima, S.; Yang, T. X.; Suzuki, A., *Chem. Phys. Lett.* **2001**, *334*, 365.
64. Vallet, V.; Wahlgren, U.; Schimmelpfennig, B.; Moll, H.; Szabo, Z.; Grenthe, I., *Inorg. Chem.* **2001**, *40*, 3516.
65. Garcia-Hernandez, M.; Willnauer, C.; Krüger, S.; Moskaleva, L. V.; Rosch, N., *Inorg. Chem.* **2006**, *45*, 1356.
66. Clark, D. L.; Conradson, S. D.; Donohoe, R. J.; Keogh, D. W.; Morris, D. E.; Palmer, P. D.; Rogers, R. D.; Tait, C. D., *Inorg. Chem.* **1999**, *38*, 1456.
67. Moll, H.; Reich, T.; Szabo, Z., *Radiochim. Acta* **2000**, *88*, 411.
68. Quiles, F.; Burneau, A., *Vibrat. Spectrosc.* **2000**, *23*, 231.
69. Quiles, F.; Chinh, N. T.; Carteret, C.; Humbert, B., *Inorg. Chem.* **2011**, *50*, 2811.
70. Zehnder, R. A.; Batista, E. R.; Scott, B. L.; Peper, S. M.; Goff, G. S.; Runde, W. H., *Radiochim. Acta* **2008**, *96*, 575.

71. Zanonato, P. L.; Di Bernardo, P.; Szabo, Z.; Grenthe, I., *Dalton T.* **2012**, Advance Article.
72. Amayri, S.; Reich, T.; Arnold, T.; Geipel, G.; Bernhard, G., *J. Solid State Chem.* **2005**, *178*, 567.
73. Barclay, G. A.; Sabine, T. M.; Taylor, J. C., *Acta Crystallogr.* **1965**, *19*, 205.
74. Allen, P. G.; Bucher, J. J.; Clark, D. L.; Edelstein, N. M.; Ekberg, S. A.; Gohdes, J. W.; Hudson, E. A.; Kaltsoyannis, N.; Lukens, W. W.; Neu, M. P.; Palmer, P. D.; Reich, T.; Shuh, D. K.; Tait, C. D.; Zwick, B. D., *Inorg. Chem.* **1995**, *34*, 4797.
75. McGlynn, S. P.; Neely, W. C.; Smith, J. K., *J. Chem. Phys.* **1961**, *35*, 105.
76. Anderson, A.; Chieh, C.; Irish, D. E.; Tong, J. P. K., *Can. J. Chem.* **1980**, *58*, 1651.
77. Hratchian, H. P.; Sonnenberg, J. L.; Hay, P. J.; Martin, R. L.; Bursten, B. E.; Schlegel, H. B., *J. Phys. Chem. A* **2005**, *109*, 8579.
78. Schreckenbach, G.; Hay, P. J.; Martin, R. L., *Inorg. Chem.* **1998**, *37*, 4442.
79. Vaughn, A. E.; Barnes, C. L.; Duval, P. B., *Angew. Chem. Int. Edit.* **2007**, *46*, 6622.
80. Villiers, C.; Thuery, P.; Ephritikhine, M., *Angew. Chem. Int. Edit.* **2008**, *47*, 5892.

## Preface to Chapter 6

This chapter is based on a manuscript published in the journal “*Chemistry-A European Journal*”.

The full citation of the paper is as follows:

Samuel O. Odoh, Pan Q. Jiang, Grigory A. Shamov, Feiyue Wang, Mostafa Fayek and Georg Schreckenbach, “Theoretical Study of the Reduction of Uranium(VI) Aquo Complexes on Titania Particles and by Alcohols”, *Chem.-A Eur. J.*, **2012**, 18, 7117-7127.

The possibility of using titania particles as a getter for radionuclides in mine tailings and at waste sites has motivated us to study the adsorption of uranium complexes on both a periodic rutile and a nanoparticulate anatase surface. The role of surface defects in inducing the reduction of adsorbed species were also explored using density functional theory. The electronic structure and roles of these surface defects were compared to the photochemical reduction of hexavalent uranium by organic alcohols.

All the calculations in the published manuscript and compiled in this chapter were carried out by Samuel O. Odoh. The manuscript was prepared together with the other authors.

Copyright permissions have been obtained from the publisher of this journal, Wiley, as well as from the other authors. Pan Q. Jiang and Grigory Shamov were postdoctoral research fellows in Professor Schreckenbach’s group. Dr Mostafa Fayek and Dr Feiyue Wang are professors in the Department of Geology and Department of Chemistry at University of Manitoba respectively.

## Chapter 6: Theoretical Study of the Reduction of Uranium (VI) Aquo Complexes on Titania Particles and by Alcohols

### Abstract

To provide insights into the adsorption and photoreduction of uranium (VI) on  $\text{TiO}_2$ , we have studied the structural and electronic properties of uranium (VI) aquo complexes adsorbed on stoichiometric and non-stoichiometric or ‘defected’  $\text{TiO}_2$  surfaces and nanoparticles. Plane wave calculations with the pure PBE density functional and the PBE+U approach were used to study U(VI) complexes on a periodic rutile (110) slab. In addition, a nanoparticulate  $\text{Ti}_{38}\text{O}_{76}$  cluster was used to simulate anatase nanoparticles. The electronic structures of the adsorbed U(VI) complexes indicate that the photoreduction process is a consequence of the photocatalytic properties of  $\text{TiO}_2$ . The reduction of the adsorbed complexes can only occur if the energy of the incident photon exceeds the semiconductor band gap. The gap states induced by single or neighboring hydrogen atoms and oxygen vacancies at the rutile (110) surface cannot reduce adsorbed U(VI) complexes as the unoccupied 5f orbitals are found deeper in the conduction band. In the absence of a solid substrate, photoreduction proceeds by abstraction of a hydrogen atom from water or organic molecules present in solution. Photoreduction by chlorophenol results in lower product yield than reduction by aliphatic alcohols. This is because the triplet uranyl-chlorophenol complex is much more stable than similar complexes formed with methanol and ethanol. In the case of water, the hydroxyl photoproduct easily re-oxidizes the pentavalent species formed. In addition, it is easier for the triplet uranyl-water complex to decompose to the photo-reactants.

## Introduction

The retention by adsorption and reduction of uranium (VI) on geological surfaces in the natural environment is of great importance to the nuclear industry. The safe disposal of high-level nuclear waste (HLNW) and the design of containment structures at mines and environmental remediation models can be improved with better understanding of the chemistry of uranium adsorption and reduction in the natural environment. It is therefore important that chemical processes involving the adsorption/desorption, reduction of U(VI) and the oxidation of U(IV) in natural solid and aqueous systems are investigated. These processes have been the subject of many scientific studies.<sup>1-14</sup> In addition to surface adsorption, the reduction of the soluble and environmentally mobile U(VI) to the less soluble and relatively immobile U(IV) species represents a very potent avenue for uranium immobilization.

Experimentally, the reduction of U(VI) has been observed on abiotic solid systems.<sup>2-3, 8, 13, 15-16</sup> The most widely studied of these involves the redox coupling of the Fe(II)/Fe(III) system to that of U(VI)/U(V) with the U(V) produced undergoing disproportionation to give U(IV) and U(VI). Liger and co-workers observed the reduction of U(VI) by Fe(II) adsorbed on colloidal hematite at high pH.<sup>8</sup> The reduction of U(VI) by Fe(II) adsorbed on corundum (Al<sub>2</sub>O<sub>3</sub>) has also been observed.<sup>10</sup> In the design of trappings for mine tailings or stored nuclear waste, it is important to ensure that the trap or its products do not constitute mobile systems that can easily leach into the environment as a contaminant. Thus, although the sulfides and oxides of iron as well as zero-valent iron have been shown to effectively reduce U(VI), their practical use in trappings may be limited due to the leaching of the oxidation byproducts such as sulfates and sulfites into the ecosystem. Although the Fe(III) oxidation products are unreactive and immobile,

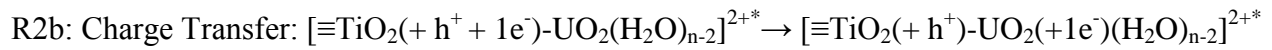
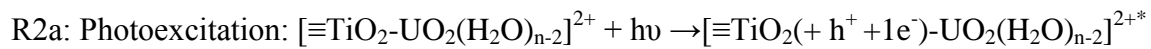
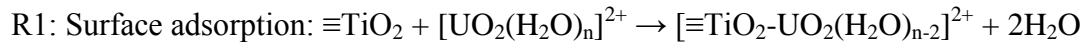
the by-products acidify the surrounding waters and remobilize other resident heavy metals such as lead and cadmium.<sup>11-12</sup>

Roberts<sup>17</sup> and Helean<sup>18-19</sup> have suggested the use of titanium-based materials such as titanate-containing ceramics as radionuclide getters because they are generally more resistant to radiation damage and to geological alteration. The strong association of uranium with titanium oxide (TiO<sub>2</sub>) in naturally uraniferous systems<sup>20</sup> and kaolinite with titanium impurities<sup>21</sup> allows us to propose TiO<sub>2</sub> as a novel uranium getter. In addition, uranium has been found to be intimately associated as uraninite with anatase grains at the Nopal I uranium deposit in Mexico at a depth of 191 meters.<sup>20</sup> Although TiO<sub>2</sub> is more expensive, it has the advantages of greater adsorption capacity, stability and relative environmental benignness in comparison to Al<sub>2</sub>O<sub>3</sub>, iron oxides and iron pyrites. The reduction of U(VI) to U(IV) by rutile and anatase nanoparticles under dark conditions has also been mentioned in very rare instances.<sup>2</sup>

Theoretical studies of the adsorption of the aquo-uranyl complex, [UO<sub>2</sub>(H<sub>2</sub>O)<sub>3</sub>]<sup>2+</sup> and other uranyl complexes<sup>22-24</sup> at the rutile (110) and other mineral surfaces<sup>14, 25-28</sup> have been reported. Most of these theoretical reports have focused on elucidating the nature of the uranyl adsorption (outer or inner-shell coordination) to the metal or metal oxide surface as well as gauging the agreement between calculated and experimental geometrical parameters. The current report summarizes a theoretical study of the electronic and structural properties of the uranyl moiety adsorbed at the rutile (110) surface with a view to describing the mechanism for the photoreduction of the adsorbed complexes. The electronic properties of uranyl complexes adsorbed on non-stoichiometric titania systems with surface defects are also examined to determine the relative energy positions of the unoccupied uranium 5f bands and the gap states

induced by the point defects. Finally, the photoreduction of U(VI) on TiO<sub>2</sub> crystals is compared to the quenching of the photoexcited U(VI) luminescent state by water and organic compounds.

The role of photoexcitation in the reductive immobilization of U(VI) on photocatalytic titania surfaces is of interest.<sup>3, 13</sup> A model involving the creation of an electron-hole (e<sup>-</sup>-h<sup>+</sup>) pair after photoexcitation has been used to describe the photocatalyzed reduction of CO<sub>2</sub> and NO<sub>2</sub> on semiconducting metal oxide surfaces like rutile and anatase.<sup>29</sup> Here, the photoexcited electron is promoted into an orbital localized on the surface-adsorbed species. The highest occupied molecular orbitals (HOMO) or valence band on TiO<sub>2</sub> systems are dominated by contributions from oxygen 2p atomic orbitals. Photoexcitation from the HOMO and subsequent electronic relaxation, Figure 6.1a, could result in the creation of a hole at the top of the valence band and the promotion of an electron into the uranium 5f orbital. Rapid disproportionation of the U(V) thus formed could provide a pathway from this excited state to the formation of U(IV), R1-R5. These reactions will be discussed in detail below.



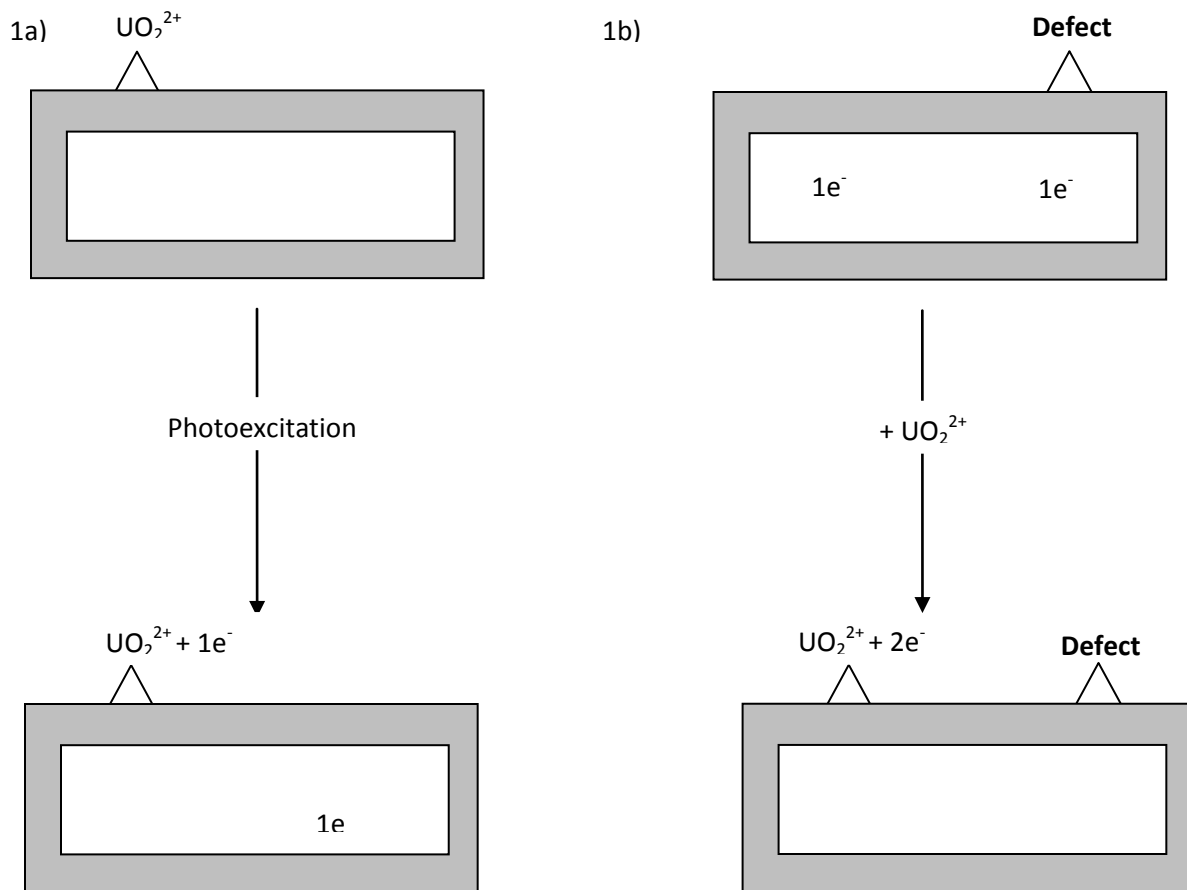


**Figure 6.1:** Possibilities for charge transfer to U(VI) complexes adsorbed on TiO<sub>2</sub> crystals or nanoparticles. a) Creation of an electron-hole ( $e^-h^+$ ) pair after photoexcitation of a surface-adsorbate complex. b) Excess electrons induced by surface or bulk defects are transferred to the adsorbed U(VI) group initiating reduction.

Surface and bulk oxygen vacancies, single or neighboring surface hydroxyls and titanium interstitials are commonly found on real TiO<sub>2</sub> systems. They are crucial to the catalytic behavior and chemistry of TiO<sub>2</sub> crystals and surfaces.<sup>30-34</sup> This is mainly due to the very high chemical reactivities of these defects as a result of their excess electron(s). These defects and associated unpaired electron states on TiO<sub>2</sub> particles and surfaces have been extensively studied

theoretically and experimentally. Periodic density functional theory (DFT) calculations have recently been used to show that the excess electrons from these defects can drive surface-adsorbate charge transfer.<sup>31-32</sup> The influence of the adsorbate's electronegativity on the charge transfer from the point defects was also noted. From this perspective, it would be interesting to determine the possibility of electron transfer from gap states on non-stoichiometric titania systems to adsorbed U(VI) complexes, Figure 6.1b, as a possible pathway towards reductive immobilization of uranium. The physical implication of this suggestion is the possibility of reducing U(VI) by defected TiO<sub>2</sub> crystals and surfaces under dark conditions (without photocatalysis). The reduction of adsorbed U(VI) complexes by the unpaired electrons induced by dopants, defects and impurities in TiO<sub>2</sub> systems would be very important in the storage of nuclear waste materials as the less mobile U(IV) in dark underground repositories.

In this work we employ relativistic density functional theory (DFT) calculations to evaluate the suggestions posed above: 1) Can theoretical examination of the structural and electronic properties of U(VI) complexes adsorbed on TiO<sub>2</sub> systems provide insights into the photocatalytic reduction process (Figure 6.1a)? (2) Can electron transfer from gap states induced by single and neighboring surface hydroxyls result in the reduction of adsorbed uranyl complexes (Figure 6.1b)? The first question relates to the behavior of TiO<sub>2</sub> as a photocatalyst while the second question concerns the ability of surface or sub-surface electrons induced by defects, dopants or impurities to reduce U(VI) complexes adsorbed on TiO<sub>2</sub> systems in the dark. Finally, after elucidating the photoreduction mechanism on TiO<sub>2</sub> systems, the quenching of photoexcited U(VI) complexes by water and organic molecules in the absence of a semiconductor substrate is also explored. The energetics of the hydrogen abstraction reaction as well as the nature and stability of the triplet state uranyl-organic complexes are examined.

The current report is organized as follows: The first part of the discussion section is focused on the description of the structural and electronic parameters of free U(VI) complexes as well as stoichiometric and non-stoichiometric TiO<sub>2</sub> surfaces and nanoparticles. Next, the electronic and structural properties of U(VI) complexes adsorbed on stoichiometric TiO<sub>2</sub> systems are examined. The photoreduction of adsorbed uranyl complexes is then examined in light of the electronic structures of the surface-adsorbate complexes. A periodic rutile (110) surface is employed as a sample TiO<sub>2</sub> surface while a Ti<sub>38</sub>O<sub>76</sub> cluster is used to simulate a nanoparticle. The quenching of photoexcited uranyl complexes by water and organic molecules are then examined. Finally, the results of this work are summarized in the conclusions section.

### **Computational Details**

Scalar relativistic periodic calculations were carried out with the VASP 5.2<sup>35-38</sup> package using the projector augmented wave (PAW)<sup>39-40</sup> approach with plane wave basis while employing the PBE functional.<sup>41-42</sup> To adequately localize and stabilize defect states using the PBE+U approach, Hubbard correction terms, U, of 4.2<sup>43</sup> and 4.0 eV were used for titanium and uranium atoms respectively.<sup>44</sup> The U value of 4.2 eV has been shown to result in band gaps for the rutile (110) and anatase (101) surfaces that agree well with experimental data in addition to adequately reproducing the energetics of the electronic gap states induced by oxygen vacancies on these surfaces.<sup>45</sup> The spin-polarized calculations were carried out with a plane wave cutoff set at 520 eV and a 3×3×1 k-point Monkhorst-Pack (MP) mesh was used. The electronic energy convergence at each step and the geometry convergence criteria were stipulated as 10<sup>-4</sup> eV and 0.01 eV Å<sup>-1</sup> respectively. A rutile (110) slab with 192 atoms was cut from a bulk supercell constructed from the optimized unit cell. Point defects were created by adding one or two neighboring hydrogen atoms to the rutile (110) surface. The bottom layer in this slab was held

fixed at the bulk-optimized coordinates. Periodic slab images were separated by a vacuum of no less than 12 Å to prevent interaction. Complexes belonging to the  $[\text{UO}_2(\text{OH})_m(\text{H}_2\text{O})_{3-m}]^{2-m}$  series with the uranyl group bonded to two bridging surface oxygen atoms,  $O_{bb^-}$ , were used as the U(VI) adsorbates in this work. As the adsorbates were added on only one side of the slab, monopole, dipole and quadrupole corrections were carefully accounted for.

Anatase nanoparticles were represented by the  $\text{Ti}_{38}\text{O}_{76}$  cluster model. This cluster is about 12 Å × 16 Å in size and is therefore of nanoparticulate size. Gas phase geometry optimizations were also carried out using the PBE and BP86 density functionals. Single point calculations were then carried out with the B3LYP functional in aqueous solution using the conductor-like screening model (COSMO).<sup>46-48</sup> The atomic radii of the uranium, titanium, oxygen and hydrogen atoms were chosen as 2.18 Å, 2.18 Å, 1.72 Å and 1.30 Å respectively. The free uranyl complexes, water, methanol, ethanol, chlorophenol and all the complexes formed between the uranyl and organic molecules were optimized in the gas phase and aqueous phases with the PBE and B3LYP functionals. All atoms were described using all-electron basis sets of triple- $\zeta$  polarized (TZP) quality while relativistic effects were included using the zeroth order regular approximation (ZORA).<sup>49-51</sup> All optimized geometries were characterized as local minima on the potential energy surface using vibrational frequency analysis. The calculations on the discrete clusters were carried out with the ADF suite of programs.<sup>52-53</sup>

## Results and Discussion

**Free Uranyl Complexes.** The calculated structural and electronic properties of bare  $\text{UO}_2^{2+}$  and the aquo and aquo-hydroxo complexes of the uranyl moiety are presented in Table 6.1.  $[\text{UO}_2(\text{H}_2\text{O})_5]^{2+}$  is one of the dominant species in very acidic solutions while  $[\text{UO}_2(\text{H}_2\text{O})_3]^{2+}$  is the

**Table 6.1:** Calculated structural features and properties of U(VI) complexes obtained with the PBE functional in the gas phase. The PBE functional and PBE+U approach (*shown in italics*) were used with plane wave basis sets for the adsorbed complexes at the rutile (110) surface. The U-OH<sub>2</sub><sup>a</sup> average bond lengths are given.

|  | U-O <sub>y1</sub> (Å) | U-OH <sub>2</sub> <sup>a</sup> (Å) | $\nu$ UO <sub>2</sub> (cm <sup>-1</sup> )    | Gap (eV)                                      |
|--|-----------------------|------------------------------------|--|---|
| UO <sub>2</sub> <sup>2+</sup>  | 1.724                 |                                    | 963.2, 1058.8                                | 2.286   |
| [UO <sub>2</sub> (H <sub>2</sub> O) <sub>3</sub> ] <sup>2+</sup>     | 1.762                 | 2.381                              | 909.1, 997.0                                 | 2.955   |
| [UO <sub>2</sub> (H <sub>2</sub> O) <sub>5</sub> ] <sup>2+</sup>     | 1.776                 | 2.475                              | 882.8, 970.0                                 | 2.921   |
| [UO <sub>2</sub> (H <sub>2</sub> O) <sub>4</sub> (OH)] <sup>1+</sup> | 1.804                 | 2.569                              | 837.4, 914.5                                 | 2.466   |
| [UO <sub>2</sub> (H <sub>2</sub> O) <sub>3</sub> (OH) <sub>2</sub> ] | 1.817                 | 2.484                              | 819.6, 899.6                                 | 2.636   |
| Adsorbed on a rutile (110) surface                                   |                       |                                    |  |   |
|  | U-O <sub>y1</sub> (Å) | U-OH <sub>2</sub> <sup>a</sup> (Å) | U-O <sub>bb</sub> (Å)                        | U-Ti <sub>surf</sub> (Å)                      |
| [UO <sub>2</sub> ] <sup>2+</sup>                                     | 1.790                 |                                    | 2.170  | 3.310   |
|  | <i>1.758</i>          |                                    | <i>2.218</i>                                 | <i>3.304</i>                                  |
| [UO <sub>2</sub> (H <sub>2</sub> O) <sub>3</sub> ] <sup>2+</sup>     | 1.800                 | 2.593                              | 2.277/2.333                                  | 3.355   |
|  | <i>1.770</i>          | <i>2.587</i>                       | <i>2.353/2.330</i>                           | <i>3.385</i>                                  |
| <b>EXAFS (Ref. <sup>29</sup>)</b>                                    | <b>1.78</b>           | <b>2.46</b>                        | <b>2.31</b>                                  | <b>3.02-3.56</b>                              |
| [UO <sub>2</sub> (H <sub>2</sub> O) <sub>2</sub> (OH)] <sup>1+</sup> | 1.815                 | 2.557                              | 2.510  | 3.493   |
| Adsorbed on an anatase Ti <sub>38</sub> O <sub>76</sub> cluster.     |                       |                                    |  |   |
|  | U-O <sub>y1</sub> (Å) | U-OH <sub>2</sub> <sup>a</sup> (Å) | U-O <sub>bb</sub> / U-Ti <sub>surf</sub> (Å) | $\square$ UO <sub>2</sub> (cm <sup>-1</sup> ) |
| [UO <sub>2</sub> ] <sup>2+</sup>                                     | 1.790                 |                                    | 2.170/3.340                                  | 862.5, 933.2                                  |
| [UO <sub>2</sub> (H <sub>2</sub> O) <sub>3</sub> ] <sup>2+</sup>     | 1.800                 | 2.572                              | 2.281/3.405                                  | 846.9, 921.8                                  |

remaining motif after two equatorial ligands have been replaced by bridging oxygen atoms belonging to the  $\text{TiO}_2$  surface or nanoparticle, Figure 6.2. The addition of aquo ligands to the uranyl equatorial region results in a slight elongation of the  $\text{U-O}_{\text{yl}}$  bonds. The elongation of the  $\text{U-O}_{\text{yl}}$  bonds results in the reduction of the symmetric and asymmetric vibrational stretching frequencies of the uranyl cation, Table 6.1. The replacement of aquo ligands by hydroxo ligands results in further elongation of the  $\text{U-O}_{\text{yl}}$  bonds and corresponding decrease in the uranyl vibrational stretching frequencies.

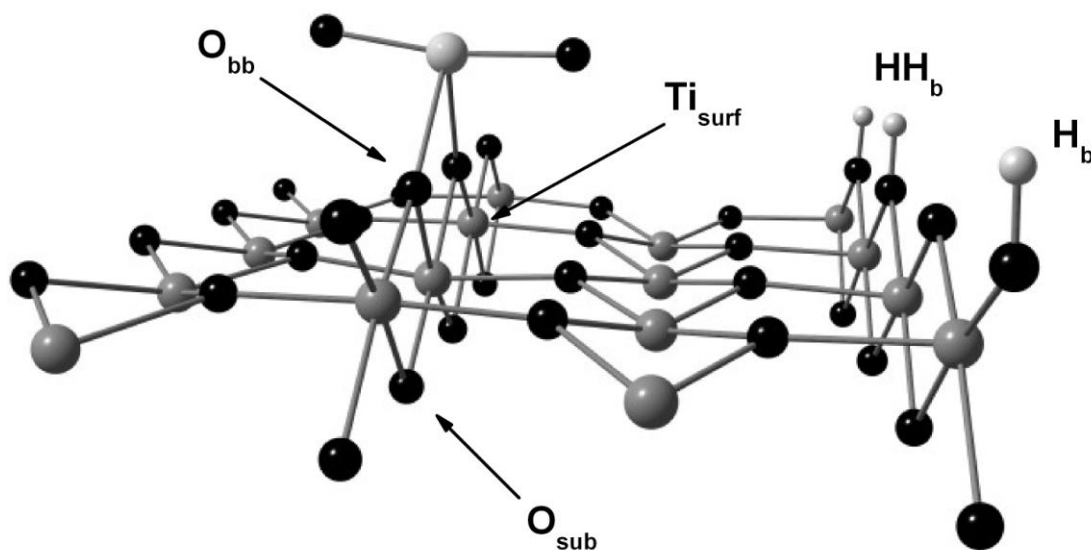


**Figure 6.2:** Structure of  $\text{UO}_2^{2+}$  adsorbed at the rutile (110) surface at the bridging oxygen atoms. The  $\text{O}_{\text{sub}}$ ,  $\text{O}_{\text{bb}}$  and  $\text{Ti}_{\text{surf}}$ ,  $\text{H}_b$  and  $\text{HH}_b$  atoms are labeled for easy identification. The oxygen, titanium and uranium atoms correspond to the black, grey and white spheres respectively. The  $\text{H}_b$  and  $\text{HH}_b$  atoms are respectively the isolated and neighboring surface hydroxyl defects.

The lowest unoccupied orbitals of these U(VI) complexes are a set of empty 5f orbitals while the HOMO in  $\text{UO}_2^{2+}$  is of  $\sigma$ -type character between the uranium and  $\text{O}_{yl}$  atoms. The calculated HOMO-LUMO band gaps of the aquo complexes obtained with the PBE functional are around 2.9 eV. The use of the B3LYP functional widens the gap between the occupied and virtual orbitals. As an example, the calculated HOMO-LUMO gap of  $[\text{UO}_2(\text{H}_2\text{O})_5]^{2+}$  obtained with the hybrid functional is 5.508 eV. Alignment of the MO energy diagrams of  $\text{UO}_2^{2+}$  (HOMO and LUMO at -11.08 and -5.52 eV respectively) and  $[\text{UO}_2(\text{H}_2\text{O})_5]^{2+}$  (HOMO and LUMO at -10.27 and -4.77 eV respectively) at the B3LYP level in aqueous solution reveals a slight shift of the frontier orbitals to higher energies by about 0.8 eV in the pentaquo complex. This form of comparison is possible as they have the same total charge.

**Clean Stoichiometric  $\text{TiO}_2$  Systems.** Rutile surfaces and anatase nanoparticles were modeled using periodic DFT calculations on a rutile (110) slab containing 192 atoms and molecular calculations on a  $\text{Ti}_{38}\text{O}_{76}$  cluster model respectively. The molecular cluster, which was cut from a bulk anatase supercell is of nano-particulate size. We have used an anatase cluster rather than a rutile cluster as the anatase phase is most stable for  $\text{TiO}_2$  nanoparticles below a size of 14 nm.<sup>54</sup> The periodic calculations continue a line of theoretical and experimental investigations of the adsorption of U(VI) complexes on the rutile (110) surface.<sup>22-24, 55</sup> The (110) surface is known to be the most stable compared to all other surfaces cut on crystalline rutile.<sup>56</sup> This surface constitutes about 56% of the exposed surfaces of crystalline rutile.<sup>57</sup>

The HOMO-LUMO gap for the optimized  $\text{Ti}_{38}\text{O}_{76}$  cluster was calculated with the BP86 functional as 2.54 and 2.75 eV in the gas and aqueous phases respectively. These values are smaller than the experimental value of 3.20 eV for bulk anatase.<sup>58</sup> The first few highest occupied frontier orbitals for this cluster were all found to possess predominantly O-2p atomic orbital

character while the lowest unoccupied MOs are mainly of Ti-3d character. The total and partial electronic density of states (DOS) of a periodic rutile (110) slab optimized with the PBE functional and the PBE+U approach using plane wave basis sets are presented in Figure 6.3.

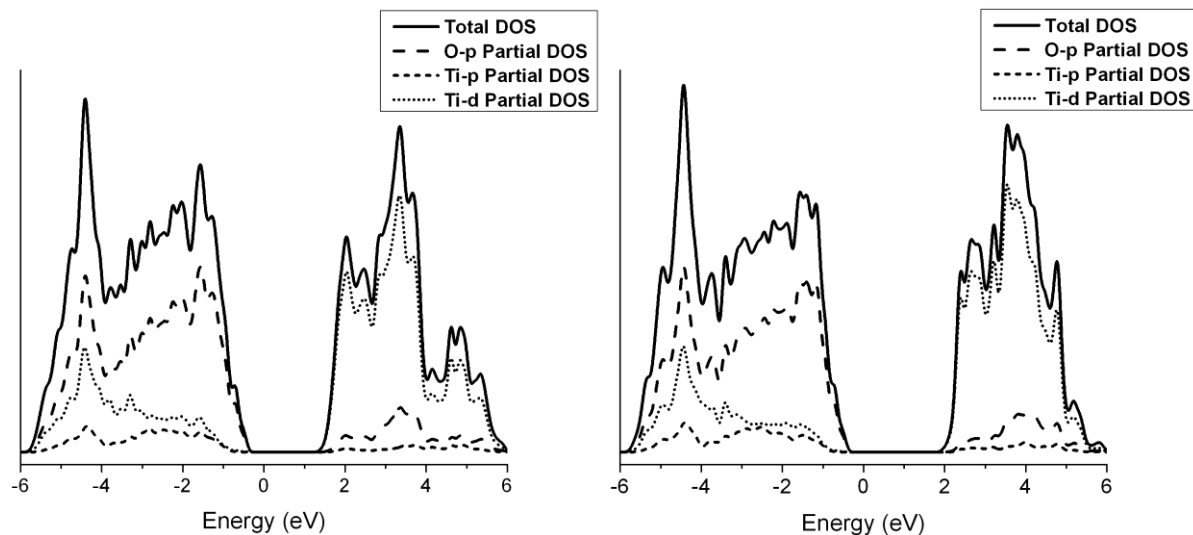


**Figure 6.3:** Total and partial electronic density of states (DOS) obtained for a clean rutile (110) slab while using with the PBE functional (left) and the PBE+U approach (right,  $U=4.2$  eV). Employing the  $U=4.2$  eV correction increases the calculated band gap from 1.859 eV obtained with the pure GGA functional to 2.418 eV.

These DOS show that the valence and conduction bands near the Fermi level are dominated by the oxygen 2p and titanium 3d contributions respectively. In addition, the electronic band gap was calculated as 1.859 with the PBE functional and 2.418 eV with the PBE+U approach. These values are in good agreement with reports from other theoretical investigations but significantly underestimate the experimental band gap of 3.03 eV for rutile.<sup>59-</sup>

<sup>60</sup> The applied U-value of 4.2 eV appears sufficient for our needs as it has been shown to adequately describe the energetics of the electronic gap states induced by surface defects.<sup>61</sup>

**Non-Stoichiometric TiO<sub>2</sub> Systems.** The defect states induced by the presence of single (H<sub>b</sub>) and neighboring (HH<sub>b</sub>) surface hydroxyls on a periodic rutile (110) slab are shown in Figure 6.4. The labeling of these surface hydroxyl defects are presented in Figure 6.2. The two excess electrons in the HH<sub>b</sub> slab were calculated to be nearly degenerate in energy. The calculated energies of the HH<sub>b</sub> gap states relative to bottom of the conduction band is in

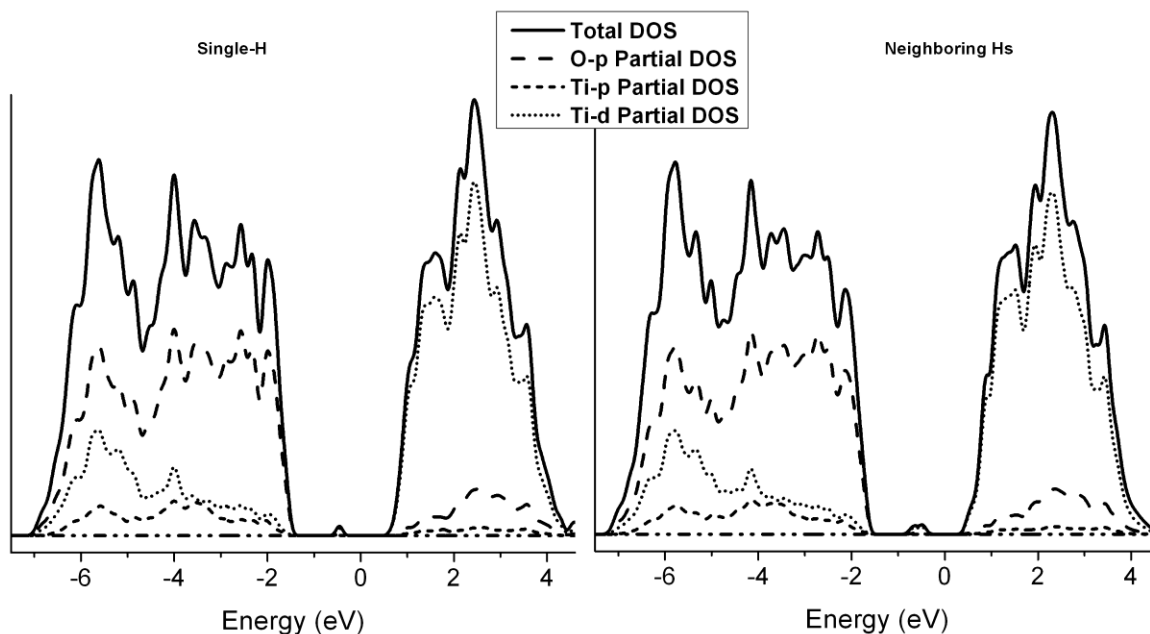


**Figure 6.4:** Total and partial electronic density of states (DOS) obtained for hydroxylated rutile (110) slabs with the PBE+U approach (U=4.2 eV for Ti 3d and U=4.0 eV for U 5f). The Ti-3d gap states were calculated to be about 1 eV below the conduction band. The gap states caused by two neighboring hydroxyl defects were calculated to be nearly degenerate in energy and are also of Ti<sup>3+</sup> character.

good agreement with the previous report of Bonapasta et al.<sup>62</sup> The gap states are found at 1.097 and 0.906 eV below the conduction band for the slabs with H<sub>b</sub> and HH<sub>b</sub> defects respectively. They are therefore in the region observed from with photoelectron and electron energy loss spectroscopic measurements.<sup>63-64</sup> In addition, the gaps between the valence and conduction bands on the hydroxylated slabs were calculated as around 2.191 and 2.141 eV for the H<sub>b</sub> and HH<sub>b</sub> slabs respectively, Figure 6.4. The band gap has been decreased by about 0.3-0.4 eV from the value of 2.415 eV obtained for the clean stoichiometric surface. Finally, it is important to mention that the excess unpaired electron(s) are localized on subsurface Ti atoms in both the H<sub>b</sub> and HH<sub>b</sub> slabs in essence turning these sites into Ti<sup>3+</sup> centers.

**U(VI) Complexes Adsorbed on Stoichiometric TiO<sub>2</sub> Systems.** The structural parameters of [UO<sub>2</sub>]<sup>2+</sup> and [UO<sub>2</sub>(H<sub>2</sub>O)<sub>3</sub>]<sup>2+</sup> species adsorbed on a periodic rutile (110) slab are given in Table 6.1. These calculations were carried out with the PBE functional using plane wave basis sets. The values obtained with the PBE+U approach are also included. The U-O<sub>yl</sub> bond length in the adsorbate complex, [UO<sub>2</sub>(H<sub>2</sub>O)<sub>2</sub>(OH)]<sup>1+</sup> was calculated as 1.815 Å. This is longer than that obtained for the adsorbed [UO<sub>2</sub>(H<sub>2</sub>O)<sub>3</sub>]<sup>2+</sup> and [UO<sub>2</sub>]<sup>2+</sup> complexes. It is however shorter than the value of 1.843 Å obtained in the case of an adsorbed [UO<sub>2</sub>(OH)<sub>3</sub>]<sup>1-</sup> group.<sup>55</sup> In addition, there is an increase in the U-O<sub>bb</sub> bond lengths (bonds between the uranium atom and the bridging surface oxygen atoms, O<sub>bb</sub>, Figure 6.2) upon addition of an equatorial hydroxide ligand, Table 6.1. This indicates a decrease in the surface adsorption strength with increasing pH. This decrease in surface adsorption is confirmed by the increasing distances between the uranium atom and the surface titanium atoms, U-Ti<sub>surf</sub>, Table 6.1. The increase in the U-O<sub>yl</sub> and U-O<sub>bb</sub> bond lengths upon addition of a hydroxide group is similar to the situation in the free complexes. This is seen as a result of the uranyl ion forming stronger complexes with hydroxide and carbonate anions

than with water and the bridging oxygen atoms at the rutile surface.<sup>55</sup> The use of the PBE+U results in reduction of the calculated U-O<sub>y1</sub> and U-O<sub>bb</sub> bond-lengths. The calculated U-O<sub>y1</sub> and U-O<sub>bb</sub> bond lengths obtained for the complex [UO<sub>2</sub>(H<sub>2</sub>O)<sub>3</sub>]<sup>2+</sup> using the PBE+U approach are in good agreement with EXAFS results<sup>65</sup>, Table 6.1.

The bonds between the bridging oxygen atoms and the hexa-coordinated Ti atoms beneath them at the clean rutile (110) surface, O<sub>bb</sub>-Ti<sub>surf</sub>, were calculated to be between 1.858 and 1.860 Å when the PBE+U approach was employed, Figure 6.2, in comparison with the experimental value of 1.85 Å.<sup>66</sup> The adsorption of UO<sub>2</sub><sup>2+</sup> and [UO<sub>2</sub>(H<sub>2</sub>O)<sub>3</sub>]<sup>2+</sup> results in significant elongation of these surface bonds to about 1.994-2.027 and 1.948-1.973 Å respectively. In addition, the bonds between the Ti atom directly beneath the adsorbed uranyl complex and the tri-coordinated sub-surface oxygen atoms, Ti<sub>surf</sub>-O<sub>sub</sub>, were calculated as 1.908 and 1.936 Å for the UO<sub>2</sub><sup>2+</sup> and [UO<sub>2</sub>(H<sub>2</sub>O)<sub>3</sub>]<sup>2+</sup> adsorbates respectively, Figure 6.2. These are much shorter than was obtained from calculations, 2.060 Å and experimental work, 2.08 Å on the clean surface.<sup>66</sup>

It should also be noted that complexation of the bare uranyl or pentaquo complex to the TiO<sub>2</sub> surface or nanoparticle results in slight elongation of the U-O<sub>y1</sub> bonds by 0.01-0.07 Å. This is in agreement with the results of EXAFS studies, Table 6.1.<sup>65</sup> The elongation of the U-O<sub>y1</sub> bond lengths upon surface adsorption is reminiscent of a similar effect when equatorial aquo ligands are replaced by hydroxide ligands, as has been discussed above. The effect of this is a reduction in the calculated stretching modes of the uranyl group. The calculated symmetric and asymmetric vibrational modes of the UO<sub>2</sub><sup>2+</sup> and [UO<sub>2</sub>(H<sub>2</sub>O)<sub>3</sub>]<sup>2+</sup> groups adsorbed on the anatase nanocluster are much lower than was obtained for the similar free complexes, Table 6.1. Experimental confirmation (using Fourier transform infra-red spectroscopy, FTIR) of this change in the uranyl vibrational wavenumbers has been recently reported.<sup>67</sup>

The electronic DOS for the surface-adsorbate complexes with  $\text{UO}_2^{2+}$  and  $[\text{UO}_2(\text{H}_2\text{O})_3]^{2+}$  adsorbed on the bridging oxygen atoms of a periodic rutile (110) slab are presented in Figure 6.5. Overall, the DOS for the surface-adsorbate complex is similar to that of the clean (110) slab and dominated by contributions from the rutile slab. This is most likely a result of the low uranyl surface coverages used in this work. The electronic band gap of the surface-adsorbate complex with a  $[\text{UO}_2]^{2+}$  adsorbate was calculated as 1.442 and 2.060 eV with the PBE functional and PBE+U approach respectively. These are about 0.417 and 0.352 eV respectively

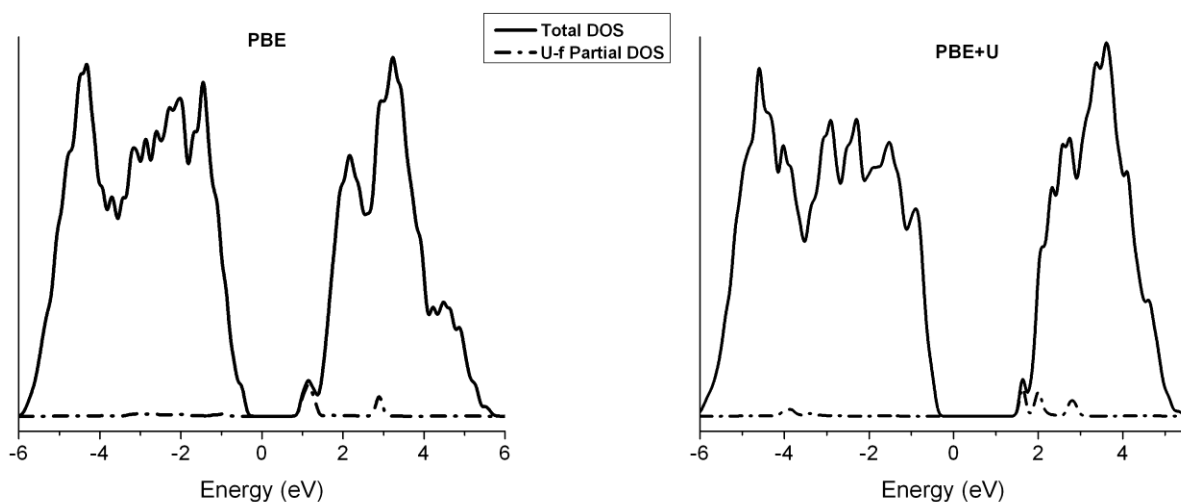


**Figure 6.5:** Total and partial electronic density of states (DOS) obtained for rutile (110) slabs with an adsorbed  $\text{UO}_2^{2+}$  group obtained with the PBE+U approach ( $U=4.2$  eV for Ti-3d and  $U=4.0$  eV for U-5f). The empty U-5f states were calculated to be just beneath the Ti-3d dominated conduction band.

lower than those obtained for the clean (110) surface respectively. The  $U$  value of 4.0 eV has been shown to be sufficient in describing the unoccupied 5f orbitals of uranium fuels and

clusters.<sup>68-69</sup> Given that the experimental band gap of rutile is 3.0 eV, the results of the PBE+U calculations suggest that the empty 5f bands can be expected to be found between 0 and 1 eV beneath the Ti-3d conduction band. At the current level however a 5f band is found just beneath the conduction band.

For the periodic slab with a  $[\text{UO}_2(\text{H}_2\text{O})_3]^{2+}$  adsorbate, the empty 5f band is shifted to slightly higher energies and is now buried in the Ti-3d conduction band, Figure 6.6. The electronic band gap of the rutile- $[\text{UO}_2(\text{H}_2\text{O})_3]^{2+}$  surface adsorbate complex was calculated to be 2.136 eV. A look at the calculated DOS however suggests that given accurate replication of the experimental rutile band gap, the 5f band should be just below (-0.2 to 0.8 eV) the Ti-3d

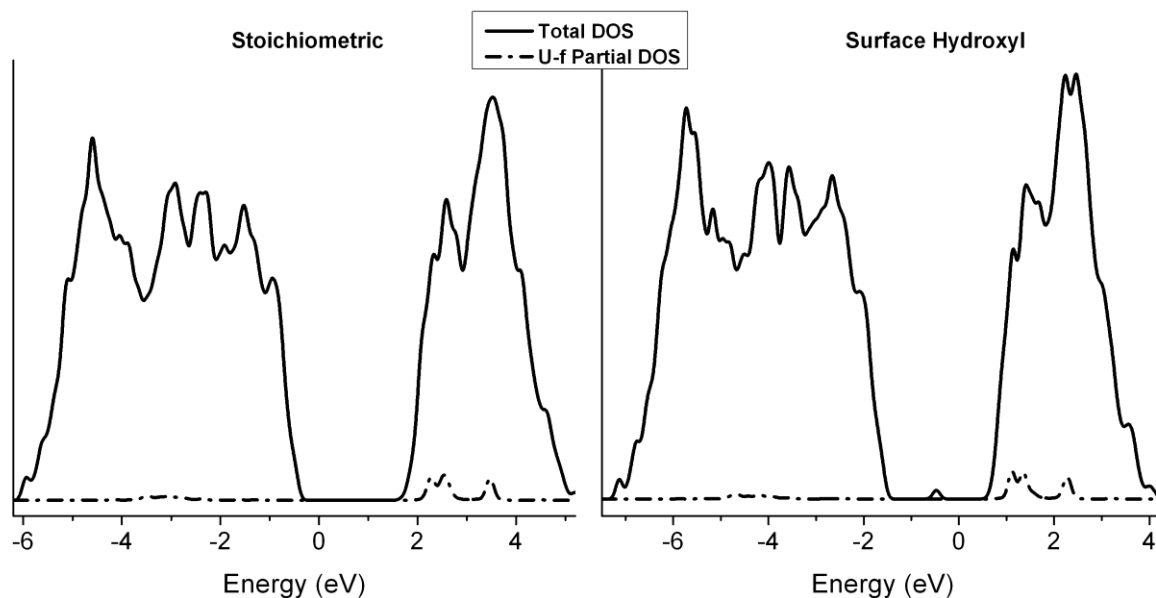


**Figure 6.6:** Total and partial electronic density of states (DOS) obtained for stoichiometric (left) and surface hydroxyl defected (right) rutile (110) slabs with adsorbed  $[\text{UO}_2(\text{H}_2\text{O})_3]^{2+}$  obtained with the PBE+U approach ( $U=4.2$  eV for Ti-3d and  $U=4.0$  eV for U-5f). The gap state induced by the surface hydroxyl lies at lower energies than the empty U-5f bands.

conduction band. Examination of the electronic structure of the  $\text{Ti}_{38}\text{O}_{76}\text{-}[\text{UO}_2(\text{H}_2\text{O})_3]^{2+}$  and  $\text{Ti}_{38}\text{O}_{76}\text{-}[\text{UO}_2]^{2+}$  complexes also reveals the presences of empty U-5f states between the O-2p and Ti-3d bands of the anatase cluster. Figure 6.7. In agreement with the PBE+U calculations on the periodic slab, the empty U-5f band is located between 1 and 0.0 eV of the Ti-3d band. The ordering and general description of the bands dominated by the O-2p, U-5f and Ti-3d remains the same for the surface-adsorbate complexes of  $\text{UO}_2^{2+}$  and  $[\text{UO}_2(\text{H}_2\text{O})_3]^{2+}$ .

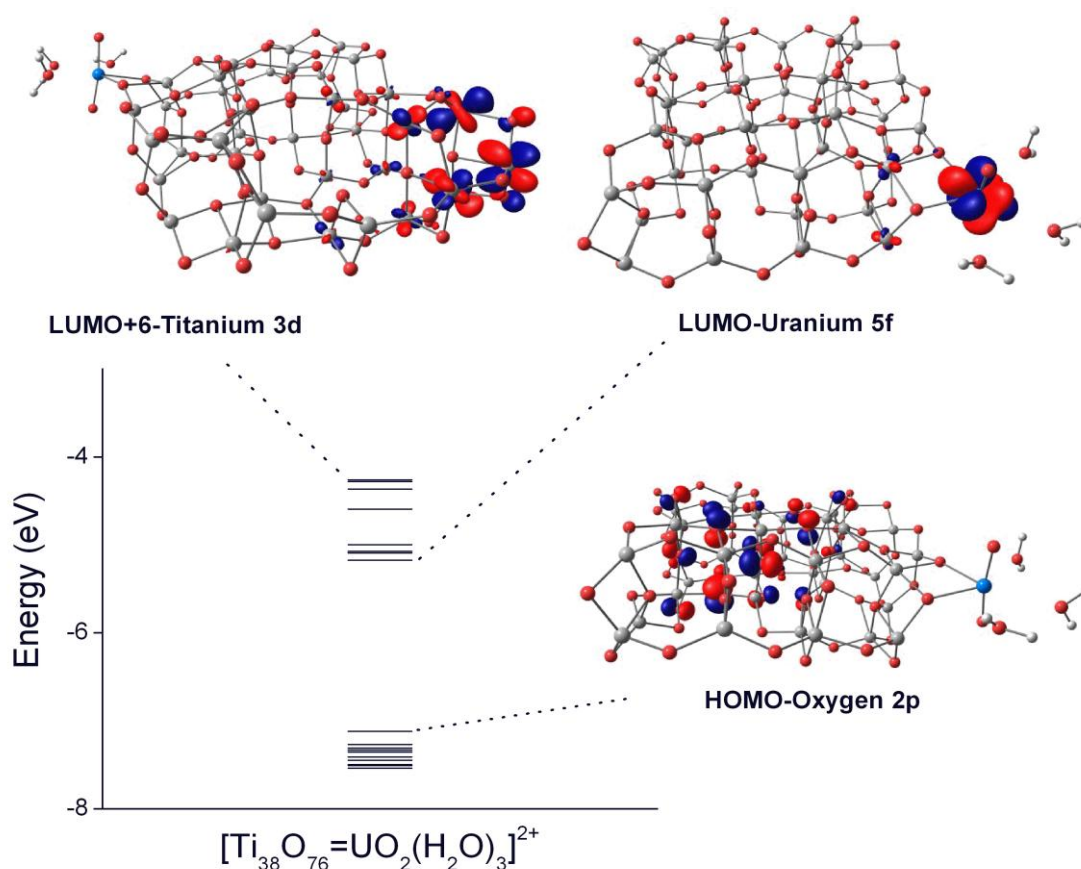


**Figure 6.7:** Electronic energy levels and frontier molecular orbitals obtained at the BP86/TZP level for the a  $\text{Ti}_{38}\text{O}_{76}\text{-}[\text{UO}_2(\text{H}_2\text{O})_3]^{2+}$  surface-adsorbate complex. The empty U-5f orbitals are between 1.0 and 0.0 eV of the onset of the Ti-3d virtual orbitals.

The empty 5f states might be occupied during photoexcitation from the O-2p dominated valence band. In this event, the adsorbed uranyl group acquires a pentavalent, U(V) character with the simultaneous creation of a hole in the titania system. Indeed, examination of the lowest triplet excited states of the  $\text{Ti}_{38}\text{O}_{76}\text{-}[\text{UO}_2]^{2+}$  and  $\text{Ti}_{38}\text{O}_{76}\text{-}[\text{UO}_2(\text{H}_2\text{O})_3]^{2+}$  clusters reveals that an electron is invariably excited from an O-2p orbital localized in the  $\text{TiO}_2$  cluster into a uranium 5f orbital. For example, the calculated Mulliken spin densities on the  $\text{Ti}_{38}\text{O}_{76}$  and  $[\text{UO}_2(\text{H}_2\text{O})_3]^{2+}$  groups in the lowest triplet state of  $\text{Ti}_{38}\text{O}_{76}\text{-}[\text{UO}_2(\text{H}_2\text{O})_3]^{2+}$  are 1.014 and 0.986 respectively. Indeed TDDFT calculations of the first 50 excitations of the  $\text{Ti}_{38}\text{O}_{76}\text{-}[\text{UO}_2(\text{H}_2\text{O})_3]^{2+}$  cluster reveal the final orbitals to be of distinctly U-5f character. The trapping of the excited electron in the actinide 5f orbitals is in contrast to the localization of the electron-hole pair on the subsurface atoms of a photoexcited rutile (110)-water surface adsorbate complex containing associatively adsorbed water.<sup>70</sup> Electronic transitions from the ground state to the triplet excited states are forbidden however due to spin selection rules. This might indicate low probabilities for the photoreduction pathway initiated by direct excitation into the lowest triplet states.

Conversely, initial photoexcitation into the Ti-3d dominated virtual orbitals (LUMO+5 and above) or the conduction band for the periodic slab may also be followed by fast electronic decay and charge transfer into the 5f-band/orbitals of the adsorbed U(VI) species. This indirect process of excitation of the valence electrons into the  $\text{TiO}_2$  conduction band followed by charge transfer into the uranium-5f atomic orbitals is likely to be more plausible given the spatial overlap of the MOs involved in the initial excitation, Figure 6.7. The nature of this charge-transfer mechanism for the photoreduction of the adsorbed uranyl complexes indicates that the incident energy must be equal or greater than the semiconductor band gap. This is in accordance with the experimental work of Amadelli et al.<sup>1</sup> It also indicates that the role of the  $\text{TiO}_2$  surface

or nanoparticle is mainly photocatalytic. A sequence of reactions, R1-R5 occurring between the formation of the surface-adsorbate complex to the formation of mixed U(VI)/U(IV) oxides can be posited. It should be noted that the direct photoexcitation ( $O-2p \rightarrow U-5f$ ) and indirect charge transfer ( $O-2p \rightarrow Ti-3d \rightarrow U-5f$ ) processes both involve excitation of electrons from the  $TiO_2$  valence band. In the case of the latter, the yield of the U(IV) formed would match the absorption spectrum of the  $TiO_2$  system. This was also found to be the case by Amadelli et al.<sup>1</sup>

Concerning reactions R4 and R5, the presence of adsorbed polymeric uranyl species and hole-scavengers will appear to favor the disproportionation process, R4 as these species afford a polynuclear framework allowing disproportionation of the pentavalent intermediates. The oxidation of the U(V) species by dissolved molecular oxygen is known to be relatively slow and the precipitation of the adsorbed U(IV) would drive R4 forward under sustained irradiation.<sup>4, 71-72</sup> The suspension of photo-irradiation results in the re-oxidation of U(IV) species by molecular oxygen. This could lead to the formation of U(IV)/U(VI) mixed oxides, R5.<sup>1, 3, 13</sup>

**U(VI) Complexes Adsorbed on Non-Stoichiometric  $TiO_2$ .** The possible reduction of U(VI) complexes adsorbed on defected surfaces, Figure 6.1b, is similar to the photocatalyzed reduction process on stoichiometric  $TiO_2$  slabs, Figure 6.1a. The only difference being that the U(VI) complex would be reduced by the transfer of an electron from a deep-lying  $3d^1$  electronic state formed by the point defects on adsorption rather than by a photoexcited electron.

The electronic DOS of periodic rutile (110) slabs with an adsorbed  $[UO_2(H_2O)_3]^{2+}$  group and a surface hydroxyl defect obtained using the PBE+U approach is presented in Figure 6.6. The uranyl and surface hydroxyl groups were placed on adjacent  $O_{bb}$  bridging rows. In the absence of the equatorial aquo ligands, the excess electron from the single hydroxyl defect is

localized on a Ti atom in the rutile slab in the most stable electronic state. Although this result might suggest that the unpaired electron is not transferred to the adsorbed U(VI) complex, it has been shown that the gap states predicted by the PBE+U approach are not as deeply localized as those predicted by hybrid functionals.<sup>31, 34</sup> Enforcing the localization of the unpaired electron on the uranium atom of the adsorbed uranyl group increases the total energy by about 0.11 eV. This is done by using the MAGMOM keyword in the VASP software package. The introduction of three aquo ligands on the uranyl group,  $[\text{UO}_2(\text{H}_2\text{O})_3]^{2+}$ , Figure 6.8, further increases the energy barrier to localization of the excess electrons on the uranium atom. A similar situation was observed when the surface hydroxyl group was replaced by either neighboring hydroxyls or an oxygen vacancy.

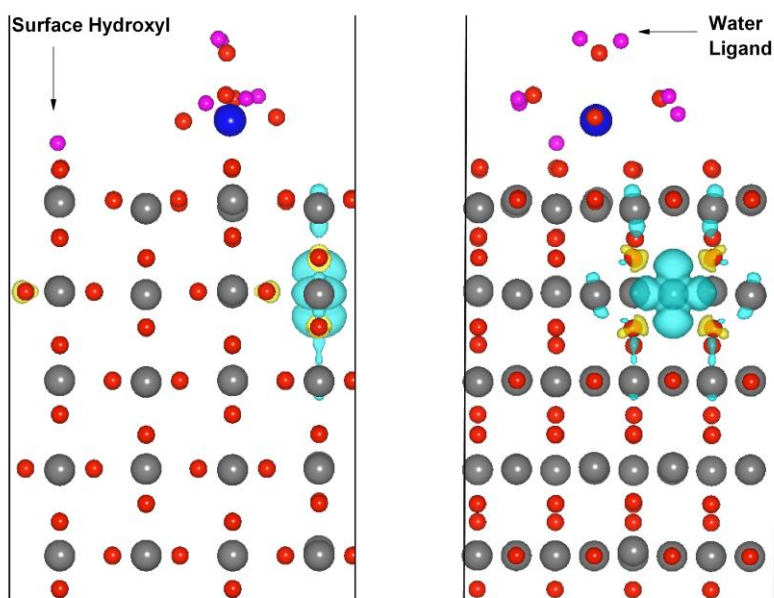


**Figure 6.8:** Calculated spin distributions of a rutile (110) slab with a surface-adsorbed  $[\text{UO}_2(\text{H}_2\text{O})_3]^{2+}$  moiety and a surface hydroxyl defect. These calculations were carried out with the PBE+U approach. Two side views of each slab are presented [Titanium: grey, Oxygen: red, Uranium: blue and Hydrogen: pink].

Going back to the anatase molecular clusters, the MO energy level diagram of the defected  $\text{Ti}_{38}\text{O}_{76}\text{H}$  (surface hydroxyl) cluster with an adsorbed  $[\text{UO}_2(\text{H}_2\text{O})_3]^{2+}$  is presented in Figure 6.9. The delocalization of the excess electron state on several titanium atoms with a small portion on the uranyl moiety is most likely an artifact of the geometry optimization with the GGA functional.<sup>34</sup> The gap state induced by the surface defect is found below the virtual U-5f dominated orbitals. This state possesses appreciable U-5f atomic orbital contributions. The U-5f contribution to the gap state was calculated to be about 28% with the BP86 functional but was decreased to around 12% after a the single point calculation with the B3LYP functional. This results in the reduction of the spin density on the adsorbed uranyl group by about 50%.

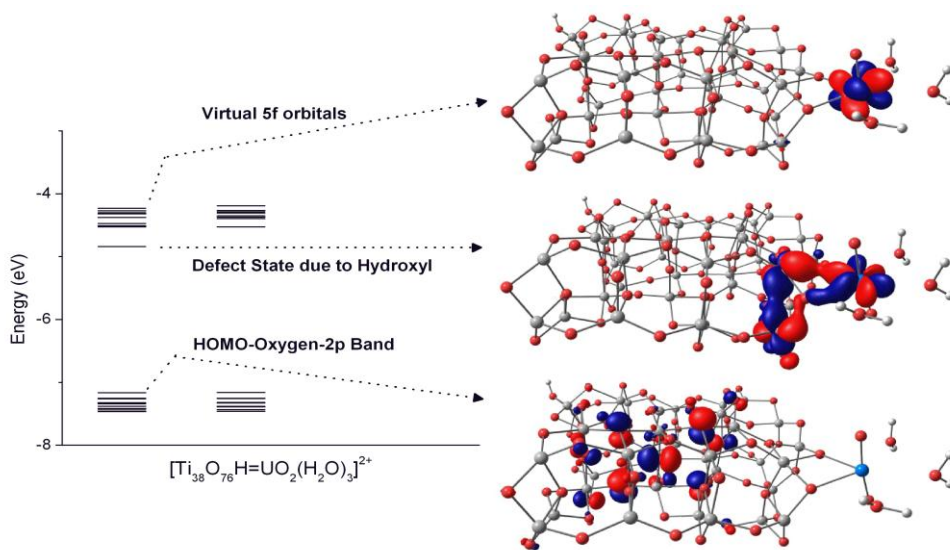


**Figure 6.9:** Electronic energy levels and MOs of a non-stoichiometric cluster (with a surface hydroxyl)-adsorbate complex. The defect state induced by the hydroxyl is predominantly of Ti-3d character. The Mulliken spin density on the uranyl complex is reduced by 50 % from 0.30 to 0.15 after a single point calculation with the B3LYP functional.

The combination of the results of the calculations on the periodic slab and the nanoparticulate cluster model indicates that surface hydroxyl and oxygen vacancy defects play little role in the reduction of adsorbed U(VI) complexes. The gap states induced by these defects occur at lower energies than the empty U-5f bands. The addition of aquo ligands to the equatorial region of the adsorbed uranyl further shifts the empty U-5f band away from the band gap. It should also be noted that these defect species have tremendous affinities for adsorbed or dissolved oxygen suggesting their role in U(VI) reduction would be even further limited under oxic conditions.

**Quenching of Photoexcited U(VI) Complexes by Water and Organic Molecules.** As discussed thus far, the role of TiO<sub>2</sub> in the reductive immobilization of U(VI) complexes appears to be mainly photocatalytic while surface defects play little or no role in the reduction of surface adsorbed U(VI) complexes. In contrast, the photoreduction of U(VI) complexes by organic molecules in the absence of a solid photocatalytic surface is well known from experimental studies.<sup>5, 9, 72-74</sup> Theoretical studies directed at understanding the quenching of photoexcited actinyl dications, [AnO<sub>2</sub>]<sup>2+</sup> by water have been done.<sup>74-77</sup> A more generic reaction involving the abstraction of a hydrogen atom from water and organic molecules in quenching the photoexcited pentaquo uranyl complex can be written as R6.



Thermochemically, the quenching of the lowest triplet excited state of [UO<sub>2</sub>(H<sub>2</sub>O)<sub>5</sub>]<sup>2+</sup> by abstracting an hydrogen atom from water is significantly endoergic in comparison to similar processes by aliphatic alcohols or 4-chlorophenol, Table 6.2. Photoreduction via abstraction of the α-hydrogen atoms of methanol is more exoergic than abstraction from its alcohol-hydrogen

atom by about 6.6 to 8.1 kcal/mol. A similar preference for the  $\alpha$ -hydrogen atom of ethanol was also observed. The calculated reaction energies for R6 actually reflect the relative stability of the radicals formed by either abstraction of the  $\alpha$ -,  $\beta$ - and OH hydrogen atoms and is in very good agreement with the experimental observation that the lowest triplet state of U(VI)<sup>9, 73</sup> like carbonyl radicals<sup>78</sup> tend to preferentially abstract the  $\alpha$ -hydrogen atoms of aliphatic alcohols. Accounting for solvent polarity by performing single point calculations in methanol using optimized gas phase structures did not alter the conclusions that can be drawn from the results presented in Table 6.2. In the case of 4-chlorophenol, it appears that abstraction of the phenolic hydrogen atom represents the only feasible photoreduction pathway. Abstraction of hydrogen atoms from the 2- and 3- position of the phenyl ring were calculated to be endoergic at the PBE/TZP level. In addition, the results of the DFT calculations suggest that the photooxidation of chlorophenol is energetically more favored than quenching by the aliphatic alcohols or water. It should however be noted that these thermodynamic calculations on R6 do not involve a description of the interaction between the triplet excited state  $[\text{UO}_2(\text{H}_2\text{O})_5]^{2+}$  complex and the ROH (quenching) molecules.

The nature of the complexes formed between the triplet excited state of  $[\text{UO}_2(\text{H}_2\text{O})_5]^{2+}$  and the quenching molecules (water, aliphatic alcohols or phenols) can be probed using unrestricted DFT calculations. Examination of the calculated  $S(S+1)$  values for these uranyl-quencher complexes indicates little or no spin contamination. The calculated lengths of the U-O<sub>yl</sub> bonds and the bonds between the uranyl oxo atom and the hydrogen atom to be abstracted in the uranyl-quencher complex, O<sub>oxo</sub>-H<sub>abs</sub> are presented in Table 6.2. Attempts to optimize the geometries of the triplet state uranyl-quencher complex formed through the 2- and 3- hydrogen atoms of chlorophenol and the  $\beta$ -hydrogen atoms of ethanol were unsuccessful. The instability of

**Table 6.2:** Calculated reaction energies (kcal/mol) obtained for R6 in aqueous solution obtained at the PBE/TZP and B3LYP/TZP levels in addition to the calculated structural and electronic properties of the triplet state uranyl-quencher complexes.

| Quencher       | R6 Reaction Energies |        |        | Uranyl-Quencher Complexes <sup>a</sup> |   |                   |
|----------------|----------------------|--------|--------|--|---|-------------------|
|                | H atom               | PBE    | B3LYP  | U-O <sub>yl</sub> <sup>b</sup>         | O <sub>yl</sub> -H <sub>abstracted</sub> <sup>b</sup> | Spin <sup>c</sup> |
| Water          | OH                   | 14.25  | 2.24   | 1.809/1.898                            | 2.357/2.361   | 0.411             |
| Methanol       |                      |        |        |  |   |                   |
|                | $\alpha$ -H          | -12.20 | -20.33 | 1.803/1.996                            | 1.019   | 0.959             |
|                | OH                   | -4.13  | -13.52 | 1.806/1.969                            | 1.025   | 1.002             |
| Ethanol        |                      |        |        |  |   |                   |
|                | $\alpha$ -H          | -14.59 | -22.36 | 1.808/1.966                            | 1.041   | 0.947             |
|                | $\beta$ -H           | -4.54  | -13.22 |  |   |                   |
|                | OH                   | -4.81  | -13.63 | 1.808/1.956                            | 1.034   | 1.001             |
| 4-chlorophenol |                      |        |        |  |   |                   |
|                | 2-H                  | 5.62   | -2.40  |  |   |                   |
|                | 3-H                  | 5.89   | -1.95  |  |   |                   |
|                | OH                   | -22.31 | -31.28 | 1.822/1.882                            | 1.430   | 1.001             |

<sup>a</sup> The structural features and electronic properties presented are from triplet uranyl-quencher complexes whose geometries were optimized in aqueous solution at the B3LYP/TZP level. <sup>b</sup> The longer U-O<sub>yl</sub> bonds belong to the oxo atom involved in hydrogen abstraction. <sup>c</sup> This denotes the partial spin localized on the radical formed after H abstraction from the quenching molecule.

the triplet state uranyl-quencher complexes formed via the hydrogen atoms at the 2- and 3-phenyl positions reinforces the thermochemical calculations which indicated that the

photoreduction of U(VI) by chlorophenol can only proceed via the formation of the chlorophenoxy radical.

In all the optimized triplet state uranyl-quencher complexes considered, there is complete transfer of an electron to the uranyl group with the uranium atom being formally pentavalent, Table 6.2. The distance between the uranyl oxo atom and the hydrogen atom being abstracted from the quenching molecule,  $O_{\text{oxo}}-H_{\text{abs}}$ , was calculated to be about 2.36 Å in the triplet  $[\text{UO}_2(\text{H}_2\text{O})_5][\text{H}_2\text{O}]^{2+,*}$  complex. This distance is rather large in comparison to the distances of about 1.0 Å in the complexes formed with the aliphatic alcohols. The distance in the  $[\text{UO}_2(\text{H}_2\text{O})_5][\text{chlorophenol}]^{2+,*}$  complex is about 0.5 Å longer than observed for the aliphatic alcohols. In addition, the triplet state uranyl-quencher complex formed with chlorophenol was calculated to be significantly relatively more stable (relative to the photo-products) than those formed with water, methanol or ethanol, Figure 6.10. The longer  $O_{\text{oxo}}-H_{\text{abs}}$  distance as well as the greater stability of the triplet uranyl-chlorophenol complex is most likely due to stabilization via electron delocalization from the aromatic ring.

The yield of any reduction products (e.g. U(IV) precipitate, alkene and alkyl radical oxidation products) depends on the susceptibility of the ability of the triplet uranyl-quencher complex to decomposition. If the triplet uranyl-quencher complex is ‘too’ stable relative to photoreduction products, decomposition subsequent to hydrogen abstraction will be more endoergic. This will result in low yields for U(V) species, U(IV) formed on disproportionation of the pentavalent complex, alkoxy or hydroxyl radical and ketones formed from the alkoxy radicals. This is most likely the case for the photoreduction by chlorophenol, Figure 6.10, and is in some agreement with the experimental work of Sarakha et al.<sup>72</sup> They observed low product yields even while obtaining very high charge transfer rates between the chlorophenol molecule

and the excited uranyl complex. This correlates well with the significant spin/charge transfer in the triplet uranyl-chlorophenol complex, Table 6.2, and its high stability relative to the photo-reactants and photo-products, Figure 6.10. In contrast, the triplet uranyl-water complex was found to be the least stable with respect to the photo-reactants and the most stable relative to the photo-products, Figure 6.10. This indicates that the uranyl-water triplet state complex would most likely decompose back to the photo-reactants. This is in stark contrast to the other triplet state complexes which would progress to the photo-products given the relative energies of the forward and backward reactions. It should however be noted that we have only examined the quenching of the lowest triplet excited state of the uranyl complex. Higher electronic excited states might be involved in the photooxidation of water by uranyl complexes.

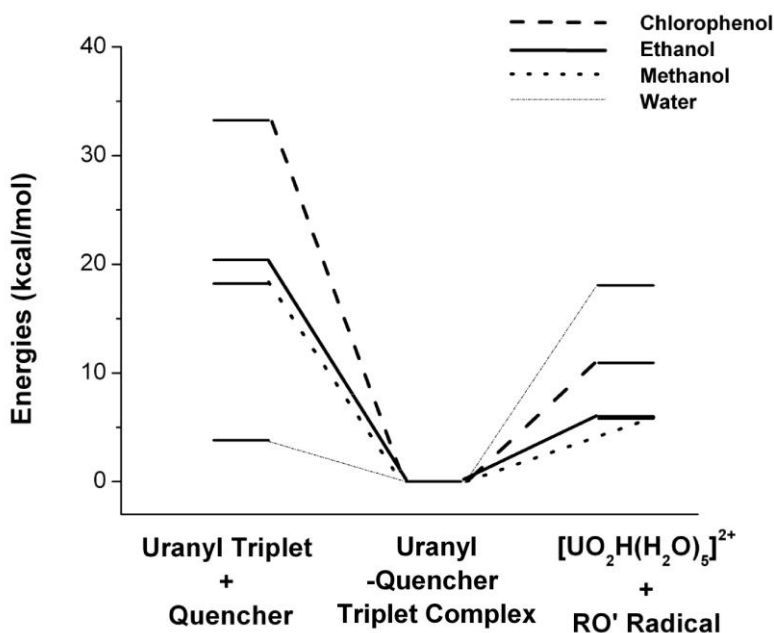


**Figure 6.10:** The quenching of the lowest triplet excited state of  $[\text{UO}_2(\text{H}_2\text{O})_5]^{2+}$  by water and organic alcohols. The relative energies ( $\Delta G$ , calculated at the BP86/TZVP level in aqueous

solution) of the reactants and products of reaction R6 are given with respect to the triplet uranyl-quencher complex.

## Conclusions

We have carried out a study of the structural and electronic properties of U(VI) complexes adsorbed on TiO<sub>2</sub> surfaces to obtain insights into the photoreduction mechanism of uranium compounds on such surfaces. The possibility of charge transfer from surface defects such as hydroxyls and oxygen vacancies to the adsorbed U(VI) complexes was explored as well. The quenching of the lowest triplet excited state of U(VI) complexes by water and small organic molecules was also elucidated for comparison to the photocatalytic role of the TiO<sub>2</sub> surface. All these calculations were carried out using DFT either on periodic extended systems with plane waves or on cluster models with all-electron basis sets.

The structures of rutile surfaces as well as the structures of the adsorbed uranyl complexes are well reproduced both in terms of absolute values and in structural trends by using the PBE+U method in the periodic calculations. When compared with available experimental data, the cluster model calculations with the PBE functional provide accurate descriptions of the IR spectra of the uranyl complexes adsorbed on nanoparticles. Electronically, the empty 5f states of the adsorbed uranyl complexes were calculated to be just below the Ti-3d conduction band. The selection rules indicate that a charge-transfer mechanism which is O-2p → Ti-3d → U-5f is most likely responsible for the photoreduction of U(VI) on TiO<sub>2</sub> surfaces. This implies that the photoreduction process on TiO<sub>2</sub> surfaces and nanoparticles is photocatalytic in nature and does not involve direct excitation of the uranyl complex. For such surface catalyzed reduction processes to occur, the energy of the incident light must be equal to or exceed the semiconductor band gap. The implication of this constraint is that the photoreduction yield must match the

absorption spectrum of the semiconductor. This is in agreement with previous experimental reports further demonstrating the potency of the approach employed.

According to the computations, electron transfer from surface oxygen vacancies and hydroxyl defects do not appear to be able to induce U(VI) reduction under dark conditions. This is because the gap states induced by these defects are found nearer the valence band than the empty 5f bands. The equatorial aquo ligands of the uranyl complex further shift the empty U-5f band into the conduction band. This decreases the possibility of localizing the excess electrons on the uranium atom.

In contrast to photoreduction on TiO<sub>2</sub>, the photoreduction by water, aliphatic alcohols and chlorophenol is initiated by initial photoexcitation of the uranyl complex. The calculated reaction energies indicate that, the hydroxyl radical formed by abstracting an hydrogen atom from a water molecule is able to rapidly re-oxidize the U(V) species formed. The aliphatic alcohols and 4-chlorophenol more easily quench the photoexcited uranyl complex by donating their  $\alpha$ - and phenolic hydrogen atoms respectively. The relative stabilities of the triplet state uranyl-quencher complexes with respect to the pentavalent and alkoxy (or phenoxy) photoreduction products appear crucial to the photo-product yield observed. The uranyl-chlorophenol triplet state complex is more stable relative to the photo-products than similar complexes formed with the aliphatic alcohols. This correlates well with previous experimental work in which very high charge transfer quantum yields with very low yields for the photo-products were obtained for the uranyl-chlorophenol system.

## References

1. Amadelli, R.; Maldotti, A.; Sostero, S.; Carassiti, V., *J. Chem. Soc. Faraday T.* **1991**, *87* (19), 3267-3273.
2. Bonato, M.; Allen, G. C.; Scott, T. B., *Micro Nano. Lett.* **2008**, *3* (2), 57-61.
3. Eliet, V.; Bidoglio, G., *Environ. Sci. Technol.* **1998**, *32* (20), 3155-3161.
4. Formosinho, S. J.; Burrows, H. D.; Miguel, M. D.; Azenha, M.; Saraiva, I. M.; Ribeiro, A.; Khudyakov, I. V.; Gasanov, R. G.; Bolte, M.; Sarakha, M., *Photoch. Photobio. Sci.* **2003**, *2* (5), 569-575.
5. Formosinho, S. J.; Miguel, M. D. M.; Burrows, H. D., *J. Chem. Soc. Faraday T. I* **1984**, *80*, 1717-1733.
6. Harazono, T.; Sato, S.; Fukutomi, H., *B. Chem. Soc. Jpn.* **1984**, *57* (3), 768-770.
7. Lefevre, G.; Kneppers, J.; Fedoroff, M., *J. Colloid Interf. Sci.* **2008**, *327* (1), 15-20.
8. Liger, E.; Charlet, L.; Van Cappellen, P., *Geochim. Cosmochim. Ac.* **1999**, *63* (19-20), 2939-2955.
9. Nagaishi, R.; Katsumura, Y.; Ishigure, K.; Aoyagi, H.; Yoshida, Z.; Kimura, T., *J. Photoch. Photobio. A.* **1996**, *96* (1-3), 45-50.
10. Regenspurg, S.; Schild, D.; Schafer, T.; Huber, F.; Malmstrom, M. E., *Appl. Geochem.* **2009**, *24* (9), 1617-1625.
11. Scott, T. B.; Allen, G. C.; Heard, P. J.; Randell, M. G., *Geochim. Cosmochim. Ac.* **2005**, *69* (24), 5639-5646.
12. Scott, T. B.; Tort, O. R.; Allen, G. C., *Geochim. Cosmochim. Ac.* **2007**, *71* (21), 5044-5053.

13. Selli, E.; Eliet, V.; Spini, M. R.; Bidoglio, G., *Environ. Sci. Technol.* **2000**, *34* (17), 3742-3748.
14. Sherman, D. M.; Peacock, C. L.; Hubbard, C. G., *Geochim. Cosmochim. Ac.* **2008**, *72* (2), 298-310.
15. Evans, C. J.; Nicholson, G. P.; Faith, D. A.; Kan, M. J., *Green Chem.* **2004**, *6* (4), 196-197.
16. Yusov, A. B.; Shilov, V. P., *Russ. Chem. B+* **2000**, *49* (2), 285-290.
17. Roberts, S. K.; Bourcier, W. L.; Shar, H. F., *Radiochim. Acta* **2000**, *88*, 539-543.
18. Helean, K. B.; Ushakov, S. V.; Brown, C. E.; Navrotsky, A.; Lian, J.; Ewing, R. C.; Farmer, J. M.; Boatner, L. A., *J. Solid State Chem.* **2004**, *177*, 1858-1866.
19. Helean, K. B.; Navrotsky, A.; Lumpkin, G. R.; Colella, M.; Lian, J.; Ewing, R. C.; Ebbinghaus, B.; Catlano, J. G., *J. Nucl. Mater.* **2003**, *320*, 231-244.
20. Fayek, M.; Ren, M.; Goodell, P.; Dobson, P.; Saucedo, A. L.; Kelts, A.; Utsunomiya, S.; Ewing, R. C.; Riciputi, L. R.; Reyes, I., *International High Level Radioactive Waste Management Conference Proc.* **2006**.
21. Payne, T. E.; Davis, J. A.; Lumpkin, G. R.; Chisari, R.; Waite, T. D., *Appl. Clay Sci.* **2004**, *26* (1-4), 151-162.
22. Perron, H.; Domain, C.; Roques, J.; Drot, R.; Simoni, E.; Catalette, H., *Radiochim. Acta* **2006**, *94* (9-11), 601-607.
23. Perron, H.; Domain, C.; Roques, J.; Drot, R.; Simoni, E.; Catalette, H., *Inorg. Chem.* **2006**, *45* (17), 6568-6570.
24. Perron, H.; Roques, J.; Domain, C.; Drot, R.; Simoni, E.; Catalette, H., *Inorg. Chem.* **2008**, *47* (23), 10991-10997.

25. Hattori, T.; Saito, T.; Ishida, K.; Scheinost, A. C.; Tsuneda, T.; Nagasaki, S.; Tanaka, S., *Geochim. Cosmochim. Ac.* **2009**, *73* (20), 5975-5988.
26. Kremleva, A.; Krüger, S.; Rösch, N., *Radiochim. Acta* **2010**, *98* (9-11), 635-646.
27. Roques, J.; Veilly, E.; Simoni, E., *Int. J. Mol. Sci.* **2009**, *10* (6), 2633-2661.
28. Veilly, E.; Roques, J.; Jodin-Caumon, M. C.; Humbert, B.; Drot, R.; Simoni, E., *J. Chem. Phys.* **2008**, *129* (24).
29. Usubharatana, P.; McMartin, D.; Veawab, A.; Tontiwachwuthikul, P., *Ind. Eng. Chem. Res.* **2006**, *45* (8), 2558-2568.
30. Bowker, M.; Bennett, R. A., *J. Phys-Condens. Mat.* **2009**, *21* (47).
31. Deskins, N. A.; Rousseau, R.; Dupuis, M., *J. Phys. Chem. C* **2009**, *113* (33), 14583-14586.
32. Deskins, N. A.; Rousseau, R.; Dupuis, M., *J. Phys. Chem. C* **2010**, *114* (13), 5891-5897.
33. Diebold, U., *Surf. Sci. Rep.* **2003**, *48* (5-8), 53-229.
34. Finazzi, E.; Di Valentin, C.; Pacchioni, G.; Selloni, A., *J. Chem. Phys.* **2008**, *129* (15).
35. Kresse, G.; Furthmüller, J., *Comput. Mat. Sci* **1996**, *6*, 15.
36. Kresse, G.; Furthmüller, J., *Phys. Rev. B* **1996**, *54*, 11169.
37. Kresse, G.; Hafner, J., *Phys. Rev. B* **1993**, *47*, 558.
38. Kresse, G.; Hafner, J., *Phys. Rev. B* **1994**, *49*, 14251.
39. Blöchl, P. E., *Phys. Rev. B* **1994**, *50*, 17953.
40. Kresse, G.; Joubert, D., *Phys. Rev. B* **1999**, *59*, 1758.
41. Perdew, J. P.; Burke, K.; Ernzerhof, M., *Phys. Rev. Lett.* **1996**, *77* (18), 3865-3868.
42. Perdew, J. P.; Burke, K.; Ernzerhof, M., *Phys. Rev. Lett.* **1997**, *78* (7), 1396-1396.
43. Calzado, C. J.; Hernandez, N. C.; Sanz, J. F., *Phys. Rev. B* **2008**, *77* (4).

44. Dudarev, S. L.; Botton, G. A.; Savrasov, S. Y.; Humphreys, C. J.; Sutton, A. P., *Phys. Rev. B* **1998**, *57*, 1505
45. Morgan, B. J.; Watson, G. W., *J. Phys. Chem. C* **2010**, *114* (5), 2321-2328.
46. Klamt, A., *J. Phys. Chem.* **1995**, *99* (7), 2224-2235.
47. Klamt, A.; Schuurmann, G., *J. Chem. Soc. Perk T. 2* **1993**, (5), 799-805.
48. Pye, C. C.; Ziegler, T., *Theor. Chem. Acc.* **1999**, *101* (6), 396-408.
49. Faas, S.; Snijders, J. G.; van Lenthe, J. H.; van Lenthe, E.; Baerends, E. J., *Chem. Phys. Lett.* **1995**, *246* (6), 632-640.
50. van Lenthe, E., *J. Comput. Chem.* **1999**, *20* (1), 51-62.
51. van Lenthe, E.; Baerends, E. J.; Snijders, J. G., *J. Chem. Phys.* **1993**, *99* (6), 4597-4610.
52. ADF2010.01, Theoretical Chemistry, Vrije Universiteit, Amsterdam, The Netherlands, <http://www.scm.com> 2010.
53. te Velde, G.; Bickelhaupt, F. M.; van Gisbergen, S. J. A.; Fonseca Guerra, C.; Baerends, E. J.; Snijders, J. G.; Ziegler, T., *J. Comput. Chem.* **2001**, *22*, 931-967.
54. Zhang, H. Z.; Banfield, J. F., *J. Mater. Chem.* **1998**, *8* (9), 2073-2076.
55. Pan, Q.-J.; Odoh, S. O.; Asaduzzaman, A. M.; Schreckenbach, G., *Chem-Eur. J.* *accepted*.
56. Purton, J.; Bullett, D. W.; Oliver, P. M.; Parker, S. C., *Surf. Sci.* **1995**, *336* (1-2), 166-180.
57. Ramamoorthy, M.; Vanderbilt, D.; Kingsmith, R. D., *Phys. Rev. B* **1994**, *49* (23), 16721-16727.
58. Reyes-Coronado, D.; Rodriguez-Gattorno, G.; Espinosa-Pesqueira, M. E.; Cab, C.; de Coss, R.; Oskam, G., *Nanotechnology* **2008**, *19* (14).

59. Jedidi, A.; Markovits, A.; Minot, C.; Bouzriba, S.; Abderraba, M., *Langmuir* **2010**, *26* (21), 16232-16238.
60. Li, S. C.; Wang, J. G.; Jacobson, P.; Gong, X. Q.; Selloni, A.; Diebold, U., *J. Am. Chem. Soc.* **2009**, *131* (3), 980-984.
61. Morgan, B. J.; Watson, G. W., *J. Phys. Chem. C* **2009**, *113* (17), 7322-7328.
62. Bonapasta, A. A.; Filippone, F.; Mattioli, G.; Alippi, P., *Catal. Today* **2009**, *144* (1-2), 177-182.
63. Henderson, M. A.; Epling, W. S.; Peden, C. H. F.; Perkins, C. L., *J. Phys. Chem. B* **2003**, *107* (2), 534-545.
64. Wendt, S.; Matthiesen, J.; Schaub, R.; Vestergaard, E. K.; Laegsgaard, E.; Besenbacher, F.; Hammer, B., *Phys. Rev. Lett.* **2006**, *96* (6).
65. Den Auwer, C.; Drot, R.; Simoni, E.; Conradson, S. D.; Gailhanou, M.; de Leon, J. M., *New J. Chem.* **2003**, *27* (3), 648-655.
66. Bondarchuk, O.; Kim, Y. K.; White, J. M.; Kim, J.; Kay, B. D.; Dohnalek, Z., *J. Phys. Chem. C* **2007**, *111* (29), 11059-11067.
67. Comarmond, M. J.; Payne, T. E.; Harrison, J. J.; Thiruvoth, S.; Wong, H. K.; Aughterson, R. D.; Lumpkin, G. R.; Muller, K.; Foerstendorf, H., *Environ. Sci. Technol.* **2011**, *45* (13), 5536-5542.
68. Dorado, B.; Amadon, B.; Freyss, M.; Bertolus, M., *Phys. Rev. B* **2009**, *79* (23).
69. Kotani, A.; Yamazaki, T., *Prog. Theor. Phys. Suppl.* **1992**, (108), 117-131.
70. Shapovalov, V.; Stefanovich, E. V.; Truong, T. N., *Surf. Sci.* **2002**, *498* (1-2), L103-L108.
71. Bakac, A.; Espenson, J. H., *Inorg. Chem.* **1995**, *34* (7), 1730-1735.

72. Sarakha, M.; Bolte, M.; Burrows, H. D., *J. Phys. Chem. A* **2000**, *104* (14), 3142-3149.
73. Nagaishi, R.; Katsumura, Y.; Ishigure, K.; Aoyagi, H.; Yoshida, Z.; Kimura, T.; Kato, Y., *J. Photoch. Photobio. A* **2002**, *146* (3), 157-161.
74. Tsushima, S., *Inorg. Chem.* **2009**, *48* (11), 4856-4862.
75. Moskaleva, L. V.; Krüger, S.; Spörl, A.; Rösch, N., *Inorg. Chem.* **2004**, *43* (13), 4080-4090.
76. Vallet, V.; Maron, L.; Schimmelpfennig, B.; Leininger, T.; Teichteil, C.; Gropen, O.; Grenthe, I.; Wahlgren, U., *J. Phys. Chem. A* **1999**, *103* (46), 9285-9289.
77. Vallet, V.; Schimmelpfennig, B.; Maron, L.; Teichteil, C.; Leininger, T.; Gropen, O.; Grenthe, I.; Wahlgren, U., *Chem. Phys.* **1999**, *244* (2-3), 185-193.
78. Formosinho, S. J., *J. Chem. Soc. Faraday T. II* **1976**, *72*, 1313-1331.

## Preface to Chapter 7

This chapter is based on a manuscript published in the journal “*Inorganic Chemistry*”. The full citation of the paper is as follows:

Samuel O. Odoh, Sean M. Walker, Markus Meier, Jörg Stetefeld and Georg Schreckenbach, “QM and QM/MM Study of Uranyl Fluorides in the Gas Phase, Aqueous Phase and in the Hydrophobic Cavities of Tetrabrachion”, *Inorganic Chem.* **2010**, 50, 3141-3152.

The existence, orientation and electronic properties of an uranyl fluoride complex ( $\text{UO}_2\text{F}_5^{3-}$ ) in the hydrophobic cavities of tetrabrachion protein unit were examined using density functional theory and molecular mechanics in a QM/MM formalism.

All the calculations in the published manuscript and compiled in this chapter were carried out by Samuel O. Odoh. The manuscript was prepared together with the other authors.

Copyright permissions have been obtained from the American Chemical Society and the other authors. Sean M. Walker was an undergraduate research fellow in Professor Schreckenbach’s group. Dr Markus Meier and Dr Jörg Stetefeld are affiliated with the Department of Chemistry at University of Manitoba.

# Chapter 7: QM and QM/MM Study of Uranyl Fluorides in the Gas Phase, Aqueous Phase and in the Hydrophobic Cavities of Tetrabrachion

## Abstract

The structural properties and electronic structures of pentacoordinated uranyl complexes belonging to the  $[\text{UO}_2\text{F}_n(\text{H}_2\text{O})_{5-n}]^{2-n}$  series have been studied in the gas and aqueous phases using density functionals with relativistic pseudopotentials and all electron basis sets in the gas phase calculations in combination with the COSMO solvation model in the aqueous phase. In addition, the conformational orientation, structural and electronic properties of  $[\text{UO}_2\text{F}_5]^{3-}$  in the hydrophobic cavities of the right handed coiled coil (RHCC) protein of tetrabrachion have been determined using the hybrid QM/MM method. Although, there is good agreement between the available experimental geometrical parameters and the values obtained in the aqueous phase using pseudopotentials or all electron basis sets, the variation of the uranyl U=O bond with the number of fluoride ligands is only truly captured after the inclusion of five water molecules in the second coordination sphere around the molecules. The docking procedure used in this work shows that there are only two possible orientations of the uranyl group of  $[\text{UO}_2\text{F}_5]^{3-}$  embedded in the hydrophobic cavities of the RHCC protein. The two orientations are exclusively along the axes perpendicular to the protein axial channel with no possible orientation of the uranyl group along the axial channel due to both steric effects and interaction with the alkyl chain of the isoleucine residues pointing into the axial channel. In addition, the embedded complex is always positioned nearer the isoleucine residues at the N-terminal ends of the hydrophobic cavities.

Energy analysis however reveals that both conformations can only be observed in cavity two, the largest hydrophobic cavity. The structural and electronic properties of the ligand embedded in this cavity are very similar to those of the gas-phase structure. Comparable study of  $[\text{Pt}(\text{CN})_6]^{2-}$  and the anticancer drug, cisplatin,  $[\text{PtCl}_2(\text{NH}_3)_2]$ , in cavity two, revealed the existence of just two orientations for the former, similar to the uranyl complex and multiple orientations for the latter.

## Introduction

The tetrabrachion complex of archaebacterium *Staphylothermus marinus* has been shown to contain a right-handed coiled coil (RHCC) protein.<sup>1-5</sup> The thermodynamically stable RHCC contains four parallel  $\alpha$ -helical chains oriented in a right-handed fashion with four hydrophobic cavities aligned along the axis of the protein, Figure 7.1. In the native crystal structure, the largest hydrophobic cavity of tetrabrachion contains nine water molecules aggregated into a cluster while the other cavities contain five, one and two water molecules respectively according to their sizes. The aggregation of the water molecules in the cavities of tetrabrachion is due to the exclusively aliphatic and hydrophobic lining of the cavity walls. Yin et al have shown that metastable water complexes held together by hydrogen bonds exist in the largest cavity of RHCC both at room (298 K) and high (365 K) temperatures.<sup>6-7</sup> They also demonstrated the existence of significant entropic contributions to the thermodynamics of the filling of the largest hydrophobic cavity by multiple water molecules.

A recent review on the nature and structure of coiled-coil proteins as well as their potential use for therapeutic purposes has been published by McFarlane et al.<sup>8</sup> The presence of large cavities in such proteins and the ability of these cavities to bind or hold cargo molecules make them ideal drug delivery vehicles. Modification of the terminal amino acids of coiled coils with specific labeling groups can be used for specific drug targeting thus reducing the overall

cytotoxicity of a therapeutic molecule. Perhaps the most important potential use of coiled-coil proteins is for delivery of cancer drugs to tumor cells. In fact, the ability of the RHCC

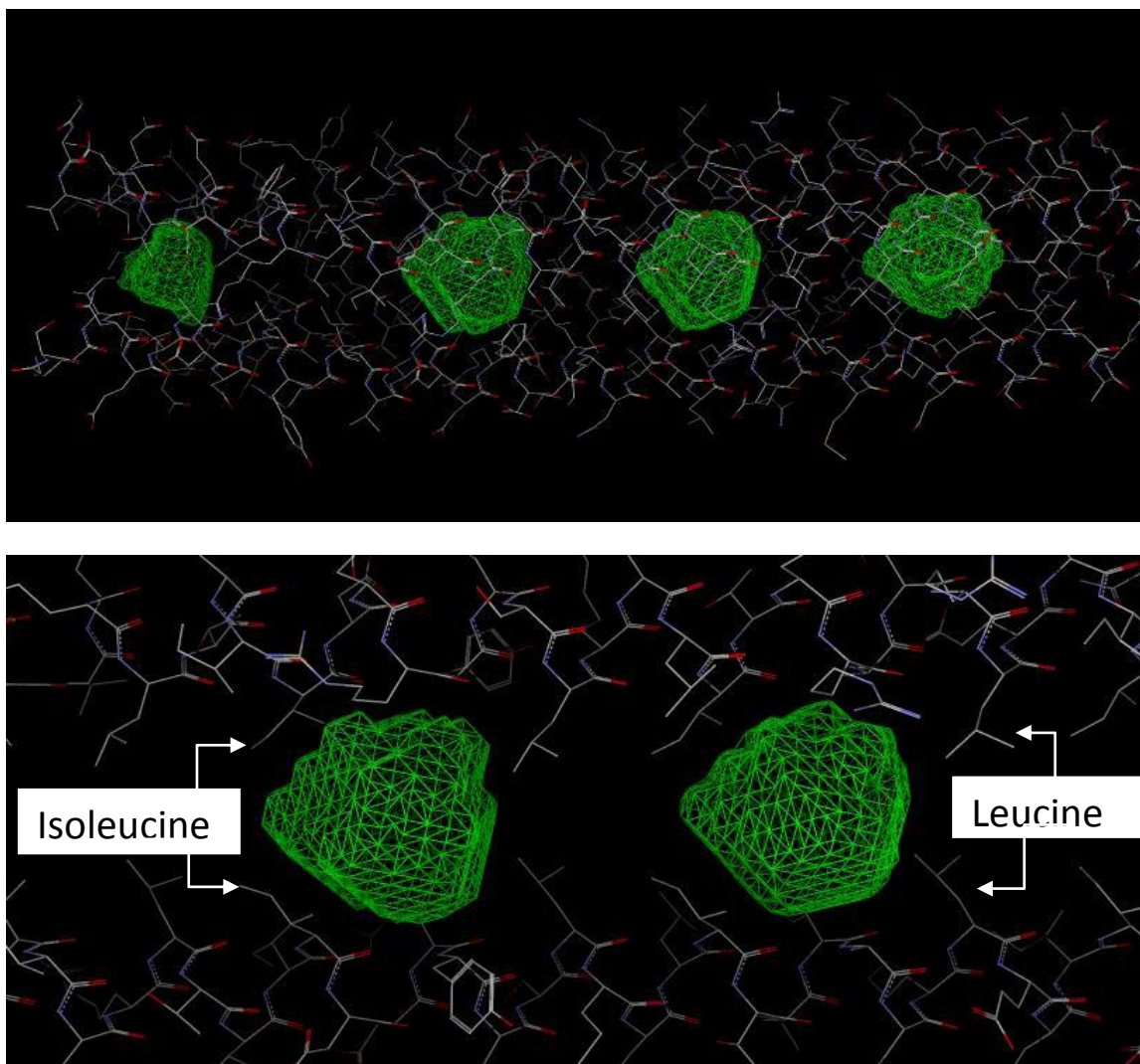


**Figure 7.1:** Top: The Right Handed Coiled Coil Protein of Tetrabrachion. Cavities One-Four from the N-Terminus (Left) to the C-Terminus (Right) are Shown. Bottom: Two Monomer Chains of the RHCC Tetramer. Isoleucine and Leucine Side Chains are Found at the N-Terminal and C-Terminal Ends Respectively of Cavities Two and Three.

of tetrabrachion to incorporate and transfer cisplatin,  $[\text{PtCl}_2(\text{NH}_3)_2]$ , into mammalian cells has been studied by Eriksson et al.<sup>2</sup> They found that RHCC stably incorporates cisplatin at room temperature and that the RHCC-cisplatin (RHCC-C) complex rather efficiently binds to cells. The RHCC-C complex was found to be equally or sometimes more effective against cancer cells as the pure cisplatin drug. Their work raises the possibility of the RHCC protein being used as a carrier for cisplatin in therapeutic usage. However, an obstacle to the long-term goal of using the RHCC as a drug delivery vehicle is the issue of diseased cell targeting. Theoretical studies of cisplatin in the cavities of the RHCC could potentially be used in designing modifications to either the cargo molecule or the aliphatic chains lining the cavities.

Moreover, cancer drugs are not the only kind of molecular systems that can be embedded in the hydrophobic cavities of RHCC. Indeed several heavy metals and their compounds were incorporated into the cavities of the tetrabrachion RHCC during X-ray crystallographic studies of its structure.<sup>5</sup> It would thus appear that the hydrophobic cavities are filled with water clusters in the native structure while the occupying water clusters are displaced by any compact molecular or ionic system present in solution. The displacement of water clusters embedded in the hydrophobic cavities by a single ionic complex will be favored by an increase in total entropy which will dominate the positive-leaning enthalpy of transferring ionic or hydrophilic species from the polar aqueous solvent into a cavity lined exclusively with aliphatic side chains.<sup>6-7</sup>

Actinide complexes like uranyl fluoride used in the determination of the phase information of the RHCC are also incorporated into the hydrophobic cavities.<sup>4-5, 9-10</sup> Uranyl fluorides have been extensively studied theoretically and experimentally in both the gaseous and aqueous phases.<sup>11-26</sup> The hydrophobic cavities of the RHCC of tetrabrachion represent a rather unique and 'different' environment in which to study the structure and bonding of uranyl

fluorides. The extent to which the wavefunction of a cargo molecule is perturbed by the protein environment can be determined by comparing the geometrical and electronic structures of uranyl fluorides in the hydrophobic cavities of RHCC, in the gas phase and in solution. In addition, as the cavities of the RHCC are non-polar, it will be interesting to see if there is any ‘local-order’ (or favored orientations) to the alignment of polar molecules like uranyl fluoride.

Full quantum mechanical (QM) calculations on the protein-actinide species complex are currently very computationally expensive not in the least because of the large number of degrees of freedom in the protein.<sup>27</sup> Indeed, the large number of loose degrees of freedom in biological macromolecules makes the concept of a ‘global or local’ structural minimum less important than in stiff molecules and hence the need for selection of a probabilistic ensemble corresponding to all possible configurations in which the macromolecule could exist at a certain temperature.<sup>27</sup> The quantum mechanical/molecular mechanics (QM/MM) method is a hybrid method in which the active or interesting site is treated with computationally more demanding QM methods while the remainder of the system (remainder of the macromolecule and/or environmental water) is treated classically using molecular mechanics (MM).<sup>28-42</sup> This method has been used extensively in literature to study large systems and represents a balance between the accuracy of full quantum mechanical treatment and the computational efficiency of a full classical treatment using molecular mechanics.<sup>43-46</sup>

There have been very few theoretical studies of actinide complexes using the QM/MM method. Infante *et al* studied the nature of the water solvation shells around both the tetrafluoro- and tetrahydroxo- complexes of the uranyl dication.<sup>15-16, 47-48</sup> The solvent water molecules were treated with MM while the uranyl complexes were treated with density functional theory (DFT) with relativistic effects included using the zeroth order regular approximation, ZORA.<sup>49-51</sup> The

interaction between the solvent water MM region and the wavefunction of the actinide complex QM region was restricted to mechanical coupling. Comparison of the results of QM/MM calculations with those obtained with full QM calculations indicated qualitative and some quantitative agreements in the computed geometric and electronic properties.

Here we present QM/MM simulation studies on uranyl pentafluoride,  $[\text{UO}_2\text{F}_5]^{3-}$  incorporated in the hydrophobic cavities of the RHCC using DFT with relativistic effective core potentials (RECPs) to include relativistic effects on the QM region while classically representing the RHCC using the popular AMBER95 force field.<sup>52</sup> Electrostatic coupling of the MM charges to the wavefunction of the QM region and other non-bonded interactions like Van der Waals and electrostatic interactions are included in the calculations. The structural and electronic properties of  $[\text{UO}_2\text{F}_5]^{3-}$  in the hydrophobic cavities are compared to those in both gaseous and aqueous phases. The presence of favored configurations for the embedded actinide complex with respect to the axial channel of the protein is reliably proven using the QM/MM method. This is in agreement with preliminary experimental evidence for the existence of two orientations for uranyl fluoride in the largest hydrophobic cavity of the RHCC.<sup>53</sup> Finally, the incorporation of the anticancer drug, cisplatin, and  $[\text{Pt}(\text{CN})_6]^{2-}$  into the largest hydrophobic cavity is examined using the same methodology used for uranyl fluoride. It should be fully noted that current theoretical calculations of cisplatin in the hydrophobic cavities were stimulated by the possibility of therapeutic use while similar work on  $[\text{UO}_2\text{F}_5]^{3-}$  in these cavities was motivated by structural and electronic considerations (the presence of local order in the arrangement of this molecule in the cavities and the effect of the cavity walls on the electronic structure of the actinide complex). The common theme connecting the two subjects (cisplatin and uranyl complexes) is provided in the common protein environment with its unique cavity structure and the resulting application of

a common methodology. There is undoubtedly little therapeutic potential for this actinide complex.

The remainder of this report is organized as follows. The computational calculations carried out are first described followed by a discussion of the geometric and electronic structure of uranyl fluorides in the gas and aqueous phases. The chemistry of uranyl fluorides in the hydrophobic cavities of tetrabrachion is then described using  $[\text{UO}_2\text{F}_5]^{3-}$  as a representative complex. Finally, we compare the incorporation of  $[\text{UO}_2\text{F}_5]^{3-}$  in the hydrophobic cavities to that of other ligands such as cisplatin and  $[\text{Pt}(\text{CN})_6]^{2-}$ .

### Computational Details

The molecular geometries of all members of the  $[\text{UO}_2\text{F}_n(\text{H}_2\text{O})_{5-n}]^{2-n}$  series and cisplatin were optimized in the gaseous and aqueous phases using the B3LYP<sup>54-57</sup> and BP86<sup>57-58</sup> functionals. The uranium and platinum atoms were described with the Stuttgart small-core (60 core electrons represented by a pseudopotential) RECP and associated valence basis sets while all other atoms were described with the 6-311++G\*\* basis set.<sup>59-61</sup> All g-functions in the valence basis associated with the Stuttgart pseudopotentials were removed. In addition, a set of diffuse f-type basis functions ( $\alpha = 0.005$ ) was added to allow for an accurate description of the lowest unoccupied molecular orbitals of the uranyl complexes. All the RECP calculations were carried out in the NWChem 5.1.1 package.<sup>62-63</sup> The aqueous phase calculations employed the conductor-like screening solvation model (COSMO)<sup>64-65</sup>. The atomic radii used in forming solvation cavities around the molecules in these calculations are 2.18, 1.72, 1.72 and 1.30 for the uranium, fluorine, oxygen and hydrogen atoms, respectively.

Also the ZORA relativistic approach<sup>49-51</sup> with triple- $\zeta$  polarized (TZP) all electron basis sets and the BP86 functional was used in optimizing the geometries of all the molecules. No core atomic orbitals were frozen. These ZORA-DFT calculations were carried out using the Amsterdam Density Functional (ADF 2009) package with an integration parameter of 6.0.<sup>66-68</sup> Multipole derived atomic charges, Mayer bond orders and Mulliken atomic charges were obtained from these all-electron calculations.<sup>69</sup> In ADF,<sup>70</sup> the aqueous phase calculations were carried out using the COSMO solvation model<sup>64-65</sup> and identical atomic radii to those used in the RECP calculations were employed. Modern approaches in theoretical calculations of actinide chemistry in the gaseous and aqueous phases have recently been reviewed.<sup>71</sup>

The starting configurations for the QM/MM simulations of  $[\text{UO}_2\text{F}_5]^{3-}$ ,  $[\text{Pt}(\text{CN})_6]^{2-}$  and cisplatin encapsulated in the hydrophobic cavities of the RHCC were generated using AutoDock.<sup>72</sup> The water clusters,  $(\text{H}_2\text{O})_n$  (where  $n=9, 5, 1$  and  $2$  for the largest, second-largest, third-largest and smallest cavities, respectively) in the cavities were evacuated prior to docking.<sup>5</sup> Ligand-optimized geometries and multipole-derived atomic charges obtained from the BP86-ZORA-TZP calculations were used in the docking. The van der Waals parameters used for the uranium atom were taken from the work of Guilbaud and Wipff.<sup>73</sup> The parameters used for platinum atoms when cisplatin was docked in the cavity were obtained from the work of Spiegel et al.<sup>74</sup> The hydrophobic cavities or binding sites for the ligands were determined from the amino acid sequence of the X-ray structure<sup>3</sup> and confirmed using various grids in AutoDock. The simulated annealing algorithm was used to generate structures, which were then clustered and ranked by their energies. Several initial temperatures for the annealing were tried in addition to using 25, 50 and 75 cooling runs.

The atoms of the RHCC protein and crystal waters were represented with the AMBER95 force field in the QM/MM calculations.<sup>52</sup> The QM/MM calculations were performed using the NWChem 5.1.1 and 6.0 codes.<sup>62-63</sup> There was no necessity for link atoms as there are no formal bonds between the embedded molecules and the cavity walls of the protein. DFT calculations using the BP86 functional as well as the Stuttgart small-core RECP for the uranium and platinum atoms and the 6-311++G\*\* basis for all other atoms were performed on the embedded molecules.<sup>61</sup> The cutoff for all non-bonded interactions was set at 15 Å. The ligands considered in this work are  $[\text{UO}_2\text{F}_5]^{3-}$  and cisplatin embedded in the protein hydrophobic cavities. Electrostatic coupling (polarization of the wave function of the QM region by the charges of neighboring MM atoms), Coulombic electrostatic and van der Waal (vdW) interactions of the protein and ligand atoms were included in the calculations. The geometry optimization procedure included sequential optimization of both the embedded ligands (QM) and the RHCC protein (MM) till energy convergence ( $5.0 \times 10^{-5}$  Hartree) was attained. The vibrational frequencies of the embedded ligands were also determined after the geometry optimization by numerical differentiation. All the MM atoms were held frozen during the finite-difference vibrational calculations.

## Results and Discussion

**$[\text{UO}_2\text{F}_n(\text{H}_2\text{O})_{5-n}]^{2-n}$  Complexes: Gaseous and Aqueous Phases.** The structural parameters and uranyl vibrational stretching frequencies of the  $[\text{UO}_2\text{F}_n(\text{H}_2\text{O})_{5-n}]^{2-n}$  compounds, Figure 7.2, obtained using DFT with the small-core RECP and the all-electron ZORA approaches are given in Table 7.1. Methodologically, the U=O bond lengths computed using the B3LYP hybrid functional are generally shorter than those obtained with the BP86 functional. This agrees with literature experience, Table 7.1.<sup>21, 75-77</sup> Also, given comparable basis set size and the same

density functional, nearly identical bond lengths and vibrational frequencies are obtained from the RECP and ZORA approaches, Table 7.1. This agrees with recent estimates that the bond lengths obtained with small-core RECPs agree with those obtained using a four component relativistic approach while the calculated vibrational wavenumbers are lower than the all-electron basis set results.<sup>21, 75</sup>

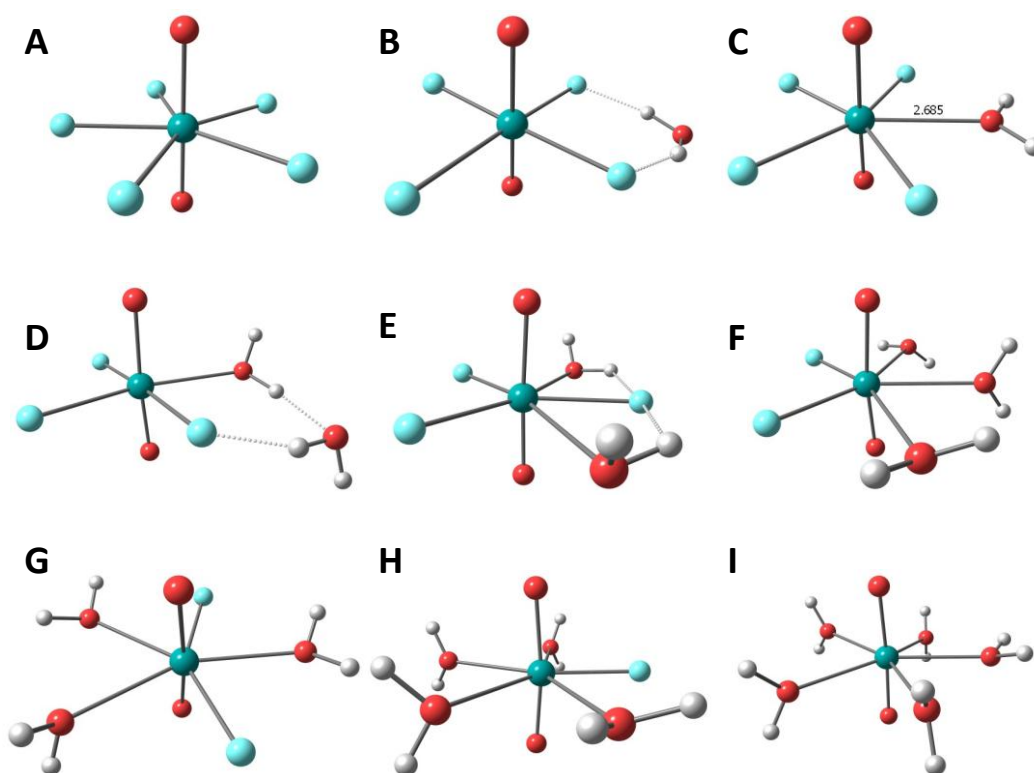


**Figure 7.2:** Aqueous Phase Structures of the  $[\text{UO}_2\text{F}_n(\text{H}_2\text{O})_{5-n}]^{2-n}$  Complexes Optimized at the BP86/TZP/ZORA/COSMO Level. A)  $[\text{UO}_2\text{F}_5]^{3-}$ , B)  $[\text{UO}_2(\text{H}_2\text{O})\text{F}_4]^{2-}$  Structure 1, C)  $[\text{UO}_2(\text{H}_2\text{O})\text{F}_4]^{2-}$  Structure 2 D)  $[\text{UO}_2(\text{H}_2\text{O})_2\text{F}_3]^{1-}$  Structure 1, E)  $[\text{UO}_2(\text{H}_2\text{O})_2\text{F}_3]^{1-}$  Structure 2 F)  $[\text{UO}_2(\text{H}_2\text{O})_3\text{F}_2]^0$  Structure 1, G)  $[\text{UO}_2(\text{H}_2\text{O})_3\text{F}_2]^0$  Structure 2 H)  $[\text{UO}_2(\text{H}_2\text{O})_4\text{F}]^{1+}$  and I)  $[\text{UO}_2(\text{H}_2\text{O})_5]^{2+}$ .

**Table 7.1a:** Calculated and experimental structural parameters of the  $[\text{UO}_2\text{F}_n(\text{H}_2\text{O})_{5-n}]^{2-n}$  complexes obtained at the RECP/BP86 level. The ADF/ZORA/BP86/TZP results values are given in parenthesis. The experimental data are from Reference <sup>24</sup>.

|  | $[\text{UO}_2(\text{H}_2\text{O})_5]^{2+}$ |                   |         |                   | $[\text{UO}_2(\text{H}_2\text{O})_5]^{2+} \cdot 5\text{H}_2\text{O}$ |              |         |              | Expt. <sup>b</sup> |
|--|--|-------------------|---------|-------------------|--|--------------|---------|--------------|--------------------|
|  | Gas  |                   | Aqueous |                   | Gas  |              | Aqueous |              |                    |
|  | B3LYP                                      | BP86 <sup>a</sup> | B3LYP   | BP86 <sup>a</sup> | B3LYP  | BP86         | B3LYP   | BP86         |                    |
| U=O  | 1.748                                      | 1.773 (1.772)     | 1.758   | 1.783(1.787)      | 1.759  | 1.789(1.789) | 1.768   | 1.800(1.797) | 1.76               |
| U-OH <sub>2</sub>                                  | 2.499                                      | 2.481(2.494)      | 2.469   | 2.458(2.450)      | 2.466  | 2.464(2.468) | 2.428   | 2.431(2.439) | 2.41               |
| v <sub>symm</sub>                                  | 927  | 864 (891)         | 898     | 840 (859)         | 899  | 843(867)     | 878     |              | 870                |
| v <sub>asymm</sub>                                 | 1015                                       | 958 (883)         | 960     | 911(922)          | 991  | 922(940)     | 939     |              | 965                |
| $[\text{UO}_2(\text{H}_2\text{O})_4\text{F}]^{1+}$ |  |                   |         |                   |  |              |         |              |                    |
|  | Gas  |                   | Aqueous |                   |  |              |         |              |                    |
|  | B3LYP                                      | BP86              | B3LYP   | BP86              |  |              |         |              |                    |
| U=O  | 1.771                                      | 1.795 (1.798)     | 1.776   | 1.802(1.807)      |  |              |         |              |                    |
| U-OH <sub>2</sub>                                  | 2.548                                      | 2.539(2.557)      | 2.515   | 2.510(2.510)      |  |              |         |              |                    |
| U-F  | 2.107                                      | 2.104(2.091)      | 2.146   | 2.134(2.128)      |  |              |         |              |                    |
| v <sub>symm</sub>                                  | 881  | 827(846)          | 863     | 808(825)          |  |              |         |              |                    |

| $v_{\text{asymm}}$   | 962   | 910(927)      | 917   | 869(877)      |  |               |                      |               |
|--|-------|---------------|-------|---------------|--|---------------|----------------------|---------------|
| [UO <sub>2</sub> (H <sub>2</sub> O) <sub>3</sub> F <sub>2</sub> ] <sup>0</sup> Structure 1 |       |               |       |               | [UO <sub>2</sub> (H <sub>2</sub> O) <sub>3</sub> F <sub>2</sub> ] <sup>0</sup> Structure 2 |               |                      |               |
| Gas  |       | Aqueous       |       |               | Gas <sup>c</sup>   |               | Aqueous <sup>c</sup> |               |
|  | B3LYP | BP86          | B3LYP | BP86          | B3LYP  | BP86 [2.5]    | B3LYP                | BP86 [0.02]   |
| U=O  | 1.785 | 1.814 (1.813) | 1.792 | 1.820 (1.826) | 1.783  | 1.809 (1.809) | 1.792                | 1.820 (1.825) |
| U-OH <sub>2</sub>  | 2.666 | 2.657 (2.663) | 2.652 | 2.579 (2.577) | 2.594  | 2.594 (2.605) | 2.559                | 2.562 (2.568) |
| U-F  | 2.157 | 2.150 (2.154) | 2.167 | 2.165 (2.160) | 2.180  | 2.170 (2.210) | 2.183                | 2.170 (2.164) |
| $v_{\text{symm}}$  | 851   | 798 (824)     | 831   | 779 (793)     | 856  | 806 (826)     | 831                  | 779 (793)     |
| $v_{\text{asymm}}$   | 928   | 876 (898)     | 881   | 831 (835)     | 935  | 886 (905)     | 879                  | 832 (838)     |

**Table 7.1b:** Calculated and experimental structural parameters of the  $[\text{UO}_2\text{F}_n(\text{H}_2\text{O})_{5-n}]^{2-n}$  complexes obtained at the RECP/BP86 level. The ADF/ZORA/BP86/TZP results values are given in parenthesis. The experimental data are from Reference <sup>24</sup>.

|                    | $[\text{UO}_2(\text{H}_2\text{O})_2\text{F}_3]^{1-}$ Structure 1 |               |         |               | $[\text{UO}_2(\text{H}_2\text{O})_2\text{F}_3]^{1-}$ Structure 2 |               |                      |               | Expt. |
|--------------------|--|---------------|---------|---------------|--|---------------|----------------------|---------------|-------|
|                    | Gas  |               | Aqueous |               | Gas <sup>c</sup>   |               | Aqueous <sup>c</sup> |               |       |
|                    | B3LYP  | BP86          | B3LYP   | BP86          | B3LYP,8.6  | BP86,9.4      | B3LYP,6.6            | BP86,6.9      |       |
| U=O                | 1.805  | 1.841 (1.842) | 1.803   | 1.834 (1.838) | 1.799  | 1.828 (1.828) | 1.807                | 1.832 (1.842) | 1.80  |
| U-OH <sub>2</sub>  | 2.620,   | 2.594,3.614   | 2.566,  | 2.588,4.033   | 2.776  | 2.804 (2.790) | 2.610                | 2.625 (2.625) | 2.47  |
|                    | 3.715  | (2.605,3.658) | 4.172   | (2.507,3.888) |  |               |                      |               |       |
| U-F                | 2.192  | 2.183 (2.183) | 2.215   | 2.196 (2.203) | 2.221  | 2.211 (2.219) | 2.221                | 2.226 (2.203) | 2.25  |
| $v_{\text{symm}}$  | 812  | 777 (783)     | 807     | 761 (777)     | 831  | 814 (822)     | 805                  | 761 (767)     |       |
| $v_{\text{asymm}}$ | 884  | 832 (869)     | 854     | 809 (814)     | 901  | 850 (853)     | 848                  | 809 (804)     |       |
|                    | $[\text{UO}_2(\text{H}_2\text{O})\text{F}_4]^{2-}$ Structure 1   |               |         |               | $[\text{UO}_2(\text{H}_2\text{O})\text{F}_4]^{2-}$ Structure 2   |               |                      |               |       |
|                    | Gas  |               | Aqueous |               | Gas <sup>c</sup>   |               | Aqueous <sup>c</sup> |               |       |
|                    | B3LYP  | BP86          | B3LYP   | BP86          | B3LYP,34.7   | BP86,35.1     | B3LYP,11.            | BP86 ,11.9    |       |
| U=O                | 1.820  | 1.850         | 1.819   | 1.850         | 1.824  | 1.856         | 1.824                | 1.857 (1.860) | 1.80  |
| U-OH <sub>2</sub>  | 4.022  | 4.003         | 3.958   | 3.917         | 2.710  | 2.701         | 2.672                | 2.685 (2.715) | 2.48  |

|                                |       |               |         |               |  |              |         |               |      |
|--------------------------------|-------|---------------|---------|---------------|--|--------------|---------|---------------|------|
| U-F                            | 2.250 | 2.240         | 2.230   | 2.220         | 2.260  | 2.270        | 2.250   | 2.244 (2.248) | 2.26 |
| $V_{\text{symm}}$              | 789   | 741 (757)     | 786     | 737 (755)     | 776  | 727          | 778     | 726 (740)     |      |
| $V_{\text{asymm}}$             | 861   | 815 (830)     | 825     | 778 (784)     | 845  | 794          | 814     | 765(771)      |      |
| $[\text{UO}_2\text{F}_5]^{3-}$ |       |               |         |               | $[\text{UO}_2\text{F}_5]^{3-} \cdot 5\text{H}_2\text{O}$ |              |         |               |      |
|                                | Gas   |               | Aqueous |               | Gas  |              | Aqueous |               |      |
|                                | B3LYP | BP86          | B3LYP   | BP86          | B3LYP  | BP86         | B3LYP   | BP86          |      |
| U=O                            | 1.842 | 1.878 (1.876) | 1.835   | 1.871 (1.874) | 1.804  | 1.832(1.831) | 1.811   | 1.837(1.840)  | 1.80 |
| U-F                            | 2.343 | 2.337 (2.338) | 2.300   | 2.294 (2.281) | 2.365  | 2.361(2.370) | 2.328   | 2.330(2.326)  | 2.26 |
| $V_{\text{symm}}$              | 740   | 688 (694)     | 757     | 705(716)      | 803  | 754(775)     | 799     | 751(764)      | 784  |
| $V_{\text{asymm}}$             | 806   | 752 (768)     | 790     | 739(745)      | 865  | 825(843)     | 836     | 788(808)      | 850  |

There is a gradual increase in the calculated U=O and U-F bond lengths as the number of fluoride ligands is increased down the  $[\text{UO}_2\text{F}_n(\text{H}_2\text{O})_{5-n}]^{2-n}$  series, Table 7.1. This is especially true for conformers in which the five ligands are in the first coordination sphere about the equatorial plane. The calculated Mayer bond orders of the U=O bonds in the complexes are presented in Table 7.2. Concomitant with the increasing U=O bond lengths, there is a decrease in the calculated U=O bond order as the number of fluoride ligands in the complexes is increased. This lengthening of the U=O bond is accompanied by a decrease in the calculated Mulliken charges on both the uranium atom and the uranyl group, Figure 7.3 and Table 7.2. Based on the calculated Mayer bond orders and atomic charges in the molecules, an additive-ionic Lewis base effect of multiple fluoride ligands could be used as an explanation for the increasing U-F bonds<sup>13</sup> even as such an approach can be used in explaining the increase in the U=O and U-OH<sub>2</sub> bond lengths.

The sequential-average ligand binding energies of the uranyl complexes provide an alternative way of examining the effect of greater number of fluoride ligands. The ligand binding energy,  $\Delta E_{\text{binding}}$ , to the uranyl moiety of a  $[\text{UO}_2\text{F}_n(\text{H}_2\text{O})_{5-n}]^{2-n}$  complex is given by  $E_{\text{complex}} - E_{\text{uranyl}} - nE_{\text{fluoride ion}} - (5-n)E_{\text{water}}$ . The difference between the ligand binding energies of successive members of the  $[\text{UO}_2\text{F}_n(\text{H}_2\text{O})_{5-n}]^{2-n}$  series represents the average energy required for the sequential replacement of an aquo ligand by a fluoride ion. The average ligand binding energies calculated for the  $[\text{UO}_2\text{F}_n(\text{H}_2\text{O})_{5-n}]^{2-n}$  complexes in solution increases as the number of fluoride ligands increases, Table 7.2. This is to be expected given the replacement of a neutral aquo ligand coordinated to the uranyl cation by an anionic fluoride ligand. However the calculated energies for introduction of a subsequent fluoride anion reduces from -43.8 kcal/mol

in the case of  $[\text{UO}_2(\text{H}_2\text{O})_5]^{2+}$  to 3.70 kcal/mol in the case of  $[\text{UO}_2(\text{H}_2\text{O})_4]^{1+}$ . Further examination Table 7.2 shows that the calculated successive ligand binding energies overestimate

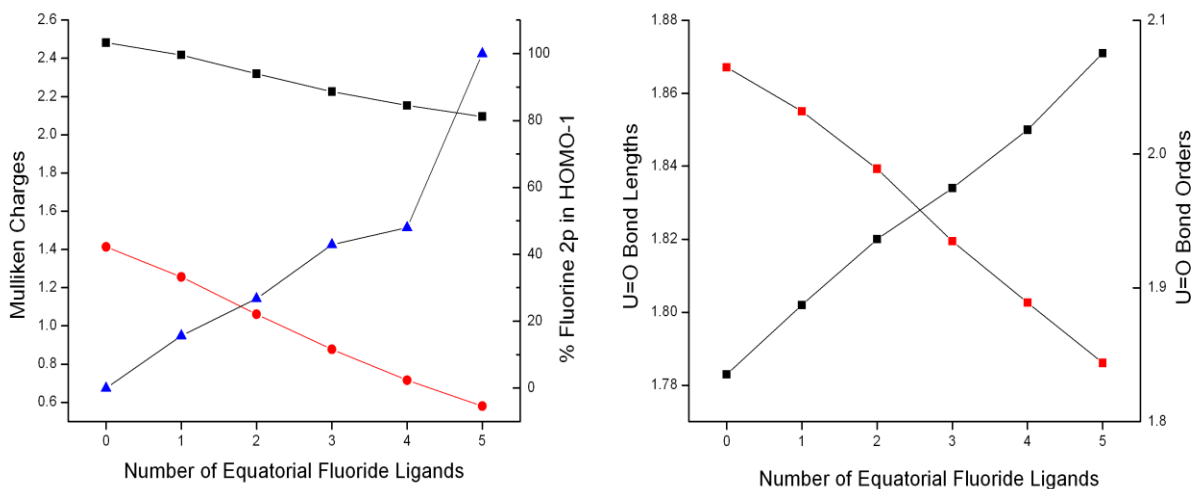


**Figure 7.3:** Left: Variation of the Mulliken Charges on the Uranium Atom (Black) and Uranyl Moiety (Red) and the Fluoro-2p Contribution to the HOMO-1 Orbital (Blue) with Increasing Number of Fluoride Ligands. Right: Variation of the U=O Bond Lengths (Black) and Bond Orders (Red) with Increasing Number of Fluoride Ligands.

the experimental values significantly, likely a result of the poor performance of the solvation model for calculating ligand binding and activation energies.<sup>12, 24, 78</sup> The use of extended second and third aquo-coordination spheres in addition to the implicit PCM model around the uranyl complexes would lead to improvements in the calculated ligand binding energies.<sup>79</sup>

Electronically, the first few virtual molecular orbitals in all the uranyl compounds are all of uranium 5f character, Figures 7.4a and 7.4b. This is generally expected for  $5f^0$  U(VI) complexes. The highest occupied orbitals (HOMO) are all uranyl based and are almost identical

**Table 7.2:** Aqueous phase calculated ligand binding energies in kcal/mol, Mayer bond orders for the U=O Bond and atomic Mulliken charges on uranium atoms in the  $UO_2F_n(H_2O)_{5-n}]^{2-n}$  complexes obtained at the ADF/ZORA/TZP/BP86/COSMO level.

| n              | Calculated Ligand B. E. <sup>b</sup> | Experimental Successive Ligand B. E. <sup>86</sup> | Mulliken Charges on Uranium Atom |         | U=O Mayer Bond Orders |         |
|----------------|--------------------------------------|--|----------------------------------|---------|-----------------------|---------|
|                |                                      |  | Gas                              | Aqueous | Gas                   | Aqueous |
| 0              | -95.8                                |  | 2.364                            | 2.482   | 2.150                 | 2.065   |
| 1              | -139.6 (-43.8)                       | -7.04  | 2.304                            | 2.418   | 2.105                 | 2.032   |
| 2              | -176.2 (-36.6)                       | -5.00  | 2.286                            | 2.330   | 2.060                 | 1.989   |
| 2 <sup>a</sup> | -176.0 (-36.4)                       |  | 2.321                            | 2.319   | 2.060                 | 1.982   |
| 3              | -205.2 (-29.0)                       | -2.82  | 2.215                            | 2.257   | 1.987                 | 1.935   |
| 3 <sup>a</sup> | -210.5 (-34.3)                       |  | 2.260                            | 2.275   | 2.000                 | 1.960   |
| 4              | -234.3 (-23.8)                       | -1.28  | 2.235                            | 2.241   | 1.944                 | 1.920   |
| 4 <sup>a</sup> | -222.9 (-17.8)                       |  | 2.200                            | 2.154   | 1.907                 | 1.889   |
| 5              | -230.6 (+3.70)                       | 1.00   | 2.094                            | 2.095   | 1.854                 | 1.844   |

<sup>a</sup> These are structures 2 for the species with n=2, 3 and 4 respectively, Figure 2 and text.

in all optimized structures of the  $[UO_2F_n(H_2O)_{5-n}]^{2-n}$  compounds. They are of  $\sigma$ -character with 5f atomic contribution from the uranium atom and 2p-contributions from the oxygen atoms of the uranyl group, Figures 7.4c and 7.4d. Contributions from the 6p-atomic orbitals of uranium are also

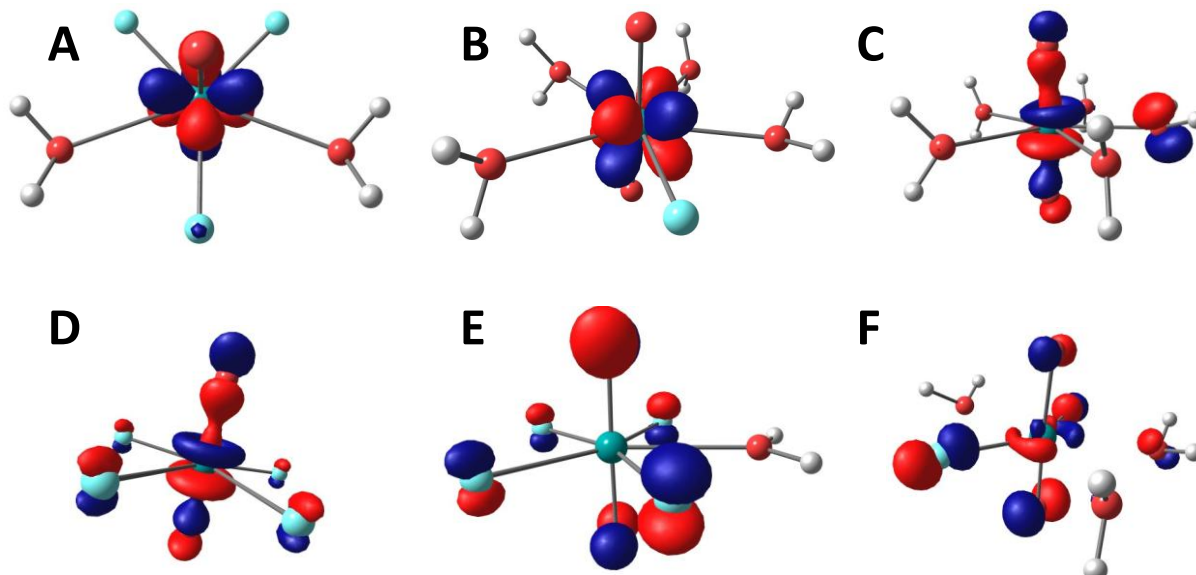


**Figure 7.4:** Selected Frontier Molecular Orbitals of  $[\text{UO}_2\text{F}_n(\text{H}_2\text{O})_{5-n}]^{2-n}$  Member Structures Optimized at the ADF/ZORA/BP86/TZP/COSMO Level: A) LUMO of  $[\text{UO}_2(\text{H}_2\text{O})_2\text{F}_3]^{1-}$  Structure 2 B) LUMO of  $[\text{UO}_2(\text{H}_2\text{O})_4\text{F}]^{1+}$  C) HOMO of  $[\text{UO}_2(\text{H}_2\text{O})_5]^{2+}$  D) HOMO of  $[\text{UO}_2\text{F}_5]^{3-}$ , E) HOMO-1 of  $[\text{UO}_2(\text{H}_2\text{O})\text{F}_4]^{2-}$  and F) HOMO-1 of  $[\text{UO}_2(\text{H}_2\text{O})_3\text{F}_2]^0$  Structure 2.

found in the HOMO  $\sigma$ -orbitals for these complexes. However, there are sometimes very minor contributions from the ligand 2p orbitals in a  $\pi$ -character to the HOMO in these complexes. The HOMO-1 to HOMO-4 orbitals in all the complexes are generally  $\pi$ -type orbitals formed from the 2p-type atomic orbitals of the equatorial ligands as well as in most cases 2p-orbital contributions from the uranyl oxo atoms in a  $\pi$ -bonding scheme. Contributions from the uranium 6p and 6d-orbitals to the HOMO to HOMO-4 orbitals are minor and amount to not more than 1.3% and 2.5% respectively. The increase in the number of fluoride ligands down the series can be observed in the evolution of the fluorine 2p contributions to the HOMO-1, Figure 7.3. There is

scant evidence for any form of  $\pi$ -competition between the uranyl oxo-atoms and the equatorial ligands. A more ionic Lewis base effect appears to be a more plausible explanation for the increase in U=O and U-F bond lengths with increasing number of fluoride ligands in the equatorial plane. In general, the HOMO-1 orbitals are similar in all the complexes except in  $[\text{UO}_2\text{F}_5]^{3-}$  and  $[\text{UO}_2(\text{H}_2\text{O})_5]^{2+}$  for which there are no contributions to their HOMO-1 orbitals from the uranyl oxo atoms, Figure 7.4.

Structurally, the  $[\text{UO}_2\text{F}_5]^{3-}$  complex belongs to the  $D_{5H}$  symmetry group in both the gas and aqueous phases (some slight loss in symmetry) in agreement with experimental solution<sup>24</sup> and solid state<sup>26</sup> observations. Optimization in solution results in a slight contraction of the U-F bonds by approximately 0.04 Å while having little effect on the U=O bonds. The calculated symmetric and asymmetric stretching vibrational frequencies of the uranyl group of  $[\text{UO}_2\text{F}_5]^{3-}$  deviate significantly from the experimental values.<sup>80-81</sup> The discrepancy is most likely due to the insufficient description of the aqueous environment around the ionic complex by the implicit COSMO solvation model used. Indeed, better agreement was obtained after inclusion of five water molecules in the second coordination sphere around the uranyl group, Table 7.1. The presence of a second coordination sphere with five water molecules results in the shortening of the U=O bond by 0.02-0.04 Å while causing an increase in the U-F bonds.

The U-OH<sub>2</sub> bonds of the optimized C1 structure of  $[\text{UO}_2(\text{H}_2\text{O})_5]^{2+}$  are generally of two types in aqueous solution: 4 water ligands arranged orthogonally to the equatorial plane and the last aquo ligand almost parallel to the equatorial plane. This orientation is only slightly more stable than the symmetrical  $D_5$  and  $D_{5H}$  structures. Electronically, the introduction of  $D_5$  and  $D_{5H}$  high symmetries alters the orbital ordering in the complex. The major effect of imposing the  $D_5$  and  $D_{5H}$  symmetries is a stabilization of the  $\sigma$ -type HOMO in the C1 structure relative to the  $\pi$ -

type HOMO-1. The calculated U=O and U-OH<sub>2</sub> bond lengths in the minimum structure are in good agreement with both experimental results and previous theoretical calculations.<sup>76, 82</sup> Although the O=U=O bond angles in this molecule are slightly bent by 0.0-4.0°, it should be noted that Perron *et al* have mentioned that the XANES data of [UO<sub>2</sub>(H<sub>2</sub>O)<sub>5</sub>]<sup>2+</sup> could actually be explained with O=U=O bond angles not less than 160 degrees.<sup>83</sup> Similar to [UO<sub>2</sub>F<sub>5</sub>]<sup>3-</sup>, Table 7.1, the addition of five water molecules in the second coordination sphere results in better agreement between the calculated and experimental uranyl stretching vibrational frequencies.

The addition of a second coordination sphere containing five water molecules to the structures of [UO<sub>2</sub>(H<sub>2</sub>O)<sub>5</sub>]<sup>2+</sup> and [UO<sub>2</sub>F<sub>5</sub>]<sup>3-</sup> not only results in greater agreement between the experimental and calculated vibrational frequencies, it allows the experimental range of the U=O bond lengths in the [UO<sub>2</sub>F<sub>n</sub>(H<sub>2</sub>O)<sub>5-n</sub>]<sup>2-n</sup> complexes to be accurately captured by the theoretical calculations, Table 7.1. The difference in the experimental U=O bond lengths of [UO<sub>2</sub>(H<sub>2</sub>O)<sub>5</sub>]<sup>2+</sup> and [UO<sub>2</sub>F<sub>5</sub>]<sup>3-</sup> is 0.04 Å in contrast to the 0.08-0.09 Å obtained using the COSMO solvation model but in full agreement with the 0.037-0.043 Å using a combination of the COSMO model with five water molecules in the second coordination sphere. This is particularly important given that recent experimental work has revealed little evidence for variation in the U=O bond lengths among the species in the [UO<sub>2</sub>F<sub>n</sub>(H<sub>2</sub>O)<sub>5-n</sub>]<sup>2-n</sup> series<sup>24</sup>.

The structure of the [UO<sub>2</sub>(H<sub>2</sub>O)<sub>4</sub>F]<sup>1+</sup> complex, Figure 7.2h, is a simple arrangement of the oxygen atoms of the four water ligands and the fluoride ion in the equatorial plane. The uranyl O=U=O angle in this complex ranges from 168.8° to 174.4° in the gaseous and aqueous phases. Comparison to [UO<sub>2</sub>(H<sub>2</sub>O)<sub>5</sub>]<sup>2+</sup> indicates a slight increase in the U=O (0.02 Å) and U-OH<sub>2</sub> (0.045 Å) bond lengths accompanied by a subsequent decrease in the vibrational wavenumbers of the U=O bond stretch. This increase in the U=O bond lengths (and also in the U-F bond lengths

down the series) is directly related to the decrease in the calculated charges on the uranium atom and the uranyl group, Figure 7.3. The electron-donating fluoride ligand leads to the decrease in charge on the actinide center resulting in weaker U-F bonds as more fluoride ligands are added with an added effect of some electrostatic repulsion with the uranyl oxo atoms and equatorial water ligands.<sup>13</sup>

There are many possible arrangements of the fluoro- and aquo-ligands in the complexes intermediate between  $[\text{UO}_2(\text{H}_2\text{O})_4\text{F}]^{1+}$  and  $[\text{UO}_2(\text{H}_2\text{O})_4\text{F}_2]^{2-}$ . For  $[\text{UO}_2(\text{H}_2\text{O})_3\text{F}_2]^0$ , only the structures in which all the aquo- and fluoro-ligands lie in the equatorial region were considered. Structure 1 (or cis-structure with neighboring fluoro-ligands), Figure 7.2f, was calculated to be approximately 3.4 and 1.6 kcal/mol less stable than structure 2 (or trans-structure with non-neighboring fluoro-ligands), Figure 7.2g, at the B3LYP/6-311++G\*\* level in the gas and aqueous phases respectively. The energy difference between these structural isomers is however 0.02 and 0.12 kcal/mol at the RECP-BP86 and ZORA-BP86 levels respectively in aqueous solution. The small magnitude of this energy difference might suggest co-existence or facile inter-convertibility. In addition, the calculated geometrical parameters and vibrational frequencies for both structures are identical especially in the aqueous phase. The only exception to this is a U-OH<sub>2</sub> bond in structure 1 which was calculated to be about 0.22 Å longer than all the U-OH<sub>2</sub> bonds in structure 2.

The structure corresponding to the alignment of three neighboring fluoro-ligands as well as one aquo ligand in the equatorial plane represents the most stable conformation of the  $[\text{UO}_2(\text{H}_2\text{O})_2\text{F}_3]^{1-}$  complex, Structure 1, Figure 7.2d. The other aquo ligand is at a long-distance of 3.57-4.17 Å from the uranium atom. This long distance representing an aquo-ligand outside the first coordination sphere was however not observed experimentally.<sup>24</sup> Structure 1 was calculated

to be approximately 6.6-9.4 kcal/mol more stable than the structure corresponding to two non-neighboring aquo ligands with the fluoro-ligands aligned in a triangular fashion at the equatorial plane, Structure 2, Figure 7.2e. The calculated U=O and U-F bond lengths for Structure 2 are in good agreement with experimental data in contrast to the U-OH<sub>2</sub> bonds which were calculated to be 0.14-0.16 Å longer than was experimentally observed.<sup>24</sup> It might be that addition of counter-ions further stabilizes Structure 2 enough to reach quantitative agreement with experimental observation.<sup>11</sup>

Computed local minimum structures for the [UO<sub>2</sub>(H<sub>2</sub>O)F<sub>4</sub>]<sup>2-</sup> complex have generally been structures with the water ligand at about 3.90-4.02 Å away from the uranium atom<sup>12</sup> (Structure 1, Figure 7.2b). However, experimental studies in crystal structures and solution have indicated the presence of a short U-OH<sub>2</sub> bond about 2.48 or 2.11 Å in length respectively.<sup>24, 81</sup> The C<sub>2v</sub> structure (Structure 2, Figure 7.2c) corresponding to this arrangement has two imaginary frequencies in both gas and continuum phase DFT calculations. Structure 2 was calculated to convert to structure 1 or to dissociate to [UO<sub>2</sub>F<sub>4</sub>]<sup>2-</sup> and an outgoing water molecule with conversion or dissociation energies of 10-13 and 5.4-6.3 kcal/mol respectively in aqueous solution, Table 7.1. Carr-Parrinello MD (CPMD) simulations by Bühl et al<sup>11</sup> have been used to show that the addition of two ammonium counter-ions stabilizes the ‘experimental’ geometry of structure 2 by about 2-4 kcal/mol thus possibly justifying the experimental observation.<sup>24, 81</sup> It would therefore appear that the inclusion of counter-ions according to Bühl et al in calculations on the [UO<sub>2</sub>(H<sub>2</sub>O)F<sub>4</sub>]<sup>2-</sup> complex is essential.<sup>11</sup>

**[UO<sub>2</sub>F<sub>5</sub>]<sup>3-</sup> Docked in the Cavities of the RHCC.** The terminal (N- and C-terminal or cavities one and four respectively) cavities of the RHCC protein are lined at the N-terminal and C-terminal ends by isoleucine residues. The intermediate cavities two and three are however

bounded at their N- and C-terminal ends by isoleucine and leucine residues respectively (7.1). These hydrophobic residues are oriented such that their side chains protrude into the axial channel of the protein, Figures 7.1 and 7.5. Eight residues from each monomer unit which are amino acids less hydrophobic than leucine and isoleucine form a ring around each cavity.<sup>5</sup> The cavities range in size from 140-280 Å<sup>3</sup> in the native protein and are occupied by water clusters. In this work, [UO<sub>2</sub>F<sub>5</sub>]<sup>3-</sup> and cisplatin were docked in these cavities and optimized using QM/MM. Only preliminary docking simulations were carried out for [Pt(CN)<sub>6</sub>]<sup>2-</sup>. [UO<sub>2</sub>F<sub>5</sub>]<sup>3-</sup> was used as a representative for the [UO<sub>2</sub>F<sub>n</sub>(H<sub>2</sub>O)<sub>5-n</sub>]<sup>2-n</sup> complexes due to the rigidity of the bonds between the uranyl group and the equatorial ligands and the resulting relative ease to dock in the hydrophobic cavities. This is in spite of the fact that [UO<sub>2</sub>F<sub>5</sub>]<sup>3-</sup> is formed only at high fluoride concentrations.<sup>24</sup> [UO<sub>2</sub>F<sub>5</sub>]<sup>3-</sup> can be thought of as a model system with the protein environment having similar structural and electronic effects on the other members of the pentaquo-fluoro series.

An infinite number of possible orientations of the uranyl group can be expected if [UO<sub>2</sub>F<sub>5</sub>]<sup>3-</sup> is embedded in a chemically uniform and spherical hydrophobic cavity. However, docking of this complex in all the RHCC cavities indicates the presence of two favored orientations of the uranyl group with respect to the axial channel. The uranyl group can only be oriented along the two axes perpendicular to the RHCC axis in all the hydrophobic cavities, Table 7.3. The equatorial fluoro ligands occupy the second axis orthogonal to the axial channel and no possible alignment of the O=U=O group along the RHCC axial channel was found.

The presence of these minima orientations of the embedded complex along axes orthogonal to the axial channel can be explained by two observations. Firstly, the cavities of the RHCC protein are chemically heterogeneous and roughly cylindrical cavities with isoleucine and

or leucine residues (ah-layer) pointing into the center of the helix while the backbone of the arginine and tyrosine residues (de-layer) form a ring bounding the cavity.<sup>5, 10</sup> The uranyl complex embedded in the cavities is always positioned closest to the isoleucine residues at the N-terminal end of the cavities except in cavity four, the C-terminal cavity, in which the complex is positioned nearest to the residues at the C-terminal end due to exposure to the aqueous environment. Maximum separation from the leucine residues at the C-terminal end of the cavities could be explained based on steric considerations. The leucine residues simply penetrate deeper into the axial channel affording lesser space for the embedded ligand. On the other hand, the isoleucine side chains at the N-terminal ends of the cavities are more ‘open’ and have greater access into the axial channel, Figure 7.1, and the aqueous environment in the case of cavity one, the N-terminal cavity.

Secondly, the side-chains of the isoleucine residues pointing into the axial channel from each monomer backbone form a cross-like space bounded at the four edges by the protein backbone, Figure 7.5. It is near this cross-like opening in the isoleucine residues partitioning the axial channel that the two possible arrangements of the uranyl moiety and the five equatorial fluoride ligands of the  $[\text{UO}_2\text{F}_5]^{3-}$  complex fit. Typical distances between the alkyl-hydrogen atoms of the isoleucine residues and the atoms of the  $[\text{UO}_2\text{F}_5]^{3-}$  complex ranged from 2.0 to 4.8 Å after the docking.

**QM/MM Calculations on  $[\text{UO}_2\text{F}_5]^{3-}$  Embedded in the RHCC Cavities.** Structurally, the  $D_{5h}$  symmetry of the  $[\text{UO}_2\text{F}_5]^{3-}$  complex is lifted and five different U-F bond lengths were observed after QM/MM optimization in all the cavities. For each cavity, the orientation with longer U-F bonds or shorter distance between its fluoro ligand and the hydrogen atoms of the isoleucine residues is less favorable energetically, Table 7.3. Electronically, there is some correspondence

between the U-F bond lengths and the calculated HOMO-LUMO gaps of the embedded ligands. After considering energy constraints and the calculated structural parameters, it can be concluded that there is a possibility of experimentally observing the two ligand orientations in only cavity two.

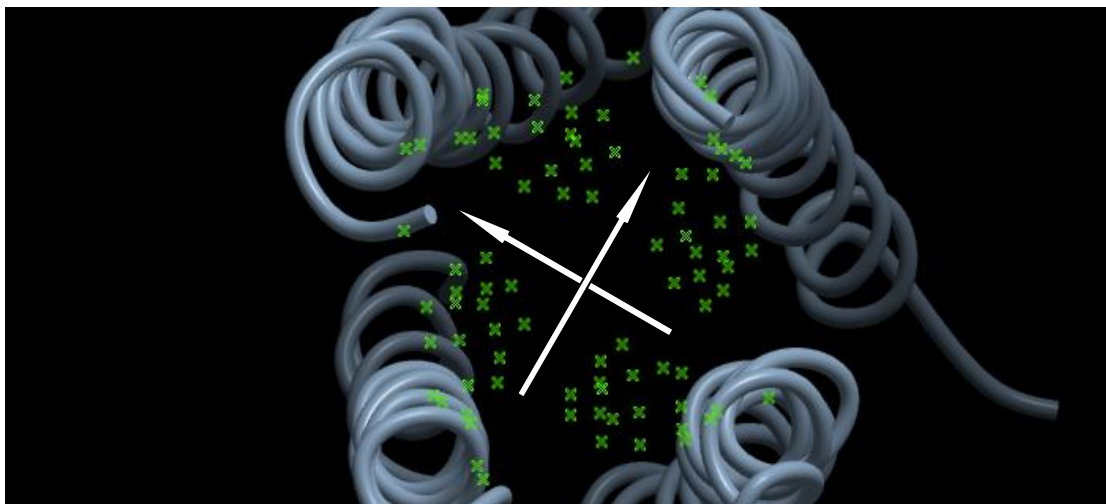


**Figure 7.5:** The Atoms of the Isoleucine Residues (Represented as Green Crosses) at the N-Terminal End of Cavity Two. The Protruding Side-Chains Form a Cross-Like Space into which the Uranyl Group and Equatorial Fluoride Ligands of  $[\text{UO}_2\text{F}_5]^{3-}$  are Embedded. The Two White Arrows Depict the two Possible Alignments of the Uranyl Moiety and the Equatorial Ligands.

The maximum energy difference between the two orientations in the four cavities obtained using the docking procedure,  $\Delta\Delta G_{\text{Docking}}$ , is 0.03 kcal/mol, Table 7.3. The orientations are therefore essentially iso-energetic and the magnitude of this energy barrier suggests that both orientations should be experimentally observed in all the cavities with a high probability of inter-conversion. However, the calculated energy barriers,<sup>84</sup>  $\Delta\Delta G_{\text{QM/MM}}$ , Table 7.3, indicate that the two orientations of the embedded QM/MM optimized  $[\text{UO}_2\text{F}_5]^{3-}$  complex should be observable only in cavity two, the largest cavity. Only in this cavity are they still iso-energetic, even at the

**Tables 7.3:** Calculated relative energies (kcal/mol), frontier gaps (eV) and structural features of the two orientations of the  $[\text{UO}_2\text{F}_5]^{3-}$  complex in the hydrophobic cavities of tetrabrachion.

| Cav.    | Allign. <sup>a</sup> | $\Delta\Delta\text{G}$<br>Docking <sup>b</sup> | $\Delta\Delta\text{G}$<br>QM/MM | Gap<br>(eV) | $\text{R}_{\text{U}=\text{O}}$<br>(Å) | $\text{R}_{\text{U}-\text{F}}$<br>(Å) | $\angle\text{UO}_2$<br>(°) |
|---------|----------------------|--|---------------------------------|-------------|---------------------------------------|---------------------------------------|----------------------------|
| 1       | a                    |  |                                 | 2.709       | 1.877-1.892                           | 2.272-2.372                           | 177.2                      |
|         | b                    | 0.00   | 10.12                           | 2.634       | 1.874-1.877                           | 2.273-2.420                           | 176.8                      |
| 2       | a                    |  |                                 | 2.677       | 1.865-1.876                           | 2.321-2.348                           | 179.2                      |
|         | b                    | 0.03   | 0.05                            | 2.702       | 1.878-1.894                           | 2.324-2.355                           | 178.9                      |
| 3       | a                    |  |                                 | 2.489       | 1.864-1.887                           | 2.266-2.391                           | 175.8                      |
|         | b                    | 0.03   | 5.77                            | 2.366       | 1.860-1.892                           | 2.260-2.405                           | 172.1                      |
| 4       | a                    |  |                                 | 2.794       | 1.877-1.909                           | 2.268-2.391                           | 177.9                      |
|         | b                    | 0.01   | 8.33                            | 2.793       | 1.854-1.866                           | 2.214-2.365                           | 177.5                      |
| Gas     |                      |  |                                 | 2.694       | 1.878                                 | 2.337                                 | 180.0                      |
| Aqueous |                      |  |                                 | 2.728       | 1.871                                 | 2.294                                 | 180.0                      |

<sup>a</sup> The two alignments of  $[\text{UO}_2\text{F}_5]^{3-}$  in the cavities are labeled 'a' and 'b' according to their relative energies. <sup>b</sup> The free energies,  $\Delta\Delta\text{G}$  are given as the difference,  $\Delta\text{G}_\text{A}-\Delta\text{G}_\text{B}$ .

QM/MM level. There is strong experimental evidence for the existence of the two orientations of uranyl fluoride in this cavity as found by the calculations.<sup>53</sup> The other cavities all have one high-energy conformation resulting in a low probability of experimental observation.

The calculation of the free energies associated with the replacement of the water clusters in the native RHCC cavities by the  $[\text{UO}_2\text{F}_5]^{3-}$  ligand is difficult and requires averaging over the configuration space of the protein-ligand system. This is particularly important as the water clusters move on much faster timescales than the uranyl complex. Using a few snapshots of the protein-ligand system in calculating the free energies associated with displacement of the native water clusters by  $[\text{UO}_2\text{F}_5]^{3-}$  may therefore be misleading. However intuitively, the exchange of the water clusters with uranyl fluorides would be expected to be exergonic.<sup>4-5</sup> The free energy associated with the displacement of the water clusters could be expected to be dominated by a large entropic contribution<sup>6</sup> even though the enthalpy contribution is expected to be slightly positive due to the transfer of the uranyl complex from the aqueous medium into a cavity surrounded by hydrophobic residues.

Both orientations in cavity one, the N-terminal cavity, have U=O and U-F bond lengths within 0.02 Å and 0.08 Å of the gas-phase structural parameters respectively, Table 7.3. An examination of the electronic structure of the embedded ligands reveals a reduction of the HOMO-LUMO gap by approximately 0.06 eV in the less energetically favored orientation. This orientation also has the larger U-F bond deformation and a greater change in the O=U=O bond angle.

The structural parameters of the embedded ligands in cavity two (the largest cavity) are essentially identical to those calculated for the gas-phase structure. The U=O and U-F bond

lengths are all within 0.03 Å of the calculated gas-phase values. In addition, the uranyl bond angles are within 1.2° of the gas-phase structures. The similarity of the ligands embedded in this cavity to the gas-phase complex is also reflected in the calculated uranyl stretching vibrational frequencies. Electronically, the HOMO-LUMO gaps and the description of the frontier orbitals for the ligand embedded in this cavity are similar (to within about 0.02 eV) to those calculated for the gas phase structure. The similarity of both uranyl conformations to the gas-phase structure is most likely due to the size of the cavity, the large size of the cavity allowing for minimal interaction with the hydrogen atoms of the isoleucine residues.

The effects of the RHCC framework on the geometries of the embedded ligands are more pronounced in cavity three than in the first two cavities. Deviations of the U=O and U-F bond lengths by 0.03 Å and 0.07 Å respectively from the gas-phase values were calculated in cavity three. The uranyl bond angle was decreased by 4.2 and 7.9° in the two possible orientations in this cavity. A significant decrease in the HOMO-LUMO gap by 0.21-0.33 eV was calculated in the ligands embedded in this cavity compared to the gas phase complex.

The less energetically favorable orientation in cavity four, the C-terminal cavity, has significant deformation of the U-F bonds by up to 0.12 Å. There is lesser deformation of the U-F bonds (0.02-0.07 Å) and longer U=O bonds in the more energetically accessible orientation, Table 7.3. The U=O bonds in both orientations are however within 0.03 Å of the gas-phase structure. In addition, the HOMO-LUMO gaps for both orientations of the ligand are similar and are about 0.1 eV larger than the gas-phase value.

**Other Ligands Embedded in the RHCC.** Due to the potential use of the cavities of this coiled-coil protein as a delivery vehicle for therapeutic molecules, we have also explored the enclosure

of a cisplatin molecule in cavity two of the RHCC. Unlike in the case of  $[\text{UO}_2\text{F}_5]^{3-}$ , docking and subsequent QM/MM calculations of cisplatin in this cavity indicate that there are more than two possible orientations with respect to the axial channel. Also, there is no preference for alignment or location towards the isoleucine residues at the N-terminal end of the cavity unlike the uranyl complex.

An explanation for this is the absence of a strong oxo- axial group that can preferentially anchor towards the isoleucine residues at the N-terminal end of the cavity. The chloro- and ammine ligands of cisplatin can therefore be oriented in a fairly large number of possible orientations with respect to the RHCC axis. The chemical nature of the ammine ligands also allows for interaction with the carbonyl groups of the cavity wall. On the other hand, preliminary docking of the hexacyano platinate complex,  $[\text{Pt}(\text{CN})_6]^{2-}$  in the largest cavity revealed only two orientations reminiscent of those observed for the uranyl complex. The presence of two favored orientations for  $[\text{UO}_2\text{F}_5]^{3-}$  and  $[\text{Pt}(\text{CN})_6]^{2-}$  in the protein cavities suggests that these alignments will exist for molecules with strong axial groups in an octahedral or pentagonal bipyramidal framework.

The calculated structural parameters for two randomly selected poses of cisplatin embedded in the largest cavity of the RHCC protein are compared to the calculated gas and aqueous-phase structures as well as the experimental crystal structure<sup>85</sup> in Table 7.4. Overall the optimized structures of these two poses are essentially similar to the gas phase structure even though there is a minute elongation of the Pt-Cl bond as well as contraction of the N-Pt-N bond angle. This is largely not surprising as very few water molecules actually penetrate the axial channel of the RHCC protein and cavity two is large enough to allow the molecule to exist in a ‘pseudo-gaseous’ state.

**Table 7.4:** Computed Structural Parameters Cisplatin in the Gaseous and Aqueous Phases and of Two Randomly Selected Orientations of Cisplatin Embedded in the Cavity Two (Largest Cavity) of the RHCC Protein Obtained Using RECPs.

| Parameter | Gaseous |       | Solution |       | Expt.* | Structure-1 | Structure-2 |
|-----------|---------|-------|----------|-------|--------|-------------|-------------|
|           | B3LYP   | BP86  | B3LYP    | BP86  |        | BP86        | BP86        |
| Pt-Cl     | 2.310   | 2.303 | 2.349    | 2.336 | 2.330  | 2.312       | 2.314       |
| Pt-N      | 2.104   | 2.092 | 2.079    | 2.068 | 2.010  | 2.099       | 2.101       |
| N-Pt-N    | 98.19   | 99.27 | 92.22    | 92.99 | 87.0   | 98.81       | 98.26       |
| Cl-Pt-Cl  | 95.54   | 95.78 | 93.92    | 94.10 | 91.9   | 95.53       | 95.63       |

\* Crystal Structure from Reference <sup>82</sup>.

## Conclusions

A systematic study of pentacoordinated aquo and fluoro uranyl complexes has been carried out using two different relativistic methods, the relativistic effective core potentials and ZORA with all electron basis set, in conjunction with the B3LYP and BP86 density functionals. The effects of an aqueous medium on the geometrical structure, ligand binding energies and electronic structure were investigated using the COSMO solvation model as well as an explicit second coordination sphere. The conformational alignments, electronic structures and geometrical parameters of  $[\text{UO}_2\text{F}_5]^{3-}$  and cisplatin embedded in the hydrophobic cavities of the tetrabrachion coiled coil have been determined with the hybrid QM/MM approach. The studies of cisplatin and  $[\text{UO}_2\text{F}_5]^{3-}$  inside the hydrophobic cavities were motivated by a need for insight

into therapeutic usage of the protein in drug delivery and structural or conformational alignment reasons, respectively.

The inclusion of solvation effects using the COSMO model generally leads to only slight increases in the U=O bonds lengths in contrast to a contraction of the U-F bonds. This effect is associated with decreases in the uranyl stretching vibrational frequencies. The calculated U=O bond lengths increase as the number of fluoride ligands are increased in both the gas and aqueous phases. The range of the U=O bond lengths from  $[\text{UO}_2(\text{H}_2\text{O})_5]^{2+}$  to  $[\text{UO}_2\text{F}_5]^{3-}$  is however only accurately captured after the inclusion of five water molecules in the second coordination sphere. The inclusion of water molecules in the second coordination sphere also results in better agreement between the calculated and experimental uranyl vibrational frequencies.

Although, the docking procedure used in this contribution indicates the presence of two favored orientations of the  $[\text{UO}_2\text{F}_5]^{3-}$  complex in all four hydrophobic cavities of the tetrabrachion coiled-coil protein, the calculated relative free energies of embedded complexes optimized at the QM/MM level however reveal that both orientations can only be experimentally observed in cavity two, the largest cavity. There is strong experimental evidence for these orientations as found by the calculations.<sup>53</sup> In the other three cavities, only one conformation is energetically accessible. The two possible orientations of the uranyl complexes in the protein cavities are along the two axes perpendicular to the protein channel axis. There is no possible orientation of the embedded ligands along the channel axis. The uranyl pentafluoride is generally associated with the isoleucine residues at the N-terminus end of the protein cavities. This is due to a combination of steric effects and interaction with the alkyl side chains of the isoleucine residues. The presence of two ordered orientations of the uranyl complexes in the hydrophobic cavities is not unique. Docking of the hexacoordinated  $[\text{Pt}(\text{CN})_6]^{2-}$  complex also reveals a similar

structure in cavity two of the protein. On the other hand, the anticancer drug, cisplatin, shows no preferred orientations in the protein cavities.

In general, there is little change in the U=O bond lengths upon embedding of the complexes, with a maximum change of 0.03 Å from the gas phase value of 1.878 Å at the BP86/RECP level. The largest structural changes are seen in the U-F bonds and O=U=O bond angles. An examination of the structural features, HOMO-LUMO gaps and uranyl stretching vibrational frequencies of the uranyl complexes embedded in cavity two reveal great similarity to the gas phase structure.

## References

1. Burkhard, P.; Stetefeld, J.; Strelkov, S. V., *Trends Cell Biol.* **2001**, *11*, 82.
2. Eriksson, M.; Hassan, S.; Larsson, R.; Linder, S.; Ramqvist, T.; Lovborg, H.; Vikinge, T.; Figgemeier, E.; Muller, J.; Stetefeld, J.; Dalianis, T.; Ozbek, S., *Anticancer Res.* **2009**, *29*, 11.
3. <http://www.pdb.org/pdb/explore/explore.do?structureId=1FE6>.
4. Ozbek, S.; Muller, J. F.; Figgemeier, E.; Stetefeld, J., *Acta Crystallogr. D.* **2005**, *61*, 477.
5. Stetefeld, J.; Jenny, M.; Schulthess, T.; Landwehr, R.; Engel, J.; Kammerer, R. A., *Nat. Struct. Biol.* **2000**, *7*, 772.
6. Yin, H.; Hummer, G.; Rasaiah, J. C., *J. Am. Chem. Soc.* **2007**, *129*, 7369.
7. Yin, H.; Hummer, G.; Rasaiah, J. C., *JACS* **2007**, *129*, 7369.
8. McFarlane, A. A.; Orriss, G. L.; Stetefeld, J., *Eur. J. Pharmacol.* **2009**, *625*, 101.
9. Ozbek, S.; Muller, J. F.; Figgemeier, E.; Stetefeld, J., *Acta Crystallogr., Sect. D: Biol. Crystallogr.* **2005**, *61*, 477.

10. Stetefeld, J.; Jenny, M.; Schulthess, T.; Landwehr, R.; Engel, J.; Kammerer, R. A., *Nat. Struct. Biol.* **2000**, *7*, 772.
11. Bühl, M.; Schreckenbach, G.; Sieffert, N.; Wipff, G., *Inorg. Chem.* **2009**, *48*, 9977.
12. Bühl, M.; Sieffert, N.; Wipff, G., *Chem. Phys. Lett.* **2009**, *467*, 287.
13. Gaillard, C.; El Azzi, A.; Billard, I.; Bolvin, H.; Hennig, C., *Inorg. Chem.* **2005**, *44*, 852.
14. Garcia-Hernandez, M.; Willnauer, C.; Krüger, S.; Moskaleva, L. V.; Rösch, N., *Inorg. Chem.* **2006**, *45*, 1356.
15. Infante, I.; Van Stralen, B.; Visscher, L., *J. Comput. Chem* **2006**, *27*, 1156.
16. Infante, I.; Visscher, L., *J. Comput. Chem* **2004**, *25*, 386.
17. Macak, P.; Tsushima, S.; Wahlgren, U.; Grenthe, I., *Dalton T.* **2006**, 3638.
18. Paez-Hernandez, D.; Ramirez-Tagle, R.; Codorniu-Hernandez, E.; Montero-Cabrera, L. A.; Arratia-Perez, R., *Polyhedron* **2010**, *29*, 975.
19. Schreckenbach, G., *Inorg. Chem.* **2002**, *41*, 6560.
20. Schreckenbach, G.; Hay, P. J.; Martin, R. L., *J. Comput. Chem* **1999**, *20*, 70.
21. Shamov, G. A.; Schreckenbach, G.; Vo, T. N., *Chem-Eur. J.* **2007**, *13*, 4932.
22. Straka, M.; Dyall, K. G.; Pyykkö, P., *Theor. Chem. Acc.* **2001**, *106*, 393.
23. Straka, M.; Kaupp, M., *Chem. Phys.* **2005**, *311*, 45.
24. Vallet, V.; Wahlgren, U.; Schimmelpfennig, B.; Moll, H.; Szabo, Z.; Grenthe, I., *Inorg. Chem.* **2001**, *40*, 3516.
25. Wang, Q.; Pitzer, R. M., *J. Phys. Chem. A.* **2001**, *105*, 8370.
26. Zachariasen, W. H., *Acta Crystallogr.* **1954**, *7*, 783.
27. Cramer, C. J., *Essentials of Computational Chemistry: Theories and Models*. 2nd ed.; John Wiley & Sons Ltd: West Sussex, 2004; p 17.

28. Eichinger, M.; Tavan, P.; Hutter, J.; Parrinello, M., *J. Chem. Phys.* **1999**, *110*, 10452.
29. Field, M. J., *J. Comput. Chem* **2002**, *23*, 48.
30. Friesner, R. A.; Guallar, V., *Ann. Rev. Phys. Chem.* **2005**, *56*, 389.
31. Hu, H.; Elstner, M.; Hermans, J., *Proteins* **2003**, *50*, 451.
32. Lin, H.; Truhlar, D. G., *Theor. Chem. Acc.* **2007**, *117*, 185.
33. Murphy, R. B.; Philipp, D. M.; Friesner, R. A., *J. Comput. Chem* **2000**, *21*, 1442.
34. Schoneboom, J. C.; Lin, H.; Reuter, N.; Thiel, W.; Cohen, S.; Ogliaro, F.; Shaik, S., *J. Am. Chem. Soc.* **2002**, *124*, 8142.
35. Senn, H. M.; Thiel, W., QM/MM methods for biological systems. In *Atomistic Approaches in Modern Biology: From Quantum Chemistry to Molecular Simulations*, 2007; Vol. 268, pp 173.
36. Sherwood, P.; de Vries, A. H.; Guest, M. F.; Schreckenbach, G.; Catlow, C. R. A.; French, S. A.; Sokol, A. A.; Bromley, S. T.; Thiel, W.; Turner, A. J.; Billeter, S.; Terstegen, F.; Thiel, S.; Kendrick, J.; Rogers, S. C.; Casci, J.; Watson, M.; King, F.; Karlsen, E.; Sjovoll, M.; Fahmi, A.; Schafer, A.; Lennartz, C., *J. Mol. Struc-Theochem.* **2003**, *632*, 1.
37. Vreven, T.; Morokuma, K.; Farkas, O.; Schlegel, H. B.; Frisch, M. J., *J. Comput. Chem* **2003**, *24*, 760.
38. Warshel, A., *Ann. Rev. Bioph. Biom.* **2003**, *32*, 425.
39. Woo, T. K.; Cavallo, L.; Ziegler, T., *Theor. Chem. Acc.* **1998**, *100*, 307.
40. Warshel, A.; Levitt, M., *J. Mol Biol.* **1976**, *103*, 227.
41. Singh, U. C.; Kollman, P. A., *J. Comput. Chem* **1986**, *7*, 718.
42. Valiev, M.; Yang, J.; Adams, J. A.; S., T. S.; Weare, J. H., *J. Phys. Chem. B* **2007**, *111*, 13455.

43. Friesner, R. A.; Guallar, V., *Annu. Rev. Phys. Chem.* **2005**, *56*, 389.
44. Sauer, J.; Sierka, M., *J. Comput. Chem.* **2000**, *21*, 1470.
45. Senn, H. M.; Thiel, W., *Atomistic Approaches in Modern Biology: From Quantum Chemistry to Molecular Simulations* **2007**, *268*, 173.
46. Shurki, A.; Warshel, A., *Protein Simulations* **2003**, *66*, 249.
47. Infante, I.; Van Stralen, B.; Visscher, L., *J. Comput. Chem.* **2006**, *27*, 1156.
48. Infante, I.; Visscher, L., *J. Comput. Chem.* **2004**, *25*, 386.
49. Faas, S.; Snijders, J. G.; van Lenthe, J. H.; van Lenthe, E.; Baerends, E. J., *Chem. Phys. Lett.* **1995**, *246*, 632.
50. van Lenthe, E., *J. Comp. Chem.* **1999**, *20*, 51.
51. van Lenthe, E.; Baerends, E. J.; Snijders, J. G., *J. Chem. Phys.* **1993**, *99*, 4597.
52. Cornell, W. D.; Cieplak, P.; Bayly, C. I.; Gould, I. R.; Merz, K. M.; Ferguson, D. M.; Spellmeyer, D. C.; Fox, T.; Caldwell, J. W.; Kollman, P. A., *J. Am. Chem. Soc.* **1995**, *117*, 5179.
53. Stetefeld, J.; Meier, M., *Unpublished Results*.
54. Stephens, P. J.; Devlin, F. J.; Chabalowski, C. F.; Frisch, M. J., *J. Phys. Chem.* **1994**, *98*, 11623.
55. Becke, A. D., *J. Chem. Phys.* **1993**, *98*, 5648.
56. Lee, C. T.; Yang, W. T.; Parr, R. G., *Phys. Rev. B* **1988**, *37*, 785.
57. Becke, A. D., *Phys. Rev. A* **1988**, *38*, 3098.
58. Perdew, J. P., *Phys. Rev. B* **1986**, *33*, 8822.
59. Küchle, W.; Dolg, M.; Stoll, H.; Preuss, H., *J. Chem. Phys.* **1994**, *100*, 7535.
60. Cao, X. Y.; Moritz, A.; Dolg, M., *Chem. Phys.* **2008**, *343*, 250.
61. <http://www.theochem.uni-stuttgart.de/pseudopotentials/clickpse.en.html>.

62. Bylaska, E. J. d. J., W. A.; Govind N.; Kowalski K.; Straatsma, T. P.; Valiev, M.; Wang, D.; Apra, E.; Windus, T. L.; Hammond, J.; Nichols, P.; Hirata, S.; Hackler, M. T.; Zhao, Y.; Fan, P. -D.; Harrison, R. J.; Dupuis, M.; Smith, D. M. A.; Nieplocha, J.; Tipparaju, V.; Krishnan, M.; Wu, Q.; Van Voorhis, T.; Auer, A. A.; Nooijen, M.; Brown, E.; Cisneros, G.; Fann, G. I.; Fruchtl, H.; Garza, J.; Hirao, K.; Kendall, R.; Nichols, J. A.; Tsemekhman, K.; Wolinski, K.; Anchell, J.; Bernholdt, D.; Borowski, P.; Clark, T.; Clerc, D.; Dachsel, H.; Deegan, M.; Dyall, K.; Elwood, D.; Glendening, E.; Gutowski, M.; Hess, A.; Jaffe, J.; Johnson, B.; Ju, J.; Kobayashi, R.; Kutteh, R.; Lin, Z.; Littlefield, R.; Long, X.; Meng, B.; Nakajima, T.; Niu, S.; Pollack, L.; Rosing, M.; Sandrone, G.; Stave, M.; Taylor, H.; Thomas, G.; van Lenthe, J.; Wong, A.; and Zhang, Z. NWChem, A Computational Chemistry Package for Parallel Computers, Version 5.1". 2007.
63. Valiev, V.; Bylaska, E. J.; Govind, N.; Kowalski, K.; Straatsma, T. P.; van Dam, H. J. J.; Wang, D.; Nieplocha, J.; Apra, E.; Windus, T. L.; de Jong, W. A., *Comput. Phys. Commun.* **2010**, *181*, 1477.
64. Klamt, A., *J. Phys. Chem.* **1995**, *99*, 2224.
65. Klamt, A.; Schuurmann, G., *J. Chem. Soc. Perk T. 2* **1993**, 799.
66. te Velde, G.; Bickelhaupt, F. M.; van Gisbergen, S. J. A.; Fonseca Guerra, C.; Baerends, E. J.; Snijders, J. G.; Ziegler, T., *J. Comput. Chem.* **2001**, *22*, 931.
67. Fonseca Guerra, C.; Snijders, J. G.; te Velde, G.; Baerends, E. J., *Theor. Chem. Acc.* **1998**, *99*, 391.
68. ADF2007.01, Theoretical Chemistry, Vrije Universiteit, Amsterdam, The Netherlands, <http://www.scm.com>.
69. Swart, M.; van Duijnen, P. T.; Snijders, J. G., *J Comput Chem* **2001**, *22*, 79.

70. Pye, C. C.; Ziegler, T., *Theor. Chem. Acc.* **1999**, *101*, 396.
71. Schreckenbach, G.; Shamov, G. A., *Accounts Chem. Res.* **2009**, in print  
10.1021/ar800271r.
72. Goodsell, D. S.; Morris, G. M.; Olson, A. J., *J. Mol. Recognit.* **1996**, *9*, 1.
73. Guilbaud, P.; Wipff, G., *J. Mol. Struct. THEOCHEM* **1996**, *366*, 55.
74. Spiegel, K.; Rothlisberger, U.; Carloni, P., *J. Phys. Chem. B* **2004**, *108*, 2699.
75. Odoh, S. O.; Schreckenbach, G., *J. Phys. Chem. A* **2010**, *114*, 1957.
76. Shamov, G. A.; Schreckenbach, G., *J. Phys. Chem. A* **2005**, *109*, 10961.
77. Schultz, N. E.; Zhao, Y.; Truhlar, D. G., *J. Phys. Chem. A* **2005**, *109*, 4388.
78. Vallet, V.; Wahlgren, U.; Szabo, Z.; Grenthe, I., *Inorg. Chem.* **2002**, *41*, 5626.
79. Vallet, V.; Wahlgren, U.; Grenthe, I., *J. Am. Chem. Soc.* **2003**, *125*, 14941.
80. Flint, C. D.; Tanner, P. A., *Mol. Phys.* **1981**, *43*, 933.
81. Mak, T. C. W.; Yip, W. H., *Inorg. Chim. Acta* **1985**, *109*, 131.
82. Jones, L. H.; Penneman, R. A., *J. Chem. Phys.* **1953**, *21*, 542.
83. Perron, H.; Roques, J.; Domain, C.; Drot, R.; Simoni, E.; Catalette, H., *Inorg. Chem.* **2008**, *47*, 10991.
84. Valiev, M.; Garrett, B. C.; Tsai, M. K.; Kowalski, K.; Kathmann, S. M.; Schenter, G. K.; Dupuis, M., *J. Chem. Phys.* **2007**, *127*.
85. Milburn, G. H. W.; Truter, M. R., *J. Chem. Soc. A* **1966**, *1*, 1609.
86. Guillaumont, R.; Fanghänel, T.; Grenthe, I.; Neck, V.; Palmer, D. A.; Rand, M. H., *Update on the Chemical Thermodynamics of Uranium, Neptunium, Plutonium, Americium and Technetium*, . Elsevier: Amsterdam, 2003; Vol. 5, p 970.

## Preface to Chapter 8

This chapter is based on two manuscripts. The full citations of these manuscripts are:

- 1) P. L. Arnold, G. M. Jones, **S. O. Odoh**, G. Schreckenbach and J. B. Love. “Strongly coupled binuclear uranium-oxo complexes from uranyl oxo rearrangement and reductive silylation”. *Nature Chemistry*, **2012**, 4, 221.
- 2) P. L. Arnold, E. Holis, J. B. Love, N. Magnani, E. Colineau, R. Caciuffo, N. Edelstein, L. Castro, A. Yahia, L. Maron, **S. O. Odoh** and G. Schreckenbach.. “Oxo-Functionalization and Reduction of the Uranyl Ion through Lanthanide-Element Bond Homolysis; Synthetic, Structural, and Bonding Analysis of a Series of Singly Reduced Uranyl - Rare Earth 5f<sup>1</sup>-4f<sup>n</sup> Complexes”. **2012**, to be submitted.

In this chapter, the results of our theoretical calculations on two types of complexes synthesized and characterized by our experimental collaborators are presented. In the first manuscript, a bis-oxo-silyl uranium (V) complex with a butterfly shaped U<sub>2</sub>O<sub>4</sub> core was characterized. This novel U<sub>2</sub>O<sub>4</sub> core is unique as a result of the fact that one of the UO<sub>2</sub> groups was transformed from the traditionally linear format (as found in the starting material) into a bent/cis orientation. In contrast, in the second manuscript two complexes with U<sub>2</sub>O<sub>4</sub> cores in which the UO<sub>2</sub> groups interact by side-on cation-cation interactions were characterized. The two classes of complexes studied in this work are stable U(V)/U(V) bi-nuclear complexes in which reduction from the hexavalent state was achieved either by oxo-silylation (in the case of the butterfly-shaped complex) and oxo-metallation by transition metals (in the case of the side-on cation-cation complexes).

In the first manuscript, all theoretical DFT calculations of the structure and electronic properties of the bis-nuclear butterfly-type complex were carried out by Samuel O. Odoh. The second manuscript contains two sets of calculations: a) a B3LYP/RECP approach was employed by the Maron group from France and b) the all-electron approach with the PBE functional was used in the calculations carried out by me as part of the contributions from the Schreckenbach group in Manitoba, Canada.

Although this chapter is based on our contributions to the two manuscripts, it has been completely re-written to emphasize our contributions. Our studies of the two types of complexes were deliberately collated in one chapter due to the similarity of a U(V)/U(V) framework as well as reduction from the hexavalent to pentavalent state facilitated by oxo-functionalization.

Copyright permissions have been obtained from the publishers of this article and from all the other authors. Polly L. Arnold, Emmalina Hollis, G.M. Jones, Gary S. Nichols and Jason B. Love are affiliated with the School of Chemistry, University of Edinburgh, Edinburgh, United Kingdom. Jean-Christophe Griveau, Roberto Caciuffo are affiliated with the European Commission, Joint research centre, Institute for Transuranium Elements, Karlsruhe, Germany. Nicola Magnani and Norman Edelstein are affiliated with the Lawrence Berkeley National Laboratory, Berkeley, U.S.A. Laurent Maron, Ludovic Castro and Ahmed Yahia are affiliated with the University of Toulouse, Toulouse, France.

# Chapter 8: Bis-Uranium (V) Dioxo Complexes formed after Oxo-functionalization of Uranyl Axial Oxo Atoms

## Abstract

Bis-uranium (V) dioxo complexes of the Pacman-type macrocycle have been characterized using scalar relativistic density functional theory. The class of bimetallic complexes studied included cases in which the  $U_2O_4$  unit is aggregated in either a butterfly-shaped fashion or via cation-cation interactions between the pentavalent uranyl groups in a diamond-shaped motif. The axial oxo atoms of the butterfly-shaped moiety are functionalized by silyl groups while transition metals, yttrium and samarium, were used in reductively functionalization of the axial oxo atoms in the diamond-shaped complexes. The formation of the butterfly-shaped motif most likely proceeds via a pentavalent intermediate rather than via a hexavalent complex. For the complexes with a diamond-shaped motif, the calculated structural parameters agree well with the experimental data. Accurate prediction of the energetic ordering of the low-lying electronic states in these complexes appear to be problematic for the methods used in this study.

## Introduction

There has been a significant resurgence in the synthesis and characterization of various uranium complexes with organic ligands such as macrocycles and expanded porphyrins.<sup>1-11</sup> The pentavalent state of the uranyl moiety is however difficult to isolate and characterize in an aqueous environment due to its susceptibility to disproportionation and oxidation. Ikeda and co-workers used a spectro-electrochemical approach to study uranyl pentavalent complexes by

electrochemically reducing hexavalent complexes.<sup>12-16</sup> The properties of the quasi-stable pentavalent complexes produced in the optically transparent electrochemical cell were then measured using spectroscopic approaches such as nuclear magnetic resonance (NMR)<sup>13</sup>, infrared (IR)<sup>15</sup> and extended X-ray absorption fine structure (EXAFS)<sup>12</sup>. The capability to synthesize and isolate pentavalent UO<sub>2</sub> complexes has increased greatly since the isolation of a pentavalent uranyl triphenyl phosphine oxide cation with a triflate anion pair by Berthet et al.<sup>17</sup> More recently, an approach involving reductive oxo-functionalization of the oxo- atoms of UO<sub>2</sub><sup>2+</sup> complexes has been used by a number of workers.<sup>3, 18-21</sup> Complexes in which one or both oxo- atoms of the uranyl have been functionalized with strong Lewis acids such as silyl groups<sup>19-20</sup>, hydrogen atoms<sup>20</sup> and B(C<sub>6</sub>F<sub>5</sub>)<sub>3</sub><sup>22</sup> have all been reported.

Discrete complexes in which an oxo- atom(s) of a uranyl group interacts with the uranium atom of another uranyl group have also been synthesized.<sup>6, 23-27</sup> Cation-cation complexes involving uranyl-uranyl interactions constitute a significant fraction of kinetically stable pentavalent uranyl complexes.<sup>3</sup> There are generally two structural motifs for cation-cation interactions in multinuclear uranyl complexes, the diamond motif in which the two uranyl groups are in (nearly) parallel arrangement<sup>22</sup> and the aptly named T- shaped motif, in which the uranyl groups are (nearly) perpendicular, Figure 8.1. An example of note is the tetrameric cation-cation complex reported by Burdet et al.<sup>23</sup> The adjacent uranyl groups interact through a T-shaped cation-cation motif, Figure 8.1.

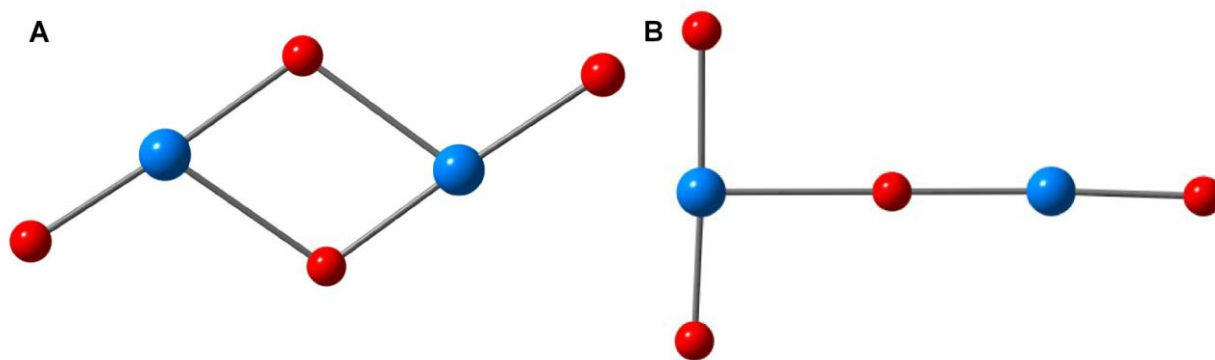


**Figure 8.1:** Two common motifs for cation-cation interactions (CCI) between uranyl groups. (A) The diamond motif in which the UO<sub>2</sub> groups are arranged in a parallel fashion. (B) The T-shaped motif in which an oxo-atom of one uranyl group interacts with the uranium atom of a neighboring uranyl group. All oxygen, uranium and carbon atoms in this work are depicted as red, blue and grey colors respectively.

In the first part of this chapter the structural and electronic properties of a recently synthesized and characterized complex, **1**, Figure 8.2, featuring a butterfly-shaped U<sub>2</sub>O<sub>4</sub> motif is presented.<sup>28</sup> The butterfly-shaped U<sub>2</sub>O<sub>4</sub> motif is different from the common uranyl-uranyl CCI motifs shown in Figure 8.1. In this complex, the U<sub>2</sub>O<sub>4</sub> core is encased in a Pacman-type, H<sub>4</sub>L ligand, Figure 8.2 with the two *exo*-oxo atoms reductively functionalized by silyl groups. There is a particular feature of the binuclear butterfly-shape that is worthy of note. The orientation of the O<sub>exo</sub>-U-O<sub>cis</sub> moiety implies that one of the traditionally linear UO<sub>2</sub> groups has been bent into a cis/bent dioxouranium moiety.

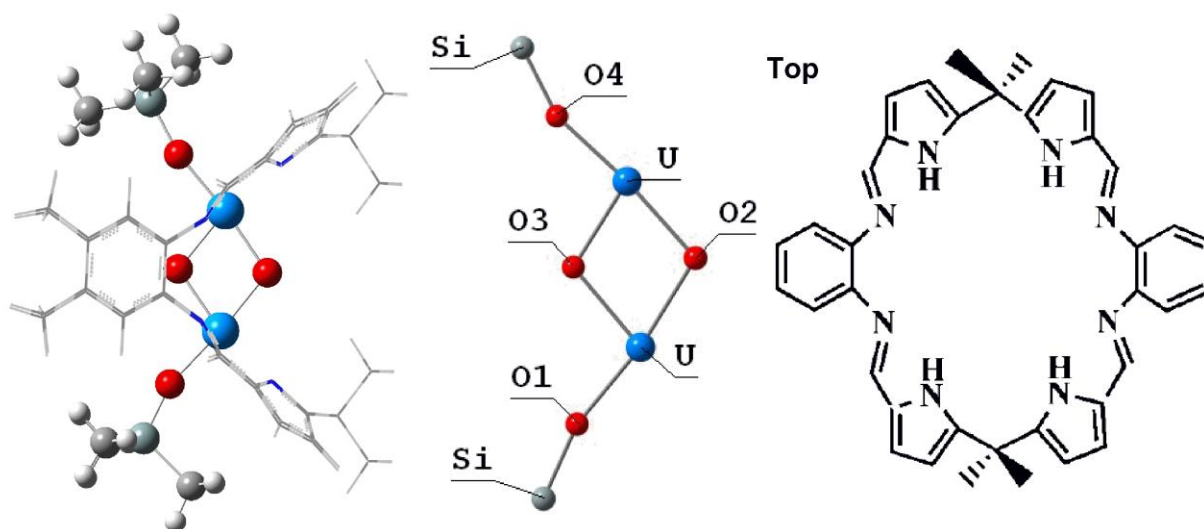


**Figure 8.2:** The recently synthesized  $\text{U}_2\text{O}_4$  Pacman complex, **1a**. (Left) A side-on view of complex **1a**. The  $\text{U}_2\text{O}_4$  core in this complex is butterfly-shaped. O1 and O4 are the *exo*-oxo atoms while O2 and O3 are the *endo*- and *cis*-oxo atoms respectively. The top view of the Pacman-type  $\text{H}_4\text{L}$  ligand is shown on the right. The two amine sites of this ligand are occupied by U(V) centers in **1a**.

Reductive oxo-functionalization of the axial oxo atoms of the  $\text{UO}_2^{2+}$  moiety has been achieved with silyl-type groups as in **1**, metal ions and other groups.<sup>1, 3, 18-20, 22, 29</sup> Arnold et al. have reported the synthesis and characterization of several uranyl Pacman complexes in which the axial oxo atoms have been reductively functionalized by manganese, iron and other transition metals ions.<sup>18</sup> Theoretical characterization of these species was carried out by Berard et al.<sup>30</sup> These complexes can be labeled as  $\text{XOUO}(\text{py})\text{H}_2\text{L}$  species with X being either the proton, methyl, silyl or the metal ion. The equatorial coordination of the dioxouranium (V) units in these species is satisfied by two linkages to the amine groups of the Pacman-type ligand, two to the pyrrole groups of the Pacman-type ligand, and a pyridine solvent ligand. Arnold et al.<sup>31</sup> have

however synthesized and characterized a new class of oxo-functionalized complexes. In their work, the dimerization of the  $XO(UO)(py)H_2L$  complexes (where X is Y or Sm) results in the formation of  $(XO(UO))_2L_2$  species. In this work, the yttrium salt is labeled as **2** while its samarium counterpart is labeled as **3**. The yttrium salt is shown in Figure 8.3. The dioxouranium units in these binuclear complexes are arranged in a diamond  $U_2O_4$  motif, Figure 8.1. During follow-up studies of their synthesis of **2** and **3**, Arnold et al. have been able to isolate and characterize the monomer precursors, as lithium chloride salts, of these binuclear complexes.<sup>32</sup> The geometry of the lithium chloride monomer salt of the yttrium dimer is shown in Figure 8.4. The monomer salts are labeled in a similar manner to the corresponding dimer species. The yttrium monomer is labeled as **2M** and its samarium counterpart as **3M**. The M is used to signify that these are the monomeric salts.

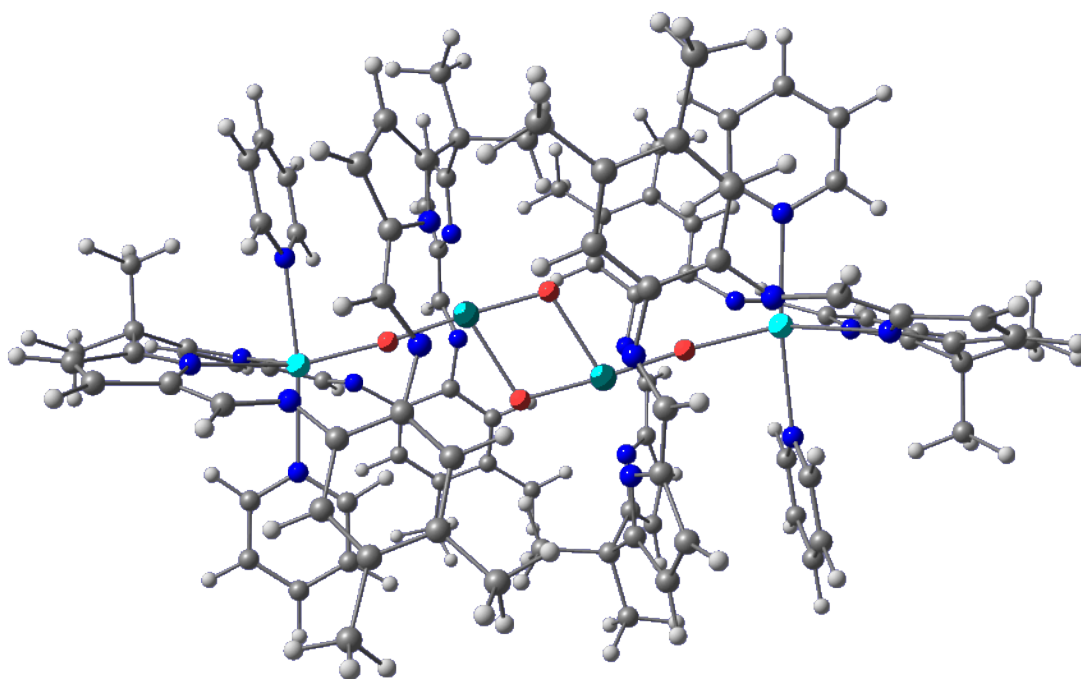


**Figure 8.3:** Optimized structure of the yttrium dimer complex, **2**, obtained at the PBE/L1 level. The O, U and Y atoms are in red, dark green and light green colours respectively.

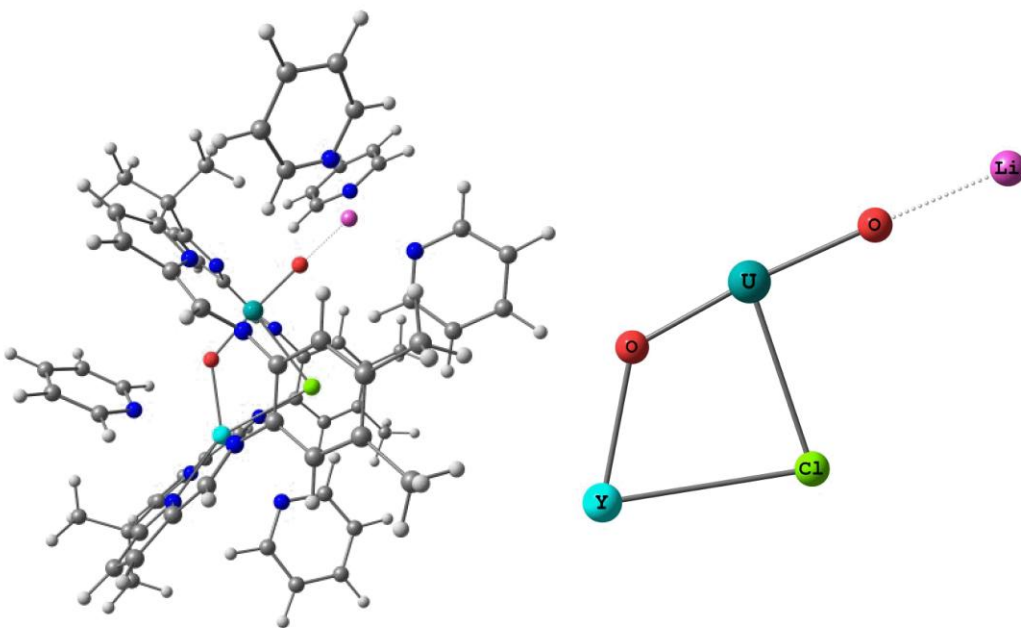


**Figure 8.4:** The lithium-chloride monomer salt of the yttrium dimer complex, **2M**. The dioxo-uranium core with Li and Y oxo-functionalization are shown on the right.

In this report, the structural and electronic properties of the novel uranium-Pacman complexes, **1**, **2** and **3** have been studied using density functional theory (DFT) calculations. The aim is to characterize their structures with particular emphasis on the nature of their  $U_2O_4$  cores, their ground electronic states as well as the possibility of interaction between their actinide centers. The structure and electronic properties of the lithium-chloride monomer salts, **2M** and **3M** are also examined.<sup>32</sup> We have employed DFT in the calculations in this work. Scalar relativistic DFT is increasingly the favorite approach for computing the properties of actinide complexes due to its speed, good treatment of electron correlation effects and general accuracy. The ability of DFT to provide accurate structural properties, redox potentials and vibrational frequencies for open-shell actinide complexes has been established by various workers.<sup>33</sup>

## Computational Details

The geometries of **1**, **2** and **3** as well as the lithiated monomers, **2M** and **3M**, were optimized in the gas phase using DFT calculations with the B3LYP functional.<sup>34-35</sup> Single point calculations in the pyridine solvent were carried out on the optimized structures by employing the polarizable continuum solvation (PCM) model<sup>36-37</sup> in the DFT calculations. The uranium atom was described with the Stuttgart relativistic pseudopotential<sup>38-39</sup> while all other atoms were described with the 6-31G\*\* basis set. These calculations were performed with the Gaussian 03<sup>40</sup> suite of programs and are labeled the B3LYP/RECP calculations. Natural bond orbital (NBO) analyses were also performed.<sup>41</sup> This allowed us to calculate the Mayer-Mulliken bond orders and the Wiberg bond indices.<sup>42</sup> Scalar relativistic calculations with all-electron (AE) basis sets using a four-component approach were also carried out with the Priroda program.<sup>43</sup> The PBE functional was employed in these calculations while using a triple- $\zeta$  (cc-pVTZ) basis set. These calculations were labeled as the PBE/AE/4-component calculations. The small-component portion was described using appropriate kinetically balanced basis sets. The Mayer bond orders were calculated after the geometry optimization.<sup>42</sup>

## Results and Discussion

**Electronic structure analysis of 1.** Analysis of the bonding in the  $U_2O_4$  core of **1** was undertaken using density functional theory (DFT) and natural bond order (NBO) calculations. Single point calculations in a pyridine solvent continuum were carried out on a molecule of **1** whose geometry had been optimised in the gas phase. Three possible arrangements of the two uranium-centered  $f$ -electrons were considered: triplet (ferromagnetically-coupled,  $f^\alpha f^\alpha$ ); anti-ferromagnetic unrestricted broken-symmetry singlet ( $f^\alpha f^\beta$  independently-localised orbitals); and restricted singlet ( $f^{\alpha\beta}$  configuration). The anti-ferromagnetic singlet state was calculated to be

more stable than the triplet state by 1.5 and 1.4 kcal/mol in the gas and pyridine solvent phases when the B3LYP functional was employed with relativistic pseudopotentials. The energy difference between these states was calculated as 2.8 kcal/mol in all-electron calculations with the PBE functional. At this level, the restricted singlet is about 16.0 and 14.2 kcal/mol higher in energy than the unrestricted singlet and triplet states respectively.

The calculated structural properties of **1** obtained at the B3LYP/RECP and PBE/AE/4-component levels are compiled in Table 8.1. For the unrestricted singlet state of **1**, the bonds between the uranium and the *endo*- and *cis*- oxo atoms were calculated to be between 2.092 and 2.099 Å while the U-O<sub>exo</sub> bond lengths were calculated as 2.053 Å, within 0.01 Å of those obtained experimentally. The experimental structural parameters were obtained from X-ray diffraction studies.<sup>28</sup> Overall the best agreement between the calculated and experimental structural parameters was obtained for the unrestricted antiferromagnetic singlet electronic state, Table 8.1. The U...U separation was calculated as 3.366 and 3.379 Å in the unrestricted broken-symmetry singlet and triplet states respectively. The calculated Mayer bond orders for the O<sub>exo</sub>-Si, U-O<sub>exo</sub>, U-O<sub>endo</sub> and U-O<sub>cis</sub> were calculated as 1.04, 1.27, 1.20 and 1.19 respectively. The bonds within the U<sub>2</sub>O<sub>4</sub> core can therefore be considered formally as single bonds with some double bond character, although the U-O<sub>exo</sub> bonds are slightly stronger. This is the case for both the electronic triplet and unrestricted singlet states.

The  $\alpha$ -(HOMO-27) and  $\beta$ -(HOMO-27) orbitals obtained with the B3LYP functional for the unrestricted singlet state are depicted in Figure 8.5(a) and (b) and describe the primary  $\sigma$ -bonding interaction in the U<sub>2</sub>O<sub>4</sub> core. The contributions from the *trans-endo*-oxo atom to these orbitals are significantly larger than those from the *cis*-oxo atom. There is another set of  $\sigma$ -type orbitals at slightly higher energy with greater contributions from the *cis*-oxo atom. Thus,

although the  $\sigma$ -framework is weaker in **1a** than in the calculated structure of the hexavalent uranyl analogue<sup>44</sup>, a strongly bound *cis*-oxo component can be identified in **1a**. In addition, there is a weaker  $\pi$ -type bonding interaction in the  $U_2O_2$  core, Figure 8.5c and 8.5d. The  $\pi$ -type orbitals, Figure 8.5(c) and (d), are dominated by 2p-contributions from the *cis*-oxo atom and appear to be only remnants of more prominent and stable  $\pi$ -interactions in the calculated structure of the hexavalent, non-silylated counterpart<sup>44</sup>.

The combined structural and computational data show that the butterfly  $U_2O_4Si_2$  motif, Figure 8.2, can be formulated as singly bonded uranium oxo and siloxide groups combined with a significant  $\pi$ -bonding contribution from the *cis*-oxo group. Formally, this has resulted from the rearrangement of two linear, pentavalent actinyls into a new bonding mode for uranium in which one oxo group is shared and *trans*- and one has adopted a *cis*-position. The diamond  $U_2O_2$  geometry adopted in **1** has been observed in related Group 6 chemistry.<sup>28</sup> For example, oxidation reactions of the quadruply metal-metal bonded Mo acetate dimer in the presence of good  $\pi$ -accepting ligands form  $Mo^V(\mu-O)_2Mo^V$  complexes which have single M-M bonds. It is therefore tempting to look for a direct metal-metal interaction in **1** since no f-block metal-metal bonded complex has been reported. The calculated  $U\cdots U$  separation of 3.366 Å is particularly short (twice the covalent radius of the uranium atom = 3.92 Å) which may indicate some bonding interaction. This is reflected in the non-trivial calculated Mayer bond order of 0.34 between the uranium atoms, which is only slightly lower than those calculated for some of the U-N bonds in **1** (range 0.38-0.55). NBO analysis allows the identification of a set of bonding and antibonding orbitals, Figure 8.6(a) and (b) respectively, between the uranium centers. While there are no reported examples of molecular bonds between two f-block elements, multiple U-U bonds with distinctly different interactions compared to transition metals have been predicted by

**Table 8.1:** Calculated and experimental structural parameters of **1** in the ferromagnetic triplet and antiferromagnetic broken-symmetry electronic states. The properties obtained for the antiferromagnetic state are enclosed in parentheses.

|                        | <b>B3LYP/RECP</b>           |                 | <b>PBE/AE/4-Component</b>   |                             | <b>Expt.</b> |
|------------------------|-----------------------------|-----------------|-----------------------------|-----------------------------|--------------|
|                        | <b>Bond Lengths</b><br>(Å)  | <b>Mayer BO</b> | <b>Bond Lengths</b><br>(Å)  | <b>Mayer BO</b>             |              |
|                        | <i>fafa</i> ( <i>faff</i> ) | ( <i>faff</i> ) | <i>fafa</i> ( <i>faff</i> ) | <i>fafa</i> ( <i>faff</i> ) |              |
| U-U                    | 3.379 (3.366)               | 0.219           | 3.372 (3.372)               | 0.34 (0.34)                 | 3.3556(5)    |
| U-O <sub>exo</sub>     | 2.056 (2.053)               | 0.991           | 2.055 (2.050)               | 1.26 (1.27)                 | 2.041(6)     |
| U-O <sub>endo</sub>    | 2.048, (2.092)              | 0.925-0.950     | 2.093, (2.076)              | 1.18-1.22                   | 2.086(5),    |
|                        | 2.048, (2.099)              |                 | 2.099, (2.099)              | (1.19-1.20)                 | 2.098(5),    |
|                        | 2.142, (2.093)              |                 | 2.101, (2.095)              |                             | 2.094(5),    |
|                        | 2.165 (2.096)               |                 | 2.105, (2.102)              |                             | 2.096(5)     |
| U-O <sub>endo</sub> -U | 107.5 (107.1)               |                 | 107.1 (107.5)               |                             | 106.6        |
| U-O <sub>cis</sub> -U  | 106.6 (106.6)               |                 | 106.6 (106.8)               |                             | 106.4        |
| U-N <sub>imine</sub>   | 2.539-2.563                 | 0.370           | 2.537-2.562                 | 0.38-0.41                   | 2.490-2.515  |
|                        | (2.538-2.540)               |                 | (2.543-2.572)               | (0.37-0.40)                 |              |
| U-N <sub>pyrrole</sub> | 2.432-2.480                 | 0.435           | 2.457-2.474                 | 0.52-0.55                   | 2.420-2.442  |
|                        | (2.468-2.471)               |                 | (2.443-2.484)               | (0.51-0.57)                 |              |

|      |               |       |               |             |       |
|------|---------------|-------|---------------|-------------|-------|
| O-Si | 1.688 (1.688) | 0.829 | 1.703 (1.700) | 1.04 (1.04) | 1.663 |
|------|---------------|-------|---------------|-------------|-------|

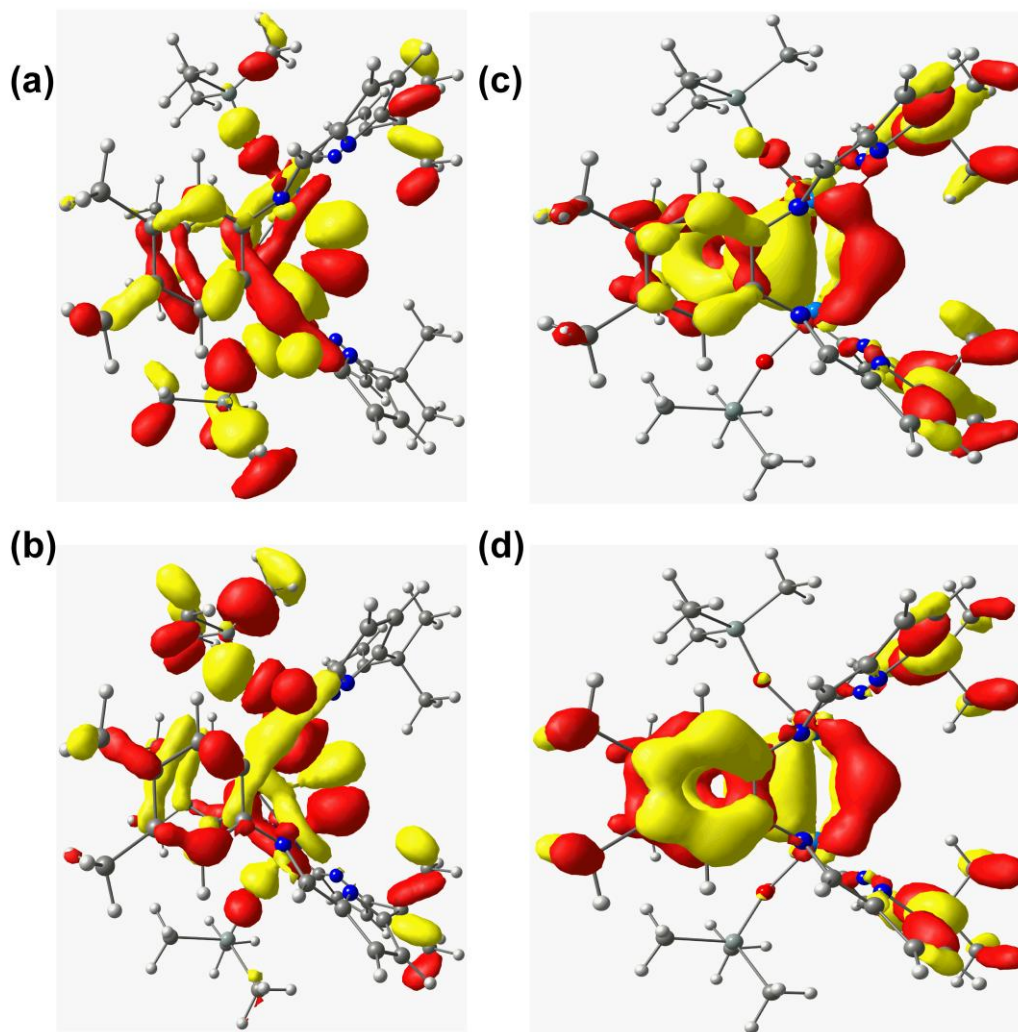


**Figure 8.5:** Molecular orbitals of primary  $\sigma$ - and  $\pi$ - character in the unrestricted singlet state of **1a**: (a)  $\alpha$ -(HOMO-27) with energy of  $-0.333$  a.u. and contributions of 27% *endo*-oxo 2p, 13 % *exo*-oxo 2p, 3 % *cis*-oxo 2p and 13 % U-5f; (b)  $\beta$ -(HOMO-27), with energy of  $-0.333$  a.u. and contributions of 25 % *endo*-oxo 2p, 11 % *exo*-oxo 2p, 3 % *cis*-oxo 2p and 13% U-5f. These  $\sigma$ -type orbitals extend across the  $U_2O_2$  core; (c)  $\alpha$ -HOMO-28 with energy of  $-0.334$  a.u. and

contributions of 34 % *cis*-oxo 2p and 9 % *endo*-oxo 2p, 5% U-5f and 6 % U-6d; (d)  $\beta$ -HOMO-28, with energy of  $-0.334$  a.u. and contributions of 37 % *cis*-oxo 2p, 9 % *endo*-oxo 2p, 5 % U-5f and 5 % U-6d. These orbitals depict the weaker  $\pi$ -type interaction across the  $U_2O_2$  core.

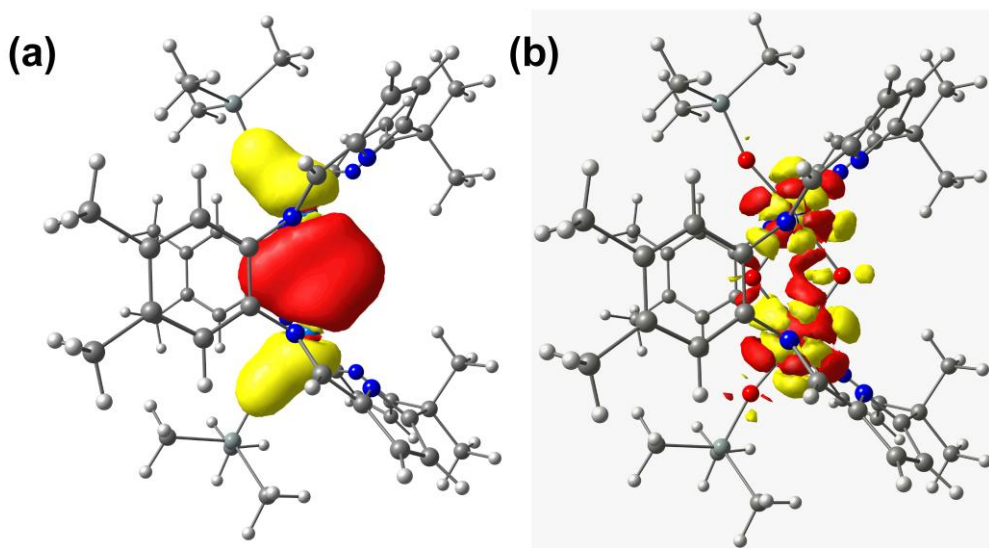


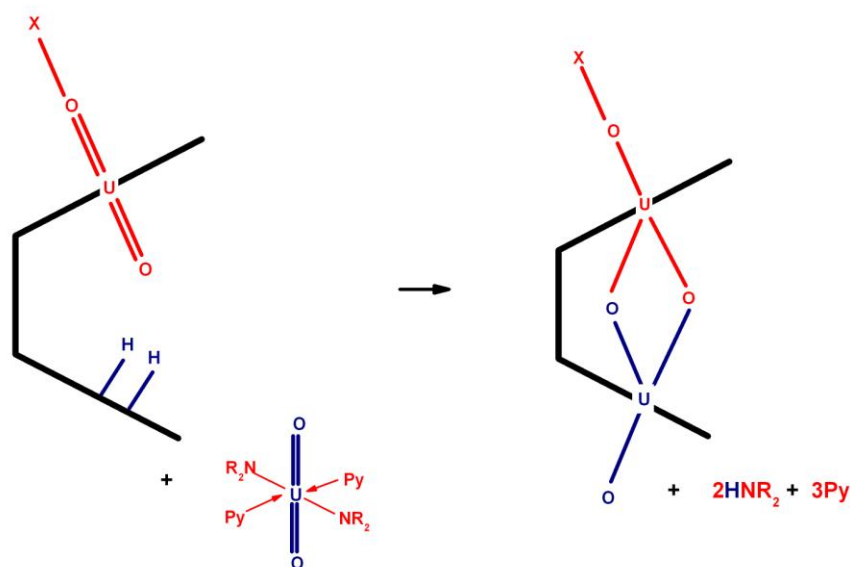
**Figure 8.6:** The (a) HOMO-172 (bonding with respect to the two U atoms) with an energy of  $-1.094$  a.u. and (b) its antibonding counterpart, LUMO+35, both containing contributions from U-5f and O-2s orbitals.

theory.<sup>45</sup> There is a need to further explore the presence of any covalent interaction between the actinide centers in this and similar complexes. The calculated Mayer bond orders for the U-U internuclear distances are intriguing at best.

## Formation of **1**

The formation of **1** can occur with a uranyl-Pacman,  $\text{UO}_2(\text{py})(\text{H}_2\text{L})$ , starting complex. It is however unclear whether the insertion of the second uranyl group of **1** proceeds via a hexavalent or pentavalent complex. There is also the possibility of formation via the oxo-silylated complex,  $\text{Me}_3\text{SiOUO}(\text{py})(\text{H}_2\text{L})$  as dictated by the oxo-functionalized nature of **1**. This is interesting as  $\text{UO}_2(\text{py})(\text{H}_2\text{L})$  and its pentavalent and oxo-functionalized pentavalent derivatives most likely provide different reactivities for the transamination of the second amine site of  $\text{UO}_2(\text{py})(\text{H}_2\text{L})$ . The incoming uranyl group is inserted into the Pacman complexes in a *cis*-orientation in order to achieve the butterfly-shaped  $\text{U}_2\text{O}_4$  core found in **1**. We have used the uranyl silylamide complex,  $\text{UO}_2[\text{N}(\text{SiMe}_3)_2]_2(\text{py})_2$ , to supply the incoming uranyl units as it is the same reagent that was used in the experimental synthesis of **1**. These reactions are depicted in Scheme 8.1 and their calculated energies are presented in Table 8.2. The B3LYP/RECP and PBE/AE/4-component calculations are in agreement that the insertion of a *cis*-uranyl entity into the hexavalent complex is an endothermic reaction while it is exothermic, and significantly so, for the pentavalent complex. This is not surprising given the greater Lewis basicity of the oxo atoms in the pentavalent state. For the oxo-silylated complex, Reaction 3, we find that the reaction energy is exothermic but less so than the case of the pentavalent complex, Reaction 2, Table 8.2. The formation of a binuclear complex from a pentavalent oxo-silylated complex is expected to be aided by increased Lewis basicity of the *endo*-oxo atoms of the Pacman complexes in comparison to the hexavalent complex, Table 8.3. Examination of the calculated atomic charges on the hexavalent, pentavalent and oxo-silylated starting complexes reveals an increase in the polarization of the U-O bonds in the oxo-functionalized complexes, indicative of an increase in ionicity and a decrease in bond covalency. This effect is especially more pronounced in the

functionalized U-O bonds. The increased acidity of the uranium atoms in the functionalized complexes and to a smaller extent the greater basicity of the *endo*-oxo atoms suggest increased reactivity with Lewis bases and acids respectively, Table 8.2. It should be noted that, although the changes in the calculated atomic charges are minute, they are in line with the previous work of Wang et al, who studied NUN and NUNH (proton-functionalization of a uranyl analog).<sup>46</sup> Overall, the reaction energies for these transamination reactions suggest that reductive oxosilylation has a lesser effect on the basicity of the *endo*-oxo atom than reduction to the pentavalent uranyl complex. We can basically conclude from the results presented in Table 8.2 that the formation of the U<sub>2</sub>O<sub>4</sub> core of **1** most likely involves the pentavalent uranyl Pacman complex.



**Scheme 8.1:** Insertion of a cis-type UO<sub>2</sub> group into the empty, un-transaminated site of the uranyl Pacman complex. X is R<sub>3</sub>Si, R<sub>3</sub>C and H for the oxo-silylated, alkylated and protonated complexes respectively.

**Table 8.2:** Calculated reaction free energies ( $\Delta G_{298}$ , kcal/mol)<sup>47</sup> required to transaminate the unoccupied amine site of several Pacman complexes with a *cis*-uranyl group. These reactions result in the formation of butterfly  $U_2O_4$  motif similar to that found in complex **1**. R is  $SiMe_3$ .

| Reactions   | PBE/L1 | B3LYP/RECP |                 |
|---|--------|------------|-----------------|
|   | Gas    | Gas        | Py <sup>a</sup> |
| <b>1.</b> $UO_2(py)(H_2L) + UO_2(NR_2)_2(py)_2 \rightarrow (UO_2)_2L + 3py + 2HNR_2$  | 4.8    | 13.5       | 9.3             |
| <b>2.</b> $[UO_2(py)(H_2L)]^+ + UO_2(NR_2)_2(py)_2 \rightarrow [(UO_2)_2L]^+ + 3py + 2HNR_2$ (Pentavalent)                        | -12.8  | -12.5      | -14.2           |
| <b>3.</b> $Me_3SiOUO(py)(H_2L) + UO_2(NR_2)_2(py)_2 \rightarrow (Me_3SiOUO_2UO)L + 3py + 2HNR_2$ (Oxo-functionalized pentavalent) | -3.1   | -3.8       | -5.1            |

<sup>a</sup> In pyridine solvent using gas phase geometries and the PCM/UA0 approach

**Table 8.3:** Calculated atomic charges on the uranium and oxo- atoms of the uranyl Pacman complex,  $UO_2(py)(H_2L)$ , and its pentavalent and reductively oxo-functionalized derivatives obtained at the PBE/AE/4-component level (and at the B3LYP/RECP level).

|                   | $U(VI)O_2(py)(H_2L)$ | $[U(V)O_2(py)(H_2L)]^+$ | $HOU(V)O(py)(H_2L)$ | $Me_3SiOU(V)O(py)(H_2L)$ |
|-------------------|----------------------|-------------------------|---------------------|--------------------------|
| U                 | 1.38 (1.76)          | 1.24 (1.52)             | 1.42 (1.76)         | 1.61 (1.87)              |
| O <sub>endo</sub> | -0.39 (-0.62)        | -0.46 (-0.74)           | -0.42 (-0.67)       | -0.42 (-0.67)            |
| O <sub>exo</sub>  | -0.27 (-0.46)        | -0.32 (-0.56)           | -0.39 (-0.66)       | -0.50 (-0.78)            |

## Electronic structure analysis of the lithiated monomer complexes, 2M and 3M

The structural properties of the lithium-functionalized monomer complexes of the yttrium and samarium dimer salts were optimized at the PBE/AE/4-component level. The calculated structural properties are compiled in Table 8.4. The structure of the Y monomer complex is shown in Figure 8.4. For the Sm monomer complex, the quintet ( $4f_{\alpha}^5 5f_{\beta}^1$ ) and septet ( $4f_{\alpha}^5 5f_{\alpha}^1$ ) electronic states were considered. The septet state was found to be slightly more stable than the quintet indicating that ferromagnetic coupling of the Sm and U centers is slightly favored. The energy difference between these states, 0.6 kcal/mol, is quite small. However, the structural parameters for the quintet state are in much better agreement with the experimental crystal structure, Table 8.4. The  $\text{UO}_2$  stretching vibrations in the calculated IR spectrum of the yttrium complex at 698 and 757  $\text{cm}^{-1}$  are in good agreement with the peaks found at 764 ( $\text{UO}_2$  asymmetric stretch) and 725 ( $\text{UO}_2$  asymmetric stretch)  $\text{cm}^{-1}$  in the measured FTIR spectrum.

In the Sm and Y monomer complexes, the calculated Mayer bond orders indicate significant double bond characters in the U-O<sub>1</sub> and U-O<sub>2</sub> bonds, Table 8.4. On the other hand, the M-Cl, M-O<sub>1</sub> and U-Cl interactions are single bonds with appreciable ionic characters. The bond orders for the U-O bonds in these complexes are much lower than was obtained for the hexavalent uranyl Pacman complex,  $\text{UO}_2(\text{py})(\text{H}_2\text{L})$ .<sup>30</sup> The loss of a whole bond order is due to the interaction of the oxo atoms with the Li and lanthanide atoms, as the triple bond character of the U-O bonds in the uranyl group is preserved on single electron reduction of  $\text{UO}_2(\text{py})(\text{H}_2\text{L})$  to  $\text{UO}_2(\text{py})(\text{H}_2\text{L})^-$ . This phenomenon was also observed in Wang et al.'s study of NUN and NUNH.<sup>46</sup> Examination of the molecular orbitals of the yttrium complex however reveals the  $\sigma$  and  $\pi$  orbital manifolds similar to those of uranyl groups. The symmetry (Lewis acid-base interaction between the oxo- and electropositive metal atoms on both sides of the uranium center

**Table 8.4:** The structural properties (bond lengths in Å and angles in degrees) for the monomer complexes obtained at the PBE/L1 level. The calculated Mayer bond orders are given in parenthesis. The experimental data are taken from Reference 31.

|  | Sm-monomer  |             | Y-monomer |             |
|--|-------------|-------------|-----------|-------------|
|  | Septet      | Quintet     | Expt.     | Calc.       |
| Li-O <sub>2</sub>                              | 1.91 (0.53) | 1.89 (0.58) |           | 1.90 (0.57) |
| U-O <sub>1</sub>                               | 1.86 (2.02) | 1.90 (1.83) | 1.91      | 1.92 (1.79) |
| U-O <sub>2</sub>                               | 1.87 (1.79) | 1.89 (1.75) | 1.86      | 1.89 (1.76) |
| M-O <sub>1</sub>                               | 2.45 (0.34) | 2.32 (0.51) |           | 2.24 (0.53) |
| M-Cl   | 2.94 (0.29) | 2.87 (0.35) |           | 2.80 (0.36) |
| U-Cl   | 2.74 (0.78) | 2.79 (0.67) |           | 2.79 (0.66) |
| U-M  | 3.70        | 3.65        | 3.63      | 3.63        |
| Li-O <sub>2</sub> -U <sub>2</sub>              | 175.0       | 175.0       | 173.4     | 175.0       |
| O <sub>1</sub> -U <sub>1</sub> -O <sub>2</sub> | 176.4       | 176.2       | 174.7     | 175.2       |
| U-O <sub>1</sub> -M                            | 118.1       | 120.1       |           | 122.3       |
| U-Cl-M   | 82.0        | 81.1        |           | 80.7        |

) preserves the optimal geometry for interaction of the valence orbitals of the uranium and oxygen atoms. However depletions of the Y-O<sub>1</sub> 2p atomic contributions to the  $\pi$  orbitals are characteristic of oxo-functionalized uranyl systems and explain the weakening of the U-O<sub>1</sub> bonds.

### Electronic structure analysis of the dimer complexes, **2** and **3**

We also performed geometry optimizations on **2** and **3**, the direct representations of the Sm and Y dimer complexes produced experimentally.<sup>31</sup> For the yttrium dimer complex, **2**, the triplet and broken symmetry singlet states were calculated as being essentially iso-energetic (energy difference of 0.1 kcal/mol) in the gas phase at the PBE/L1 level. The optimized structure of the broken symmetry singlet state obtained at the PBE/L1 level is shown in Figure 8.3. The experimental IR spectrum for this complex has dominant peaks at 897, 836, 791, 751, 722, 702, 668, 621, 603 and 569 cm<sup>-1</sup>. These are well matched by the calculated vibrational modes at 570, 600, 605, 623, 685, 691, 709, 730, 737, 792, 851 and 884 cm<sup>-1</sup>, in order. The peaks between 570 and 709 cm<sup>-1</sup> in the calculated spectrum corresponds to several motions of the U and O atoms in the U<sub>2</sub>O<sub>4</sub> core, amongst which are the U-O<sub>1</sub> stretching and flexing of the U<sub>2</sub>O<sub>2</sub> core.

For the samarium dimer complex, **3**, the  $4f_{\alpha}^5 5f_{\alpha}^1 5f_{\beta}^1 4f_{\beta}^5$  singlet state (i.e. antiferromagnetic coupling between the two uranium f<sup>1</sup> centers and ferromagnetic interaction between the Sm and U centers, **3s**) was calculated to be 9.2 kcal/mol more stable than the  $4f_{\beta}^5 5f_{\alpha}^1 5f_{\alpha}^1 4f_{\beta}^5$  state (total multiplicity of 9, **3n**). The greater stability of the antiferromagnetic singlet state is in contrast to the experimental magnetic results which reveal greater superexchange interaction between the Sm and U centers rather than between the two uranium centers.

The calculated and experimental U-M distances in the dimer complexes, Table 8.5, are significantly larger than those in the Li(py)<sub>3</sub>(μ-Cl) complexes, Table 8.4. This is most likely due to the presence of the bridging chloride groups in the monomers which occupy an acute angle above the U-M distance, despite similar M-O distances in the monomers and dimers. Like in the

**Table 8.5:** The calculated and experimental structural parameters (bond lengths in Å and angles in degrees) for the dimer complexes obtained at the PBE/L1 level. The Mayer bond orders are given in parenthesis.

|          | Sm-Dimer, <b>3</b> |                  |       | Y-Dimer, <b>2</b> |       |
|----------|--------------------|------------------|-------|-------------------|-------|
|          | Singlet, <b>3s</b> | Nonet, <b>3n</b> | Expt. | Singlet           | Expt. |
| U-O1     | 1.88 (2.00)        | 1.92 (1.83)      | 1.89  | 1.94 (1.79)       | 1.92  |
| U-O2     | 1.95 (1.71)        | 1.98 (1.63)      | 1.94  | 1.98 (1.61)       | 1.97  |
| U-O2'    | 2.34 (0.63)        | 2.31 (0.71)      | 2.35  | 2.30 (0.73)       | 2.32  |
| M-O1     | 2.32 (0.35)        | 2.25 (0.53)      | 2.24  | 2.18 (0.55)       | 2.16  |
| U-U      | 3.47               | 3.47 (0.34)      | 3.47  | 3.47              | 3.45  |
| U-M      | 4.20               | 4.18             | 4.12  | 4.11              | 4.07  |
| O1-U1-O2 | 175.4              | 175.4            | 174.4 | 175.6             | 175.3 |
| U1-O1-M  | 176.1              | 178.6            | 174.5 | 176.2             | 177.3 |

monomer complexes, the U-O<sub>1</sub> and U-O<sub>2</sub> distances in the dimers have double bond characters.

The CCIs across the U<sub>2</sub>O<sub>2</sub> core, depicted by the U-O2' bonds, are however weaker and more ionic bonds than the other U-O bonds. The calculated U-U distances in the dimer complexes are about 3.47 Å. This is shorter than the sum of the covalent radii of two singly bonded uranium atoms, 3.92 Å but slightly longer than the value of 3.37 Å recently obtained by us in the butterfly oxo-silylated complex in which a U<sub>2</sub>O<sub>2</sub> core is formed from two pentavalent uranyl units within the same pyrrolic macrocycle as used here, Table 8.1.<sup>28</sup>

## Conclusions

In this work we have studied the structural and electronic properties of three binuclear U<sub>2</sub>O<sub>4</sub> complexes with U(V)/U(V) configuration using scalar relativistic DFT calculations. The ground electronic states of these complexes as well as the possibilities for U-U interactions were also examined. For the formation of the butterfly-shaped complex, **1**, the Lewis basicities of the *endo*-oxo atoms of the oxo-functionalized complexes are intermediate between those of the hexavalent and pentavalent uranyl complexes. As a result of this, the transamination reactions leading to the butterfly-shaped U<sub>2</sub>O<sub>4</sub> motif are more exothermic for the pentavalent and oxo-functionalized pentavalent species than the hexavalent complexes. The reaction energies point to the possible involvement of a pentavalent intermediate in the synthesis of **1**.

The f<sup>I</sup> uranium centers in **1** were found to be anti-ferromagnetically coupled in agreement with low temperature magnetic experiments. In contrast, for **2** and **3**, antiferromagnetic coupling amongst the U centers and ferromagnetic coupling between the actinide and lanthanide centers is predicted by the PBE/L1 all-electron basis set approach in disagreement with the experimental work. However, this is only severe in the Sm-dimer complex, **3**, with the ferromagnetic and

antiferromagnetic U-U or M-U coupling being degenerate ( $< 1$  kcal/mol) for the yttrium dimer, **2**. It should however be noted that we were simply unable to converge to the  $4f_{\beta}^5 5f_{\alpha}^1 5f_{\beta}^1 4f_{\alpha}^5$  electronic state of the Sm-dimer that was indicated by the experimental magnetic measurements. The bonding characteristics reveal that the U-O bonds in **2** and **3** as well as their monomeric precursors, are mainly of double bond character, representing a loss of a full bond order, in comparison to  $\text{UO}_2(\text{py})(\text{H}_2\text{L})$ , upon oxo-metallation by either Li (for the monomeric precursors, **2M** and **3M**) or lanthanide metals (for **2** and **3**).

## References

1. Arnold, P. L.; Love, J. B.; Patel, D., *Coordin. Chem. Rev.* **2009**, *253* (15-16), 1973-1978.
2. Ephritikhine, M., *Dalton T.* **2006**, (21), 2501-2516.
3. Fortier, S.; Hayton, T. W., *Coordin. Chem. Rev.* **2010**, *254* (3-4), 197-214.
4. Graves, C. R.; Kiplinger, J. L., *Chem. Commun.* **2009**, (26), 3831-3853.
5. Melfi, P. J.; Kim, S. K.; Lee, J. T.; Bolze, F.; Seidel, D.; Lynch, V. M.; Veauthier, J. M.; Gaunt, A. J.; Neu, M. P.; Ou, Z.; Kadish, K. M.; Fukuzumi, S.; Ohkubo, K.; Sessler, J. L., *Inorg. Chem.* **2007**, *46* (13), 5143-5145.
6. Nocton, G.; Horeglad, P.; Vetere, V.; Pecaut, J.; Dubois, L.; Maldivi, P.; Edelstein, N. M.; Mazzanti, M., *J. Am. Chem. Soc.* **2010**, *132* (2), 495-508.
7. Seidel, D.; Lynch, V.; Sessler, J. L., *Angew. Chem. Int. Edit.* **2002**, *41* (8), 1422-1425.
8. Sessler, J. L.; Gorden, A. E. V.; Seidel, D.; Hannah, S.; Lynch, V.; Gordon, P. L.; Donohoe, R. J.; Tait, C. D.; Keogh, D. W., *Inorg. Chim. Acta* **2002**, *341*, 54-70.
9. Sessler, J. L.; Melfi, P. J.; Pantos, G. D., *Coordin. Chem. Rev.* **2006**, *250* (7-8), 816-843.
10. Sessler, J. L.; Seidel, D.; Vivian, A. E.; Lynch, V.; Scott, B. L.; Keogh, D. W., *Andw. Chem. Int. Edit.* **2001**, *40* (3), 591-594.

11. Sessler, J. L.; Vivian, A. E.; Seidel, D.; Burrell, A. K.; Hoehner, M.; Mody, T. D.; Gebauer, A.; Weghorn, S. J.; Lynch, V., *Coordin. Chem. Rev.* **2001**, *216*, 411-434.
12. Ikeda, A.; Hennig, C.; Tsushima, S.; Takao, K.; Ikeda, Y.; Scheinost, A. C.; Bernhard, G., *Inorg. Chem.* **2007**, *46* (10), 4212-4219.
13. Mizuoka, K.; Grenthe, I.; Ikeda, Y., *Inorg. Chem.* **2005**, *44* (13), 4472-4474.
14. Mizuoka, K.; Ikeda, Y., *Inorg. Chem.* **2003**, *42* (11), 3396-3398.
15. Mizuoka, K.; Ikeda, Y., *Radiochim. Acta* **2004**, *92* (9-11), 631-635.
16. Mizuoka, K.; Kim, S. Y.; Hasegawa, M.; Hoshi, T.; Uchiyama, G.; Ikeda, Y., *Inorg. Chem.* **2003**, *42* (4), 1031-1038.
17. Berthet, J. C.; Nierlich, M.; Ephritikhine, M., *Angew. Chem. Int. Edit.* **2003**, *42* (17), 1952-1954.
18. Arnold, P. L.; Patel, D.; Blake, A. J.; Wilson, C.; Love, J. B., *J. Am. Chem. Soc.* **2006**, *128* (30), 9610-9611.
19. Arnold, P. L.; Patel, D.; Wilson, C.; Love, J. B., *Nature* **2008**, *451* (7176), 315-U3.
20. Arnold, P. L.; Pecharman, A. F.; Love, J. B., *Angew. Chem. Int. Edit.* **2011**, *50* (40), 9456-9458.
21. Schnaars, D. D.; Wu, G.; Hayton, T. W., *J. Am. Chem. Soc.* **2009**, *131* (48), 17532-17533.
22. Hayton, T. W.; Wu, G., *Inorg. Chem.* **2009**, *48* (7), 3065-3072.
23. Burdet, F.; Pecaut, J.; Mazzanti, M., *J. Am. Chem. Soc.* **2006**, *128* (51), 16512-16513.
24. Mougel, V.; Horeglad, P.; Nocton, G.; Pecaut, J.; Mazzanti, M., *Angew. Chem. Int. Edit.* **2009**, *48* (45), 8477-8480.

25. Mougel, V.; Horeglad, P.; Nocton, G.; Pecaut, J.; Mazzanti, M., *Chem-Eur. J.* **2010**, *16* (48), 14365-14377.
26. Natrajan, L.; Burdet, F.; Pecaut, J.; Mazzanti, M., *J. Am. Chem. Soc.* **2006**, *128* (22), 7152-7153.
27. Nocton, G.; Horeglad, P.; Pecaut, J.; Mazzanti, M., *J. Am. Chem. Soc.* **2008**, *130* (49), 16633-16645.
28. Arnold, P. L.; Jones, G. M.; Odoh, S. O.; Schreckenbach, G.; Magnani, N.; Love, J. B., *Nature Chem.* **2012**, *4* (3), 221-227.
29. Arnold, P. L.; Blake, A. J.; Wilson, C.; Love, J. B., *Inorg. Chem.* **2004**, *43* (26), 8206-8208.
30. Berard, J. J.; Schreckenbach, G.; Arnold, P. L.; Patel, D.; Love, J. B., *Inorg. Chem.* **2008**, *47* (24), 11583-11592.
31. Arnold, P. L.; Hollis, E.; White, F. J.; Magnani, N.; Caciuffo, R.; Love, J. B., *Angew. Chem. Int. Edit.* **2011**, *50* (4), 887-890.
32. Arnold, P. L.; Holis, E.; Love, J. B.; Magnani, N.; Colineau, E.; Caciuffo, R.; Edelstein, N.; Maron, L.; Castro, L.; Yahia, A.; O., O. S.; G., S., **2012**.
33. Odoh, S. O.; Schreckenbach, G., *J. Phys. Chem. A* **2011**, *115* (48), 14110-14119.
34. Becke, A. D., *J. Chem. Phys.* **1993**, *98* (7), 5648-5652.
35. Stephens, P. J.; Devlin, F. J.; Chabalowski, C. F.; Frisch, M. J., *J. Phys. Chem.* **1994**, *98* (45), 11623-11627.
36. Miertus, S.; Scrocco, E.; Tomasi, J., *Chem. Phys.* **1981**, *55* (1), 117-129.
37. Miertus, S.; Tomasi, J., *Chem. Phys.* **1982**, *65* (2), 239-245.
38. Küchle, W.; Dolg, M.; Stoll, H.; Preuss, H., *Mol. Phys.* **1991**, *74* (6), 1245-1263.

39. Küchle, W.; Dolg, M.; Stoll, H.; Preuss, H., *J. Chem. Phys.* **1994**, *100* (10), 7535-7542.
40. Frisch, M. J.; Trucks, G. W.; Schlegel, H. B.; Scuseria, G. E.; Robb, M. A.; Cheeseman, J. R.; Scalmani, G.; Barone, V.; Mennucci, B.; Petersson, G. A.; Nakatsuji, H.; Caricato, M.; Li, X.; Hratchian, H. P.; Izmaylov, A. F.; Bloino, J.; Zheng, G.; Sonnenberg, J. L.; Hada, M.; Ehara, M.; Toyota, K.; Fukuda, R.; Hasegawa, J.; Ishida, M.; Nakajima, T.; Honda, Y.; Kitao, O.; Nakai, H.; Vreven, T.; Montgomery, J., J. A.; Peralta, J. E.; Ogliaro, F.; Bearpark, M.; Heyd, J. J.; Brothers, E.; Kudin, K. N.; Staroverov, V. N.; Kobayashi, R.; Normand, J.; Raghavachari, K.; Rendell, A.; Burant, J. C.; Iyengar, S. S.; Tomasi, J.; Cossi, M.; Rega, M.; Millam, N. J.; Klene, M.; Knox, J. E.; Cross, J. B.; Bakken, V.; Adamo, C.; Jaramillo, J.; Gomperts, R. E.; Stratmann, O.; Yazyev, A. J.; Austin, R.; Cammi, C.; Pomelli, J. W.; Ochterski, R.; Martin, R. L.; Morokuma, K.; Zakrzewski, V. G.; Voth, G. A.; Salvador, P.; Dannenberg, J. J.; Dapprich, S.; Daniels, A. D.; Farkas, O.; Foresman, J. B.; Ortiz, J. V.; Cioslowski, J.; Fox, D. J. *Gaussian 09, Revision A.2*, Gaussian, Inc.: Wallingford CT, 2009.
41. Glendening, E. D.; Reed, A. E.; Carpenter, J. E.; F., W. *NBO Version 3.1*.
42. Bridgeman, A. J.; Cavigliasso, G.; Ireland, L. R.; Rothery, J., *J. Chem. Soc. Dalton* **2001**, (14), 2095-2108.
43. Laikov, D. N.; Ustynyuk, Y. A., *Russ. Chem. B+* **2005**, *54* (3), 820-826.
44. Pan, Q.-J.; Shamov, G. A.; Schreckenbach, G., *Chem-Eur. J.* **2010**, *16* (7), 2282-2290.
45. Gagliardi, L.; Roos, B. O., *Nature* **2005**, *433* (7028), 848-851.
46. Wang, X. F.; Andrews, L.; Vlasisavljevich, B.; Gagliardi, L., *Inorg. Chem.* **2011**, *50* (8), 3826-3831.
47. Shamov, G. A.; Schreckenbach, G., *J. Phys. Chem. A* **2005**, *109* (48), 10961-10974.

## Preface to Chapter 9

This chapter is based on manuscript that would soon be submitted for publication in the journal “*Inorganic Chemistry*”. The full citation of the paper is as follows:

Samuel O. Odoh, Bert W. de Jong and Georg Schreckenbach, “Theoretical Study of a Gas-Phase Binuclear Uranyl Hydroxo Complex,  $(\text{UO}_2)_2(\text{OH})_5^-$ .” *Inorganic Chemistry*, **2012**, to be submitted.

The work in this chapter provides a detailed description of our search for the lowest energy structures of the bis-uranyl complex,  $(\text{UO}_2)_2(\text{OH})_5^-$ . This complex was identified in laser ablation studies of uranium trioxide solids. The relative energies of the various structures were calculated out at the density functional theory (DFT) level and using ab initio wavefunction approaches.

All the DFT as well as the full-MP2 calculations in this chapter were carried out by Samuel O. Odoh. The frozen-core MP2 and CCSD(T) calculations were carried out by Bert de Jong. The manuscript was prepared together with the other authors.

Copyright permissions have been obtained from all the other authors. Bert de Jong is affiliated with the Pacific Northwest National Laboratory.

## Chapter 9: Theoretical Study of a Gas-Phase Binuclear Uranyl

### Hydroxo Complex, $(\text{UO}_2)_2(\text{OH})_5^-$ .

#### Abstract

The low energy structures and bonding of gas-phase  $(\text{UO}_2)_2(\text{OH})_5^-$ , a product of laser ablation studies on uranium trioxide solids, have been studied using density functional theory (DFT) and ab initio methods while employing scalar relativistic effective core potentials. As  $(\text{UO}_2)_2(\text{OH})_5^-$  is a member of the  $(\text{UO}_2)_2(\text{OH})_n^{4-n}$ , series of complexes, the structures of the di, tri, tetra and hexa-hydroxo bis-uranyl complexes were also determined with particular emphasis on structures featuring cation-cation interactions between the uranyl groups. We found that the most stable structures obtained for  $(\text{UO}_2)_2(\text{OH})_5^-$  feature this type of interactions. This was confirmed at the MP2 and CCSD(T)//MP2 levels. Analysis of the bonding in the structures of  $(\text{UO}_2)_2(\text{OH})_5^-$  shows that the  $\text{UO}_2(\text{OH})_2$  and  $\text{UO}_2(\text{OH})_3^-$  units are held together mainly by electrostatic effects. In addition, there is no evidence for covalent interactions between the actinide atoms even in structures where the U-U distances are significantly lesser than the sum of the covalent radii of the actinide centers. The calculated IR vibrational frequencies provide signature probes that can be used in differentiating the low-energy structures and in experimentally confirming the existence of the structures featuring cation-cation interactions.

#### Introduction

There is a synergistic convergence between the application of computational approaches to the study of actinide complexes<sup>1-24</sup> and the resurgence of synthetic actinide chemistry. Novel actinide complexes produced via “wet” chemical synthesis are being reported regularly. A few

examples of these are stable U(V) complexes<sup>25</sup>, imido-analogs of actinyl species<sup>26-27</sup> among others. In addition to these wet chemical approaches, there is a long tradition of identifying gaseous actinide compounds produced from laser-ablated solids by mass spectrometric analyses.<sup>28-52</sup> The transfer of actinide compounds from the solvent phase into the gaseous phase has also been demonstrated. In addition, the species produced after the laser ablation and solution-to-gas transfer processes have been reacted with other compounds (such as nebulized alcohols, water and oxygen).<sup>33-36, 39, 47-49</sup> In several cases, the products of such reactions were found to themselves be new actinide species. As an example, the discovery of gas-phase hypercoordinated complexes of the actinyl dications has been reported by van Stipdonk et al.<sup>47</sup> A collision-induced dissociation (CID) approach has also been applied to gaseous actinide systems.<sup>34, 48</sup> The fragmentation patterns and product yields have provided insights into the redox chemistries of actinyl complexes as well as the nature of the chemical bonds in these compounds.

Marcalo et al. identified multinuclear uranates with molecular formulas ranging between  $\text{UO}_n^-$  and  $\text{U}_{14}\text{O}_n^-$  in their ablative work on solid uranium trioxide.<sup>53</sup> Anionic species, such as  $\text{U}_2\text{O}_7\text{H}^-$  and  $\text{U}_3\text{O}_{10}\text{H}^-$ , containing hydrogen atoms were also detected in their mass spectrometric data. They noted that the hydrogen atoms were produced from water or hydroxyl groups in their samples. More recently, a comprehensive mass-spectrometric study on the gaseous species produced from laser ablation of solid uranium trioxide in the presence of water has led to the identification of highly hydroxylated  $(\text{UO}_2)_n(\text{OH})_{2n+1}^-$  and  $(\text{UO}_2)_n(\text{OH})_{2n}(\text{O}_2)^-$  clusters.<sup>54</sup> The fragmentation patterns of these clusters were also examined using state of the art CID techniques. A recent ablation study of titanium dioxide solids resulted in the detection of similar oxy-hydroxide anions,  $(\text{TiO}_2)_x(\text{H}_2\text{O})_y\text{OH}^-$  and  $(\text{TiO}_2)_x(\text{H}_2\text{O})_y(\text{O}_2)^-$ .<sup>55</sup>

One of the gaseous species identified in the mass spectrometric work is  $(\text{UO}_2)_2(\text{OH})_5^-$ . It is an interesting complex as it is one of the simplest of the bis-uranyl hydroxo complexes identified, in addition to having the largest yields in the mass spectra of the ablated gases.<sup>54</sup> In many cases, the experimental identification and characterization of gaseous actinide compounds have been accompanied or followed by detailed theoretical examination of their structural and electronic properties as well as their fragmentation or reaction pathways.<sup>6, 40, 44, 50</sup> The relatively small size of  $(\text{UO}_2)_2(\text{OH})_5^-$  means it is relatively tractable in terms of computational expense. It should however be noted that given its bis-uranyl nature (and the multi-nuclear nature of the  $(\text{UO}_2)_n(\text{OH})_{2n+1}^-$  and  $(\text{UO}_2)_n(\text{OH})_{2n}\text{O}_2^-$  clusters in general) as well as the relatively large number of ligands, there is a need to examine a large number of low-energy structures while searching for the global minimum point on the potential energy surface.

The crystal structures of  $\text{UO}_3$ <sup>56</sup> and  $\text{UO}_3 \cdot \text{H}_2\text{O}$ <sup>57</sup> are known to possess cation-cation interactions (CCIs) between neighboring uranyl groups. CCIs are intermolecular interactions between cationic species. In the case of bis-actinyl species, these are usually formed through oxo atoms. CCIs are found in  $\text{UO}_3$  as the uranium atoms in the crystal structure have only oxo-type neighbors. As the  $(\text{UO}_2)_n(\text{OH})_{2n+1}^-$  anionic clusters are formed from  $\text{UO}_3$  (and reaction of the ablated gases with water or hydroxyl), it is important that structural frameworks retaining the CCIs found in the solid structure are considered in any search for the lowest energy structures for these complexes. Another perspective involves examining the individual components of the  $(\text{UO}_2)_2(\text{OH})_5^-$  complex. The  $\text{UO}_2^{2+}$  group contains a  $d^0f^0$  uranium atom, is rigorously linear and is known to possess very inert oxo atoms.<sup>58-60</sup> On the other hand, the hydroxo ligand is a strong  $\sigma$  and  $\pi$  donor. The coordination of electron donors to the equatorial region of the uranyl moiety generally results in an increase in the Lewis basicities of the uranyl oxo atoms. This increased

Lewis basicities of the oxo atoms has been found to favor the formation of CCIs between uranyl groups or with other cations.<sup>61</sup> From this point of view, the role of CCIs in the  $(\text{UO}_2)_n(\text{OH})_{2n+1}^-$  complexes would be expected to increase as the number of hydroxo ligands are increased. It can then be concluded that a search for the lowest energy structures of  $(\text{UO}_2)_2(\text{OH})_5^-$  is incomplete without a search for structures containing CCIs between the uranyl groups.

On the other hand, the structural and electronic properties of bis-uranyl hydroxo-aquo complexes, formed at high pH values in aqueous solutions, have been examined with experimental and theoretical approaches. In their calculations, Tsushima et al. obtained a  $\mu_2$ -dihydroxo structure for  $(\text{UO}_2)_2(\text{H}_2\text{O})_6(\text{OH})_2^{2+}$  complex as well as a  $\mu$ -hydroxo structure for the  $(\text{UO}_2)_2(\text{H}_2\text{O})_8(\text{OH})^{3+}$  complex in aqueous solution.<sup>19</sup> The  $\mu_2$ -dihydroxo structure that was obtained for  $(\text{UO}_2)_2(\text{H}_2\text{O})_6(\text{OH})_2^{2+}$  is in good agreement with the crystallographic work of Aberg.<sup>62</sup> In this structure, the uranyl groups are bridged by hydroxo ligands and their equatorial coordination sphere is satisfied by aquo ligands. Similar  $\mu$ -hydroxo bridged structures have also been obtained for other actinide complexes.<sup>63-65</sup> It should however be noted that there is no guarantee that these  $\mu_2$ -dihydroxo structures would be the most stable motifs for the highly hydroxylated complexes belonging to the  $(\text{UO}_2)_n(\text{OH})_{2n+1}^-$  series in the gaseous phase.

We report here a theoretical study of the structural features and electronic properties of the low energy structures of  $(\text{UO}_2)_2(\text{OH})_5^-$ . Particular emphasis was given to the search of stable structures featuring CCIs between the uranyl groups in this complex. The structure of other members of the  $(\text{UO}_2)_2(\text{OH})_n^{4-n}$  series of complexes were also examined to further determine if CCIs are pervasive in gaseous bis-uranyl hydroxide complexes. The density functional theory (DFT), second order Møller-Plesset perturbation (MP2) and coupled cluster approaches were used in this work.

## Computational Details

All the calculations were performed with the NWChem 6.0 package of programs.<sup>66</sup> Scalar relativistic calculations were carried out with the Stuttgart small-core effective core potential for the uranium atom.<sup>67-69</sup> The valence basis associated with this pseudopotential is of 10s9p5d5f contraction while all-electron DFT optimized valence triple- $\zeta$  polarized (TZVP) basis sets were used for the oxygen and hydrogen atoms.<sup>70</sup> This combination of basis set and pseudopotentials have been previously used in calculating accurate structural parameters, vibrational frequencies and reaction energies of actinide and transition metal complexes.<sup>5, 7, 71-72</sup> The geometries of many possible structural motifs of  $(\text{UO}_2)_2(\text{OH})_5^-$  and other members of the  $(\text{UO}_2)_2(\text{OH})_n^{4-n}$  series of complexes were optimized using the hybrid B3LYP functional. These structural motifs were obtained by rigorous examination of many possible structures without symmetry constraints. This approach allows for a sampling of the potential energy surface with the aim of detecting the lowest energy structures. Structures containing CCIs between the uranyl groups and those featuring bridging hydroxo- ligands were included in this search. In addition, structures containing equatorial aquo ligands (while maintaining the molecular formula of  $\text{U}_2\text{O}_9\text{H}_5^-$ ) were considered. To further ascertain the relative energies of the lowest energy structures, their geometries were also optimized with the local density approximation (LDA), the half and half functional of Becke, as implemented in NWChem (BeckeHandH), and MP2. The U-U distances between the two uranium atoms of the title complex and several of the structures studied in this work are less than 3.92 Å (twice the covalent radius of a uranium atom<sup>73</sup>). In addition some ligands bonded to each uranium atom are within the second coordination sphere of the adjacent uranium atom. These two effects suggest the possibility of substantial long-range correlation effects on the structure and relative energies of these complexes. For this reason, single point

calculations on the MP2 optimized geometries were carried out with the coupled cluster, CCSD(T), approach as well as a variety of modified density functionals: CAM-B3LYP<sup>74</sup>, BeckeHandH as well as the B3LYP functional corrected for dispersion effects using Grimme's third scheme, B3LYP-D3.<sup>75</sup> To characterize the bonding in the different structures, the Mayer-Mulliken bond order<sup>76</sup> and Mulliken atomic charges were calculated at the B3LYP/TZVP level.

## Results and Discussion

**Structures of  $(\text{UO}_2)_2(\text{OH})_5^-$ .** The three lowest energy structures obtained for  $(\text{UO}_2)_2(\text{OH})_5^-$  at the B3LYP/TZVP level are presented in Figure 9.1. The calculated relative energies of these structures obtained while employing a variety of density functional and ab initio methods are collected in Table 9.1. At the B3LYP/TZVP level, the  $\mu_2$ -dihydroxo structure was found to be the least stable of these three structures. The two lower-energy structures that were calculated both feature CCIs between their uranyl groups and are essentially degenerate. One of these CCI structures possesses a bridging hydroxo group between the uranium centers, Figure 9.1 in addition to an oxo linkage. This structure is labeled as  $\mu$ -hydroxo-CCI, Figure 9.1. The uranyl group whose oxo atom participates in the CCI essentially lies in the equatorial plane of the other uranyl group. In this structure, each uranyl group possesses two equatorially coordinated pendant hydroxo ligands in addition to the bridging hydroxo group. The bonds between the bridging hydroxo group and the uranium atoms were calculated as 2.28 and 2.51 Å, Table 9.2. As would be expected, the bridging hydroxo ligand is much more strongly bonded to the equatorial uranyl group, whose oxo atom is involved in the CCI, Figure 9.1. The  $\text{U}-\text{O}_{\text{y1}}$  bonds for the three oxo atoms not involved in the CCIs were calculated to be about 1.80 Å long, Table 9.2. This is within the range calculated for  $\text{UO}_2(\text{OH})_2$ , 1.79 Å and  $\text{UO}_2(\text{OH})_3^-$ , 1.81 Å, at the B3LYP/TZVP level, Table 9.3. A similar case was also observed for the bonds between the uranium atoms and the

pendant hydroxo ligands, the  $\text{U-OH}_{\text{pendant}}$  bonds, Table 9.2. The  $\text{U-O}_{\text{CCI}}$  bond for the equatorial uranyl group and  $\text{U}_1\text{-O}_{\text{CCI}}$  between the uranyl groups were calculated as 1.84 and 2.62 Å respectively.

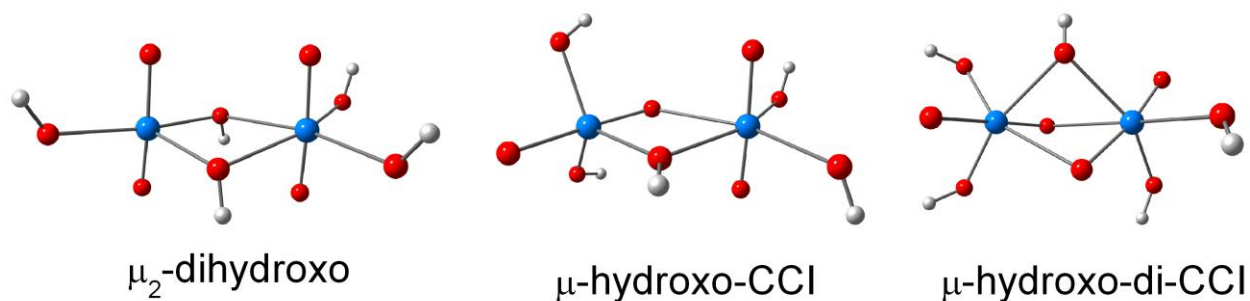


**Figure 9.1:** The three low energy structures of  $(\text{UO}_2)_2(\text{OH})_5^-$  obtained at the B3LYP/TZVP level.

The second CCI structure is labeled as  $\mu$ -hydroxo-di-CCI, Figure 9.1. The uranyl groups in this structure are not fully parallel to each other with their orientations such that the pendant hydroxo groups are all in the equatorial region. However, the fifth hydroxo group is a bridging hydroxo group coordinated to both uranyl groups. The  $\text{U-O}_{\text{CCI}}$  bonds for both uranyl groups (bonds between the uranium atoms and the oxo groups involved in CCIs) are about 1.86-1.87 Å long, Table 9.2. These are much longer than the free  $\text{U-O}_{\text{yl}}$  bonds which were calculated to be 1.80-1.81 Å in length. As noted, this was also the case for the  $\mu$ -hydroxo-CCI structure, Table 9.2, suggesting involvement in CCIs results in elongation of  $\text{U-O}_{\text{yl}}$  bonds by 0.04-0.07 Å. The  $\text{U}_1\text{-O}_{\text{CCI}}$  bonds between the uranyl groups were calculated as 2.56 and 2.63 Å, confirming the presence of some asymmetry in this structure, Table 9.2. Attempts at removing this asymmetry

**Table 9.1:** Calculated relative energies (kcal/mol) of the three low energy structures of  $(\text{UO}_2)_2(\text{OH})_5^-$ .

|                 | $\mu_2$ -dihydroxo | $\mu$ -hydroxo-CCI | $\mu$ -hydroxo-di-CCI |
|-----------------|--------------------|--------------------|-----------------------|
| LDA             | 8.92               | 9.10               | 0.00                  |
| B3LYP           | 1.83               | 0.00               | 0.17                  |
| MP2//B3LYP      | 4.29               | 3.89               | 0.00                  |
| CAM-B3LYP       | 1.12               | 0.00               | 0.71                  |
| BeckeHandH      | 12.97              | 7.82               | 0.00                  |
| MP2             | 6.31               | 5.45               | 0.00                  |
| B3LYP//MP2      | 5.87               | 2.75               | 0.00                  |
| B3LYP-D3//MP2   | 4.58               | 2.54               | 0.00                  |
| CAM-B3LYP//MP2  | 6.49               | 3.69               | 0.00                  |
| BeckeHandH//MP2 | 9.02               | 4.67               | 0.00                  |
| CCSD(T)//MP2    | 5.13               | 3.04               | 0.00                  |

by stipulating a  $C_2$  axis through the  $\mu$ -hydroxo ligand increases the total energy by 1.42 kcal/mol and results in a transition state structure at the B3LYP/TZVP level. The pendant U-OH bonds in the  $\text{UO}_2(\text{OH})_2$  groups of this structure were calculated to be 2.16 -2.17 Å long. They are within the range of the U-OH bond lengths calculated for  $\text{UO}_2(\text{OH})_2$  (2.11 Å) and  $\text{UO}_2(\text{OH})_3^-$  (2.22 Å), similar to the case for the  $\mu$ -hydroxo-CCI.

The third low-energy framework obtained at the B3LYP/TZVP level appears to be formed through the agglomeration of  $\text{UO}_2(\text{OH})_2$  and  $\text{UO}_2(\text{OH})_3^-$  via two bridging hydroxo ligands. This structure is labeled as the  $\mu_2$ -dihydroxo structure, Figure 9.1. The U- $\text{O}_{yl}$  bond lengths in this

**Table 9.2:** Calculated bond lengths ( $\text{\AA}$ ) and bond orders of the low energy structures of  $(\text{UO}_2)_2(\text{OH})_5^-$  obtained at the B3LYP/TZVP level.

|                                  | $\mu_2$ -dihydroxo |           | $\mu$ -hydroxo-CCI |           | $\mu$ -hydroxo-di-CCI |           |
|----------------------------------|--------------------|-----------|--------------------|-----------|-----------------------|-----------|
|                                  | Length             | Order     | Length             | Order     | Length                | Order     |
| U-O <sub>yl</sub>                | 1.79-1.81          | 2.02-2.08 | 1.80               | 2.04      | 1.80-1.81             | 2.04      |
| U-O <sub>CCI</sub>               |                    |           | 1.84               | 1.71      | 1.86-1.87             | 1.63-1.68 |
| U <sub>1</sub> -O <sub>CCI</sub> |                    |           | 2.62               | 0.25      | 2.56                  | 0.32      |
|                                  |                    |           |                    |           | 2.63                  | 0.29      |
| U-OH <sub>bridging</sub>         | 2.26-2.29          | 0.56-0.58 | 2.28               | 0.49      | 2.44                  | 0.37      |
|                                  | 2.56               |           | 2.51               | 0.21      | 2.36                  | 0.46      |
| U-OH <sub>pendant</sub>          | 2.18-2.19          | 0.27      | 2.17-2.19          | 0.87-0.91 | 2.16-2.17             | 0.88-0.91 |
| U-U                              | 3.84               | 0.02      | 3.78               | 0.04      | 3.39                  | 0.10      |

structure were calculated to be about 1.79-1.81  $\text{\AA}$ . The bonds between the bridging hydroxo uranyl groups are significantly longer for the uranyl group with two pendant hydroxo groups. The U-OH bonds for the pendant hydroxo groups were predicted to be about 2.18-2.19  $\text{\AA}$  long, Table 9.2. This  $\mu_2$ -dihydroxo structure was calculated to be 1.66 and 1.82 kcal/mol respectively

higher in energy than the  $\mu$ -hydroxo-di-CCI and  $\mu$ -hydroxo-CCI structures at the B3LYP/TZVP level, Table 9.1.

It is interesting that two of the lowest energy structures of  $(\text{UO}_2)_2(\text{OH})_5^-$  obtained at the B3LYP/TZVP level feature CCIs between the uranyl groups. CCIs have been observed in the solid-state structures of  $\text{UO}_3$ <sup>56</sup> and  $\text{UO}_3 \cdot \text{H}_2\text{O}$ <sup>56</sup>. The  $\text{U}-\text{O}_{\text{yl}}$  distances in solid state  $\text{UO}_3 \cdot \text{H}_2\text{O}$  range from 2.38 Å to 2.56 Å.<sup>56</sup> The  $\text{U}_1-\text{O}_{\text{CCI}}$  distances in  $\mu$ -hydroxo-CCI and  $\mu$ -hydroxo-di-CCI structures were however calculated to be between 2.56 and 2.63 Å, suggesting some retention of the general structure found in the solid phase after ablation and reaction in the gas phase. The longer  $\text{U}_1-\text{O}_{\text{CCI}}$  distances in the gas-phase structures are most likely due to the highly hydroxylated nature of the  $(\text{UO}_2)_2(\text{OH})_5^-$  complex.

The calculated U-U distances in these structures were all found to be less than the sum of the covalent radii of the uranium centers (3.92 Å).<sup>73</sup> The U-U distances were calculated as 3.39, 3.78 and 3.84 Å for the  $\mu$ -hydroxo-di-CCI,  $\mu$ -hydroxo-CCI and  $\mu_2$ -dihydroxo structures respectively, Table 9.2. The contraction of the U-U distance as the degree of CCIs is increased is consistent with the geometrical arrangements of the different structures.

**Relative Energies of the Most Stable Structures.** The calculated energy differences between these stable structures are found to be rather small at the B3LYP/TZVP level, Table 9.1. There is a possibility of substantial long-range effects on the calculated relative-energies of these structures due to the short U-U distances as well as the fact that some ligands bonded to each uranium atom are within the second-coordination sphere of the other uranium atom. There is also a need to confirm the stability of the structures featuring CCIs by employing other theoretical approaches. Towards this end, structural optimizations were carried out with the LDA,

BeckeHandH and CAM-B3LYP functionals as well as at the MP2 level. In addition, single point calculations at the MP2 optimized geometries were carried out using a coupled-cluster, CCSD(T), approach and several of long-range corrected density functionals, Table 9.1.

Optimization at the MP2/TZVP level breaks the degeneracy found between the  $\mu$ -hydroxo-di-CCI and  $\mu$ -hydroxo-CCI structures at the B3LYP/TZVP level, Table 9.1. Similarly, the LDA, BeckeHandH and CAM-B3LYP functionals predict the  $\mu$ -hydroxo-di-CCI structure to be lower in energy than the  $\mu$ -hydroxo-CCI structure. This is confirmed by the single-point energy calculations with the CCSD(T) approach at the MP2 optimized geometries. These calculations confirm the rather high-energy nature of the  $\mu_2$ -dihydroxo structure (4.5-9.0 kcal/mol) in comparison to the two structures featuring CCIs. Methodologically, the general trend in the relative energies obtained at the CCSD(T)//MP2 and MP2 levels are replicated by the BeckeHandH functional. The half and half functional however predicts the  $\mu_2$ -dihydroxo structure to be significantly higher in energy than is obtained with the ab initio approaches, Table 9.1. Optimization with the local density approximation (LDA) correctly predicts the  $\mu$ -hydroxo-di-CCI structure as the lowest energy structure, although the  $\mu$ -hydroxo-CCI and  $\mu_2$ -dihydroxo structures were found to be iso-energetic. Lastly, optimization with CAM-B3LYP, yields disappointing results for the overall trend as well as the magnitude of the relative energies when compared to the MP2 and CCSD(T)//MP2 results, Table 9.1.

**Calculated Vibrational Frequencies.** The calculated harmonic infra-red (IR) frequencies associated with the uranyl and hydroxo groups in the three most stable structures of  $(\text{UO}_2)_2(\text{OH})_5^-$  are presented in Table 9.3. Firstly, the O-H stretching of the hydroxo groups are found at around  $3791 \text{ cm}^{-1}$  in all the three structures. This is typical of uranium complexes containing hydroxo groups and is also present in the mono-nuclear uranyl hydroxo complexes.<sup>77</sup>

The U-OH stretching modes were calculated to be around 546-573 and 597-612  $\text{cm}^{-1}$  in  $\text{UO}_2(\text{OH})_2$  and  $\text{UO}_2(\text{OH})_3^-$  complexes respectively at the B3LYP/TZVP level. The calculated values for  $\text{UO}_2(\text{OH})_2$  are in good agreement with the experimental (547-569  $\text{cm}^{-1}$ ) and theoretical (534-572  $\text{cm}^{-1}$ ) values obtained by Wang et al.<sup>77</sup> In  $(\text{UO}_2)_2(\text{OH})_5^-$ , the U-O-H stretching modes of the pendant hydroxo ligands were calculated to be between 560 and 580  $\text{cm}^{-1}$  for the  $\mu_2$ -dihydroxo structure. These modes are found at 513-555  $\text{cm}^{-1}$  for the  $\mu$ -hydroxo-di-CCI and 533-577  $\text{cm}^{-1}$  for the  $\mu$ -hydroxo-CCI structures, Figure 9.2. Overall the peaks centered at around 570  $\text{cm}^{-1}$  are of modest intensities in the  $\mu_2$ -dihydroxo and  $\mu$ -hydroxo-CCI structures. The intense peaks between 420 and 520  $\text{cm}^{-1}$  correspond to the U-O-H bending and H-O-U-O-H asymmetric stretching modes among others. The U-O-H vibrational modes of the bridging hydroxo groups are however found at much higher wavenumbers. These were predicted to be at 748 and 734  $\text{cm}^{-1}$  in the  $\mu_2$ -dihydroxo structure at the B3LYP/TZVP level, Table 9.3. They are found at around 630 and 649  $\text{cm}^{-1}$  in the  $\mu$ -hydroxo-CCI and  $\mu$ -hydroxo-di-CCI structures respectively.

The uranyl groups in mononuclear uranyl complexes are generally involved in a set of IR active asymmetric and an IR inactive symmetric stretching vibrations. The symmetric uranyl stretching modes were calculated to be at 883 and 832  $\text{cm}^{-1}$  for  $\text{UO}_2(\text{OH})_2$  and  $\text{UO}_2(\text{OH})_3^-$  respectively at the B3LYP/TZVP level while the asymmetric stretching modes were respectively calculated at about 955 and 905  $\text{cm}^{-1}$ , Table 9.3. Wang et al. reported values of 920 and 944  $\text{cm}^{-1}$  from their experimental and theoretical work on  $\text{UO}_2(\text{OH})_2$  respectively.<sup>77</sup> The calculated IR spectra for the three low energy structures of  $(\text{UO}_2)_2(\text{OH})_5^-$ , Figure 9.2, show the presence of

**Table 9.3:** Calculated IR vibrational frequencies ( $\text{cm}^{-1}$ ) of the low energy structures of  $(\text{UO}_2)_2(\text{OH})_5^-$  obtained at the B3LYP/TZVP level. The normalized intensities are given in parenthesis.

|  | $\mu_2$ -dihydroxo                            | $\mu$ -hydroxo-CCI                            | $\mu$ -hydroxo-di-CCI              |
|--|---|---|------------------------------------|
| Uranyl Modes                             |   |   |                                    |
| Asymmetric*                              |   |   |                                    |
| $\text{O}_{1a}\text{-U}_1\text{-O}_{1b}$ | 921 (0.9)                                     | 899 (0.6)                                     | 871 (0.2)                          |
| $\text{O}_{2a}\text{-U}_1\text{-O}_{2b}$ | 895 (0.2)                                     | 882 (0.7)                                     | 867 (1.0)                          |
| Symmetric*                               |   |   |                                    |
| $\text{O}_{1a}\text{-U}_1\text{-O}_{1b}$ | 843 (0.0)                                     | 828 (0.0)                                     | 783 (0.2)                          |
| $\text{O}_{2a}\text{-U}_1\text{-O}_{2b}$ | 823 (0.0)                                     | 783 (0.2)                                     | 732 (0.1)                          |
| Bridging Hydroxo                         | 748 (0.2), 734 (0.1)                          | 631 (0.1)                                     | 649 (0.1)                          |
| Pendant Hydroxo                          | 587 (0.0), 578 (0.2),<br>573 (0.1), 563 (0.2) | 577 (0.1), 571 (0.2),<br>537 (0.0), 534 (0.0) | 555 (0.0), 535 (0.1),<br>532 (0.0) |
| Mixed hydroxo                            | 518 (0.5)                                     | 520 (0.1)                                     | 524 (0.0)                          |

\* The  $\text{O}_{1a}\text{-U}_1\text{-O}_{1b}$  and  $\text{O}_{2a}\text{-U}_2\text{-O}_{2b}$  stretching modes correspond to stretching of each of the uranyl groups.

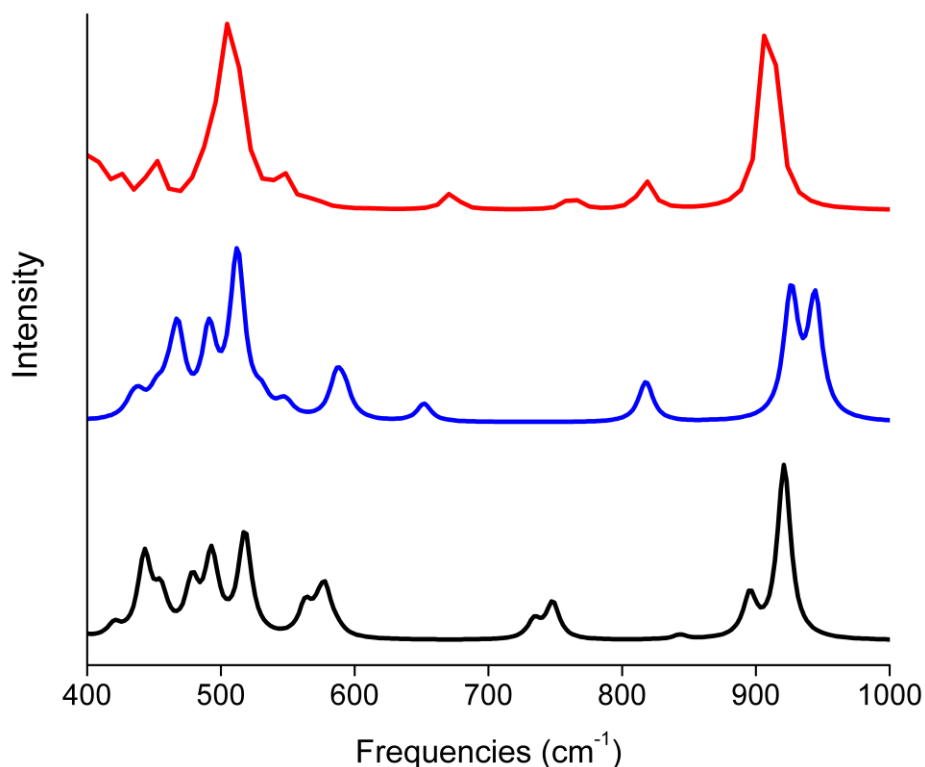


**Figure 9.2:** Calculated IR spectra for the  $\mu_2$ -dihydroxo (black),  $\mu$ -hydroxo-CCI (blue) and  $\mu$ -hydroxo-di-CCI (red) structures of  $(\text{UO}_2)_2(\text{OH})_5^-$  obtained using the B3LYP functional.

four uranyl stretching modes between  $750\text{--}950\text{ cm}^{-1}$ . These modes can be divided into two sets between  $750\text{--}860$  and  $860\text{--}950\text{ cm}^{-1}$ . The sets found at higher wavenumbers involve asymmetric uranyl stretching while the sets at lower wavenumbers correspond to symmetric uranyl stretching modes. It should however be noted that there is some variability in the degree of coupling between the stretching modes of the individual uranyl groups. Interestingly, the lowest uranyl stretching mode ( $783\text{ cm}^{-1}$ ) in the  $\mu$ -hydroxo-CCI structure and the two lowest ( $783$  and  $732\text{ cm}^{-1}$ ) in the  $\mu$ -hydroxo-di-CCI structures were predicted to yield peaks of modest IR intensities. These peaks correspond largely to the stretching vibrations of the  $\text{U-O}_{\text{CCI}}$  bonds. The modest

intensities of these vibrational modes are in contrast to the weak IR activity of the symmetric stretching vibrations of the uranyl group in the  $\mu_2$ -dihydroxo structure, Figure 9.2. This provides a tantalizing suggestion of the possibility of confirming the presence of CCIs in the ground state structure of  $(\text{UO}_2)_2(\text{OH})_5^-$ . A measurement of the IR and Raman spectra of gaseous  $(\text{UO}_2)_2(\text{OH})_5^-$  could provide equivocal confirmation of the existence or otherwise of CCIs in the gas phase structure, as the symmetric stretching modes of the uranyl group in the  $\mu_2$ -dihydroxo structure are significantly weaker (IR) and are found at about  $50\text{ cm}^{-1}$  higher wavenumbers than those in the  $\mu$ -hydroxo-CCI and  $\mu$ -hydroxo-di-CCI structures. In addition, the peaks corresponding to wagging of the bridging hydroxo ligands at around  $750\text{ cm}^{-1}$  for the  $\mu_2$ -dihydroxo structure and those corresponding to the stretching of the U-O<sub>yl</sub> bonds in the CCI structures peaks (near  $800\text{ cm}^{-1}$ ) can also be used as probes to distinguish the  $\mu_2$ -dihydroxo structure from those featuring CCIs. Overall, the calculated relative intensities of the peaks obtained with the LDA and BeckeHandH functionals confirm the usefulness of these vibrational modes.

**Bonding.** The Mayer-Mulliken bond order has been very useful in the description of bonding in inorganic molecules.<sup>76, 78</sup> The U-O<sub>yl</sub> bonds in the bare uranyl group were calculated to have a bond order of 2.42, Table 9.4, indicating significant triple bond character. Addition of hydroxo ligands to the mononuclear uranyl species gradually decreases the multiplicity of the U-O<sub>yl</sub> bonds to 2.01 in  $\text{UO}_2(\text{OH})_3^-$ . A similar elongation and accompanying decrease in the bond orders of the U-OH bonds is seen with larger number of equatorial hydroxo ligands.

Examination of the calculated bond orders in the structures of  $(\text{UO}_2)_2(\text{OH})_5^-$  allows for several conclusions, Table 9.2. Firstly, for the pendant hydroxo ligands, the U-OH bond orders are between 0.86 and 0.92, intermediate between the values obtained for  $\text{UO}_2(\text{OH})_2$ , 1.01, and  $\text{UO}_2(\text{OH})_3^-$ , 0.81 respectively, Table 9.4. The calculated bond orders of the U-O<sub>yl</sub> bonds in the

**Table 9.4:** Calculated bond lengths (Å), bond orders and vibrational frequencies (cm<sup>-1</sup>) of a few gas-phase mono-nuclear uranium complexes obtained at the B3LYP/TZVP level.

|  | Bond Lengths (Å)  |       |       | Bond Orders       |      |      | Frequencies (cm <sup>-1</sup> ) |
|--|-------------------|-------|-------|-------------------|------|------|---------------------------------|
|  | U-O <sub>yl</sub> | U-O   | U-OH  | U-O <sub>yl</sub> | U-O  | U-OH |                                 |
| UO <sub>2</sub> <sup>2+</sup>                  | 1.701             |       |       | 2.42              |      |      | 1049, 1149                      |
| UO <sub>2</sub> (OH) <sup>+</sup>              | 1.745             |       | 2.010 | 2.27              |      | 1.21 | 955, 1033                       |
| UO <sub>2</sub> (OH) <sub>2</sub>              | 1.785             |       | 2.114 | 2.12              |      | 1.01 | 883, 955                        |
| UO <sub>2</sub> (OH) <sub>3</sub> <sup>-</sup> | 1.811             |       | 2.221 | 2.01              |      | 0.81 | 832, 905                        |
| UO <sub>3</sub>                                | 1.807             | 1.849 |       | 2.13              | 2.18 |      | 789, 893, 893                   |

uranyl groups of the  $\mu_2$ -dihydroxo structure and the free U-O<sub>yl</sub> bonds of the CCI structures range between 2.02 and 2.08. In contrast for the oxo atoms involved in CCIs, the U-O<sub>CCI</sub> bond orders are significantly decreased, ranging in value between 1.63 and 1.71. The reduction in bond order is similar but lesser than the significant decrease of up to a full bond order usually observed upon reductive oxo-functionalization.<sup>50, 79</sup> Regarding the oxo and hydroxo bridges across the uranium centers, the U<sub>1</sub>-O<sub>CCI</sub> bonds possess bond orders between 0.25 and 0.32 while the U-OH<sub>bridging</sub> bonds have bond orders between 0.21 and 0.58.

Lastly, the short U-U distances, especially in the  $\mu$ -hydroxo-di-CCI structure, are most likely due to the hard-hard nature of the uranium-oxygen interactions. We draw this conclusion

because the calculated bond orders across the U-U distances are negligible (0.02-0.10). This certainly suggests that covalent interactions between the actinide centers are essentially non-existent.

The dissociation of the three low-energy structures of  $(\text{UO}_2)_2(\text{OH})_5^-$  into  $\text{UO}_2(\text{OH})_2$  and  $\text{UO}_2(\text{OH})_3^-$  were calculated to be endothermic at the B3LYP/TZVP level. The energy required ranges from 50.0 kcal/mol in the case of the  $\mu_2$ -dihydroxo structure to 51.6 kcal/mol for the  $\mu$ -hydroxo-di-CCI structure. This confirms the stability of the structures, with the bridging U-OH and U-O'<sub>CCI</sub> bonds sufficiently holding the two units together. Given the low bond orders obtained for the bridging U-OH and U-O'<sub>CCI</sub> bonds, we examined the calculated Mulliken charges of the involved atoms. The effective charges on the oxygen atoms of the pendant hydroxo groups are generally between -0.72 and -0.75 while the charges for the free uranyl oxo atoms are between -0.51 and -0.56. In contrast, the uranyl oxo atoms involved in CCIs possess effective charges between -0.60 and -0.63 while for the bridging hydroxo groups the effective charges were calculated to be between -0.78 and -0.85. It appears that the bridging oxo and hydroxo groups are overall more polarized than the free oxo and pendant hydroxo groups respectively. A reflection of this is seen in the fact that the uranium centers with oxo atoms participating in CCIs possess larger effective charges. This is in line with lower overlap with the oxo atoms (smaller bond order for the U-O<sub>CCI</sub> bonds in contrast to the free U-O<sub>yl</sub> bonds) as well as larger electrostatic interaction of the CCI oxo atoms with the adjacent uranium atoms (very low bond orders for the U<sub>1</sub>-O<sub>CCI</sub> bonds).

**Other Structures of  $(\text{UO}_2)_2(\text{OH})_5^-$ .** There are many other possible structures for  $(\text{UO}_2)_2(\text{OH})_5^-$ . We present a few of them in Figure 9.3. The complexes with aquo ligands, **A**, **B** and **C**, are of significantly higher energies than the hydroxylated ones. This is the case at both the B3LYP and

MP2//B3LYP level. Single point MP2 calculations on the B3LYP/TZVP optimized geometries appear sufficient as they also predict the removal of the degeneracy between the  $\mu$ -hydroxo-CCI and  $\mu$ -hydroxo-di-CCI that was obtained at the B3LYP level, Table 9.1. The aquo complexes are essentially  $(\text{UO}_3)_n(\text{OH})^-.n\text{H}_2\text{O}$  adducts formed as intermediates to the hydroxylated complexes. Other structures include those with only one bridging oxo, **D**, or one hydroxo group, **E**, which are higher in energy than the structures in Figure 9.1, a reflection of the fact that the hydroxo bridges as well as the CCIs confer stability on the structural framework. The relative energy of **E** with respect to the  $\mu$ -hydroxo-di-CCI structure increases to 12.3 kcal/mol at the MP2//B3LYP level. This is unsurprising and is in line with the results presented in Table 9.1, MP2 favors the CCI structures. Of the remaining structures presented in Figure 9.3, **G** is particularly interesting. It is very similar to the  $\mu$ -hydroxo-CCI structure, with a pendant hydroxo group now converted into a second bridging ligand. This structure was predicted to be about 13.7 and 2.4 kcal/mol higher in energy than the  $\mu$ -hydroxo-di-CCI structure at the B3LYP and MP2//B3LYP levels respectively. The implication of this is that it is even more stable than the  $\mu$ -hydroxo-CCI structure at the MP2//B3LYP level. Attempts at re-optimizing the structure of **G** at the MP2 level however results in it collapsing to the  $\mu$ -hydroxo-di-CCI structure.

**Structures of other  $(\text{UO}_2)_2(\text{OH})_n^{4-n}$  complexes.**  $(\text{UO}_2)_2(\text{OH})_5^-$  is a member of the  $(\text{UO}_2)_2(\text{OH})_n^{4-n}$  series of complexes and was identified in a mass spectrometric study.<sup>54</sup> To determine the role of CCIs in the gas phase structures of the other complexes in this series, the structures of  $(\text{UO}_2)_2(\text{OH})_2^{2+}$ ,  $(\text{UO}_2)_2(\text{OH})_3^+$ ,  $(\text{UO}_2)_2(\text{OH})_4$ , and  $(\text{UO}_2)_2(\text{OH})_6^{2-}$  were all optimized using similar approaches and basis sets employed for  $(\text{UO}_2)_2(\text{OH})_5^-$ . The most stable structure for  $(\text{UO}_2)_2(\text{OH})_2^{2+}$  was found to be a  $\mu_2$ -dihydroxo structure at the B3LYP/TZVP level. A  $\mu$ -hydroxo-CCI structure, Figure 9.4, was calculated to be about 4.2 kcal/mol higher in energy than

the  $\mu_2$ -dihydroxo structure at this level, Table 9.5. In addition, another structure in which two  $\text{UO}_2(\text{OH})^+$  groups interact via their oxo atoms was predicted to be 16.5 kcal/mol higher in energy than the  $\mu_2$ -dihydroxo structure. This structure is labeled as di-CCI. The general trend in the relative stabilities of the  $\mu_2$ -dihydroxo,  $\mu$ -dihydroxo-CCI and di-CCI structures of  $(\text{UO}_2)_2(\text{OH})_2^{2+}$  obtained with the B3LYP functional is in agreement with those obtained at the MP2 and CCSD(T)//MP2 levels, Table 9.5.

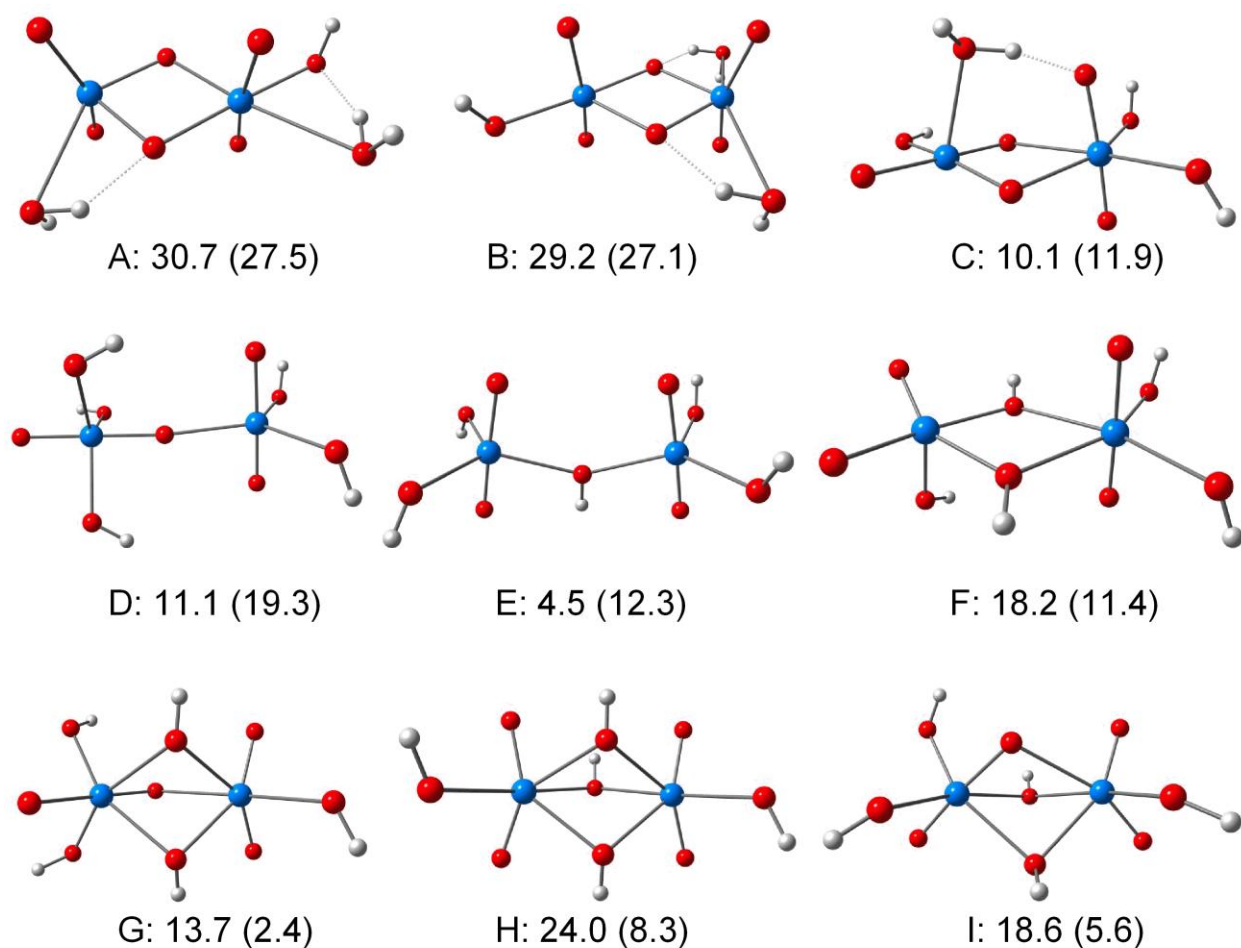


**Figure 9.3:** Other possible structure of  $(\text{UO}_2)_2(\text{OH})_5^-$ . Their energies at the B3LYP (and MP2//B3LYP) levels are given relative to that of the  $\mu$ -hydroxo-di-CCI structure.

The  $\mu_2$ -dihydroxo framework was also found as the lowest energy structures of the tetrahydroxo,  $(\text{UO}_2)_2(\text{OH})_4$ , and hexahydroxo,  $(\text{UO}_2)_2(\text{OH})_6^{2-}$ , complexes at the B3LYP/TZVP level, Figure 9.4. Structurally, the trend towards increasingly longer U-O<sub>y1</sub> and U-OH bonds with increasing numbers of equatorial hydroxo ligands is evident in these complexes. Energetically, the  $\mu$ -hydroxo-CCI structures were calculated to be higher in energy than the  $\mu_2$ -dihydroxo ones by about 4.05 and 6.11 kcal/mol for the tetra- and hexahydroxo complexes at the B3LYP/TZVP level respectively, Table 9.5. Similar to the case in the dihydroxo complex, the di-CCI structures were found at much higher energies (11.13 and 18.37 kcal/mol for the tetra- and hexahydroxo complexes). The trends in the relative energies of these three structures calculated at the MP2 and CCSD(T)//MP2 levels are in good agreement with those obtained at the B3LYP level. We note that the tetrahydroxo complexes were predicted to be stable with respect to fragmentation into two units of  $\text{UO}_2(\text{OH})_2$ . The decompositions of the di-CCI,  $\mu$ -hydroxo-CCI and  $\mu_2$ -dihydroxo structures of  $(\text{UO}_2)_2(\text{OH})_4$  were calculated to be endothermic by about 33.19, 40.00 and 43.12 kcal/mol respectively at the B3LYP/TZVP level. The stability of these structures is understandable given that the charge on each monomeric  $\text{UO}_2(\text{OH})_2$  unit is zero. This also indicates that while the di-CCI structure of the tetrahydroxo complex, Figure 9.4, is significantly higher in energy than the lowest energy structure, the CCIs can still bind the monomer units together with a significant amount of energy (33.19 kcal/mol). We also explored a variety of other structures for  $(\text{UO}_2)_2(\text{OH})_4$  and  $(\text{UO}_2)_2(\text{OH})_6^{2-}$ , amongst which are those with a butterfly shaped  $\text{U}_2\text{O}_4$  core, similar to the recently reported complex,<sup>80</sup> and those similar to structure **G** in Figure 9.3.

**Table 9.5:** Relative energies (kcal/mol) of the low energy structures of  $(\text{UO}_2)_2(\text{OH})_n^{4-n}$ , ( $n=2, 3, 4$  and  $6$ ) obtained at the DFT and ab initio levels.

|                                     | B3LYP | MP2   | CCSD(T)//MP2 |
|-------------------------------------|-------|-------|--------------|
| $(\text{UO}_2)_2(\text{OH})_2^{2+}$ |       |       |              |
| $\mu_2$ -dihydroxo                  | 0.00  | 0.00  | 0.00         |
| $\mu$ -hydroxo-CCI                  | 4.15  | 3.89  | 7.60         |
| di-CCI                              | 16.51 | 12.66 | 35.86        |
| $(\text{UO}_2)_2(\text{OH})_3^+$    |       |       |              |
| $\mu_2$ -dihydroxo                  | 0.00  | 0.48  | 0.00         |
| $\mu$ -hydroxo-CCI                  | 0.80  | 1.36  | 1.19         |
| $\mu$ -hydroxo-di-CCI               | 3.49  | 0.00  | 3.55         |
| $(\text{UO}_2)_2(\text{OH})_4$      |       |       |              |
| $\mu_2$ -dihydroxo                  | 0.00  | 0.00  | 0.00         |
| $\mu$ -hydroxo-CCI                  | 4.04  | 3.76  | 4.03         |
| di-CCI                              | 11.13 | 9.68  | 10.98        |
| $(\text{UO}_2)_2(\text{OH})_6^{2-}$ |       |       |              |
| $\mu_2$ -dihydroxo                  | 0.00  | 0.00  | 0.00         |

|                    |       |       |       |
|--------------------|-------|-------|-------|
| $\mu$ -hydroxo-CCl | 6.11  | 7.63  | 8.70  |
| di-CCl             | 18.37 | 17.97 | 20.09 |

---

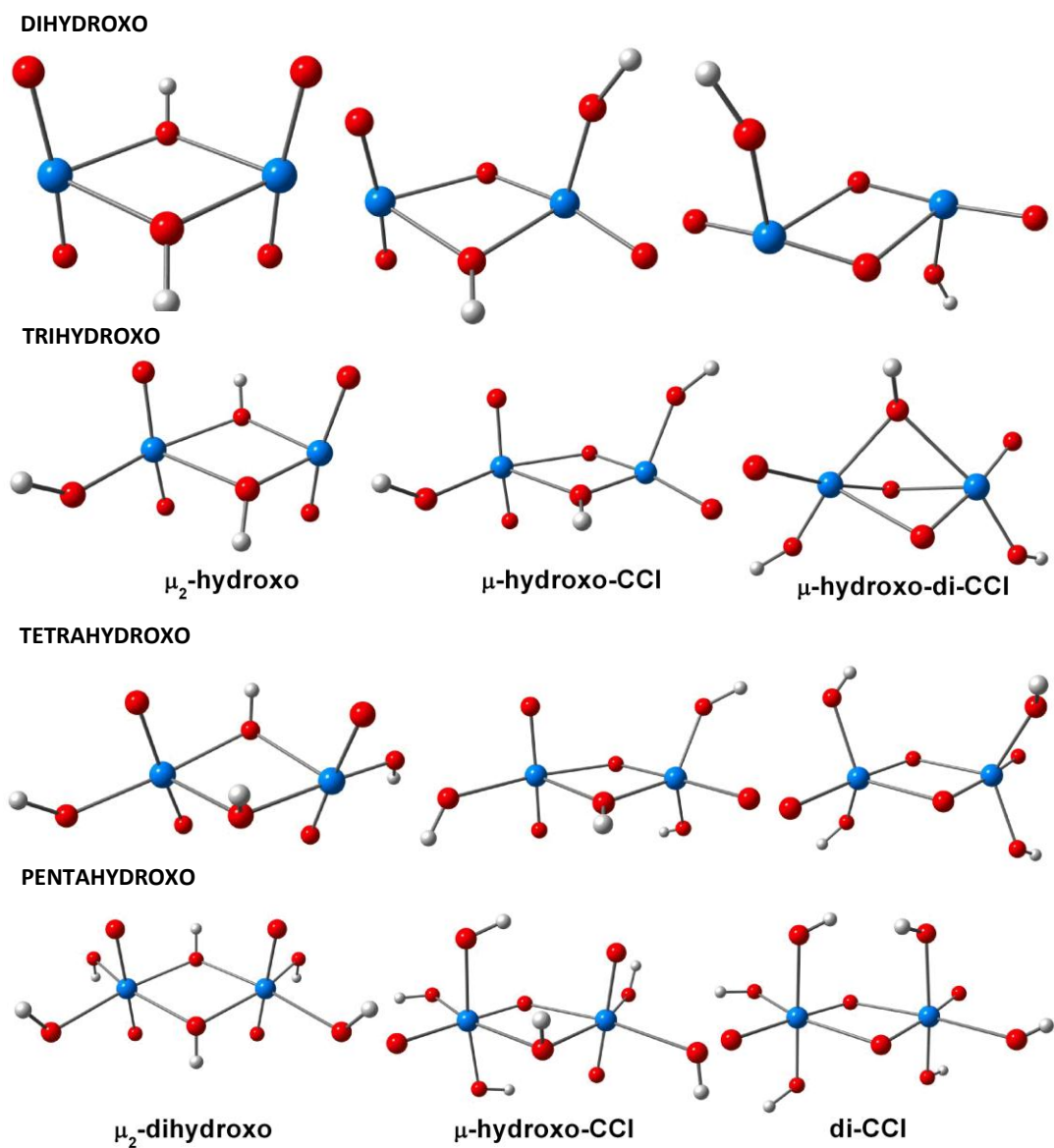


**Figure 9.4:** Low energy structures of the bis-uranyl hydroxo complexes,  $(\text{UO}_2)_2(\text{OH})_n^{4-n}$ .

The trihydroxo complex is similar to the title complex,  $(\text{UO}_2)_2(\text{OH})_5^-$ , in that they both have an odd number of hydroxo groups. This, like in the pentahydroxo complex, allows for a bridging hydroxide in between two  $\text{UO}_2(\text{OH})^+$  entities. For this complex, Figure 9.4, the  $\mu_2$ -dihydroxo structure was calculated to be only 0.80 kcal/mol higher in energy than the  $\mu$ -hydroxo-CCI structure at the B3LYP/TZVP level while the  $\mu$ -hydroxo-di-CCI structure was calculated to be 3.50 kcal/mol higher in energy, Table 9.5. The small relative energies of these structures are in distinct contrast to the relative energies of similar structures in the di-, tetra- and hexahydroxo species, Table 9.5. Overall this suggests that the increased stability of structural frameworks featuring CCIs between the uranyl groups begins in the trihydroxo complex. It would appear that the odd number of hydroxo ligands confers increased stabilization by a bridging ligand across the uranyl groups. The  $\mu$ -hydroxo-di-CCI and  $\mu_2$ -dihydroxo structures were found to be the most stable structure at the MP2 and CCSD(T)//MP2 levels respectively. The  $\mu$ -hydroxo-CCI and  $\mu$ -hydroxo-di-CCI structures were calculated to be about 1.19 and 3.55 kcal/mol higher energy than the  $\mu_2$ -dihydroxo structure at the CCSD(T)//MP2 level. The smaller energy differences between these structures and the greater stabilities of the CCI structures in the pentahydroxo complex, Table 9.1, indicate the role of molecular symmetry (with respect to the pendant and bridging ligands).

## Conclusions

We have examined the structural and electronic properties of several structures of the gas phase bis-uranyl hydroxo complex,  $[(\text{UO}_2)_2(\text{OH})_5]^-$ , using a range of DFT and ab initio methods. A similar approach was also employed in the search for the stable structures of the  $(\text{UO}_2)_2(\text{OH})_n^{4-n}$  ( $n=2, 3, 4$  and  $6$ ) complexes. Particular emphasis was given to low energy structures featuring CCIs between the two uranyl groups.

Structurally, the bis-uranyl complexes are similar to their uranyl counterparts. The progressive elongation of the U-O<sub>y1</sub> and U-OH bonds as the number of equatorial hydroxo ligands in the [(UO<sub>2</sub>)<sub>2</sub>(OH)<sub>n</sub>]<sup>4-n</sup> complexes is similar to the observation in the uranyl complexes. A search of the low energy structures for the [(UO<sub>2</sub>)<sub>2</sub>(OH)<sub>n</sub>]<sup>4-n</sup> complexes shows that the μ<sub>2</sub>-dihydroxo structures are significantly more stable than those featuring CCIs for the dihydroxo, tetrahydroxo and hexahydroxo complexes. In contrast, structures featuring uranyl CCIs were however found to be more stable than the μ<sub>2</sub>-dihydroxo structures for the trihydroxo and pentahydroxo complexes. A combination of the role of hydroxo ligands as σ-donors increasing the Lewis basicity of the uranyl oxo atoms and symmetry is most likely responsible for the greater stability of the CCI structures in the gaseous trihydroxo and pentahydroxo complexes. It remains to be seen whether the CCI structural arrangements have been overlooked in aqueous phase chemistry.

For the calculated structural parameters of (UO<sub>2</sub>)<sub>2</sub>(OH)<sub>5</sub><sup>-</sup>, the U-O bonds for the oxo-atoms involved in CCIs are significantly elongated in comparison to their free counterparts. This is similar to the popular case of oxo-functionalized pentavalent and hexavalent uranyl complexes. The formation of CCIs creates discrepancies in the calculated IR vibrational frequencies associated with the stretching of the U-O<sub>y1</sub> bonds suggesting that the existence or otherwise of the CCI structures can be experimentally confirmed by measuring the IR spectrum of gas-phase (UO<sub>2</sub>)<sub>2</sub>(OH)<sub>5</sub><sup>-</sup>. In addition, signature U-O-H stretching of the bridging hydroxo group at around 750 cm<sup>-1</sup> and U-O<sub>y1</sub> stretching peaks around 800 cm<sup>-1</sup> should allow for a conclusive differentiation of the CCI and dihydroxo structures.

Examination of the bonding in  $[(\text{UO}_2)_2(\text{OH})_5]^-$  reveals the ionic nature of the  $\mu$ -hydroxo and CCI's oxo bridges. Negligible covalent interactions were found between the two actinide centers even in structures with significantly short U-U distances.

## References

1. Barros, N.; Maynau, D.; Maron, L.; Eisenstein, O.; Zi, G. F.; Andersen, R. A., *Organometallics* **2007**, *26*, 5059.
2. Bolvin, H.; Wahlgren, U.; Moll, H.; Reich, T.; Geipel, G.; Fanghanel, T.; Grenthe, I., *J. Phys. Chem. A* **2001**, *105*, 11441.
3. Brynda, M.; Wesolowski, T. A.; Wojciechowski, K., *J. Phys. Chem. A* **2004**, *108*, 5091.
4. Clavaguera-Sarrio, C.; Vallet, V.; Maynau, D.; Marsden, C. J., *J. Chem. Phys.* **2004**, *121*, 5312.
5. de Jong, W. A.; Harrison, R. J.; Nichols, J. A.; Dixon, D. A., *Theor. Chem. Acc.* **2001**, *107*, 22.
6. Gagliardi, L.; Roos, B. O., *Chem. Phys. Lett.* **2000**, *331*, 229.
7. Groenewold, G. S.; Gianotto, A. K.; McIlwain, M. E.; Van Stipdonk, M. J.; Kullman, M.; Moore, D. T.; Polfer, N.; Oomens, J.; Infante, I.; Visscher, L.; Siboulet, B.; De Jong, W. A., *J. Phys. Chem. A* **2008**, *112*, 508.
8. Groenewold, G. S.; Oomens, J.; de Jong, W. A.; Gresham, G. L.; McIlwain, M. E.; Van Stipdonk, M. J., *Phys. Chem. Chem. Phys.* **2008**, *10*, 1192.
9. Gutowski, K. E.; Cocalia, V. A.; Griffin, S. T.; Bridges, N. J.; Dixon, D. A.; Rogers, R. D., *J. Am. Chem. Soc.* **2007**, *129*, 526.

10. Hemmingsen, L.; Amara, P.; Ansoborlo, E.; Field, M. J., *J. Phys. Chem. A* **2000**, *104*, 4095.
11. Kozimor, S. A.; Yang, P.; Batista, E. R.; Boland, K. S.; Burns, C. J.; Clark, D. L.; Conradson, S. D.; Martin, R. L.; Wilkerson, M. P.; Wolfsberg, L. E., *J. Am. Chem. Soc.* **2009**, *131*, 12125.
12. Nocton, G.; Horeglad, P.; Vetere, V.; Pecaut, J.; Dubois, L.; Maldivi, P.; Edelstein, N. M.; Mazzanti, M., *J. Am. Chem. Soc.* **2010**, *132*, 495.
13. Real, F.; Vallet, V.; Marian, C.; Wahlgren, U., *J. Chem. Phys.* **2007**, *127*.
14. Schreckenbach, G.; Hay, P. J.; Martin, R. L., *Inorg. Chem.* **1998**, *37*, 4442.
15. Schreckenbach, G.; Hay, P. J.; Martin, R. L., *J. Comput. Chem.* **1999**, *20*, 70.
16. Schreckenbach, G.; Shamov, G. A., *Accounts Chem. Res.* **2010**, *43*, 19.
17. Shamov, G. A.; Schreckenbach, G., *J. Am. Chem. Soc.* **2008**, *130*, 13735.
18. Sundararajan, M.; Campbell, A. J.; Hillier, I. H., *J. Phys. Chem. A* **2008**, *112*, 4451.
19. Tsushima, S.; Rossberg, A.; Ikeda, A.; Muller, K.; Scheinost, A. C., *Inorg. Chem.* **2007**, *46*, 10819.
20. Vallet, V.; Wahlgren, U.; Schimmelpfennig, B.; Moll, H.; Szabo, Z.; Grenthe, I., *Inorg. Chem.* **2001**, *40*, 3516.
21. Vazquez, J.; Bo, C.; Poblet, J. M.; de Pablo, J.; Bruno, J., *Inorg. Chem.* **2003**, *42*, 6136.
22. Wahlin, P.; Danilo, C.; Vallet, V.; Real, F.; Flament, J. P.; Wahlgren, U., *J. Chem. Theory Comput.* **2008**, *4*, 569.
23. Wander, M. C. F.; Kerisit, S.; Rosso, K. M.; Schoonen, M. A. A., *J. Phys. Chem. A* **2006**, *110*, 9691.
24. Yahia, A.; Arnold, P. L.; Love, J. B.; Maron, L., *Chem. Commun.* **2009**, 2402.

25. Graves, C. R.; Kiplinger, J. L., *Chem. Commun.* **2009**, 3831.
26. Hayton, T. W.; Boncella, J. M.; Scott, B. L.; Batista, E. R.; Hay, P. J., *J. Am. Chem. Soc.* **2006**, *128*, 10549.
27. Hayton, T. W.; Boncella, J. M.; Scott, B. L.; Palmer, P. D.; Batista, E. R.; Hay, P. J., *Science* **2005**, *310*, 1941.
28. Andrews, L.; Liang, B. Y.; Li, J.; Bursten, B. E., *Angew. Chem. Int. Edit.* **2000**, *39*, 4565.
29. Chertihin, G. V.; Andrews, L.; Neurock, M., *J. Phys. Chem-US* **1996**, *100*, 14609.
30. Chien, W.; Anbalagan, V.; Zandler, M.; Van Stipdonk, M.; Hanna, D.; Gresham, G.; Groenewold, G., *J. Am. Soc. Mass. Spectr.* **2004**, *15*, 777.
31. Cornehl, H. H.; Wesendrup, R.; Diefenbach, M.; Schwarz, H., *Chem-Eur. J.* **1997**, *3*, 1083.
32. Di Santo, E.; Santos, M.; Michelini, M. C.; Marcalo, J.; Russo, N.; Gibson, J. K., *J. Am. Chem. Soc.* **2011**, *133*, 1955.
33. Gibson, J. K., *Int. J. Mass Spectrom.* **2002**, *214*, 1.
34. Gibson, J. K.; Marcalo, J., *Coordin. Chem. Rev.* **2006**, *250*, 776.
35. Gresham, G. L.; Gianotto, A. K.; Harrington, P. D.; Cao, L. B.; Scott, J. R.; Olson, J. E.; Appelhans, A. D.; Van Stipdonk, M. J.; Groenewold, G. S., *J. Phys. Chem. A* **2003**, *107*, 8530.
36. Hunt, R. D.; Andrews, L., *J. Chem. Phys.* **1993**, *98*, 3690.
37. Hunt, R. D.; Yustein, J. T.; Andrews, L., *J. Chem. Phys.* **1993**, *98*, 6070.
38. Jackson, G. P.; Gibson, J. K.; Duckworth, D. C., *J. Phys. Chem. A* **2004**, *108*, 1042.
39. Jackson, G. P.; King, F. L.; Goeringer, D. E.; Duckworth, D. C., *J. Phys. Chem. A* **2002**, *106*, 7788.

40. Lyon, J. T.; Andrews, L.; Malmqvist, P. A.; Roos, B. O.; Yang, T. X.; Bursten, B. E., *Inorg. Chem.* **2007**, *46*, 4917.
41. Marcalo, J.; Gibson, J. K., *J. Phys. Chem. A* **2009**, *113*, 12599.
42. Michelini, M. D.; Marcalo, J.; Russo, N.; Gibson, J. K., *Inorg. Chem.* **2010**, *49*, 3836.
43. Michelini, M. D.; Russo, N.; Sicilia, E., *J. Am. Chem. Soc.* **2007**, *129*, 4229.
44. Pereira, C. C. L.; Marsden, C. J.; Marcalo, J.; Gibson, J. K., *Phys. Chem. Chem. Phys.* **2011**, *13*, 12940.
45. Ricks, A. M.; Gagliardi, L.; Duncan, M. A., *J. Phys. Chem. Lett.* **2011**, *2*, 1662.
46. Santos, M.; Marcalo, J.; Leal, J. P.; de Matos, A. P.; Gibson, J. K.; Haire, R. G., *Int. J. Mass Spectrom.* **2003**, *228*, 457.
47. Van Stipdonk, M. J.; Chien, W.; Anbalagan, V.; Bulleigh, K.; Hanna, D.; Groenewold, G. S., *J. Phys. Chem. A* **2004**, *108*, 10448.
48. Van Stipdonk, M. J.; Chien, W.; Anbalagan, V.; Gresham, G. L.; Groenewold, G. S., *Int. J. Mass Spectrom.* **2004**, *237*, 175.
49. Van Stipdonk, M. J.; Chien, W.; Bulleigh, K.; Wu, Q.; Groenewold, G. S., *J. Phys. Chem. A* **2006**, *110*, 959.
50. Wang, X. F.; Andrews, L.; Vlasisavljevich, B.; Gagliardi, L., *Inorg. Chem.* **2011**, *50*, 3826.
51. Zhou, M. F.; Andrews, L.; Ismail, N.; Marsden, C., *J. Phys. Chem. A* **2000**, *104*, 5495.
52. Zhou, M. F.; Andrews, L.; Li, J.; Bursten, B. E., *J. Am. Chem. Soc.* **1999**, *121*, 9712.
53. Marcalo, J.; Santos, M.; de Matos, A. P.; Gibson, J. K., *Inorg. Chem.* **2009**, *48*, 5055.
54. Groenewold, G.; de Jong, W. A., *Personal Communication* **2011**.
55. Barthen, N.; Millon, E.; Aubriet, F., *J. Am. Soc. Mass. Spectr.* **2011**, *22*, 508.

56. Siegel, S.; Hoekstra, H.; Sherry, E., *Acta Crystallogr.* **1966**, *20*, 292.
57. Siegel, S.; Tani, B.; Viste, A.; Hoekstra, H. R., *Acta Crystallogr. B-Stru.* **1972**, *B 28*, 117.
58. Denning, R. G., *Struct. Bond.* **1992**, *79*, 215.
59. Denning, R. G., *J. Phys. Chem. A* **2007**, *111*, 4125.
60. Denning, R. G.; Snellgrove, T. R.; Woodward, D. R., *Mol. Phys.* **1979**, *37*, 1109.
61. Fortier, S.; Hayton, T. W., *Coordin. Chem. Rev.* **2010**, *254*, 197.
62. Aberg, M., *Acta. Chem. Scand. A* **1978**, *32*, 101.
63. Henry, N.; Lagrenee, M.; Loiseau, T.; Clavier, N.; Dacheux, N.; Abraham, F., *Inorg. Chem. Commun.* **2011**, *14*, 429.
64. Thuery, P., *Acta Crystallogr. C* **2007**, *63*, M54.
65. Thuery, P.; Masci, B., *Acta Crystallogr. C* **2002**, *58*, m556.
66. Valiev, M.; Bylaska, E. J.; Govind, N.; Kowalski, K.; Straatsma, T. P.; Van Dam, H. J. J.; Wang, D.; Nieplocha, J.; Apra, E.; Windus, T. L.; de Jong, W., *Comput. Phys. Commun.* **2010**, *181*, 1477.
67. Bergner, A.; Dolg, M.; Kuchle, W.; Stoll, H.; Preuss, H., *Mol. Phys.* **1993**, *80*, 1431.
68. Kuchle, W.; Dolg, M.; Stoll, H.; Preuss, H., *Mol. Phys.* **1991**, *74*, 1245.
69. Kuchle, W.; Dolg, M.; Stoll, H.; Preuss, H., *J. Chem. Phys.* **1994**, *100*, 7535.
70. Godbout, N.; Salahub, D. R.; Andzelm, J.; Wimmer, E., *Can. J. Chem.-Rev. Can. Chim.* **1992**, *70*, 560.
71. Aubriet, F.; Gaumet, J. J.; de Jong, W. A.; Groenewold, G. S.; Gianotto, A. K.; McIlwain, M. E.; Van Stipdonk, M. J.; Leavitt, C. M., *J. Phys. Chem. A* **2009**, *113*, 6239.

72. Groenewold, G. S.; Gianotto, A. K.; Cossel, K. C.; Van Stipdonk, M. J.; Oomens, J.; Polfer, N.; Moore, D. T.; de Jong, W. A.; McIlwain, M. E., *Phys. Chem. Chem. Phys.* **2007**, *9*, 596.
73. Cordero, B.; Gomez, V.; Platero-Prats, A. E.; Reves, M.; Echeverria, J.; Cremades, E.; Barragan, F.; Alvarez, S., *Dalton T.* **2008**, 2832.
74. Yanai, T.; Tew, D. P.; Handy, N. C., *Chem. Phys. Lett.* **2004**, *393*, 51.
75. Grimme, S.; Antony, J.; Ehrlich, S.; Krieg, H., *J. Chem. Phys.* **2010**, *132*.
76. Bridgeman, A. J.; Cavigliasso, G.; Ireland, L. R.; Rothery, J., *J. Chem. Soc. Dalton* **2001**, 2095.
77. Wang, X. F.; Andrews, L.; Li, J., *Inorg. Chem.* **2006**, *45*, 4157.
78. Bridgeman, A. J.; Cavigliasso, G., *Faraday Discuss.* **2003**, *124*, 239.
79. Berard, J. J.; Schreckenbach, G.; Arnold, P. L.; Patel, D.; Love, J. B., *Inorg. Chem.* **2008**, *47*, 11583.
80. Arnold, P. L.; Jones, G. M.; Odoh, S. O.; Schreckenbach, G.; Magnani, N.; Love, J. B., *Nature Chem.* **2011**, *4*, 221

## Chapter 10: Summary and Future Studies of Actinide Complexes

### 10.1 Summary

The studies presented in this thesis have provided a great amount of information regarding the use and performance of computational techniques for studying actinide complexes. The performance of modern DFT and relativistic ECPs were benchmarked with an aim of determining the degrees of accuracy that could be expected when they are used for calculations on actinide systems. These approaches were then used in studying the speciation and properties of actinyl hydroxides in solution (Chapter 4), monomeric uranium peroxides in solution (Chapter 5), uranium fluorides in the gas and aqueous phases as well as in a cell-wall protein (Chapter 7), reduction of U(V) complexes on geochemical surfaces such as rutile and anatase (Chapter 6), novel and highly stable pentavalent uranium complexes formed by reductive oxo-functionalization of axial oxo atoms in a bimetallic bis-uranium dioxo motif (Chapter 8) and lastly the structure and properties of a novel homobimetallic U(VI) hydroxide complexes in the gas-phase (Chapter 9).

The linkages between these works revolve around the role and existence of actinide species in the environment. Based on the studies compiled in this thesis, we can make a general statement like this: *Some components of highly radioactive nuclear waste decompose by emission of  $\alpha$ -particles. This induces the  $\alpha$ -hydrolysis of water giving hydrogen peroxide. It is important to study monomeric uranyl peroxide complexes, Chapter 5, as they are the building blocks of crystalline polynuclear species characterized by Burns et al.<sup>1-7</sup> They might be of great importance at low  $H_2O_2$  concentrations, confirmed by the existence of only thin peroxide films on depleted uranium rods.<sup>8-11</sup> The nuclear waste tanks at most repositories as well as ground water*

usually have modest to high pH values. At these pH ranges, complexation with hydroxide and carbonate ligands becomes important due to the strengths with which these ligands bind the actinyl moiety.<sup>12-13</sup> The speciation of plutonyl hydroxide complexes at modest to high pH values has been found to be different from that of its uranyl counterpart.<sup>14-16</sup> The origins of this difference have been probed using DFT calculations in Chapter 4. It is indubitable that during migration in underground soils, radionuclides will be in contact with air, water and biota<sup>17-20</sup>. A good understanding of the differences in the electronic and structural properties of uranium complexes in the gas and aqueous phases needs to be complemented with studies on their interactions with the cell-walls of microorganisms. To this end we have studied the encapsulation of uranyl fluorides in the tetrabrachion protein found in the cell wall of archaeobacterium *Staphylothermus marinus*, Chapter 7. Due to the high solubility of U(VI) complexes, two approaches can be taken to ensure slower migration in underground waters. The first approach involves adsorption onto the cell walls of microorganisms<sup>17-20</sup> or onto geochemical surfaces.<sup>21-24</sup> The use of titania as a possible sorbent or getter for extracting waste radionuclides from soil was explored. We studied the structural and electronic properties of uranyl complexes adsorbed on periodic and molecular rutile and anatase clusters, Chapter 6. The second approach involves reduction of the U(VI) complexes to the less soluble U(IV) complexes. The role of titania surface defects on the U(VI)-U(IV) reduction process was also explored in Chapter 6. It needs to be however kept in mind that the intermediate U(V) complexes were until recently difficult to isolate and characterize as they disproportionate to the +6 and +4 oxidation states. The synthesis and characterization of new U(V) complexes, might provide a better understanding of approaches to induce oxidation state and solubility changes at nuclear waste sites. Oxo-functionalization of the axial oxo atoms of the uranyl moiety has been shown to

be a feasible route to stable U(V) complexes.<sup>25-35</sup> We have characterized two classes of U(V) dimer complexes in Chapter 8. The first was formed by oxo-silylation of two axial oxo atoms resulting in a butterfly shaped dimer while the second class of U(V) dimer complexes have a di-CCI structure with two axial oxo atoms functionalized by transition metals. The dioxo-uranium species in these stable U(V) dimers interact with each other via oxo cation-cation linkages (cation-cation interactions, CCIs). The existence of these type of interactions in U(V) complexes is understandable given the increased Lewis basicities of the axial oxo atoms upon U(VI)-U(V) reduction.<sup>36</sup> These types of interactions are however rare for U(VI) complexes, with the exception of  $UO_3$  and  $UO_3 \cdot nH_2O$  crystals.<sup>32</sup> In Chapter 9, we performed a comprehensive examination of dimeric uranyl hydroxide species and found that the lowest energy structures of  $[(UO_2)_2(OH)_5]^+$  possess CCIs.

Overall, the work in this dissertation has provided further confirmation of the rich chemistry of actinide species in the gaseous, aqueous and solid phases. The use of relativistic DFT calculations is found to be suitable for examining actinide chemistry in various environmental phases. Relativistic DFT calculations are suitable for examining the structure and properties of actinide species in their ground electronic states. This applies to small systems like  $UO_3$  (Chapter 1) or bulky systems like the Pacman complexes (Chapter 8) or the solid surface (Chapter 6). When coupled with implicit solvation models, DFT is a powerful tool for examining the properties of actinide species in solution and for making in-silico predictions regarding their speciation.

## 10.2. Future studies of actinide complexes specific to this thesis

The following are possible directions for continuing the computational work on actinide complexes studied in this thesis:

**Chapter 2-** The performance of the B3LYP, PBE0 and PBE functionals for calculating the structural properties and reaction energies of actinide complexes have been extensively examined. In this chapter, we examined the degree of accuracy that could be expected when these functionals are combined with either relativistic pseudopotentials or all-electron basis sets. There has however been considerable progress in the development of new density functionals over the last 3-4 years. The meta-GGA, meta-hybrid and dispersion-corrected functionals are examples of these new functionals.<sup>37-39</sup> It is however unknown how well these functionals predict the structure and reaction energies of actinide complexes. Recent indications by several authors, studying isolated reactions,<sup>40-41</sup> seem to suggest that the M06 functional might be particularly well suited for studying actinide complexes.<sup>42-45</sup> To this effect, a full examination of the performance of these and other new functionals is desirable.

**Chapters 3 and 4-** Theoretical studies of the structural and electronic properties of plutonyl (VI) complexes is complicated not in the least by energy convergence problems but also by the fact that Kohn-Sham DFT is not particularly suited to studying open-shell multi-reference systems. Although we have had some success in predicting the structure of plutonyl (VI) and plutonium (IV) complexes, Chapter 3, as well the speciation and formation of plutonyl hydroxides, Chapter 4, using DFT, the next line of attack involves a study of the spectroscopy of these complexes. A computational regimen based on DFT prediction of structure/energetics and prediction of electronic spectra using some multi-reference approach (examples included complete active space approaches (CASSCF and CASPT2) and various configuration interaction schemes) would

provide a direct counterpart to experimental plutonium chemists. The use of multi-reference approaches in studying the spectra of actinide complexes is at the moment limited to small actinyl species.<sup>46-47</sup>

**Chapter 5-** The motivation behind our study of the monomeric uranyl peroxo complexes was the recent synthesis and characterization of the uranyl peroxo dicarbonate complex by Goff et al.<sup>48</sup> It should however be noted that regarding uranyl peroxo species, our study represents one extreme, while most studies have focused on the other extreme, the multinuclear crystalline peroxo species. The mechanism by which the polynuclear crystals are formed from the monomeric species is currently not fully understood. Insights into the agglomeration of uranyl peroxo groups might be very important in the migration of nuclear waste in underground alkaline soils and in soils with high carbonate contents.<sup>3,7</sup>

**Chapter 8-** The characterization of the stable U(V)/U(V) binuclear complexes in this chapter is very interesting as a result of the novel structural motifs (butterfly or di-CCI shaped  $U_2O_4$  cores) as well as a result of the roles these complexes could possibly play in the retardation of U(VI) complexes in natural ecosystems.<sup>25, 27</sup> Currently, however, we are very much interested in determining the degree of interaction between the two uranium centers in the  $U_2O_4$  structures. A computational study of the various  $U_2O_4$  motifs and involving U(VI), U(V) and oxo-functionalized U(V) centers is in order. The atoms in molecules approach of Bader would be particularly suited for such a study.<sup>49</sup> Such a study also has general applicability to actinyl complexes containing CCIs.

**Chapter 9-** In this chapter, the results of our DFT calculations showed that the lowest energy structures of the U(VI)/U(VI) complex,  $[(UO_2)_2(OH)_5]^+$ , possess CCIs. As stated previously, this

complex was identified in mass-spectrometric studies of the gases formed after laser ablation of a slab of  $\text{UO}_3$  in a vacuum chamber with trace amounts of water and oxygen. The step by step reaction pathway leading to the formation of this complex from gaseous  $\text{UO}_3$  remains unknown. The mechanisms through which this particular complex decomposes to smaller uranyl hydroxides or through which it agglomerates to higher hydroxides such as  $[(\text{UO}_2)_3(\text{OH})_7]^-$ , remains unknown. Theoretical exploration of the hydration of  $\text{UO}_3$ , the kinetics of  $\text{UO}_3$  hydrolysis and the thermochemistry of the agglomeration of the monomeric and dimeric complexes are in order.

### 10.3. General directions for computational studies of actinide complexes

The field of computational actinide chemistry continues to expand. The amount of time that can be (reasonably) spent in a doctoral program is however limited. The following are the general directions towards which computational actinide chemistry appears to be going:

**1) Increased focus on molecular dynamics simulations:** At the current stage in computational chemistry, static calculations based on the DFT, MP2, HF, CC or CI approaches can be performed with varying degrees of ease and accuracy. The modeling of macromolecular or nanoscale behavior however remains somewhat of a challenge even though the basic principles and methods of molecular dynamics and mechanics have been established for more than 50 years. The speciation, structure, hydrolysis and spectra of actinide and actinyl ions in solvent boxes of water as well as at water-solid interfaces would benefit from hybrid methods combining molecular dynamics and quantum mechanical calculations. There have been several recent studies of actinide species using these approaches.<sup>50-54</sup>

**2) Actinide Bonding:** The extent to which the various valence and semi-core actinide orbitals participate in actinide-ligand bonding still remains of significant interest to computational chemists. In addition, while the bonding schemes within actinyl groups are well understood,<sup>55-57</sup> the role of electrostatic and covalent contributions to the bonding between actinyl groups and equatorial groups is still not completely understood. Orbital decomposition schemes such as the natural bond orbitals approach and the natural orbitals for chemical valence (NOCV) theory of Ziegler et al.<sup>58-59</sup> and the localized orbital bonding analysis of Head-Gordon et al.<sup>60</sup> are particularly suited for studying the bonding between equatorial ligands and actinide centers.

## References

1. Armstrong, C. R.; Nyman, M.; Shvareva, T.; Sigmon, G. E.; Burns, P. C.; Navrotsky, A., *P. Natl. Acad. Sci. USA* **2012**, *109* (6), 1874-1877.
2. Kubatko, K. A.; Forbes, T. Z.; Klingensmith, A. L.; Burns, P. C., *Inorg. Chem.* **2007**, *46* (9), 3657-3662.
3. Ling, J.; Wallace, C. M.; Szymanowski, J. E. S.; Burns, P. C., *Angew. Chem. Int. Ed.* **2010**, *49* (40), 7271-7273.
4. Sigmon, G. E.; Ling, J.; Unruh, D. K.; Moore-Shay, L.; Ward, M.; Weaver, B.; Burns, P. C., *J. Am. Chem. Soc.* **2009**, *131* (46), 16648-16649.
5. Sigmon, G. E.; Weaver, B.; Kubatko, K. A.; Burns, P. C., *Inorg. Chem.* **2009**, *48* (23), 10907-10909.
6. Unruh, D. K.; Burtner, A.; Pressprich, L.; Sigmon, G. E.; Burns, P. C., *Dalton T.* **2010**, *39* (25), 5807-5813.
7. Vlaisavljevich, B.; Gagliardi, L.; Burns, P. C., *J. Am. Chem. Soc.* **2010**, *132* (41), 14503-14508.

8. Amme, M.; Svedkauskaite, J.; Bors, W.; Murray, M.; Merino, J., *Radiochim. Acta* **2007**, 95 (12), 683-692.
9. Corbel, C.; Sattonnay, G.; Guilbert, S.; Garrido, F.; Barthe, M. F.; Jegou, C., *J. Nucl. Mater.* **2006**, 348 (1-2), 1-17.
10. Hanson, B.; McNamara, B.; Buck, E.; Friese, J.; Jenson, E.; Krupka, K.; Arey, B., *Radiochim. Acta* **2005**, 93 (3), 159-168.
11. Sunder, S.; Miller, N. H.; Shoesmith, D. W., *Corros. Sci.* **2004**, 46 (5), 1095-1111.
12. Clark, D. L.; Conradson, S. D.; Donohoe, R. J.; Keogh, D. W.; Morris, D. E.; Palmer, P. D.; Rogers, R. D.; Tait, C. D., *Inorg. Chem.* **1999**, 38 (7), 1456-1466.
13. Kaplan, D. I.; Gervais, T. L.; Krupka, K. M., *Radiochim. Acta* **1998**, 80 (4), 201-211.
14. Rao, L. F.; Tian, G. X.; Di Bernardo, P.; Zanonato, P., *Chem-Eur. J.* **2011**, 17 (39), 10985-10993.
15. Reilly, S. D.; Neu, M. P., *Inorg. Chem.* **2006**, 45 (4), 1839-1846.
16. Zanonato, P.; Di Bernardo, P.; Bismondo, A.; Liu, G. K.; Chen, X. Y.; Rao, L. F., *J. Am. Chem. Soc.* **2004**, 126 (17), 5515-5522.
17. Anderson, R. T.; Vrionis, H. A.; Ortiz-Bernad, I.; Resch, C. T.; Long, P. E.; Dayvault, R.; Karp, K.; Marutzky, S.; Metzler, D. R.; Peacock, A.; White, D. C.; Lowe, M.; Lovley, D. R., *Appl. Environ. Microb.* **2003**, 69 (10), 5884-5891.
18. Caccavo, F.; Lonergan, D. J.; Lovley, D. R.; Davis, M.; Stolz, J. F.; McInerney, M. J., *Appl. Environ. Microb.* **1994**, 60 (10), 3752-3759.
19. Lovley, D. R., *Annu. Rev. Microbiol.* **1993**, 47, 263-290.
20. Lovley, D. R.; Phillips, E. J. P., *Appl. Environ. Microb.* **1992**, 58 (3), 850-856.

21. Fredrickson, J. K.; Zachara, J. M.; Kennedy, D. W.; Duff, M. C.; Gorby, Y. A.; Li, S. M. W.; Krupka, K. M., *Geochim. Cosmochim. Acta* **2000**, *64* (18), 3085-3098.
22. Liger, E.; Charlet, L.; Van Cappellen, P., *Geochim. Cosmochim. Acta* **1999**, *63* (19-20), 2939-2955.
23. Liu, C. X.; Gorby, Y. A.; Zachara, J. M.; Fredrickson, J. K.; Brown, C. F., *Biotechnol. Bioeng.* **2002**, *80* (6), 637-649.
24. O'Loughlin, E. J.; Kelly, S. D.; Cook, R. E.; Csencsits, R.; Kemner, K. M., *Environ. Sci. Technol.* **2003**, *37* (4), 721-727.
25. Arnold, P. L.; Holis, E.; Love, J. B.; Magnani, N.; Colineau, E.; Caciuffo, R.; Edelstein, N.; Maron, L.; Castro, L.; Yahia, A.; O., O. S.; G., S., **2012**.
26. Arnold, P. L.; Hollis, E.; White, F. J.; Magnani, N.; Caciuffo, R.; Love, J. B., *Angew. Chem. Int. Ed.* **2011**, *50* (4), 887-890.
27. Arnold, P. L.; Jones, G. M.; Odoh, S. O.; Schreckenbach, G.; Magnani, N.; Love, J. B., *Nature Chem.* **2012**, *4* (3), 221-227.
28. Arnold, P. L.; Love, J. B.; Patel, D., *Coordin. Chem. Rev.* **2009**, *253* (15-16), 1973-1978.
29. Arnold, P. L.; Patel, D.; Blake, A. J.; Wilson, C.; Love, J. B., *J. Am. Chem. Soc.* **2006**, *128* (30), 9610-9611.
30. Arnold, P. L.; Patel, D.; Wilson, C.; Love, J. B., *Nature* **2008**, *451* (7176), 315-U3.
31. Arnold, P. L.; Pecharman, A. F.; Love, J. B., *Angew. Chem. Int. Edit.* **2011**, *50* (40), 9456-9458.
32. Fortier, S.; Hayton, T. W., *Coordin. Chem. Rev.* **2010**, *254* (3-4), 197-214.
33. Graves, C. R.; Kiplinger, J. L., *Chem. Commun.* **2009**, (26), 3831-3853.
34. Hayton, T. W.; Wu, G., *Inorg. Chem.* **2009**, *48* (7), 3065-3072.

35. Schnaars, D. D.; Wu, G.; Hayton, T. W., *J. Am. Chem. Soc.* **2009**, *131* (48), 17532-17533.
36. Wang, X. F.; Andrews, L.; Vlasisavljevich, B.; Gagliardi, L., *Inorg. Chem.* **2011**, *50* (8), 3826-3831.
37. Baer, R.; Livshits, E.; Salzner, U., Tuned Range-Separated Hybrids in Density Functional Theory. In *Annual Review of Physical Chemistry, Vol 61*, Leone, S. R.; Cremer, P. S.; Groves, J. T.; Johnson, M. A.; Richmond, G., Eds. 2010; Vol. 61, pp 85-109.
38. Cohen, A. J.; Mori-Sanchez, P.; Yang, W. T., *Chem. Rev.* **2012**, *112* (1), 289-320.
39. Grimme, S., *Wiley Interdisciplinary Reviews-Computational Molecular Science* **2011**, *1* (2), 211-228.
40. Austin, J. P.; Burton, N. A.; Hillier, I. H.; Sundararajan, M.; Vincent, M. A., *Phys. Chem. Chem. Phys.* **2009**, *11* (8), 1143-1145.
41. Averkiev, B. B.; Mantina, M.; Valero, R.; Infante, I.; Kovacs, A.; Truhlar, D. G.; Gagliardi, L., *Theor. Chem. Acc.* **2011**, *129* (3-5), 657-666.
42. Zhao, Y.; Schultz, N. E.; Truhlar, D. G., *J. Chem. Theory Comput.* **2006**, *2* (2), 364-382.
43. Zhao, Y.; Truhlar, D. G., *Acc. Chem. Res.* **2008**, *41* (2), 157-167.
44. Zhao, Y.; Truhlar, D. G., *Theor. Chem. Acc.* **2008**, *120* (1-3), 215-241.
45. Zhao, Y.; Truhlar, D. G., *Chem. Phys. Lett.* **2011**, *502* (1-3), 1-13.
46. Infante, I.; Eliav, E.; Vilkas, M. J.; Ishikawa, Y.; Kaldor, U.; Visscher, L., *J. Chem. Phys.* **2007**, *127* (12).
47. Seijo, L.; Barandiaran, Z., *J. Chem. Phys.* **2003**, *118* (12), 5335-5346.
48. Goff, G. S.; Brodnax, L. F.; Cisneros, M. R.; Peper, S. M.; Field, S. E.; Scoft, B. L.; Runde, W. H., *Inorg. Chem.* **2008**, *47* (6), 1984-1990.

49. Bader, R. F. W., *Chem. Rev.* **1991**, *91* (5), 893-928.
50. Atta-Fynn, R.; Bylaska, E. J.; Schenter, G. K.; de Jong, W. A., *J. Phys. Chem. A* **2011**, *115* (18), 4665-4677.
51. Atta-Fynn, R.; Johnson, D. F.; Bylaska, E. J.; Ilton, E. S.; Schenter, G. K.; de Jong, W. A., *Inorg. Chem.* **2012**, *51* (5), 3016-3024.
52. Bühl, M.; Sieffert, N.; Chaumont, A.; Wipff, G., *Inorg. Chem.* **2012**, *51* (3), 1943-1952.
53. Duvail, M.; Martelli, F.; Vitorge, P.; Spezia, R., *J. Chem. Phys.* **2011**, *135* (4).
54. Spezia, R.; Beuchat, C.; Vuilleumier, R.; D'Angelo, P.; Gagliardi, L., *J. Phys. Chem. B* **2012**, *116* (22), 6465-6475.
55. Denning, R. G., *Struct. Bond.* **1992**, *79*, 215-276.
56. Denning, R. G., *J. Phys. Chem. A* **2007**, *111* (20), 4125-4143.
57. Denning, R. G.; Green, J. C.; Hutchings, T. E.; Dallera, C.; Tagliaferri, A.; Giarda, K.; Brookes, N. B.; Braicovich, L., *J. Chem. Phys.* **2002**, *117* (17), 8008-8020.
58. Michalak, A.; Mitoraj, M.; Ziegler, T., *J. Phys. Chem. A* **2008**, *112* (9), 1933-1939.
59. Mitoraj, M. P.; Michalak, A.; Ziegler, T., *J. Chem. Theory Comput.* **2009**, *5* (4), 962-975.
60. Thom, A. J. W.; Sundstrom, E. J.; Head-Gordon, M., *Phys. Chem. Chem. Phys.* **2009**, *11* (47), 11297-11304.

## List of Publications

1. P. L. Arnold, E. Holis, J. B. Love, N. Magnani, E. Colineau, R. Caciuffo, N. Edelstein, L. Castro, A. Yahia, L. Maron, **S. O. Odoh** and G. Schreckenbach. Oxo-Functionalization and Reduction of the Uranyl Ion through Lanthanide-Element Bond Homolysis; Synthetic, Structural, and Bonding Analysis of a Series of Singly Reduced Uranyl - Rare Earth  $5f^1$ - $4f^n$  Complexes. *To be submitted*, 2012.
2. **S. O. Odoh**, G. Schreckenbach and W. B. de Jong. Gas phase structure of dimeric uranyl hydroxides,  $(\text{UO}_2)_2(\text{OH})_5^-$ . *To be submitted*, 2012.
3. Y.-R. Guo, Q. Wu, **S. O. Odoh**, G. Schreckenbach and Q. Pan. Substituent tuning of the structural, spectroscopic and reaction properties of trans-bis(imido) uranium complexes: A relativistic density functional study. *To be submitted*, 2012.
4. **S. O. Odoh** and G. Schreckenbach. Energy and density analysis of axial and equatorial bonding in uranyl complexes. *To be submitted*, 2012.
5. **S. O. Odoh** and G. Schreckenbach. DFT study of oxo-functionalized dioxo-uranium pentavalent complexes (structure, bonding, ligand exchange, dimerization and U(V)/U(IV) reduction of  $\text{OUOH}$  and  $\text{OUOSiH}_3$  complexes). *Inorganic Chemistry* (ic-2012-01762g), *submitted August 10th 2012*.
6. **S. O. Odoh** and G. Schreckenbach. DFT Study of Uranyl Peroxo Complexes with  $\text{H}_2\text{O}$ ,  $\text{F}^-$ ,  $\text{OH}^-$ ,  $\text{CO}_3^{2-}$  and  $\text{NO}_3^-$ . *Inorganic Chemistry*, *submitted June 29th 2012*.
7. **S. O. Odoh**, J. A. Reyes and G. Schreckenbach. Theoretical Study of the Structural and Electronic Properties of Plutonyl Hydroxides. *Inorganic Chemistry*, *submitted May 17th 2012*.

8. Q. Pan, **S. O. Odoh**, G. Schreckenbach, P. L. Arnold, and J. B. Love. Theoretical exploration of uranyl complexes with a designed polypyrrolic macrocycle: Effects of hinge size in the Pacman-like complexes on their structures and properties. *Dalton Transactions*, **2012**, 41, 8878-8885.
9. **S. O. Odoh**, Q. Pan, G. A. Shamov, F. Wang, M. Fayek and G. Schreckenbach. Theoretical study of the reduction of uranium (VI) aquo-complexes on titania particles and by alcohols. *Chemistry: A European Journal*, **2012**, 18, 7117-7127.
10. P. L. Arnold, G. M. Jones, **S. O. Odoh**, G. Schreckenbach, N. Magnani and J. B. Love. Strongly coupled binuclear uranium-oxo complexes from uranyl oxo-rearrangement and reductive silylation. *Nature Chemistry*, **2012**, 4, 221-227.
11. Q. Pan, **S. O. Odoh**, A. M. Asaduzzaman and G. Schreckenbach. Adsorption of uranyl species onto the rutile (110) Surface: A periodic density functional theory study. *Chemistry: A European Journal*, **2012**, 18, 1458-1466.
12. **S. O. Odoh** and G. Schreckenbach. Theoretical study of the structural properties of Pu(IV) and Pu(VI) Complexes. *Journal of Physical Chemistry A*, **2011**, 115, 14110-14119.
13. Q. Pan, Y. Guo, L. Li, **S. O. Odoh**, H. Fu and H. Zhang. Structures, spectroscopic properties and redox potentials of quaterpyridyl Ru(II) photosensitizer and its derivatives for solar energy cell: A density functional theory study. *Phys. Chem. Chem. Phys.*, **2011**, 32, 14481-14489.
14. **S. O. Odoh**, S. Walker, M. Meier, J. Stetefeld and G. Schreckenbach. QM and QM/MM study of uranyl fluorides in the gas phase, aqueous phase and in the hydrophobic cavities of tetrabrachion. *Inorganic Chemistry*, **2011**, 50, 3141-3152.

15. **S. O. Odoh** and G. Schreckenbach. Performance of relativistic effective core potentials in DFT calculations on actinide compounds. *Journal of Physical Chemistry A*, **2010**, 114, 1957-1963.
16. J. J. Neville, N. P. Appathurai, Y. Fan, **S. Odoh** and L. Yang. F 1s spectroscopy and ionic fragmentation of trifluoropropyne. *Canadian Journal of Chemistry*, **2008**, 86, 761-768.